frontiers | Research Topics

Advanced biomaterials for hard tissue repair and regeneration

Edited by
Hongye Yang, Jian Yu, Dandan Pei and Wenjie Zhang

Published in
Frontiers in Bioengineering and Biotechnology

ISSN 1664-8714
ISBN 978-2-8325-5534-7
DOI 10.3389/978-2-8325-5534-7

About Frontiers

Frontiers is more than just an open access publisher of scholarly articles: it is a pioneering approach to the world of academia, radically improving the way scholarly research is managed. The grand vision of Frontiers is a world where all people have an equal opportunity to seek, share and generate knowledge. Frontiers provides immediate and permanent online open access to all its publications, but this alone is not enough to realize our grand goals.

Frontiers journal series

The Frontiers journal series is a multi-tier and interdisciplinary set of open-access, online journals, promising a paradigm shift from the current review, selection and dissemination processes in academic publishing. All Frontiers journals are driven by researchers for researchers; therefore, they constitute a service to the scholarly community. At the same time, the *Frontiers journal series* operates on a revolutionary invention, the tiered publishing system, initially addressing specific communities of scholars, and gradually climbing up to broader public understanding, thus serving the interests of the lay society, too.

Dedication to quality

Each Frontiers article is a landmark of the highest quality, thanks to genuinely collaborative interactions between authors and review editors, who include some of the world's best academicians. Research must be certified by peers before entering a stream of knowledge that may eventually reach the public - and shape society; therefore, Frontiers only applies the most rigorous and unbiased reviews. Frontiers revolutionizes research publishing by freely delivering the most outstanding research, evaluated with no bias from both the academic and social point of view. By applying the most advanced information technologies, Frontiers is catapulting scholarly publishing into a new generation.

What are Frontiers Research Topics?

Frontiers Research Topics are very popular trademarks of the *Frontiers journals series*: they are collections of at least ten articles, all centered on a particular subject. With their unique mix of varied contributions from Original Research to Review Articles, Frontiers Research Topics unify the most influential researchers, the latest key findings and historical advances in a hot research area.

Find out more on how to host your own Frontiers Research Topic or contribute to one as an author by contacting the Frontiers editorial office: frontiersin.org/about/contact

Advanced biomaterials for hard tissue repair and regeneration

Topic editors
Hongye Yang — Wuhan University, China
Jian Yu — University of British Columbia, Canada
Dandan Pei — Xi'an Jiaotong University, China
Wenjie Zhang — Shanghai Jiao Tong University, China

Citation
Yang, H., Yu, J., Pei, D., Zhang, W., eds. (2024). *Advanced biomaterials for hard tissue repair and regeneration*. Lausanne: Frontiers Media SA.
doi: 10.3389/978-2-8325-5534-7

Table of contents

05 Editorial: Advanced biomaterials for hard tissue repair and regeneration
Hongye Yang, Dandan Pei, Wenjie Zhang and Jian Yu

08 Dual effectiveness of a novel all-in-one endodontic irrigating solution in antibiofilm activity and smear layer removal
Xuyan Sheng, Jian Yu, He Liu, Zhejun Wang, Shuli Deng and Ya Shen

18 Advances in materials used for minimally invasive treatment of vertebral compression fractures
Pengfei Sui, Tong Yu, Shouye Sun, Bo Chao, Cheng Qin, Jingwei Wang, Erwei Wang and Changjun Zheng

38 Recent advances of responsive scaffolds in bone tissue engineering
Tongyu Zhu, Hongbo Zhou, Xiaojing Chen and Yuanjing Zhu

52 Effects of background color and restoration depth on color adjustment potential of a new single-shade resin composite versus multi-shade resin composites
Jiakang Zhu, Siyang Chen, Annikaer Anniwaer, Yue Xu and Cui Huang

62 Enhancing dentin bonding quality through Acetone wet-bonding technique: a promising approach
Shikai Zhao, Zhiyi Zhu, Jian Yu, Chenmin Yao, Miaoyang Yu, Hongye Yang and Cui Huang

73 Bioceramic micro-fillers reinforce antibiofilm and remineralization properties of clear aligner attachment materials
Wenhui Jiang, Zhejun Wang, Yinghong Zhou, Ya Shen, Edwin Yen and Bingshuang Zou

84 Mineral coated microparticles doped with fluoride and complexed with mRNA prolong transfection in fracture healing
Anna Laura Nelson, Gianluca Fontana, Laura Chubb, Josh Choe, Katherine Williams, Dan Regan, Johnny Huard, William Murphy, Nicole Ehrhart and Chelsea Bahney

97 Antibiofilm peptides enhance the corrosion resistance of titanium in the presence of *Streptococcus mutans*
Dan Wang, Yingying Yue, He Liu, Tian Zhang, Evan F. Haney, Robert E. W. Hancock, Jian Yu and Ya Shen

109 Establishment of a mandible defect model in rabbits infected with multiple bacteria and bioinformatics analysis
Yuan Zhao, Jun Su, Chong-yan Xu, Yan-bo Li, Tong Hu, Yi Li, Li Yang, Qiang Zhao and Wen-yun Zhang

125 Small organic molecules containing amorphous calcium phosphate: synthesis, characterization and transformation
Abhishek Indurkar, Pawan Kudale, Vitālijs Rjabovs, Ivo Heinmaa, Öznur Demir, Matvejs Kirejevs, Kristaps Rubenis, Ganesh Chaturbhuj, Māris Turks and Janis Locs

139 The possibility of clinical bonding between metal/ceramic brackets to zirconia: *in vitro* study
Yichun Hu, Jiayang Gao, Xinyue Huang, Yutong Li, Ziyi Chen, Desong Zhan, Hidehiko Sano, Ricardo M. Carvalho and Jiale Fu

151 Corrigendum: The possibility of clinical bonding between metal/ceramic brackets to zirconia: *in vitro* study
Yichun Hu, Jiayang Gao, Xinyue Huang, Yutong Li, Ziyi Chen, Desong Zhan, Hidehiko Sano, Ricardo M. Carvalho and Jiale Fu

153 Evaluate the effects of low-intensity pulsed ultrasound on dental implant osseointegration under type II diabetes
Yingying Wang, Ximeng Cao, Yingyi Shen, Qi Zhong, Ziang Wu, Yaqin Wu, Weimin Weng and Chun Xu

163 Enhancing the inhibition of dental erosion and abrasion with quercetin-encapsulated hollow mesoporous silica nanocomposites
Jia-Min Chen, Yi-Ling Cheng, Meng-Hui Yang, Chen Su and Hao Yu

175 Evaluation of osteogenic properties of a novel injectable bone-repair material containing strontium *in vitro* and *in vivo*
Lishuang Liu, Sha Hou, Guangya Xu, Jingjing Gao, Junyu Mu, Min Gao, Jianrong He, Xiaoyu Su, Zheng Yang, Yi Liu, Tengzhuo Chen, Zhihong Dong, Lijia Cheng and Zheng Shi

188 Enhancing osteogenesis and angiogenesis functions for Ti-24Nb-4Zr-8Sn scaffolds with methacrylated gelatin and deferoxamine
Qian Xu, Yun Bai, Shujun Li, Wentao Hou, Yulin Hao, Rui Yang, Xiaowu Li and Xing Zhang

199 A submicron forest-like silicon surface promotes bone regeneration by regulating macrophage polarization
Guo Sun, Tianyu Shu, Shaoyang Ma, Meng Li, Zhiguo Qu and Ang Li

211 Emerging roles of hydrogel in promoting periodontal tissue regeneration and repairing bone defect
Wendi Guo, Hongbin Dong and Xing Wang

224 The treatment efficacy of bone tissue engineering strategy for repairing segmental bone defects under diabetic condition
Xiangsheng Wang, Can Xiang, Chunhua Huang, Hanxiao Cheng, Zhentao Zhou, Jufang Zhang and Hui Xie

233 Theaflavin –3,3′-digallate/ethanol: a novel cross-linker for stabilizing dentin collagen
Zhiyong Chen, Yingxian Wei, Likun Liang, Xu Wang, Fangfei Peng, Yiying Liang, Xin Huang, Kaiqi Yan, Yunxia Gao, Kangjing Li, Xiaoman Huang, Xinglu Jiang and Wenxia Chen

248 The effects of antimicrobial peptides buCaTHL4B and Im-4 on infectious root canal biofilms
Ziqiu Hu, Haixia Ren, Yifan Min, Yixin Li, Yuyuan Zhang, Min Mao, Weidong Leng and Lingyun Xia

frontiers | Frontiers in Bioengineering and Biotechnology

TYPE Editorial
PUBLISHED 25 September 2024
DOI 10.3389/fbioe.2024.1476088

OPEN ACCESS

EDITED AND REVIEWED BY
Yunbing Wang,
Sichuan University, China

*CORRESPONDENCE
Hongye Yang,
yang_hongye@126.com
Dandan Pei,
peidandan@xjtu.edu.cn
Wenjie Zhang,
zhangwenjie586@126.com
Jian Yu,
yujiandoctor@whu.edu.cn

RECEIVED 05 August 2024
ACCEPTED 17 September 2024
PUBLISHED 25 September 2024

CITATION
Yang H, Pei D, Zhang W and Yu J (2024) Editorial: Advanced biomaterials for hard tissue repair and regeneration.
Front. Bioeng. Biotechnol. 12:1476088.
doi: 10.3389/fbioe.2024.1476088

Editorial: Advanced biomaterials for hard tissue repair and regeneration

Hongye Yang[1]*, Dandan Pei[2]*, Wenjie Zhang[3]* and Jian Yu[1,4]*

[1]State Key Laboratory of Oral and Maxillofacial Reconstruction and Regeneration, Key Laboratory of Oral Biomedicine Ministry of Education, Hubei Key Laboratory of Stomatology, School and Hospital of Stomatology, Wuhan University, Wuhan, China, [2]Key Laboratory of Shaanxi Province for Craniofacial Precision Medicine Research, College of Stomatology, Xi'an Jiaotong University, Xi'an, China, [3]College of Stomatology, Shanghai Jiao Tong University, National Center for Stomatology, National Clinical Research Center for Oral Diseases, Shanghai Key Laboratory of Stomatology, Shanghai Engineering Research Center of Advanced Dental Technology and Materials, Shanghai, China, [4]Division of Endodontics, Department of Oral Biological and Medical Sciences, Faculty of Dentistry, University of British Columbia, Vancouver, Canada

KEYWORDS

bone, tooth, hard tissue, repair, regeneration, tissue engineering

Editorial on the Research Topic
Advanced biomaterials for hard tissue repair and regeneration

Bone and tooth are typical hard tissues in vertebrates. Due to hierarchical structural characteristics and excellent mechanical properties, hard tissues play important roles for human body, such as health protection, movement support, and food mastication. Once hard tissue defect occurs, our living quality will be seriously affected. In general, hard tissues lack the ability of self-repair, except for the regeneration ability of bone for small-scale defects. As a result, the past few decades have witnessed great progress in the field of biomaterials for hard tissue repair. Actually, both bone and tooth are masterpieces of biomineralization in nature, the repair and regeneration of hard tissues should be performed in a biomimetic way. Therefore, this Research Topic provides a comprehensive overview of the current state of the art regarding advanced biomaterials used to repair or regenerate damaged hard tissues, as well as to highlight the most promising advanced strategies other than suggest the future direction in the field. In the present Research Topic, 154 authors from all over the world decided to publish their outstanding and promising results.

1. For bone regeneration, biomaterials should serve as desirable scaffolds not only to offer a microenvironment closer to *in vivo* conditions, but also to exhibit excellent bioactivity, biocompatibility, and osteogenic properties. Combined with cell seeding and bioactive molecule functionalization, a faster repair rate and better regeneration quality in bone defects would be expected.

In particular, Zhu et al. present a comprehensive review of recent developments in responsive scaffolds, thereby contributing novel insights to the field of bone defect repair.

Nelson et al. tested the efficacy of mineral coated microparticles (MCM) and fluoride-doped MCM (FMCM) to effectively deliver firefly luciferase (FLuc) mRNA lipoplexes (LPX) to the fracture site, and found that FMCM-LPX-FLuc could serve as a promising mRNA delivery platform for fracture healing applications.

Sui et al. described the advances in materials used for minimally invasive treatment of vertebral compression fractures and enumerated the types of bone cement commonly used in current practice. They also discussed the limitations of the materials themselves, and summarized the approaches for improving the characteristics of bone cement.

Zhao et al. established a model of chronic infectious mandibular defect (IMD) by mixed infection with *Staphylococcus aureus* and *Pseudomonas aeruginosa*, further explored the occurrence and development of IMD and identified key genes by transcriptome sequencing and bioinformatics analysis.

Sun et al. proposed a submicron forest-like (Fore) silicon surface based on photoetching, and found that the upregulation of macrophage M2 polarization on the Fore surface contributed to enhance osteogenesis *in vitro* and accelerate bone regeneration *in vivo*.

Wang et al. assessed the impact of low-intensity pulsed ultrasound (LIPUS) therapy on the peri-implant osteogenesis in a Type II diabetes mellitus (T2DM) rat model. The results showed that LIPUS has a great potential for T2DM patients to attain improved peri-implant osteogenesis.

Xu et al. developed Ti-24Nb-4Zr-8Sn scaffolds with methacrylated gelatin and deferoxamine, providing a new strategy to improve the osteogenesis and angiogenesis for repair of large bone defects.

Wang et al. suggested that, biomaterial scaffolds seeded with allogenic fetal BMSCs represent a promising strategy to induce and improve bone regeneration under diabetic condition.

Liu et al. constructed a novel injectable strontium-doped hydroxyapatite bone-repair material, which demonstrated good antibacterial properties, biocompatibility, and osteoinductivity.

Finally, Guo et al. reviewed the current mainstream types and characteristics of hydrogels, and summarized the relevant basic research on hydrogels in promoting periodontal tissue regeneration and bone defect repair in recent years.

2. For tooth repair, biomimetic approaches should be developed to remineralize dentin, manage root canal, enhance the restorative materials with bonding/antibacterial ability, or mimic natural teeth from multiple perspectives (such as morphology, strength, and color). Accordingly, new biomaterials, methodologies, and approaches for tooth repair are continually invented.

In particular, Zhao et al. suggested that the acetone-wet bonding (AWB) technique was effective in enhancing the dentin bond durability by increasing the wettability of dentin surface to adhesives, removing residual water in the hybrid layer, improving the penetration of adhesive monomer, and inhibiting the collagenolytic activities.

Sheng et al. investigated the antimicrobial properties of Triton, an all-in-one irrigant, on *Enterococcus faecalis* and multispecies oral biofilms in dentin canals, as well as its ability to remove the smear layer.

Zhu et al. found that color adjustment potential was dependent on resin composite type, background color, and restoration depth, so shade selection is indispensable for multi-shade resin composites. Charisma Diamond One exhibited the highest color adjustment potential and the most pronounced color shifting, contributing to simplifying the process of shade selection and improving the efficiency of clinical work.

Indurkar et al. present the synthesis of ACP with naturally occurring organic compounds (ascorbate, glutamate, and itaconate) ubiquitously found in mitochondria and vital for bone remodeling and healing. This research contributes to the expanding field of biomaterial science by bridging the gap between the biomineralization process and synthetic material.

Wang et al. demonstrated that antibiofilm peptides are effective in promoting corrosion resistance of titanium against *Streptococcus mutans*, suggesting a promising strategy to enhance the stability of dental implants by endowing them with antibiofilm and anticorrosion properties.

Chen et al. synthesized quercetin-encapsulated hollow mesoporous silica nanocomposites (Q@HMSNs), which held promise for inhibiting dentine erosion and abrasion by promoting tubule occlusion and demineralized organic matrix preservation.

Jiang et al. illustrated that proper incorporation of bioceramic micro-fillers in attachments provides an innovative approach for clear aligner therapy with reinforced antibiofilm and remineralization effects without weakening shear bonding strength.

Hu et al. reported that the bond strength between ceramic brackets and zirconia was significantly lower after thermocycling compared to that of metal brackets and zirconia. SBPM exhibited consistent and robust bond strength between ceramic/metal brackets and zirconia across various storage conditions.

Chen et al. evaluated the ability of theaflavin-3,3′-digallate (TF3)/ethanol solution to crosslink demineralized dentin collagen, resist collagenase digestion, and explore the potential mechanism.

Finally, Hu et al. proved that two antimicrobial peptides (AMPs), buCaTHL4B and Im-4, possessed remarkable antibacterial and anti-biofilm capabilities against pathogenic root canal biofilms *in vitro*, indicating their potential as promising additives to optimize the effectiveness of root canal treatment as alternative irrigants.

In summary, we have gathered an array of cutting-edge research articles that delve into the exciting realm of advanced biomaterials for hard tissue repair and regeneration, particularly focusing on the domains of bone and tooth restoration. The compilation of 20 meticulously curated contributions not only

showcases the remarkable progress made in this interdisciplinary field but also offers a glimpse into the promising avenues that lie ahead.

Future research should strive to address the limitations of current biomaterials, such as their long-term stability, biocompatibility, and the potential for immune rejection. The integration of advanced manufacturing techniques, such as 3D printing and precision engineering, can further refine the design and fabrication of biomaterials, enabling the creation of customized, patient-specific solutions. Moreover, a deeper understanding of the cellular and molecular mechanisms underlying hard tissue repair and regeneration is crucial for the rational design of next-generation biomaterials.

Author contributions

HY: Writing–original draft, Writing–review and editing. DP: Writing–original draft, Writing–review and editing. WZ: Writing–original draft, Writing–review and editing. JY: Writing–original draft, Writing–review and editing.

Funding

The author(s) declare that no financial support was received for the research, authorship, and/or publication of this article.

Conflict of interest

The authors declare that the research was conducted in the absence of any commercial or financial relationships that could be construed as a potential conflict of interest.

Publisher's note

frontiers | Frontiers in Bioengineering and Biotechnology

TYPE Original Research
PUBLISHED 01 August 2023
DOI 10.3389/fbioe.2023.1254927

OPEN ACCESS

EDITED BY
Jian Yang,
The Pennsylvania State University (PSU), United States

REVIEWED BY
Xiaofei Zhu,
Boston University, United States
Jianfeng Jin,
Academic Centre for Dentistry Amsterdam, Netherlands

*CORRESPONDENCE
Ya Shen,
yashen@dentistry.ubc.ca
Shuli Deng,
ytys090116@zju.edu.cn

†These authors have contributed equally to this work and share first authorship

RECEIVED 07 July 2023
ACCEPTED 24 July 2023
PUBLISHED 01 August 2023

CITATION
Sheng X, Yu J, Liu H, Wang Z, Deng S and Shen Y (2023), Dual effectiveness of a novel all-in-one endodontic irrigating solution in antibiofilm activity and smear layer removal.
Front. Bioeng. Biotechnol. 11:1254927.
doi: 10.3389/fbioe.2023.1254927

Dual effectiveness of a novel all-in-one endodontic irrigating solution in antibiofilm activity and smear layer removal

Xuyan Sheng[1,2†], Jian Yu[2,3†], He Liu[2], Zhejun Wang[2], Shuli Deng[1*] and Ya Shen[2*]

[1]Stomatology Hospital, School of Stomatology, Zhejiang University School of Medicine, Zhejiang Provincial Clinical Research Center for Oral Diseases, Key Laboratory of Oral Biomedical Research of Zhejiang Province, Cancer Center of Zhejiang University, Engineering Research Center of Oral Biomaterials and Devices of Zhejiang Province, Hangzhou, China, [2]Division of Endodontics, Department of Oral Biological and Medical Sciences, Faculty of Dentistry, University of British Columbia, Vancouver, BC, Canada, [3]State Key Laboratory of Oral and Maxillofacial Reconstruction and Regeneration, Key Laboratory of Oral Biomedicine Ministry of Education, Hubei Key Laboratory of Stomatology, School and Hospital of Stomatology, Wuhan University, Wuhan, China

The continuous destruction of dental hard tissues increases the risk of bacterial invasion, which leads to pulp infections. Irrigation is critical for successful root canal treatment in terms of infection control. However, no single irrigant covers all of the functions demanded, including antibiofilm and tissue-dissolving activities. The aim of this study was to investigate the antimicrobial properties of Triton, an all-in-one irrigant, on *Enterococcus faecalis* and multispecies oral biofilms in dentin canals, as well as its ability to remove the smear layer. Dentin blocks (192 specimens) were prepared from single-root human teeth and then assigned to 48 groups (24 groups for each biofilm type). Serial centrifugation was used for bacterial introduction into dentinal tubules. After 3 weeks, half of the specimens were created a uniform smear layer. The following treatments were applied: short time (separate): Triton, 6% NaOCl, 2% NaOCl, and water (all for 3 min); short time (combined): Triton (3 + 1 min), 6% NaOCl +17% EDTA (3 + 1 or 2 + 1 min), and 2% NaOCl +17% EDTA (3 + 1 min); and long time: Triton (3 + 3 min), 6% NaOCl (5 min), 6% NaOCl +17% EDTA (5 + 1 min), and water (3 + 3 min). Confocal laser scanning microscopy and scanning electron microscopy were employed to examine the antimicrobial activity and smear layer removal, respectively. The results revealed that despite the absence or presence of the smear layer, Triton (3 + 3 min) showed the highest killing for both tested biofilms (61.53%–72.22%) among all groups ($p < 0.05$). Furthermore, the smear layer was removed by Triton after 3 + 3 min, exposing open dentin canals. These findings demonstrated that Triton can provide dual benefits of antibiofilm and smear layer removal capabilities simultaneously, indicating a simplified and effective strategy for application in root canal treatment.

KEYWORDS

antimicrobial, biofilm, dentin, irrigant, smear layer

1 Introduction

Human teeth are effective in combating external adverse challenges to protect the internal pulp tissues because of their delicate microstructure and ordered crystal arrangement (An et al., 2012). In nature, dental hard tissues are rarely self-repairing; the destruction of enamel and dentin allows bacteria to invade the pulp and cause infection and pain (Lawn et al., 2010; Yu et al., 2023). The primary purpose of endodontic treatment focuses on eradicating microorganisms within the infected root canals and preventing reinfection, thereby saving the natural tooth (Zehnder and Belibasakis, 2015). The necrotic, inflamed tissue/dentin debris and microbes inside the root canal can be removed under constant irrigation following mechanical instrumentation (Neelakantan et al., 2017). Irrigating solutions play a vital role in influencing canal wall areas that are not touched by the instruments (Boutsioukis and Arias-Moliz, 2022) and are beneficial in preventing bacterial extrusion into the periapical areas; their distinguishing features include organic or inorganic tissue-dissolving ability or antimicrobial/antibiofilm activities (Haapasalo et al., 2014). Despite advancements in disinfectants, instruments, and techniques have made endodontic treatment more predictable nowadays, there is no single irrigant that adequately covers all of the functions demanded. As a result, the combined, sequential use of irrigants is crucial to the clinical success of root canal treatment.

Sodium hypochlorite (NaOCl) is the most commonly used irrigant in endodontic treatment, due to its ability to dissolve organic tissues (including collagen, pulpal remnants, and organic components of the smear layer) and its broad-spectrum antimicrobial activity against *Enterococcus faecalis* (*E. faecalis*) and multispecies biofilms (Gu et al., 2017). Whereas, removal of dentin debris and inorganic components of the smear layer is also required for the complete cleaning of the root canal system (Bilvinaite et al., 2022). Ethylenediaminetetraacetic acid (EDTA) or citric acid (CA) is generally applied following NaOCl to effectively dissolve the inorganic substances of the smear layer and dentin (Turk et al., 2015). However, neither has any or little organic tissue-dissolving ability (Prado et al., 2015). Because of its favorable antibacterial properties, chlorhexidine digluconate (CHX) has long been employed in dental disinfection and plaque controlling (Kamolnarumeth et al., 2021). CHX, on the other hand, cannot replace NaOCl since it is incapable of dissolving organic debris and killing oral biofilms (Wang et al., 2020). Given that the successive use of these irrigants prolongs root canal cleaning, using combination products of irrigants with multiple functions would be desirable to simplify the clinical procedures.

The past few decades have witnessed the introduction of several combination products for root canal irrigation. Previous studies have shown that 2-in-1 solutions incorporating EDTA or CA and CHX or doxycycline can provide benefits (Andrabi et al., 2013; Balto et al., 2015; Giardino et al., 2018), but incorporating NaOCl in these solutions is not practical as EDTA neutralizes NaOCl (Rossi-Fedele et al., 2012). Additionally, concerns cover cytotoxicity, tooth staining, and drug resistance exist with the use of CHX or doxycycline (Shen et al., 2016; Liu et al., 2018; Wang et al., 2020). To address these concerns, a new all-in-one endodontic irrigant, Triton, has recently been developed, which avoids the use of EDTA, CHX, and antibiotics. Triton comprises two parts with distinct components, with Part A containing chelators (CA), surfactants, pH modifiers, and stabilizers, while Part B containing 8% NaOCl and a pH modifier. The automix technique precisely mixes the two parts to deliver the final solution (4% NaOCl), allowing for simultaneous organic and inorganic tissue dissolution. Despite its potential benefits, no related information on the antibiofilm activity and smear layer removal of Triton is currently available.

The objective of this study was to evaluate the antibiofilm and smear layer removal effectiveness of Triton as an endodontic irrigant. The null hypotheses were that: i) there is no significant difference in the antimicrobial efficacy between Triton and NaOCl or NaOCl + EDTA against *E. faecalis* and multispecies oral biofilms in dentin canals; and ii) Triton does not remove the smear layer.

2 Materials and methods

2.1 Dentin block preparation

In accordance with the protocol approved by the Clinical Research Ethics Committee of the University of British Columbia (certificate H12-02430), 48 single-root, non-caries human teeth subjected to orthodontic extraction were collected. All procedures were performed following the Declaration of Helsinki. As the same procedure described in our previous studies (Wang et al., 2018; Huang et al., 2019), 96 dentin blocks (with a dimension of 4 × 4 × 2 mm) were prepared to yield 192 specimens. The schematic diagram of this study is presented in Figure 1.

2.2 Disinfecting solution preparation

Triton (Brasseler, Savannah, United States) was prepared by mixing components from Parts A and B at a 1: 1 volume ratio. The composition of ingredients of Triton is summarized in Supplementary Table S1. Seventeen percent EDTA (pH 7.0) (Vista, Racine, United States) and 6% NaOCl (Clorox, Oakland, United States) were achieved from the manufacturers. The iodometric titration was used to verify the available chlorine concentration. Sterilized deionized water was used to dilute 6% NaOCl for 2% NaOCl preparation.

2.3 Dentin block infection

The bacterial strain, *E. faecalis* VP3-181, was initially isolated from an infected root canal as previously reported (Peciuliene et al., 2000). Brain-heart infusion (BHI) agar (BD Corp., Sparks, United States) plates were used to anaerobically incubate *E. faecalis* overnight at 37°C. Supra- and subgingival plaque from one healthy adult volunteer was collected after informed consent was obtained. BHI broth was utilized to suspend *E. faecalis* and plaque mixed bacteria, respectively. In line with a previously published protocol (Ma et al., 2011), suspensions of *E. faecalis* and plaque were centrifuged into dentinal tubules after being adjusted to the same optical density (0.05 at 405 nm). A 3-week anaerobic incubation was implemented at 37°C for dentin blocks with bacterial suspensions in BHI broth. During the incubation

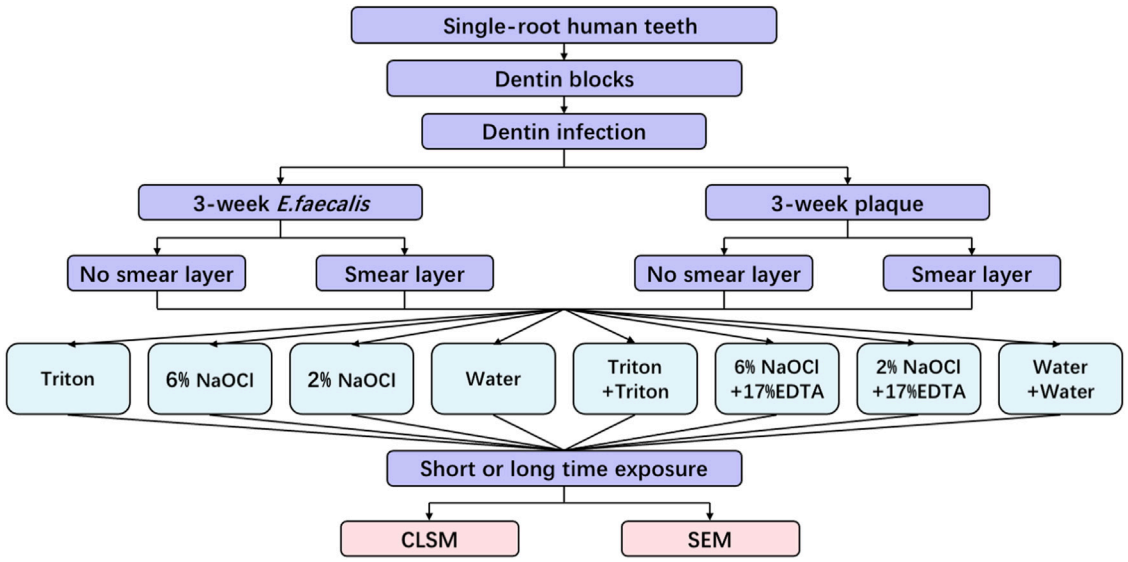

FIGURE 1
Schematic illustration of the experimental design in this study.

TABLE 1 Times of exposure to the experimental solutions used in this study.

Solutions	Short time (min)		Long time (min)	
	No smear layer	Smear layer	No smear layer	Smear layer
Triton	3	3	–	–
6% NaOCl	3	3	5	5
2% NaOCl	3	3	–	–
Water (control)	3	3	–	–
Triton + Triton	3 + 1	3 + 1	3 + 3	3 + 3
6% NaOCl + 17% EDTA	3 + 1/2 + 1	3 + 1/2 + 1	5 + 1	5 + 1
2% NaOCl + 17% EDTA	3 + 1	3 + 1	–	–
Water + Water (control)	–	–	3 + 3	3 + 3

period, fresh BHI broth was used to change the old broth once a week.

2.4 Dentin disinfection

After 3 weeks, the infected specimens were removed from the tubes. The nail varnish was employed to mimic the cement layer on the root surface by sealing the outer side of the specimens after sterile water rinse and air drying. According to different solutions and treatment times as shown in Table 1, the prepared specimens were randomly assigned to 48 groups (24 groups for *E. faecalis* and the other 24 groups for plaque; 4 specimens in each group). For groups with the smear layer, a medium-grit cylinder flat-end bur (Patterson Dental, Halifax, Canada) was used to create a smear layer on the root canal side of each block for 4 s each at 1,500 rpm prior to treatments. After that, 50 μL of each solution was applied on the root canal side of the specimens for designated short and long periods of time. To expose fresh surfaces of longitudinally fractured dentinal tubules (Wang et al., 2017), each specimen was vertically split across the center of the root canal into two-halves after rinsing for 1 min with sterile water. Each specimen in the groups treated with two solutions was rinsed with PBS for 30 s and dried before being treated with the second solution.

2.5 Examination of confocal laser scanning microscopy (CLSM)

Following gentle rinsing with PBS for 1 min, each specimen was stained with a live/dead bacterial viability kit (L7012, Molecular

Probes, Eugene, United States) protected from light according to the manufacturer's protocols. SYTO-9 and propidium iodide included in this kit enable live and dead bacteria to show green and red fluorescence, respectively (Huang et al., 2019; Yu et al., 2021). CLSM (FV10i-LIV, Olympus, Tokyo, Japan) was employed to scan biofilm images (512 × 512 pixels) from four randomly selected areas for each specimen with a z-stack of 20 slices at 0.5-μm step, and a minimum of 16 scans were obtained for each group. An Imaris 7.4.2 software (Bitplane, Zurich, Switzerland) was used to reconstruct three-dimensional volume stacks and quantitatively determine the proportions of live and dead bacteria (Guo et al., 2021; Zhu et al., 2023).

2.6 Smear layer removal

Additional dentin disk specimens were prepared in accordance with previously proposed approach (Wang et al., 2017). These specimens were exposed to one of five freshly prepared solutions (2 mL) as follows: i) 6% NaOCl +17% EDTA (3 + 1 min), ii) 6% NaOCl +17% EDTA (5 + 1 min), iii) 6% NaOCl + water (5 + 1 min), iv) Triton (3 min), and v) Triton + Triton (3 + 3 min). This process was conducted with gentle vibration (60 rpm) at room temperature. Sterilized deionized water was used to rinse the specimens for 1 min between exposure to two solutions, and a final rinse for 1 min was applied for all specimens. Scanning electron microscopy (SEM, SU3500, Hitachi, Toronto, Canada) was utilized to observe the smear layer removal at 3 kV.

2.7 Colony forming unit (CFU) test

Sterile hydroxyapatite (HA) disks (Clarkson Chromatography Products, Williamsport, United States) with 1.52 mm thickness and 9.65 mm diameter were used as the growth substrates of plaque biofilms. The formation of biofilms on HA disks was performed based on a well-established model, as previously reported (Wang et al., 2020). The 3-week-old biofilms formed on the surface of disks were scraped off into BHI broth medium, and the suspension was adjusted to an optical density of 0.25 at 405 nm. One hundred μL of each plaque suspension was then added to 400 μL of sterile water, 6% NaOCl, and Triton for 30 s. After that, 100 μL of each suspension was added to 900 μL of BHI broth medium to perform ten-fold serial dilution. A droplet of 20 μL of diluent from each of three solutions was overspread onto blood agar plates (BHI agar with 5% heparinized sheep's blood; BD Difco, Detroit, United States) and anaerobically cultivated at 37°C for 48 h, followed by calculating the total number of CFU. The percentage of bacteria killed was defined as previously described (Wang et al., 2020). Three repeated tests were accomplished for the CFU test.

2.8 Statistical analysis

Statistical analysis was carried out using SPSS 22.0 (IBM, Armonk, United States). The Shapiro-Wilk test and Levene's test were utilized to confirm the normality of the distribution and the homogeneity of variance, respectively. Univariate analysis of variance (ANOVA) with *post hoc* multiple comparisons was employed to analyze the CLSM and CFU data. The significance level was set at 0.05.

3 Results

3.1 Antimicrobial effects by CLSM analysis

CLSM images of 3-week-old *E. faecalis* and plaque multispecies biofilms in dentin canals after exposure to different irrigants are shown in Figure 2 and Figure 3, respectively, and the corresponding proportions of dead bacterial cells in the biofilms are summarized in Figure 2. In the absence of the smear layer (Figures 2–4), large proportions of two types of bacteria (64.09% ± 3.81% for *E. faecalis* and 61.73% ± 4.72% for multispecies biofilms) were killed by Triton alone in 3 min, while 6% NaOCl induced approximately half of the bacterial death. The use of Triton by 3 + 3 min killed 71.05% ± 6.68% in *E. faecalis* and 72.22% ± 6.81% in multispecies biofilms, achieving the highest biofilm killing among all groups ($p < 0.05$), irrespective of bacterial type or short or long exposure.

In the presence of the smear layer (Figures 2–4), Triton alone was as effective as 6% NaOCl (without the smear layer) in killing *E. faecalis* and multispecies biofilms in 3 min, while outperforming 6% NaOCl (with the smear layer) ($p < 0.05$). Six percent or 2% NaOCl +17% EDTA was more effective in bacterial killing than NaOCl alone, and the weakest effects were found when 2% NaOCl was used alone. Long exposure to Triton by 3 + 3 min resulted in significantly higher bacterial death for both *E. faecalis* (61.53% ± 5.36%) and multispecies (63.65% ± 5.05%) biofilms, when compared to all other groups ($p < 0.05$).

3.2 Smear layer removal

Figure 5 shows the typical SEM images of smear layer removal by different treatments. Groups containing Triton or EDTA removed the smear layer to varying degrees, leaving open dentin canals exposed. In contrast, the 6% NaOCl + water (without EDTA) group did not cause the removal of the smear layer, and no open dentinal tubules were visible.

3.3 Bacterial killing by CFU test

Supplementary Figure S1 displays CFU results for 3-week-old dispersed plaque multispecies biofilms after exposure to different medicaments for 30 s. The use of 6% NaOCl killed 99.46% ± 0.15% of the bacteria. As for Triton, all of the bacteria were killed.

4 Discussion

The effectiveness of Triton on killing mono- and multispecies oral biofilms and removing the smear layer in dentin canals was evaluated in the present study. The results demonstrated that Triton showed significantly higher bacterial killing for both *E. faecalis* and multispecies biofilms in dentin canals when compared to NaOCl or

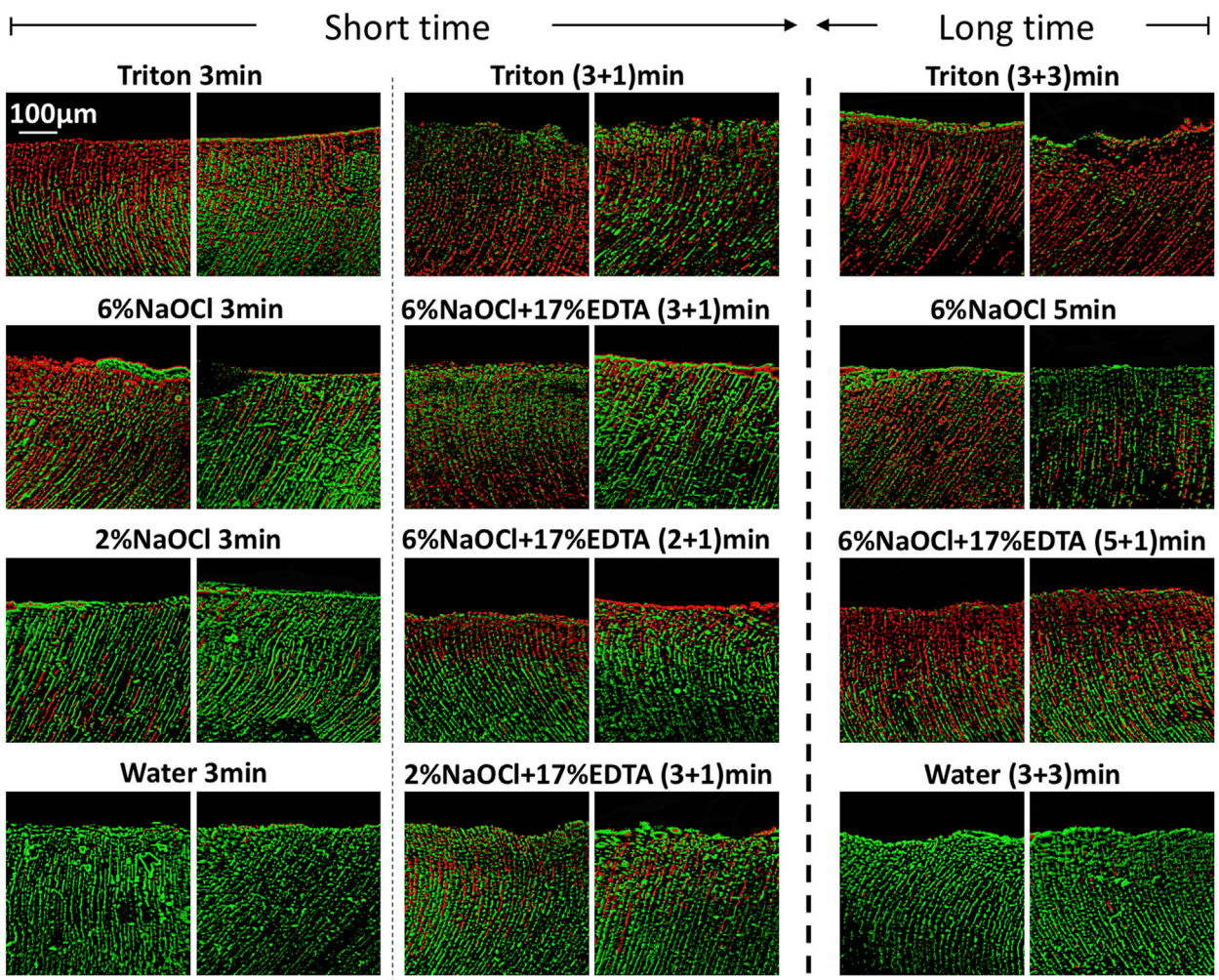

FIGURE 2
Three-dimensional reconstructed CLSM images of 3-week-old *Enterococcus faecalis* biofilms in dentin canals after exposure to different irrigants (live bacteria, green; dead bacteria, red). For each medication, pictures on the left and right respectively show the absence and presence of the smear layer.

NaOCl + EDTA and can remove the smear layer with open dentin canals exposed. As a result, Triton is effective in providing the antibiofilm and smear layer removal activities, and the two null hypotheses have to be rejected.

The prerequisite for successful endodontic treatment derives from effective bacterial biofilm elimination in the root canal systems. Both *E. faecalis* and multispecies biofilms were tested since the former is generally detected in chronic endodontic infection and the latter could better mimic actual oral conditions (Shen et al., 2011; Rosa et al., 2017). Treatment with Triton for 3 min resulted in significant bacterial killing in both biofilms (Figures 2–4). Interestingly, when Triton was used for 3 min, followed by another 3 min of treatment, it showed significantly higher biofilm bacterial death compared to 6% NaOCl (5 min) and 6% NaOCl + 17% EDTA (5 + 1 min), regardless of the presence of the smear layer. It is worth noting that clinical cases may involve more than one canal in a tooth, potentially necessitating longer irrigant exposure. Therefore, both short-time and long-time irrigation were employed in this study to account for such scenarios. The findings suggest that Triton exhibits superior antimicrobial effects on oral mono- and multispecies biofilms within dentin canals, outperforming NaOCl or NaOCl + EDTA. Additionally, the long-time treatment with Triton resulted in even more pronounced antimicrobial effects compared to the short-time treatment. These results underscore the potential of Triton as an effective antimicrobial agent for endodontic procedures. Unlike conventional irrigants or 2-in-1 products, Triton avoids the use of EDTA and/or CHX to work differently because NaOCl neutralizes upon contact with EDTA rapidly. Two separate components are designed in Triton, and the automix mechanism will precisely mix Part A (contains CA and surfactants) and Part B (contains 8% NaOCl) to produce the final solution (4% NaOCl). Interestingly, Triton with 4% NaOCl had higher antibiofilm activity than 6% NaOCl alone or in combination with 17% EDTA. The reasons may ascribe to the following perspectives. CA may promote the antibiofilm effectiveness of hypochlorite in deeper layers of dentin with the removal of the smear layer (Campello et al., 2022). Previous studies have highlighted that the antimicrobial and tissue-dissolving effects

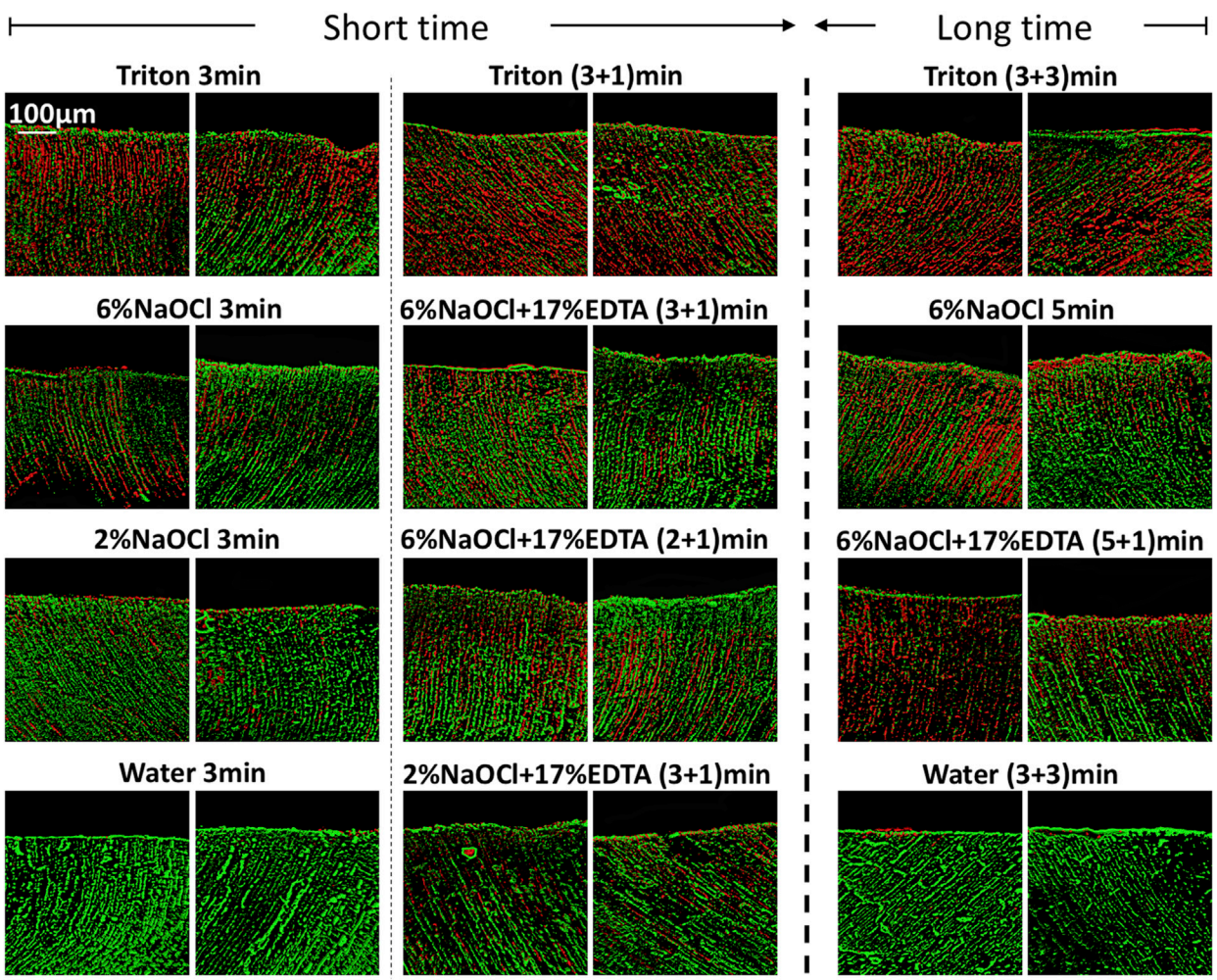

FIGURE 3
Three-dimensional reconstructed CLSM images of 3-week-old plaque multispecies biofilms in dentin canals after exposure to different irrigants (live bacteria, green; dead bacteria, red). For each medication, pictures on the left and right respectively show the absence and presence of the smear layer.

of hypochlorite also can be enhanced by the addition of surfactants (Stojicic et al., 2010; Iglesias et al., 2019). It is worth mentioning that differences in solution concentrations and tissue types may lead to partially contradictory outcomes (Poggio et al., 2010; Clarkson et al., 2012). Furthermore, pH modifiers (specifically sodium hydroxide) contained in Triton could maintain NaOCl solutions at an alkaline pH. As a result, the alkaline environment inside dentin canals is beneficial to combat acidic by-products generated by microbial metabolism within biofilms to enhance the cleansing effects (Ran et al., 2015).

In addition to eradicating biofilms in root canal systems, the dissolution of necrotic, infected organic and inorganic substances with irrigating solutions is required for complete cleaning. The smear layer is typically created during instrumentation and may act as an impediment to microbial killing of antimicrobial agents in the canals (Wang et al., 2013). In this regard, it is crucial that the smear layer should be removed. Since hypochlorite can only remove the organic components of the smear layer, the activity of irrigants against inorganic components and dentin debris is preferred. Hence, the ability of Triton on the smear layer removal was determined in this study. SEM observation confirmed that Triton treatment for 3 and 3 + 3 min removed the smear layer with open dentin canals exposed (Figure 5), which is as effective as NaOCl + EDTA, implying a favorable tissue-dissolving activity. This finding could be related to the function of CA incorporated in Triton. Despite the scarce antibacterial activity, CA as a chelator is capable of effectively dissolving inorganic materials, including dentin remnants and apatite crystals (Gandolfi et al., 2018). Recent literature has reported that synergistic action of mode interacting with other chemicals can be provided by CA (Olivieri et al., 2016; Wilkoński et al., 2021). Furthermore, the stable, high pH condition of NaOCl solutions created by pH modifiers plays a vital role in exerting stronger proteolytic effects. Significantly more necrotic, inflamed tissue, dentin debris, and inorganic components of the smear layer are likely to be dissolved according to previous evidence (Jungbluth et al., 2011; Trautmann et al., 2021). In other words, the all-in-one design in Triton demonstrated positive effects for the combination of NaOCl, CA, surfactants, and pH modifiers. It should be emphasized that

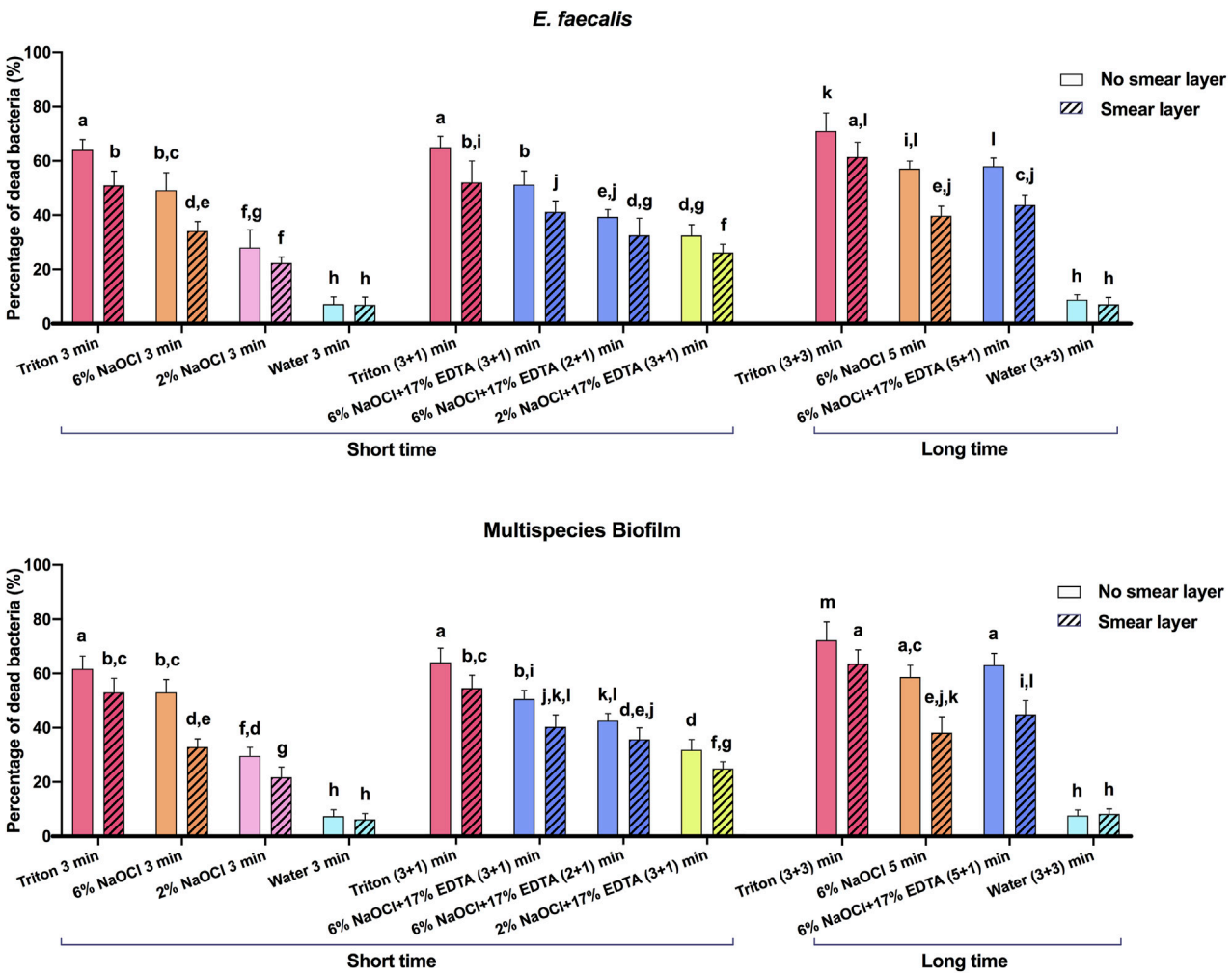

FIGURE 4
The proportions of dead bacterial cell volumes in 3-week-old biofilms of dentin canals after short and long exposure to different irrigants. Data are represented as means ± standard deviations. Different letters indicate statistical differences ($p < 0.05$).

the use of Triton did not weaken or compromise the efficacy of any of the components included. Instead, effective antimicrobial and tissue-dissolving activities can be achieved simultaneously.

As a critical field of research in endodontics, ideal dentin disinfection has been pursued for decades. The role of microorganisms in dentin canals may vary in different cases (Bergenholtz, 2016). In clinical practice, the effectiveness of various antimicrobial strategies can be considered one of the most useful indicators for dentin disinfection (Han et al., 2021; Yan et al., 2022; Hu et al., 2023). To simulate the clinical conditions more realistically in this study, short and long time exposure to different irrigating solutions was evaluated on the basis of previous investigations (Wang et al., 2018; Huang et al., 2019). Although it appears to be a relatively long irrigation exposure of 3 + 3 or 5 + 1 min, the significance is that searching for potential curved, calcified, or missing canals in multirooted teeth cases that require a prolonged time is available. Additionally, serial centrifugation for dentin blocks was implemented by introducing *E. faecalis* and multispecies bacteria into the dentinal tubules in our model. In this regard, it will be possible to make comparisons between specimens since all dentin blocks secure the bacteria inside the dentinal tubules via centrifugation (Ma et al., 2011; Al-Zuhair et al., 2023).

The application of Triton succeeds in the synergistic killing of oral bacterial biofilms and removal of the smear layer as an alternative irrigant. The action of mode of the all-in-one strategy also simplifies procedural steps for endodontic treatment. However, the limitations of this study should not be omitted. Given the complexity of dentin canal and apical structure, an *ex vivo* model (instead of an *in vitro* model) of dentin infection should also be employed to investigate the antimicrobial efficacy of the irrigants in future studies. Although promising findings have been demonstrated, it should be noted that the *in vitro* conditions tested in the present study may not exactly mimic actual oral conditions. In addition, to further determine the molecular biological mechanism of antibiofilm activity, additional analyses, such as polymerase chain reaction assay, need be considered apart

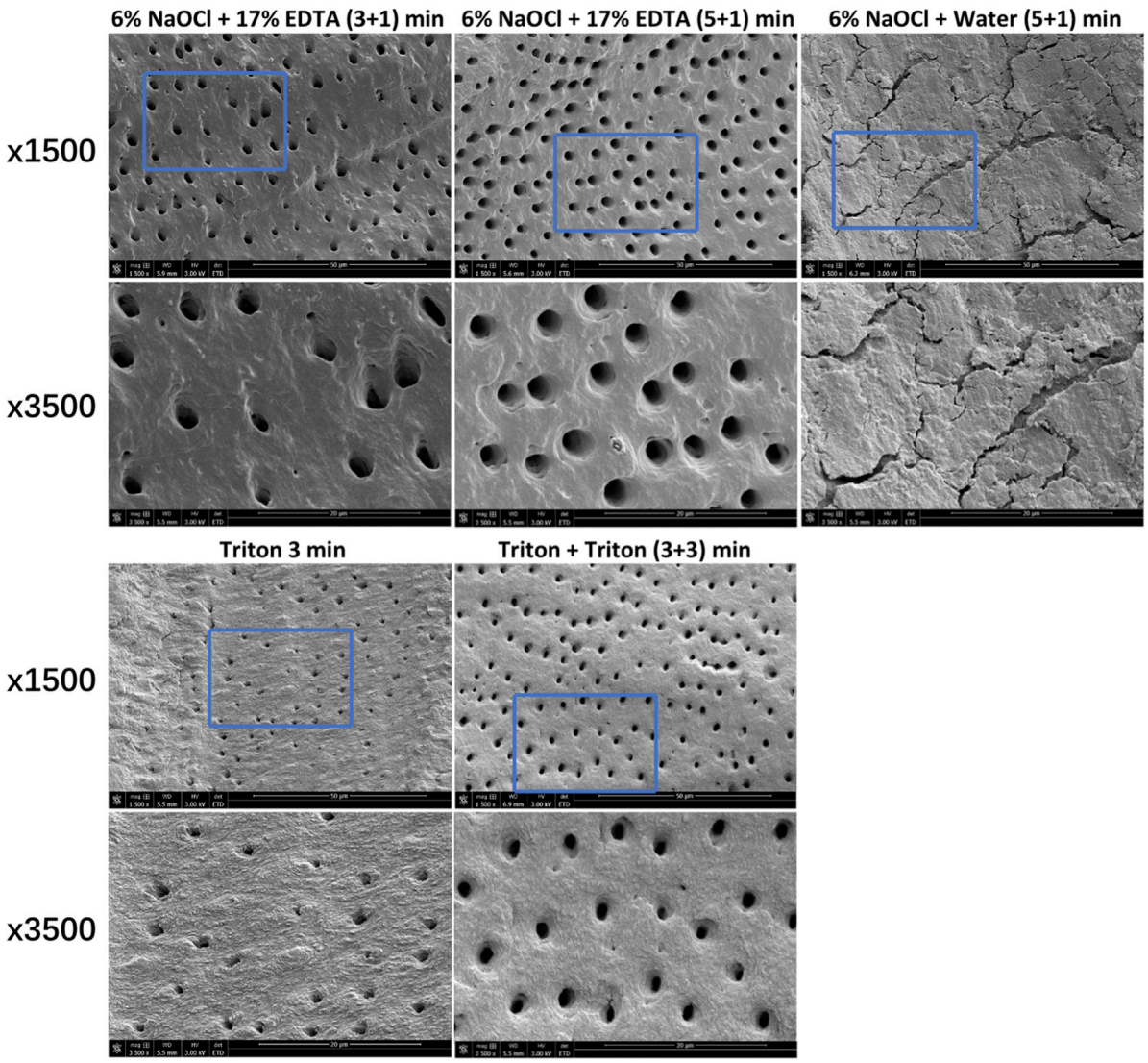

FIGURE 5
Characteristic SEM images of smear layer removal by different treatments. For each group, images (×3,500) correspond to high-magnification images of the blue box region (1,500 ×).

from CLSM examination. Further research is also demanded to investigate the detailed mechanism and wide-ranging application of Triton.

5 Conclusion

The use of Triton effectively killed *E. faecalis* and multispecies oral biofilms in dentin canals and demonstrated a higher killing ability than 6% NaOCl and 6% NaOCl +17% EDTA. Meanwhile, Triton can be used to remove the smear layer while leaving the open dentinal tubules exposed. The all-in-one design for offering dual effectiveness of antibiofilm and smear layer removal capabilities indicates a promising strategy to optimize the mode of action of irrigation in root canal treatment. Thus, the development of Triton may serve as an alternative irrigant to provide significant benefits in leading a simplified and effective irrigation era in clinical practice.

Data availability statement

The original contributions presented in the study are included in the article/Supplementary Material, further inquiries can be directed to the corresponding authors.

Ethics statement

The studies involving humans were approved by the Clinical Research Ethics Committee of the University of British Columbia (certificate H12-02430). The studies were conducted in accordance with the local legislation and institutional requirements. The

participants provided their written informed consent to participate in this study.

Author contributions

XS: Conceptualization, Formal Analysis, Investigation, Writing–original draft. JY: Conceptualization, Formal Analysis, Investigation, Writing–original draft. HL: Investigation, Writing–original draft, Data curation. ZW: Investigation, Writing–original draft, Validation. SD: Conceptualization, Supervision, Writing–review and editing. YS: Conceptualization, Supervision, Writing–review and editing.

Funding

This work was financially supported by Key R&D Program of Zhejiang (2022C03060). JY research conducted at the UBC Faculty of Dentistry was supported by China Scholarship Council (No. 202006275049).

Conflict of interest

The authors declare that the research was conducted in the absence of any commercial or financial relationships that could be construed as a potential conflict of interest.

Publisher's note

Supplementary material

The Supplementary Material for this article can be found online at: https://www.frontiersin.org/articles/10.3389/fbioe.2023.1254927/full#supplementary-material

References

Al-Zuhair, H., Su, Z., Liu, H., Wang, Z., Haapasalo, M., Hieawy, A., et al. (2023). Antimicrobial effects of agitational irrigation on single- and multispecies biofilms in dentin canals. *Odontology* 111, 49–56. doi:10.1007/s10266-022-00719-3

An, B., Wang, R., and Zhang, D. (2012). Role of crystal arrangement on the mechanical performance of enamel. *Acta. Biomater.* 8, 3784–3793. doi:10.1016/j.actbio.2012.06.026

Andrabi, S. M., Kumar, A., Mishra, S. K., Tewari, R. K., Alam, S., and Siddiqui, S. (2013). Effect of manual dynamic activation on smear layer removal efficacy of ethylenediaminetetraacetic acid and SmearClear: An *in vitro* scanning electron microscopic study. *Aust. Endod. J.* 39, 131–136. doi:10.1111/j.1747-4477.2012.00350.x

Balto, H. A., Shakoor, Z. A., and Kanfar, M. A. (2015). Combined effect of a mixture of tetracycline, acid, and detergent, and nisin against *Enterococcus faecalis* and Actinomyces viscosus biofilms. *Saudi Med. J.* 36, 211–215. doi:10.15537/smj.2015.2.9947

Bergenholtz, G. (2016). Assessment of treatment failure in endodontic therapy. *J. Oral Rehabil.* 43, 753–758. doi:10.1111/joor.12423

Bilvinaite, G., Zongolaviciute, R., Drukteinis, S., Bukelskiene, V., and Cotti, E. (2022). Cytotoxicity and efficacy in debris and smear layer removal of HOCl-based irrigating solution: An *in vitro* study. *J. Funct. Biomater.* 13, 95. doi:10.3390/jfb13030095

Boutsioukis, C., and Arias-Moliz, M. T. (2022). Present status and future directions - irrigants and irrigation methods. *Int. Endod. J.* 55 (Suppl. 3), 588–612. doi:10.1111/iej.13739

Campello, A. F., Rodrigues, R. C. V., Alves, F. R. F., Miranda, K. R., Brum, S. C., Mdala, I., et al. (2022). Enhancing the intracanal antibacterial effects of sodium hypochlorite with etidronic acid or citric acid. *J. Endod.* 48, 1161–1168. doi:10.1016/j.joen.2022.06.006

Clarkson, R. M., Kidd, B., Evans, G. E., and Moule, A. J. (2012). The effect of surfactant on the dissolution of porcine pulpal tissue by sodium hypochlorite solutions. *J. Endod.* 38, 1257–1260. doi:10.1016/j.joen.2012.05.013

Gandolfi, M. G., Taddei, P., Pondrelli, A., Zamparini, F., Prati, C., and Spagnuolo, G. (2018). Demineralization, collagen modification and remineralization degree of human dentin after EDTA and citric acid treatments. *Materials* 12, 25. doi:10.3390/ma12010025

Giardino, L., Del Fabbro, M., Cesario, F., Fernandes, F. S., and Andrade, F. B. (2018). Antimicrobial effectiveness of combinations of oxidant and chelating agents in infected dentine: An *ex vivo* confocal laser scanning microscopy study. *Int. Endod. J.* 51, 448–456. doi:10.1111/iej.12863

Gu, L. S., Huang, X. Q., Griffin, B., Bergeron, B. R., Pashley, D. H., Niu, L. N., et al. (2017). Primum non nocere - the effects of sodium hypochlorite on dentin as used in endodontics. *Acta Biomater.* 61, 144–156. doi:10.1016/j.actbio.2017.08.008

Guo, R., Peng, W., Yang, H., Yao, C., Yu, J., and Huang, C. (2021). Evaluation of resveratrol-doped adhesive with advanced dentin bond durability. *J. Dent.* 114, 103817. doi:10.1016/j.jdent.2021.103817

Haapasalo, M., Shen, Y., Wang, Z., and Gao, Y. (2014). Irrigation in endodontics. *Br. Dent. J.* 216, 299–303. doi:10.1038/sj.bdj.2014.204

Han, X., Chen, Y., Jiang, Q., Liu, X., and Chen, Y. (2021). Novel bioactive glass-modified hybrid composite resin: Mechanical properties, biocompatibility, and antibacterial and remineralizing activity. *Front. Bioeng. Biotechnol.* 9, 661734. doi:10.3389/fbioe.2021.661734

Hu, J., Yu, J., Liu, H., Wang, Z., Haapasalo, M., Haney, E. F., et al. (2023). Dynamic killing effectiveness of mouthrinses and a d-enantiomeric peptide on oral multispecies biofilms grown on dental restorative material surfaces. *J. Dent.* 134, 104552. doi:10.1016/j.jdent.2023.104552

Huang, X., Haapasalo, M., Wang, Z., Hancock, R. E. W., Wei, X., and Shen, Y. (2019). Effect of long-term exposure to peptides on mono- and multispecies biofilms in dentinal tubules. *J. Endod.* 45, 1522–1528. doi:10.1016/j.joen.2019.09.003

Iglesias, J. E., Pinheiro, L. S., Weibel, D. E., Montagner, F., and Grecca, F. S. (2019). Influence of surfactants addition on the properties of calcium hypochlorite solutions. *J. Appl. Oral Sci.* 27, e20180157. doi:10.1590/1678-7757-2018-0157

Jungbluth, H., Marending, M., De-Deus, G., Sener, B., and Zehnder, M. (2011). Stabilizing sodium hypochlorite at high pH: Effects on soft tissue and dentin. *J. Endod.* 37, 693–696. doi:10.1016/j.joen.2011.02.019

Kamolnarumeth, K., Thussananutiyakul, J., Lertchwalitanon, P., Rungtanakiat, P., Mathurasai, W., Sooampon, S., et al. (2021). Effect of mixed chlorhexidine and hydrogen peroxide mouthrinses on developing plaque and stain in gingivitis patients: A randomized clinical trial. *Clin. Oral Investig.* 25, 1697–1704. doi:10.1007/s00784-020-03470-7

Lawn, B. R., Lee, J. W., and Chai, H. (2010). Teeth: Among nature's most durable biocomposites. *Annu. Rev. Mat. Res.* 40, 55–75. doi:10.1146/annurev-matsci-070909-104537

Liu, J. X., Werner, J., Kirsch, T., Zuckerman, J. D., and Virk, M. S. (2018). Cytotoxicity evaluation of chlorhexidine gluconate on human fibroblasts, myoblasts, and osteoblasts. *J. Bone Jt. Infect.* 3, 165–172. doi:10.7150/jbji.26355

Ma, J., Wang, Z., Shen, Y., and Haapasalo, M. (2011). A new noninvasive model to study the effectiveness of dentin disinfection by using confocal laser scanning microscopy. *J. Endod.* 37, 1380–1385. doi:10.1016/j.joen.2011.06.018

Neelakantan, P., Romero, M., Vera, J., Daood, U., Khan, A. U., Yan, A., et al. (2017). Biofilms in endodontics-current status and future directions. *Int. J. Mol. Sci.* 18, 1748. doi:10.3390/ijms18081748

Olivieri, J. G., García Font, M., Stöber, E., de Ribot, J., Mercadé, M., and Duran-Sindreu, F. (2016). Effect of manual dynamic activation with citric acid solutions in smear layer removal: A scanning electron microscopic evaluation. *J. Dent. Sci.* 11, 360–364. doi:10.1016/j.jds.2016.01.006

Peciuliene, V., Balciuniene, I., Eriksen, H. M., and Haapasalo, M. (2000). Isolation of *Enterococcus faecalis* in previously root-filled canals in a Lithuanian population. *J. Endod.* 26, 593–595. doi:10.1097/00004770-200010000-00004

Poggio, C., Arciola, C. R., Dagna, A., Chiesa, M., Sforza, D., and Visai, L. (2010). Antimicrobial activity of sodium hypochlorite-based irrigating solutions. *Int. J. Artif. Organs.* 33, 654–659. doi:10.1177/039139881003300911

Prado, M., Silva, E. J., Duque, T. M., Zaia, A. A., Ferraz, C. C., Almeida, J. F., et al. (2015). Antimicrobial and cytotoxic effects of phosphoric acid solution compared to other root canal irrigants. *J. Appl. Oral Sci.* 23, 158–163. doi:10.1590/1678-775720130691

Ran, S., Gu, S., Wang, J., Zhu, C., and Liang, J. (2015). Dentin tubule invasion by *Enterococcus faecalis* under stress conditions *ex vivo*. *Eur. J. Oral Sci.* 123, 362–368. doi:10.1111/eos.12202

Rosa, R. A. D., Santini, M. F., Figueiredo, J. A. P., Visioli, F., Pereira, J. R., Vivan, R. R., et al. (2017). Effectiveness of photodynamic therapy associated with irrigants over two biofilm models. *Photodiagnosis Photodyn. Ther.* 20, 169–174. doi:10.1016/j.pdpdt.2017.10.003

Rossi-Fedele, G., Doğramaci, E. J., Guastalli, A. R., Steier, L., and de Figueiredo, J. A. (2012). Antagonistic interactions between sodium hypochlorite, chlorhexidine, EDTA, and citric acid. *J. Endod.* 38, 426–431. doi:10.1016/j.joen.2012.01.006

Shen, Y., Stojicic, S., and Haapasalo, M. (2011). Antimicrobial efficacy of chlorhexidine against bacteria in biofilms at different stages of development. *J. Endod.* 37, 657–661. doi:10.1016/j.joen.2011.02.007

Shen, Y., Zhao, J., de la Fuente-Núñez, C., Wang, Z., Hancock, R. E., Roberts, C. R., et al. (2016). Experimental and theoretical investigation of multispecies oral biofilm resistance to chlorhexidine treatment. *Sci. Rep.* 6, 27537. doi:10.1038/srep27537

Stojicic, S., Zivkovic, S., Qian, W., Zhang, H., and Haapasalo, M. (2010). Tissue dissolution by sodium hypochlorite: Effect of concentration, temperature, agitation, and surfactant. *J. Endod.* 36, 1558–1562. doi:10.1016/j.joen.2010.06.021

Trautmann, E., Attin, T., Mohn, D., and Zehnder, M. (2021). Hydrogen peroxide versus sodium hypochlorite: All a matter of pH? *J. Endod.* 47, 297–302. doi:10.1016/j.joen.2020.10.016

Turk, T., Kaval, M. E., and Şen, B. H. (2015). Evaluation of the smear layer removal and erosive capacity of EDTA, boric acid, citric acid and desy clean solutions: An *in vitro* study. *BMC Oral Health* 15, 104. doi:10.1186/s12903-015-0090-y

Wang, D., Shen, Y., Hancock, R. E. W., Ma, J., and Haapasalo, M. (2018). Antimicrobial effect of peptide DJK-5 used alone or mixed with EDTA on mono- and multispecies biofilms in dentin canals. *J. Endod.* 44, 1709–1713. doi:10.1016/j.joen.2018.07.018

Wang, D., Shen, Y., Ma, J., Hancock, R. E. W., and Haapasalo, M. (2017). Antibiofilm effect of D-enantiomeric peptide alone and combined with EDTA *in vitro*. *J. Endod.* 43, 1862–1867. doi:10.1016/j.joen.2017.06.037

Wang, Z., Shen, Y., and Haapasalo, M. (2020). Dynamics of dissolution, killing, and inhibition of dental plaque biofilm. *Front. Microbiol.* 11, 964. doi:10.3389/fmicb.2020.00964

Wang, Z., Shen, Y., and Haapasalo, M. (2013). Effect of smear layer against disinfection protocols on Enterococcus faecalis-infected dentin. *J. Endod.* 39, 1395–1400. doi:10.1016/j.joen.2013.05.007

Wilkoński, W., Jamróz-Wilkońska, L., Zapotoczny, S., Opiła, J., and Giardino, L. (2021). Real-time co-site optical microscopy study on the morphological changes of the dentine's surface after citric acid and sodium hypochlorite: A single-tooth model. *BMC Oral Health* 21, 454. doi:10.1186/s12903-021-01815-6

Yan, Y., Guan, Y., Luo, L., Lu, B., Chen, F., and Jiang, B. (2022). Effects of immunoglobulin Y-loaded amorphous calcium phosphate on dentinal tubules occlusion and antibacterial activity. *Front. Bioeng. Biotechnol.* 10, 921336. doi:10.3389/fbioe.2022.921336

Yu, J., Bian, H., Zhao, Y., Guo, J., Yao, C., Liu, H., et al. (2023). Epigallocatechin-3-gallate/mineralization precursors co-delivery hollow mesoporous nanosystem for synergistic manipulation of dentin exposure. *Bioact. Mat.* 23, 394–408. doi:10.1016/j.bioactmat.2022.11.018

Yu, J., Yi, L., Guo, R., Guo, J., Yang, H., and Huang, C. (2021). The stability of dentin surface biobarrier consisting of mesoporous delivery system on dentinal tubule occlusion and Streptococcus mutans biofilm inhibition. *Int. J. Nanomedicine* 16, 3041–3057. doi:10.2147/IJN.S290254

Zehnder, M., and Belibasakis, G. N. (2015). On the dynamics of root canal infections-what we understand and what we don't. *Virulence* 6, 216–222. doi:10.4161/21505594.2014.984567

Zhu, M., Dang, J., Dong, F., Zhong, R., Zhang, J., Pan, J., et al. (2023). Antimicrobial and cleaning effects of ultrasonic-mediated plasma-loaded microbubbles on *Enterococcus faecalis* biofilm: An *in vitro* study. *BMC Oral Health* 23, 133. doi:10.1186/s12903-023-02813-6

frontiers | Frontiers in Bioengineering and Biotechnology

TYPE Review
PUBLISHED 25 October 2023
DOI 10.3389/fbioe.2023.1303678

OPEN ACCESS

EDITED BY
Hongye Yang,
Wuhan University, China

REVIEWED BY
Peng Yin,
Capital Medical University, China
Samer Zaky,
University of Pittsburgh, United States

*CORRESPONDENCE
Changjun Zheng,
zhengchangjun9616@126.com

RECEIVED 28 September 2023
ACCEPTED 16 October 2023
PUBLISHED 25 October 2023

CITATION
Sui P, Yu T, Sun S, Chao B, Qin C, Wang J, Wang E and Zheng C (2023), Advances in materials used for minimally invasive treatment of vertebral compression fractures.
Front. Bioeng. Biotechnol. 11:1303678.
doi: 10.3389/fbioe.2023.1303678

Advances in materials used for minimally invasive treatment of vertebral compression fractures

Pengfei Sui, Tong Yu, Shouye Sun, Bo Chao, Cheng Qin, Jingwei Wang, Erwei Wang and Changjun Zheng*

Orthopaedic Medical Center, Second Hospital of Jilin University, Changchun, China

Vertebral compression fractures are becoming increasingly common with aging of the population; minimally invasive materials play an essential role in treating these fractures. However, the unacceptable processing-performance relationships of materials and their poor osteoinductive performance have limited their clinical application. In this review, we describe the advances in materials used for minimally invasive treatment of vertebral compression fractures and enumerate the types of bone cement commonly used in current practice. We also discuss the limitations of the materials themselves, and summarize the approaches for improving the characteristics of bone cement. Finally, we review the types and clinical efficacy of new vertebral implants. This review may provide valuable insights into newer strategies and methods for future research; it may also improve understanding on the application of minimally invasive materials for the treatment of vertebral compression fractures.

KEYWORDS

bone cement, minimally invasive surgery, vertebral compression fracture, biomaterial, vertebral implant

1 Introduction

A vertebral compression fracture (VCF) is defined as a reduction in the height of a single vertebral body by 20% or 4 mm (Black et al., 1999). It is caused by either trauma or a pathological process that causes bone destruction (such as osteoporosis and vertebral tumors). Although osteoporosis is the most common cause of VCFs, tumors, trauma, and infections are also commonly implicated (Liang et al., 2022). Their incidence is usually related to age, occurring in 30% of individuals aged more than 80 years and only 5%–10% of those aged younger (Beall et al., 2018). This condition is becoming increasingly common with aging of the population; approximately 1.5 million individuals are affected each year in the United States. VCF can lead to severe physical limitations including back pain, functional disability, and progressive kyphosis, and ultimately leads to a loss of appetite, malnutrition, and impaired lung function. Recent reports indicate that the thoracolumbar junction (T12 to L2) is the most commonly affected area, accounting for 60%–75% of cases; this is followed by the L2 to L5 region, which accounts for 30% of fractures (Hoyt et al., 2020). Low back pain is therefore the most common clinical manifestation; this severely affects function and quality of life (Ashammakhi et al., 2019). Conservative treatments including medications and physical support cannot offer effective pain control and functional recovery in the long term (Ong et al., 2018). In addition, patients are predisposed to the development of cardiorespiratory complications, which increase patient mortality. Surgery offers an alternative treatment modality for VCF; however, the inability to offer adequate

mechanical support often leads to residual postoperative pain. In patients with osteoporotic VCF, surgery is associated with a risk of pedicle screw loosening due to a reduction in bone quality and quantity (Girardo et al., 2019).

Percutaneous vertebroplasty (PVP) and kyphoplasty (PKP) are currently the most common modalities employed for the treatment of VCFs (Hoyt et al., 2020). The procedure involves puncture of the vertebral body with a needle and the injection of cement or other injectable biomaterials via a cannula. This surgical procedure re-stabilizes the height and kyphotic angle of the vertebral body, thereby offering rapid pain relief and an improvement in the quality of life (Roux et al., 2021). Polymethyl methacrylate (PMMA) is widely used in orthopedics and dentistry owing to its high mechanical strength, short setting time, rheological properties, and biocompatibility, making it the most commonly used injectable bone cement for PVP/PKP. However, non-degradability, lack of bioactivity, the presence of unreacted toxic monomers, and the need for high curing temperatures are some of the factors that lead to clinical complications (Martikos et al., 2019). This issue can be partially addressed by using injectable calcium phosphate bone cement (CPC), which has been used as an injectable material in orthopedic surgery due to its chemical similarity to bone and its ability to harden *in situ* (Deng et al., 2020). However, it is brittle and has uncontrollable porosity that does not allow ingrowth of bone; in addition, the paste decomposes when in contact with body fluids and has poor injectability. This led investigators to incorporate certain biomaterials that may enhance its properties (Le Ferrec et al., 2018). In this context, newer materials including magnesium phosphate bone cement (MPC) and calcium silicate (CSC) have been used for minimally invasive treatment due to their unique properties (Huang et al., 2019; Liu et al., 2022). In recent years, vertebral implants composed of implantable materials are being used in third-generation spinal augmentation systems for treating VCFs (Khan and Kushchayev, 2019). The process involves the placement of expandable implants via percutaneous puncture; these are placed either bilaterally or unilaterally through the pedicles. The transition from cement injection alone to the combined use of cement injection and vertebral body implants allows for effective restoration of the height of the collapsed vertebral body; it also improves restoration of vertebral kyphosis and reduces the risk of cement leakage (Moura and Gabriel, 2021). Four vertebral body implant systems are currently in common use; these include the Vertebral Body Stenting, SpineJack, Kiva, and Osseofix systems (Jacobson, 2020; Chang et al., 2021; Gandham et al., 2021; Vendeuvre et al., 2021). Notably, an individualized approach needs to be adopted for implantation; different implants need to be selected for different cases and anatomical locations.

Materials used for minimally invasive treatment of VCFs have been widely studied in recent years. However, their clinical application is limited by limitations of the materials used. In this review, we describe the various types of bone cement used for minimally invasive treatment of VCFs, starting from the most commonly used material, namely, PMMA; we also discuss their limitations. In addition, we enumerate the materials that are commonly used to improve the properties of bone cement (including bioactive ceramics (Gao et al., 2019), bioactive glass (Golubevas et al., 2017), nanomaterials (Miola et al., 2021), and natural or synthetic polymers (Guo et al., 2021a)) and elaborate on their beneficial impact on the properties of bone cement (Table 1). We additionally describe the types of novel vertebral implants and their clinical efficacy (Scheme 1). Finally, we discuss the prospects for the development of materials used for minimally invasive treatment of VCFs and the directions for further investigation.

2 Bone cement

Bone cement is widely used in orthopedics and other fields due to the properties of injectability and curing. The treatment of VCF primarily involves the injection of PMMA bone cement into the diseased vertebral body via a minimally invasive surgical approach (Zhu et al., 2020). Notably, other bone cement materials including CPC, MPC, and CSC are being increasingly investigated due to their unique properties.

2.1 Classification of bone cement

2.1.1 PMMA-based cement

PMMA, as a representative bone cement, is widely used in the treatment of VCFs due to its outstanding mechanical strength and biocompatibility (Sun et al., 2022b). In 2004, the United States Food and Drug Administration formally approved PMMA bone cement for the treatment of vertebral fractures caused by osteoporosis and tumors. It consists of solid and liquid phases; the PMMA bone cement is formed via an exothermic curing reaction after mixing of both phases. PMMA has become the most widely used material for minimally invasive treatment of VCFs due to its excellent mechanical properties, biocompatibility, and ability to act as a drug-carrying platform (Zheng et al., 2021). Despite its considerable success in clinical applications, it has certain limitations; these include excessive mechanical strength, the occurrence of an exothermic reaction, low viscosity, the lack of osteogenic activity, and the propensity to cause various clinical complications (Sue et al., 2019).

2.1.1.1 Excessive mechanical strength

Owing to the inherent excessive compressive strength and elastic modulus of PMMA, differences in mechanical strength between PMMA and the adjacent vertebral bone may easily lead to fractures in the latter following injection. Finite element analysis suggests that filling the vertebrae with bone cement may significantly alter their stiffness and lead to shifting of load on to the intervertebral disc; this may be responsible for fractures in the adjacent vertebrae (Baroud et al., 2003). Clinical findings have shown that injecting excessive amounts of cement during vertebral kyphoplasty may increase the risks of postoperative vertebral re-fracture (Zhai et al., 2021); in this context, Hu et al. (2019) concluded that injection of more than 40.5% of cement resulted in fractures of the adjacent vertebrae. However, some investigators believe that adjacent vertebral fracture represents a natural evolutionary process in patients with osteoporosis or neoplastic disease, and is not related to the injected PMMA. Notably, several studies have shown that the mechanical properties of PMMA are reduced by mineralized collagen and other materials; clinical results from studies using these cement composites have indicated a significant reduction in

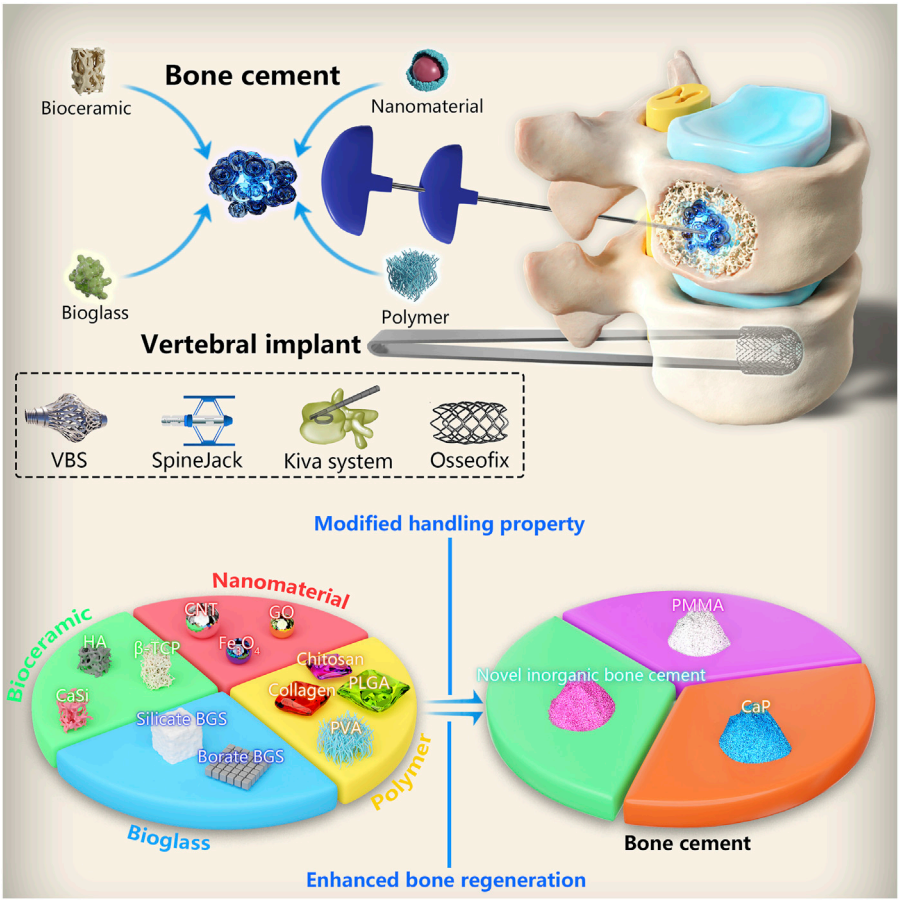

SCHEME 1
Classification of materials used for minimally invasive treatment of vertebral compression fractures and modification of bone cements.

the incidence of postoperative adjacent vertebral fractures (from 13.3% to 2%) (Wang et al., 2018a). We therefore believe that it is essential to modify PMMA. In this context, a common approach used for reducing the excessive mechanical strength involves the addition of polymers. The degradation and absorption of these materials lead to the formation of pores within the PMMA and effectively reduce the mechanical strength (Tavakoli et al., 2020).

2.1.1.2 Excessive exothermic reaction

The exothermic reaction associated with polymerization of bone cement can reach temperatures of between 70°C and 120°C, resulting in thermal burns of the surrounding tissue (De Mori et al., 2019). Severe damage to neuromuscular structures have been reported; these can lead to serious complications including paralysis, bleeding, and even death. Bone necrosis and the resultant fiber healing caused by thermal injuries may weaken the interface between the implant and host bone; this may lead to aseptic loosening of the implant (Stoops et al., 2022). Appropriate temperature reduction can be achieved by decreasing the amount of PMMA powder; however, this tends to prolong setting times and reduce the viscosity of bone cement, thereby increasing intraoperative manipulation times and the risk of postoperative cement leakage. The incorporation of biocompatible materials such as polymers, linseed oil, and metamorphic materials may allow absorption of the excess heat generated by polymerization and achieve significant improvement (Lv et al., 2015; Tai et al., 2016; De Mori et al., 2019).

2.1.1.3 Low viscosity

Leakage of bone cement due to low viscosity is a common postoperative complication. Entry into blood vessels can lead to serious consequences including compression of the spinal cord and nerve damage, pulmonary embolism, and cardiac perforation (Hsieh et al., 2019; Naud et al., 2020; Zhang et al., 2022). Guo et al. retrospectively analyzed data from 1,373 patients who underwent PKP and demonstrated significant leakage from the paravertebral venous plexus to be an important risk factor for pulmonary embolism (Guo et al., 2021b). Although symptoms are not observed in most cases, the consequences are often fatal (Hassani et al., 2019). In their retrospective study, Wang et al. found the use of high-viscosity bone cement in PVP/PKP to be a potential option for reducing the risk of leakage (Wang et al., 2022). Similarly, Zhang et al. observed a lower risk of intervertebral disc space or venous leakage with high-viscosity cement (Zhang et al., 2018b). Investigators added polyvinyl alcohol (PVA) to increase the viscosity of PMMA bone cement and prevent cement leakage; the introduction of ethylene via the surface of the PVA membrane allowed the glycidyl methacrylate-PVA membrane to firmly adhere to PMMA-based bone cement. This enabled the cement to

covalently react with the PVA membrane (Zhang et al., 2018b). Gelatin particles can also be incorporated to achieve this purpose; notably, particle size and polymer density also regulate cement viscosity (Meng et al., 2013).

2.1.1.4 Lack of bioactivity

As PMMA lacks bioactivity, the major inorganic phases of natural bone are less likely to form on the surface of this polymer; in addition, its surface is not conducive to osteoblast adhesion, proliferation, and differentiation. The formation of a fibrous layer at the PMMA-bone interface prevents direct bone contact, leading to loss of the interface between cement and bone; this further contributes to cement loosening in the postoperative period (Freeman et al., 1982). In their retrospective study, Nakamae et al. found that 25% of patients developed cement loosening after 6 months of PVP; patients with cement loosening had significantly higher mean visual analog scale scores than those without loosening (Nakamae et al., 2018). The incorporation of bioactive materials such as hydroxyapatite (HA) into PMMA represents a good strategy for improving the bioactivity of the latter and enhancing bonding between cement and bone. These materials can allow direct chemical bonding between bone and PMMA cement to enhance interface stability and enhance osteoconductivity (Choi et al., 2010).

2.1.2 Calcium phosphate-based cement

Bone is an organic-inorganic tissue and is composed primarily of collagen and calcium phosphate apatite crystals (Wang et al., 2020a). CPC has a natural affinity for bone tissue, as it resembles the inorganic components of bone. It has become the focus of new developments in injectable bone cement owing to its bioactivity, biocompatibility, osteoconductivity, injectability, and rapid setting time. However, its material properties are relatively immature and there are obvious limitations to its use; investigators are therefore attempting to address these major issues (Klein et al., 2017).

2.1.2.1 Insufficient mechanical properties

Inadequacies in the mechanical property of CPC remain one of the main reasons limiting its application. As per the specifications of International Organization for Standardization 5,833, bone cement needs to have a compressive strength of ≥70 MPa; however, CPC often fails to meet this standard (Schroeter et al., 2020). In addition, the load applied to human bones includes a complex combination of compression, tension, torsion, and bending; parameters such as compressive strength alone often do not accurately reflect the ability of CPC to resist fracture under cyclic loading in clinical settings (Paknahad et al., 2020). As CPC is an inorganic salt material, it is highly brittle; this may make it susceptible to fatigue from cyclic loading and destruction during long-term implantation in the human skeleton. This represents a major limitation that restricts its use in load-bearing sites (Ding et al., 2021). In addition, its low fracture toughness makes CPC considerably sensitive to the presence of defects and imperfections (e.g., porosity); this exacerbates crack propagation. Therefore, the brittleness of CPC and its mechanical properties can be effectively improved by either modifying its microstructure (e.g., porosity and pore size) or activating toughening mechanisms (increasing the resistance to crack extension by using processes such as fiber reinforcement) (Gong et al., 2023).

A denser and more homogeneous matrix composed of smaller crystals is needed to produce smaller pores; this may improve mechanical properties while preserving inward bone growth and other key biological properties. Factors such as porosity, pore size, and particle size of the initial material are key to the mechanical properties of CPC (Lu et al., 2019). In addition to the mentioned effects of densification and homogenization of the cement matrix, the incorporation of fibers or polymers into CPC can enhance mechanical properties. Similar to fiber reinforcement in civil engineering, this is mainly based on three mechanisms: fiber bridging, crack deflection, and friction sliding (Li et al., 2020b). The fibers bridge the cracks to resist their further opening and propagation as the matrix begins to fracture. Crack deflection of the fibers extends the distance over which the cracks propagate; this leads to expenditure of more energy on the newly formed surface. Frictional sliding of the fibers against the matrix during drawing further consumes the applied energy and increases fracture resistance of the composite (Kucko et al., 2019).

2.1.2.2 Poor degradability

CPC is a highly interconnected and porous material; it is almost exclusively composed of micropores and lacks a macroporous structure. The pores in CPCs can be categorized according to their size; micropores have an inner pore width of 100 μm and have a positive impact on the biological response, as they allow protein adsorption, cell attachment, and permeability of the implanted material to body fluids, all of which play a crucial role in promoting osteogenesis. However, the lack of interconnected macropores (exceeding 10 μm) in CPCs hinders angiogenesis and inward tissue growth; it can only be degraded layer-by-layer. This limits degradation at the bone-implant interface and thereby hinders the degradation process (Vezenkova and Locs, 2022). In order to improve CPC degradation, its porosity is controlled by optimizing its material structure. The porosity can be effectively increased by changing the particle size and liquid-powder ratio of the CPC powder phase. The use of powders with smaller particle-size and smaller liquid-to-powder ratios results in ample formation of smaller pores during the crystallization reaction (Lodoso-Torrecilla et al., 2021; Lofrese et al., 2021). Large pores may be introduced into CPC by adding water-soluble and polymeric pore-forming agents (Lu et al., 2021). Polymeric pore-formers are added to the CPC paste as a second solid phase. After curing of the CPC, these polymeric pore-formers begin to degrade and produce macroporous CPC composites; notably, these polymers confer unique properties, such as improved osteogenesis. In this context, CPC should ideally degrade at an appropriate rate to allow for concomitant new bone formation.

2.1.2.3 Poor injectability

The poor injectability of CPC is one of the main factors that limit its use in PVP and PKP procedures. The higher liquid content in uncured CPC leads to lower viscosity, lower cohesion, increased setting times, and lower mechanical strength. This subsequently leads to extravasation of bone cement from the surgical site, leading to complications such as pulmonary embolism. This possible deviation of the actual composition of the extruded paste may be

attributed to the filtration pressure, which affects the injectability of CPC pastes (Habib et al., 2008). During the construction of an injectable model, Bohner and Baroud found that the reduction of extrusion pressure (by increasing fluidity) and permeability of the paste improved cement injectability. Certain changes were made to the cement to address these two issues; the average particle size was reduced, the liquid-solid ratio was increased, round and de-agglomerated particles were used, a wide particle size distribution was adopted, ions or polymers were added to minimize particle interactions, and the viscosity of the mixture was increased (Bohner and Baroud, 2005). Ishikawa et al. observed that CPC pastes made from round particles could be injected more easily than those made from irregular particles (Ishikawa and Asaoka, 1995). However, in view of the favorable effect of high viscosity on resistance to disintegration, the latter two strategies appear to be the most appropriate for improving cement injectability. The addition of binders may also effectively reduce phase separation; however, this can result in several undesirable consequences, such as an increase in the force required for injection and a decrease in mechanical properties (Schickert et al., 2020b).

2.1.2.4 Poor cohesion

Cohesion represents the ability of CPC to harden and maintain the integrity of the cement paste in a static aqueous environment without disintegrating into small particles; it prevents attrition of the paste by the surrounding liquid (Vezenkova and Locs, 2022). The cohesion of CPC paste often depends on the forces between the constituent particles and the interaction between the paste and the surrounding fluid. Spatial stabilization is usually associated with the presence of dissolved polymers on the surface or space between particles. Thus, the addition of polymers can spatially stabilize the cement paste and increase cohesion. Increasing the viscosity of the mix is another effective approach for increasing cohesion. Numerous biopolymers, including hydroxypropyl methylcellulose and starch, have been blended into powders or liquids of CPC (Liu et al., 2014; Tian et al., 2021). Small amounts of these biopolymers can significantly improve cohesion and erosion resistance of CPC. However, although these viscous solutions may significantly improve paste cohesion, they may affect the setting time and mechanical properties in certain cases.

2.1.3 Novel inorganic bone cement

The study of magnesium phosphate for bone cement is a relatively recent development. The excellent osteogenic and vasculogenic properties of MPC are the key factors that contribute to its use in research; these factors are mainly attributed to magnesium ions, which exert an osteogenic effect via the activation of osteoblast activity. They promote the proliferation of osteoblasts via the mitogen-activated protein kinase/extracellular signal-regulated kinase signaling pathway by increasing phosphorylation of the latter (thereby enhancing the level of c-FOS) and inducing the phosphorylation of glycogen synthase kinase-β (thereby enhancing the level of β-conjugated proteins) (Wang et al., 2018b). Magnesium ions also promote osteogenesis by promoting angiogenesis (Zhang et al., 2021). Recent studies have found that depletion of magnesium content is associated with low bone mineral density, reduced bone progression, the development of osteoporosis, and skeletal improvement; they have also found that higher magnesium intake effectively inhibits a reduction in bone mineral solids in patients with osteoporosis. In this context, a magnesium alloy was found to release magnesium ions after implantation in osteoporotic rats; this increased bone morphogenetic protein 2-related osteogenesis and reduced the deleterious effects of osteoporosis (Guo et al., 2013). The localized release of magnesium ions from magnesium implants in an animal model of osteoporosis was also found to contribute to the formation of a condensate around the implant; significantly higher volumes of new bone were observed in magnesium-containing specimens (Galli et al., 2018). Although MPC does not currently meet the criteria for clinical application in terms of handling properties, it can be improved considerably by employing a wide variety of modifications. Its mechanical properties allow it to withstand loads of up to 112 MPa; this is equivalent to the mechanical strength of human cortical bone (Liu et al., 2022). Liu et al. demonstrated the acceptable injectibility and filling properties of MPC; they injected MPC into 3 dimensional-printed artificial vertebral bodies and porcine spine models and were able to achieve a good distribution. This could allow it to be successfully used in PVP/PKP or for filling other bone defects (Liu et al., 2023). Chitosan has been added to MPC to improve its handling properties; chitosan-MPC has a longer setting time, lower reaction temperature, higher strength, and more neutral pH than MPC (Yu et al., 2020).

CSC has also been used in orthopedic applications due to its superior biocompatibility and bone regeneration properties, which are similar to those of MPC. CSC generates less heat during the exothermic curing reaction and demonstrates superior bioactivity, excellent osteoconductive activity, and degradability. Huang et al. proposed a method to synthesize biodegradable calcium silicate cement by incorporating strontium into cement through solid-state sintering. The degradation rate of the cements increased with increasing content of strontium, consequentially raised the levels of released strontium and silicon ions. The elevated dissolving products may contribute to the enhancement of the cytocompatibility, alkaline phosphatase activity and osteocalcin secretion (Huang et al., 2019). Furthermore, the MPC/CS composite bone cement demonstrated apatite mineralization ability and osteogenic potential. This composite was experimentally shown to stimulate the proliferation of MC3T3-E1 cells (Liu et al., 2022). However, it demonstrates poor scour resistance, deficiencies in mechanical properties, and long curing times. These deficiencies limit its application as a clinical material and warrant modification (Zanfir et al., 2019).

3 Materials used to improve bone cement

3.1 Bioceramics

Bioactive materials are defined as those that stimulate a beneficial response in the body, especially in terms of binding to host tissues (Jones, 2013). Bioactive ceramics and glass have been added to bone cement due to their superior biocompatibility and osteogenic capacity. Traditional bioactive ceramics such as HA, β-tricalcium phosphate (TCP), and calcium silicate ceramics have

TABLE 1 Summary of bone cements and modified materials.

Category	Disadvantages	Modifications
Polymethyl methacrylate cement	Excessive mechanical strength	Chitosan, Collagen
	Excessive exothermic reaction	Chitosan, Collagen, Hyaluronic acid
	Low viscosity	Linseed oil, Silk fibroin, Polyvinyl alcohol
	Lack of bioactivity	Chitosan, Collagen, Hyaluronic acid, Bioglass, Bioceramics, Layered double hydroxide
Calcium phosphate cement	Insufficient mechanical properties	Carbon nanotubes, Polyvinyl alcohol, Graphene oxide
	Poor degradability	Chitosan, Hyaluronic acid
	Poor injectability	Collagen, Hyaluronic acid, HPMC
	Poor cohesion	Hyaluronic acid, Starch, HPMC, Chitosan
Calcium sulphate bone cement	Poor washout resistance	Gelatin, Polyvinyl alcohol
	Low compressive strength	Carbon nanotubes, Graphene oxide
	Longer setting time	Silk fibroin, Chitosan
Magnesium phosphate cement	Poor washout resistance	Hyaluronic acid, Gelatin, Chitosan
	Low compressive strength	Bioceramics, Graphene oxide, Bioglass
	Longer setting time	Hyaluronic acid, Chitosan

been widely used in the modification of bone cement (Liu et al., 2023b) (Figure 1).

HA has been used as an inorganic filler in bone cement to improve its biocompatibility, as it has a chemical composition and crystal structure similar to that of apatite found in human bone tissue. HA is highly osteoinductive; this promotes chemical interactions with osteoblasts and the local microenvironment and thereby promotes the formation of new bone (Thorfve et al., 2014). In terms of processing properties, researchers have extensively investigated the feasibility of combining HA/brushite with PMMA. Aghyarian et al. prepared two composite bone cements, namely, HA-PMMA and brushite-PMMA, and found that the addition of both materials increased cement viscosity. These cements also exhibited high shear thinning, which aided injection (Aghyarian et al., 2014) and an appropriate increase in compressive strength. They subsequently prepared bone cement with various concentrations of brushite; PMMA was replaced by a 40% mass concentration of brushite to prepare dual solution cement, which could provide an optimal combination of the studied properties. The cement was viscous, highly injectable, and had high compressive strength (Rodriguez et al., 2014). Further characterization was performed in porcine vertebral bone and in two functional cadaveric spinal units, where the biomechanical properties of calcium phosphate-PMMA were found to be comparable to those of commercial bone cement; this indicated excellent prospects for clinical application (Aghyarian et al., 2015; Aghyarian et al., 2017). Although β-TCP demonstrates a good dissolution rate and bone regeneration capacity, the mechanical strength of TCP/PMMA composite bone cement was found to be lower than that of its conventional counterpart; it therefore failed to meet the enhancement requirements of clinical implants (Yang et al., 2015). Biphasic calcium phosphate, a mixture of β-TCP and HA, can effectively harmonize the properties of both materials. Its implantation improves biodegradability of TCP, leading to supersaturation of the local microenvironment with calcium and hydrogen phosphate; this accelerates the formation of calcium-deficient HA microcrystals, ultimately promoting mineralization of the extracellular matrix and subsequent generation of new bone during healing (Zhang et al., 2018a).

Calcium silicate bioceramics are being increasingly investigated as potential novel bioceramic materials for bone grafting, as their osteogenic properties are superior to those of HA (Vallet-Regi and Arcos, 2005). Several studies have shown that in a physiological environment, silicon ions released from calcium silicate ceramics play an important role in promoting bone regeneration by stimulating the proliferation of mesenchymal stem cells, osteogenic differentiation, and osteoblastic gene expression (Lin et al., 2015). In their study using a goat vertebral defect model, Sun et al. used new PMMA/calcium silicate hybrid cements for PVP and PKP; these cements optimally filled and stabilized vertebral defects and significantly promoted new bone formation in defective vertebrae at 6 months after injection (Sue et al., 2019). However, silicate bioceramics offer insufficient mechanical strength due to degradation. A series of silicate-based bioceramics have therefore been developed, including those that incorporate iron, magnesite, akermanite ($Ca_2MgSi_2O_7$, AKT), and tremolite ($CaO\text{-}MgO\text{-}2SiO_2$) (Chen et al., 2015b; Choudhary et al., 2020). The compressive strength of akermanite/PMMA composite bone cement is approximately 100 MPa, which is comparable to that of commercial PMMA bone cement (at 73–120 MPa) (Chen et al., 2015b). Notably, the compressive strength and Young's modulus of PMMA-diopside composites match the lower limit of those of cancellous bone (Choudhary et al., 2020).

3.2 Bioglass

Bioactive glass (BG) includes glass that can produce a specific biological response at the material-bone interface and promote

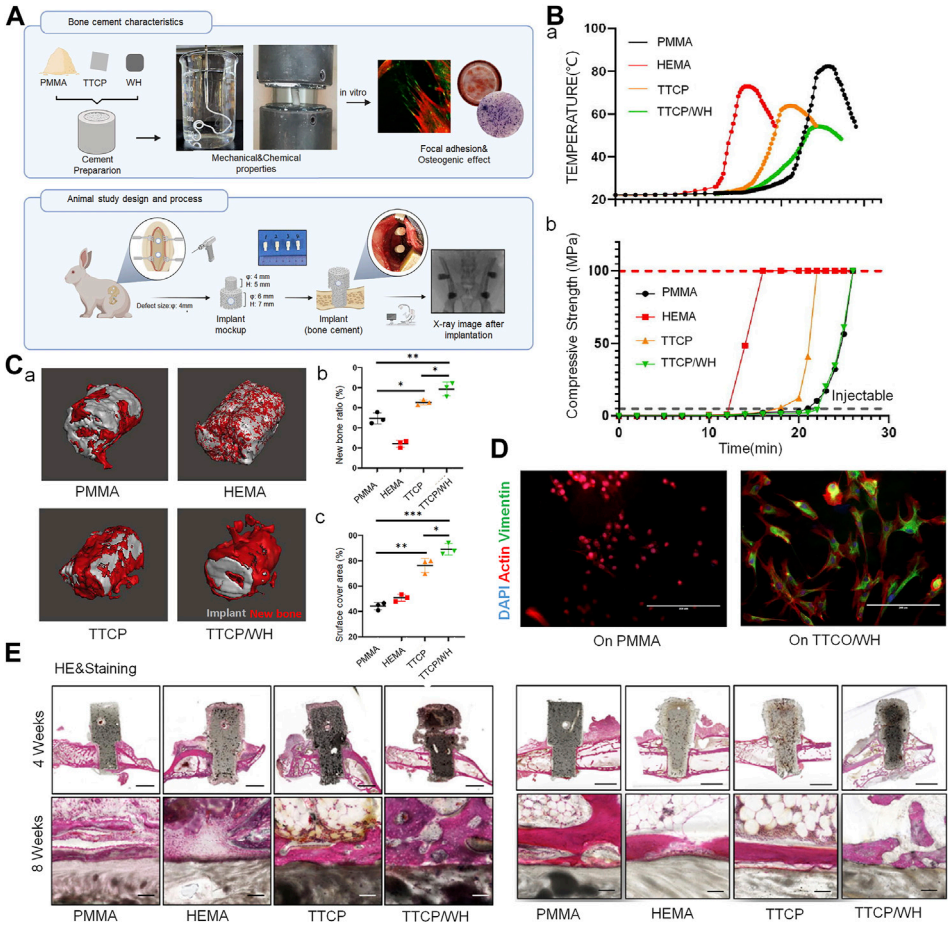

FIGURE 1
Bioactive ceramics as bone cement additives for enhancing osseointegration and bone regeneration. **(A)** Bone cement preparation and study design of *in vitro* and *in vivo* models. **(B) (A)** Temperature measurement of cement from mixing to setting. **(B)** Compressive strength measurement of cement during reaction. **(C)** (a) New bone formation around implanted scaffolds. (b) New bone generation ratio and (c) new bone covered area of cement scaffold at 4 weeks after implantation into bone defect. **(D)** Actin, vimentin and DAPI immunostaining of BMSCs after seeding on cement scaffold. **(E)** Representative histological findings from implant sites at 4 weeks (sagittal plane) and 8 weeks (coronal plane) post-implantation (the scale bar = 4 mm and 100 μm); hematoxylin and eosin stain.

efficient bonding between them (Shearer et al., 2023). Silicate and borate BGs are the most commonly used. Notably, BGs bond to bone faster than other bioceramics (Zhang et al., 2022a) (Figure 2). The process of osseointegration begins with the release of silica ions from the surface of the BG; the released ions form a layer of silica on the surface and then form an amorphous calcium phosphate precipitate, which initiate the formation of a HA layer that bonds to the bone cortex, further activating cell migration and triggering new bone formation (Cole et al., 2020a). Its osteogenic properties are an area of considerable interest as its dissolution products stimulate bone progenitor cells at the genetic level (Rahaman et al., 2011). BG stimulates bone formation by polarizing macrophages from the M1 to M2 phenotype and thereby increasing the activity of relevant genes. M1 macrophages produce pro-inflammatory cytokines and exhibit strong microbicidal properties in the early stages of inflammation. However, in the later stages of bone regeneration, persistent and excessive inflammation hinders complete local bone tissue remodeling. M2 macrophages produce anti-inflammatory cytokines to promote the tissue healing process. Therefore, regulation of the transition from M1 to M2 phenotypes represents a crucial step in the process of bone regeneration (Gomez-Cerezo et al., 2018). In this context, an alkaline environment may enhance bone formation in osteoporosis by inhibiting osteoclast activity and increasing osteoblast viability. A moderately alkaline pH of 7.8–8.5 has been reported to provide a favorable environment for new bone formation (Ding et al., 2023). Numerous researchers have prepared novel BGs that release boron and strontium ions, which create an alkaline environment; this is of particular significance in the treatment of osteoporotic VCFs. In their study on osteoporotic rabbits, Chen et al. constructed a porous injectable composite by combining silicate BG with PMMA; they found that injection of the composite into the vertebrae of the rabbits increased the bone volume fraction (trabecular bone to total bone volume) from 28.27% ± 1.69% to 38.43% ± 1.34% (Chen et al., 2015a). Hu et al. also reported similar findings in an osteoporotic rabbit model. The application of BG-modified CPC to the bone defects resulted in significant upregulation of osteogenic marker expression (including Runx2, alkaline phosphatase, osteopontin,

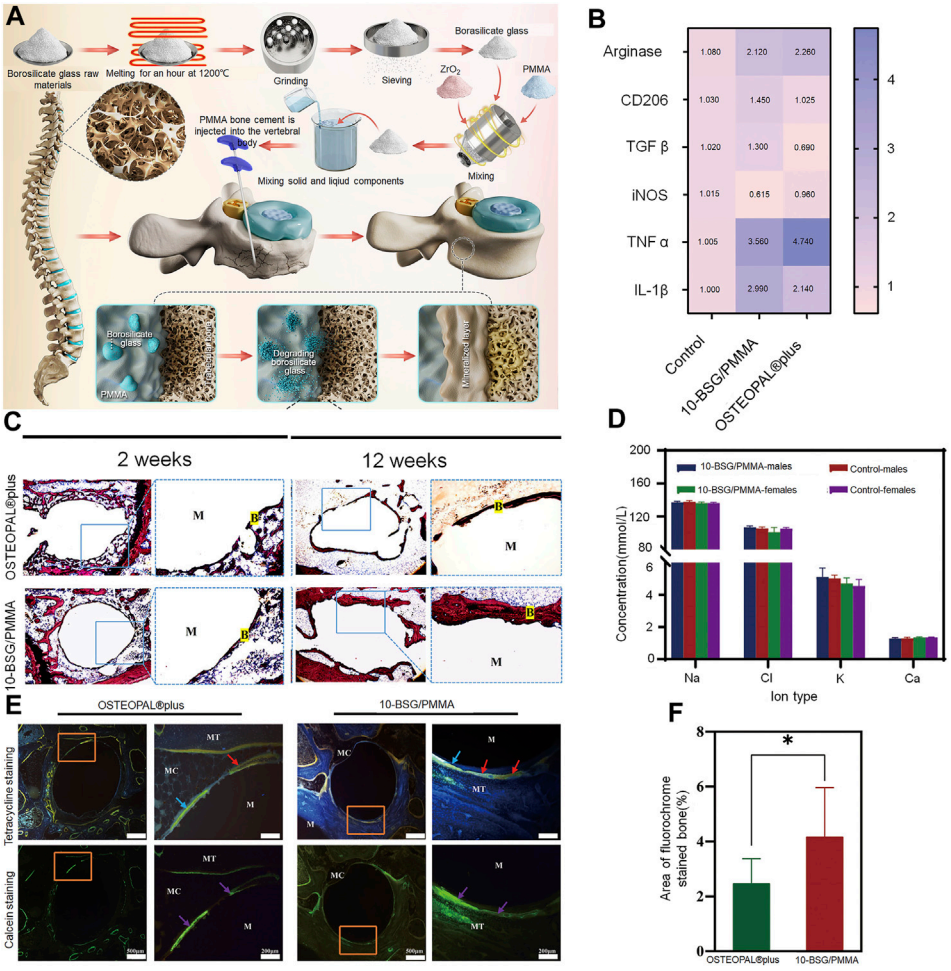

FIGURE 2
Borosilicate glass (BSG)-reinforced PMMA bone cement used for vertebroplasty. **(A)** Schematic diagram illustrating the preparation of BSG/PMMA cement and the its use for promoting bone repair. **(B)** Expression of pro-inflammatory genes and anti-inflammatory genes after culture with 10-BSG/PMMA or OSTEOPAL® plus cement for 3 days. **(C)** Van Gieson staining of rat tibia defects after 2 and 12 weeks of cement implantation. The images on the left and right are from the same group; they represent the overall picture and the partial images. **(D)** Results of subchronic systemic toxicity in the experimental and control groups, including rat serum electrolyte indices at different time points. **(E)** Overall and partial images of sequential fluorescence staining, and **(F)** semi-quantitative evaluation of new bone formation based on calculation of the area with fluorescent staining (as determined from panel **E**). Results are shown as means ± standard deviation (*: $p < 0.05$). Copyright © 2022, American Chemical Society.

and osteocalcin) and a significant decrease in osteoblastic marker expression (including tartrate-resistant acid phosphatase, matrix metalloprotease 9, and histone K) in the osteoblasts (Hu and Xu, 2019).

Although numerous experiments have demonstrated that the addition of BG sufficiently enhances the bioactivity of bone cement, it impacts the mechanical properties (including injectability) of the cement. In this context, borate-based BG demonstrates a controlled degradation rate; the bioactivity and degradation rate of borosilicate-based BG can be regulated by the introduction of variable quantities of boric oxide to match the growth rate of new bone tissue (Cui et al., 2016). In their study, Cole et al. added borate-based BG to PMMA; long-term dissolution of BG could be achieved without affecting short-term degradation. Ion release was also maintained without affecting mechanical strength. The compressive properties remained higher than those required by the American Society for Testing and Materials and International Organization for Standardization (Cole et al., 2020b). BG also enhances the compressive strength of CPC, as it becomes smaller and denser after pore sintering; this increases the compressive strength of HA/BG composites. This increase improves its load-bearing capacity and implant stability in the tissue (Ebrahimi and Sipaut, 2021). BG also improves the initial and long-term compressive strength of calcium sulfate bone cement and demonstrates good injectability and controlled setting times; all of these make it suitable for vertebral augmentation (Mansoori-Kermani et al., 2023). However, the introduction of BG adversely affects the handling properties of bone cement to varying degrees. A decrease in BG particle size has been found to reduce injectability of the cement. The fine BG particles agglomerate and absorb more water; this increases the friction between them. The setting time of formulated cement also increases significantly with a decrease in BG particle size, as the cohesion in the cement paste weakens (Hasan et al., 2019; Mabroum et al., 2022).

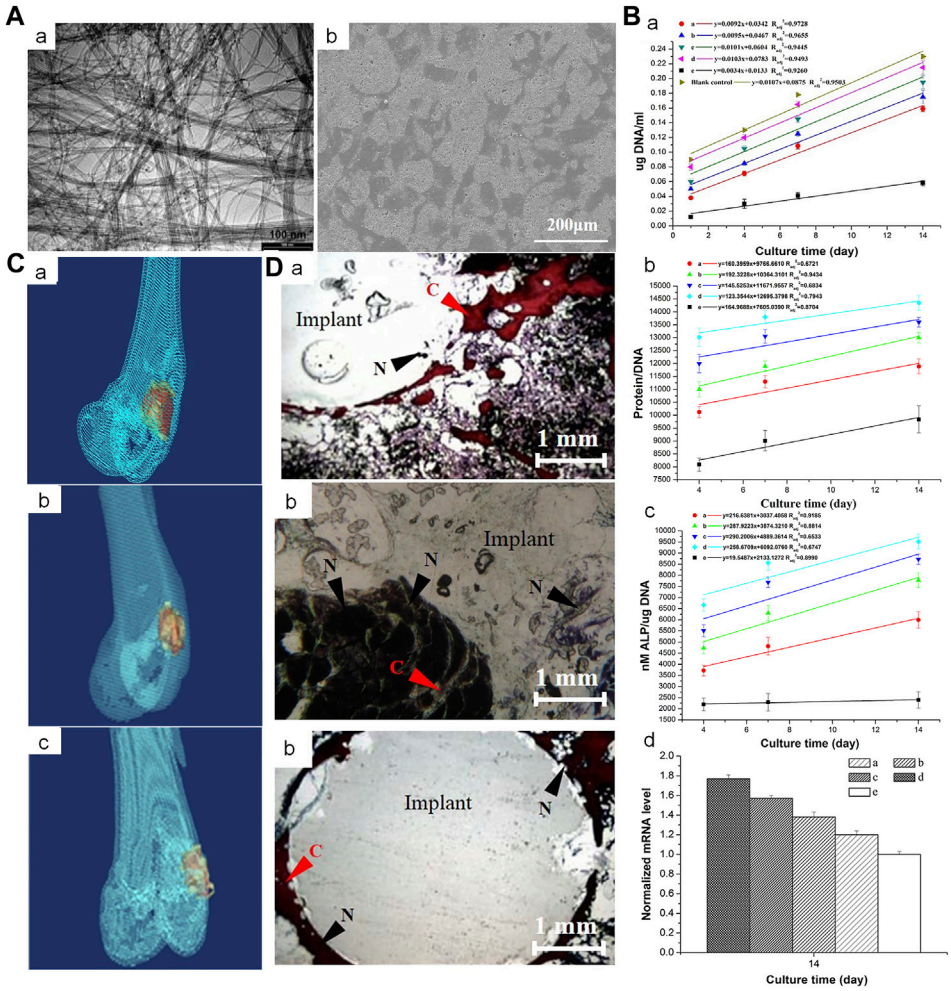

FIGURE 3
Incorporation of multi-walled CNTs into PMMA bone cement improves cytocompatibility and osseointegration. **(A)** (a) Transmission electron microscopy image of NC3151 grade multi-walled CNT. (b) Scanning electron microscope images of PMMA bone cement loaded with multi-walled CNT powder affecting the proliferation of rabbit BMSCs. **(B)** (a) deoxyribonucleic acid (DNA) content, (b) Protein/DNA content and (c) ALP/DNA (mean ± SD) of the rabbit BMSCs when exposed to blank control and PMMA bone cements loaded with different concentrations of multi-walled CNT powder. **(C)** 3-dimensional reconstruction of computed tomography images of PMMA-multi-walled CNT bone cement specimens from Group D after 4, 8, and 12 weeks. **(D)** Van Gieson-stained images of PMMA-MWCNT bone cement specimens from group D (1.0 percent by weight) after 4, 8, and 12 weeks: (a) 4 weeks, (b) 8 weeks, (c) 12 weeks. Collagen fibers **(C)** are stained red. The nucleus (N) is stained brown-black.

3.3 Nanomaterials

3.3.1 Carbon nanotubes

Carbon nanotubes (CNTs) can significantly improve the mechanical properties of bone cement. This may be mainly attributed to certain unique properties including nanoscale diameters, longer length, higher strength and stiffness, and considerably high aspect ratios. Multi-walled CNTs prevent cracks in the cement from expanding; they provide a bridging effect at the tails of the crack in a direction perpendicular to that of crack expansion. In their study, Sadati et al. found that the incorporation of 0.5% of multi-walled CNTs into PMMA significantly increased tensile strength, elastic modulus, and bending strengths by 37%. The finite element method was used to simulate the bridging mechanism of PMMA/multi-walled CNT nanocomposites (Sadati et al., 2022). Combining the functionalized CNTs with PMMA significantly reduces the high polymerization temperature of PMMA. The reduction in generated heat translates to a reduction in the thermal necrosis index value of the corresponding nanocomposite cement; this may reduce the high temperatures *in vivo* and decrease the possibility of heat-induced bone tissue necrosis induced by polymerization of PMMA cement. In their study, Ormsby et al. found that the addition of functionalized multi-walled CNTs led to a significant reduction in the quantity of heat generated by the exothermic polymerization reaction of PMMA bone cement; it also significantly reduced thermal necrosis index values from 3% to 99% (Ormsby et al., 2011). Mabroum et al. had combined CNT with commercial bone cement; they also observed a significant reduction in the heat generated by the exothermic polymerization reaction of Simplex PTM bone cement. They suggested that the carboxylated multi-

walled CNTs acted as a heat trap in the bone cement matrix to reduce the generated heat (Ormsby et al., 2014).

The possibility of nanotoxicity needs to be considered in the case of CNT-based biomaterials (Wang et al., 2019) (Figure 3). Pahlevanzadeh et al. incorporated CNT into PMMA-monticellite bone cement; they found that the cement retained good bioactivity after incorporation of CNT, as evidenced by the absence of cytotoxic effects in MG63 cells (Pahlevanzadeh et al., 2019). Similarly, the addition of CNT to MPC exerted no cytotoxic effects; the cells exhibited appropriate adhesion to the bone cement and acceptable proliferation (Esnaashary et al., 2020). However, Medvecky et al. reported conflicting results; their experiments, that involved material testing and live/dead staining of CNT-CPC, suggested that multi-walled CNT composite cement surfaces were cytotoxic (Medvecky et al., 2019). Notably, some believe that an optimal CNT content is required for cellular activity. An increase in the concentration of CNT in PMMA nanocomposites allows for adequate survival and proliferation of mesenchymal stem cells (MSCs) on their surface; the cell density decreases significantly when the number of CNTs exceeds 0.25 percent by weight (Sadati et al., 2022).

3.3.2 Graphene oxide

As graphene has a lower metal impurity content than CNTs, the purification processes for removal of trapped nanoparticles require less time. Based on the method of fabrication, graphene can be categorized into numerous subtypes; these include graphene, graphene oxide (GO), and reduced GO, which is of particular interest. GO has a larger number of hydrophilic groups than simple CNT and graphene; these allow it to form chemical bonds (between functional groups) with molecules in the bone cement. This facilitates good dispersion, thereby enhancing mechanical strength and improving biological properties. In their study, Paz et al. loaded different proportions of graphene and GO onto PMMA; they found that the PMMA cement with a lower load of graphene or GO powder (≤0.25 percent by weight) showed significantly superior fracture toughness and fatigue properties (Paz et al., 2017). In addition, GO powder demonstrated greater dispersion and improvement in mechanical properties than those obtained with graphene powder. In their study, Arici et al. compared the mechanical properties and cellular activity of CNT with those of GO. They found that GO further improved the percentage of cell viability, conferred superior mechanical properties, and offered a more stable pH and cell viability than CNT; this may be attributed to the larger surface area of GO (Arici et al., 2023). The introduction of GO has also been found to improve cell viability and osteogenic differentiation. All anabolic genes including *COL1A1*, *BMP4*, *BMP2*, *RUNX2*, and *ALP* demonstrate stimulatory effects, while catabolic genes (*MMP2* and *MMP9*) exert inhibitory effects (Mirza et al., 2019). Another mixing approach involves the incorporation of hybridized GO/CNT into bone cement. This approach offers better dispersion properties than CNTs and GO alone; it also shortens the final setting time and reduces the mobility of MPC. In this context, a study showed that the addition of 13.77% GO/CNTs (by weight of cement) increased the compressive and flexural strength of MPC by 17.50% and 0.05%, respectively (Du et al., 2020).

3.3.3 Magnetite (Fe_3O_4)

The combination of nanomaterials with PMMA represents an important area of interest in the treatment of tumor-induced VCFs. While the PMMA implanted in the fracture site plays a role in supporting the fractured vertebrae and relieving pain, the magnetic nanomaterials act as heat-seeded materials in magnetic thermotherapy; they generate heat due to loss of magnetism in the presence of an external magnetic field (Yu et al., 2019) (Figure 4). Heating of the cancerous area to temperatures of over 42°C kills the cancer cells, while allowing normal cells to survive. Magnetite is well suited for use as a heat seed material due to its excellent heat-generating properties and biocompatibility. In their study, Ling et al. placed PMMA-Fe_3O_4 in an *ex vivo* magnetic field; the increase in temperature of resected bovine liver was found to positively correlate with the iron content and time. This suggested that the intratumoral temperature is controllable (Ling et al., 2017). However, as the heat generated by magnetothermic materials may damage surrounding healthy tissues (especially the spinal cord), Harabech et al. evaluated the heating effect of Fe_3O_4 nanomaterials in bovine vertebrae in an *ex vivo* alternating magnetic field. The temperature in the PMMA-magnetic nanoparticle composite rose by approximately 7°C; however, that in the spinal column only rose by only 1°C, thereby creating a smaller thermal impact on the spinal cord (Harabech et al., 2017). Although Fe_3O_4 demonstrates excellent heat generation properties as a magneto-thermal material, its rate of warming and bioactivity need to be improved. Certain investigators have attempted to increase the weight percentage of magnetic nanoparticles in PMMA in order to improve the magneto-thermal efficiency of nanomaterials. However, an inappropriately high weight ratio of magnetic nanoparticles affects the physicochemical properties and increases cytotoxicity (Miola et al., 2021). Ren et al. attempted to improve performance by adding 1 percent by weight of $Zn_0.3Fe_2.7O_4$ nanoparticles to PMMA; in addition to providing reliable mechanical support, the resulting bone cement demonstrated high thermal efficiency (Ren et al., 2022). The wrapping of Fe_3O_4 with GO (which has superior thermal conductivity) addresses the important issue of non-uniform heating of magnetic thermal materials; this allows for more rapid heating of the composite materials and achievement of thermal equilibrium. This shortens the time of thermal therapy and reduces heat-resistance caused by an excessively long heating time (Yan et al., 2019).

3.3.4 Other nanomaterials

Layered double hydroxide has recently provoked considerable interest owing to its excellent properties. Liquid MMA monomer was added to the pre-polymerized PMMA and powders of COL-I and/or LDH, and the polymerization reaction of MMA was initiated at room temperature (25°C) for 20 min after the powders were thoroughly mixed. It demonstrates outstanding thermal insulating properties, which may inhibit thermal diffusion during the polymerization reaction of methylmethacrylate and help protect the surrounding osteoblast-associated cells. In addition, the magnesium ions released by LDH promote osteogenesis. The larger micro sheets of layered double hydroxide are able to produce a certain number of holes on the surface of PMMA; this is beneficial for osseointegration between cement and bone (Wang

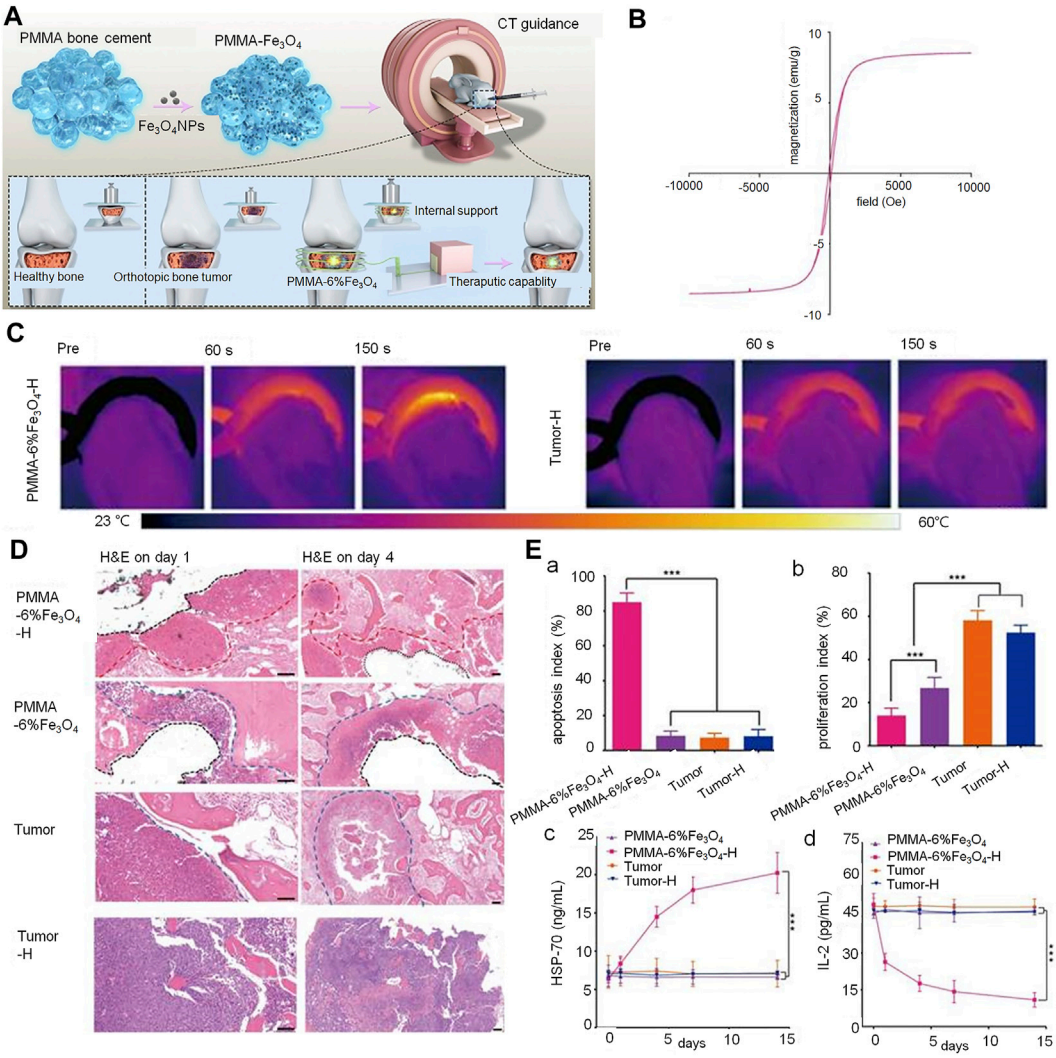

FIGURE 4
PMMA-Fe_3O_4 composite used for internal mechanical support and magnetic thermal ablation of bone tumors. **(A)** Prepared magnetic PMMA bone cement for magnetic thermal ablation of tumors. **(B)** Magnetic hystersis loop of polymerized PMMA-6% Fe_3O_4. **(C)** Thermal images of rabbit leg in the PMMA-6% Fe_3O_4-H group and Tumor-H group. **(D)** Hematoxylin and eosin staining on day 1 (scale bar: 50 μm) and day 4 (scale bar: 100 μm) (red dotted line: edge of ablation, blue dotted line: edge of the tumor, black dotted line: edge of removed PMMA-6% Fe_3O_4 composite). **(E)** (a) and (b) indicate the apoptosis index (AI) and proliferation index (PI) of each group. (c) Heat shock protein-70 levels of rabbit serum in different groups before and after magnetic thermal ablation. (d) Interleukin-2 levels of rabbit serum in different groups before and after magnetic thermal ablation. Copyright © 2019, Ivyspring International Publisher.

et al., 2021). Titanium dioxide and magnesium oxide nanoparticles have also been added to PMMA due to their excellent osteogenic activity (Li et al., 2020a; Vedhanayagam et al., 2020).

3.4 Polymer materials

3.4.1 Natural polymers

Natural polymers are used as biomaterials in medicine due to their excellent biomimetic properties and biocompatibility (Guo et al., 2021c). Chitosan, a linear polysaccharide obtained by deacetylation of chitin, is one of the most common natural polymers used (Sultankulov et al., 2019). Given its excellent biocompatibility, biodegradability, and bioactivity, it has been used for the modification of bone cement. As chitosan is degraded *in vivo*, its incorporation into PMMA bone cement creates appreciable porosity. The increase in porosity facilitates osseointegration between bone and cement and promotes more stable fixation; it also reduces the mechanical strength of PMMA-based bone cement, thereby reducing the difference with bone (Sun et al., 2022a). The improvement in bioactivity and polymerization temperature were found to be dose-dependent; an increase in the loading concentration of chitosan (to >10%) significantly reduced the heat generated by PMMA during polymerization (De Mori et al., 2019). In their study, Zapata et al. obtained similar outcomes compared to CS when using <15% loading; the composite PMMA/CS bone cement having >15% loading achieved more rapid deposition of calcium and phosphorus ions, and showed

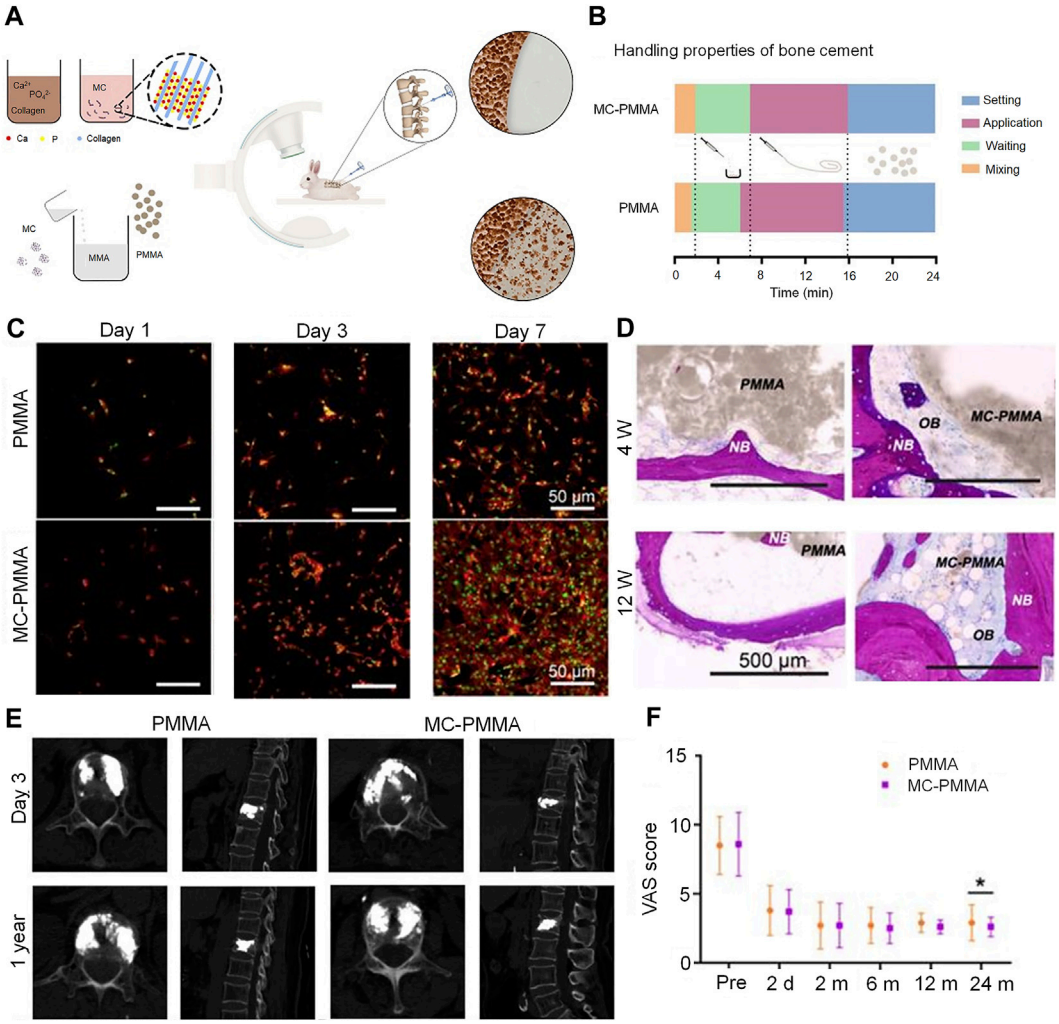

FIGURE 5
Mineralized collagen-reinforced PMMA bone cement for the treatment of osteoporotic vertebral compression fractures. **(A)** Preparation of mineralized collagen and PMMA bone cement. **(B)** Handling properties of bone cements. **(C)** Morphology of BMSCs on days 1, 3, and 7 with MC-PMMA or PMMA bone cement. Cells stained with rhodamin-phalloidin for F-actin (red) and SYTOX Green for nuclei (green). **(D)** Histological staining in the PMMA and MC-PMMA groups after 4 and 12 weeks using methylene blue (light blue) and basic fuchsin (red). The bone cement is in gray. **(E)** Lateral projection re-examination by computed tomography at 3 days and 1 year after surgery. **(F)** The visual analog scale score was evaluated by three doctors. Results are presented as the mean ± standard deviation; $*p < 0.05$. Copyright © 2020, Ivyspring International Publisher.

more rapid bioactivity (Valencia Zapata et al., 2020). Incorporating different forms of chitosan may also produce different effects. In their study, Zamora Lagos et al. incorporated different forms of chitosan into PMMA; CS sheets provided greater porosity to the cement than CS spheres (Zamora Lagos et al., 2020). However, CS microspheres demonstrated greater degradation in bone cement, thereby effectively improving the osteoconductivity and degradation of CPC (Meng et al., 2019).

Collagen is a natural antigenic biomaterial found in the skin, ligaments, bone, and cartilage (Li et al., 2021). Type I collagen accounts for 90% of the total collagen and is present in large quantities in the bone extracellular matrix secreted by osteoblasts. Collagen can be easily combined with other biomaterials; mineralized collagen (MC) can be formed by mineralization of HA and collagen molecules. Owing to similarities in structure and chemical composition between MC and natural bone components, the former demonstrates good osteogenic activity; it also increases the differentiation of MSCs to osteoblasts (Zhu et al., 2023). MC-modified bone cement significantly improves the adhesion of preosteoblasts and their proliferation; this promotes good osseointegration between the cement and host bone tissue. It also promotes higher alkaline phosphatase activity (secreted by human bone marrow MSCs) and higher expression of osteoblast-specific genes (Jiang et al., 2015). Notably, osteogenic differentiation has been found to be more than twice as high in MC-PMMA than in PMMA after 21 days of culture (Wu et al., 2016). In addition, the introduction of this material can effectively improve the maneuverability properties of bone cement. In their study, Li et al. used 15.0% by weight-impregnated MC-PMMA; this material significantly reduced the modulus of elasticity of PMMA bone cement from 1.91 to 1.21 GPa (Li et al., 2015). The results also revealed that the addition of MC significantly reduced the

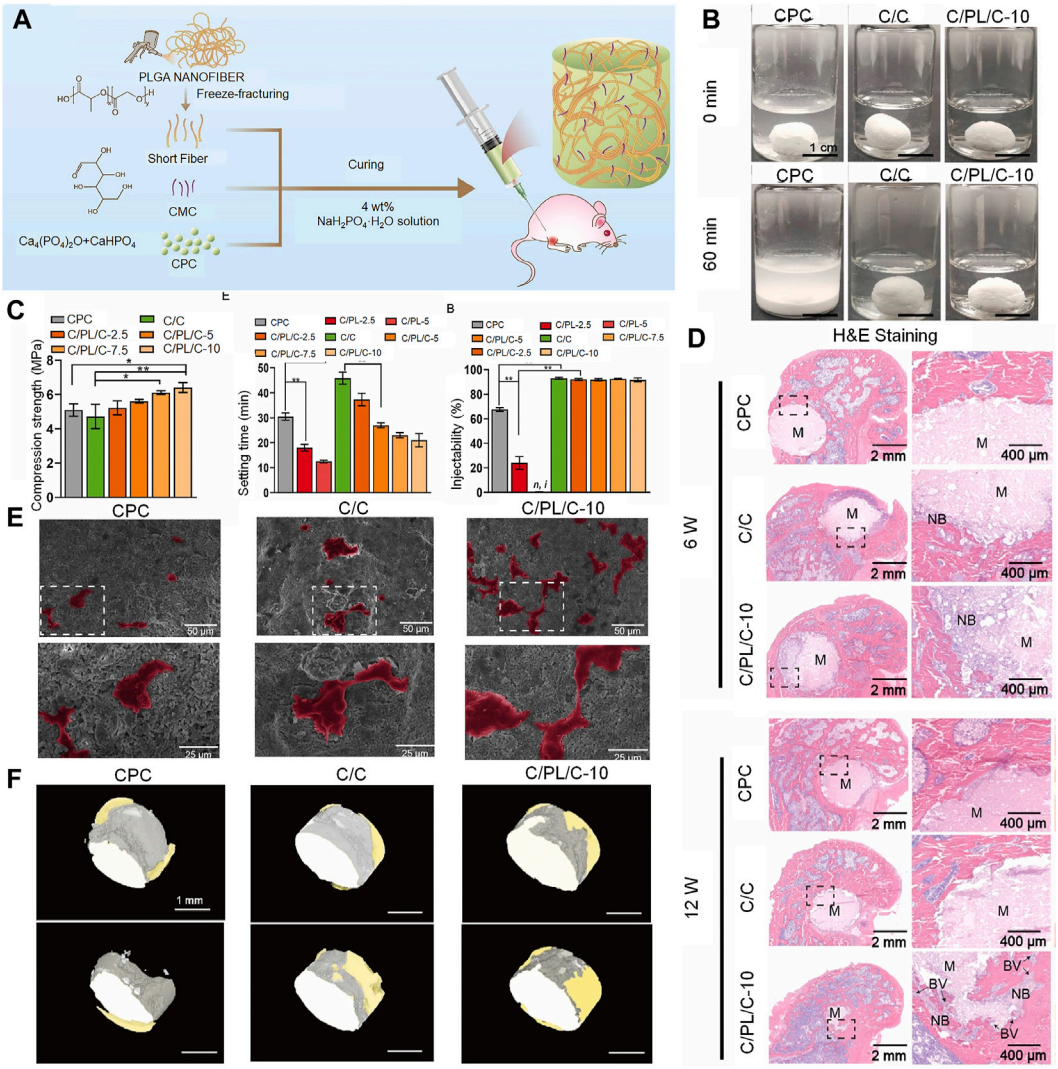

FIGURE 6
Injectable PLGA nanofiber-reinforced bone cement with controlled biodegradability for bone regeneration after minimally-invasive surgery. **(A)** Schematic representation of fabrication of C/PL/C injectable bone cement for bone regeneration. **(B)** Anti-washout performance of CPC, C/C, and C/PL/C-10, respectively. **(C)** Injectability, compressive strength, and setting time of cements. Data are presented as the mean ± standard deviation; n = 3; *significant difference compared with control group, $*p < 0.05$ and $**p < 0.01$. **(D)** Hematoxylin and eosin staining of non-decalcified femoral condyle sections 6 and 12 weeks after implantation. NB: newly formed bone; BV: blood vessels; M: materials. **(E)** Scanning electron microscope images of human umbilical vein endothelial cells on the cement surface after 24 h of incubation (human umbilical vein endothelial cells are in color for ease of observation). **(F)** 3-dimensional reconstruction of the implants in different groups; gray: cement; yellow: newly formed bone.

compressive elastic modulus of PMMA, thereby reducing the pressure on adjacent vertebrae. However, addition of MC had no significant effect on the injectibility and processing time of the cement. Similarly, Zhu et al. found that the addition of MC improved the handling properties of this composite bone cement in the clinical setting (Zhu et al., 2020) (Figure 5). Clinical evidence suggests that patients treated with MC-PMMA show significant improvement in postoperative low back pain, dyskinesia, and vertebral height (Bai et al., 2017). Notably, patients in a study who were treated with MC-PMMA demonstrated greater improvements in bone density at 6-month and 1-year follow-up than those treated conventionally; the incidence of adjacent vertebral fractures decreased to 2% after modified cementing. This represented a significant improvement over the rate of 13% observed after conventional cementing (Wang et al., 2018a).

3.4.2 Synthetic polymers

Synthetic polymers offer more possibilities for chemical modifications and molecular alterations than their natural counterparts. This may help tailor system performance to specific application requirements (Wong et al., 2023). These polymers have customized matrix structures and chemical properties. In this context, poly (lactide-co-glycolide) (PLGA) is a linear copolymer of lactic and glycolic acid monomers (Jin et al., 2021). The time needed to degrade PLGA can be adjusted (to align with that of bone regeneration) by adjusting the ratio of lactic and glycolic acid. The

degradation of PLGA gradually enhances stress stimulation of new bone; it may therefore promote bone regeneration and structural remodeling. PLGA is currently incorporated into bone cement to improve its properties. CPC scaffolds are doped with novel PLGA microspheres; these microspheres provide pores that allow CPC to grow into the new bone tissue. In a study using a rat femoral defect model, the PLGA microspheres were found to be nearly filled with mature new bone upon degradation at 24 weeks (Liang et al., 2020). Composites of dense PLGA particles have also been found to be suitable for use as pore generators in CPC; in a study, they accelerated degradation and were more effective in promoting murine BMSC proliferation (Qian et al., 2020; Lu et al., 2021). In their study, Yu et al. found that the addition of fibrous PLGA to bone defects effectively improved the brittleness of CPC. A two-fold increase in toughness was observed in addition to a moderate improvement in compressive strength (Yu et al., 2018; Cai et al., 2023) (Figure 6).

PLGA is effective in improving the handling properties of bone cement; it has also been widely used as a drug delivery system for molecules such as proteins, peptides, and genes due to its excellent carrier properties. PLGA was first used in a study on the treatment of infectious osteomyelitis; it was used in the form of microspheres after immobilizing ciprofloxacin and triclosan-containing PLGA microspheres on PMMA (Wang et al., 2020b). In their study, Qiao et al. loaded rifampicin/moxifloxacin onto PLGA microspheres for local drug delivery; microspheres prepared using PLGA and embedded with moxifloxacin and rifampicin/moxifloxacin using the water-in-oil-in-water double emulsion solvent evaporation technique were used for local delivery (Qiao et al., 2019). The results from these studies provide valuable insights into the treatment of osteoporotic and neoplastic VCFs. PLGA can also be used as a drug carrier for the treatment of oncologic bone disease. In their study, Jayaram et al. added zoledronic acid to PLGA, which released it at a concentration of 8% over 97 weeks. In contrast, PMMA released 13%–17% of zoledronic acid; PLGA therefore offered better release kinetics (Jayaram et al., 2021). PLGA loaded with doxorubicin was combined with bone cement in a study; it prolonged the release of doxorubicin and has a positive impact on the treatment of sarcoma (Dewhurst et al., 2020). In the treatment of osteoporotic VCFs, nano-sized PLGA particles were able to encapsulate and release the functional recombinant protein (ICOS-F) into cement formulations to provide an anti-osteoclastic effect and stimulate an appropriate bone remodeling response, which was conducive to effective healing (Banche-Niclot et al., 2023). On injecting CPC/PLGA composites loaded with alendronate in an osteoporotic rat model, the composites exhibited a suitable setting time, appropriate compressive strength, and controlled release of alendronate; bone formation was also demonstrated under osteoporotic conditions (van Houdt et al., 2018).

PVA fibers have been added to other gel matrices (as high-tenacity materials) due to their excellent high modulus of elasticity and tensile strength (Shi, 2021). The area of fiber reinforcement of cement matrices (used in civil engineering) has been researched extensively. However, the findings have been less frequently applied to medical bone cementing. It is believed that PVA fibers are usually covered by a hydrophobic oil-based coating, which reduces their hydrophilicity and optimizes energy dissipation via a friction-sliding mechanism; this hydrophobic PVA improves toughness and ductility (Kucko et al., 2019). In view of its high toughness, it may be a good candidate for incorporation into brittle bone cements such as CPC. In the dental field, reinforcement of the cement matrix with PVA fibers has led to the successful development of tough fiber-reinforced CPCs. The incorporation of PVA fibers reinforces CPCs to improve cement toughness and structural stability upon degradation; however, it does not affect biocompatibility and the osseointegration process (Schickert et al., 2020a). Reinforcement with PVA fibers increases the flexural strength and toughness of CPCs by more than 3 and 435-fold, respectively; this makes reinforcement an extremely effective strategy for strengthening and toughening (Kucko et al., 2019). In their study, Luo et al. found that cement containing 5 percent by weight of fibers offer a good compromise, with compressive strengths of 46.5 ± 4.6 MPa (compared to 62.3 ± 12.8 MPa without fibers), which are considerably greater than that of human trabecular bone (0.1–14 MPa) (Luo et al., 2019).

4 Vertebral implants

Unlike minimally invasive injectable cement materials, vertebral implants are primarily composed of implantable metals (Cornelis et al., 2019) (Figure 7). These include the Vertebral Body Stenting (VBS), SpineJack, Kiva, and Osseofix systems, which are based on a similar principle of percutaneous implantation of an expandable vertebral body stent (to restore vertebral height) and the correction of kyphosis; this procedure is referred to as third-generation vertebral body augmentation (Dong et al., 2022).

The goal of restoring mechanical stability to the diseased vertebral body is achieved by use of a vertebral body implant. An *in vitro* biomechanical study on the Osseofix system used human cadaveric vertebrae; it showed that the yield and ultimate loads of the vertebrae repaired by the system were similar to those of intact vertebrae. In addition, the Osseofix system was effective in restoring the original biomechanical strength of fractured vertebrae, unlike kyphoplasty (Ghofrani et al., 2010). An *in vitro* study that compared the mechanical properties of the SpineJack system and balloon kyphoplasty in human cadaveric bone found that both procedures restored height; strength and stiffness were partially restored without any significant differences. Although the mechanical properties of most vertebral implants have been well documented, further investigation is needed to assess the clinical effectiveness and scope of application of these metallic implants in posterior convex VCFs (Sietsma et al., 2009). Certain recent clinical studies have found this new type of implant to be effective in the treatment of traumatic VCFs or pathological fractures caused by osteoporosis or metastatic tumors of the spine. A study evaluated the extent of height recovery offered by the VBS in cases of acute traumatic VCFs among young non-osteoporotic patients. The values for mean postoperative vertebral height gain, vertebral kyphosis angle correction, and Beck index improvement were 3.8 mm, 4.3°, and 0.07, respectively. The results from the study confirmed that VBS can significantly restore vertebral height in young patients with traumatic VCFs (Garnon et al., 2019). A study had retrospectively evaluated the safety and efficacy of the VBS in patients with post-

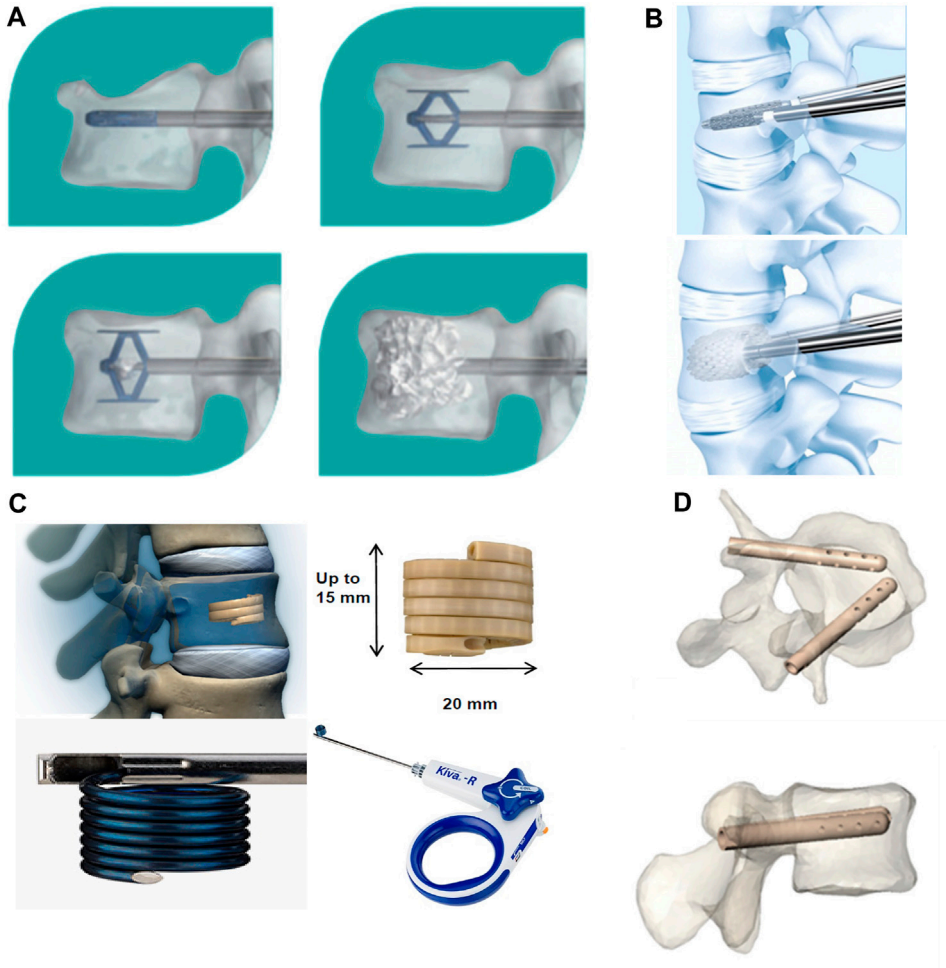

FIGURE 7
Innovative spine implants for improved augmentation and stability in neoplastic vertebral compression fractures. **(A)** SpineJack® implantation procedure. **(B)** Vertebral Body Stent® (VBS®) deployment procedure. **(C)** KIVA® implant design and delivery ancillaries. **(D)** Views of V-STRUT© implants in a vertebra, perspective and top view. © 2019 The Authors. Published by MDPI.

traumatic A3.2 and A2 type fractures (single traumatic thoracolumbar fractures) who were treated between 2010 and 2019. The results confirmed an improvement in posterior convexity and restoration of vertebral height in all patients (Salle et al., 2022). In a prospective study on type A1.3 and A3.1 fractures, the VBS offered satisfactory improvements in pain, function, posterior convexity correction, and even endplate repositioning in osteoporotic and traumatic fractures (Klezl et al., 2011). The system was also found to be effective in correcting kyphotic deformities and restoring loss of vertebral height in patients with chronic osteoporosis who had VCFs; these findings confirm the feasibility of its clinical application (Premat et al., 2018). A recent study evaluated the utility of the OsseoFix system for the treatment of VCFs caused by multiple myeloma; it found that the implant provided significant improvements in terms of both pain and prognostic scores, thereby significantly reducing complications. The total number of implants used in this study was the highest to be reported in the literature to date; the use of expandable titanium mesh cages allowed safe and effective treatment (Gandham et al., 2021).

Although, new implant materials have been able to address certain limitations of PVP and PKP, various clinical adverse events continue to occur. For instance, stent tumbling prevents the contralateral stent from providing adequate support (Kanematsu et al., 2023). In this context, a randomized controlled trial evaluated the impact of two different augmentation procedures, namely, the KIVA system and PKP, on the readmission rate due to serious adverse events. The patients with a previous history of VCF or significant osteoporosis who were treated using the KIVA system demonstrated a greater risk of readmission due to serious adverse events (at 1-year after treatment) than those who underwent PKP (Beall et al., 2017). Therefore, future studies need to evaluate the issue of appropriate selection of metallic implants for different vertebral body fractures.

5 Conclusion and prospects

The appropriate selection of implantable materials is crucial to the clinical outcomes of minimally invasive treatment for VCFs.

However, the materials in current use have various limitations, which hinder clinical application. As the first and second generation of minimally invasive implantable materials for vertebral body augmentation, traditional bone cement (represented by PMMA) is widely used in the clinic. However, it lacks bioactivity and leads to a series of clinical complications. Therefore, newer bone cements including MPC and CSC have been developed; these have been favored by researchers owing to their superior osteoclastogenic and angiogenic effects. Biomaterials with various beneficial properties have been mixed with bone cement to improve its handling properties and bioactivity in a targeted manner. A review of the types and clinical efficacy of new vertebral implants used in third-generation vertebroplasty show that a wide variety of options are available for the treatment of different types of VCFs.

Although the implant materials developed for minimally invasive treatment have various outstanding properties, their clinical effectiveness and safety remain unclear. In addition, clinical validation of processing properties such as injectability and setting time are lacking for new composite bone cement materials. Large-scale controlled clinical studies evaluating the efficacy of new vertebral implants are also lacking; the scope of their application warrants further investigation. Clinicians also need to address the issue of selection of appropriate materials for minimally invasive surgery. In conclusion, the ongoing improvements in technology and biomaterials are expected to make minimally invasive surgery for VCFs safer and more effective.

Author contributions

PS: Writing–original draft. TY: Supervision. SS: Conceptualization. BC: Conceptualization. CQ: Supervision. JW: Conceptualization. EW: Supervision. CZ: Funding acquisition, Writing–review and editing.

Funding

The author(s) declare financial support was received for the research, authorship, and/or publication of this article. This work was supported by Jilin province department of finance (YDZJ202201ZYTS125).

Conflict of interest

The authors declare that the research was conducted in the absence of any commercial or financial relationships that could be construed as a potential conflict of interest.

Publisher's note

All claims expressed in this article are solely those of the authors and do not necessarily represent those of their affiliated organizations, or those of the publisher, the editors and the reviewers. Any product that may be evaluated in this article, or claim that may be made by its manufacturer, is not guaranteed or endorsed by the publisher.

References

Aghyarian, S., Hu, X. B., Lieberman, I. H., Kosmopoulos, V., Kim, H. K. W., and Rodrigues, D. C. (2015). Two novel high performing composite PMMA-CaP cements for vertebroplasty: an *ex vivo* animal study. *J. Mech. Behav. Biomed. Mater.* 50, 290–298. doi:10.1016/j.jmbbm.2015.06.022

Aghyarian, S., Hu, X., Haddas, R., Lieberman, I. H., Kosmopoulos, V., Kim, H. K. W., et al. (2017). Biomechanical behavior of novel composite PMMA-CaP bone cements in an anatomically accurate cadaveric vertebroplasty model. *J. Orthop. Res.* 35, 2067–2074. doi:10.1002/jor.23491

Aghyarian, S., Rodriguez, L. C., Chari, J., Bentley, E., Kosmopoulos, V., Lieberman, I. H., et al. (2014). Characterization of a new composite PMMA-HA/Brushite bone cement for spinal augmentation. *J. Biomaterials Appl.* 29, 688–698. doi:10.1177/0885328214544770

Arici, S., Kacmaz, E. G., Kamali, A. R., and Ege, D. (2023). Influence of graphene oxide and carbon nanotubes on physicochemical properties of bone cements. *Mater. Chem. Phys.* 293, 126961. doi:10.1016/j.matchemphys.2022.126961

Ashammakhi, N., Clerk-Lamalice, O., Baroud, G., Darabi, M. A., Georgy, B., Beall, D., et al. (2019). Spine intervention-an update on injectable biomaterials. *Can. Assoc. Radiologists Journal-Journal De L Assoc. Can. Des Radiologistes* 70, 37–43. doi:10.1016/j.carj.2018.11.003

Bai, M., Yin, H., Zhao, J., Li, Y., Yang, Y., and Wu, Y. (2017). Application of PMMA bone cement composited with bone-mineralized collagen in percutaneous kyphoplasty. *Regen. Biomater.* 4, 251–255. doi:10.1093/rb/rbx019

Banche-Niclot, F., Corvaglia, I., Cavalera, C., Boggio, E., Gigliotti, C. L., Dianzani, U., et al. (2023). Optimization of an injectable, resorbable, bioactive cement able to release the anti-osteoclastogenic biomolecule ICOS-fc for the treatment of osteoporotic vertebral compression fractures. *Biomolecules* 13, 94. doi:10.3390/biom13010094

Baroud, G., Nemes, J., Heini, P., and Steffen, T. (2003). Load shift of the intervertebral disc after a vertebroplasty: a finite-element study. *Eur. Spine J.* 12, 421–426. doi:10.1007/s00586-002-0512-9

Beall, D. P., Coe, J. D., Mcilduff, M., Bloch, D., Hornberger, J., Warner, C., et al. (2017). Serious adverse events associated withReadmission through one year after VertebralAugmentation with either a PolyetheretherketoneImplant or balloon kyphoplasty. *Pain Physician* 20, 521–528. doi:10.36076/ppj.20.5.521

Beall, D., Lorio, M. P., Yun, B. M., Runa, M. J., Ong, K. L., and Warner, C. B. (2018). Review of vertebral augmentation: an updated meta-analysis of the effectiveness. *Int. J. Spine Surg.* 12, 295–321. doi:10.14444/5036

Black, D. M., Palermo, L., Nevitt, M. C., Genant, H. K., Christensen, L., Cummings, S. R., et al. (1999). Defining incident vertebral deformity: a prospective comparison of several approaches. *J. Bone Mineral Res.* 14, 90–101. doi:10.1359/jbmr.1999.14.1.90

Bohner, M., and Baroud, G. (2005). Injectability of calcium phosphate pastes. *Biomaterials* 26, 1553–1563. doi:10.1016/j.biomaterials.2004.05.010

Cai, P., Lu, S., Yu, J., Xiao, L., Wang, J., Liang, H., et al. (2023). Injectable nanofiber-reinforced bone cement with controlled biodegradability for minimally-invasive bone regeneration. *Bioact. Mater.* 21, 267–283. doi:10.1016/j.bioactmat.2022.08.009

Chang, M., Zhang, C., Shi, J., Liang, J., Yuan, X., Huang, H., et al. (2021). Comparison between 7 osteoporotic vertebral compression fractures treatments: systematic review and network meta-analysis. *World Neurosurg.* 145, 462–470.e1. doi:10.1016/j.wneu.2020.08.216

Chen, J., Yu, J., He, Q., Zhao, X., Sang, H. X., Lei, W., et al. (2015a). A novel injectable porous surface modified bioactive bone cement for vertebroplasty: an *in vivo* biomechanical and osteogenic study in a rabbit osteoporosis model. *Am. J. Transl. Res.* 7, 548–552.

Chen, J., Zhai, D., Huan, Z., Ma, N., Zhu, H., Wu, C., et al. (2015b). Silicate bioceramic/PMMA composite bone cement with distinctive physicochemical and bioactive properties. *Rsc Adv.* 5, 37314–37322. doi:10.1039/c5ra04646g

Choi, S.-M., Yang, W.-K., Yoo, Y.-W., and Lee, W.-K. (2010). Effect of surface modification on the *in vitro* calcium phosphate growth on the surface of poly(methyl methacrylate) and bioactivity. *Colloids Surfaces B-Biointerfaces* 76, 326–333. doi:10.1016/j.colsurfb.2009.11.012

Choudhary, R., Venkatraman, S. K., Bulygina, I., Senatov, F., Kaloshkin, S., and Swamiappan, S. (2020). Designing of porous PMMA/diopside bone cement for non-load bearing applications. *J. Asian Ceram. Soc.* 8, 862–872. doi:10.1080/21870764.2020.1793476

Cole, K. A., Funk, G. A., Rahaman, M. N., and Mciff, T. E. (2020a). Characterization of the conversion of bone cement and borate bioactive glass

composites. *J. Biomed. Mater. Res. Part B-Applied Biomaterials* 108, 1580–1591. doi:10.1002/jbm.b.34505

Cole, K. A., Funk, G. A., Rahaman, M. N., and Mciff, T. E. (2020b). Mechanical and degradation properties of poly(methyl methacrylate) cement/borate bioactive glass composites. *J. Biomed. Mater. Res. Part B-Applied Biomaterials* 108, 2765–2775. doi:10.1002/jbm.b.34606

Cornelis, F. H., Joly, Q., Nouri-Neuville, M., Ben-Ammar, M., Kastler, B., Kastler, A., et al. (2019). Innovative spine implants for improved augmentation and stability in neoplastic vertebral compression fracture. *Medicina-Lithuania* 55, 426. doi:10.3390/medicina55080426

Cui, X., Zhang, Y., Wang, H., Gu, Y., Li, L., Zhou, J., et al. (2016). An injectable borate bioactive glass cement for bone repair: preparation, bioactivity and setting mechanism. *J. Non-Crystalline Solids* 432, 150–157. doi:10.1016/j.jnoncrysol.2015.06.001

de Mori, A., Di Gregorio, E., Kao, A. P., Tozzi, G., Barbu, E., Sanghani-Kerai, A., et al. (2019). Antibacterial PMMA composite cements with tunable thermal and mechanical properties. *Acs Omega* 4, 19664–19675. doi:10.1021/acsomega.9b02290

Deng, X.-G., Xiong, X.-M., Cui, W., Gu, T., Wan, D., Shi, H.-G., et al. (2020). Preliminary application of CPC/PMMA composite bone cement in kyphoplasty for the elderly. *Zhongguo gu shang = China J. Orthop. traumatology* 33, 831–836. doi:10.12200/j.issn.1003-0034.2020.09.008

Dewhurst, R. M., Scalzone, A., Buckley, J., Mattu, C., Rankin, K. S., Gentile, P., et al. (2020). Development of natural-based bone cement for a controlled doxorubicin-drug release. *Front. Bioeng. Biotechnol.* 8, 754. doi:10.3389/fbioe.2020.00754

Ding, J., Zhao, J., Wang, L., Chen, X., Jiang, D., Qin, M., et al. (2023). Regulated contribution of local and systemic immunity to new bone regeneration by modulating B/Sr concentration of bioactive borosilicate glass. *Mater. Today Bio* 19, 100585. doi:10.1016/j.mtbio.2023.100585

Ding, L., Wang, H., Zhang, W., Li, J., Liu, D., Han, F., et al. (2021). Calcium phosphate bone cement with enhanced physicochemical properties via *in situ* formation of an interpenetrating network. *J. Mater. Chem. B* 9, 6802–6810. doi:10.1039/d1tb00867f

Dong, C., Zhu, Y., Zhou, J., and Dong, L. (2022). Therapeutic efficacy of third-generation percutaneous vertebral augmentation system (pvas) in osteoporotic vertebral compression fractures (OVCFs): a systematic review and meta-analysis. *Biomed Res. Int.* 2022, 1–17. doi:10.1155/2022/9637831

Du, Y., Yang, J., Thomas, B. S., Li, L., Li, H., Shaban, W. M., et al. (2020). Influence of hybrid graphene oxide/carbon nanotubes on the mechanical properties and microstructure of magnesium potassium phosphate cement paste. *Constr. Build. Mater.* 260, 120449. doi:10.1016/j.conbuildmat.2020.120449

Ebrahimi, S., and Sipaut, C. S. (2021). The effect of liquid phase concentration on the setting time and compressive strength of hydroxyapatite/bioglass composite cement. *Nanomaterials* 11, 2576. doi:10.3390/nano11102576

Esnaashary, M. H., Khavandi, A., Rezaie, H. R., and Javadpour, J. (2020). Mg-P/c-SWCNT bone cement: the effect of filler on setting behavior, compressive strength and biocompatibility. *J. Bionic Eng.* 17, 100–112. doi:10.1007/s42235-020-0008-5

Freeman, M. A., Bradley, G. W., and Revell, P. A. (1982). Observations upon the interface between bone and polymethylmethacrylate cement. *J. bone Jt. Surg. Br. volume* 64, 489–493. doi:10.1302/0301-620x.64b4.7096429

Galli, S., Stocchero, M., Andersson, M., Karlsson, J., He, W., Lilin, T., et al. (2018). Correction to: the effect of magnesium on early osseointegration in osteoporotic bone: a histological and gene expression investigation. *Osteoporos. Int.* 29, 1931–1931. doi:10.1007/s00198-018-4497-6

Gandham, S., Islim, A., Alhamad, S., and Thambiraj, S. (2021). The outcome of expandable titanium mesh implants for the treatment of multi-level vertebral compression fractures caused by multiple myeloma. *Sicot-J* 7, 28. doi:10.1051/sicotj/2021026

Gao, S., Lv, Y., Yuan, L., Ren, H., Wu, T., Liu, B., et al. (2019). Improved bone ingrowth of tricalcium phosphate filled Poly(methyl methacrylate) (PMMA) bone cements *in vivo*. *Polym. Test.* 76, 513–521. doi:10.1016/j.polymertesting.2019.02.015

Garnon, J., Dore, B., Auloge, P., Caudrelier, J., Dalili, D., Ramamurthy, N., et al. (2019). Efficacy of the vertebral body stenting system for the restoration of vertebral height in acute traumatic compression fractures in a non-osteoporotic population. *Cardiovasc. Interventional Radiology* 42, 1579–1587. doi:10.1007/s00270-019-02265-y

Ghofrani, H., Nunn, T., Robertson, C., Mahar, A., Lee, Y., and Garfin, S. (2010). An evaluation of fracture stabilization comparing kyphoplasty and titanium mesh repair techniques for vertebral compression fractures is bone cement necessary?. *Spine* 35, E768–E773. doi:10.1097/brs.0b013e3181d260bf

Girardo, M., Rava, A., Coniglio, A., Cinnella, P., Aprato, A., Masse, A., et al. (2019). Importance of polymethylmethacrylate augmentation in the treatment of thoracolumbar osteoporotic vertebral fractures. *Minerva Ortop. E Traumatol.* 70, 65–69. doi:10.23736/s0394-3410.19.03920-1

Golubevas, R., Zarkov, A., Alinauskas, L., Stankeviciute, Z., Balciunas, G., Garskaite, E., et al. (2017). Fabrication and investigation of high-quality glass-ceramic (GC)-polymethyl methacrylate (PMMA) composite for regenerative medicine. *Rsc Adv.* 7, 33558–33567. doi:10.1039/c7ra05188c

Gomez-Cerezo, N., Casarrubios, L., Morales, I., Feito, M. J., Vallet-Regi, M., Arcos, D., et al. (2018). Effects of a mesoporous bioactive glass on osteoblasts, osteoclasts and macrophages. *J. Colloid Interface Sci.* 528, 309–320. doi:10.1016/j.jcis.2018.05.099

Gong, T., Ji, X., Liu, X., Zhou, J., Zhang, J., Chen, Y., et al. (2023). Different cellulose nanofibers impact properties of calcium phosphate silicate cement for bone tissue engineering. *Cellulose* 30, 1011–1029. doi:10.1007/s10570-022-04942-7

Guo, C., Huang, H., Shao, Y., Qin, Q., Liang, D., Zhang, S., et al. (2021b). Risk factors for pulmonary cement embolism (PCE) after polymethylmethacrylate augmentation: analysis of 32 PCE cases. *Neurospine* 18, 806–815. doi:10.14245/ns.2142616.308

Guo, C., Liang, Z., Yang, L., Du, W., Yu, T., Tang, H., et al. (2021c). The role of natural polymers in bone tissue engineering. *J. Control. Release* 338, 571–582. doi:10.1016/j.jconrel.2021.08.055

Guo, C., Niu, D., Liu, J., Bao, X., and Xu, G. (2021a). Application of biodegradable PLGA-PEG-PLGA/CPC composite bone cement in the treatment of osteoporosis. *Coatings* 11, 827. doi:10.3390/coatings11070827

Guo, Y., Ren, L., Liu, C., Yuan, Y., Lin, X., Tan, L., et al. (2013). Effect of implantation of biodegradable magnesium alloy on BMP-2 expression in bone of ovariectomized osteoporosis rats. *Mater. Sci. Eng. C-Materials Biol. Appl.* 33, 4470–4474. doi:10.1016/j.msec.2013.05.042

Habib, M., Baroud, G., Gitzhofer, F., and Bohner, M. (2008). Mechanisms underlying the limited injectability of hydraulic calcium phosphate paste. *Acta Biomater.* 4, 1465–1471. doi:10.1016/j.actbio.2008.03.004

Harabech, M., Kiselovs, N. R., Maenhoudt, W., Crevecoeur, G., Van Roost, D., and Dupre, L. (2017). Experimental *ex-vivo* validation of PMMA-based bone cements loaded with magnetic nanoparticles enabling hyperthermia of metastatic bone tumors. *Aip Adv.* 7. doi:10.1063/1.4973499

Hasan, M. L., Kim, B., Padalhin, A. R., Faruq, O., Sultana, T., and Lee, B.-T. (2019). *In vitro* and *in vivo* evaluation of bioglass microspheres incorporated brushite cement for bone regeneration. *Mater. Sci. Eng. C-Materials Biol. Appl.* 103, 109775. doi:10.1016/j.msec.2019.109775

Hassani, S. F., Cormier, E., Shotar, E., Drir, M., Spano, J.-P., Morardet, L., et al. (2019). Intracardiac cement embolism during percutaneous vertebroplasty: incidence, risk factors and clinical management. *Eur. Radiol.* 29, 663–673. doi:10.1007/s00330-018-5647-0

Hoyt, D., Urits, I., Orhurhu, V., Orhurhu, M. S., Callan, J., Powell, J., et al. (2020). Current concepts in the management of vertebral compression fractures. *Curr. Pain Headache Rep.* 24, 16. doi:10.1007/s11916-020-00849-9

Hsieh, M.-K., Kao, F.-C., Chiu, P.-Y., Chen, L.-H., Yu, C.-W., Niu, C.-C., et al. (2019). Risk factors of neurological deficit and pulmonary cement embolism after percutaneous vertebroplasty. *J. Orthop. Surg. Res.* 14, 406. doi:10.1186/s13018-019-1459-4

Huang, T.-H., Kao, C.-T., Shen, Y.-F., Lin, Y.-T., Liu, Y.-T., Yen, S.-Y., et al. (2019). Substitutions of strontium in bioactive calcium silicate bone cements stimulate osteogenic differentiation in human mesenchymal stem cells. *J. Mater. Science-Materials Med.* 30, 68. doi:10.1007/s10856-019-6274-2

Hu, L., Sun, H., Wang, H., Cai, J., Tao, Y., Feng, X., et al. (2019). Cement injection and postoperative vertebral fractures during vertebroplasty. *J. Orthop. Surg. Res.* 14, 228. doi:10.1186/s13018-019-1273-z

Hu, Y., and Xu, G. (2019). The study on the repair of rabbit bone defect by injection of calcium phosphate cements and bioglass (CPC-BG) composite biomaterial. *J. Biomaterials Tissue Eng.* 9, 100–103. doi:10.1166/jbt.2019.1943

Ishikawa, K., and Asaoka, K. (1995). Estimation of ideal mechanical strength and critical porosity of calcium phosphate cement. *J. Biomed. Mater. Res.* 29, 1537–1543. doi:10.1002/jbm.820291210

Jacobson, R. E. (2020). The use of SpineJack intravertebral implant for the correction of recurrent vertebral fracture after kyphoplasty. *Cureus* 12, e7599. doi:10.7759/cureus.7599

Jayaram, R., O'Donnell, P. W., and Puleo, D. A. (2021). Systems for local, sustained release of zoledronic acid as a potential treatment for metastatic bone disease. *Mater. Sci. Eng. C-Materials Biol. Appl.* 118, 111395. doi:10.1016/j.msec.2020.111395

Jiang, H.-J., Xu, J., Qiu, Z.-Y., Ma, X.-L., Zhang, Z.-Q., Tan, X.-X., et al. (2015). Mechanical properties and cytocompatibility improvement of vertebroplasty PMMA bone cements by incorporating mineralized collagen. *Materials* 8, 2616–2634. doi:10.3390/ma8052616

Jin, S., Xia, X., Huang, J., Yuan, C., Zuo, Y., Li, Y., et al. (2021). Recent advances in PLGA-based biomaterials for bone tissue regeneration. *Acta Biomater.* 127, 56–79. doi:10.1016/j.actbio.2021.03.067

Jones, J. R. (2013). Review of bioactive glass: from Hench to hybrids. *Acta Biomater.* 9, 4457–4486. doi:10.1016/j.actbio.2012.08.023

Kanematsu, R., Hanakita, J., Takahashi, T., Minami, M., Nakamura, S., Tokunaga, S., et al. (2023). Intraoperative complications of vertebral body stenting system. *Surg. Neurol. Int.* 14, 156–156. doi:10.25259/sni_299_2023

Khan, M., and Kushchayev, S. V. (2019). Percutaneous vertebral body augmentations. *Neuroimaging Clin. N. Am.* 29, 495–513. doi:10.1016/j.nic.2019.07.002

Klein, R., Tetzlaff, R., Weiss, C., Schaefer, M.-K., Tanner, M., Wiedenhoefer, B., et al. (2017). Osteointegration and resorption of intravertebral and extravertebral calcium phosphate cement. *Clin. Spine Surg.* 30, E291–E296. doi:10.1097/bsd.0b013e3182aab2df

Klezl, Z., Majeed, H., Bommireddy, R., and John, J. (2011). Early results after vertebral body stenting for fractures of the anterior column of the thoracolumbar spine. *Injury-International J. Care Inj.* 42, 1038–1042. doi:10.1016/j.injury.2011.04.006

Kucko, N. W., Schickert, S. D. L., Marques, T. S., Herber, R.-P., Van Den Beuken, J. J. J. P., Yi, Z., et al. (2019). Tough and osteocompatible calcium phosphate cements reinforced with poly(vinyl alcohol) fibers. *Acs Biomaterials Sci. Eng.* 5, 2491–2505. doi:10.1021/acsbiomaterials.9b00226

Le Ferrec, M., Mellier, C., Boukhechba, F., Le Corroller, T., Guenoun, D., Fayon, F., et al. (2018). Design and properties of a novel radiopaque injectable apatitic calcium phosphate cement, suitable for image-guided implantation. *J. Biomed. Mater. Res. Part B-Applied Biomaterials* 106, 2786–2795. doi:10.1002/jbm.b.34059

Liang, B., Burley, G., Lin, S., and Shi, Y.-C. (2022). Osteoporosis pathogenesis and treatment: existing and emerging avenues. *Cell. Mol. Biol. Lett.* 27, 72. doi:10.1186/s11658-022-00371-3

Liang, W., Gao, M., Lou, J., Bai, Y., Zhang, J., Lu, T., et al. (2020). Integrating silicon/zinc dual elements with PLGA microspheres in calcium phosphate cement scaffolds synergistically enhances bone regeneration. *J. Mater. Chem. B* 8, 3038–3049. doi:10.1039/c9tb02901j

Li, C., Sun, J., Shi, K., Long, J., Li, L., Lai, Y., et al. (2020a). Preparation and evaluation of osteogenic nano-MgO/PMMA bone cement for bone healing in a rat critical size calvarial defect. *J. Mater. Chem. B* 8, 4575–4586. doi:10.1039/d0tb00074d

Li, G., Zhang, K., Pei, Z., Liu, P., Chang, J., Zhang, K., et al. (2020b). Basalt fibre reinforced calcium phosphate cement with enhanced toughness. *Mater. Technol.* 35, 152–158. doi:10.1080/10667857.2019.1659536

Ling, Y., Tang, X., Wang, F., Zhou, X., Wang, R., Deng, L., et al. (2017). Highly efficient magnetic hyperthermia ablation of tumors using injectable polymethylmethacrylate-Fe3O4. *Rsc Adv.* 7, 2913–2918. doi:10.1039/c6ra20860f

Lin, K., Liu, Y., Huang, H., Chen, L., Wang, Z., and Chang, J. (2015). Degradation and silicon excretion of the calcium silicate bioactive ceramics during bone regeneration using rabbit femur defect model. *J. Mater. Science-Materials Med.* 26, 197. doi:10.1007/s10856-015-5523-2

Li, T., Weng, X. S., Bian, Y. Y., Zhou, L., Cui, F. Z., and Qiu, Z. Y. (2015). Influence of nano-HA coated bone collagen to acrylic (polymethylmethacrylate) bone cement on mechanical properties and bioactivity. *Plos One* 10, e0129018. doi:10.1371/journal.pone.0129018

Liu, J., Hou, W., Wei, W., Peng, J., Wu, X., Lian, C., et al. (2023). Design and fabrication of high-performance injectable self-setting trimagnesium phosphate. *Bioact. Mater.* 28, 348–357. doi:10.1016/j.bioactmat.2023.05.019

Liu, Q., Kim, J. H., Cho, M., Kim, S. H., Xu, B., Amirthalingam, S., et al. (2023b). Bioactive magnesium-based whitlockite ceramic as bone cement additives for enhancing osseointegration and bone regeneration. *Mater. Des.* 229, 111914. doi:10.1016/j.matdes.2023.111914

Liu, W., Huan, Z., Wu, C., Zhou, Z., and Chang, J. (2022). High-strength calcium silicate-incorporated magnesium phosphate bone cement with osteogenic potential for orthopedic application. *Compos. Part B-Engineering* 247, 110324. doi:10.1016/j.compositesb.2022.110324

Liu, W., Zhang, J., Rethore, G., Khairoun, K., Pilet, P., Tancret, F., et al. (2014). A novel injectable, cohesive and toughened Si-HPMC (silanized-hydroxypropyl methylcellulose) composite calcium phosphate cement for bone substitution. *Acta Biomater.* 10, 3335–3345. doi:10.1016/j.actbio.2014.03.009

Li, Y., Liu, Y., Li, R., Bai, H., Zhu, Z., Zhu, L., et al. (2021). Collagen-based biomaterials for bone tissue engineering. *Mater. Des.* 210, 110049. doi:10.1016/j.matdes.2021.110049

Lodoso-Torrecilla, I., Van Den Beucken, J. J. J. P., and Jansen, J. A. (2021). Calcium phosphate cements: optimization toward biodegradability. *Acta Biomater.* 119, 1–12. doi:10.1016/j.actbio.2020.10.013

Lofrese, G., Ricciardi, L., de Bonis, P., Cultrera, F., Cappuccio, M., Scerrati, A., et al. (2021). Use of the SpineJack direct reduction for treating type A2, A3 and A4 fractures of the thoracolumbar spine: a retrospective case series. *J. Neurointerventional Surg.* 14, 931–937. doi:10.1136/neurintsurg-2021-017682

Luo, J., Faivre, J., Engqvist, H., and Persson, C. (2019). The addition of poly(vinyl alcohol) fibers to apatitic calcium phosphate cement can improve its toughness. *Materials* 12, 1531. doi:10.3390/ma12091531

Lu, Q., Liu, C., Wang, D., Liu, H., Yang, H., and Yang, L. (2019). Biomechanical evaluation of calcium phosphate-based nanocomposite versus polymethylmethacrylate cement for percutaneous kyphoplasty. *Spine J.* 19, 1871–1884. doi:10.1016/j.spinee.2019.06.007

Lu, T., He, F., and Ye, J. (2021). Physicochemical properties, *in vitro* degradation, and biocompatibility of calcium phosphate cement incorporating poly(lactic-co-glycolic acid) particles with different morphologies: a comparative study. *Acs Omega* 6, 8322–8331. doi:10.1021/acsomega.1c00031

Lv, Y., Li, A., Zhou, F., Pan, X., Liang, F., Qu, X., et al. (2015). A novel composite PMMA-based bone cement with reduced potential for thermal necrosis. *Acs Appl. Mater. Interfaces* 7, 11280–11285. doi:10.1021/acsami.5b01447

Mabroum, H., Noukrati, H., Youcef, H. B., Oudadesse, H., and Barroug, A. (2022). The effect of bioactive glass particle size and liquid phase on the physical-chemical and mechanical properties of carbonated apatite cement. *Ceram. Int.* 48, 28207–28220. doi:10.1016/j.ceramint.2022.06.126

Mansoori-Kermani, A., Mashayekhan, S., Kermani, F., and Abdekhodaie, M. J. (2023). The effect of tricalcium silicate incorporation on bioactivity, injectability, and mechanical properties of calcium sulfate/bioactive glass bone cement. *Ceram. Int.* 49, 15003–15014. doi:10.1016/j.ceramint.2023.01.083

Martikos, K., Greggi, T., Vommaro, F., Boriani, L., Scarale, A., Zarantonello, P., et al. (2019). Vertebroplasty in the treatment of osteoporotic vertebral compression fractures: patient selection and perspectives . *Open Access Rheumatology-Research Rev.* 11, 157–161. doi:10.2147/oarrr.s174424

Medvecky, L., Giretova, M., Kralikova, R., Medvecka, S., and Briancin, J. (2019). *In vitro* cytotoxicity of calcium phosphate cement reinforced with multiwalled carbon nanotubes. *J. Mater. Science-Materials Med.* 30, 54. doi:10.1007/s10856-019-6256-4

Meng, B., Qian, M., Xia, S.-X., Yang, H.-L., and Luo, Z.-P. (2013). Biomechanical characteristics of cement/gelatin mixture for prevention of cement leakage in vertebral augmentation. *Eur. Spine J.* 22, 2249–2255. doi:10.1007/s00586-013-2886-2

Meng, D., Dong, L., Yuan, Y., and Jiang, Q. (2019). *In vitro* and *in vivo* analysis of the biocompatibility of two novel and injectable calcium phosphate cements. *Regen. Biomater.* 6, 13–19. doi:10.1093/rb/rby027

Miola, M., Bellare, A., Gerbaldo, R., Laviano, F., and Verne, E. (2021). Synthesis and characterization of magnetic and antibacterial nanoparticles as filler in acrylic cements for bone cancer and comorbidities therapy. *Ceram. Int.* 47, 17633–17643. doi:10.1016/j.ceramint.2021.03.082

Mirza, E. H., Khan, A. A., Al-Khureif, A. A., Saadaldin, S. A., Mohamed, B. A., Fareedi, F., et al. (2019). Characterization of osteogenic cells grown over modified graphene-oxide-biostable polymers. *Biomed. Mater.* 14, 065004. doi:10.1088/1748-605x/ab3ab2

Moura, D. L., and Gabriel, J. P. (2021). Expandable intravertebral implants: a narrative review on the concept, biomechanics, and outcomes in traumatology. *Cureus* 13, e17795. doi:10.7759/cureus.17795

Nakamae, T., Yamada, K., Tsuchida, Y., Osti, O. L., Adachi, N., and Fujimoto, Y. (2018). Risk factors for cement loosening after vertebroplasty for osteoporotic vertebral fracture with intravertebral cleft: a retrospective analysis. *Asian Spine J.* 12, 935–942. doi:10.31616/asj.2018.12.5.935

Naud, R., Guinde, J., and Astoul, P. (2020). Pulmonary cement embolism complicating percutaneous kyphoplasty: a case report. *Respir. Med. Case Rep.* 31, 101188. doi:10.1016/j.rmcr.2020.101188

Ong, K. L., Beall, D. P., Frohbergh, M., Lau, E., and Hirsch, J. A. (2018). Were VCF patients at higher risk of mortality following the 2009 publication of the vertebroplasty "sham" trials?. *Osteoporos. Int.* 29, 375–383. doi:10.1007/s00198-017-4281-z

Ormsby, R. W., Modreanu, M., Mitchell, C. A., and Dunne, N. J. (2014). Carboxyl functionalised MWCNT/polymethyl methacrylate bone cement for orthopaedic applications. *J. Biomaterials Appl.* 29, 209–221. doi:10.1177/0885328214521252

Ormsby, R., Mcnally, T., Mitchell, C., Halley, P., Martin, D., Nicholson, T., et al. (2011). Effect of MWCNT addition on the thermal and rheological properties of polymethyl methacrylate bone cement. *Carbon* 49, 2893–2904. doi:10.1016/j.carbon.2011.02.063

Pahlevanzadeh, F., Bakhsheshi-Rad, H. R., Ismail, A. F., Aziz, M., and Chen, X. B. (2019). Development of PMMA-Mon-CNT bone cement with superior mechanical properties and favorable biological properties for use in bone-defect treatment. *Mater. Lett.* 240, 9–12. doi:10.1016/j.matlet.2018.12.049

Paknahad, A., Kucko, N. W., Leeuwenburgh, S. C. G., and Sluys, L. J. (2020). Experimental and numerical analysis on bending and tensile failure behavior of calcium phosphate cements. *J. Mech. Behav. Biomed. Mater.* 103, 103565. doi:10.1016/j.jmbbm.2019.103565

Paz, E., Forriol, F., Del Real, J. C., and Dunne, N. (2017). Graphene oxide versus graphene for optimisation of PMMA bone cement for orthopaedic applications. *Mater. Sci. Eng. C-Materials Biol. Appl.* 77, 1003–1011. doi:10.1016/j.msec.2017.03.269

Premat, K., Vande Perre, S., Cormier, E., Shotar, E., Degos, V., Morardet, L., et al. (2018). Vertebral augmentation with the SpineJack® in chronic vertebral compression fractures with major kyphosis. *Eur. Radiol.* 28, 4985–4991. doi:10.1007/s00330-018-5544-6

Qian, G., Lu, T., Zhang, J., Liu, R., Wang, Z., Yu, B., et al. (2020). Promoting bone regeneration of calcium phosphate cement by addition of PLGA microspheres and zinc silicate via synergistic effect of in -situ pore generation, bioactive ion stimulation and macrophage immunomodulation. *Appl. Mater. Today* 19, 100615. doi:10.1016/j.apmt.2020.100615

Qiao, Z., Yuan, Z., Zhang, W., Wei, D., and Hu, N. (2019). Preparation, *in vitro* release and antibacterial activity evaluation of rifampicin and moxifloxacin-loaded poly(D,L-lactide-co-glycolide) microspheres. *Artif. Cells Nanomedicine Biotechnol.* 47, 790–798. doi:10.1080/21691401.2019.1581792

Rahaman, M. N., Day, D. E., Bal, B. S., Fu, Q., Jung, S. B., Bonewald, L. F., et al. (2011). Bioactive glass in tissue engineering. *Acta Biomater.* 7, 2355–2373. doi:10.1016/j.actbio.2011.03.016

Ren, B., Han, Z., Li, W., and Liu, J. (2022). Feasibility study of a novel magnetic bone cement for the treatment of bone metastases. *Life-Basel* 12, 1342. doi:10.3390/life12091342

Rodriguez, L. C., Chari, J., Aghyarian, S., Gindri, I. M., Kosmopoulos, V., and Rodrigues, D. C. (2014). Preparation and characterization of injectable brushite filled-poly (methyl methacrylate) bone cement. *Materials* 7, 6779–6795. doi:10.3390/ma7096779

Roux, C., Cortet, B., Bousson, V., and Thomas, T. (2021). Vertebroplasty for osteoporotic vertebral fracture. *Rmd Open* 7, e001655. doi:10.1136/rmdopen-2021-001655

Sadati, V., Khakbiz, M., Chagami, M., Bagheri, R., Chashmi, F. S., Akbari, B., et al. (2022). Experimental investigation and finite element modelling of PMMA/carbon nanotube nanobiocomposites for bone cement applications. *Soft Matter* 18, 6800–6811. doi:10.1039/d2sm00637e

Salle, H., Van Tran, G., Faure, P., Mounayer, C., Rouchaud, A., Salle, L., et al. (2022). Treatment of A3.2 and A2 traumatic thoracolumbar spine compression fractures using vertebral body stenting: a 63-patient series. *J. Neurointerventional Surg.* 15, 86–90. doi:10.1136/neurintsurg-2021-018628

Schickert, S. D. L., Jansen, J. A., Bronkhorst, E. M., Van Den Beucken, J. J. J. P., and Leeuwenburgh, S. C. G. (2020a). Stabilizing dental implants with a fiber-reinforced calcium phosphate cement: an *in vitro* and *in vivo* study. *Acta Biomater.* 110, 280–288. doi:10.1016/j.actbio.2020.03.026

Schickert, S. D. L., Pinto, J. C., Jansen, J., Leeuwenburgh, S. C. G., and Van Den Beucken, J. J. J. P. (2020b). Tough and injectable fiber reinforced calcium phosphate cement as an alternative to polymethylmethacrylate cement for vertebral augmentation: a biomechanical study. *Biomaterials Sci.* 8, 4239–4250. doi:10.1039/d0bm00413h

Schroeter, L., Kaiser, F., Stein, S., Gbureck, U., and Ignatius, A. (2020). Biological and mechanical performance and degradation characteristics of calcium phosphate cements in large animals and humans. *Acta Biomater.* 117, 1–20. doi:10.1016/j.actbio.2020.09.031

Shearer, A., Montazerian, M., Sly, J. J., Hill, R. G., and Mauro, J. C. (2023). Trends and perspectives on the commercialization of bioactive glasses. *Acta Biomater.* 160, 14–31. doi:10.1016/j.actbio.2023.02.020

Shi, Y. (2021). Application of rehabilitation of cruciate ligament injury during exercise based on nano-biomaterials tissue engineering treatment plan. *Int. J. Nanotechnol.* 18, 113–126. doi:10.1504/ijnt.2021.114219

Sietsma, M. S., Hosman, A. J. F., Verdonschot, N. J. J., Aalsma, A. M. M., and Veldhuizen, A. G. (2009). Biomechanical evaluation of the vertebral jack tool and the inflatable bone tamp for reduction of osteoporotic spine fractures. *Spine* 34, E640–E644. doi:10.1097/brs.0b013e3181b1fed8

Stoops, K., Brown, J. M., Santoni, B., and Groundland, J. (2022). Thermal properties of polymethyl methacrylate vary depending on brand and type. *J. Orthop. Res.* 41, 614–618. doi:10.1002/jor.25389

Sue, X., Wu, Z., He, D., Shen, K., Liu, X., Li, H., et al. (2019). Bioactive injectable polymethylmethacrylate/silicate bioceramic hybrid cements for percutaneous vertebroplasty and kyphoplasty. *J. Mech. Behav. Biomed. Mater.* 96, 125–135. doi:10.1016/j.jmbbm.2019.04.044

Sultankulov, B., Berillo, D., Sultankulova, K., Tokay, T., and Saparov, A. (2019). Progress in the development of chitosan-based biomaterials for tissue engineering and regenerative medicine. *Biomolecules* 9, 470. doi:10.3390/biom9090470

Sun, X., Zhang, X., Jiao, X., Ma, J., Liu, X., Yang, H., et al. (2022a). Injectable bioactive polymethyl methacrylate-hydrogel hybrid bone cement loaded with BMP-2 to improve osteogenesis for percutaneous vertebroplasty and kyphoplasty. *Bio-Design Manuf.* 5, 318–332. doi:10.1007/s42242-021-00172-1

Sun, X., Zhang, X., Jiao, X., Ma, J., Liu, X., Yang, H., et al. (2022b). Injectable bioactive polymethyl methacrylate-hydrogel hybrid bone cement loaded with BMP-2 to improve osteogenesis for percutaneous vertebroplasty and kyphoplasty. *Bio-Design Manuf.* 5, 318–332. doi:10.1007/s42242-021-00172-1

Tai, C.-L., Lai, P.-L., Lin, W.-D., Tsai, T.-T., Lee, Y.-C., Liu, M.-Y., et al. (2016). Modification of mechanical properties, polymerization temperature, and handling time of polymethylmethacrylate cement for enhancing applicability in vertebroplasty. *Biomed Res. Int.* 2016, 1–8. doi:10.1155/2016/7901562

Tavakoli, M., Bakhtiari, S. S. E., and Karbasi, S. (2020). Incorporation of chitosan/graphene oxide nanocomposite in to the PMMA bone cement: physical, mechanical and biological evaluation. *Int. J. Biol. Macromol.* 149, 783–793. doi:10.1016/j.ijbiomac.2020.01.300

Thorfve, A., Lindahl, C., Xia, W., Igawa, K., Lindahl, A., Thomsen, P., et al. (2014). Hydroxyapatite coating affects the Wnt signaling pathway during peri-implant healing *in vivo*. *Acta Biomater.* 10, 1451–1462. doi:10.1016/j.actbio.2013.12.012

Tian, Y., Liu, H., He, L., Zhang, R., Lu, Q., Liu, C., et al. (2021). Calcium phosphate-based composite cement: impact of starch type and starch pregelatinization on its physicochemical properties and performance in the vertebral fracture surgical models *in vitro*. *J. Biomed. Mater. Res. Part B-Applied Biomaterials* 109, 2068–2078. doi:10.1002/jbm.b.34855

Valencia Zapata, M. E., Mina Hernandez, J. H., and Grande Tovar, C. D. (2020). Acrylic bone cement incorporated with low chitosan loadings. *Polymers* 12, 1617. doi:10.3390/polym12071617

Vallet-Regi, M., and Arcos, D. (2005). Silicon substituted hydroxyapatites. A method to upgrade calcium phosphate based implants. *J. Mater. Chem.* 15, 1509–1516. doi:10.1039/b414143a

Van Houdt, C. I. A., Gabbai-Armelin, P. R., Lopez-Perez, P. M., Ulrich, D. J. O., Jansen, J. A., Renno, A. C. M., et al. (2018). Alendronate release from calcium phosphate cement for bone regeneration in osteoporotic conditions. *Sci. Rep.* 8, 15398. doi:10.1038/s41598-018-33692-5

Vedhanayagam, M., Anandasadagopan, S., Nair, B. U., and Sreeram, K. J. (2020). Polymethyl methacrylate (PMMA) grafted collagen scaffold reinforced by PdO-TiO2 nanocomposites. *Mater. Sci. Eng. C-Materials Biol. Appl.* 108, 110378. doi:10.1016/j.msec.2019.110378

Vendeuvre, T., Brossard, P., Pic, J.-B., Billot, M., Gayet, L.-E., Pries, P., et al. (2021). Vertebral balloon kyphoplasty versus vertebral body stenting in non-osteoporotic vertebral compression fractures at the thoracolumbar junction: a comparative radiological study and finite element analysis (BONEXP study). *Eur. Spine J.* 30, 3089–3098. doi:10.1007/s00586-021-06785-5

Vezenkova, A., and Locs, J. (2022). Sudoku of porous, injectable calcium phosphate cements - path to osteoinductivity. *Bioact. Mater.* 17, 109–124. doi:10.1016/j.bioactmat.2022.01.001

Wang, C., Huang, W., Zhou, Y., He, L., He, Z., Chen, Z., et al. (2020a). 3D printing of bone tissue engineering scaffolds. *Bioact. Mater.* 5, 82–91. doi:10.1016/j.bioactmat.2020.01.004

Wang, C., Xiao, D., Lu, M., Liu, Q., Xie, T., Feng, G., et al. (2020b). Immobilization of poly(lactide-co-glycolide) microspheres on bone implant materials for antibiotic release and the binding mechanisms. *Rsc Adv.* 10, 7251–7258. doi:10.1039/c9ra08246h

Wang, C., Yu, B., Fan, Y., Ormsby, R. W., Mccarthy, H. O., Dunne, N., et al. (2019). Incorporation of multi-walled carbon nanotubes to PMMA bone cement improves cytocompatibility and osseointegration. *Mater. Sci. Eng. C-Materials Biol. Appl.* 103, 109823. doi:10.1016/j.msec.2019.109823

Wang, Q., Sun, C., Zhang, L., Wang, L., Ji, Q., Min, N., et al. (2022). High-versus low-viscosity cement vertebroplasty and kyphoplasty for osteoporotic vertebral compression fracture: a meta-analysis. *Eur. Spine J.* 31, 1122–1130. doi:10.1007/s00586-022-07150-w

Wang, X., Geng, Z., Huang, Y., Jia, Z., Cui, Z., Li, Z., et al. (2018b). Unraveling the osteogenesis of magnesium by the activity of osteoblasts *in vitro*. *J. Mater. Chem. B* 6, 6615–6621. doi:10.1039/c8tb01746h

Wang, X., Kou, J.-M., Yue, Y., Weng, X.-S., Qiu, Z.-Y., and Zhang, X.-F. (2018a). Clinical outcome comparison of polymethylmethacrylate bone cement with and without mineralized collagen modification for osteoporotic vertebral compression fractures. *Medicine* 97, e12204. doi:10.1097/md.0000000000012204

Wang, Y., Shen, S., Hu, T., Williams, G. R., Bian, Y., Feng, B., et al. 2021. Layered double hydroxide modified bone cement promoting osseointegration via multiple osteogenic signal pathways. *Acs Nano*, 15, 9732–9745. doi:10.1021/acsnano.1c00461

Wong, S. K., Yee, M. M. F., Chin, K.-Y., and Ima-Nirwana, S. (2023). A review of the application of natural and synthetic scaffolds in bone regeneration. *J. Funct. Biomaterials* 14, 286. doi:10.3390/jfb14050286

Wu, J., Xu, S., Qiu, Z., Liu, P., Liu, H., Yu, X., et al. (2016). Comparison of human mesenchymal stem cells proliferation and differentiation on poly(methyl methacrylate) bone cements with and without mineralized collagen incorporation. *J. Biomaterials Appl.* 30, 722–731. doi:10.1177/0885328215582112

Yan, F., Liu, Z., Zhang, T., Zhang, Q., Chen, Y., Xie, Y., et al. (2019). Biphasic injectable bone cement with Fe3O4/GO nanocomposites for the minimally invasive treatment of tumor-induced bone destruction. *Acs Biomaterials Sci. Eng.* 5, 5833–5843. doi:10.1021/acsbiomaterials.9b00472

Yang, J., Zhang, K., Zhang, S., Fan, J., Guo, X., Dong, W., et al. (2015). Preparation of calcium phosphate cement and polymethyl methacrylate for biological composite bone cements. *Med. Sci. Monit.* 21, 1162–1172. doi:10.12659/msm.893845

Yu, Y.-H., Wu, R.-C., Lee, D., Chen, C.-K., and Liu, S.-J. (2018). Artificial membrane induced by novel biodegradable nanofibers in the masquelet procedure for treatment of segmental bone defects. *J. Nanomater.* 2018, 1–8. doi:10.1155/2018/8246571

Yu, K., Liang, B., Zheng, Y., Exner, A., Kolios, M., Xu, T., et al. (2019). PMMA-Fe3O4 for internal mechanical support and magnetic thermal ablation of bone tumors. *Theranostics* 9, 4192–4207. doi:10.7150/thno.34157

Yu, L., Xia, K., Gong, C., Chen, J., Li, W., Zhao, Y., et al. (2020). An injectable bioactive magnesium phosphate cement incorporating carboxymethyl chitosan for bone regeneration. *Int. J. Biol. Macromol.* 160, 101–111. doi:10.1016/j.ijbiomac.2020.05.161

Zamora Lagos, S. I., Murillo Salas, J., Valencia Zapata, M. E., Mina Hernandez, J. H., Valencia, C. H., Rojo, L., et al. (2020). Influence of the chitosan morphology on the properties of acrylic cements and their biocompatibility. *Rsc Adv.* 10, 31156–31164. doi:10.1039/d0ra06508k

Zanfir, A.-V., Nenu, N., Voicu, G., Badanoiu, A.-I., Ghitulica, C.-D., and Iordache, F. (2019). Modified calcium silicophosphate cements with improved properties. *Mater. Chem. Phys.* 238, 121965. doi:10.1016/j.matchemphys.2019.121965

Zhai, G., Li, A., Liu, B., Lv, D., Zhang, J., Sheng, W., et al. (2021). A meta-analysis of the secondary fractures for osteoporotic vertebral compression fractures after percutaneous vertebroplasty. *Medicine* 100, e25396. doi:10.1097/md.0000000000025396

Zhang, Z.-F., Huang, H., Chen, S., Liu, D.-H., Feng, Y.-H., Xie, C.-L., et al. (2018b). Comparison of high- and low-viscosity cement in the treatment of vertebral compression fractures A systematic review and meta-analysis. *Medicine* 97, e0184. doi:10.1097/md.0000000000010184

Zhang, H., Cui, Y., Zhuo, X., Kim, J., Li, H., Li, S., et al. (2022a). Biological fixation of bioactive bone cement in vertebroplasty: the first clinical investigation of borosilicate glass (BSG) reinforced PMMA bone cement. *Acs Appl. Mater. Interfaces* 14, 51711–51727. doi:10.1021/acsami.2c15250

Zhang, X., Huang, P., Jiang, G., Zhang, M., Yu, F., Dong, X., et al. (2021). A novel magnesium ion-incorporating dual-crosslinked hydrogel to improve bone scaffold-mediated osteogenesis and angiogenesis. *Mater. Sci. Eng. C-Materials Biol. Appl.* 121, 111868. doi:10.1016/j.msec.2021.111868

Zhang, X., Kang, T., Liang, P., Tang, Y., and Quan, C. (2018a). Biological activity of an injectable biphasic calcium phosphate/PMMA bone cement for induced osteogensis in rabbit model. *Macromol. Biosci.* 18. doi:10.1002/mabi.201700331

Zhang, Y., Liu, X., and Liu, H. (2022). Cardiac perforation caused by cement embolism after percutaneous vertebroplasty: a report of two cases. *Orthop. Surg.* 14, 456–460. doi:10.1111/os.13192

Zheng, Z., Chen, S., Liu, X., Wang, Y., Bian, Y., Feng, B., et al. (2021). A bioactive polymethylmethacrylate bone cement for prosthesis fixation in osteoporotic hip replacement surgery. *Mater. Des.* 209, 109966. doi:10.1016/j.matdes.2021.109966

Zhu, J., Yang, S., Cai, K., Wang, S., Qiu, Z., Huang, J., et al. (2020). Bioactive poly (methyl methacrylate) bone cement for the treatment of osteoporotic vertebral compression fractures. *Theranostics* 10, 6544–6560. doi:10.7150/thno.44428

Zhu, X., Wang, C., Bai, H., Zhang, J., Wang, Z., Li, Z., et al. (2023). Functionalization of biomimetic mineralized collagen for bone tissue engineering. *Mater. Today Bio* 20, 100660. doi:10.1016/j.mtbio.2023.100660

frontiers | Frontiers in Bioengineering and Biotechnology

TYPE Review
PUBLISHED 17 November 2023
DOI 10.3389/fbioe.2023.1296881

OPEN ACCESS

EDITED BY
Wenjie Zhang,
Shanghai Jiao Tong University, China

REVIEWED BY
Wanting Niu,
Regis College, United States
Gaizhen Kuang,
University of Chinese Academy of Sciences, China
Jiulong Zhao,
Naval Medical University, China

*CORRESPONDENCE
Yuanjing Zhu,
zhuyj115@csu.edu.cn

†These authors have contributed equally to this work and share first authorship

RECEIVED 19 September 2023
ACCEPTED 09 November 2023
PUBLISHED 17 November 2023

CITATION
Zhu T, Zhou H, Chen X and Zhu Y (2023), Recent advances of responsive scaffolds in bone tissue engineering.
Front. Bioeng. Biotechnol. 11:1296881.
doi: 10.3389/fbioe.2023.1296881

Recent advances of responsive scaffolds in bone tissue engineering

Tongyu Zhu†, Hongbo Zhou†, Xiaojing Chen and Yuanjing Zhu*

Hunan Clinical Research Center of Oral Major Diseases and Oral Health, Xiangya Stomatological Hospital, Xiangya School of Stomatology, Central South University, Changsha, Hunan, China

The investigation of bone defect repair has been a significant focus in clinical research. The gradual progress and utilization of different scaffolds for bone repair have been facilitated by advancements in material science and tissue engineering. In recent times, the attainment of precise regulation and targeted drug release has emerged as a crucial concern in bone tissue engineering. As a result, we present a comprehensive review of recent developments in responsive scaffolds pertaining to the field of bone defect repair. The objective of this review is to provide a comprehensive summary and forecast of prospects, thereby contributing novel insights to the field of bone defect repair.

KEYWORDS

responsive scaffolds, bone tissue engineering, stimuli, inflammatory, targeted drug delivery

1 Introduction

Bone tissue defects present a significant health risk to individuals (Buza and Einhorn, 2016). Approximately four million surgical procedures are performed annually to address bone loss, utilizing grafts and/or substitutes, thereby establishing it as the second most commonly transplanted tissue worldwide (Greenwald et al., 2001). Although bone grafting serves as the preferred method for repairing extensive defects resulting from congenital anomalies, tumor removal, and traumatic fractures, it is accompanied by challenges such as limited availability, morbidity at the donor site, and inflammation, among others (Brydone et al., 2010; Tang et al., 2016).

The primary objective of bone tissue engineering is to develop bone-graft substitutes that can overcome the limitations associated with natural bone grafts (Shrivats et al., 2014). Scaffolds, which serve as a potential approach for treating bone defects, are currently being explored. The selection of appropriate biomaterials is of utmost importance in the fabrication of these scaffolds, and various techniques and materials are under investigation. The ideal bone graft substitutes should possess biocompatibility, biodegradability, and ease of production. Additionally, they should facilitate cell infiltration, stimulate bone growth, and provide biomechanical support during the regeneration of bone by osteoblasts (Bose et al., 2012).

Researchers have employed diverse scaffold materials to facilitate endogenous regeneration. Conventional scaffold materials comprise organic polymers such as collagen and hyaluronic acid, artificial polymers like polylactic acid, and biologically active inorganic materials like calcium phosphate, which enhance bone regeneration (Khan et al., 2008; Collins et al., 2021). However, conventional scaffolds exhibit a deficiency in controlled release capabilities, rendering them incapable of effectively

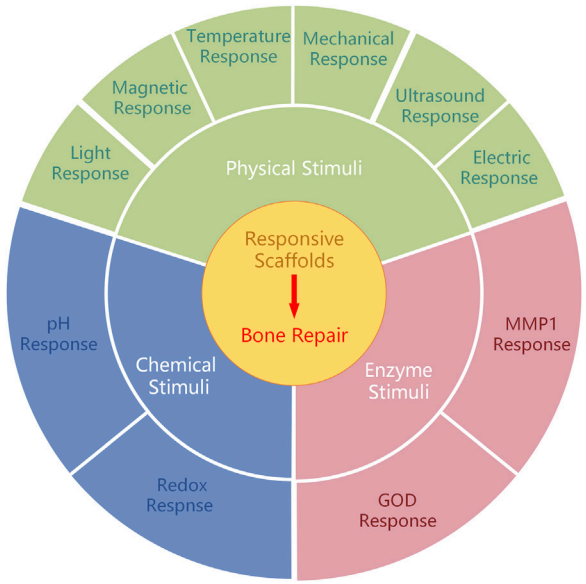

FIGURE 1
Different types of responsive scaffolds for bone repair.

regulating chronic inflammation as required (Ye et al., 2022). As a result, scholars have redirected their focus towards the advancement of responsive scaffolds.

Responsive scaffolds are considered to be groundbreaking in the field of bone repair. These scaffolds are comprised of materials that possess the capability to be activated and respond to various external stimuli, such as light, magnetism, and pH, or internal stimuli, including cytokines, enzymes, and biological signals. Responsive scaffolds demonstrate the ability to react to triggers originating from external regulatory equipment and internal microenvironment alterations, thereby enabling them to deliver drugs in a timely manner in response to a diverse array of circumstances (Wei et al., 2022). Moreover, they exhibit the capacity to react to both external and internal triggers, enabling them to deliver drugs as needed in response to a wide range of situations.

The occurrence of bone loss can lead to injury in both hard and soft tissues, with the microenvironment of diseased tissue exhibiting notable distinctions from that of healthy tissue. These disparities are believed to exploit various stimuli, including lower pH levels, elevated concentrations of reactive oxygen species (ROS), and heightened enzyme and osteoclast activities, thereby promoting bone resorption. By utilizing a responsive scaffold, it becomes possible to activate and target these specific stimuli, facilitating the precise delivery of drugs to modify the microenvironment and effectively repair the injury. For instance, researchers have developed a modified-scaffold composed of an electrospun asymmetric double-layer membrane made of polycaprolactone and collagen (PCL/Col) to address the low pH environment in bone defect sites. This composite scaffold exhibited the release of approximately 93% of Zn^{2+} ions from the PCL/Col/ZIF-8 membrane within 12 h under acidic conditions (pH 5.5). The pH-sensitive structure of the scaffold provides a favorable environment for the proliferation of osteoblasts, thereby presenting a promising approach for bone regeneration (Xue et al., 2021). Responsive scaffolds have demonstrated potential and approval in the treatment of bone injuries.

This review primarily examines the recent advancements in responsive biomaterials and scaffolds utilized in bone tissue engineering. It specifically delves into their application, material selection, scaffold design, and their efficacy in addressing bone defects. Furthermore, the review explores the current limitations and potential prospects for bone defect restoration, drawing upon substantial evidence that substantiates the favorable outcomes achieved through the implementation of functionalized responsive scaffolds.

2 The categories of responsive scaffolds

This study primarily encompasses three primary categorizations of stimulus-responsive scaffolds based on the source of stimuli: physical stimuli (e.g., light, temperature change, electric field, magnet, and ultrasound), chemical stimuli (e.g., pH level and ROS), and enzyme stimuli (Figure 1) (Table 1).

2.1 Physical stimuli

Physical-responsive scaffolds are predominantly comprised of materials that are sensitive to physical stimuli. These materials possess a structure that can be reconfigured when exposed to various factors, including light, magnetism, temperature, ultrasonic waves, and magnetic fields. Consequently, these alterations in structure facilitate the delivery of drugs. For instance, temperature-responsive scaffolds exhibit stability in healthy tissue, but undergo degradation in diseased tissue. In the initial phases of bone defects, inflammation induces a localized increase in temperature. This change in temperature can serve as an endogenous stimulus for the scaffold to respond and subsequently release the drug (Zhang et al., 2013; Karimi et al., 2016b).

Under specific circumstances, elastin-like polypeptides (ELPs) exhibit a lower critical solution temperature (LCST) in contrast to other synthetic polymers (Tamburro et al., 2005). Upon surpassing this transition temperature, ELPs undergo a first-order phase transition, resulting in the formation of a peptide and water-rich phase (Krishna et al., 2012; Zhao et al., 2016). This distinctive characteristic has sparked considerable enthusiasm in the advancement of biomaterials capable of reacting to external stimuli. In a recent study, researchers have successfully synthesized elastin-like self-assembly nanoparticles with thermos-responsive characteristics. These nanoparticles were employed for the controlled release of bone morphogenetic protein-2 (BMP-2) and bone morphogenetic protein-14 (BMP-14), exploiting the reverse temperature transition of bio-generated polymer$(VPAVG)_{220}$ (Bessa et al., 2010). This distinctive property can be harnessed to mitigate inflammation and facilitate bone regeneration under specific conditions. In the field of bone tissue engineering, a wide range of physical-responsive scaffolds are frequently utilized to modulate drug delivery.

2.1.1 Temperature response

Temperature-responsive scaffolds can undergo structural reconstruction and release drug payloads when the desired

TABLE 1 The summarization of recent responsive scaffolds.

Scaffold categories	Specific scaffold material	Growth factors or drugs	Animal model/ *in vitro* study	Function	Ref
temperature-responsive	elastin-like polymer $(VPAVG)_{220}$	bone morphogenetic protein-2 (BMP-2) and bone morphogenetic protein-14 (BMP-14)	C2C12 cells	induced osteogenic mineralization	Bessa et al. (2010)
temperature-responsive	poly(ε-caprolactone-co-lactide)-b-PEG-b-poly(ε-caprolactone-co-lactide) (PCLA) and O-phosphorylethanolamine	bone morphogenetic protein 2 (BMP-2)	subcutaneous administration into the dorsal region of Sprague-Dawley (SD) rats	biomineralized *in situ*	Kim et al. (2020)
temperature-responsive	chitosan (CS) and methylcellulose (MC)	veratric acid (VA)	mouse mesenchymal stem cells	promoted osteogenic differentiation	Durairaj et al. (2023)
temperature-responsive	hydroxyapatite (HA), Gelatin (GN) and Fe_3O_4	ibuprofen (IBU)	MTT assay within the cell environment	highly biocompatible	Sahmani et al. (2020)
light-responsive	strontium and ibuprofen-loaded black phosphorus (BP + IBU@SA microspheres) into aminated modified poly-L-lactic acid (PLLA)	ibuprofen (IBU)	MC3T3-E1 cells	improved cell adhesion and proliferation and induced apatite formation	Chen et al. (2021)
light-responsive	thin-film silicon (Si) embedded into hydroxyapatite mineralized collagen/poly(ε-caprolactone) (PLA) structures	-	5 mm-sized SD rat circular bone defect model	improved osteogenesis	Wang et al. (2023)
electric-responsive	poly (l-lactic acid)-block-aniline pentamer-block-poly (l-lactic acid) (PLA-AP) with poly (lactic-co-glycolic acid)/hydroxyapatite (PLGA/HA)	human bone morphogenetic protein-4 (hBMP-4)	rabbit radial defect model	improved cell proliferation ability, enhanced osteogenesis differentiation and bone healing	Cui et al. (2020)
electric-responsive	gelatin-graft-poly-pyrrole	H_2O_2	-	sustained oxygen release	Nejati et al. (2020)
electric-responsive	silicon dioxide with poly(dimethylsiloxane) (SiO_2/PDMS)	-	5 mm-sized SD rat circular bone defect model	facilitated bone regeneration	Qiao et al. (2022)
mechanical-responsive	hydroxyapatite/barium titanate (HA/BT)	-	MTT assay within L929 cells	highly biocompatible	Zhang et al. (2014)
magnetic-responsive	poly (vinylidene fluoride) (PVDF), and magnetostrictive particles of $CoFe_2O_4$	-	MC3T3-E1 cells	promoted preosteoblasts proliferation	Fernandes et al. (2019)
magnetic-responsive	polycaprolactone (PCL) microparticles, encapsulating magnetic nanoparticles (MNPs)	placental proteins	umbilical cord mesenchymal stem cells (UC-MSCs)	promoted osteogenic differentiation	Lanier et al. (2021)
ultrasound-responsive	polylactic acids (PLA) embedded in alginate hydrogels	stromal cell-derived factor-1 (SDF-1) and bone morphogenetic protein 2 (BMP-2)	SD rats femoral bone defect model	repaired bone defect *in situ*	He et al. (2023)
pH-responsive	polycaprolactone/collagen (PCL/Col) membrane modified by zeolitic imidazolate framework-8 (ZIF-8)	-	SD rats calvarial defect model	increased osteoinductivity along with blood vessel formation	Xue et al. (2021)
pH-responsive	chitosan loaded with ZIF-8	vancomycin (VAN)	MC3T3-E1 cells	promoted high proliferation and osteogenic activities	Karakeçili et al. (2019)
ROS-responsive	LBL-compatible poly (thioketal β-amino amide) (PTK-BAA) polycation	bone morphogenetic protein 2 (BMP-2)	8 mm-sized SD rat circular bone defect model	increased new bone formation	Martin et al. (2021)
enzyme-responsive	KLDL-MMP1 (Ac-KLDLKLDLVPMSMRGGKLDLKLDL-CONH2) peptides	bone marrow mesenchymal stromal cell-derived exosomes (BMSC-Exos)	6 mm-sized SD rat circular bone defect model	recruited stem cells and promoted osteodifferentiation in response to neovascularization and accelerate tissue regeneration	Yang et al. (2023)
enzyme-responsive	polycaprolactone/chitosan nanofibers with glucose oxidase (GOD)	dexamethasone (DEX)	MC3T3-E1 cells	promoted MC3T3-E1 cells' osteogenic differentiation in high-glucose environments	Jia et al. (2023)

temperature is achieved, as they are triggered by changes in the surrounding environment. Thermo-responsive polymers, employed in the fabrication of these scaffolds, may experience phase transitions above the LCST (Bordat et al., 2019) or expedite degradation when exposed to elevated temperatures. For instance, certain thermo-responsive polymers undergo a transition from a liquid state to a stable viscoelastic gel, while certain thermo-sensitive polymers exhibit accelerated degradation at elevated temperatures, thereby facilitating the controlled release of drugs.

In a recent study, a cohort of alginate bioconjugates comprising micrografted poly(ε-caprolactone-co-lactide)-b-PEG-b-poly(ε-caprolactone-co-lactide) (PCLA) and o-phosphorylethanolamine were synthesized with the aim of facilitating bone regeneration (Kim et al., 2020). These bioconjugated salts have the ability to undergo a conversion into durable viscoelastic gels when administered *in vivo* and subjected to physiological temperature, surpassing the LCST threshold. This conversion enhances the mechanical characteristics and fosters bone regeneration, thereby suggesting their potential utility in promoting bone formation. Methylcellulose is a cellulose polysaccharide known for its biocompatibility, biodegradability, and hydrophilicity. It demonstrates gelation properties, resulting in gel formation at specific temperatures (Lioubavina-Hack et al., 2005; Kim et al., 2018). Composite hydrogels, comprising chitosan and methylcellulose, encapsulate veratric acid and exhibit desirable biocompatibility. These hydrogels gelatinize at 37°C, making them suitable for use as a restorative agent to enhance osteoblast differentiation (Durairaj et al., 2023).

Endogenous temperature stimulation is elicited by fluctuations in temperature conditions at the site of the lesion. The lesion tissue undergoes pathological deformation and hyperthermia, which stem from trauma and tumors, thereby triggering the release of inflammatory factors and evaluation of the local environmental temperature. Consequently, the scaffold structure in pathological sites undergoes alterations when the temperature is elevated. During the initial phase of bone defect, the localized temperature elevation can serve as a stimulus for scaffold response and/or drug release (Zhang et al., 2013; Karimi et al., 2016b).

Nanocarriers engineered for thermal responsiveness have the potential to maintain stability at the physiological temperature of the human body. Upon exposure to external heat or assessment of the local environmental temperature, these carriers can efficiently release therapeutic agents either promptly upon heating or in a controlled manner at the site of disease. In a recent study, Fe_3O_4 nanoparticles were employed by researchers within a magnetic field to induce heat generation and eradicate infected cells (Abdellahi et al., 2018a). The magnetite nanoparticles (MNPs) possess the ability to elevate temperature upon exposure to an alternating magnetic field, thus facilitating the degradation of the drug carrier for drug release (Abdellahi et al., 2018b; Sahmani et al., 2018). In this particular scenario, hydroxyapatite (HA) and gelatin (GN) were integrated with MNPs to fabricate bio-nanocomposite scaffolds, which subsequently underwent degradation under magnetothermal conditions. The results indicate that the prepared scaffold exhibits promising potential for utilization in bone tissue engineering for both biological and thermal applications (Sahmani et al., 2020).

The achievement of thermal specificity in temperature-responsive systems poses a significant obstacle due to the restricted variability observed in pathological tissues within living organisms. Consequently, future research endeavors should prioritize the development of scaffold materials that are more responsive to lower temperatures, possess enhanced stability in normal tissues, and ensure greater safety.

2.1.2 Light response

Various light-responsive materials exhibit different responses to various wavelengths of light, thereby facilitating the identification of suitable materials for diverse clinical needs. Upon exposure to light, light-responsive scaffolds undergo changes in their physical properties, thereby enabling efficient drug delivery. This responsiveness of scaffolds is primarily attributed to the degradation of materials containing light-sensitive components or the modification of light-sensitive molecules. Consequently, when scaffolds are exposed to light, the drug bound or encapsulated within them is released (Mayer and Heckel, 2006; Chen and Zhao, 2018).

Black phosphorus (BP), a novel nanomaterial characterized by its two-dimensional framework, exhibits remarkable biosafety, inherent biocompatibility, and photosensitivity (Pandey et al., 2020). In a recent study, a multifunctional nanofiber scaffold was developed by incorporating ibuprofen black phosphorus (BP + IBU@SA microspheres) and sodium alginate microspheres onto aminated poly-L-lactic acid (PLLA) nanofibers. This scaffold demonstrates exceptional near-infrared light-responsive release capabilities and anti-inflammatory properties. BP was employed to induce the destruction of polymeric shells through the utilization of near-infrared (NIR)-mediated photothermal performance, thereby achieving controlled drug release. By subjecting the scaffolds to NIR light, the adverse effects of rapid drug release can be mitigated, while maintaining the drug concentration at an optimal level to meet the specific requirements of bone repair. The conducted investigations have demonstrated that the incorporation of functionalized scaffolds enhances cell adhesion, proliferation, and apatite formation, rendering it a viable and promising approach for bone tissue engineering (Chen et al., 2021).

Silicon (Si) is widely employed as a semiconductor material in bio-implantation devices (Kang et al., 2016; Parameswaran et al., 2018). When subjected to near-infrared illumination, Si structures produce electrical signals that depolarize cell potentials and trigger intracellular calcium activation. Consequently, these optoelectronic signals play a role in directing hBMSCs towards osteogenic differentiation (Wang et al., 2023). Recently, a three-dimensional (3D) biomimetic scaffold utilizing thin-film Si microstructures has been developed. Through the utilization of NIR light, researchers have discovered that the Si film facilitates the attachment and growth of cells. The Si-based hybrid scaffold offers a 3D hierarchical structure that effectively governs cell growth and regulates cell behavior via light-responsive electrical signals. These silicon structures are remotely manipulated by infrared radiation to regulate the depolarization of stem cell membranes, resulting in heightened Ca^{2+} activities for hBMSCs, as well as improved potential and intracellular calcium dynamics. Consequently, this process promotes both cell proliferation and differentiation. The utilization of silicone scaffolds resulted in

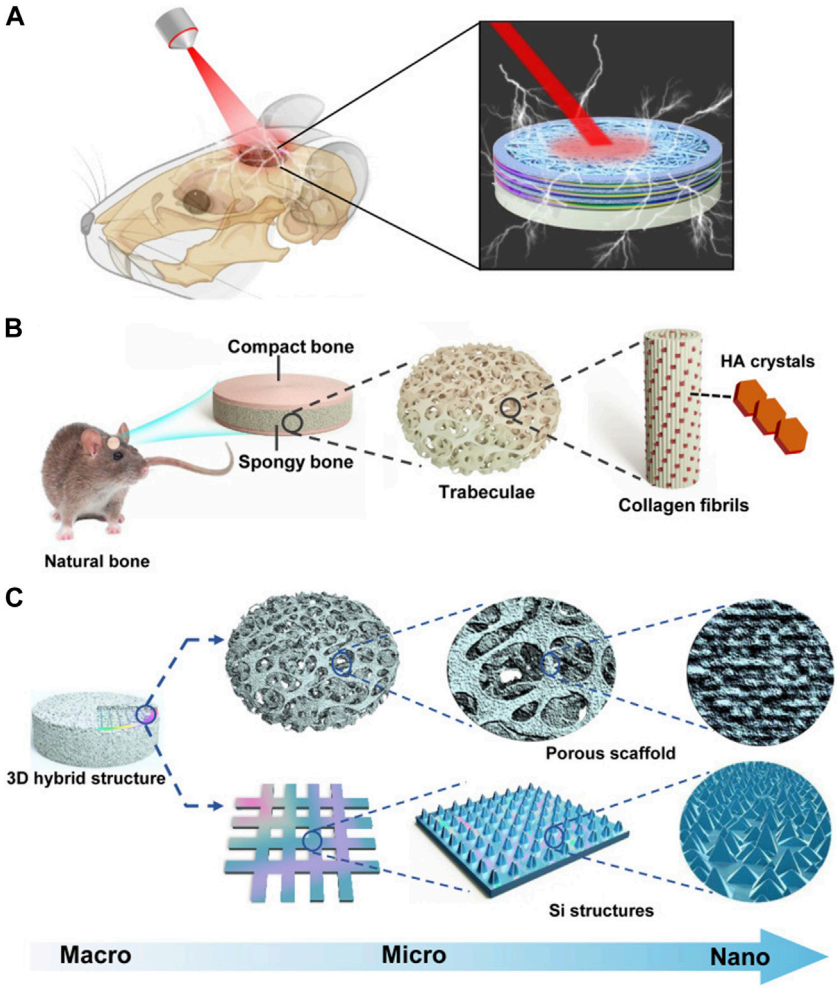

FIGURE 2
Bioregenerative 3D optoelectronic scaffold with Si nanostructures for bone regeneration. **(A)** An illustration of an implantable scaffold in concept. **(B)** Native bone hierarchical structure. **(C)** Structural design of the 3D hybrid scaffold. Reproduced from (Wang et al., 2023) with permission. Copyright 2023 AAAS.

enhanced bone formation when subjected to light stimulation (Wang et al., 2023) (Figure 2).

However, the advancement of light-responsive systems continues to encounter various obstacles. In numerous applications, the ability of radiation below 650 nm to penetrate tissue beyond a depth of 1 cm is limited, while NIR light within the range of 650–900 nm (as water absorbs wavelengths longer than 900 nm) can penetrate up to 10 cm. However, these penetration depths are not considered clinically significant due to being either too shallow or too deep *in vitro* (Weissleder, 2001; Fomina et al., 2012). Additionally, further quantitative investigation is necessary to evaluate the biological safety of light-sensitive materials and ascertain the optimal duration and intensity of light exposure.

2.1.3 Electric response

Electrical stimulation (EStim) has undergone extensive research and has proven to be an effective intervention in medical settings for the purpose of enhancing bone healing (Bhavsar et al., 2020), as it exerts influence on the migration (Yuan et al., 2014), proliferation (Ercan and Webster, 2008), differentiation (Eischen-Loges et al., 2018) of bone cells. Presently, the integration of electrostimulation therapy with electric-responsive stents is regarded as a compelling approach in clinical practice (Palza et al., 2019; Vaca-González et al., 2019).

Endogenous electrical currents exert a substantial influence on diverse physiological processes in the human body. These naturally occurring electrical fields possess the capacity to induce either depolarization or hyperpolarization of the membrane potential in living tissues, thereby eliciting the activation of signaling factors that facilitate cell proliferation and migration, including those of bone cells (Funk, 2015). Exogenous electrical stimulation including alternating current (AC), which reverses direction periodically and direct current (DC) which flows in one direction both have effects on bone tissue and scaffold (Chen et al., 2013). Electric-responsive scaffolds possess inherent bioactivity and can facilitate tissue formation with or without the need for external electrical stimulation. These scaffolds are capable of responding to electrical fields in living tissues, thereby expediting drug release. Consequently, electric-responsive scaffolds have been employed in various studies within the field of bone tissue engineering.

Conductive polymers, namely polyaniline, poly-pyrrole, polythiophene, and their derivatives (Cui et al., 2012; Xie et al., 2015) have been found to augment cellular activities, including cell adhesion, proliferation, differentiation, migration, and protein secretion, at the interface between the polymer and tissue, regardless of electrical stimulation (Hardy et al., 2013). These polymers demonstrate favorable biocompatibility in both *in vivo* and *in vitro* settings, while also exhibiting high conductivity under physiological conditions. Polyaniline (PA) is a conductive polymer that exhibits the ability to undergo transference when subjected to pulsed EStim (Wang et al., 2017). Additionally, polylactide (PLA) is a polymer known for its favorable biodegradability (Huang et al., 2007). In light of these aforementioned attributes, a novel electric-responsive scaffold has been developed, comprising a main chain composed of poly (l-lactic acid)-block-aniline pentamer-block-poly (l-lactic acid) (PLA-AP) and a triblock copolymer of poly (lactic-co-glycolic acid)/hydroxyapatite (PLGA/HA). The composite scaffold (PLGA/HA/PLA-AP/phBMP-4) underwent degradation upon electrical stimulation (Cyclic voltammograms (CV), scanning rate of 100 mVs^{-1}) to control the release of phBMP-4 and regulate gene expression of doxycycline (Dox). In an experimental model involving rabbit radius defects, the electric-responsive scaffold demonstrated enhanced cell proliferation, improved osteogenic differentiation, and influenced the process of bone healing (Cui et al., 2020).

Poly-pyrrole has garnered significant attention in academic research due to its exceptional conductivity. In this study, H_2O_2-loaded polylactic acid microparticles were manufactured, and gelatin-graft-poly-pyrrole with varying pyrrole contents and periodate-oxidized pectin were synthesized to create an injectable conductive hydrogel/microparticle scaffold. This scaffold demonstrated the ability to sustain oxygen release for a duration of 14 days. The conductivity of the scaffold can enhance the bone healing process when responding to electrical stimuli, making it a promising candidate for bone tissue engineering applications (Nejati et al., 2020).

Electret materials, known for their enduring polarization properties (Zhang et al., 2023), have the ability to generate intrinsic electrical stimulation when subjected to an external electric field (Guo et al., 2022; Lin et al., 2022; Qiao et al., 2022). In tissue engineering, electret materials commonly employed include inorganic compounds like silicon dioxide (SiO_2) (Qiao et al., 2022), zinc oxide (ZnO) (Zhu et al., 2018), HA (Nakamura et al., 2009), as well as biopolymers such as proteins (e.g., collagen), polysaccharides (e.g., chitin), and polynucleotides (e.g., DNA), also demonstrate the phenomenon of the electron effect (Zheng et al., 2020). SiO_2, a material with electret properties, exhibits favorable biocompatibility and charge retention ability (Li et al., 2015). In order to enhance its electroactive properties, researchers developed a composite membrane by integrating silicon dioxide with poly(dimethylsiloxane) (SiO_2/PDMS). The composite membranes underwent polarization through the application of an external electric field, resulting in the retention of residual charge for a duration of up to 6 weeks. The electreted SiO_2/PDMS membranes demonstrated a favorable electrical microenvironment, leading to enhanced osteogenic differentiation of BMSCs *in vitro* and accelerated bone defect healing *in vivo* (Qiao et al., 2022) (Figure 3).

The potential application of electrical stimuli-responsive scaffolds in bone repair shows promise. However, the controllability of electric field changes in organisms remains uncertain, necessitating further investigation into the application of telephony stents.

2.1.4 Mechanical response

Mechanical-responsive materials possess the ability to promptly alter their physiochemical attributes when subjected to mechanical force or deformation (Shabani and Bodaghi, 2023). Piezoelectric biomaterials are a class of intelligent materials capable of producing electrical activity in response to mechanical stimulation, independent of the need for external electrical devices (Zheng et al., 2020). Piezoelectricity arises from the inherent crystal or chemical structure of materials, leading to the development of a net dipole or charge during mechanical deformation. Additionally, piezoelectric materials possess the ability to modulate cellular behavior by generating surface charges in response to deformation caused by cellular interaction. This characteristic offers novel avenues for biomechanical simulation, bone regeneration, and bone defect repair (Tandon et al., 2018; Khare et al., 2020).

Piezoelectric materials can be classified into various categories including polymers (such as PLLA and poly (vinylidene fluoride) (PVDF)), ceramics [such as HA and barium titanate (BT)], natural materials like collagen, and composite polymers. An example of such composites is the aligned porous BT/HA composites, which have been developed to possess high piezoelectric coefficients owing to their exceptional piezoelectric property. These composites serve as a charge supplier, thereby stimulating the bone healing process, and exhibit similar charge supply properties and stress-generated potentials as natural collagen bone (Baxter et al., 2010; Zhang et al., 2014).

Collagen, a naturally occurring protein and integral component of bone, exhibits piezoelectric properties that render it well-suited for tissue engineering applications. Specifically, the piezoelectric nature of collagen within bone induces the generation of a streaming potential when subjected to stress, leading to a decrease in hydraulic permeability and an augmentation in stiffness (Ahn and Grodzinsky, 2009; Ferreira et al., 2012). The suitability of the collagen-HA piezoelectric composite scaffold for cellular growth and bone healing has been demonstrated in previous research (Silva et al., 2001). Nevertheless, this scaffold is subject to certain limitations, including low mechanical stiffness, rapid degradation, and potential toxicity resulting from the use of crosslinking agents.

Despite facing challenges related to material stability, biocompatibility, and the need to balance mechanical properties, the investigation of piezoelectric materials in the realm of bone tissue engineering presents promising opportunities for the treatment of bone defects and the regeneration of bone.

2.1.5 Magnetic response

The utilization of magnetic nanoparticles in bone tissue engineering has gained attention due to their inherent magnetism and the magnetocaloric effect, among other factors. These nanoparticles demonstrate a responsive characteristic towards magnetic fields, including both alternating magnetic field (AMF) that periodically change direction, and constant magnetic field (CMF) that remain in one direction (Goharkhah et al., 2015).

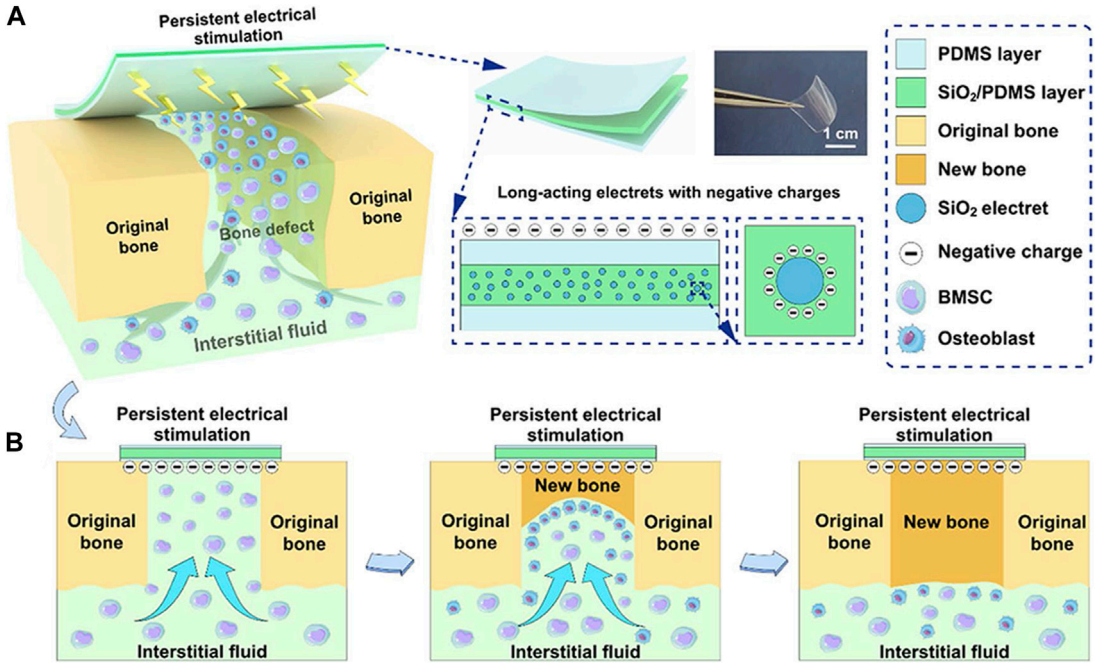

FIGURE 3
The schemes of electreted sandwich membranes. **(A)** Illustration of persistent electrical stimulation provided by electreted sandwich-like SiO_2/PDMS composite membranes. **(B)** Implanted composite membranes act as native periosteum covering the bone defect region to enhance well-integrated bone formation and regeneration. Reproduced from (Qiao et al., 2022) with permission. Copyright 2022 American Chemical Society.

Moreover, they possess the potential to augment the osteoinductive, osteoconductive, and angiogenic properties of scaffolds (Dasari et al., 2022).

A magnetic-responsive scaffold comprising of a piezoelectric polymer, PVDF, and magnetostrictive particles of $CoFe_2O_4$ has been successfully fabricated, with nylon template structures utilized to facilitate the solvent casting process. The investigation revealed that the PVDF component of the scaffold undergoes crystallization into the electroactive β-phase when subjected to magnetic and/or electromagnetic stimulation (permanent magnets, frequency of 0.3 Hz), thereby enhancing the proliferation of preosteogenic cells. This observed phenomenon can be attributed to the interplay between the magnetic and electromagnetic properties of the magnetic nanoparticles upon stimulation (Fernandes et al., 2019) (Figure 4). The magnetomechanical and magnetoelectric response of the scaffolds is believed to be a valuable resource.

In a separate investigation, the magnetic-responsive scaffold is comprised of PCL microparticles that enclose MNPs and placental proteins. The MNPs, due to their magnetocaloric effect, induce heating and subsequent melting of the PCL upon exposure to AMF (strength from−1 to 1 T), thereby facilitating the diffusion of proteins from the microparticles to stimulate bone formation. Upon deactivation of the magnetic field, the PCL solidifies once again, potentially enabling repeated administration of drugs in a cyclic manner (Lanier et al., 2021). This present study introduces a magnetic-responsive delivery system designed for localized drug release, with potential applications in bone regeneration.

The magnetic field presents a superior setting for external stimuli-responsiveness in comparison to light and temperature due to its ability to fully penetrate human tissue and initiate release, while also allowing for complete external control. Nevertheless, magnetic nanoparticle could face drawbacks of diffusion out within one or 2 days, thus preventing a continuous release (Veres et al., 2022), during the bone defect treatment and Iron oxide magnetic nanoparticles may mediate ROS generation and have an impact on other cells (Hohnholt et al., 2011; Sruthi et al., 2018).

2.1.6 Ultrasound response

Ultrasound, a mechanical wave with a high frequency (≥20 kHz), possesses the ability to be concentrated and transmitted within a particular medium, thereby finding utility in various clinical domains including *in vivo* imaging and physical therapy (Wheatley and Cochran, 2013). Furthermore, ultrasound exhibits potential in addressing bone defects as it can influence the biological aspects and drug administration characteristics of materials (Wei et al., 2021; He et al., 2023).

In order to obtain biomimetic scaffold composites (BSCs), researchers fabricated acoustically responsive hydrogel scaffolds (ARSs) that were developed and incorporated with stromal cell derived factor-1 (SDF-1) and BMP-2. The alginate hydrogel scaffold was degraded through pulsed ultrasound (p-US) irradiation, resulting in the exposure of ARSs to BMSCs due to its thermal effect. Subsequently, sinusoidal continuous wave ultrasound (s-US) irradiation was applied to stimulate the intrinsic resonance of ARSs, thereby facilitating the capture of endogenous BMSCs on the scaffolds and significantly enhancing their adhesion and growth for the *in situ* repair of bone defects (He et al., 2023).

The ultrasound-responsive scaffold facilitates the precise release of drugs and recruitment of cells in a spatiotemporal

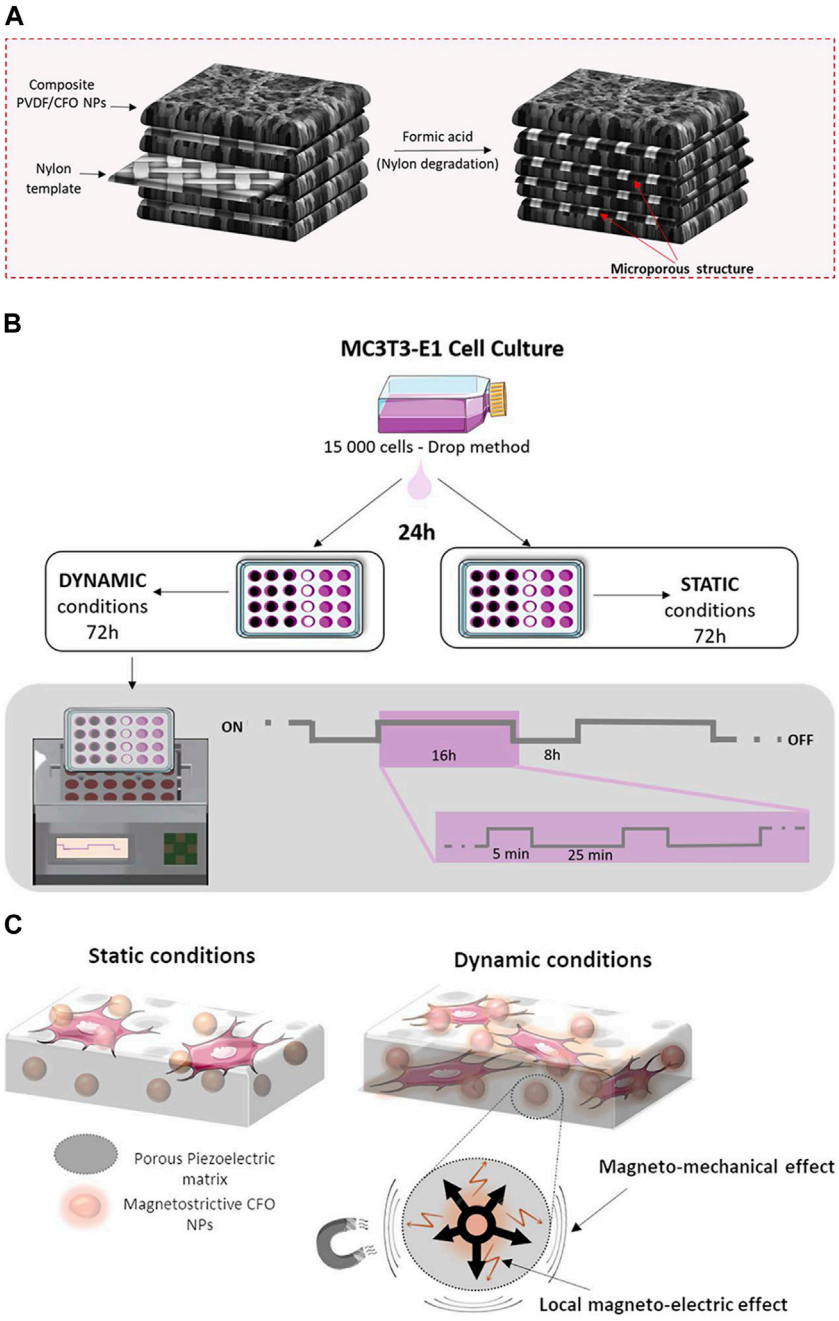

FIGURE 4
The schemes of 3D magnetoactive scaffolds for bone tissue engineering. **(A)** Schematic representation for the 3D scaffold development. **(B)** Schematic representation of the cell culture assays and stimulation profile. **(C)** Schematic representation of magnetomechanical and local magnetoelectrical properties of 3D scaffolds upon the magnetic stimuli. Reproduced from (Fernandes et al., 2019) with permission. Copyright 2019 American Chemical Society.

manner, while minimizing adverse effects through a non-toxic pathway (Pitt et al., 2004; Zardad et al., 2016). Nonetheless, the uncontrolled depth of ultrasound penetration and the potential thermal effect necessitate further investigation. In contrast to ultrasound, shockwave, which is a prevalent mechanical wave, exhibits greater shock amplitude and energy (Smallcomb et al., 2022). It is commonly employed to facilitate the biological healing processes of bones. Although shockwave is seldom reported as a stimulus source for responsive scaffolds, it offers a promising and innovative avenue for the repair of bone defects (Cheng and Wang, 2015).

2.2 Chemical stimuli

Chemically-responsive scaffolds are primarily constructed using materials that demonstrate sensitivity to specific variations in environmental concentration. When exposed to changes in the

pH value, ROS concentration, ion concentration, and other conditions, the drug-encapsulated scaffold undergoes stimulation, leading to the rupture of responsive chemical bonds or modification of the functional group structure within the scaffold. Consequently, this process triggers the release of the drug. For example, ROS concentration can be activated by phagocytes (such as granulocytes and macrophages) under inflammatory conditions after trauma, and phenylborate pinanol ester (PBAP), a compound that can be combined on scaffold, break chemical bonds and fracture under high ROS, which lead to the quickly drug releasing on the certain site (Zhang et al., 2017; Yuan et al., 2021). Therefore, the development of chemical-responsive materials holds potential in facilitating targeted drug delivery at the site of injury to promote bone repair. Here are several common types of chemical-responsive scaffolds on bone regeneration.

2.2.1 pH response

pH-responsive scaffolds are specifically engineered to react to alterations in pH levels, which are induced by the release of inflammatory factors from injured tissues. Extensive research has demonstrated that the pH value can decrease to 6.5 within a span of 60 h following the onset of inflammation (Caliceti, 2011). Furthermore, various organelles exhibit distinct pH values, such as lysosomes (4.5–5), endosomes (5.5–6), golgi apparatus (6.4), and cytosol (7.4) (Karimi et al., 2016a). Consequently, it becomes feasible to incorporate pH-responsive chemical groups into scaffold materials, thereby empowering the scaffold to regulate the release of drugs within the affected tissue.

Zeolitic imidazolate framework-8 (ZIF-8) belongs to the class of metal-organic frameworks (MOFs), which are formed through the connection of metal ions or clusters with organic ligands. Its remarkable pH-sensitivity has led to its application as a bone substitute and drug carrier (Zheng et al., 2016). Research has demonstrated that ZIF-8 is capable of releasing Zn^{2+} ions in acidic environments, thereby displaying a favorable osteogenic impact (Liu et al., 2022). To facilitate the promotion of vascularized bone regeneration, electrospun polycaprolactone/collagen (PCL/Col) membranes were modified with ZIF-8. The ZIF-8 structure experienced collapse and subsequent release of Zn^{2+} ions at a pH value of 5.5. Within a 12-h timeframe, approximately 93% of Zn^{2+} ions were discharged from the PCL/Col/ZIF-8 composite membrane under acidic conditions (pH 5.5). Utilizing this pH-responsive scaffold, concurrent restoration of blood vessels and bone was achieved in a rat model with calvarial defects (Xue et al., 2021).

In a separate study, ZIF-8 nanocrystals were employed as a carrier for vancomycin in order to achieve a delivery profile that responds to changes in pH. These nanocrystals were incorporated into chitosan fiber-scaffolds to create a potential substitute for bone tissue, which also possessed antimicrobial properties and facilitated interaction with osteoblast cells. Following a 48-h period at a pH of 5.4, the release of vancomycin reached a plateau at 77%, subsequent to the increased dissolution of ZIF-8 under acidic conditions. This dissolution served to diminish the activity of *S. aureus* and promote the differentiation of preosteoblasts into osteoblasts (García-González et al., 2018; Karakeçili et al., 2019).

The pH-responsive system presents a captivating approach for drug delivery, leveraging the pH discrepancies observed in various tissues within the living organism. Nevertheless, the exclusive reliance on pH reaction systems may encounter limitations in terms of specificity and sensitivity, given the inconsistent magnitude of pH disparity between the target tissue and healthy tissue.

2.2.2 Redox response

ROS, encompassing highly reactive ions, free radicals or molecular compounds such as superoxide (O^{2-}), hydroxyl radicals (·OH), hypochlorite ion (ClO^{-}), and hydrogen peroxide (H_2O_2), play a significant role as signaling molecules in the progression of inflammatory disorders. Given their close relationship with bone growth and remodeling, ROS hold particular appeal for augmenting material responsiveness (Martin et al., 2021).

At the site of a bone defect caused by inflammation, polymorphonuclear neutrophils (PMNs) produce an excessive amount of ROS, leading to endothelial dysfunction and tissue damage, which is detrimental to the process of bone repair. In comparison to healthy tissues, inflamed tissues exhibit ROS concentrations that are 10–100 times higher (Liu et al., 2016). Consequently, the development of a scaffold that is responsive to ROS for the purpose of regulating drug release in inflammatory sites and other afflicted tissues represents a promising approach for enhancing bone repair (Mura et al., 2013).

A critically-sized bone defect refers to a clinical situation wherein bone loss or removal occurs as a result of trauma, infection, tumor, or other factors, and is unable to undergo spontaneous healing (Huang et al., 2022). In such circumstances, the defect lacks the ability to self-repair and necessitates external interventions. A recent investigation has documented a study on a polycation that exhibits compatibility with the Layer-by-Layer (LBL) technique and is exclusively degraded by ROS produced by cells. When the concentrations of ROS increase in the surrounding environment, the thioketal-based polymers containing a scaffold structure can be activated and broken down by physiological levels of ROS. Additionally, these polymers enable the controlled release of therapeutic BMP-2 upon oxidation. The findings of this study suggest a direct correlation between ROS-responsive scaffolds and the promotion of bone growth in critically-sized bone defects (Martin et al., 2021).

In the context of pathological tissues, the maintenance of a stable structure by the ROS response system assumes critical importance. Nevertheless, the development of a ROS-responsive system that operates optimally under specific conditions presents a persistent challenge owing to the intricate and heterogeneous *in vivo* microenvironment. Despite continuous endeavors, there persist unresolved fundamental concerns that impede its attainment of perfection.

2.3 Enzyme stimuli

Enzymes have found application in the realm of nanotechnology, particularly in the development of nano-drug carriers, owing to their distinctive biological targeting and catalytic attributes. In the context of lesion tissue, enzyme levels undergo alterations within the local microenvironment as a consequence of injury and inflammation. By employing this

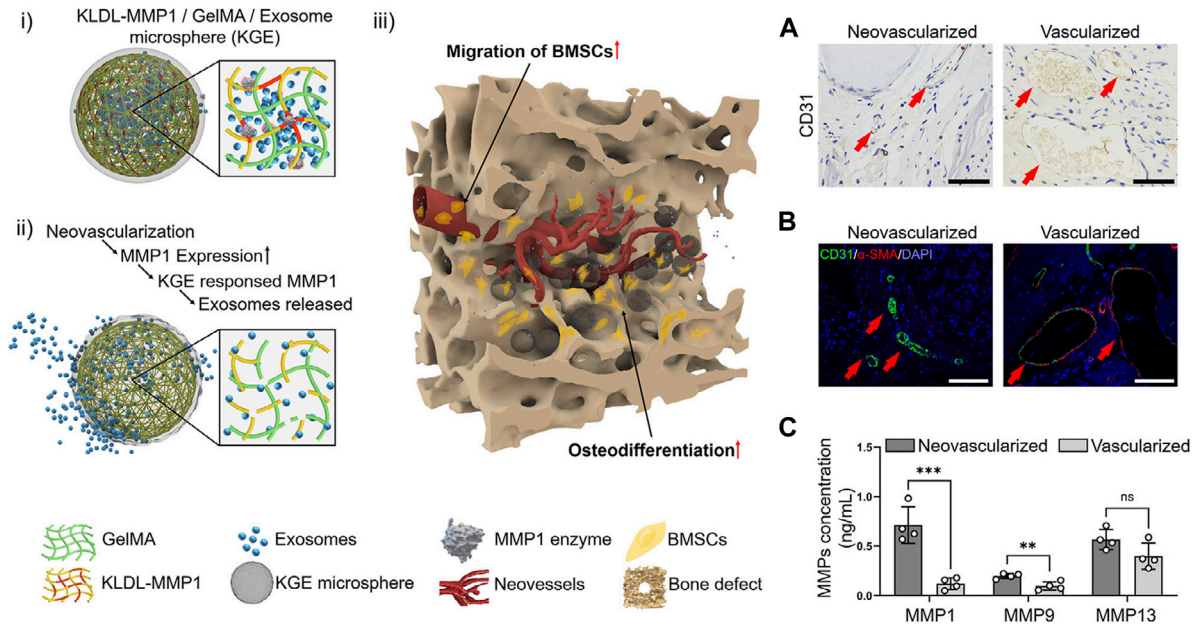

FIGURE 5
Structural design of enzyme-responsive KGE microspheres. **(i)** KGE microspheres encapsulated Exos before enzymatic hydrolysis. **(ii)** MMP1 degrades KGE, releasing Exos after injection. **(iii)** Through neovessels, Exos diffuse into bone defects to promote BMSCs migration and osteodifferentiation. **(A–C)** The MMPs expression in neovascularized and vascularized bone tissues. **(A)** CD31 immunohistochemical staining of SD rat skull defect on day 14, scale = 100 μm. **(B)** CD31/α-SMA Immunofluorescent staining of SD rat skull defect on day 14, scale = 100 μm. **(C)** Detection of MMPs concentration by ELISA, ***: $p < 0.001$, **: $p < 0.01$, ns: $p > 0.05$. Reproduced from (Jia et al., 2023) with permission. Copyright 2023 Elsevier.

TABLE 2 The advantages and limitations of responsive scaffold categories.

Scaffold categories	Advantages	Limitations
Temperature-responsive	Controllable and easy to operate	Temperature ranges are limited
Light-responsive	Little harm to the human body; No direct contact with the lesion area	Penetration depths are either too shallow or too deep; The biological safety of light-sensitive materials need to evaluate
Electric-responsive	Responds quickly and with strong sensitivity	Further investigation is required to examine the alterations in electric field intensity and frequency within organisms
Mechanical-responsive	Sensitive and quick to react	Potential toxicity resulting from the use of crosslinking agents
Magnetic-responsive	Controllable from an external source	The diffusion rate of magnetic particles is high; There exists a potential for toxicity
Ultrasound-responsive	The system can be controlled externally	The controllability of penetration depth is limited; It generates a thermal effect
pH-responsive	Utilizing the distinctions between diseased and normal tissue	Limited range of variation; Low sensitivity
Redox-responsive	Utilizing the distinctions between diseased and normal tissue	The sensitivity is relatively low
Enzyme-responsive	Distinctive biological targeting and catalytic attributes	Different types of enzymes may exhibit cross-reactivity

approach, enzymes can be directed towards specific biochemical signals within the area of bone defect, facilitating the regulation of active ingredient release.

Neovascularized bone, for example, expresses high levels of matrix metalloproteinase-1 (MMP1) (Quintero-Fabián et al., 2019). MMP1 can degrade extracellular matrix proteins by cleaving specific amino acid sequences, which can promote the migration of vascular endothelial cells by decomposing the extracellular matrix (Quintero-Fabián et al., 2019). The KLDL-MMP1 (Ac-KLDLKLDLVPMSMRGGKLDLKLDL-CONH2) peptides were synthesized by the researchers, as they can be degraded by MMP1. To develop a microfluidic chip, the

researchers utilized an injectable MMP1-sensitive hydrogel microsphere (KGE), which was created by combining self-assembling peptide (KLDL-MMP1), gelatin methacryloyl (GelMA), and bone marrow mesenchymal stromal cell-derived exosomes (BMSC-Exos). The Exo-release material, which is sensitive to enzymes, exhibits a specific response and degradation towards MMP1 originating from neovascularization during the angiogenesis phase subsequent to bone injury. This degradation process facilitates the release of exosomes within scaffolds, thereby facilitating the recruitment of cells for the purpose of bone defect repair (Yang et al., 2023) (Figure 5).

A novel enzyme-responsive scaffold has been developed utilizing glucose oxidase (GOD), an enzyme capable of selectively catalyzing the degradation of glucose. In individuals with diabetes, the process of osteogenesis is frequently hindered due to the presence of elevated glucose levels in the body, which in turn leads to inflammation that inhibits osteogenesis. In a high-glucose environment, glucose can undergo specific catalysis by glucose oxidase, resulting in the production of gluconic acid. Consequently, the researchers incorporated glucose oxidase into the nanofiber scaffold to construct a glucose oxidase responsive scaffold. As the glucose concentration increased, the nanofiber scaffolds gradually expanded, leading to the subsequent release of dexamethasone (DEX), which possesses anti-inflammatory properties and promotes bone formation. Thus, these glucose-sensitive nanofiber scaffolds present a promising therapeutic approach for individuals with diabetes and alveolar bone defects (Jia et al., 2023).

Despite the extensive development of enzymatic reaction systems, they still possess several drawbacks within an academic context. One such limitation pertains to the variability in enzyme expression levels observed among patients, thereby raising concerns regarding the adequacy of enzyme expression within the target population. Additionally, the lack of specificity poses another challenge, as different types of matrix metalloproteinases (MMPs) may exhibit cross-reactivity. For example, all of MMP1, MMP8, and MMP13 can cleave glycine–isoleucine or glycine–leucine bond (Williams and Olsen, 2009). These limitations ultimately impede the progress of enzyme-reactive scaffolds in the field of bone engineering.

3 Conclusion and discussion

Stimuli-responsive scaffolds have emerged as a promising class of intelligent biomaterials in recent years. The advantages and limitations of responsive scaffold categories are shown in Table 2. They possess the ability to detect various physical stimuli, including light, temperature, electric field, magnetic field, and ultrasound, as well as chemical stimuli such as pH and redox response, and enzyme stimuli. Upon encountering specific stimuli, these scaffolds facilitate cell adhesion, migration proliferation, and differentiation. Consequently, they hold great potential for the repair of bone defects. Despite the notable progress made in biomaterial advancements for bone tissue engineering over the past few decades, there remains a considerable amount of work to be done, particularly in three specific areas that warrant further investigation in the future: 1) Responsive scaffolds for bone tissue engineering must possess specific biocompatibility and exhibit targeted responses to particular stimuli. However, achieving a singular response is challenging due to the intricate nature of the human physiological environment and the diverse conditions found at injury sites. Consequently, the development of multi-response scaffolds is gradually gaining momentum as a means to attain optimal therapeutic outcomes; 2) Further in-vivo experiments are necessary to ascertain the interactions between biomaterials and the local microenvironment. The implantation of biomaterials can induce substantial alterations in the microenvironment, thereby exerting a significant influence on osteogenesis. Consequently, it is imperative to continuously monitor the dynamic changes of substances within the body; 3) Furthermore, the challenges pertaining to the precision and specificity of responsive tissue engineering scaffolds persist. The accurate identification of the lesion site and the implementation of targeted responses necessitate additional attention and research. Continued advances in bone tissue engineering are anticipated to facilitate the rapid development of stimuli-responsive scaffolds, offering additional treatment options for the clinical management of bone defects, and ultimately influencing clinical outcomes.

Author contributions

TZ: Writing–original draft, Funding acquisition. HZ: Supervision, Writing–original draft. XC: Writing–review and editing, Supervision. YZ: Funding acquisition, Supervision, Writing–review and editing.

Funding

The author(s) declare financial support was received for the research, authorship, and/or publication of this article. This work was supported by Natural Science Foundation for Youth of Hunan Province of China (Grant No. 2021JJ40909); Fundamental Research Funds for the Central Universities of Central South University (Grant No. 1053320213327).

Conflict of interest

The authors declare that the research was conducted in the absence of any commercial or financial relationships that could be construed as a potential conflict of interest.

Publisher's note

References

Abdellahi, M., Karamian, E., Najafinezhad, A., Ranjabar, F., Chami, A., and Khandan, A. (2018a). Diopside-magnetite; A novel nanocomposite for hyperthermia applications. *J. Mech. Behav. Biomed. Mater* 77, 534–538. doi:10.1016/j.jmbbm.2017.10.015

Abdellahi, M., Najfinezhad, A., Saber-Samanadari, S., Khandan, A., and Ghayour, H. (2018b). Zn and Zr co-doped M-type strontium hexaferrite: synthesis, characterization and hyperthermia application. *Chin. J. Phys.* 56, 331–339. doi:10.1016/j.cjph.2017.11.016

Ahn, A. C., and Grodzinsky, A. J. (2009). Relevance of collagen piezoelectricity to "Wolff's Law": a critical review. *Med. Eng. Phys.* 31, 733–741. doi:10.1016/j.medengphy.2009.02.006

Baxter, F. R., Bowen, C. R., Turner, I. G., and Dent, A. C. (2010). Electrically active bioceramics: a review of interfacial responses. *Ann. Biomed. Eng.* 38, 2079–2092. doi:10.1007/s10439-010-9977-6

Bessa, P. C., Machado, R., NüRNBERGER, S., Dopler, D., Banerjee, A., Cunha, A. M., et al. (2010). Thermoresponsive self-assembled elastin-based nanoparticles for delivery of BMPs. *J. Control Release* 142, 312–318. doi:10.1016/j.jconrel.2009.11.003

Bhavsar, M. B., Han, Z., Decoster, T., Leppik, L., Costa Oliveira, K. M., and Barker, J. H. (2020). Electrical stimulation-based bone fracture treatment, if it works so well why do not more surgeons use it? *Eur. J. Trauma Emerg. Surg.* 46, 245–264. doi:10.1007/s00068-019-01127-z

Bordat, A., Boissenot, T., Nicolas, J., and Tsapis, N. (2019). Thermoresponsive polymer nanocarriers for biomedical applications. *Adv. Drug Deliv. Rev.* 138, 167–192. doi:10.1016/j.addr.2018.10.005

Bose, S., Roy, M., and Bandyopadhyay, A. (2012). Recent advances in bone tissue engineering scaffolds. *Trends Biotechnol.* 30, 546–554. doi:10.1016/j.tibtech.2012.07.005

Brydone, A. S., Meek, D., and Maclaine, S. (2010). Bone grafting, orthopaedic biomaterials, and the clinical need for bone engineering. *Proc. Inst. Mech. Eng. H.* 224, 1329–1343. doi:10.1243/09544119jeim770

Buza, J. A., and Einhorn, T. (2016). Bone healing in 2016. *Clin. Cases Min. Bone Metab.* 13, 101–105. doi:10.11138/ccmbm/2016.13.2.101

Caliceti, P. (2011). "Targeted delivery of small and macromolecular drugs,". Editors S. Ajit, and I. Narang and Ram, 6, 2323–2325. ChemMedChem.

Cheng, J. H., and Wang, C. J. (2015). Biological mechanism of shockwave in bone. *Int. J. Surg.* 24, 143–146. doi:10.1016/j.ijsu.2015.06.059

Chen, H., and Zhao, Y. (2018). Applications of light-responsive systems for cancer theranostics. *ACS Appl. Mater Interfaces* 10, 21021–21034. doi:10.1021/acsami.8b01114

Chen, Q., Cordero-Arias, L., Roether, J. A., Cabanas-Polo, S., Virtanen, S., and Boccaccini, A. R. (2013). Alginate/Bioglass® composite coatings on stainless steel deposited by direct current and alternating current electrophoretic deposition. *Surf. Coatings Technol.* 233, 49–56. doi:10.1016/j.surfcoat.2013.01.042

Chen, S., Guo, R., Liang, Q., and Xiao, X. (2021). Multifunctional modified polylactic acid nanofibrous scaffold incorporating sodium alginate microspheres decorated with strontium and black phosphorus for bone tissue engineering. *J. Biomater. Sci. Polym. Ed.* 32, 1598–1617. doi:10.1080/09205063.2021.1927497

Collins, M. N., Ren, G., Young, K., Pina, S., Reis, R. L., and Oliveira, J. M. (2021). Scaffold fabrication technologies and structure/function properties in bone tissue engineering. *Adv. Funct. Mater.* 31, 2010609. doi:10.1002/adfm.202010609

Cui, H., Liu, Y., Deng, M., Pang, X., Zhang, P., Wang, X., et al. (2012). Synthesis of biodegradable and electroactive tetraaniline grafted poly(ester amide) copolymers for bone tissue engineering. *Biomacromolecules* 13, 2881–2889. doi:10.1021/bm300897j

Cui, L., Zhang, J., Zou, J., Yang, X., Guo, H., Tian, H., et al. (2020). Electroactive composite scaffold with locally expressed osteoinductive factor for synergistic bone repair upon electrical stimulation. *Biomaterials* 230, 119617. doi:10.1016/j.biomaterials.2019.119617

Dasari, A., Xue, J., and Deb, S. (2022). Magnetic nanoparticles in bone tissue engineering. *Nanomater. (Basel)* 12, 757. doi:10.3390/nano12050757

Durairaj, K., Balasubramanian, B., Arumugam, V. A., Easwaran, M., Park, S., Issara, U., et al. (2023). Biocompatibility of veratric acid–encapsulated chitosan/methylcellulose hydrogel: biological characterization, osteogenic efficiency with *in silico* molecular modeling. *Appl. Biochem. Biotechnol.* 195, 4429–4446. doi:10.1007/s12010-023-04311-5

Eischen-Loges, M., Oliveira, K. M. C., Bhavsar, M. B., Barker, J. H., and Leppik, L. (2018). Pretreating mesenchymal stem cells with electrical stimulation causes sustained long-lasting pro-osteogenic effects. *PeerJ* 6, e4959. doi:10.7717/peerj.4959

Ercan, B., and Webster, T. J. (2008). Greater osteoblast proliferation on anodized nanotubular titanium upon electrical stimulation. *Int. J. Nanomedicine* 3, 477–485. doi:10.2147/ijn.s3780

Fernandes, M. M., Correia, D. M., Ribeiro, C., Castro, N., Correia, V., and Lanceros-Mendez, S. (2019). Bioinspired three-dimensional magnetoactive scaffolds for bone tissue engineering. *ACS Appl. Mater Interfaces* 11, 45265–45275. doi:10.1021/acsami.9b14001

Ferreira, A. M., Gentile, P., Chiono, V., and Ciardelli, G. (2012). Collagen for bone tissue regeneration. *Acta Biomater.* 8, 3191–3200. doi:10.1016/j.actbio.2012.06.014

Fomina, N., Sankaranarayanan, J., and Almutairi, A. (2012). Photochemical mechanisms of light-triggered release from nanocarriers. *Adv. Drug Deliv. Rev.* 64, 1005–1020. doi:10.1016/j.addr.2012.02.006

Funk, R. H. (2015). Endogenous electric fields as guiding cue for cell migration. *Front. Physiol.* 6, 143. doi:10.3389/fphys.2015.00143

GarcíA-GonzáLEZ, C. A., Barros, J., Rey-Rico, A., Redondo, P., GóMEZ-Amoza, J. L., Concheiro, A., et al. (2018). Antimicrobial properties and osteogenicity of vancomycin-loaded synthetic scaffolds obtained by supercritical foaming. *ACS Appl. Mater Interfaces* 10, 3349–3360. doi:10.1021/acsami.7b17375

Goharkhah, M., Salarian, A., Ashjaee, M., and Shahabadi, M. (2015). Convective heat transfer characteristics of magnetite nanofluid under the influence of constant and alternating magnetic field. *Powder Technol.* 274, 258–267. doi:10.1016/j.powtec.2015.01.031

Greenwald, A. S., Boden, S. D., Goldberg, V. M., Khan, Y., Laurencin, C. T., and Rosier, R. N. (2001). Bone-graft substitutes: facts, fictions, and applications. *J. Bone Jt. Surg. Am.* 83-A (Suppl. 2 Pt 2), 98–103. doi:10.2106/00004623-200100022-00007

Guo, Z. F., Patil, Y., Shinohara, A., Nagura, K., Yoshida, M., and Nakanishi, T. (2022). Organic molecular and polymeric electrets toward soft electronics. *Mol. Syst. Des. Eng.* 7, 537–552. doi:10.1039/d1me00180a

Hardy, J. G., Lee, J. Y., and Schmidt, C. E. (2013). Biomimetic conducting polymer-based tissue scaffolds. *Curr. Opin. Biotechnol.* 24, 847–854. doi:10.1016/j.copbio.2013.03.011

He, Y., Li, F., Jiang, P., Cai, F., Lin, Q., Zhou, M., et al. (2023). Remote control of the recruitment and capture of endogenous stem cells by ultrasound for *in situ* repair of bone defects. *Bioact. Mater* 21, 223–238. doi:10.1016/j.bioactmat.2022.08.012

Hohnholt, M. C., Geppert, M., and Dringen, R. (2011). Treatment with iron oxide nanoparticles induces ferritin synthesis but not oxidative stress in oligodendroglial cells. *Acta Biomater.* 7, 3946–3954. doi:10.1016/j.actbio.2011.06.052

Huang, E. E., Zhang, N., Ganio, E. A., Shen, H., Li, X., Ueno, M., et al. (2022). Differential dynamics of bone graft transplantation and mesenchymal stem cell therapy during bone defect healing in a murine critical size defect. *J. Orthop. Transl.* 36, 64–74. doi:10.1016/j.jot.2022.05.010

Huang, L., Hu, J., Lang, L., Wang, X., Zhang, P., Jing, X., et al. (2007). Synthesis and characterization of electroactive and biodegradable ABA block copolymer of polylactide and aniline pentamer. *Biomaterials* 28, 1741–1751. doi:10.1016/j.biomaterials.2006.12.007

Jia, Y., Liu, J., Tan, Z., Liu, J., Meng, X., Luo, D., et al. (2023). Preparation and characterization of a biocompatible glucose-sensitive electrospun nanofibers scaffolds containing dexamethasone with enhanced osteogenic properties *in vitro* high glucose environment. *Biomed. Mater.* 18, 045006. doi:10.1088/1748-605x/acd314

Kang, S. K., Murphy, R. K., Hwang, S. W., Lee, S. M., Harburg, D. V., Krueger, N. A., et al. (2016). Bioresorbable silicon electronic sensors for the brain. *Nature* 530, 71–76. doi:10.1038/nature16492

KarakeçILI, A., Topuz, B., Korpayev, S., and Erdek, M. (2019). Metal-organic frameworks for on-demand pH controlled delivery of vancomycin from chitosan scaffolds. *Mater Sci. Eng. C Mater Biol. Appl.* 105, 110098. doi:10.1016/j.msec.2019.110098

Karimi, M., Ghasemi, A., Sahandi Zangabad, P., Rahighi, R., Moosavi Basri, S. M., Mirshekari, H., et al. (2016a). Smart micro/nanoparticles in stimulus-responsive drug/gene delivery systems. *Chem. Soc. Rev.* 45, 1457–1501. doi:10.1039/c5cs00798d

Karimi, M., Sahandi Zangabad, P., Ghasemi, A., Amiri, M., Bahrami, M., Malekzad, H., et al. (2016b). Temperature-responsive smart nanocarriers for delivery of therapeutic agents: applications and recent advances. *ACS Appl. Mater Interfaces* 8, 21107–21133. doi:10.1021/acsami.6b00371

Khan, Y., Yaszemski, M. J., Mikos, A. G., and Laurencin, C. T. (2008). Tissue engineering of bone: material and matrix considerations. *J. Bone Jt. Surg. Am.* 90 (Suppl. 1), 36–42. doi:10.2106/jbjs.g.01260

Khare, D., Basu, B., and Dubey, A. K. (2020). Electrical stimulation and piezoelectric biomaterials for bone tissue engineering applications. *Biomaterials* 258, 120280. doi:10.1016/j.biomaterials.2020.120280

Kim, M. H., Kim, B. S., Park, H., Lee, J., and Park, W. H. (2018). Injectable methylcellulose hydrogel containing calcium phosphate nanoparticles for bone regeneration. *Int. J. Biol. Macromol.* 109, 57–64. doi:10.1016/j.ijbiomac.2017.12.068

Kim, S. H., Thambi, T., Giang Phan, V. H., and Lee, D. S. (2020). Modularly engineered alginate bioconjugate hydrogel as biocompatible injectable scaffold for *in situ* biomineralization. *Carbohydr. Polym.* 233, 115832. doi:10.1016/j.carbpol.2020.115832

Krishna, O. D., Wiss, K. T., Luo, T., Pochan, D. J., Theato, P., and Kiick, K. L. (2012). Morphological transformations in a dually thermoresponsive coil-rod-coil bioconjugate. *Soft Matter* 8, 3832–3840. doi:10.1039/c2sm07025a

Lanier, O. L., Ficarrotta, J. M., Adjei, I., Wable, D., Lewis, C., Nacea, C., et al. (2021). Magnetically responsive polymeric microparticles for the triggered delivery of a complex mixture of human placental proteins. *Macromol. Biosci.* 21, e2000249. doi:10.1002/mabi.202000249

Lin, S. Z., Xu, Z. S., Wang, S. T., Cao, J. L., Zhong, J. W., Li, G. L., et al. (2022). Multiplying the stable electrostatic field of electret based on the heterocharge-synergy and superposition effect. *Adv. Sci.* 9, e2203150. doi:10.1002/advs.202203150

Lioubavina-Hack, N., Karring, T., Lynch, S. E., and Lindhe, J. (2005). Methyl cellulose gel obstructed bone formation by GBR: an experimental study in rats. *J. Clin. Periodontol.* 32, 1247–1253. doi:10.1111/j.1600-051x.2005.00791.x

Liu, D., Yang, F., Xiong, F., and Gu, N. (2016). The smart drug delivery system and its clinical potential. *Theranostics* 6, 1306–1323. doi:10.7150/thno.14858

Liu, Y., Li, T., Sun, M., Cheng, Z., Jia, W., Jiao, K., et al. (2022). ZIF-8 modified multifunctional injectable photopolymerizable GelMA hydrogel for the treatment of periodontitis. *Acta Biomater.* 146, 37–48. doi:10.1016/j.actbio.2022.03.046

Li, X., Wang, N., Fan, G., Yu, J., Gao, J., Sun, G., et al. (2015). Electreted polyetherimide-silica fibrous membranes for enhanced filtration of fine particles. *J. Colloid Interface Sci.* 439, 12–20. doi:10.1016/j.jcis.2014.10.014

Martin, J. R., Howard, M. T., Wang, S., Berger, A. G., and Hammond, P. T. (2021). Oxidation-responsive, tunable growth factor delivery from polyelectrolyte-coated implants. *Adv. Healthc. Mater* 10, e2001941. doi:10.1002/adhm.202001941

Mayer, G., and Heckel, A. (2006). Biologically active molecules with a "light switch. *Angew. Chem. Int. Ed. Engl.* 45, 4900–4921. doi:10.1002/anie.200600387

Mura, S., Nicolas, J., and Couvreur, P. (2013). Stimuli-responsive nanocarriers for drug delivery. *Nat. Mater* 12, 991–1003. doi:10.1038/nmat3776

Nakamura, S., Kobayashi, T., Nakamura, M., and Yamashita, K. (2009). Enhanced *in vivo* responses of osteoblasts in electrostatically activated zones by hydroxyapatite electrets. *J. Mater Sci. Mater Med.* 20, 99–103. doi:10.1007/s10856-008-3546-7

Nejati, S., Karimi Soflou, R., Khorshidi, S., and Karkhaneh, A. (2020). Development of an oxygen-releasing electroconductive in-situ crosslinkable hydrogel based on oxidized pectin and grafted gelatin for tissue engineering applications. *Colloids Surf. B Biointerfaces* 196, 111347. doi:10.1016/j.colsurfb.2020.111347

Palza, H., Zapata, P. A., and Angulo-Pineda, C. (2019). Electroactive smart polymers for biomedical applications. *Mater. (Basel)* 12, 277. doi:10.3390/ma12020277

Pandey, A., Nikam, A. N., Fernandes, G., Kulkarni, S., Padya, B. S., Prassl, R., et al. (2020). Black phosphorus as multifaceted advanced material nanoplatforms for potential biomedical applications. *Nanomater. (Basel)* 11, 13. doi:10.3390/nano11010013

Parameswaran, R., Carvalho-De-Souza, J. L., Jiang, Y., Burke, M. J., Zimmerman, J. F., Koehler, K., et al. (2018). Photoelectrochemical modulation of neuronal activity with free-standing coaxial silicon nanowires. *Nat. Nanotechnol.* 13, 260–266. doi:10.1038/s41565-017-0041-7

Pitt, W. G., Husseini, G. A., and Staples, B. J. (2004). Ultrasonic drug delivery--a general review. *Expert Opin. Drug Deliv.* 1, 37–56. doi:10.1517/17425247.1.1.37

Qiao, Z. G., Lian, M. F., Liu, X. Z., Zhang, X., Han, Y., Ni, B., et al. (2022). Electreted sandwich membranes with persistent electrical stimulation for enhanced bone regeneration. *Acs Appl. Mater. Interfaces* 14, 31655–31666. doi:10.1021/acsami.2c06665

Quintero-FabiáN, S., Arreola, R., Becerril-Villanueva, E., Torres-Romero, J. C., Arana-ArgáEZ, V., Lara-Riegos, J., et al. (2019). Role of matrix metalloproteinases in angiogenesis and cancer. *Front. Oncol.* 9, 1370. doi:10.3389/fonc.2019.01370

Sahmani, S., Khandan, A., Saber-Samandari, S., and Mohammadi Aghdam, M. (2020). Effect of magnetite nanoparticles on the biological and mechanical properties of hydroxyapatite porous scaffolds coated with ibuprofen drug. *Mater Sci. Eng. C Mater Biol. Appl.* 111, 110835. doi:10.1016/j.msec.2020.110835

Sahmani, S., Saber-Samandari, S., Shahali, M., Joneidi Yekta, H., Aghadavoudi, F., Montazeran, A. H., et al. (2018). Mechanical and biological performance of axially loaded novel bio-nanocomposite sandwich plate-type implant coated by biological polymer thin film. *J. Mech. Behav. Biomed. Mater* 88, 238–250. doi:10.1016/j.jmbbm.2018.08.030

Shabani, M., and Bodaghi, M. (2023). "Mechanical-responsive materials: properties, design, and applications," in *Stimuli-responsive materials for biomedical applications* (American Chemical Society).

Shrivats, A. R., Mcdermott, M. C., and Hollinger, J. O. (2014). Bone tissue engineering: state of the union. *Drug Discov. Today* 19, 781–786. doi:10.1016/j.drudis.2014.04.010

Silva, C. C. S., Thomazini, D., Pinheiro, A. G., Aranha, N., Figueiró, S. D., GóES, J. C., et al. (2001). Collagen–hydroxyapatite films: piezoelectric properties. *Mater. Sci. Eng. B-advanced Funct. Solid-state Mater.* 86, 210–218. doi:10.1016/s0921-5107(01)00674-2

Smallcomb, M., Khandare, S., Vidt, M. E., and Simon, J. C. (2022). Therapeutic ultrasound and shockwave therapy for tendinopathy: a narrative review. *Am. J. Phys. Med. Rehabil.* 101, 801–807. doi:10.1097/phm.0000000000001894

Sruthi, S., Maurizi, L., Nury, T., Sallem, F., Boudon, J., Riedinger, J. M., et al. (2018). Cellular interactions of functionalized superparamagnetic iron oxide nanoparticles on oligodendrocytes without detrimental side effects: cell death induction, oxidative stress and inflammation. *Colloids Surf. B Biointerfaces* 170, 454–462. doi:10.1016/j.colsurfb.2018.06.041

Tamburro, A. M., Pepe, A., Bochicchio, B., Quaglino, D., and Ronchetti, I. P. (2005). Supramolecular amyloid-like assembly of the polypeptide sequence coded by exon 30 of human tropoelastin. *J. Biol. Chem.* 280, 2682–2690. doi:10.1074/jbc.m411617200

Tandon, B., Blaker, J. J., and Cartmell, S. H. (2018). Piezoelectric materials as stimulatory biomedical materials and scaffolds for bone repair. *Acta Biomater.* 73, 1–20. doi:10.1016/j.actbio.2018.04.026

Tang, D., Tare, R. S., Yang, L. Y., Williams, D. F., Ou, K. L., and Oreffo, R. O. (2016). Biofabrication of bone tissue: approaches, challenges and translation for bone regeneration. *Biomaterials* 83, 363–382. doi:10.1016/j.biomaterials.2016.01.024

Vaca-GonzáLEZ, J. J., Guevara, J. M., Moncayo, M. A., Castro-Abril, H., Hata, Y., and GarzóN-Alvarado, D. A. (2019). Biophysical stimuli: a review of electrical and mechanical stimulation in hyaline cartilage. *Cartilage* 10, 157–172. doi:10.1177/1947603517730637

Veres, T., Voniatis, C., MolnáR, K., Nesztor, D., FehéR, D., Ferencz, A., et al. (2022). An implantable magneto-responsive poly(aspartamide) based electrospun scaffold for hyperthermia treatment. *Nanomater. (Basel)* 12, 1476. doi:10.3390/nano12091476

Wang, H., Tian, J., Jiang, Y., Liu, S., Zheng, J., Li, N., et al. (2023). A 3D biomimetic optoelectronic scaffold repairs cranial defects. *Sci. Adv.* 9, eabq7750. doi:10.1126/sciadv.abq7750

Wang, Z., Crandall, C., Sahadevan, R., Menkhaus, T. J., and Fong, H. (2017). Microfiltration performance of electrospun nanofiber membranes with varied fiber diameters and different membrane porosities and thicknesses. *POLYMER* 114, 64–72. doi:10.1016/j.polymer.2017.02.084

Wei, H. P., Cui, J. J., Lin, K. L., Xie, J., and Wang, X. D. (2022). Recent advances in smart stimuli-responsive biomaterials for bone therapeutics and regeneration. *Bone Res.* 10, 17. doi:10.1038/s41413-021-00180-y

Wei, P., Cornel, E. J., and Du, J. (2021). Ultrasound-responsive polymer-based drug delivery systems. *Drug Deliv. Transl. Res.* 11, 1323–1339. doi:10.1007/s13346-021-00963-0

Weissleder, R. (2001). A clearer vision for *in vivo* imaging. *Nat. Biotechnol.* 19, 316–317. doi:10.1038/86684

Wheatley, M. A., and Cochran, M. (2013). Ultrasound contrast agents. *J. Drug Deliv. Sci. Technol.* 23, 57–72. doi:10.1016/s1773-2247(13)50007-4

Williams, K. E., and Olsen, D. R. (2009). Matrix metalloproteinase-1 cleavage site recognition and binding in full-length human type III collagen. *Matrix Biol.* 28, 373–379. doi:10.1016/j.matbio.2009.04.009

Xie, M., Wang, L., Ge, J., Guo, B., and Ma, P. X. (2015). Strong electroactive biodegradable shape memory polymer networks based on star-shaped polylactide and aniline trimer for bone tissue engineering. *ACS Appl. Mater Interfaces* 7, 6772–6781. doi:10.1021/acsami.5b00191

Xue, Y., Zhu, Z., Zhang, X., Chen, J., Yang, X., Gao, X., et al. (2021). Accelerated bone regeneration by MOF modified multifunctional membranes through enhancement of osteogenic and angiogenic performance. *Adv. Healthc. Mater* 10, e2001369. doi:10.1002/adhm.202001369

Yang, Y., Zheng, W., Tan, W., Wu, X., Dai, Z., Li, Z., et al. (2023). Injectable MMP1-sensitive microspheres with spatiotemporally controlled exosome release promote neovascularized bone healing. *Acta Biomater.* 157, 321–336. doi:10.1016/j.actbio.2022.11.065

Ye, J., Gong, M., Song, J., Chen, S., Meng, Q., Shi, R., et al. (2022). Integrating inflammation-responsive prodrug with electrospun nanofibers for anti-inflammation application. *Pharmaceutics* 14, 1273. doi:10.3390/pharmaceutics14061273

Yuan, J., Li, L., Yang, Q., Ran, H., Wang, J., Hu, K., et al. (2021). Targeted treatment of ischemic stroke by bioactive nanoparticle-derived reactive oxygen species responsive and inflammation-resolving nanotherapies. *ACS Nano* 15, 16076–16094. doi:10.1021/acsnano.1c04753

Yuan, X., Arkonac, D. E., Chao, P. H., and Vunjak-Novakovic, G. (2014). Electrical stimulation enhances cell migration and integrative repair in the meniscus. *Sci. Rep.* 4, 3674. doi:10.1038/srep03674

Zardad, A. Z., Choonara, Y. E., Du Toit, L. C., Kumar, P., Mabrouk, M., Kondiah, P. P. D., et al. (2016). A review of thermo- and ultrasound-responsive polymeric systems for delivery of chemotherapeutic agents. *Polym. (Basel)* 8, 359. doi:10.3390/polym8100359

Zhang, Q., Zhang, F., Chen, Y., Dou, Y., Tao, H., Zhang, D., et al. (2017). Structure–property correlations of reactive oxygen species-responsive and hydrogen peroxide-eliminating materials with anti-oxidant and anti-inflammatory activities. *Chem. Mater.* 29, 8221–8238. doi:10.1021/acs.chemmater.7b02412

Zhang, X., Yang, P., Dai, Y., Ma, P. A., Li, X., Cheng, Z., et al. (2013). Multifunctional up-converting nanocomposites with smart polymer brushes gated mesopores for cell

imaging and thermo/pH dual-responsive drug controlled release. *Adv. Funct. Mater.* 23, 4067–4078. doi:10.1002/adfm.201300136

Zhang, X., Zhao, J., Xie, P., and Wang, S. (2023). Biomedical applications of electrets: recent advance and future perspectives. *J. Funct. Biomaterials*, 14. [Online]. doi:10.3390/jfb14060320

Zhang, Y., Chen, L., Zeng, J., Zhou, K., and Zhang, D. (2014). Aligned porous barium titanate/hydroxyapatite composites with high piezoelectric coefficients for bone tissue engineering. *Mater Sci. Eng. C Mater Biol. Appl.* 39, 143–149. doi:10.1016/j.msec.2014.02.022

Zhao, B., Li, N. K., Yingling, Y. G., and Hall, C. K. (2016). LCST Behavior is Manifested in a Single Molecule: elastin-Like polypeptide $(VPGVG)_n$. *Biomacromolecules* 17, 111–118. doi:10.1021/acs.biomac.5b01235

Zheng, H., Zhang, Y., Liu, L., Wan, W., Guo, P., NyströM, A. M., et al. (2016). One-pot synthesis of metal-organic frameworks with encapsulated target molecules and their applications for controlled drug delivery. *J. Am. Chem. Soc.* 138, 962–968. doi:10.1021/jacs.5b11720

Zheng, T., Huang, Y., Zhang, X., Cai, Q., Deng, X., and Yang, X. (2020). Mimicking the electrophysiological microenvironment of bone tissue using electroactive materials to promote its regeneration. *J. Mater Chem. B* 8, 10221–10256. doi:10.1039/d0tb01601b

Zhu, J., Zhu, Y., Song, W., Wang, H., Gao, M., Cho, M., et al. (2018). Zinc oxide-enhanced piezoelectret polypropylene microfiber for mechanical energy harvesting. *ACS Appl. Mater Interfaces* 10, 19940–19947. doi:10.1021/acsami.8b02458

frontiers | Frontiers in Bioengineering and Biotechnology

TYPE Original Research
PUBLISHED 07 December 2023
DOI 10.3389/fbioe.2023.1328673

OPEN ACCESS

EDITED BY
Wenjie Zhang,
Shanghai Jiao Tong University, China

REVIEWED BY
Xiaodong Wang,
Sun Yat-sen University, China
Yang Zhen,
Peking University Hospital of Stomatology, China

*CORRESPONDENCE
Cui Huang,
huangcui@whu.edu.cn

RECEIVED 27 October 2023
ACCEPTED 24 November 2023
PUBLISHED 07 December 2023

CITATION
Zhu J, Chen S, Anniwaer A, Xu Y and Huang C (2023), Effects of background color and restoration depth on color adjustment potential of a new single-shade resin composite versus multi-shade resin composites.
Front. Bioeng. Biotechnol. 11:1328673.
doi: 10.3389/fbioe.2023.1328673

Effects of background color and restoration depth on color adjustment potential of a new single-shade resin composite versus multi-shade resin composites

Jiakang Zhu, Siyang Chen, Annikaer Anniwaer, Yue Xu and Cui Huang*

State Key Laboratory of Oral and Maxillofacial Reconstruction and Regeneration, Key Laboratory of Oral Biomedicine Ministry of Education, Hubei Key Laboratory of Stomatology, School and Hospital of Stomatology, Wuhan University, Wuhan, China

The objectives of this study was to evaluate the effects of background color and restoration depth on color adjustment potential of a new single-shade resin composite versus multi-shade resin composites. Two multi-shade resin composites (Spectrum TPH3 and Clearfil AP-X) marked A2 shade and a new single-shade resin composite (Charisma Diamond One) were tested. Four base shades (A1, A2, A3, and A3.5) of the same resin composite (Filtek Z250) were selected as different background colors. Dual specimens with 1-, 2-, and 3-mm restoration depth and single specimens of all materials were fabricated. CIE color coordinates were measured using a spectrophotometer, then color differences (ΔE_{00}) and translucency parameter (TP_{00}) were calculated using the CIEDE2000 formula. Independent observers performed visual scoring. CAP-I and CAP-V values were calculated according to ΔE_{00} and visual scoring. The results revealed that CAP-I and CAP-V were significantly affected by resin composite type, background color, and restoration depth. CAP-I and CAP-V decreased as restoration depth increased at the same background color for all materials. Charisma Diamond One had the highest CAP-I and CAP-V values at all background colors and restoration depths, with the highest TP_{00} value. These findings demonstrated that color adjustment potential was dependent on resin composite type, background color, and restoration depth, so shade selection is indispensable for multi-shade resin composites. Charisma Diamond One exhibited the highest color adjustment potential and the most pronounced color shifting, contributing to simplifying the process of shade selection and improving the efficiency of clinical work.

KEYWORDS

color adjustment potential, resin composites, color shifting, single shade, CIEDE2000

1 Introduction

Resin composites are now widely used as esthetic restorative materials in dentistry, which can perfectly achieve the restoration of tooth defect and the modification of tooth color and shape in a conservative and inexpensive way (Korkut and Türkmen, 2021; Da Rosa Rodolpho et al., 2022). Unlike indirect restorations made of ceramic materials whose color can be achieved by external staining at the later stage of treatment, the accurate shade selection is necessary for resin composite restorations before treatment, so as to select the materials closest to the color of the surrounding teeth for good esthetic effects (Ismail et al., 2020; Diamantopoulou et al., 2021; Vargas et al., 2023). The shade of resin composite selected based on a light-cured resin ball refers to placing a resin ball on the surface of tooth, comparing the color difference between the tooth and the resin ball after light-curing, and then removing it until a resin composite with the appropriate shade is determined by clinicians. Obviously, the shade selection of resin composite is complex and time-consuming (Browning et al., 2009; Tabatabaian et al., 2021).

In clinic, we can feel that the color differences between resin composites and surrounding tooth tissues are less perceived when viewed as a whole after finishing the restorations than when viewed separately before filling treatment (Tsubone et al., 2012; de Abreu et al., 2021). This phenomenon is called "chameleon effect" in dental parlance interpreted as color shifting which includes two major aspects: the blending effect (not measurable by any instrument, an optical illusion) and the effect of physical translucency (Paravina et al., 2008; Ismail and Paravina, 2022). More recently, color adjustment potential (CAP) is a term that describes and quantifies the interaction between the physical and perceptual components of color shifting, which can be assessed both instrumentally (CAP-I) and visually (CAP-V) (Trifkovic et al., 2018; Pereira Sanchez et al., 2019). Previous studies have shown that the CAP of resin composite is affected by many factors such as the type and shade of resin composite, background color, restoration depth, etc. (Tanaka et al., 2015; Akgül et al., 2022; El-Rashidy et al., 2022; Yamashita et al., 2023).

In order to minimize the shade selection, simplify the process of resin composite restoration, and reduce the chair-side time, single-shade resin composites were created and introduced, which have only a narrow range of colors but can match the colors of different teeth (de Abreu et al., 2021; Lucena et al., 2021; Altınışık and Özyurt, 2023). In other words, single-shade resin composites have enhanced CAP.

Recently, a newly developed single-shade resin composite (Charisma Diamond One, Kulzer, Hanau, Germany) has been introduced, which can supposedly match all Vita Classical shades according to the manufacturer's information (Altınışık and Özyurt, 2023). However, no published third-party study has evaluated the CAP of the new single-shade resin composite compared with multi-shade resin composites to truly prove its superiority in color matching over conventional multi-shade resin composites.

Therefore, this study aimed to evaluate and compare the instrumental and visual color adjustment potential (CAP-I and CAP-V) of the newly developed single-shade resin composite compared with two clinically available multi-shade resin composites in relation to background color and restoration depth. The null hypotheses tested were: (1) there are no significant differences in color adjustment potential (CAP-I and CAP-V) among the resin composites evaluated, (2) background color or restoration depth would have no effect on the color adjustment potential (CAP-I and CAP-V).

2 Materials and methods

2.1 Specimen preparation

Two multi-shade resin composites marked A2 shade and a new single-shade resin composite were evaluated in this study. Four base shades (A1, A2, A3, and A3.5) of the same resin composite were selected to simulate different background colors. Details of these materials were listed in Table 1.

All specimens were made in custom-designed, Teflon molds (Figure 1). All specimens were filled in twice and each time filled the materials with a thickness of approximately 2 mm and then light-cured for 20 s using an LED light curing unit (Bluephase II; Ivoclar Vivadent, Schaan, Liechtenstein). The resin composite specimens were divided into four groups: three groups of dual specimens and one group of single specimens (Figure 2). The single specimens were disk-shaped (diameter = 10 mm, thickness = 4 mm) and fabricated for all materials included in this study (n = 9). The dual specimens consisted of an outer ring (diameter = 10 mm, thickness = 4 mm) made of base shades and an inner hole in the center (diameter = 6 mm) filled with each of the 3 tested materials after the cavities were treated with a transparent universal bonding agent (3 M-ESPE, St Paul, MN, United States) (n = 9). to According to the depth of the inner hole (corresponds to the thickness of the tested shade), dual specimens were divided into 3 groups including 1.0 mm-group, 2.0 mm-group, and 3.0 mm-group for each test material (Akgül et al., 2022; Yamashita et al., 2023).

The same operator progressively polished all specimens on both sides using wet silicon carbide paper of increasing grit number (P600-, P800-, and P1200-grit) for 10 s each, at a speed of 150 rpm, with mild hand pressure in a table-top grinder-polisher (EcoMet 250; Buehler, Lake Bluff, IL, United States). All specimens were incubated at 37°C for 24 h to ensure complete polymerization.

2.2 Instrumental evaluation

A portable clinical spectroradiometer (Vita Easyshade V; VITA Zahnfabrik, Bad Sackingen, Germany) was used for the color measurements for all specimens against both black and white backgrounds. The probe (diameter = 5 mm) of spectroradiometer faced the center of the specimen during measurement. The spectrophotometer was calibrated in compliance with the manufacturer's instructions before each measurement. L*, a*, and b* color coordinates based on the CIELAB system were recorded, where L* represents the lightness on a scale of 0 (black) to 100 (white), a* represents the hue and chroma on the red-green axis, and b* represents the hue and chroma on the yellow-blue axis.

Color coordinates measured were used for computation of color differences. The color difference (ΔE) was calculated using the

TABLE 1 Materials used in this study.

Groups		Materials	Shade	Manufacturer	Composition	Lot number
Test	T1	Clearfil AP-X	A2	Kuraray Noritake, Okayama, Japan	Base resin: Bis-GMA, TEGDMA	5C0133
					Filler: silanated barium glass filler, silanated silica filler, silanated colloidal silica	
	T2	Spectrum TPH3	A2	Dentsply, Konstanz, Germany	Base resin: Bis-GMA, Bis-EMA, TEGDMA	2111000345
					Filler: barium aluminio borosilicate, barium fluoro aluminio borosilicate, highly dispersed silicon dioxide	
	T3	Charisma Diamond One	-	Kulzer, Hanau, Germany	Base resin: TCD-Urethaneacrylate, UDMA, TEGDMA Filler: Barium Aluminium Boro Fluor Silicate Glass	K010026
Base	B1	Filtek Z250	A1	3M ESPE, St. Paul, MN	Base resin: Bis-GMA, Bis-EMA, UDMA Filler: zircon/silica	NE03476
	B2		A2			NE62695
	B3		A3			NE03675
	B4		A3.5			NA26526

Bis-EMA, ethoxylated bisphenol A glycol dimethacrylate; Bis-GMA, Bisphenol A diglycidylmethacrylate; TCD-Urethaneacrylate, Tricy clodecane-Urethaneacrylate; TEGDMA, triethylene glycol dimethacrylate; UDMA, urethane dimethacrylate.

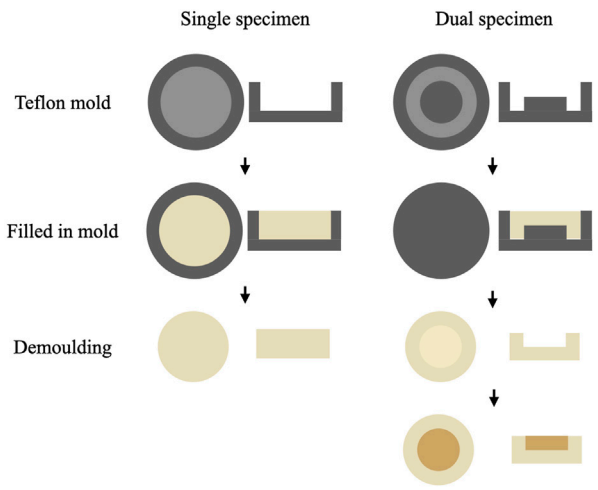

FIGURE 1
Diagram for the fabrication of single and dual specimens. The heights of raised part in the hole of Teflon molds for dual specimens were 1.0 mm, 2.0 mm, and 3.0 mm respectively in different groups.

CIEDE2000 color difference formula as follows (Perez Mdel et al., 2011):

$$\Delta E_{00} = \sqrt{\left(\frac{\Delta L'}{K_L S_L}\right)^2 + \left(\frac{\Delta C'}{K_C S_C}\right)^2 + \left(\frac{\Delta H'}{K_H S_H}\right)^2 + R_T \left(\frac{\Delta C'}{K_C S_C}\right)\left(\frac{\Delta H'}{K_H S_H}\right)},$$

where $\Delta L'$, $\Delta C'$, and $\Delta H'$ were the differences in lightness, chroma, and hue for a pair of points. S_L, S_C, and S_H were the weighing functions for the lightness, chroma, and hue components, respectively. The parametric factors (K_L, K_C, and K_H) were the expressions for experimental conditions. All parametric factors of the CIEDE2000 color difference formula were set to 1. R_T was the rotation factor that considers the interactions between hue and chroma differences in the blue area.

In addition, translucency parameter (TP_{00}) values were determined by calculating the color coordinates values between the readings over the black and white backgrounds according to the following CIEDE2000 color difference formula (Lucena et al., 2021):

$$TP_{00} = \sqrt{\left(\frac{L'_B - L'_W}{K_L S_L}\right)^2 + \left(\frac{C'_B - C'_W}{K_C S_C}\right)^2 + \left(\frac{H'_B - H'_W}{K_H S_H}\right)^2 + R_T \left(\frac{C'_B - C'_W}{K_C S_C}\right)\left(\frac{H'_B - H'_W}{K_H S_H}\right)},$$

where the subscripts "B" and "W" referred to the lightness (L'), chroma (C') and hue (H') of the specimens over the black and white backgrounds, respectively.

2.3 Visual evaluation

Visual color evaluations were performed by three dentistry specialists with demonstrated superior color discrimination competency according to ISO/TR 28642:2016. Under D65 illumination and using a 0°/45° viewing geometry, the observers performed blind visual evaluations of all specimens placed on a neutral gray paper in a random order. Color differences were graded from 0 to 4 as follows: 0 = excellent match, 1 = very good match, 2 = not so good match (border zone mismatch), 3 = obvious mismatch, and 4 = huge (pronounced) mismatch.

2.4 Color adjustment potential (CAP) indices

The CAP indices included instrumental CAP (CAP-I) index and visual CAP (CAP-V) index (Figure 3).

CAP-I was calculated as follows: $\text{CAP-I} = 1 - \Delta E_{DUAL}/\Delta E_{SINGLE}$, where ΔE_{DUAL} was the CIEDE2000 color difference between the test shade in dual specimen and the base shade both in single specimen, and ΔE_{SINGLE} was the CIEDE2000 color difference between the test shade and base shade in separate single specimen.

CAP-V was calculated as follows: $\text{CAP-V} = 1 - V_{DUAL}/V_{SINGLE}$, where V_{DUAL} was the visual scoring between the test shade and base shade both in the same dual specimen, and V_{SINGLE} is the visual scoring between the test shade and base shade in separate single specimen.

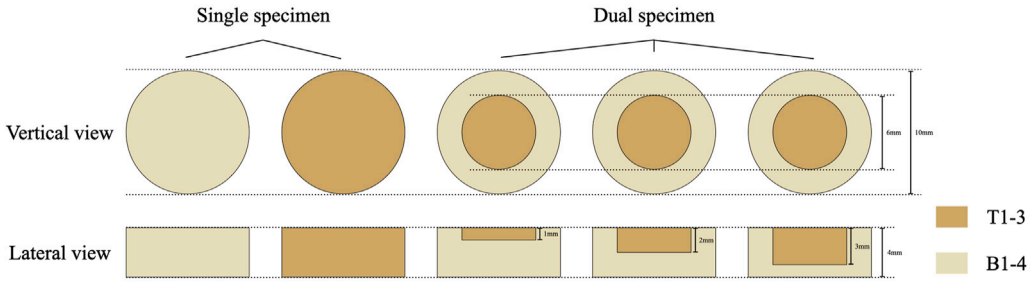

FIGURE 2
Schematic representation of single and dual specimens.

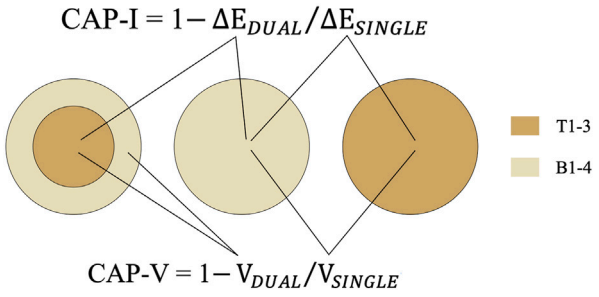

FIGURE 3
The measurement areas of instrumental and visual evaluation; the calculation method of CAP-I and CAP-V.

2.5 Statistical analysis

Statistical analysis was performed with IBM SPSS Statistics for Mac (version 26; IBM Corp., Armonk, NY, United States). The data were presented as mean and standard deviation values. The result of the Shapiro–Wilk test showed that the data presented normal distribution ($p > 0.05$). A three-way analysis of variance (ANOVA) was used to analyze the effects of material type, background color, and restoration depth on ΔE_{00}, CAP-I, and CAP-V values. The least significant difference (LSD) test and Dunnett's T3 test were applied for multiple comparisons when significant variation was detected. The test standard was bilateral ($\alpha = 0.05$ for all tests).

3 Results

Figure 4 showed representative single and dual specimens. In order to eliminate unwanted specular reflections on the surfaces of specimens caused by the flash, the photos were taken with a cross-polarization filter, which contributed to improving color selection and communication (Villavicencio-Espinoza et al., 2018; Sampaio et al., 2019; Jorquera et al., 2022).

The mean and standard deviation values of ΔE_{00} and visual scoring for the single specimens and the dual specimens with three restoration depths were respectively shown in Tables 2, 3. According to the results of multiple comparisons, ΔE_{00} values and visual scoring were both significantly affected by material type, background color, restoration depth, and specimen type ($p < 0.001$).

From the perspective of instrumental evaluation, for Charisma Diamond One, the ΔE_{00} values of all dual specimens were significantly lower than those of single specimens against the same background color. However, for Clearfil AP-X and Spectrum TPH3, the ΔE_{00} values of only a small portion of the dual specimens (mainly with 1-mm restoration depth) were significantly lower than those of the single specimens. But from the perspective of visual evaluation, the visual scorings of dual specimens were statistically significantly lower than or equal to those of single specimens at the same background color for all materials with different restoration depths. Nevertheless, for all materials, both ΔE_{00} values and visual scorings increased as restoration depth increased against the same background color.

In addition, at the same restoration depth, Clearfil AP-X showed the highest ΔE_{00} values and visual scorings against A1 base shade and the lowest mainly against A3/A3.5 base shade, Spectrum TPH3 showed the highest ΔE_{00} values and visual scorings against A3.5 base shade and the lowest mainly against A2 base shade, and Charisma Diamond One showed the highest ΔE_{00} values against A3.5 base shade and the lowest against A1 base shade.

According to the three-way ANOVA results, CAP-I and CAP-V values were both significantly affected by material type, background color, restoration depth, and their interactions ($p < 0.001$) (Table 4). Figure 5 presented the CAP-I and CAP-V values of three test materials with three restoration depths under four background colors. For all materials, both CAP-I and CAP-V decreased as restoration depth increased against the same background color. CAP-I values ranged from −0.45 to 0.79 and CAP-V values ranged from −0.02 to 0.77, both with the highest values consistently found for Charisma Diamond One among three test materials at the same background color and restoration depth ($p <$ 0. 001).

Figure 6 showed the TP_{00} values of all test materials and base materials for the single specimens. Charisma Diamond One and Filtek Z250 (A1 shade) showed, respectively, the greatest and the lowest translucency values, with significant differences ($p < 0.001$). There was no statistically significant difference among the TP_{00} value of Spectrum TPH3, Filtek Z250 (A2 shade), and Filtek Z250 (As shade) ($F = 0.396$, $p = 0.678$), as well as between the TP_{00} value of Filtek Z250 (A1 shade) and Filtek Z250 (A3.5 shade) ($F = 0.597$, $p =$ 0.560).

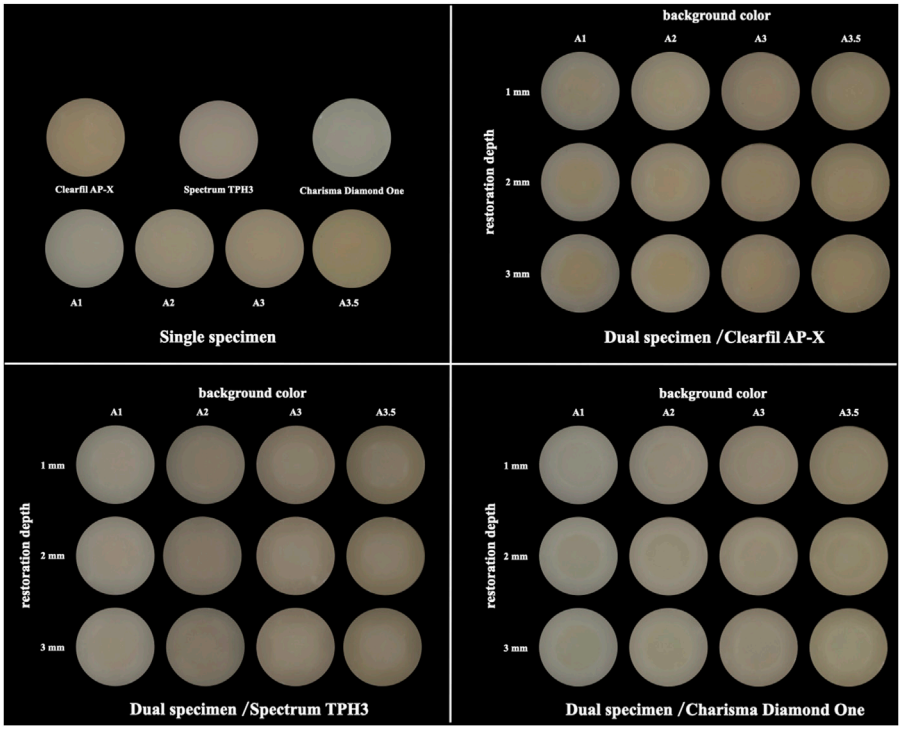

FIGURE 4
The representative single and dual specimens of all test materials and base materials.

TABLE 2 Descriptive statistics and multiple comparisons of ΔE_{00} values.

Material	Background color	Single specimen	Dual specimen (Restoration depth)		
			1 mm	2 mm	3 mm
Clearfil AP-X	A1	$7.80 \pm 0.74^{A,a,*}$	$5.19 \pm 0.67^{A,b}$	$6.92 \pm 0.59^{A,a}$	$7.38 \pm 0.55^{A,a}$
	A2	$5.53 \pm 0.42^{B,a}$	$4.09 \pm 0.35^{B,b}$	$4.83 \pm 0.43^{B,c}$	$5.57 \pm 0.63^{B,a}$
	A3	$3.08 \pm 0.37^{C,a}$	$1.97 \pm 0.23^{C,b}$	$2.91 \pm 0.39^{C,a,*}$	$4.85 \pm 0.52^{C,c,*}$
	A3.5	$2.65 \pm 0.12^{D,a}$	$2.02 \pm 0.15^{C,b}$	$2.52 \pm 0.21^{C,a}$	$3.85 \pm 0.55^{D,c}$
Spectrum TPH3	A1	$4.42 \pm 0.75^{A,a}$	$2.63 \pm 0.27^{A,b}$	$3.72 \pm 0.58^{A,a}$	$4.18 \pm 0.57^{A,a}$
	A2	$2.43 \pm 0.26^{B,a}$	$1.70 \pm 0.16^{B,b}$	$1.87 \pm 0.17^{B,b}$	$2.61 \pm 0.23^{B,a}$
	A3	$2.24 \pm 0.50^{B,a}$	$2.34 \pm 0.36^{C,a}$	$2.81 \pm 0.38^{C,b,*}$	$3.32 \pm 0.57^{C,c}$
	A3.5	$4.97 \pm 0.57^{A,a}$	$4.15 \pm 0.28^{D,b}$	$5.32 \pm 0.36^{D,a,c}$	$5.60 \pm 0.26^{D,c}$
Charisma Diamond One	A1	$7.89 \pm 0.65^{A,a,*}$	$1.65 \pm 0.29^{A,b}$	$1.84 \pm 0.22^{A,b}$	$2.76 \pm 0.45^{A,c}$
	A2	$8.56 \pm 0.51^{A,a}$	$2.69 \pm 0.19^{B,b}$	$2.92 \pm 0.19^{B,b,c}$	$3.06 \pm 0.13^{A,c}$
	A3	$8.28 \pm 0.31^{A,a}$	$4.19 \pm 0.44^{C,b}$	$4.40 \pm 0.27^{C,b}$	$5.31 \pm 0.74^{B,c,*}$
	A3.5	$9.88 \pm 0.30^{B,a}$	$4.76 \pm 0.28^{D,b}$	$6.05 \pm 0.31^{D,c}$	$7.22 \pm 0.45^{C,d}$

The same superscript uppercase letter indicates no statistical difference among the background colors at the same material type and type/restoration depth of specimen ($p > 0.05$).
The same superscript lowercase letter indicates no statistical difference among the type/restoration depth of specimen at the same material type and background color ($p > 0.05$).
* indicates no statistical difference among the material types at the same background color and type/restoration depth of specimen ($p > 0.05$).

4 Discussion

The results of present study showed significant differences in both instrumental and visual color adjustment potential among all test resin composites at different background colors and restoration depths. Therefore, both experimental hypotheses were rejected.

The color adjustment potential can be evaluated instrumentally and visually. Color measurement instruments can describe the

TABLE 3 Descriptive statistics and multiple comparisons of visual scoring.

Material	Background color	Single specimen	Dual specimen (Restoration depth)		
			1 mm	2 mm	3 mm
Clearfil AP-X	A1	$3.82 \pm 0.17^{A,a,*}$	$1.93 \pm 0.36^{A,b}$	$2.18 \pm 0.29^{A,b}$	$3.04 \pm 0.35^{A,c}$
	A2	$2.48 \pm 0.53^{B,a}$	$1.48 \pm 0.38^{A,b,*}$	$1.56 \pm 0.33^{B,b,*}$	$2.18 \pm 0.24^{B,a}$
	A3	$1.74 \pm 0.28^{C,a,*}$	$0.89 \pm 0.23^{B,b,*}$	$1.26 \pm 0.32^{B,c,*}$	$1.78 \pm 0.44^{B,C,a,*}$
	A3.5	$1.52 \pm 0.34^{C,a}$	$0.93 \pm 0.32^{B,b,*}$	$1.37 \pm 0.31^{B,a}$	$1.55 \pm 0.47^{C,a}$
Spectrum TPH3	A1	$3.07 \pm 0.36^{A,a,\#}$	$1.15 \pm 0.17^{A,B,b}$	$1.41 \pm 0.33^{A,b}$	$1.74 \pm 0.22^{A,B,c}$
	A2	$2.04 \pm 0.35^{B,a}$	$0.89 \pm 0.33^{A,b,\#}$	$0.96 \pm 0.39^{B,b}$	$1.55 \pm 0.29^{A,c,*}$
	A3	$1.81 \pm 0.34^{B,a,*}$	$1.41 \pm 0.33^{B,b}$	$1.63 \pm 0.26^{A,a,b,c}$	$1.81 \pm 0.38^{A,B,a,c,*}$
	A3.5	$2.11 \pm 0.41^{B,a}$	$1.85 \pm 0.34^{D,a}$	$2.04 \pm 0.26^{C,a,*}$	$2.07 \pm 0.36^{B,a,*}$
Charisma Diamond One	A1	$3.41 \pm 0.46^{A,a,*,\#}$	$0.81 \pm 0.34^{A,b}$	$1.07 \pm 0.32^{A,b,c}$	$1.37 \pm 0.31^{A,c}$
	A2	$3.82 \pm 0.34^{A,B,a}$	$1.19 \pm 0.44^{A,b,*,\#}$	$1.48 \pm 0.38^{B,b,c,*}$	$1.70 \pm 0.26^{B,c,*}$
	A3	$3.96 \pm 0.11^{B,a}$	$1.04 \pm 0.35^{A,b,*}$	$1.22 \pm 0.41^{A,B,b,*}$	$1.74 \pm 0.32^{B,c,*}$
	A3.5	$4.00 \pm 0.00^{B,a}$	$1.15 \pm 0.56^{A,b,*}$	$2.00 \pm 0.37^{C,c,*}$	$2.15 \pm 0.45^{C,c,*}$

The same superscript uppercase letter indicates no statistical difference among the background colors at the same material type and type/restoration depth of specimen ($p > 0.05$).
The same superscript lowercase letter indicates no statistical difference among the type/restoration depth of specimen at the same material type and background color ($p > 0.05$).
* or # indicates no statistical difference among the material types at the same background color and type/restoration depth of specimen ($p > 0.05$).

TABLE 4 Three-way ANOVA results of CAP-I and CAP-V.

Object	Source	Type III sum of squares	df	Mean square	F	*p*
CAP-I	Material type (A)	20.645	2	10.322	591.045	<0.001
	Background color(B)	6.459	3	2.153	123.286	<0.001
	Restoration depth (C)	6.675	2	3.337	191.093	<0.001
	A * B	1.094	6	0.182	10.439	<0.001
	A * C	1.549	4	0.387	22.172	<0.001
	B * C	0.750	6	0.125	7.159	<0.001
	A * B * C	1.320	12	0.110	6.299	<0.001
CAP-V	Material type (A)	9.147	2	4.573	437.432	<0.001
	Background color(B)	3.556	3	1.185	113.387	<0.001
	Restoration depth (C)	3.667	2	1.834	175.372	<0.001
	A * B	2.103	6	0.351	33.525	<0.001
	A * C	0.43	4	0.107	10.274	<0.001
	B * C	0.296	6	0.049	4.724	<0.001
	A * B * C	0.335	12	0.028	2.667	0.002

results in terms of color coordinates. Spectrophotometers have been proven to be useful and accurate instruments for measuring color in dentistry, which can improve the sensitivity and accuracy of measurement compared with visual evaluation (Karamouzos et al., 2007; Johnston, 2009). However, visual evaluation remains an important indicator for evaluating the color difference and color adjustment potential of resin composites (Chu et al., 2010), as it is the most commonly used method primary basis for clinicians and patients to determine the esthetic effect of resin composite restoration in clinic (de Abreu et al., 2021; Ruiz-López et al., 2022). Therefore, both instrumental and visual evaluation were used in present study to comprehensively compare the color adjustment potential of different resin composites. The CIELAB formula is frequently-used in the evaluation of color difference in dentistry. However, in order to achieve a better correlation between visual perception and instrumental evaluation, the recent color

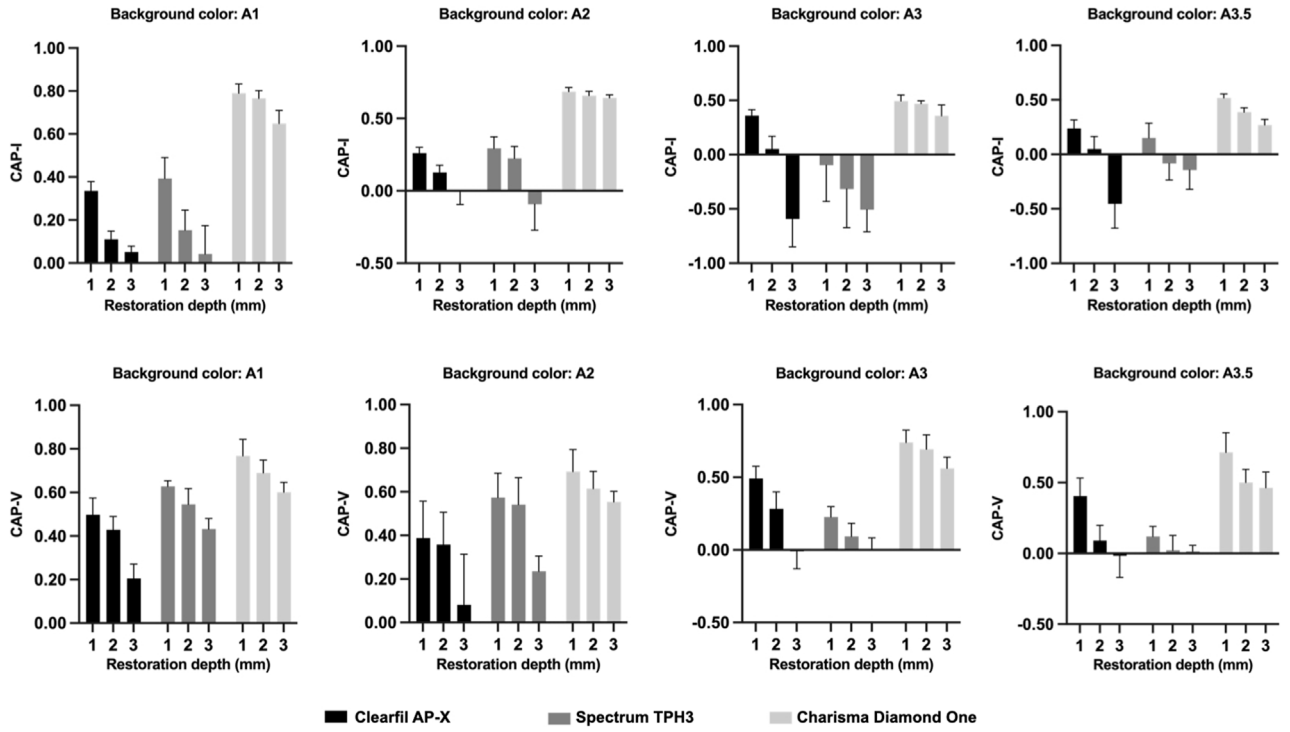

FIGURE 5
The CAP-I and CAP-V values of three test materials with different restoration depths under four background colors.

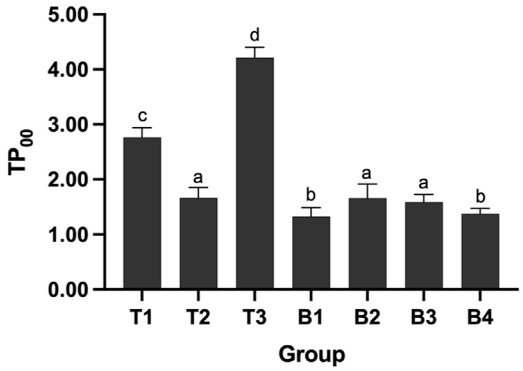

FIGURE 6
The TP_{00} values of all test materials and base materials for the single specimens. Different lowercase letters indicate the significant statistical difference ($p < 0.05$).

difference formula CIEDE2000 was developed and increasingly popular (Pecho et al., 2016; Günal-Abduljalil and Ulusoy, 2022).

The result from the present study was in accordance with previous investigations that the color difference of resin composite restoration depended on the material type and background color (Pereira Sanchez et al., 2019; de Abreu et al., 2021; Saegusa et al., 2021). Because the types and contents of base resins and fillers, as well as the size and shape of fillers, all have an impact on the color shifting ability of resin composites. Previous studies founded a positive correlation between the amount of Bis-GMA in the resin composite and its translucency because Bis-GMA has a higher translucency compared to UDMA and TEGDMA (Azzopardi et al., 2009; Miletic et al., 2017). And some studies also showed the color shifting ability of resin composites would improve with the increase in the filler contents (Altınışık and Özyurt, 2023). In addition, the size and shape of resin composite fillers determine the final surface properties of restorations, such as the size and shape of defects on the surfaces after polishing, resulting in the different wavelengths reflected from the surface and affecting the human perception of color (Sang et al., 2021; da Costa et al., 2021). Although the shade of all test resin composites (except Charisma Diamond One) was selected as A2 shade in this study, not all materials showed the lowest color difference under background of A2 shade. In this study, Spectrum TPH3 marked A2 shade matches the Filtek Z250 marked A2 shade best, with the lowest ΔE_{00} values and visual scoring among four background colors. However, Clearfil AP-X marked A2 shade matches the Filtek Z250 marked A3 or A3.5 shade best. Therefore, shade selection is indispensable in clinic when using multi-shade resin composites, especially when it comes to highly esthetic restorations (Ismail et al., 2020). The shade selection does not just determine the shade of the tooth needed treatment. More importantly, the shade of the resin composite selected based on the light-cured resin balls is necessary, because there are color differences between different resin composites marked the same shade.

CAP is a term representing color shifting referring to the interaction of dental materials with surrounding tissues, which determine the esthetic effect of resin composite (Ismail and Paravina, 2022). Equally, CAP was also depended on the material type and background color. The resin composite with positive CAP value means that it has less color differences when viewed together with

surrounding after restoration than when viewed separately (Durand et al., 2021). Currently, there has been no uniform standard for the CAP value as a threshold of effective color shifting yet. Pereira et al. and Altınışık et al. thought that a CAP value of 0.20 (corresponding to a 20% reduction in the value of color difference in dual specimen compared with single specimen) was the threshold (Pereira Sanchez et al., 2019; Altınışık and Özyurt, 2023), while Durand et al. thought a CAP value of 0.50 was the threshold (Durand et al., 2021). However, there is no doubt that among all the materials tested, Charisma Diamond One exhibited the best and effective color shifting ability at all different background colors and restoration depths, with CAP-I or CAP-V values always greater than 0.20 and the vast majority greater than 0.5.

As expected, the color difference and CAP were significantly affected by restoration depth. The color difference (both ΔE_{00} value and visual scoring) increased as restoration depth increased against the same background color for all test materials, while CAP-I and CAP-V values decreased as restoration depth increased. This result indicated that the esthetic effect of resin material was declined as restoration depth increased, which highlighted the importance of layering technique in esthetic restoration of resin composite. The color construction of natural tooth is more complex than the experimental sample, so layering technique is necessary to simulate the optical properties of a natural tooth and minimize the color difference when it comes to resin composite restoration, especially for the anterior teeth with high esthetic requirements (Romero, 2015; Miotti et al., 2017; Ricci and Fahl, 2023).

Previous studies have reported that the CAP of resin composite increased in accordance with an increase in translucency (Paravina et al., 2006). Translucency is one of the primary factors in controlling esthetics and it can be evaluated by the translucency parameter (TP_{00}) (Lucena et al., 2021). The higher the TP_{00} value is, the more light can be reflected from the background color into the composite restoration (Wang et al., 2013). This may explain the higher CAP-I and CAP-V values of Charisma Diamond One were recorded compared to other resin composites, with the highest TP_{00} value among all materials.

According to the manufacturer and literature, Charisma Diamond One utilizes "adaptive light matching" which determines the shade of the restoration by absorbing light waves reflected from the surrounding tooth shade. It contains urethane methacrylates, whose refractive index decreases as the size of side alkyl chain increases. Therefore, the translucency of Charisma Diamond One could increase after curing (Altınışık and Özyurt, 2023). On the other hand, due to the effect of the dark background in the oral cavity, the level of translucency that is incompatible with the surrounding structures can result in grayish restorations for the anterior teeth (Lucena et al., 2021). This also explains the higher ΔE_{00} value and visual scoring were recorded for Charisma Diamond One compared to other resin composites. One possible solution to this problem may be the "blocker", which is used for the restoration of anterior teeth, so as to better combine the resin composite with the adjacent tooth structure (de Abreu et al., 2021).

Apart from the CAP, color difference is also an important indicator for evaluating the color shifting ability of resin composite. Some previous studies have proposed to adjust the acceptable threshold of color difference to $\Delta E_{00} \leq 1.8$ units (Paravina et al., 2015). According to this standard, only Spectrum TPH3 with 1- and 2-mm restoration depths under A2 background color and Charisma Diamond One with 1- and 2-mm restoration depths under A1 base shade displayed the acceptable color difference. However, ΔE00 value is affected by measuring instrument, illuminant condition, environment brightness, background color, and so on (Lagouvardos et al., 2009; Lee et al., 2010; Tabatabaian et al., 2021). The result of visual evaluation showed that most of the tested groups of the dual specimens were superior or equal to "border zone mismatch" (visual scoring ≤ 2). Combined with the result of visual evaluation, the acceptable threshold value of ΔE00 in this study should be higher than 1.8.

Based on the comprehensive results of this study, Charisma Diamond One had the best color shifting ability, for its better CAP at different background colors and restoration depths. Charisma Diamond One is likely to match different teeth colors, which contributes to simplifying the process of shade selection and improving the efficiency of clinical work. However, it may only be suitable for restoration of the posterior teeth. For the restoration of the anterior teeth with high esthetic requirements, its application may be limited by the fact that the color difference evaluated instrumentally or visually was not minimal all the time for it and it may result in grayish restorations.

The current study has several limitations. Only four background colors were evaluated and the specimen cannot completely simulate the color construction of a natural tooth. And the experimental conditions for color evaluation are different from clinical treatment. In addition, the color stability of resin composites can be significantly affected by the aging process in the oral environment such as changes in temperature and the absorption of colorants contained in foods and beverages, which affects the esthetic result and clinical longevity of resin composite restorations. The evaluation of these variables needs to be further studied *in vivo* and *in vitro*, which will provide more detailed information about the color properties of resin composites.

5 Conclusion

The color adjustment potential was significantly affected by resin composite type, background color, and restoration depth, regardless of instrumental or visual evaluation. Charisma Diamond One exhibited the most pronounced color shifting ability with the highest CAP-I and CAP-V values at all background colors and restoration depths, compared to other multi-shade resin composites. These findings demonstrated that shade selection is indispensable for multi-shade resin composites and Charisma Diamond One contributes to simplifying the process of shade selection and improving the efficiency of clinical work.

Data availability statement

The original contributions presented in the study are included in the article/Supplementary Material, further inquiries can be directed to the corresponding author.

Author contributions

JZ: Conceptualization, Data curation, Formal Analysis, Investigation, Writing–original draft, Methodology. SC: Data

curation, Investigation, Writing–original draft. AA: Investigation, Validation, Writing–original draft. YX: Visualization, Writing–original draft. CH: Conceptualization, Supervision, Writing–review and editing.

Funding

The author(s) declare financial support was received for the research, authorship, and/or publication of this article. This study was funded by the National Natural Science Foundation of China (grant number 82271010) and Horizontal Research Project of Wuhan University (grant number K23-1607-002).

Conflict of interest

The authors declare that the research was conducted in the absence of any commercial or financial relationships that could be construed as a potential conflict of interest.

Publisher's note

References

Akgül, S., Gündoğdu, C., and Bala, O. (2022). Effects of storage time and restoration depth on instrumental color adjustment potential of universal resin composites. *J. Oral Sci.* 64, 49–52. doi:10.2334/josnusd.21-0290

Altınışık, H., and Özyurt, E. (2023). Instrumental and visual evaluation of the color adjustment potential of different single-shade resin composites to human teeth of various shades. *Clin. Oral Investig.* 27, 889–896. doi:10.1007/s00784-022-04737-x

Azzopardi, N., Moharamzadeh, K., Wood, D. J., Martin, N., and van Noort, R. (2009). Effect of resin matrix composition on the translucency of experimental dental composite resins. *Dent. Mater* 25, 1564–1568. doi:10.1016/j.dental.2009.07.011

Browning, W. D., Contreras-Bulnes, R., Brackett, M. G., and Brackett, W. W. (2009). Color differences: polymerized composite and corresponding Vitapan Classical shade tab. *J. Dent.* 37 (Suppl. 1), e34–e39. doi:10.1016/j.jdent.2009.05.008

Chu, S. J., Trushkowsky, R. D., and Paravina, R. D. (2010). Dental color matching instruments and systems. Review of clinical and research aspects. *J. Dent.* 38 (Suppl. 2), e2–e16. doi:10.1016/j.jdent.2010.07.001

da Costa, J. B., Ferracane, J. L., Amaya-Pajares, S., and Pfefferkorn, F. (2021). Visually acceptable gloss threshold for resin composite and polishing systems. *J. Am. Dent. Assoc.* 152, 385–392. doi:10.1016/j.adaj.2020.09.027

Da Rosa Rodolpho, P. A., Rodolfo, B., Collares, K., Correa, M. B., Demarco, F. F., Opdam, N. J. M., et al. (2022). Clinical performance of posterior resin composite restorations after up to 33 years. *Dent. Mater* 38, 680–688. doi:10.1016/j.dental.2022.02.009

de Abreu, J. L. B., Sampaio, C. S., Benalcázar Jalkh, E. B., and Hirata, R. (2021). Analysis of the color matching of universal resin composites in anterior restorations. *J. Esthet. Restor. Dent.* 33, 269–276. doi:10.1111/jerd.12659

Diamantopoulou, S., Kakaboura, A., Margaritis, V., and Papazoglou, E. (2021). Color comparison of three layered resin composite systems with three shade guides. *J. Esthet. Restor. Dent.* 33, 323–340. doi:10.1111/jerd.12610

Durand, L. B., Ruiz-López, J., Perez, B. G., Ionescu, A. M., Carrillo-Pérez, F., Ghinea, R., et al. (2021). Color, lightness, chroma, hue, and translucency adjustment potential of resin composites using CIEDE2000 color difference formula. *J. Esthet. Restor. Dent.* 33, 836–843. doi:10.1111/jerd.12689

El-Rashidy, A. A., Abdelraouf, R. M., and Habib, N. A. (2022). Effect of two artificial aging protocols on color and gloss of single-shade versus multi-shade resin composites. *BMC Oral Health* 22, 321. doi:10.1186/s12903-022-02351-7

Günal-Abduljalil, B., and Ulusoy, M. M. (2022). The effect of resin cement shade and restorative material type and thickness on the final color of resin-matrix ceramics. *J. Prosthodont Res.* 66, 75–82. doi:10.2186/jpr.JPR_D_20_00138

Ismail, E. H., Dawson, D. V., and Maia, R. R. (2020). A novel sample design for determining color compatibility between layered resin composite and vita shade guides. *J. Esthet. Restor. Dent.* 32, 34–42. doi:10.1111/jerd.12530

Ismail, E. H., and Paravina, R. D. (2022). Color adjustment potential of resin composites: optical illusion or physical reality, a comprehensive overview. *J. Esthet. Restor. Dent.* 34, 42–54. doi:10.1111/jerd.12843

Johnston, W. M. (2009). Color measurement in dentistry. *J. Dent.* 37 (Suppl. 1), e2–e6. doi:10.1016/j.jdent.2009.03.011

Jorquera, G. J., Atria, P. J., Galán, M., Feureisen, J., Imbarak, M., Kernitsky, J., et al. (2022). A comparison of ceramic crown color difference between different shade selection methods: visual, digital camera, and smartphone. *J. Prosthet. Dent.* 128, 784–792. doi:10.1016/j.prosdent.2020.07.029

Karamouzos, A., Papadopoulos, M. A., Kolokithas, G., and Athanasiou, A. E. (2007). Precision of *in vivo* spectrophotometric colour evaluation of natural teeth. *J. Oral Rehabil.* 34, 613–621. doi:10.1111/j.1365-2842.2007.01744.x

Korkut, B., and Türkmen, C. (2021). Longevity of direct diastema closure and recontouring restorations with resin composites in maxillary anterior teeth: a 4-year clinical evaluation. *J. Esthet. Restor. Dent.* 33, 590–604. doi:10.1111/jerd.12697

Lagouvardos, P. E., Fougia, A. G., Diamantopoulou, S. A., and Polyzois, G. L. (2009). Repeatability and interdevice reliability of two portable color selection devices in matching and measuring tooth color. *J. Prosthet. Dent.* 101, 40–45. doi:10.1016/s0022-3913(08)60289-9

Lee, Y. K., Yu, B., Lee, S. H., Cho, M. S., Lee, C. Y., and Lim, H. N. (2010). Variation in instrument-based color coordinates of esthetic restorative materials by measurement method-A review. *Dent. Mater* 26, 1098–1105. doi:10.1016/j.dental.2010.07.010

Lucena, C., Ruiz-López, J., Pulgar, R., Della Bona, A., and Pérez, M. M. (2021). Optical behavior of one-shaded resin-based composites. *Dent. Mater* 37, 840–848. doi:10.1016/j.dental.2021.02.011

Miletic, V., Jakovljevic, N., Manojlovic, D., Marjanovic, J., Rosic, A. A., and Dramićanin, M. D. (2017). Refractive indices of unfilled resin mixtures and cured composites related to color and translucency of conventional and low-shrinkage composites. *J. Biomed. Mater Res. B Appl. Biomater.* 105, 7–13. doi:10.1002/jbm.b.33523

Miotti, L. L., Santos, I. S., Nicoloso, G. F., Pozzobon, R. T., Susin, A. H., and Durand, L. B. (2017). The use of resin composite layering technique to mask discolored background: a CIELAB/ciede2000 analysis. *Oper. Dent.* 42, 165–174. doi:10.2341/15-368-l

Paravina, R. D., Ghinea, R., Herrera, L. J., Bona, A. D., Igiel, C., Linninger, M., et al. (2015). Color difference thresholds in dentistry. *J. Esthet. Restor. Dent.* 27 (Suppl. 1), S1–S9. doi:10.1111/jerd.12149

Paravina, R. D., Westland, S., Imai, F. H., Kimura, M., and Powers, J. M. (2006). Evaluation of blending effect of composites related to restoration size. *Dent. Mater* 22, 299–307. doi:10.1016/j.dental.2005.04.022

Paravina, R. D., Westland, S., Johnston, W. M., and Powers, J. M. (2008). Color adjustment potential of resin composites. *J. Dent. Res.* 87, 499–503. doi:10.1177/154405910808700515

Pecho, O. E., Ghinea, R., Alessandretti, R., Pérez, M. M., and Della Bona, A. (2016). Visual and instrumental shade matching using CIELAB and CIEDE2000 color difference formulas. *Dent. Mater* 32, 82–92. doi:10.1016/j.dental.2015.10.015

Pereira Sanchez, N., Powers, J. M., and Paravina, R. D. (2019). Instrumental and visual evaluation of the color adjustment potential of resin composites. *J. Esthet. Restor. Dent.* 31, 465–470. doi:10.1111/jerd.12488

Perez Mdel, M., Ghinea, R., Herrera, L. J., Ionescu, A. M., Pomares, H., Pulgar, R., et al. (2011). Dental ceramics: a CIEDE2000 acceptability thresholds for lightness, chroma and hue differences. *J. Dent.* 39 (Suppl. 3), e37–e44. doi:10.1016/j.jdent.2011.09.007

Ricci, W. A., and Fahl, N., Jr. (2023). Nature-mimicking layering with composite resins through a bio-inspired analysis: 25 years of the polychromatic technique. *J. Esthet. Restor. Dent.* 35, 7–18. doi:10.1111/jerd.13021

Romero, M. F. (2015). Esthetic anterior composite resin restorations using a single shade: step-by-step technique. *J. Prosthet. Dent.* 114, 9–12. doi:10.1016/j.prosdent.2015.02.013

Ruiz-López, J., Perez, M. M., Lucena, C., Pulgar, R., López-Toruño, A., Tejada-Casado, M., et al. (2022). Visual and instrumental coverage error of two dental shade

guides: an *in vivo* study. *Clin. Oral Investig.* 26, 5961–5968. doi:10.1007/s00784-022-04556-0

Saegusa, M., Kurokawa, H., Takahashi, N., Takamizawa, T., Ishii, R., Shiratsuchi, K., et al. (2021). Evaluation of color-matching ability of a structural colored resin composite. *Oper. Dent.* 46, 306–315. doi:10.2341/20-002-l

Sampaio, C. S., Atria, P. J., Hirata, R., and Jorquera, G. (2019). Variability of color matching with different digital photography techniques and a gray reference card. *J. Prosthet. Dent.* 121, 333–339. doi:10.1016/j.prosdent.2018.03.009

Sang, E. J., Song, J. S., Chung, S. H., Jin, B. H., and Hyun, H. K. (2021). Influence of a new polishing system on changes in gloss and surface roughness of resin composites after polishing and brushing. *Dent. Mater J.* 40, 727–735. doi:10.4012/dmj.2020-207

Tabatabaian, F., Beyabanaki, E., Alirezaei, P., and Epakchi, S. (2021). Visual and digital tooth shade selection methods, related effective factors and conditions, and their accuracy and precision: a literature review. *J. Esthet. Restor. Dent.* 33, 1084–1104. doi:10.1111/jerd.12816

Tanaka, A., Nakajima, M., Seki, N., Foxton, R. M., and Tagami, J. (2015). The effect of tooth age on colour adjustment potential of resin composite restorations. *J. Dent.* 43, 253–260. doi:10.1016/j.jdent.2014.09.007

Trifkovic, B., Powers, J. M., and Paravina, R. D. (2018). Color adjustment potential of resin composites. *Clin. Oral Investig.* 22, 1601–1607. doi:10.1007/s00784-017-2260-6

Tsubone, M., Nakajima, M., Hosaka, K., Foxton, R. M., and Tagami, J. (2012). Color shifting at the border of resin composite restorations in human tooth cavity. *Dent. Mater* 28, 811–817. doi:10.1016/j.dental.2012.04.032

Vargas, M., Saisho, H., Maharishi, A., and Margeas, R. (2023). A practical, predictable, and reliable method to select shades for direct resin composite restorations. *J. Esthet. Restor. Dent.* 35, 19–25. doi:10.1111/jerd.13019

Villavicencio-Espinoza, C. A., Narimatsu, M. H., and Furuse, A. Y. (2018). Using cross-polarized photography as a guide for selecting resin composite shade. *Oper. Dent.* 43, 113–120. doi:10.2341/16-227-t

Wang, F., Takahashi, H., and Iwasaki, N. (2013). Translucency of dental ceramics with different thicknesses. *J. Prosthet. Dent.* 110, 14–20. doi:10.1016/s0022-3913(13)60333-9

Yamashita, A., Kobayashi, S., Furusawa, K., Tichy, A., Oguro, R., Hosaka, K., et al. (2023). Does the thickness of universal-shade composites affect the ability to reflect the color of background dentin? *Dent. Mater J.* 42, 255–265. doi:10.4012/dmj.2022-197

frontiers | Frontiers in Bioengineering and Biotechnology

TYPE Original Research
PUBLISHED 07 December 2023
DOI 10.3389/fbioe.2023.1309503

OPEN ACCESS

EDITED BY
Gang Wu,
Academic Centre for Dentistry Amsterdam, VU Amsterdam, Netherlands

REVIEWED BY
Chang Lei,
The University of Queensland, Australia
Jiale Fu,
China Medical University, China
Yuhong Xiao,
The 920th Hospital of Joint Logistics Support Force, China

*CORRESPONDENCE
Hongye Yang,
yanghongye@whu.edu.cn
Cui Huang,
huangcui@whu.edu.cn

†These authors have contributed equally to this work

RECEIVED 08 October 2023
ACCEPTED 27 November 2023
PUBLISHED 07 December 2023

CITATION
Zhao S, Zhu Z, Yu J, Yao C, Yu M, Yang H and Huang C (2023), Enhancing dentin bonding quality through Acetone wet-bonding technique: a promising approach.
Front. Bioeng. Biotechnol. 11:1309503.
doi: 10.3389/fbioe.2023.1309503

Enhancing dentin bonding quality through Acetone wet-bonding technique: a promising approach

Shikai Zhao[1†], Zhiyi Zhu[2†], Jian Yu[1], Chenmin Yao[1], Miaoyang Yu[1], Hongye Yang[1*] and Cui Huang[1*]

[1]State Key Laboratory of Oral & Maxillofacial Reconstruction and Regeneration, Key Laboratory of Oral Biomedicine Ministry of Education, Hubei Key Laboratory of Stomatology, School and Hospital of Stomatology, Wuhan University, Wuhan, China, [2]Department of Stomatology, Maternal and Child Health Hospital of Hubei Province, Tongji Medical College, Huazhong University of Science and Technology, Wuhan, China

Objective: This paper aimed to assess the impact of the acetone wet-bonding (AWB) technique on dentin bonding and to investigate its potential underlying mechanisms.

Materials and Methods: Caries-free third molars were sliced, ground, etched, water-rinsed. Then the specimens were randomly allocated to four groups according to the following pretreatments: 1. water wet-bonding (WWB); 2. ethanol wet-bonding (EWB); 3. 50% (v/v) acetone aqueous solution (50%AWB); 4. 100% acetone solution (AWB). Singlebond universal adhesive was then applied and composite buildups were constructed. The microtensile bond strength (MTBS), failure modes and interface nanoleakage were respectively evaluated after 24 h of water storage, 10,000 times of thermocycling or 1-month collagenase ageing. *In situ* zymography and contact angle were also investigated.

Results: Acetone pretreatment preserved MTBS after thermocycling or collagenase ageing ($p < 0.05$) without affecting the immediate MTBS ($p > 0.05$). Furthermore, AWB group manifested fewer nanoleakage than WWB group. More importantly, the contact angle of the dentin surfaces decreased significantly and collagenolytic activities within the hybrid layer were suppressed in AWB group.

Conclusion: This study suggested that the AWB technique was effective in enhancing the dentin bond durability by increasing the wettability of dentin surface to dental adhesives, removing residual water in the hybrid layer, improving the penetration of adhesive monomer, and inhibiting the collagenolytic activities.

Clinical significance: The lifespan of adhesive restorations would be increased by utilization of acetone wet-bonding technique.

KEYWORDS

dentin, bonding, adhesive, interface, Acetone

1 Introduction

Since the 20th century, adhesive techniques played a dominant role in aesthetic dentistry (Drummond, 2008). Although the manufacturers claim that dentin adhesive system has evolved as far as eighth generation (Taneja et al., 2017), the dentin bonding durability remains inadequate despite its immediate effectiveness (Deligeorgi et al., 2001). Consequently, almost half of all aesthetic restorations require repair over a span of a decade and dentists find themselves dedicating a significant portion, approximately 60%, of their work hours to replace them (Deligeorgi et al., 2001). Therefore, urgent measures must be taken to enhance the durability of dentin bonding to prolong the service life of adhesive restorations.

The degradation of the hybrid layer at adhesive-dentin bonding interface is widely regarded as the chief contributing factor for the decline of bond durability (Tjaderhane et al., 2013). Adhesive hydrolysis, host-derived enzymatic degradation of collagen, inadequate infiltration of adhesive monomers, and secondary caries are possible threats that could lead to hybrid layer degradation (Breschi et al., 2018; Stewart and Finer, 2019). Various of measures, such as ethanol wet-bonding, biomimetic remineralization, collagen cross-linkers, and MMP inhibitors, have been suggested as potential options to protect the integrity of bonding interfaces and achieve reliable bonding durability (Ekambaram et al., 2014; R; Guo et al., 2021; Yang et al., 2016; Yi et al., 2019; Yu et al., 2022).

During dentin bonding, the dentin surface is firstly demineralized using phosphoric acid to create exposed collagen matrix with nanometer porosities. To prevent etched collagen from collapsing, water is needed to enter and maintain the interfibrillar spaces. This facilitates the infiltration of the adhesive monomers into the nanosized porosities of the collagen matrix for interlocking (Sartori et al., 2015). Consequently, the "wet bonding technique" was introduced to achieve higher bonding effectiveness, enhanced sealing of dentinal tubules and less post-operative discomfort (D. H. Pashley et al., 2011). But residual water can induce phase separation of the adhesive monomer (Spencer and Wang, 2002), leading to the formation of hydrophilic comonomer in the hybrid layer. This, in turn, results in the exclusion of hydrophobic monomers and hydrolyzation of the collagen (Wang and Spencer, 2003). Additionally, existing water in the collagen matrix actives endogenous enzymes, which triggers the proteolytic degradation process of the unprotected collagen (D. H. Pashley et al., 2004; Sartori et al., 2015). To address these issues, another solvent, ethanol, was introduced to replace water. Satisfactory laboratory results were obtained in *in vitro* studies by utilizing the "ethanol wet bonding technique", which requires experimental hydrophobic dental adhesive to contain ethanol of incremental concentrations (Ekambaram et al., 2014).

Acetone is a colorless, flammable and volatile liquid with a low-boiling point that evaporates rapidly and has a faint aroma. It is renowned as one of the most commonly employed solvents in various applications because it can readily blend with most organic solvents and completely with water. Moreover, it can be naturally synthesized by the human body during metabolic processes. Therefore, it has been considered a Generally Recognised As Safe (GRAS) substance when found in desserts, beverages and baked goods (Besinis et al., 2016). Acetone is a polar aprotic solvent capable of dissolving both polar and nonpolar compounds. It dissolves most monomers in dental adhesives (Ekambaram, Yiu and Matinlinna, 2015). Owing to its high dipole moment and good evaporation capacity (Abate, Rodriguez and Macchi, 2000), acetone possesses excellent water-removal capacities, earning it the name "water-chaser" (Jacobsen and Soderholm, 1995; Van Landuyt et al., 2007). Due to the fact that ethanol possesses a viscosity three times greater than that of acetone, dental adhesives based on acetone are less viscous than those based on ethanol, which promotes the acetone's infiltration into the demineralized dental collagen matrix (Faria-e-Silva et al., 2013). Previous studies examining acetone-based adhesives did not exclusively employ acetone as a sole preconditioning agent. Moreover, crucial parameters such as microtensile bond strength after ageing, nanoleakage, zymography and contact angle were not reported, all of which are essential for assessing dentin bond durability and dentin surface wettability (Irmak et al., 2016; X; Li, et al., 2004). Therefore, it is promising to explore the feasibility of "acetone wet-bonding" to improve the dentin bonding stability, especially when contrasted with conventional wet boding technique.

Thus, the objective of this study was to assess the impact of acetone pretreatment on dentin bonding in comparison to water and ethanol and explore possible mechanisms. The null hypotheses posited that acetone pretreatment would not result in (1) an enhancement in bond strength and a decrease in nanoleakage within the hybrid layer, and (2) any impact on collagen hydrolytic degradation within the hybrid layer, as well as the contact angle of the dentin surface.

2 Materials and methods

2.1 Chemicals and reagents

Singlebond universal adhesive and 35% phosphoric acid gel were purchased from 3M ESPE (St. Paul, MN, United States). Charism resin composite was supplied by Heraeus Kulzer (Hanau, Germany). Ethanol and acetone were provided by Aladdin Bio-Chem Technology (Shanghai, China). Kits of gelatinase/collagenase assay (E12055) was supplied by Molecular Probes (Invitrogen, Eugene, OR, United States). The chemicals and reagents were utilized in their as-received condition. Figure 1 displays the chemical structure of acetone.

2.2 Specimen preparation and bonding protocols

Sixty sound caries-free third molars were promptly cleansed and subsequently preserved in a 0.1% thymol solution at a temperature of 4 °C before utilization. Approval from the Ethics Committee for Human Studies of the School and Hospital of Stomatology, Wuhan University, China was secured for the utilization of the human third molars. A 50% (v/v) acetone aqueous solution was promptly prepared prior to use by blending acetone in sterilized deionized water.

To reveal the mid-coronal dentin surfaces, the teeth were cut below the enamel-dentinal junction using a diamond saw (Isomet,

Buehler Ltd., Lake Bluff, IL, United States). The standardized smear layer was produced by wet-polishing the dentin surfaces with 600-grit SiC paper for 60s. Subsequently, the specimens underwent a 15 s etching with 35% phosphoric acid, followed by thoroughly rinsing with deionized water. The surfaces were then blot-dried and treated with four primer solutions by using a micro-brush for 60s. The specimens were randomly distributed into four groups, with 15 teeth in each group, based on the different solutions as follows.

Group 1: deionized water (water wet-bonding, WWB group).
Group 2: absolute ethanol (ethanol wet-bonding, EWB group).
Group 3: 50% (v/v) acetone aqueous solution (water-acetone wet-bonding, 50%AWB group).
Group 4: absolute acetone (acetone wet-bonding, AWB group).

Following gentle blotting with filter paper, the dentin surface was rubbed for 20 s by a micro-brush dipped with Singlebond Universal (St. Paul, MN, United States). Then, the surfaces were subjected to 5 s of air blowing, and a LED light-curing (Bisco Inc., Schaumburg, IL, United States) was employed to polymerize the adhesive for 20 s. A 5-mm thick layer of composite (Charisma, Kulzer, Germany) was gradually added and polymerized for 20 s at a time. All the experimental procedures were performed by the same highly skilled clinician. Figure 2 illustrates the entire experimental procedure.

2.3 Microtensile bond strength test

The bonded teeth were immersed in water for 24 h. Then the specimens were longitudinally sectioned, yielding slabs with a thickness measuring 0.9 mm. To assess nanoleakage, six middle slabs from each group (n = 6) were randomly chosen and stored. Additionally, two middle slabs from each group (n = 2) were randomly chosen and set aside for *in situ* zymography. The remaining slabs were subsequently cut to produce beams measuring 0.9 mm × 0.9 mm. Following careful evaluation, unqualified beams, for example, those with enamel residual or positioned at the periphery were excluded. Twelve eligible beams were then selected from each tooth sample. Out of these, four (total $n = 36$) underwent MTBS immediately, another four (total n = 36) were subjected to 10,000 runs of thermocycling, and the remaining four (total $n = 36$) were assessed after 1 month of collagenase ageing. For the thermocycling procedure, the samples were inserted into a thermocycling apparatus (Thermo Fisher, Newington, United States) and subjected to alternate temperature cycles of 5°C and 55°C every 15 s, totaling 10,000 cycles (Deng et al., 2014). Regarding collagenase ageing, the specimens were submerged in a 0.1 mg/mL collagenase solution at 37°C in a dark environment. The ageing solution was produced by dissolving collagenase from *Clostridium histolyticum* in an artificial saliva medium (Zhang et al., 2020). The ageing solution was replenished periodically, every 3 days.

The chosen beams were individually affixed to a microtensile testing apparatus (Bisco Inc., Schaumburg, IL, United States). They were subjected to tension until fracture occurred, with a cross-head speed set at 1 mm per minute. Comprehensive data were meticulously documented, inclusive of the prematured detached beams. However, it is noteworthy that the values of these samples were excluded from the statistical analysis due to the fact that premature failure constituted less than 3 percent of the total samples tested in each group. Following the determination of the maximum load (N), the dimensions of each beam (mm^2) were assessed utilizing a digital caliper. Subsequently, the ultimate microtensile bond strength (MPa) was computed accordingly.

2.4 Fracture mode analysis

Following the MTBS assessment, the fractured beams were collected and subjected to drying. The surface of each beam underwent sputter-coating with Au-Pd alloy (JFC-1600, JEOL, Tokyo, Japan), and they were then subjected to analysis utilizing field-emission scanning electron microscopy (FESEM, Zeiss sigma, Jena, Germany). The fracture patterns were categorized into four types (Cova et al., 2011): (1) adhesive failure/A; (2) cohesive failure in dentin/CD; (3) cohesive failure in composite/CC; (4) mixed failure/M.

2.5 Interfacial nanoleakage evaluation of adhesive-dentin interface

Six middle slabs selected from each group, which had been stored, were randomly assigned for immediate evaluation ($n = 2$), evaluation after thermocycling ($n = 2$), or evaluation after 1 month of collagenase ageing ($n = 2$). The specimens underwent a double layer of nail polish application, with careful attention to maintain a consistent 1 mm distance from the bonded interface. Subsequently, all slabs were immersed in a 50% (w/v) silver nitrate/ammoniacal solution in the absence of light for a duration of 24 h. Following this, they underwent a thorough rinse in deionized water and were then immersed in a photo developing solution, exposed to fluorescent lighting for a duration of 8 h. They were subsequently wet-ground using 600, 800, 1,200, 2000 and 3000-grit silicon carbide papers. All specimens were subjected to ultrasonic cleaning, followed by drying and sputter-coating with carbon (JFC-1600, JEOL, Tokyo, Japan) before the final evaluation.

Using field-emission scanning electron microscopy (FESEM) in the back-scattered electron mode, the interfacial nanoleakage in all slabs was evaluated. In each slab, a total of 10 randomly chosen field-of-views were captured spanning the entire bonding interface and documented (20 images per subgroup). NIH ImageJ software (Bethesda, MD, United States) was employed to calculate the nanoleakage percentage of silver nitrate deposition within the dentin-adhesive layer. The interfacial nanoleakage was individually assessed by two examiners, expressed as a percentage and scored on a scale of 0–4, following a previously reported protocol (Li et al., 2017): 0, indicating no nanoleakage; 1, representing less than 25% nanoleakage; 2, denoting nanoleakage between 25% and 50%; 3, signifying nanoleakage between 50% and 75%; 4, indicating more than 75% nanoleakage. Kappa test was conducted to evaluate the consistency between the two examiners (K = 0.88).

2.6 Zymography of the hybrid layer

Two of the middle slabs, which had been preserved, were randomly chosen from each group for *in situ* zymography. The

10.3389/fbioe.2023.1309503

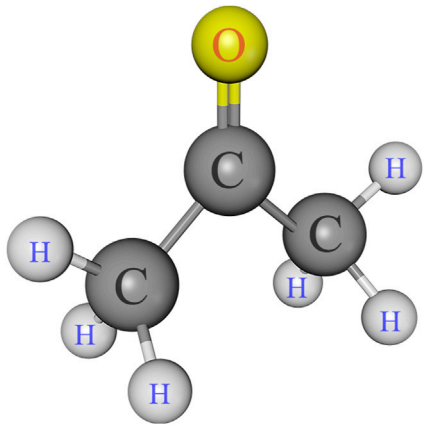

FIGURE 1
Chemical structure of acetone.

manufacturer's instructions were followed in the preparation of the gelatinase/collagenase assay kit, which contained fluorescein-tagged DQ gelatin conjugate. After wet-burnishing the specimens to achieve a thickness of approximately 50 μm, they were carefully mounted on a microscope slide. Subsequently, the specimens were covered with coverslips after applying the gelatin mixture onto these slabs. In the next 24 h, the prepared specimens were incubated in a darkened, humid chamber at a temperature of 37°C.

The slabs underwent examination through confocal laser scanning microscopy (CLSM, Leica, Wetzlar, Germany) in fluorescence mode, employing a ×40 objective lens with a numerical aperture of 0.95. The excitation/emission wavelengths were adjusted at 488/530 nm. Characteristic images were randomly captured from each slab, all at the same z layer. This was done to assess the activity of endogenous gelatinolytic proteases, encompassing MMPs and cysteine cathepsins, determined by the level of green fluorescence (Gou et al., 2018).

2.7 Surface contact angle measurements

Twelve third molars were used to acquire dentin disks, each 0.5 mm in thickness, by sectioning them below the enamel-dentinal junction with a low-speed diamond saw. These specimens were then subjected to wet-burnishing with 600, 800, 1,200, and 2000-grit SiC papers and 0.25 μm diamond paste, followed by a 5-min ultrasonic cleaning, a 15-s etching with 35% phosphoric acid gel, thorough rinsing with deionized water, and blot drying with filter papers. The disks were subsequently distributed randomly into four groups, each consisting of 6 disks: Group 1 (WWB); Group 2 (EWB); Group 3 (50%AWB); Group 4 (AWB). To measure the contact angle of each specimen, a Contact Angle System OCA (Dataphysics Instruments, Filderstadt, Germany) was utilized. A 5 μL of Singlebond universal adhesive was meticulously applied onto the surface immediately after blot-drying. The droplet's image was captured with a digital camera, and the contact angle was subsequently measured, keeping the distance between the dentin surface and the tip constant.

3 Results

3.1 Microtensile bond strength

The mean MTBS values obtained from the four groups are depicted in Figure 3. Two-factor ANOVA indicated that both pretreatments ($F = 24.730$, $p < 0.001$) and ageing methods ($F = 11.408$, $p < 0.001$) had a significant impact on dentin bond strength. For immediate bond strength, there was no significant difference observed in the EWB and AWB groups compared with the WWB group ($p > 0.05$). On the contrary, the 50%AWB group exhibited the highest value ($p < 0.05$).

In terms of bond strength after thermocycling or collagenase ageing, the AWB and 50%AWB groups displayed significantly higher values than the WWB group ($p < 0.05$). While there was no significant difference among the experimental groups ($p > 0.05$), it is worth noting that the AWB and 50%AWB groups had higher absolute values than the EWB group. The bond strength of the WWB group witnessed a significant decrease after thermocycling or collagenase ageing. However, the bond strength of the AWB group remained unaltered ($p > 0.05$).

3.2 Fracture mode analysis

Figure 4 illustrates the frequency distribution of fracture modes for the four groups. Compared to WWB group, the occurrence rate of adhesive failure increased to varying degrees in the other groups. Adhesive failure was the predominant mode in the immediate groups, whereas the occurrence rate of mixed failure showed an increase in the ageing groups. Figure 5 presents the representative FESEM images of the fractured surfaces.

3.3 Interfacial nanoleakage evaluation of adhesive-dentin interface

Table 1 exhibits the quantitative data obtained from nanoleakage evaluation. According to the Kruskal-Wallis test results, specimens pretreated with acetone exhibited significantly lower levels of nanoleakage ($p < 0.05$) compared to the control group, irrespective of the ageing method (i.e., thermocycling or collagenase ageing). Similar nanoleakage level was observed in the WWB group and 50%AWB group ($p > 0.05$).

Figure 6 shows representative FESEM micrographs of interfacial nanoleakage. Regardless of the ageing methods (immediate, thermocycling or collagenase ageing), the control and 50%AWB group showed thick and continuous silver precipitates along the adhesive-dentin interface, part of which infiltrated into the dentin tubules. However, sparse and interrupted distribution of silver particles along the interface of dentin and adhesive was observed in the EWB and AWB group. Furthermore, there were no silver granules observed within the dentin tubules, with the AWB group being particularly noteworthy in this regard. The silver uptake changes were not significant after thermocycling (Figure 6A2-D2) or collagenase ageing (Figure 6A3-D3) compared to immediate groups (Figure 6A1-D1).

10.3389/fbioe.2023.1309503

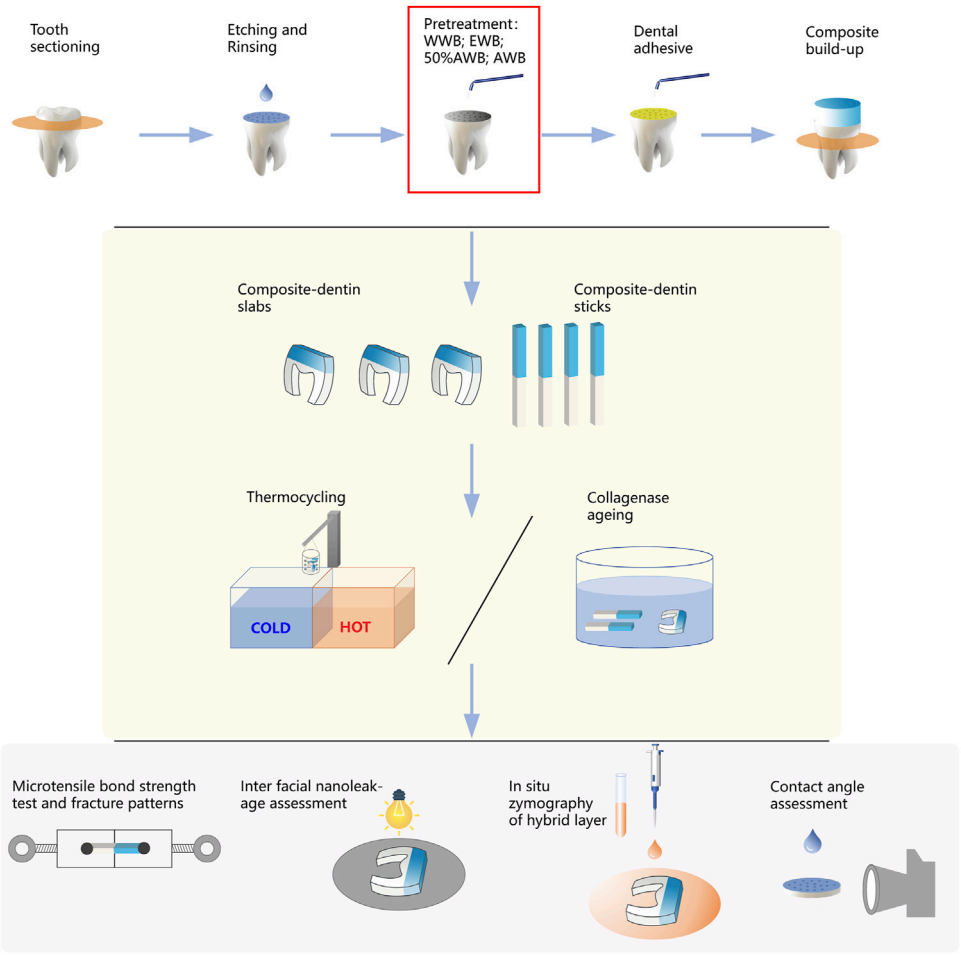

FIGURE 2
Schematic diagram illustrating the workflow of this study, including sample preparation, measurement of microtensile bond strength, nanoleakage, *in situ* zymography and contact angle.

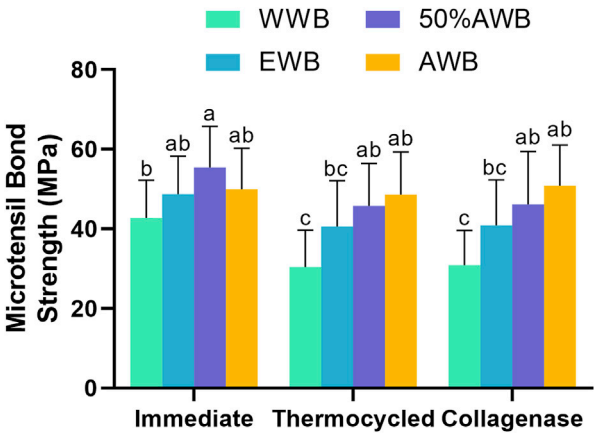

FIGURE 3
Means and standard deviations of microtensile bond strength (MTBS) for each group (groups with the same superscripts are not statistically significant ($p > 0.05$)).

3.4 Zymography of the hybrid layer

Figures 7A–D shows the typical CLSM images from the control or different pretreatment groups, which indicates the activity of endogenous proteases within the hybrid layers. In the WWB group, there was a substantial presence of green fluorescence within the hybrid layer, signifying extensive hydrolyzation of the DQ gelatine conjugate in this area compared to other groups. Conversely, the 50%AWB group displayed less green fluorescence within the hybrid layer, though the level of fluorescence was higher than that observed in the EWB and AWB groups. The EWB group showed a minimal level of green fluorescence, whereas the AWB group exhibited almost no green fluorescence along the hybrid layer.

3.5 Surface contact angle measurements

Figure 7E shows the contact angle values for each group along with their respective views. Real representative images of

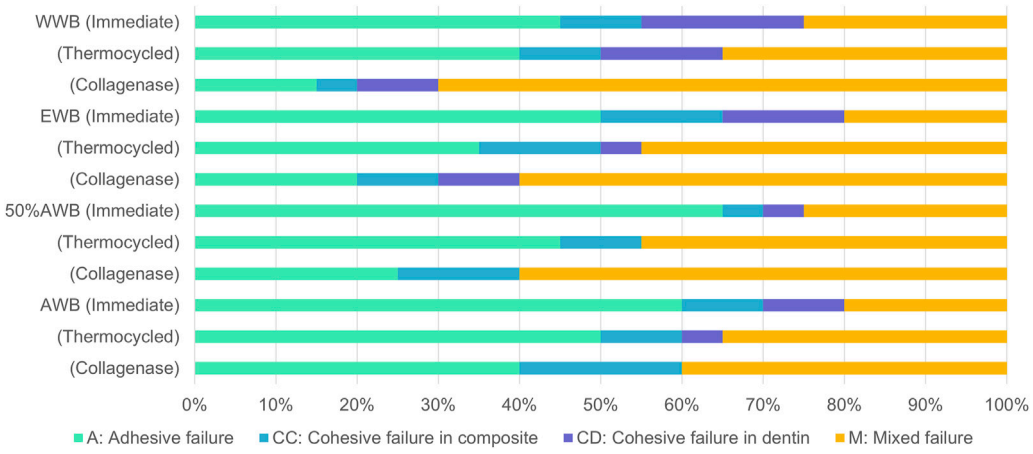

FIGURE 4
Distribution of failure modes after MTBS test.

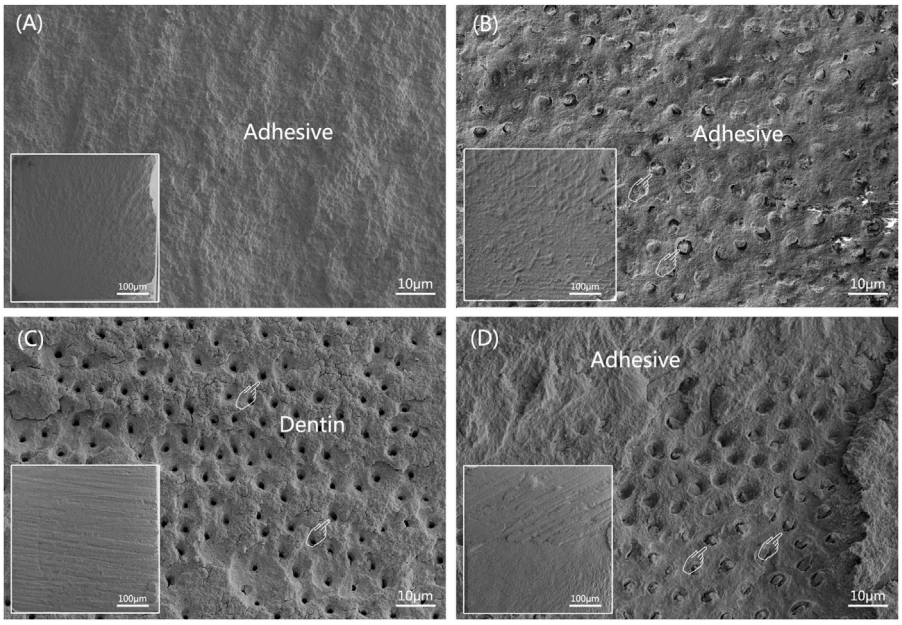

FIGURE 5
Representative FESEM images of dentin sides of fractured surfaces after MTBS test (The overall morphology is shown at the left lower corner of corresponding image). **(A)** adhesive failure; **(B)** cohesive failure in composite, pointers denoting occluded tubules; **(C)** cohesive failure in dentin, pointers denoting open dentinal tubules; **(D)** mixed failure, pointers denoting occluded tubules.

each group were displayed below the contact angle values. Among the four groups, the WWB group demonstrated the highest contact angle ($p < 0.05$). Both the EWB and 50%AWB groups exhibited significantly lower contact angles compared to the WWB group, yet notably higher angle than the AWB group ($p < 0.05$). The AWB group demonstrated the lowest contact angle ($p < 0.05$), indicating that the acetone pretreatment improved the permeability of the dental adhesive into the dentin surface.

4 Discussion

The current study assessed the impact of acetone wet-bonding (AWB) on enhancing the bonding strength of adhesive-dentin interface. The application of acetone and a 50% aqueous solution of acetone on the dentin surface as a pretreatment was found to increase the immediate bond strength. This enhanced bond strength was maintained even after undergoing different ageing methods, such as 10,000 runs of thermocycling and 1 month of collagenase

TABLE 1 Percentage distribution of nanoleakage scores from each group for immediate, 10,000 runs of thermocycled and after 1-month collagenase ageing.

Groups	Pretreatment	Score percentage (%)					Statisticaldifference
		0	1	2	3	4	
Immediate	WWB	0	0	55	45	0	ab
	EWB	15	50	30	0	5	d
	50%AWB	0	20	55	25	0	bc
	AWB	10	55	30	5	0	d
Thermocycling	WWB	0	0	35	65	0	ab
	EWB	5	45	50	0	0	d
	50%AWB	0	5	40	55	0	ab
	AWB	5	65	30	0	0	d
Collagenase ageing	WWB	0	0	15	65	20	a
	EWB	5	0	55	30	10	ab
	50%AWB	0	5	25	50	20	a
	AWB	0	50	35	10	5	cd

The Kruskal-Wallis test with Dunnett's *post hoc* test. Groups with the same letters are not statistically different ($p > 0.05$), $n = 20$.

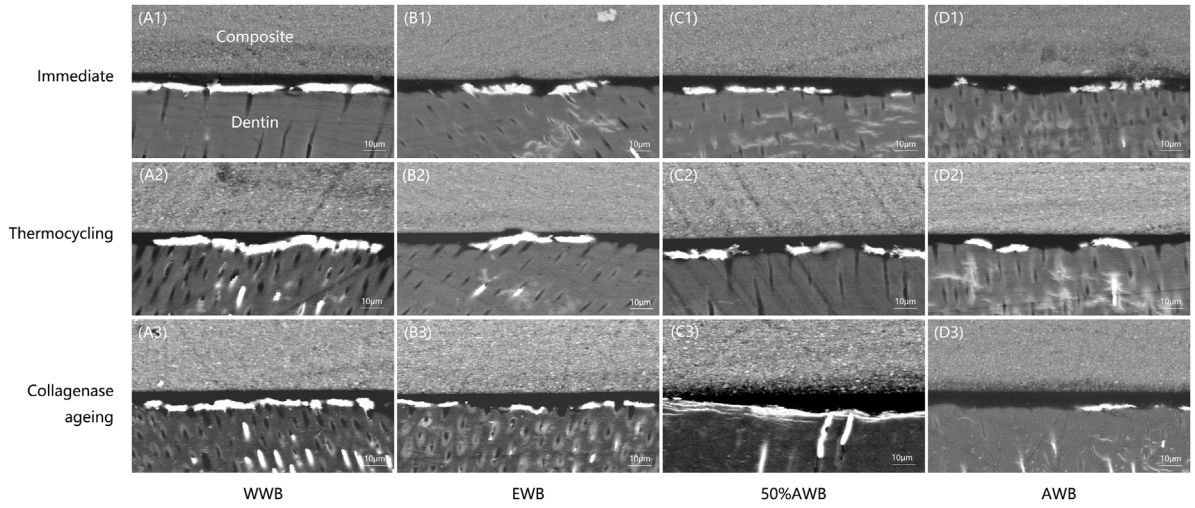

FIGURE 6
Representative FESEM images of interfacial nanoleakage expression at hybrid layer for each group. Images of **(A1-D1)**, **(A2-D2)**, and **(A3-D3)** represents nanoleakage for immediate, thermocycling, and collagenase ageing evaluation, respectively. Images of **(A1-A3)**, **(B1-B3)**, **(C1-C3)**, and **(D1-D3)** represents the WWB, EWB, 50%AWB, and AWB groups, respectively.

ageing. Furthermore, the use of the AWB method resulted in a reduction in nanoleakage compared to the water wet-bonding technique, regardless of whether the sample underwent thermocycling or collagenase ageing. Additionally, acetone pretreatment suppressed the activity of endogenous proteases, and notably, decreased the contact angle of the etched dentin surface to dental adhesives. Consequently, the null hypotheses were disproved.

During the development of dentin bonding techniques, it was discovered that moisture on the dentin surface plays an essential role in achieving high dentin bond strength (Yiu et al., 2005). Hence, the WWB technique was introduced, which involves the use of acid etching to markedly reduce the water contact angle on the dentin surface (Rosales-Leal et al., 2001). However, the low vapor pressure of water relative to other solvents necessitates a longer air-drying time, and residual water can cause hydrolytic degradation, making it less than ideal (Ekambaram et al., 2015; Jacobsen and Soderholm, 1995; E. L; Pashley, Zhang et al., 1998). As a result, alternative solvents such as ethanol were introduced (D. H. Pashley et al., 2007). Of all the bonding solvent employed in dental adhesives, acetone has the highest vapor pressure and effectively eliminates moisture from the demineralized dentin matrix (Van Landuyt et al., 2007).

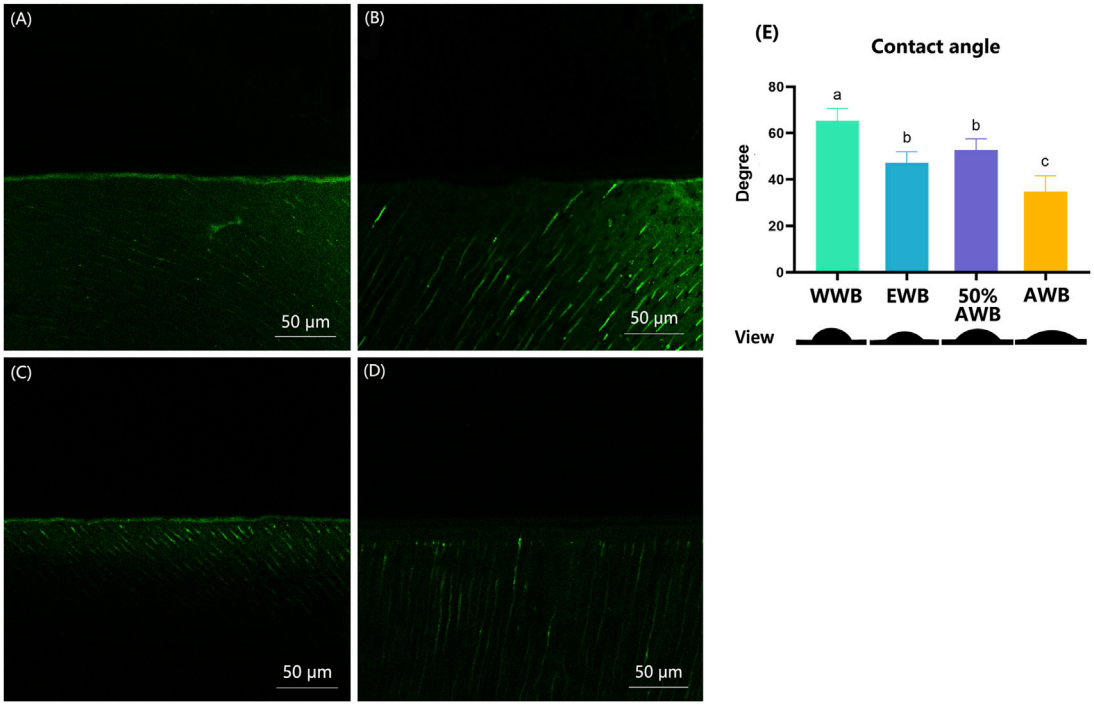

FIGURE 7
(A–D) Characteristic CLSM pictures from *in situ* zymography stained by fluorescent DQ gelatin conjugate. **(A)** water wet-bonding (WWB, **(A)**; **(B)** ethanol wet-bonding group (EWB, **(B)**; **(C)** 50% (v/v) acetone aqueous solution (50%AWB, **(C)**; **(D)** 100% acetone solution (AWB, **(D)**. **(E)** The degree of adhesive contact angle and respective views of the different pretreatment groups on the demineralized dentin surfaces. Groups with different letters are statistically different ($p < 0.05$). Real representative image of each group's anterior view was displayed below accordingly.

Additionally, acetone exhibits lower viscosity compared to ethanol, allowing it to better penetrate the demineralized dentin (Ekambaram et al., 2015; Besinis et al., 2016).

Contact angle measurement can be utilized to quantify the extent of liquid spreading on a surface. (Marshall et al., 2010). However, dentin is a non-ideal surface because of its composition and surface roughness (Besinis et al., 2016). In the wet-bonding technique process, the dentin was acid etched, water rinsed and blot-dried before the surface is treated with solvents and dental adhesives (D. H. Pashley et al., 2007). Thus, the real wettability of dentin surface after treatment is actually measurement of contact angle of the dentin surface to dental adhesives. In order to correctly measure the dentin surface wettability, a thin solvent film, according to different pretreatment groups, was cautiously left on the dentin surfaces to mask surface irregularities like smear layer and dentinal tubules, resulting in a smoother surface. If the dentin surface was dry, then the irregularities would impact the contact angle measurements necessitating the need for correction by applying the Wenzel equation (Wenzel, 1936). In this study, this method was undertaken to improve the accuracy of contact angle measurement.

In the acetone wet-bonding (AWB) technique, dentin is acid-etched and then rinsed with water, after which acetone solution is applied to interact with the residual water in the demineralized dentin. This process results in the displacement of water and transportation of adhesive monomers into the dentin collagen matrix with the help of acetone. Consequently, it enhances the dentin surface's wetting properties and improves the infiltration of adhesive (D. H. Pashley and Carvalho, 1997). In the present study, the application of acetone on the dentin led to a significant decrease in contact angle, indicating improved wettability. While pretreatment with ethanol and acetone aqueous solution also reduced the contact angle compared to water, the effect was not as pronounced as that of pure acetone. This "activation effect" of the dentin surface by the AWB technique helps to lower the surface tension of the dentin collagen matrix, creating better compatibility with primer and adhesive resins. This, in turn, facilitates the improved infiltration of adhesive monomers into the etched dentin (Besinis et al., 2016; D. H; Pashley and Carvalho, 1997). Notably, the contact angle was lowest in the AWB group, suggesting that acetone is the most effective solution for enhancing dentin wettability compared to other solvents.

The infiltration of monomer into the collagen matrix after etch-and-rinse has always been a problem (J. Guo et al., 2017). Deep penetration of the adhesive monomer can enhance the bond strength, as well as reducing the amounts of unprotected collagens which are vulnerable to hydrolysis. The breakdown of demineralized dentin matrices is a procedure that involves the swift and spontaneous establishment of fresh hydrogen bond (H-bonds) among collagen peptides (D. H. Pashley et al., 2007). Hoy's solubility parameter theory is widely used to evaluate capacity of chemicals to H-bonds (Barton, 1991). D. H. Pashley *et al* calculated Hoy's solubility parameters of collagen and found that 100% collagen has a Hoy's δ_h value of 14.8 $(J/cm^3)^{1/2}$ (Agee et al., 2006). Only solvents like water with a δ_h value of 40.4 $(J/cm^3)^{1/2}$ which is higher

than collagen have the capacity to disrupt the interpeptide hydrogen bonds, permitting the expansion of the collagen matrix. However, water is volatile and cannot polymerize and most adhesive monomers have δ_h value lower than 14.8 which means, in neat form, they cannot expand dry dentin collagen matrix (D. H. Pashley et al., 2007). In order to replace water and transport hydrophobic monomers into the gaps of collagen, amphiphilic solvents are needed. Acetone, which is amphiphilic and possesses qualities like strong permeability, can replace water and make it evaporate quickly, then transport hydrophobic monomers like MDP and hydrophilic monomers like HEMA into the gaps between collagens (Besinis et al., 2016). The immediate bond strength of 50% acetone pretreatment group (50%AWB) is notably higher than that of WWB group ($p < 0.05$), since the acetone aqueous solution can expand the collagen matrix efficiently and help the adhesive monomers infiltrate deeper simultaneously. Also, better penetration of monomers and more thorough replacement of water with the help of acetone lead to the decrease of unprotected collagens and the inhibition of enzyme hydrolysis, resulting in good bond durability. Thus, the bond strength of AWB group exhibited a notable increase compared to the WWB group following thermocycling or collagenase ageing ($p < 0.05$). Furthermore, neither thermocycling nor collagenase ageing led to a substantial decline in bond strength for the 50%AWB and AWB group.

The expression of nanoleakage is commonly utilized as a significant indicator to evaluate the durability and stability of dental bonding due to the fact that the intrusion of bacteria and the penetration of water into voids or channels within the adhesive-dentin interface can result in the deterioration of the hybrid layer (Deng et al., 2014). Kruskal-Wallis test (Table1) indicated that nanoleakage of AWB group significantly decreased in comparison to other groups ($p < 0.05$), irrespective of thermocycling or collagenase ageing. This was further demonstrated by details in Figure 6 which exhibited fewer silver deposition in AWB group. Dentin bonding is a procedure that encompasses the demineralization of dentin surface and refilling of the collagen matrix by adhesive monomers. After infiltration, adhesive monomers help form the mechanical interlock between dentin collagen and the adhesive (Pashley et al., 2003). After demineralization, it is essential to ensure that water and solvents are thoroughly eliminated from the dentin surface before curing to avoid jeopardization of the polymerization of adhesives (Yiu et al., 2005). However, the water is difficult to be removed due to its low vapor pressure (Ekambaram et al., 2015). Other solvents are then needed to replace water and help its evaporation. Acetone, which is called “water chaser”, would be the most efficient solvent because of its vapor pressure as high as 184.8 mmHg at 20 °C (Ekambaram et al., 2015). It would not only help water to evaporate but also facilitate the penetration of adhesive monomers. Therefore, the silver deposition in AWB group, which represents the holes in hybrid layer caused by the residual water after bonding, decreased significantly compared to other groups as shown in Figure 6. R. L. Sakaguchi and J. M. Powers (Sakaguchi and Powers, 2012) insisted on applying multiple coats of acetone-based adhesive due to the potential risk of evaporation during storage. However, as pretreatment solution, this would not be a problem since the concentration of pure acetone solution would not change, although the volume loss during storage is still inevitable.

The deterioration of the dentin collagen matrix can be initiated by internal enzymes such as MMPs and cysteine cathepsins and external enzymes like bacterial collagenase (Mazzoni et al., 2015). Thus, it is necessary to evaluate the activities of exogenous and endogenous enzymes. In this study, *in situ* zymography test of the hybrid layer developed by Breschi was chosen to detect the location of enzyme activities (Mazzoni et al., 2014). This method can reveal the gelatinolytic activity within the hybrid layer, which aligns with areas where collagen is left unprotected owing to incomplete resin infiltration. Results revealed a significant presence of fluorescent green within the control group, affirming the heightened activity of proteases. Conversely, the intensity of fluorescent green diminished progressively when higher concentrations of acetone were applied, suggesting the inhibition of the gelatinolytic activity. The details in Figure 7A disclosed that pretreatment with ethanol and acetone can significantly suppress the activity of endogenous proteases. There was almost none fluorescent green detected in AWB group as shown in Figure 7D. Although no direct evidence shows that acetone could inhibit dentin proteases, this phenomenon may be contributed to the better penetration of adhesive monomers with the help of acetone. After acid etching of dentin surfaces, the collagen left unprotected would be degraded by enzymes, resulting in poor dentin bonding durability (Liu et al., 2011). Since the acetone helps water evaporate, the adhesive monomers were transported deeply into the gaps of the dentin collagen. Subsequently, the collagens were enveloped and protected by adhesive monomers, thereby preventing enzymatic degradation of the collagen. The negative correlation of gelatinolytic activity and bond durability corroborated that enzyme activity could be a contributing factor to the decline in long-term bond strength.

In this study, the implementation of the acetone wet-bonding technique represents a promising approach for reducing contact angle, improving resin monomer penetration and enhancing dentin bond durability. However, limitations cannot be neglected. The high vapor pressure of acetone is a mixed blessing. Although it helps the removal of water from dentin surfaces and improves the infiltration of resin monomers into collagen matrix, the risk of evaporation can impact its longevity on the shelf. Further investigations are warranted to delve in to the underlying mechanisms of how acetone interfere with collagen hydrolytic degradation.

5 Conclusion

This study posits that the acetone wet-bonding (AWB) technique exhibits the capacity to sustain bond strength over an extended duration. Additionally, it demonstrates efficacy in improving dentin wettability to dental adhesives, facilitating adhesive monomer penetration, mitigating collagen exposure, decreasing nanoleakage, and attenuating collagen degradation. Within the confines of this *in vitro* investigation, acetone wet-bonding emerges as a promising strategy for prolonging the lifespan of adhesive restorations.

Data availability statement

The original contributions presented in the study are included in the article/Supplementary material, further inquiries can be directed to the corresponding authors.

Ethics statement

The studies involving humans were approved by the Ethics Committee for Human Studies of the School and Hospital of Stomatology, Wuhan University, China. The studies were conducted in accordance with the local legislation and institutional requirements. The participants provided their written informed consent to participate in this study.

Author contributions

SZ: Formal Analysis, Investigation, Writing–original draft. ZZ: Data curation, Investigation, Writing–original draft. JY: Validation, Writing–original draft. CY: Validation, Visualization, Writing–original draft. MY: Visualization, Writing–original draft. HY: Formal Analysis, Methodology, Writing–review and editing. CH: Conceptualization, Funding acquisition, Writing–review and editing.

Funding

The author(s) declare financial support was received for the research, authorship, and/or publication of this article. This work was supported by National Natural Science Foundation of China (82371004 and 82271010) and National Natural Science Foundation of Hubei Province (2022CFB068).

Conflict of interest

The authors declare that the research was conducted in the absence of any commercial or financial relationships that could be construed as a potential conflict of interest.

Publisher's note

All claims expressed in this article are solely those of the authors and do not necessarily represent those of their affiliated organizations, or those of the publisher, the editors and the reviewers. Any product that may be evaluated in this article, or claim that may be made by its manufacturer, is not guaranteed or endorsed by the publisher.

References

Abate, P. F., Rodriguez, V. I., and Macchi, R. L. (2000). Evaporation of solvent in one-bottle adhesives. *J. Dent.* 28 (6), 437–440. doi:10.1016/s0300-5712(00)00018-x

Agee, K. A., Becker, T. D., Joyce, A. P., Rueggeberg, F. A., Borke, J. L., Waller, J. L., et al. (2006). Net expansion of dried demineralized dentin matrix produced by monomer/alcohol saturation and solvent evaporation. *J. Biomed. Mater Res. A* 79 (2), 349–358. doi:10.1002/jbm.a.30752

Barton, A. (1991). *CRC handbook of solubility parameters and other cohesion parameters.*

Besinis, A., van Noort, R., and Martin, N. (2016). The use of acetone to enhance the infiltration of HA nanoparticles into a demineralized dentin collagen matrix. *Dent. Mater* 32 (3), 385–393. doi:10.1016/j.dental.2015.11.010

Breschi, L., Maravic, T., Cunha, S. R., Comba, A., Cadenaro, M., Tjaderhane, L., et al. (2018). Dentin bonding systems: from dentin collagen structure to bond preservation and clinical applications. *Dent. Mater* 34 (1), 78–96. doi:10.1016/j.dental.2017.11.005

Cova, A., Breschi, L., Nato, F., Ruggeri, A., Carrilho, M., Tjaderhane, L., et al. (2011). Effect of UVA-activated riboflavin on dentin bonding. *J. Dent. Res.* 90 (12), 1439–1445. doi:10.1177/0022034511423397

Deligeorgi, V., Mjor, I. A., and Wilson, N. H. (2001). An overview of reasons for the placement and replacement of restorations. *Prim. Dent. Care* 8 (1), 5–11. doi:10.1308/135576101771799335

Deng, D., Yang, H., Guo, J., Chen, X., Zhang, W., and Huang, C. (2014). Effects of different artificial ageing methods on the degradation of adhesive-dentine interfaces. *J. Dent.* 42 (12), 1577–1585. doi:10.1016/j.jdent.2014.09.010

Drummond, J. L. (2008). Degradation, fatigue, and failure of resin dental composite materials. *J. Dent. Res.* 87 (8), 710–719. doi:10.1177/154405910808700802

Ekambaram, M., Yiu, C., and Matinlinna, J. P. (2015). An overview of solvents in resin–dentin bonding. *Int. J. Adhesion Adhesives* 57, 22–33. doi:10.1016/j.ijadhadh.2014.09.007

Ekambaram, M., Yiu, C. K., Matinlinna, J. P., Chang, J. W., Tay, F. R., and King, N. M. (2014). Effect of chlorhexidine and ethanol-wet bonding with a hydrophobic adhesive to intraradicular dentine. *J. Dent.* 42 (7), 872–882. doi:10.1016/j.jdent.2014.02.006

Faria-e-Silva, A. L., Araujo, J. E., Rocha, G. P., de Oliveira Ada, S., and de Moraes, R. R. (2013). Solvent content and dentin bond strengths using water-wet, ethanol-wet and deproteinization bonding techniques. *Acta Odontol. Scand.* 71 (3-4), 710–715. doi:10.3109/00016357.2012.715195

Gou, Y. P., Meghil, M. M., Pucci, C. R., Breschi, L., Pashley, D. H., Cutler, C. W., et al. (2018). Optimizing resin-dentin bond stability using a bioactive adhesive with concomitant antibacterial properties and anti-proteolytic activities. *Acta Biomater.* 75, 171–182. doi:10.1016/j.actbio.2018.06.008

Guo, J., Lei, W., Yang, H., Zhang, Y., Zhao, S., and Huang, C. (2017). Dimethyl sulfoxide wet-bonding technique may improve the quality of dentin bonding. *J. Adhes. Dent.*, 229–237. doi:10.3290/j.jad.a38438

Guo, R., Peng, W., Yang, H., Yao, C., Yu, J., and Huang, C. (2021). Evaluation of resveratrol-doped adhesive with advanced dentin bond durability. *J. Dent.* 114, 103817. doi:10.1016/j.jdent.2021.103817

Irmak, Ö., Baltacıoğlu, İ. H., Ulusoy, N., and Bağış, Y. H. (2016). Solvent type influences bond strength to air or blot-dried dentin. *BMC Oral Health* 16 (1), 1–6. doi:10.1186/s12903-016-0247-3

Jacobsen, T., and Soderholm, K. J. (1995). Some effects of water on dentin bonding. *Dent. Mater* 11 (2), 132–136. doi:10.1016/0109-5641(95)80048-4

Li, K., Yang, H., Yan, H., Sun, Y., Chen, X., Guo, J., et al. (2017). Quercetin as a simple but versatile primer in dentin bonding. *Rsc Adv.* 7, 36392–36402. doi:10.1039/c7ra07467k

Li, X., Zhao, X., Shi, C., Zhu, G., and Li, H. (2004). Bonding strength and interface effects of different dentin surface on acetone-based adhesives bonding. *Shanghai J. Stomatology* 13 (1), 44–47. doi:10.3969/j.issn.1006-7248.2004.01.014

Liu, Y., Tjaderhane, L., Breschi, L., Mazzoni, A., Li, N., Mao, J., et al. (2011). Limitations in bonding to dentin and experimental strategies to prevent bond degradation. *J. Dent. Res.* 90 (8), 953–968. doi:10.1177/0022034510391799

Marshall, S. J., Bayne, S. C., Baier, R., Tomsia, A. P., and Marshall, G. W. (2010). A review of adhesion science. *Dent. Mater* 26 (2), e11–e16. doi:10.1016/j.dental.2009.11.157

Mazzoni, A., Apolonio, F. M., Saboia, V. P., Santi, S., Angeloni, V., Checchi, V., et al. (2014). Carbodiimide inactivation of MMPs and effect on dentin bonding. *J. Dent. Res.* 93 (3), 263–268. doi:10.1177/0022034513516465

Mazzoni, A., Tjaderhane, L., Checchi, V., Di Lenarda, R., Salo, T., Tay, F. R., et al. (2015). Role of dentin MMPs in caries progression and bond stability. *J. Dent. Res.* 94 (2), 241–251. doi:10.1177/0022034514562833

Pashley, D. H., Agee, K. A., Wataha, J. C., Rueggeberg, F., Ceballos, L., Itou, K., et al. (2003). Viscoelastic properties of demineralized dentin matrix. *Dent. Mater.* 19 (8), 700–706. doi:10.1016/s0109-5641(03)00016-2

Pashley, D. H., and Carvalho, R. M. (1997). Dentine permeability and dentine adhesion. *J. Dent.* 25 (5), 355–372. doi:10.1016/s0300-5712(96)00057-7

Pashley, D. H., Tay, F. R., Breschi, L., Tjaderhane, L., Carvalho, R. M., Carrilho, M., et al. (2011). State of the art etch-and-rinse adhesives. *Dent. Mater* 27 (1), 1–16. doi:10.1016/j.dental.2010.10.016

Pashley, D. H., Tay, F. R., Carvalho, R. M., Rueggeberg, F. A., Agee, K. A., Carrilho, M., et al. (2007). From dry bonding to water-wet bonding to ethanol-wet bonding. A review of the interactions between dentin matrix and solvated resins using a macromodel of the hybrid layer. *Am. J. Dent.* 20 (1), 7–20.

Pashley, D. H., Tay, F. R., Yiu, C., Hashimoto, M., Breschi, L., Carvalho, R. M., et al. (2004). Collagen degradation by host-derived enzymes during aging. *J. Dent. Res.* 83 (3), 216–221. doi:10.1177/154405910408300306

Pashley, E. L., Zhang, Y., Lockwood, P. E., Rueggeberg, F. A., and Pashley, D. H. (1998). Effects of HEMA on water evaporation from water-HEMA mixtures. *Dent. Mater* 14 (1), 6–10. doi:10.1016/s0109-5641(98)00003-7

Rosales-Leal, J. I., Osorio, R., Holgado-Terriza, J. A., Cabrerizo-Vilchez, M. A., and Toledano, M. (2001). Dentin wetting by four adhesive systems. *Dent. Mater* 17 (6), 526–532. doi:10.1016/s0109-5641(01)00014-8

Sakaguchi, R. L., and Powers, J. M. (2012). *Craig's restorative dental materials*. Maryland Heights, Missouri: Mosby Elsevier.

Sartori, N., Peruchi, L. D., Phark, J. H., Lopes, M. M., Araujo, E., Vieira, L. C., et al. (2015). Permeation of intrinsic water into ethanol- and water-saturated, monomer-infiltrated dentin bond interfaces. *Dent. Mater* 31 (11), 1385–1395. doi:10.1016/j.dental.2015.08.159

Spencer, P., and Wang, Y. (2002). Adhesive phase separation at the dentin interface under wet bonding conditions. *J. Biomed. Mater Res.* 62 (3), 447–456. doi:10.1002/jbm.10364

Stewart, C. A., and Finer, Y. (2019). Biostable, antidegradative and antimicrobial restorative systems based on host-biomaterials and microbial interactions. *Dent. Mater* 35 (1), 36–52. doi:10.1016/j.dental.2018.09.013

Taneja, S., Kumari, M., and Bansal, S. (2017). Effect of saliva and blood contamination on the shear bond strength of fifth-seventh-and eighth-generation bonding agents: an *in vitro* study. *J. Conserv. Dent.* 20 (3), 157–160. doi:10.4103/0972-0707.218310

Tjaderhane, L., Nascimento, F. D., Breschi, L., Mazzoni, A., Tersariol, I. L., Geraldeli, S., et al. (2013). Strategies to prevent hydrolytic degradation of the hybrid layer-A review. *Dent. Mater* 29 (10), 999–1011. doi:10.1016/j.dental.2013.07.016

Van Landuyt, K. L., Snauwaert, J., De Munck, J., Peumans, M., Yoshida, Y., Poitevin, A., et al. (2007). Systematic review of the chemical composition of contemporary dental adhesives. *Biomaterials* 28 (26), 3757–3785. doi:10.1016/j.biomaterials.2007.04.044

Wang, Y., and Spencer, P. (2003). Hybridization efficiency of the adhesive/dentin interface with wet bonding. *J. Dent. Res.* 82 (2), 141–145. doi:10.1177/154405910308200213

Wenzel, R. W. (1936). Resistance of solid surfaces to wetting by water. *Trans. Faraday Soc.* 28 (8), 988–994. doi:10.1021/ie50320a024

Yang, H., Guo, J., Deng, D., Chen, Z., and Huang, C. (2016). Effect of adjunctive application of epigallocatechin-3-gallate and ethanol-wet bonding on adhesive-dentin bonds. *J. Dent.* 44, 44–49. doi:10.1016/j.jdent.2015.12.001

Yi, L., Yu, J., Han, L., Li, T., Yang, H., and Huang, C. (2019). Combination of baicalein and ethanol-wet-bonding improves dentin bonding durability. *J. Dent.* 90, 103207. doi:10.1016/j.jdent.2019.103207

Yiu, C. K., Pashley, E. L., Hiraishi, N., King, N. M., Goracci, C., Ferrari, M., et al. (2005). Solvent and water retention in dental adhesive blends after evaporation. *Biomaterials* 26 (34), 6863–6872. doi:10.1016/j.biomaterials.2005.05.011

Yu, J., Zhao, Y., Shen, Y., Yao, C., Guo, J., Yang, H., et al. (2022). Enhancing adhesive-dentin interface stability of primary teeth: from ethanol wet-bonding to plant-derived polyphenol application. *J. Dent.* 126, 104285. doi:10.1016/j.jdent.2022.104285

Zhang, Z., Yu, J., Yao, C., Yang, H., and Huang, C. (2020). New perspective to improve dentin-adhesive interface stability by using dimethyl sulfoxide wet-bonding and epigallocatechin-3-gallate. *Dent. Mater* 36 (11), 1452–1463. doi:10.1016/j.dental.2020.08.009

frontiers | Frontiers in Bioengineering and Biotechnology

TYPE Original Research
PUBLISHED 09 January 2024
DOI 10.3389/fbioe.2023.1346959

OPEN ACCESS

EDITED BY
Dandan Pei,
Xi'an Jiaotong University, China

REVIEWED BY
Wei Fan,
Wuhan University, China
Jianbin Guo,
Fujian Medical University, China

*CORRESPONDENCE
Bingshuang Zou,
drzou@dentistry.ubc.ca

†These authors have contributed equally to this work

RECEIVED 30 November 2023
ACCEPTED 28 December 2023
PUBLISHED 09 January 2024

CITATION
Jiang W, Wang Z, Zhou Y, Shen Y, Yen E and Zou B (2024), Bioceramic micro-fillers reinforce antibiofilm and remineralization properties of clear aligner attachment materials.
Front. Bioeng. Biotechnol. 11:1346959.
doi: 10.3389/fbioe.2023.1346959

Bioceramic micro-fillers reinforce antibiofilm and remineralization properties of clear aligner attachment materials

Wenhui Jiang[1†], Zhejun Wang[2†], Yinghong Zhou[3], Ya Shen[2], Edwin Yen[1] and Bingshuang Zou[1*]

[1]Division of Orthodontics, Department of Oral Health Science, Faculty of Dentistry, The University of British Columbia, Vancouver, BC, Canada, [2]Division of Endodontics, Department of Oral Biological and Medical Sciences, Faculty of Dentistry, The University of British Columbia, Vancouver, BC, Canada, [3]School of Dentistry, The University of Queensland, Brisbane, QLD, Australia

Introduction: Clear aligners, while offering a more hygienic alternative to fixed appliances, are still associated with challenges including plaque accumulation and enamel demineralization. The aim of the present study was to investigate the antibiofilm and remineralization effectiveness of innovative flowable composite attachments containing bioceramic micro-fillers.

Methods: Four experimental attachments were formulated and bonded to human enamel specimens: 3M Filtek Supreme flowable composite (Filtek SF) + 10% bioactive glass 45S5 (BAG), Filtek SF + 30% BAG, Filtek SF + 10% Bredigite (BRT), Filtek SF + 30% BRT. Plaque biofilms were grown on the bonded enamel using a standardized protocol and the biofilm-killing effect was assessed by confocal laser scanning microscopy and scanning electron microscopy. Vickers microhardness was measured to evaluate the remineralization effect of the attachments containing bioceramic fillers after acid challenge. Shear bond test was performed to assess the bonding strength.

Results: Attachments with bioceramic fillers significantly inhibited plaque biofilm growth in 3 weeks on enamel, contributing over 20% bacterial cell killing in 10% filler groups and over 30% killing in 30% filler groups. All four experimental groups demonstrated significantly higher microhardness values than the control group without fillers on the attachment side. The shear bonding strength was not compromised in the attachments with micro-fillers.

Discussion: Proper incorporation of bioceramic micro-fillers in attachments provides an innovative approach for clear aligner therapy with reinforced antibiofilm and remineralization effects without weakening shear bonding strength.

KEYWORDS

bioactive glass, bioceramic filler, bredigite, clear aligner attachment, plaque biofilm

1 Introduction

Over the past few decades, there has been a growing demand for alternatives to conventional fixed orthodontic appliances, driving the development of more comfortable and aesthetically pleasing appliances. This shift has led to the emergence of clear aligner therapy (Khosravi et al., 2017). Removable thermoplastic clear aligners, worn sequentially by patients, have gained popularity for achieving targeted orthodontic results (Weir, 2017). However, it's worth noting that composite clear aligner attachments tend to exhibit increased biofilm accumulation compared to other restorative materials (Bourbia et al., 2013; Bichu et al., 2023).

Despite claims of a more hygienic design and expectations of fewer white spot lesions with clear aligners compared to traditional fixed appliances (Buschang et al., 2019), enamel demineralization and plaque accumulation remain critical side effects, particularly with prolonged wear (Santonocito and Polizzi, 2022). A significant increase in the total bacterial load with both types of appliances was reported (Mummolo et al., 2020). A recent randomized clinical trial has reported a significantly larger lesion area in the clear aligner group at T1 (3 months after treatment) than at T0 (beginning of treatment) and the fixed appliance group (Albhaisi et al., 2020). This increase in white spot lesions during clear aligner therapy may be attributed to limitations in saliva flow, natural buffering, and remineralizing properties (Azeem and Hamid, 2017). Resin composites, known to enhance bacterial growth (Beyth et al., 2008), contribute to a high cariogenic challenge due to bacterial biofilm accumulation around attachments during intraoral wear.

Previous antibiofilm studies have predominantly focused on fixed orthodontic appliances rather than clear aligner attachments (Badawi et al., 2003; Zhang et al., 2015a; Ferreira et al., 2019), often employing single-species bacteria (e.g., *Streptococcus mutans* and *Lactobacilli*) rather than the multispecies bacteria commonly found in white spot lesions (Chin et al., 2006; Zhang et al., 2015b). However, bacteria in white spot lesions all originate from multispecies plaque on the tooth surface (Cheng et al., 2012; Beerens et al., 2017). Most commercially available composite resins exhibit minimal antibiofilm effects, with biofilms tending to accumulate on them over time (Beyth et al., 2007; Khalichi et al., 2009). Additionally, these composites can be degraded by enzymes from saliva and bacteria (Montoya et al., 2021). The acid produced by bacterial biofilms can cause enamel demineralization around the clear aligner attachments (Zhang et al., 2017). Therefore, exploring novel bioactive attachment materials that enhance antibiofilm and remineralization properties without compromising bonding strength is essential in clear aligner therapy.

Existing antibacterial/antibiofilm agents containing leachable compounds (e.g., chlorhexidine), antibiofilm peptides, and filler nanoparticles (e.g., zinc and silver) have major limitations of short-term effectiveness and an inability to regenerate mineral content lost due to hard enamel damage (Stewart and Finer, 2019; Makvandi et al., 2020). Bioactive glass (BAG) has been identified for its ability to inhibit enamel demineralization in orthodontic bonding resins (Lee et al., 2018). Two studies have highlighted the robust antimicrobial activity of bioactive glass S53P4 against *S. aureus* and *Pseudomonas aeruginosa* (Coraça-Huber et al., 2014; Drago et al., 2014). Bredigite (BRT) bioceramics have demonstrated osteogenic effects on dentin and plaque growth suppression (Shen et al., 2016). However, the effects of using BAG and BRT as micro-fillers in clear aligner attachments remain relatively unexplored.

Achieving long-term clinical success necessitates an ideal material that is multifunctional, capable of overcoming limitations of individual formulations. Despite the potential offered by bioactive fillers, there is a lack of standardized protocols to systematically assess antibiofilm, remineralization, and bonding in one study, specifically mirroring the clinical situation of clear aligner therapy. Existing *in vitro* studies have often focused on evaluating the antimicrobial effect of bonding materials independently on composite resin disks (Zhang et al., 2015a; Zhang et al., 2015b; Altmann et al., 2017) rather than on attachment bonded enamel. Thus, the development of a standardized model is crucial to simulate the clinical reality of clear aligner therapy.

This project aimed to formulate two bioceramic micro-filler-based attachments and systematically investigate their antibiofilm and remineralization effects, as well as assess shear bond strength on a standardized platform, providing a comprehensive evaluation of their performance in a manner that closely replicates the clinical conditions of clear aligner therapy.

2 Materials and methods

2.1 Enamel sample and attachment mould preparation

This study was approved by the Clinical Research Ethics Committee of the University of British Columbia (certificate H22-01985). Sixty caries-free human premolars subjected to orthodontic extraction were collected. The extracted teeth were stored in deionized water at 4°C. The crown of each premolar was sectioned perpendicularly to the long axis of the tooth at the cementoenamel junction using a low-speed water-cooled diamond saw (Isomet, Buehler, Lake Bluff, IL, United States).

A platinum-catalyzed silicone rubber (Ecoflex™ Smooth-on, Macungie, PA, United States) was used to fabricate flexible silicone moulds used for the preparation of attachments. Each mould featured an inner diameter of 2 mm (length) × 4 mm (width) × 3 mm (thickness) and an outer diameter of 4 mm (length) × 6 mm (width) × 3 mm (thickness), following the manufacturer's guidelines.

The experimental design is outlined in the schematic diagram presented in Figure 1.

2.2 Bioceramic fillers and attachment material preparation

The composition of bioactive glass 45S5 (BAG), bredigite (BRT), and the flowable composite attachment material (Filtek SF) is listed in Table 1. Bioactive glass 45S5 contains 45 wt% SiO_2, 24.5 wt% CaO, 24.6 wt% Na_2O, and 5.8 wt% P_2O_5. According to a previously described protocol, BRT powders were synthesized by a sol-gel method using raw materials including $(C_2H_5O)_4Si$,

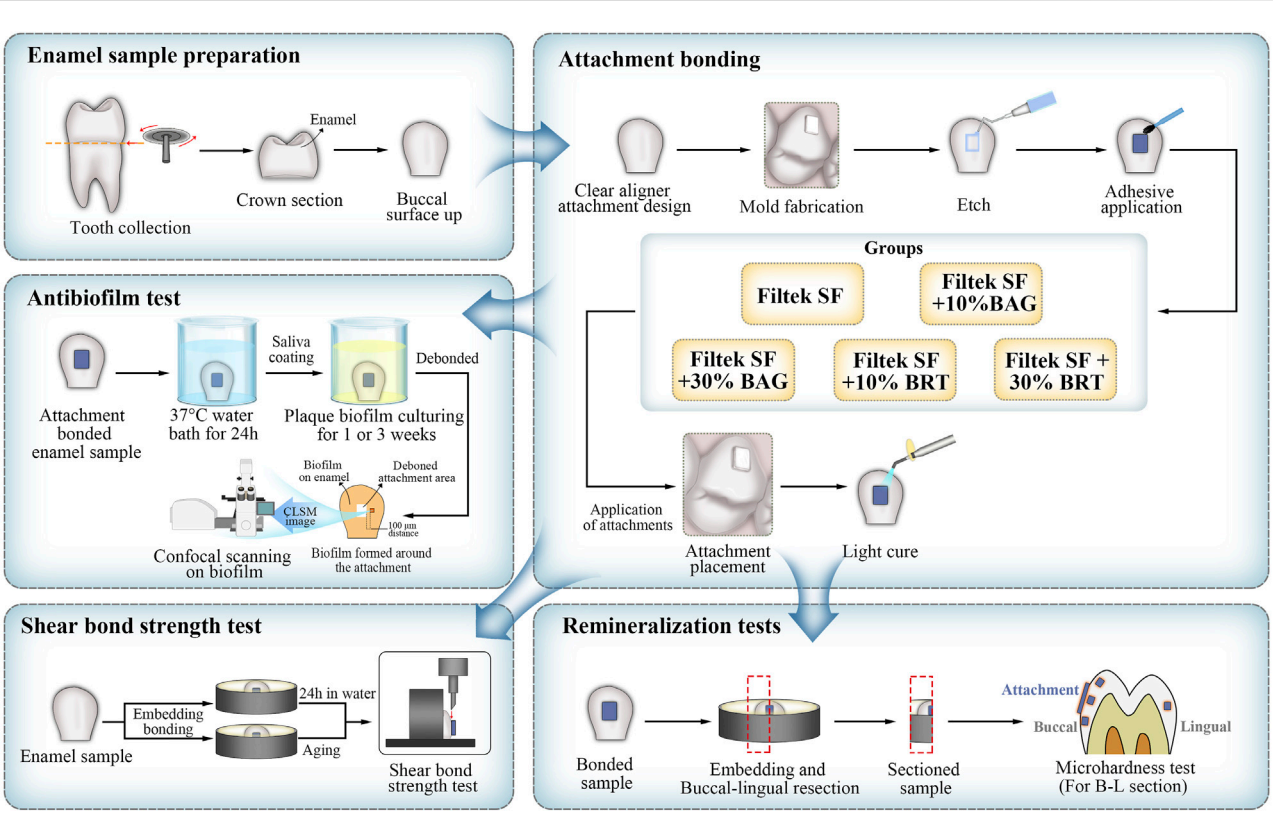

FIGURE 1
Schematic illustration of the experimental design in the present study.

TABLE 1 Composition of the bioceramic micro-fillers and their incorporated flowable composite attachments.

Materials	Manufacturer	Components
Bioactive glass 45S5 (BAG)	OSspray Ltd., London, United Kingdom	SiO_2, CaO, Na_2O, P_2O_5
Bredigite (BRT)	—	$(C_2H_5O)_4Si$, $Mg(NO_3)_2{\cdot}6H_2O$, $Ca(NO_3)_2{\cdot}4H_2O$
3M Filtek Supreme Flowable (Filtek SF)	3M ESPE, St Paul, MN, United States	BIS-GMA, TEGDMA, Si, Zr, YbF_3

BIS-GMA, Bisphenol A dimethacrylate; TEGDMA, triethyleneglycol dimethacrylate.

$Mg(NO_3)_2{\cdot}6H_2O$ and $Ca(NO_3)_2{\cdot}4H_2O$ (Sigma Aldrich, St Louis, MO, United States) (Wu and Chang, 2007).

Flowable composite attachments containing four different types of experimental bioceramic micro-filler were formulated freshly before the attachment bonding. The flowable composite attachment, 3M Filtek Supreme Flowable (Filtek SF), was manually blended with 10 wt% BAG, 30 wt% BAG, 10 wt% BRT and 30 wt% BRT powders respectively using a metallic spatula. This mixture was further homogenized in an amalgamator (Ivoclar Vivadent, Mississauga, ON, Canada) for 30 s. Subsequently, the mixture was dispensed into a resin dispenser and injected into the attachment molds.

2.3 Enamel-attachment bonding

The 60 teeth were randomly divided into 5 groups, each consisting of 12 teeth. The groups were defined as follows: 3M Filtek Supreme Flowable (Filtek SF) only (control group), Filtek SF + 10% BAG, Filtek SF + 30% BAG, Filtek SF + 10% BRT, and Filtek SF + 30% BRT.

The buccal enamel surface of each tooth was etched with 35% phosphoric acid (Pulpdent, Watertown, MA, United States) for 30 s, followed by a thorough 30-s water rinse and complete drying with oil-and-moisture-free air. A thin uniform layer of Assure universal bond (Reliance orthodontic products, Itasca, IL, United States) was applied to the etched surfaces and cured for 10 s. Subsequently, a silicone mold, as described in Section 2.1 was gently positioned on the center of the buccal enamel surface and pressed firmly into place. The various attachment materials, corresponding to the five groups, were dispensed into the rubber mold.

Excess adhesive around the attachment was meticulously removed using a cotton pellet, ensuring the integrity of the mold. The attachment underwent light-curing (LED-B, Woodpeck Inc., Guilin, China) for 30 s with the mold in place. Following mold

removal, an additional 20 s of light-curing was administered. All attachment-bonded samples were then immersed in deionized water at 37°C for 24 h before further utilization.

2.4 Biofilm model

Supragingival plaque samples were obtained from the first or second premolars of two adult volunteers: one non-clear aligner wearer (donor 1) and another wearing clear aligner for 3 months (donor 2). Collected plaques from both donors were separately mixed in brain–heart infusion broth (BHI) (Becton Dickinson, Sparks, MD) by pipetting. Bacterial suspensions from each donor were standardized to an optical density (OD) of 0.10 (150 μL at 405 nm) using a microplate reader (Model 3350; Bio-Rad Laboratories, Richmond, CA, United States).

In an effort to replicate clinical conditions, enamel samples with attached attachments were coated with saliva. The saliva was collected from each volunteer (at least 1.5 h after meal) in sterile 14-mL polypropylene tubes (Corning, NY, United States) and filtrated using sterilized 0.2 μm syringe filters. Each bonded enamel surface was coated with 500 μL infiltrated saliva for 4 h in a well of a sterile 24-well polystyrene cell culture plate (Corning, NY, United States) before initiating biofilm culturing.

Subsequently, the saliva-coated enamel samples were placed in the wells of a 24-well cell culture plate, each containing 1.8 mL of BHI. Each well was inoculated with 0.2 mL of dispersed plaque suspension from either donor 1 or donor 2. The samples were incubated in the BHI-plaque suspension in air at 37°C for 1 and 3 weeks. For each time point in each group and from each donor, three attachment-bonded samples were utilized. Fresh BHI broth was replaced weekly for the 3-week specimens.

2.5 Evaluation of the antibiofilm effect

The plaque biofilm on the enamel around attachments was subjected to bacterial viability staining and observed under a confocal laser scanning electron microscopy (CLSM). Attachment-bonded samples cultured with biofilm for 1 and 3 weeks were rinsed in 0.85% physiological saline for 1 min. Subsequently, the attachments on the enamel samples were meticulously removed using debonding pliers (HuFriedy Group, Chicago, IL, United States).

LIVE/DEAD BacLight Bacterial Viability kit L-7012 (Molecular Probes, Eugene, OR, United States), containing a two-component dye (SYTO 9 and propidium iodide in a 1: 1 mixture) in a solution, was used for staining the biofilm following the manufacturer's protocols. The excitation/emission maxima for these dyes were 480/500 nm for the SYTO 9 whole cell stain and 490/635 nm for the dead cell stain propidium iodide. A confocal laser scanning electron microscopy (FV10i-LIV, Olympus, Tokyo, Japan) was used to analyze the plaque biofilm fluorescence. Fluorescence from each stained cell was viewed using a CLSM at a 512 × 512 pixel scan area with a 10 × lens.

For each subgroup, five randomly selected biofilm areas at a distance of 100 μm away from the debonded attachment and biofilm interface were scanned by CLSM. The biofilms were scanned with a 1.5 μm step size from top to bottom, resulting in 15 scanned areas (n = 15) for each subgroup. The confocal images were analyzed and quantitated (live/dead ratios) using the Imaris 7.2 software (Bitplane Inc., St Paul, MN, United States). The total biovolume of the biofilm in the scanned area was calculated, and the volume ratio of red fluorescence to green and red fluorescence indicated the proportion of killed plaque bacteria.

The morphology of plaque biofilms cultivated around various attachments after a 3-week culturing period was investigated through scanning electron microscopy (SEM). An additional three samples from each group with plaque biofilm growth were prepared following the biofilm sample preparation procedure described above. The samples for SEM were prefixed with phosphate-buffered 2.5% glutaraldehyde for 10 min and then immersed in 2 mL 1% osmium tetroxide for 1 h. Subsequently, the specimens were dehydrated through a series of increasing ethanol concentrations (50%, 70%, 80%, and 100%). The dehydrated samples were dried by using a critical point drier (Samdri-795; Tousimis Research Corporation, Rockville, MD), sputter-coated with iridium (Leica EM MED020 Coating System, Tokyo, Japan), and examined by SEM (Helios Nanolab 650, FEI, Eindhoven, the Netherlands) at an accelerating voltage of 3 kV.

2.6 Remineralization test

An additional set of 30 enamel samples (6 for each attachment-bonded group) were prepared as outlined in Section 2.3 for microhardness evaluation.

Demineralization was conducted using 0.1 M lactic acid, with the pH adjusted to 4.0 (Zhang et al., 2018). Each attachment-bonded enamel sample was placed flat in a well of a 12-well plate (Corning, NY, United States) with the buccal surface in contact with the bottom of the well. The attachment bonded interface was fully immersed in 3 mL of lactic acid solution at 37°C for 28 days (Liu et al., 2018) and the lingual enamel surface was exposed. The demineralization solution was refreshed on a weekly basis.

Each attachment-bonded tooth was hemi-sectioned sagittally through the center of the attachment into mesial and distal halves (12 tooth-halves; n = 12) using a low-speed diamond saw (Isomet, Buehler, Lake Bluff, IL, United States) under water cooling. The sectioned specimens were embedded in self-curing epoxy-resin (Epo Thin 2, Buehler, Lake Bluff, IL, United States), leaving the sectioning side exposed. The resin-embedded specimens were wet polished using 600-grit, 1000-grit and 1200-grit silicon carbide grinding papers (CarbiMet; Buehler Ltd., Lake Bluff, IL, United States) under constant water irrigation. Final polishing was achieved with 1 μm diameter diamond cream and polishing-cloth disk (Buehler, Lake Bluff, IL, United States).

The Vickers microhardness of each specimen was measured using a microhardness tester (Micromet 3 microhardness tester; Buehler Ltd., United States) equipped with a Vickers diamond indenter at a load of 200 g and a dwell time of 15 s. The Vickers hardness (HV) was calculated using the formula: $HV = 1.8549 (F/d^2)$, where F is the load and d is the mean of the two diagonals produced by the indenter (Nekoofar et al., 2010).

Four indentations were made in each embedded tooth-half from four different locations. On the buccal surfaces, three indentations

were made under the attachment, at the coronal and cervical edges of the attachment, respectively. An additional indentation was made on the lingual enamel surface. All four indentations were made at 60 μm from the external enamel surface. In total, 12 indentations were made for each position per group (n = 12). The mean and standard deviation of microhardness values for each group were calculated.

2.7 Shear bond testing

Thirty enamel samples were prepared as described in Section 2.1 with six samples for each group. The shear bond test was performed according to a previously published protocol (Hong et al., 2022). Teeth samples were mounted in an acrylic mold (Ultradent Products, South Jordan, UT, United States) using self-curing resin (Epo Thin 2, Buehler, Lake Bluff, IL, United States), positioning the buccal surface for exposure. Specimens (height = 2.38 mm, diameter = 2.00 mm) of flowable composites from different groups were fabricated using a bonding clamp and bonding mold inserts (Ultradent Products, South Jordan, UT, United States). Enamel surfaces were etched and bonded with different flowable composites from the five groups using the same bonding protocol outlined in Section 2.3. Each group was equally divided into two subgroups. The first subgroup samples were immersed in deionized water for 24 h before shear bond testing. Samples from the second subgroup were aged in 0.1 M lactic acid (pH = 4) for 28 days before shear bond testing.

Individual specimens were secured using a metal base clamp (Ultradent Products, South Jordan, UT, United States). The buccal axis of the sample was oriented so that the labial surface was parallel to the applied force. A crosshead assembly chisel (Ultradent Products, South Jordan, UT, United States) attached to a universal Testing Machine (Instron, ElectroPuls E10000 Linear-Torsion, Shimadzu, Japan) was positioned over the upper part of the attachment and parallel to the bonded interface. An occlusogingival load was applied at a crosshead test speed of 0.5 mm/min until the attachment detached. The force required for debonding was recorded and expressed in megapascals (MPa). Shear bond strength (MPa) was calculated as the debonding force divided by the attachment surface area (mm^2).

Following detachment, each enamel surface was examined under a stereomicroscope (Nikon Eclipse Ci, Tokyo, Japan) to analyze the failure mode. The adhesive remnant index (ARI) was determined based on the presence of remaining adhesive on enamel, classified as follows: 0 = no adhesive remaining on enamel; 1 = less than half of the adhesive remaining on enamel; 2 = more than half of the adhesive remaining on enamel; 3 = all the adhesive remaining on enamel.

2.8 Statistical analysis

Statistical analyses were conducted using SPSS 29 software (SPSS, Chicago, IL, United States) for Windows. The mean values with standard deviation were used to present all data derived from confocal and microhardness tests, as well as shear bond strength assessments. The homogeneity of variance was evaluated using the Levene's test. Univariate analysis of variance (ANOVA) was applied, and *post hoc* multiple comparisons were conducted to isolate and compare the significant results at a 5% significance level. The differences in the ARI scores between groups were analyzed by the Kruskal–Wallis test and the Mann-Whitney test at a significance level of $p < 0.05$.

3 Results

3.1 Antibiofilm effect

No significant difference was found in the sensitivity of biofilms (both biovolume and percentage of killed biofilm bacteria) from the two donors for attachments containing different bioceramic micro-fillers ($p > 0.05$) (Figures 2C, D, G, H).

Significant reductions in 3-week-old biofilm biovolume were observed with the addition of 10% and 30% bioceramic micro-fillers in comparison to the Filtek SF control, particularly evident in 3-week-old biofilms (Figures 2B–D, F–H). Filtek SF + 30% BAG demonstrated up to 29.7% reduction in 3-week-old biofilm biovolume compared to Filtek SF controls (Figures 2C, G; Supplementary Datasheet S1). While 1-week-old biofilm groups with 10% BAG and 10% BRT exhibited similar biovolume to Filtek SF controls, the 30% micro-filler groups displayed increased resistance to biofilm growth (Figures 2C, G).

Attachments containing either BAG or BRT demonstrated statistically significant increase in biofilm bacteria killing compared to attachment with no fillers ($p < 0.05$) (Figures 2A, B, D–F, H). The proportion of killed biofilm bacterial cells was significantly correlated with the portion of bioceramic fillers in the flowable composite attachments. Attachments containing 30% bioceramic micro-fillers were superior to groups with 10% fillers in biofilm-killing efficacy for both donors ($p < 0.05$) (Figures 2D, H). The combination of Filtek SF and 30% BAG or 30% BRT killed 35%–37% of the 1-week-old plaque bacteria for both donors (Figures 2D, H; Supplementary Datasheet S1). The addition of 10% BAG or 10% BRT into Filtek SF resulted in 24%–26% biofilm killed (Figures 2D, H; Supplementary Datasheet S1). When 30% of bioceramic fillers were added, the rate of biofilm killing was lower in the 3-week-old plaque biofilm compared to the 1-week-old biofilm except for the 30% BRT group from donor 1 (Figures 2D, H). No statistically significant difference was detected between 1-week-old biofilm and 3-week-old biofilm in 10% bioceramic micro-fillers and no-filler control groups ($p > 0.05$) (Figures 2D, H).

The multispecies composition and distribution of the plaque biofilm after debonding was validated by SEM, showing cocci, rods and filaments within the biofilms forming mixed communities along the debonded interface (Figures 2I, K, M, O, Q, S). Control biofilms growing around non-filler-containing Filtek SF demonstrated well-organized network structures with smooth surfaces and no disrupted bacterial cells (Figures 2I–K, L). In contrast, cell lysis was evident in biofilms grown around attachments containing bioceramic micro-fillers (Figures 2N, P, R, T). The bacterial cell membranes of 1-week-old biofilms became wrinkled in the 30% BRT group (Figure 2R), and both the 30% BAG and BRT groups exhibited fine particles released within the biofilm structures (Figures 2N, P, R, T).

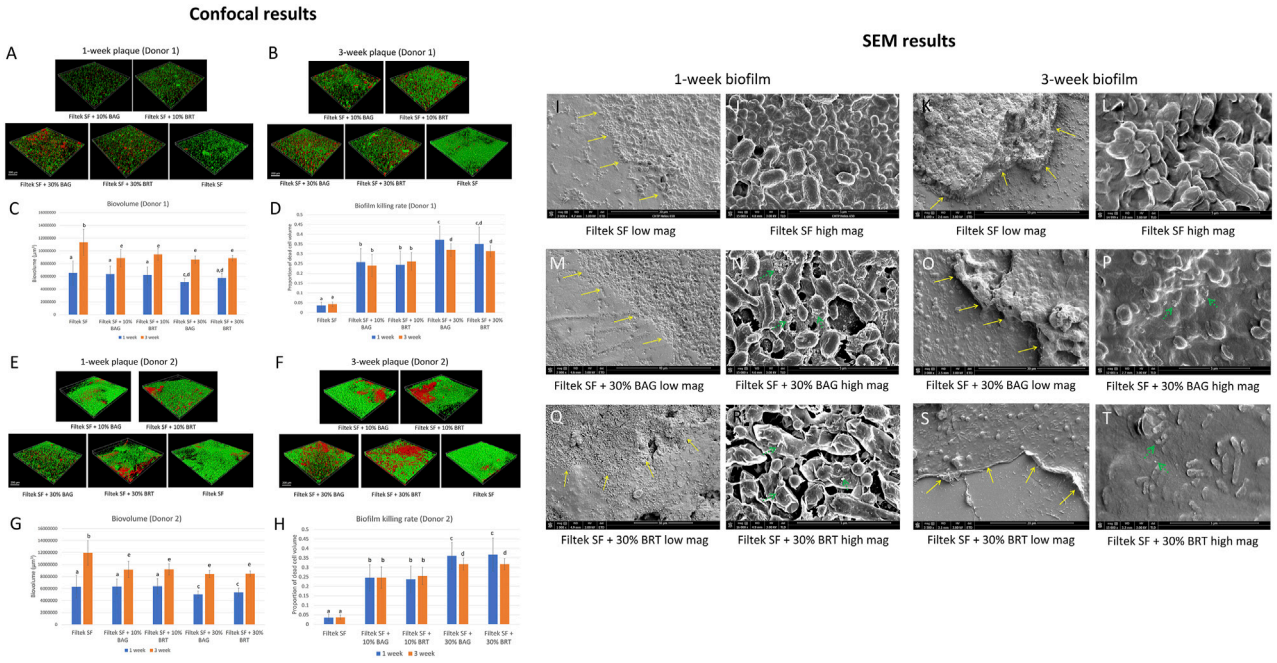

FIGURE 2
Bioceramic micro-filler containing clear aligner attachment impacts on oral plaque biofilm. **(A)** Three-dimensional constructions of CLSM scans of 1-week plaque biofilm (donor 1) formation around the attachments; **(B)** Three-dimensional constructions of CLSM scans of 3-week plaque biofilm (donor 1) formation around the attachments; **(C)** Total biovolume of plaque biofilm formed in 1 and 3 weeks from donor 1; **(D)** The proportion of the killed biofilm microbial cells of the entire plaque biofilm from donor 1. **(E)** Three-dimensional constructions of CLSM scans of 1-week plaque biofilm (donor 2) formation around the attachments; **(F)** Three-dimensional constructions of CLSM scans of 3-week plaque biofilm (donor 2) formation around the attachments; **(G)** Total biovolume of plaque biofilm formed in 1 and 3 weeks from donor 2; **(H)** The proportion of the killed biofilm microbial cells of the entire plaque biofilm from donor 2; SEM micrographs of 1-week-old biofilm exposure to Filtek SF under low **(I)** and high **(J)** magnifications. SEM micrographs of 3-week-old biofilm exposure to Filtek SF under low **(K)** and high **(L)** magnifications. SEM micrographs of 1-week-old biofilm exposure to Filtek SF + 30% BAG under low **(M)** and high **(N)** magnifications. SEM micrographs of 3-week-old biofilm exposure to Filtek SF + 30% BAG under low **(O)** and high **(P)** magnifications. SEM micrographs of 1-week-old biofilm exposure to Filtek SF + 30% BRT under low **(Q)** and high **(R)** magnifications. SEM micrographs of 3-week-old biofilm exposure to Filtek SF + 30% BRT under low **(S)** and high **(T)** magnifications. The yellow arrow shows interface of attachment and biofilm. The green arrow shows the cell lysis effect. Different letters in C, D, G and H indicate statistical differences ($p < 0.05$).

3.2 Microhardness test

Significant differences in microhardness values were found depending on the concentration of bioceramic micro-fillers in the attachments. Vickers hardness values (VHN) derived from microhardness testing were illustrated in Figure 3; Supplementary Datasheet S1. Lingual enamel surfaces that were not exposed to the demineralization solution displayed the highest microhardness values ranging between 299 and 306 (Figure 3; Supplementary Datasheet S1). In contrast, the enamel hardness on the buccal surface was significantly reduced in the Filtek SF group without the addition of bioceramic micro-fillers. No statistically significant difference in microhardness was detected among the positions of the indentation on the buccal enamel (coronal, under attachment, and cervical) for all groups ($p > 0.05$) (Figure 3).

With the inclusion of 10% bioceramic micro-fillers, the Filtek SF + 10% BAG group exhibited significantly higher microhardness values than the Filtek SF control ($p < 0.05$). The Filtek SF + 10% BRT group showed no significant difference compared to the Filtek SF + 10% BAG group ($p > 0.05$). However, groups with 10% micro-fillers still demonstrated significantly lower microhardness than the lingual control ($p < 0.05$). As the percentage of BAG and BRT reached 30% in weight, microhardness values from coronal, under attachment, and cervical enamel surfaces showed no statistically significant difference from the lingual controls ($p > 0.05$) (Figure 3).

3.3 Shear bond strength

The incorporation of BAG and BRT into Filtek SF did not compromise the bond strength of the Flitek flowable composite. The highest bond strength was 10.8 MPa from the Filtek SF group after 24 h of storage in water (Figure 4A; Supplementary Datasheet S1). No statistically significant difference was observed between all four experimental groups and the Filtek SF group ($p > 0.05$). However, the bond strength was significantly reduced after 28 days of aging in the pH 4 demineralization solution for the Filtek SF and Filtek SF + 10% BRT groups (Figure 4A). No statistically significant difference in bond strength was detected between the 24 h in water and 28 days in acid storage conditions in the BAG and 30% BRT groups ($p > 0.05$). The 30% BAG and 30% BRT groups exhibited significantly higher shear bond strength than the Filtek SF control ($p < 0.05$).

The ARI scores are depicted in Figure 4B. After the acid challenge, there were more score “0” samples in the aging in demineralization solution groups than the 24 h in water groups. However, no significant difference in debonding patterns was

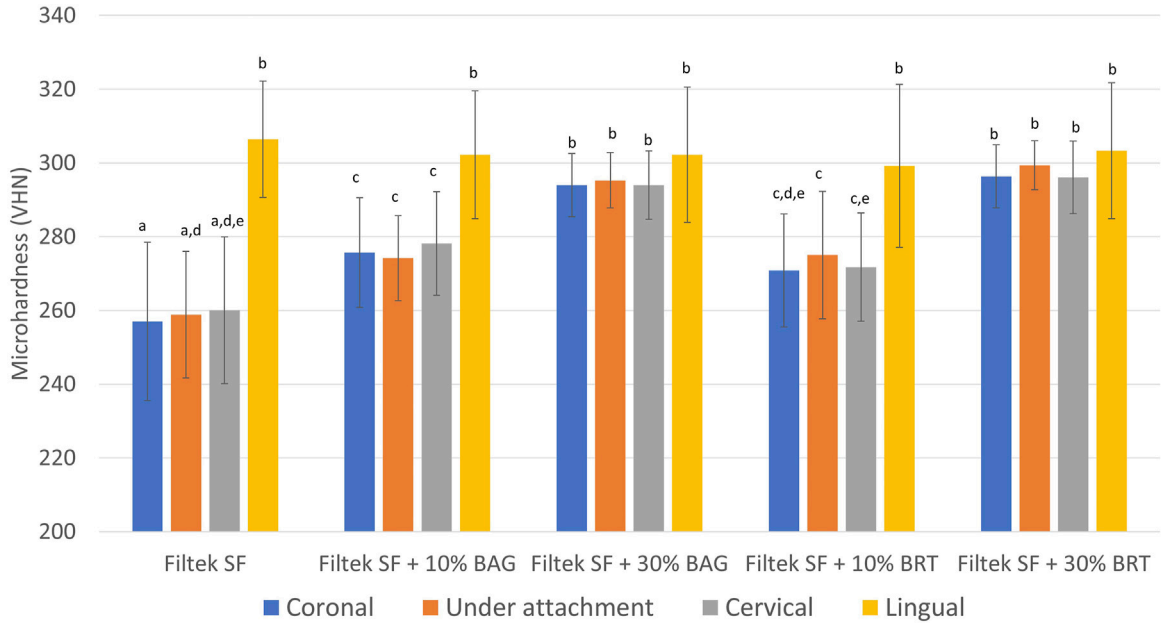

FIGURE 3
Mean surface Vickers microhardness (VHN) obtained from different locations in enamel samples bonded with Filtek SF, Filtek SF + 10% BAG, Filtek SF + 30% BAG, Filtek SF + 10% BRT, Filtek SF + 30% BRT. Columns labeled with different letters are statistically significantly different ($p < 0.05$).

observed between groups. Furthermore, no statistically significant difference was detected among all the groups regardless of the storage types ($p > 0.05$).

4 Discussion

The current study enabled us to investigate, for the first time, the antibiofilm and remineralization effects of bioceramic micro-fillers containing clear aligner attachments on human enamels, which brought us one step closer to establishing *in vitro* models representing clinical clear aligner therapy. The observed outcomes highlight the potential fortification achievable through the integration of bioceramic micro-fillers in clear aligner applications. While previous studies have explored the antibiofilm effects of various orthodontic cements, one major limitation was the predominant use of *S. mutans* in assessing the antimicrobial effects of orthodontic adhesives (Altmann et al., 2015; Kim et al., 2018; Liu et al., 2018). Often only a single strain (e.g., *Streptococcus Sobrinus* and *Lactobacillus casei*) was used (Imazato et al., 2003; Salehi et al., 2015). It is crucial to note that bacteria in white spot lesions and dental caries all originate from tooth surface plaque (Jakubovics and Kolenbrander, 2010). Unlike previous studies using resin disks for antibiofilm tests, our approach involved a plaque microcosm biofilm to assess the antibiofilm effects of restorative dental adhesives (Zhang et al., 2015a; Zhang et al., 2015b). Moreover, the lack of available data on the anti-plaque effectiveness of bioceramic micro-fillers containing clear aligner attachment on enamel surfaces underscores the novelty of our findings. Importantly, our minimally invasive approach preserves the biofilm around the clear aligner attachments, providing a more realistic representation of the clinical scenario.

Clinical studies have highlighted the challenge of biofilm accumulation with orthodontic appliances and emphasized the importance of managing plaque to prevent adverse effects on oral health. The present study addressed this challenge by demonstrating reduction in biofilm growth and bactericidal effects of attachments with bioceramic micro-fillers on human enamels. The value of clear aligner attachments with inherent antibiofilm properties lies in the sustained protection against plaque biofilm growth. Unlike intermittent mechanical cleaning, an attachment with intrinsic antibiofilm effects serves as a continuous source of protection. In the present study, the incorporation of bioceramic micro-fillers at a rate of 30% resulted in over 35% killing of 1-week-old plaque (Figure 2). Even at the lower incorporation percentage of 10%, there was a notable 25% reduction in 1-week-old biofilm. This aligns with a previous study showing that BRT successfully inhibited plaque biofilm formation, suppressing over 40% of biovolume in 2 weeks (Shen et al., 2016). Our findings indicated that older plaque biofilm exhibited increased resistance to antibiofilm effects compared to younger biofilm. Three-week-old plaque displayed amore mature structural development of the biofilm compared to the 1-week-old plaque. The physical barrier provided by the extracellular polymeric matrix and the presence of more persister cells both contributed to the higher resistance of mature biofilm (Xiao et al., 2012).

While both BAG and BRT groups showed comparable antibiofilm efficacy, their mechanism may differ slightly. Our study chose the well-studied bioactive glass 45S5 due to its widespread recognition as the most utilized bioactive glass with established antibacterial and remineralization potentials (Waltimo et al., 2007). The antibiofilm effect of BAG-containing attachments appears to be associated with the high surface area of BAG micro-fillers and the release of ionic components (e.g., K^+, Na^+, and Ca^{2+})

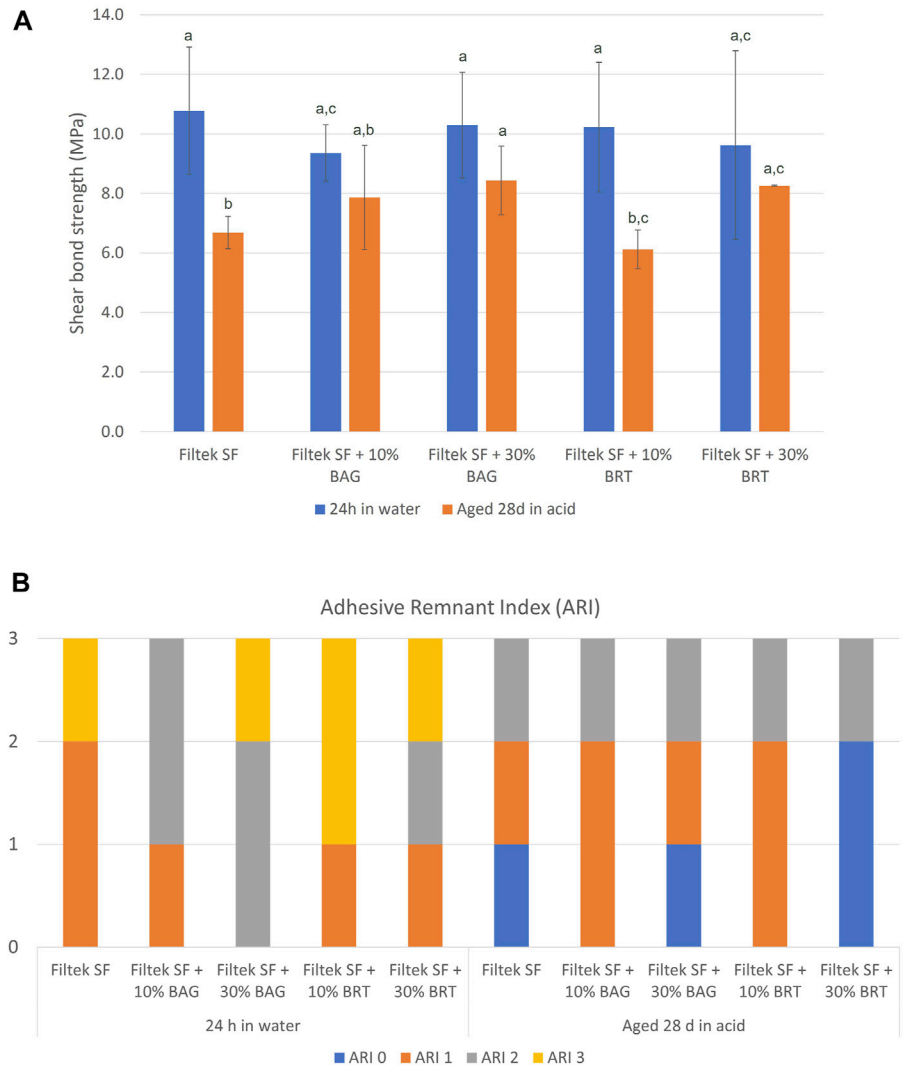

FIGURE 4
Shear testing of bioceramic micro-filler containing clear aligner attachments bonded to enamel using. **(A)** Shear bond strength. Columns labeled with different letters are statistically significantly different ($p < 0.05$). **(B)** Adhesive remnant index in different subgroups.

(Waltimo et al., 2007). The exchange of network-modifier ions with H^+ and H_3O^+ ions from surrounding gingival fluids results in an alkaline microenvironment with high local pH (Drago et al., 2015). Additionally, the release of PO_4^{3-}, Si^{4+}, and Ca^{2+} from the BAG enhances perturbations of the membrane potential of bacteria, leading to increased osmotic pressure (Begum et al., 2016). The sudden rise in the external solutes concentration induces rapid water efflux and a pressure drop across the bacterial cell membrane, resulting in altered cell size and cell lysis as shown in the SEM (Figure 3). On the other hand, the antibiofilm effects of BRT-containing attachments may be more related to the Mg^{2+} ions (Robinson et al., 2010). Upon interaction with surrounding body fluid, $Mg(OH)_2$ can formed with a pH above 11 (Shen et al., 2016). The released Si at a high pH environment may synergistically inhibit bacterial viability by acting as a surfactant to modify the cellular integrity of bacteria (Shen et al., 2016). A recent study has highlighted BRT's ability to reinforce biological properties of a Mg–Zn bio-composite (Zhang et al., 2023). The addition of BRT to the bio-composite effectively prevented the growth and invasion of *Escherichia coli* and *Staphylococcus aureus*. This evidence supported the positive impact of BRT on flowable composite in the present study. Interestingly, there was no significant difference in the antibiofilm effects of different attachments against plaque from the two donors ($p > 0.05$). This result suggests that the source and possible differences in the species composition of biofilms from patient wearing clear aligners had no substantial impact on their susceptibility to the bioceramic micro-fillers.

Enamel demineralization is a common clinical issue during orthodontic treatment. Preserving enamel health is a priority in clinical orthodontic practice, and the innovative attachments may contribute to minimizing the risk of white spot lesions and caries (Azeem and Hamid, 2017). The present study used cross-sectional microhardness to evaluate the remineralization effects of the clear aligner attachments. The microhardness values of the lingual enamel surfaces were the highest, consistent with previously published human enamel hardness values (Galo et al., 2015). Lactic acid

was used as the demineralization solution. This mimicked the biofilm acids that the orthodontic adhesive-enamel bonded areas would encounter *in vivo*, potentially affecting the resin-enamel bond strength (Langhorst et al., 2009). With the addition of bioceramic microfillers, the microhardness values significantly increased on the attachment side. When the proportion of bioceramic microfillers reached 30%, no statistically significant difference was detected between the buccal side with attachments and lingual enamel with no demineralization ($p > 0.05$). This result revealed a significant remineralization potential of BAG and BRT. Bioactive glass degrades and releases calcium and phosphate ions, acting as an external mineral ion source that accelerates remineralization (Wang et al., 2011). Apatite growth on the demineralized surfaces filled the gaps, leading to a relatively intact subsurface. Subsequent precipitation of a polycondensated silica-rich layer (Si-gel) served as a template for the formation of a calcium phosphate (Ca/P), which then crystallized into hydroxycarbonate apatite (Chen et al., 2008). The intact subsurface might be the primary reason for the higher subsurface hardness found in the experimental groups containing BAG.

A prior study demonstrated that BRT could activate the Wnt/β-catenin signalling pathway in periodontal ligament cells, promoting cementogenic/osteogenic differentiation (Zhou et al., 2013). The observed increase in microhardness may be attributed to its potential to stimulate periodontal bone formation (Shen et al., 2016), which is beneficial for restoring dental hard tissues. However, when only 10% BRT was added to the flowable composite, the microhardness in the cervical area showed no statistically significant difference with the control group (Figure 3). The lack of significance could be attributed to the crystallization of BRT in the presence of Mg^{2+}, which differs from the BAG remineralization process where hydroxycarbonate apatite dominates the precipitation in the demineralized lesions.

The ability to maintain robust shear bond strength is aligned with the contemporary emphasis on attachment resilience over the course of orthodontic treatment (Weir, 2017). The shear bond strength results provided valuable insights into the performance of the developed bioceramic filler-containing clear aligner attachment. Importantly, no statistically significant difference in shear bond strength was found between the experimental groups and the control group. This suggested that the incorporation of bioceramic micro-fillers did not adversely affect the bonding efficacy (Figure 4). This finding is consistent with previous research indicating that the addition of micro-fillers can maintain bond strength without compromising shear bond properties (Guan et al., 2001; Yang et al., 2022).

The significant reduction in bond strength observed after 28 days of storage in a pH 4 demineralization solution for the Filtek SF and Filtek SF + 10% BRT groups aligns with findings from studies that highlight the susceptibility of certain adhesive systems to acidic challenges (Fan et al., 2022; Garma and Ibrahim, 2022). In contrast, the 30% BAG and 30% BRT groups exhibited significantly higher shear bond strength than the Filtek SF control under the same acidic conditions, suggesting a potential protective effect conferred by the higher concentration of bioceramic micro-fillers to enhance bond durability in acidic environments. This corresponds with previous work emphasizing the acid-resistant properties of bioactive glass in dental applications (Wang et al., 2011).

The specific reasons for the reduction in bond strength in the 10% BRT group, while not observed in the 30% BRT and BAG groups, could be influenced by various factors including the particle distribution and interaction with matrix material (Nabiyev et al., 2021). It's possible that the particle distribution in the 10% BRT group was not ideal for promoting strong adhesion, whereas the 30% BRT and BAG groups had a more favorable particle arrangement. In addition, the 10% BRT group may have exhibited less favorable chemical interactions with the resin matrix, resulting in a weaker bond compared to the 30% BRT and BAG groups.

The ARI scores provided additional insights, revealing consistent debonding patterns across all groups. While the present study did not identify significant differences in debonding patterns between groups, there were more score "0" samples in the aging in demineralization solution groups than the 24 h in water groups. This result shows that the acid environment could have affected the enamel bonding interface (Liu et al., 2018).

Within the limitation of this study, our primary focus was on establishing the short-term efficacy of the new attachments. It is indeed crucial to investigate the attachment performance over prolonged durations, ultimately contributing to improved patient outcomes. Subsequent studies may also explore other bioceramic variants including other types of BAG, building upon the results gained from this foundational investigation. Future investigations could also expand the scope by examining more types of clear aligner attachments, contributing to the continuous advancement of attachment technologies in orthodontic practice.

5 Conclusion

The bioceramic micro-fillers modified clear aligner attachment materials revealed significant advancements in antibiofilm and remineralization properties. The attachments demonstrated bactericidal and biofilm inhibition effects proportional to the micro-filler concentration. Moreover, the innovative materials exhibited an enhanced potential for enamel remineralization, as indicated by increased microhardness compared to control groups. Importantly, the shear bond strength remained uncompromised with the addition of micro-fillers. Overall, the incorporation of bioceramic micro-fillers represents a promising approach for enhancing oral health outcomes during clear aligner therapy.

Data availability statement

The original contributions presented in the study are included in the article/Supplementary Material, further inquiries can be directed to the corresponding author.

Ethics statement

The studies involving humans were approved by the Clinical Research Ethics Committee of the University of British Columbia. The studies were conducted in accordance with the local legislation and institutional requirements. The human samples used in this study were acquired from primarily isolated as part of your previous study for which ethical approval was obtained. Written informed consent for participation was not required from the participants or

the participants' legal guardians/next of kin in accordance with the national legislation and institutional requirements.

Author contributions

WJ: Conceptualization, Formal Analysis, Investigation, Writing–original draft. ZW: Conceptualization, Formal Analysis, Investigation, Writing–original draft. YZ: Investigation, Validation, Writing–review and editing. YS: Conceptualization, Supervision, Writing–review and editing. EY: Conceptualization, Supervision, Writing–review and editing. BZ: Conceptualization, Supervision, Writing–review and editing.

Funding

The author(s) declare financial support was received for the research, authorship, and/or publication of this article. This work was financially supported by 2023 American Association of Orthodontists Foundation Biomedical Research Award.

Acknowledgments

We thank Dr. Rizhi Wang (Department of Materials Engineering, University of British Columbia) for supporting us to perform microhardness and shear bond tests. We also thank Dr. Qiong Wang (Department of Materials Engineering, University of British Columbia) for his assistance in preparing samples for microhardness and shear bond tests.

Conflict of interest

The authors declare that the research was conducted in the absence of any commercial or financial relationships that could be construed as a potential conflict of interest.

Publisher's note

All claims expressed in this article are solely those of the authors and do not necessarily represent those of their affiliated organizations, or those of the publisher, the editors and the reviewers. Any product that may be evaluated in this article, or claim that may be made by its manufacturer, is not guaranteed or endorsed by the publisher.

Supplementary material

The Supplementary Material for this article can be found online at: https://www.frontiersin.org/articles/10.3389/fbioe.2023.1346959/full#supplementary-material

References

Albhaisi, Z., Al-Khateeb, S. N., and Alhaija, E. S. A. (2020). Enamel demineralization during clear aligner orthodontic treatment compared with fixed appliance therapy, evaluated with quantitative light-induced fluorescence: a randomized clinical trial. *Am. J. Orthod. Dentofac. Orthop.* 157, 594–601. doi:10.1016/j.ajodo.2020.01.004

Altmann, A. S., Collares, F. M., Ogliari, F. A., and Samuel, S. M. (2015). Effect of methacrylated-based antibacterial monomer on orthodontic adhesive system properties. *Am. J. Orthod. Dentofac. Orthop.* 147, S82–S87. doi:10.1016/j.ajodo.2015.01.015

Altmann, A. S. P., Collares, F. M., Leitune, V. C. B., Arthur, R. A., Takimi, A. S., and Samuel, S. M. W. (2017). *In vitro* antibacterial and remineralizing effect of adhesive containing triazine and niobium pentoxide phosphate inverted glass. *Clin. Oral. Investig.* 21, 93–103. doi:10.1007/s00784-016-1754-y

Azeem, M., and Hamid, W. U. (2017). Incidence of white spot lesions during orthodontic clear aligner therapy. *J. World Fed. Orthod.* 6, 127–130. doi:10.1016/j.ejwf.2017.07.001

Badawi, H., Evans, R. D., Wilson, M., Ready, D., Noar, J. H., and Pratten, J. (2003). The effect of orthodontic bonding materials on dental plaque accumulation and composition *in vitro*. *Biomaterials* 24, 3345–3350. doi:10.1016/s0142-9612(03)00166-2

Beerens, M. W., Jacob, M., and van der Veen, M. H. (2017). Microbial profile of dental plaque associated to white spot lesions in orthodontic patients immediately after the bracket removal. *Arch. Oral. Biol.* 78, 88–93. doi:10.1016/j.archoralbio.2017.02.011

Begum, S., Johnson, W. E., Worthington, T., and Martin, R. A. (2016). The influence of pH and fluid dynamics on the antibacterial efficacy of 45S5 Bioglass. *Biomed. Mater* 11, 015006. doi:10.1088/1748-6041/11/1/015006

Beyth, N., Bahir, R., Matalon, S., Domb, A. J., and Weiss, E. I. (2008). *Streptococcus mutans* biofilm changes surface-topography of resin composites. *Dent. Mater.* 24, 732–736. doi:10.1016/j.dental.2007.08.003

Beyth, N., Domb, A. J., and Weiss, E. I. (2007). An *in vitro* quantitative antibacterial analysis of amalgam and composite resins. *J. Dent.* 35, 201–206. doi:10.1016/j.jdent.2006.07.009

Bichu, Y., Alwafi, A., Liu, X., Andrews, J., Ludwig, B., Bichu, A., et al. (2023). Advances in orthodontic clear aligner materials. *Bioact. Mater.* 22, 384–403. doi:10.1016/j.bioactmat.2022.10.006

Bourbia, M., Ma, D., Cvitkovitch, D., Santerre, J., and Finer, Y. (2013). Cariogenic bacteria degrade dental resin composites and adhesives. *J. Dent. Res.* 92, 989–994. doi:10.1177/0022034513504436

Buschang, P. H., Chastain, D., Keylor, C. L., Crosby, D., and Julien, K. C. (2019). Incidence of white spot lesions among patients treated with clear aligners and traditional braces. *Angle. Orthod.* 89, 359–364. doi:10.2319/073118-553.1

Chen, X., Wu, T., Wang, Q., and Shen, J. W. (2008). Shield effect of silicate on adsorption of proteins onto silicon-doped hydroxyapatite (100) surface. *Biomaterials* 29, 2423–2432. doi:10.1016/j.biomaterials.2008.02.002

Cheng, L., Weir, M. D., Xu, H. H., Antonucci, J. M., Kraigsley, A. M., Lin, N. J., et al. (2012). Antibacterial amorphous calcium phosphate nanocomposites with a quaternary ammonium dimethacrylate and silver nanoparticles. *Dent. Mater.* 28, 561–572. doi:10.1016/j.dental.2012.01.005

Chin, M. Y., Busscher, H. J., Evans, R., Noar, J., and Pratten, J. (2006). Early biofilm formation and the effects of antimicrobial agents on orthodontic bonding materials in a parallel plate flow chamber. *Eur. J. Orthod.* 28, 1–7. doi:10.1093/ejo/cji094

Coraça-Huber, D. C., Fille, M., Hausdorfer, J., Putzer, D., and Nogler, M. (2014). Efficacy of antibacterial bioactive glass S53P4 against *S. aureus* biofilms grown on titanium discs *in vitro*. *J. Orthop. Res.* 32, 175–177. doi:10.1002/jor.22463

Drago, L., De Vecchi, E., Bortolin, M., Toscano, M., Mattina, R., and Romano, C. L. (2015). Antimicrobial activity and resistance selection of different bioglass S53P4 formulations against multidrug resistant strains. *Future. Microbiol.* 10, 1293–1299. doi:10.2217/FMB.15.57

Drago, L., Vassena, C., Fenu, S., Vecchi, E. D., Signori, V., Francesco, R. D., et al. (2014). *In vitro* antibiofilm activity of bioactive glass S53P4. *Future. Microbiol.* 9, 593–601. doi:10.2217/fmb.14.20

Fan, M., Li, M., Yang, Y., Weir, M. D., Liu, Y., Zhou, X., et al. (2022). Dual-functional adhesive containing amorphous calcium phosphate nanoparticles and dimethylaminohexadecyl methacrylate promoted enamel remineralization in a biofilm-challenged environment. *Dent. Mater.* 38, 1518–1531. doi:10.1016/j.dental.2022.07.003

Ferreira, C. J., Leitune, V. C. B., Balbinot, G. S., Degrazia, F. W., Arakelyan, M., Sauro, S., et al. (2019). Antibacterial and remineralizing fillers in experimental orthodontic adhesives. *Mater. (Basel)* 12, 652. doi:10.3390/ma12040652

Galo, R., Contente, M., Galafassi, D., and Borsatto, M. C. (2015). Hardness and modulus of elasticity of primary and permanent teeth after wear against different dental materials. *Eur. J. Dent.* 9, 587–593. doi:10.4103/1305-7456.172635

Garma, N. M. H., and Ibrahim, A. I. (2022). Bond strength survival of a novel calcium phosphate-enriched orthodontic self-etching system after various ageing protocols: an *in vitro* study. *Int. J. Dent.* 2022, 1–9. doi:10.1155/2022/3960362

Guan, G., Takano-Yamamoto, T., Miyamoto, M., Yamashiro, T., Noguchi, H., Ishikawa, K., et al. (2001). An approach to enhance the interface adhesion between an orthodontic plastic bracket and adhesive. *Eur. J. Orthod.* 23, 425–432. doi:10.1093/ejo/23.4.425

Hong, Q., Pierre-Bez, A. C., Kury, M., Curtis, M. E., Hiers, R. D., Esteban Florez, F. L., et al. (2022). Shear bond strength and color stability of novel antibacterial nanofilled dental adhesive resins. *Nanomater. (Basel)* 13, 1. doi:10.3390/nano13010001

Imazato, S., Kinomoto, Y., Tarumi, H., Ebisu, S., and Tay, F. R. (2003). Antibacterial activity and bonding characteristics of an adhesive resin containing antibacterial monomer MDPB. *Dent. Mater.* 19, 313–319. doi:10.1016/s0109-5641(02)00060-x

Jakubovics, N. S., and Kolenbrander, P. E. (2010). The road to ruin: the formation of disease-associated oral biofilms. *Oral. Dis.* 16, 729–739. doi:10.1111/j.1601-0825.2010.01701.x

Khalichi, P., Singh, J., Cvitkovitch, D. G., and Santerre, J. P. (2009). The influence of triethylene glycol derived from dental composite resins on the regulation of *Streptococcus mutans* gene expression. *Biomaterials* 30, 452–459. doi:10.1016/j.biomaterials.2008.09.053

Khosravi, R., Cohanim, B., Hujoel, P., Daher, S., Neal, M., Liu, W., et al. (2017). Management of overbite with the Invisalign appliance. *Am. J. Orthod. Dentofac. Orthop.* 151, 691–699.e2. doi:10.1016/j.ajodo.2016.09.022

Kim, Y. M., Kim, D. H., Song, C. W., Yoon, S. Y., Kim, S. Y., Na, H. S., et al. (2018). Antibacterial and remineralization effects of orthodontic bonding agents containing bioactive glass. *Korean. J. Orthod.* 48, 163–171. doi:10.4041/kjod.2018.48.3.163

Langhorst, S., O'donnell, J., and Skrtic, D. (2009). *In vitro* remineralization of enamel by polymeric amorphous calcium phosphate composite: quantitative microradiographic study. *Dent. Mater.* 25, 884–891. doi:10.1016/j.dental.2009.01.094

Lee, S. M., Yoo, K. H., Yoon, S. Y., Kim, I. R., Park, B. S., Son, W. S., et al. (2018). Enamel anti-demineralization effect of orthodontic adhesive containing bioactive glass and graphene oxide: an *in-vitro* study. *Materials* 11, 1728. doi:10.3390/ma11091728

Liu, Y., Zhang, L., Niu, L. N., Yu, T., Xu, H. H. K., Weir, M. D., et al. (2018). Antibacterial and remineralizing orthodontic adhesive containing quaternary ammonium resin monomer and amorphous calcium phosphate nanoparticles. *J. Dent.* 72, 53–63. doi:10.1016/j.jdent.2018.03.004

Makvandi, P., Gu, J. T., Zare, E. N., Ashtari, B., Moeini, A., Tay, F. R., et al. (2020). Polymeric and inorganic nanoscopical antimicrobial fillers in dentistry. *Acta. Biomater.* 101, 69–101. doi:10.1016/j.actbio.2019.09.025

Montoya, C., Jain, A., Londono, J. J., Correa, S., Lelkes, P. I., Melo, M. A., et al. (2021). Multifunctional dental composite with piezoelectric nanofillers for combined antibacterial and mineralization effects. *Acs. Appl. Mater. Interfaces.* 13, 43868–43879. doi:10.1021/acsami.1c06331

Mummolo, S., Nota, A., Albani, F., Marchetti, E., Gatto, R., Marzo, G., et al. (2020). Salivary levels of *Streptococcus mutans* and Lactobacilli and other salivary indices in patients wearing clear aligners versus fixed orthodontic appliances: an observational study. *PLoS One* 15, e0228798. doi:10.1371/journal.pone.0228798

Nabiyev, A. A., Olejniczak, A., Islamov, A. K., Pawlukojc, A., Ivankov, O. I., Balasoiu, M., et al. (2021). Composite films of HDPE with SiO(2) and ZrO(2) nanoparticles: the structure and interfacial effects. *Nanomater. (Basel)* 11, 2673. doi:10.3390/nano11102673

Nekoofar, M. H., Oloomi, K., Sheykhrezae, M. S., Tabor, R., Stone, D. F., and Dummer, P. M. (2010). An evaluation of the effect of blood and human serum on the surface microhardness and surface microstructure of mineral trioxide aggregate. *Int. Endod. J.* 43, 849–858. doi:10.1111/j.1365-2591.2010.01750.x

Robinson, D. A., Griffith, R. W., Shechtman, D., Evans, R. B., and Conzemius, M. G. (2010). *In vitro* antibacterial properties of magnesium metal against *Escherichia coli, Pseudomonas aeruginosa* and *Staphylococcus aureus*. *Acta. Biomater.* 6, 1869–1877. doi:10.1016/j.actbio.2009.10.007

Salehi, S., Davis, H. B., Ferracane, J. L., and Mitchell, J. C. (2015). Sol-gel-derived bioactive glasses demonstrate antimicrobial effects on common oral bacteria. *Am. J. Dent.* 28, 111–115.

Santonocito, S., and Polizzi, A. (2022). Oral microbiota changes during orthodontic treatment. *Front. Biosci. (Elite Ed.* 14, 19. doi:10.31083/j.fbe1403019

Shen, Y., Wang, Z., Wang, J., Zhou, Y., Chen, H., Wu, C., et al. (2016). Bifunctional bioceramics stimulating osteogenic differentiation of a gingival fibroblast and inhibiting plaque biofilm formation. *Biomater. Sci.* 4, 639–651. doi:10.1039/c5bm00534e

Stewart, C. A., and Finer, Y. (2019). Biostable, antidegradative and antimicrobial restorative systems based on host-biomaterials and microbial interactions. *Dent. Mater.* 35, 36–52. doi:10.1016/j.dental.2018.09.013

Waltimo, T., Brunner, T. J., Vollenweider, M., Stark, W. J., and Zehnder, M. (2007). Antimicrobial effect of nanometric bioactive glass 45S5. *J. Dent. Res.* 86, 754–757. doi:10.1177/154405910708600813

Wang, Z., Jiang, T., Sauro, S., Wang, Y., Thompson, I., Watson, T. F., et al. (2011). Dentine remineralization induced by two bioactive glasses developed for air abrasion purposes. *J. Dent.* 39, 746–756. doi:10.1016/j.jdent.2011.08.006

Weir, T. (2017). Clear aligners in orthodontic treatment. *Aust. Dent. J.* 62, 58–62. doi:10.1111/adj.12480

Wu, C., and Chang, J. (2007). Synthesis and *in vitro* bioactivity of bredigite powders. *J. Biomater. Appl.* 21, 251–263. doi:10.1177/0885328206062360

Xiao, J., Klein, M. I., Falsetta, M. L., Lu, B., Delahunty, C. M., Yates, J. R., 3rd, et al. (2012). The exopolysaccharide matrix modulates the interaction between 3D architecture and virulence of a mixed-species oral biofilm. *PLoS. Pathog.* 8, e1002623. doi:10.1371/journal.ppat.1002623

Yang, S. Y., Han, A. R., Kim, K. M., and Kwon, J. S. (2022). Acid neutralizing and remineralizing orthodontic adhesive containing hydrated calcium silicate. *J. Dent.* 123, 104204. doi:10.1016/j.jdent.2022.104204

Zhang, H., Saberi, A., Heydari, Z., and Baltatu, M. S. (2023). Bredigite-CNTs reinforced Mg-Zn Bio-Composites to enhance the mechanical and biological properties for biomedical applications. *Materials* 16, 1681. doi:10.3390/ma16041681

Zhang, J., Lynch, R. J. M., Watson, T. F., and Banerjee, A. (2018). Remineralisation of enamel white spot lesions pre-treated with chitosan in the presence of salivary pellicle. *J. Dent.* 72, 21–28. doi:10.1016/j.jdent.2018.02.004

Zhang, K., Zhang, N., Weir, M. D., Reynolds, M. A., Bai, Y., and Xu, H. H. (2017). Bioactive dental composites and bonding agents having remineralizing and antibacterial characteristics. *Dent. Clin. North. Am.* 61, 669–687. doi:10.1016/j.cden.2017.05.002

Zhang, N., Chen, C., Weir, M. D., Bai, Y., and Xu, H. H. (2015a). Antibacterial and protein-repellent orthodontic cement to combat biofilms and white spot lesions. *J. Dent.* 43, 1529–1538. doi:10.1016/j.jdent.2015.09.006

Zhang, N., Weir, M. D., Romberg, E., Bai, Y., and Xu, H. H. (2015b). Development of novel dental adhesive with double benefits of protein-repellent and antibacterial capabilities. *Dent. Mater.* 31, 845–854. doi:10.1016/j.dental.2015.04.013

Zhou, Y., Wu, C., Zhang, X., Han, P., and Xiao, Y. (2013). The ionic products from bredigite bioceramics induced cementogenic differentiation of periodontal ligament cells via activation of the Wnt/β-catenin signalling pathway. *J. Mater. Chem. B* 1, 3380–3389. doi:10.1039/c3tb20445f

frontiers | Frontiers in Bioengineering and Biotechnology

TYPE Original Research
PUBLISHED 09 January 2024
DOI 10.3389/fbioe.2023.1295313

OPEN ACCESS

EDITED BY
Hongye Yang,
Wuhan University, China

REVIEWED BY
Jingang Xiao,
Southwest Medical University, China
Tang Ying,
Wuhan University, China

*CORRESPONDENCE
Nicole Ehrhart,
nehrhart@colostate.edu
Chelsea Bahney,
cbahney@sprivail.org

RECEIVED 16 September 2023
ACCEPTED 12 December 2023
PUBLISHED 09 January 2024

CITATION
Nelson AL, Fontana G, Chubb L, Choe J, Williams K, Regan D, Huard J, Murphy W, Ehrhart N and Bahney C (2024), Mineral coated microparticles doped with fluoride and complexed with mRNA prolong transfection in fracture healing. *Front. Bioeng. Biotechnol.* 11:1295313. doi: 10.3389/fbioe.2023.1295313

Mineral coated microparticles doped with fluoride and complexed with mRNA prolong transfection in fracture healing

Anna Laura Nelson[1,2], Gianluca Fontana[3], Laura Chubb[4], Josh Choe[3], Katherine Williams[4,5], Dan Regan[5], Johnny Huard[1,4], William Murphy[3,6], Nicole Ehrhart[4]* and Chelsea Bahney[1,4,7]*

[1]Center for Regenerative and Personalized Medicine, Steadman Philippon Research Institute (SPRI), Vail, CO, United States, [2]School of Biomedical Engineering, Colorado State University, Fort Collins, CO, United States, [3]Department of Orthopedics and Rehabilitation, University of Wisconsin-Madison, Madison, WI, United States, [4]Department of Clinical Sciences, Colorado State University, Fort Collins, CO, United States, [5]Department of Microbiology, Colorado State University, Fort Collins, CO, United States, [6]Department of Biomedical Engineering, University of Wisconsin-Madison, Madison, WI, United States, [7]Orthopaedic Trauma Institute, University of California, San Francisco, CA, United States

Introduction: Impaired fracture healing, specifically non-union, has been found to occur up to 14% in tibial shaft fractures. The current standard of care to treat non-union often requires additional surgeries which can result in long recovery times. Injectable-based therapies to accelerate fracture healing have the potential to mitigate the need for additional surgeries. Gene therapies have recently undergone significant advancements due to developments in nanotechnology, which improve mRNA stability while reducing immunogenicity.

Methods: In this study, we tested the efficacy of mineral coated microparticles (MCM) and fluoride-doped MCM (FMCM) to effectively deliver firefly luciferase (FLuc) mRNA lipoplexes (LPX) to the fracture site. Here, adult mice underwent a tibia fracture and stabilization method and all treatments were locally injected into the fracture. Level of osteogenesis and amount of bone formation were assessed using gene expression and histomorphometry respectively. Localized and systemic inflammation were measured through gene expression, histopathology scoring and measuring C-reactive protein (CRP) in the serum. Lastly, daily IVIS images were taken to track and measure transfection over time.

Results: MCM-LPX-FLuc and FMCM-LPX-FLuc were not found to cause any cytotoxic effects when tested *in vitro*. When measuring the osteogenic potential of each mineral composition, FMCM-LPX-FLuc trended higher in osteogenic markers through qRT-PCR than the other groups tested in a murine fracture and stabilization model. Despite FMCM-LPX-FLuc showing slightly elevated *il-1β* and *il-4* levels in the fracture callus, inflammation scoring of the fracture callus did not result in any differences. Additionally, an acute systemic inflammatory response was not observed in any of the samples tested. The concentration of MCM-LPX-FLuc and FMCM-LPX-FLuc that was used in the murine fracture model did not stimulate bone when analyzed through stereological principles. Transfection efficacy and kinetics of delivery platforms revealed that FMCM-LPX-FLuc prolongs the luciferase signal both *in vitro* and *in vivo*.

Discussion: These data together reveal that FMCM-LPX-FLuc could serve as a promising mRNA delivery platform for fracture healing applications.

KEYWORDS

bone regeneration, mRNA delivery, biomimetic, transfection, fluoride

Introduction

Fractures continue to be one of the most frequent type of hospitalized traumas with reports of about 32.7 million new cases of lower leg fractures globally in 2019 (Ekegren et al., 2018; Cauley, 2021). Additionally, tibial shaft fractures account for about 36.7% of all long-bone fractures in adults and are frequently associated with high-energy trauma events, like falls and transport accidents (Weiss et al., 2008; Papakostidis et al., 2011; Ekegren et al., 2018). Open tibial fractures are often associated with higher rates of complications, like non-union or delayed union (Gaebler et al., 2001; Papakostidis et al., 2011). In fact, reports of non-union have been found to occur up to 14% within tibial shaft fractures in a large study over the course of 2 years (Bisignano et al., 2021). Non-union is typically treated through repeated surgeries resulting in long recovery times leading to increased frailty, depression, loss of independence, and, in some cases, a downward spiral that ends in death (Colón-Emeric and Saag, 2006; Gruber et al., 2006). Bone morphogenetic protein-2 (BMP2) is a well-studied osteoanabolic that accelerates fracture healing in preclinical models, yet only has FDA approval in lumbar fusion and acute open tibial fractures (9–13) Recombinant human proteins have short half-lives and require supraphysiologic concentrations to achieve the desired biologic effect (12) In order to sustain protein release, typically proteins are delivered on an absorbable collagen sponge, necessitating surgical implantation (13–15) Despite this controlled release system, adverse side effects have continued to be reported with BMP-2 including abnormal inflammatory responses, poor bone quality, heterotopic ossification, and osteolysis (14, 16–18) Given the few approved therapeutics to accelerate fracture healing, and the limitations of those available, there is a clinical need to develop novel, and injectable-based therapies to accelerate fracture healing and minimize the incidence of delayed and non-union fractures.

Over the past few decades, the demand for orthopaedic-based technologies has followed the substantial growth in orthopaedic surgeries being performed each year (Su et al., 2022). Of these emerging orthopaedic technologies, gene therapy has undergone significant advancements due to developments in delivery carriers and their capabilities to maximize gene stability, minimize off-target effects, and reduce immunogenicity (Mockey et al., 2006; Zohra et al., 2007; Mukherjee and

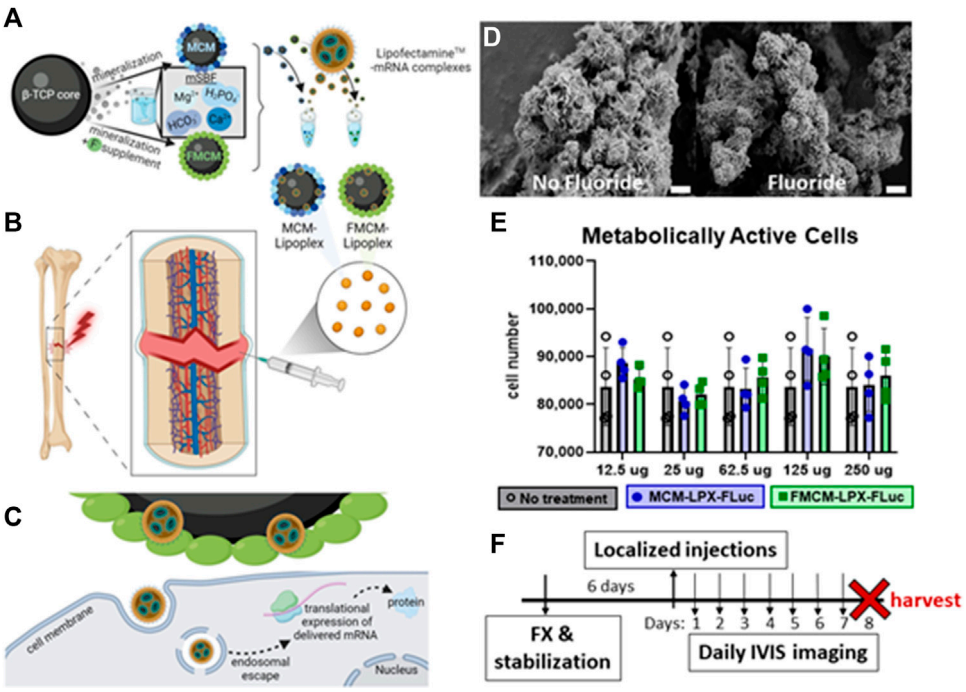

FIGURE 1
Schematic of MCM and FMCM synthesis, delivery, cell interactions and characterization of microparticles. Schematic of MCM and FMCM synthesis and lipoplex interaction **(A)**. Delivery of test article and controls were localized at the site of the fracture callus **(B)**, where MCM-LPX-FLuc and FMCM-LPX-FLuc are not endocytosed by the cells **(C)**. SEM imaging of MCM (left) and FMCM (right) **(D)**. Scale bars represent 2 μm. Metabolic activity was measured to determine cytotoxicity of MCM-LPX-FLuc and FMCM-LPX-FLuc **(E)**. Timeline of *in vivo* studies, where injections were performed 6 days after fracture and stabilization in a murine model **(F)**. Schematic created with Biorender.com.

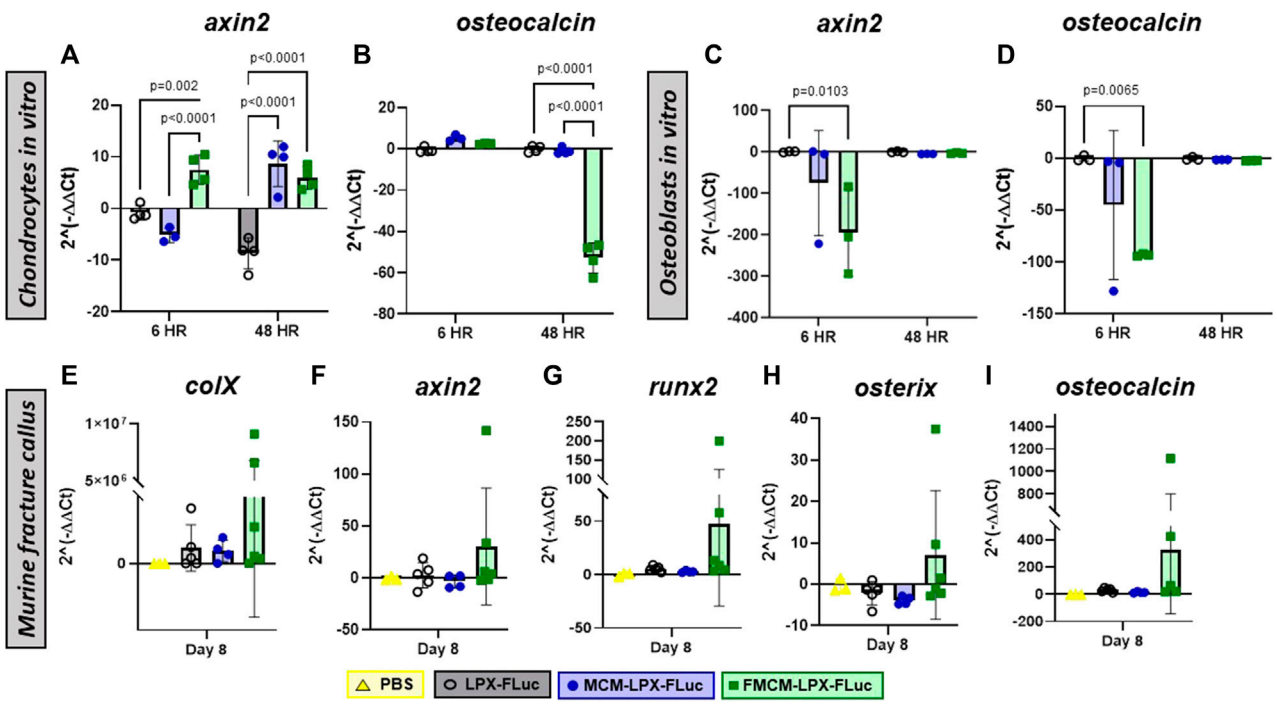

FIGURE 2
Osteogenic potential was tested through qRT-PCR in chondrocytes **(A, B)** and osteoblasts **(C, D)** *in vitro*, and within the fracture callus in a murine model *in vivo* **(E–I)**.

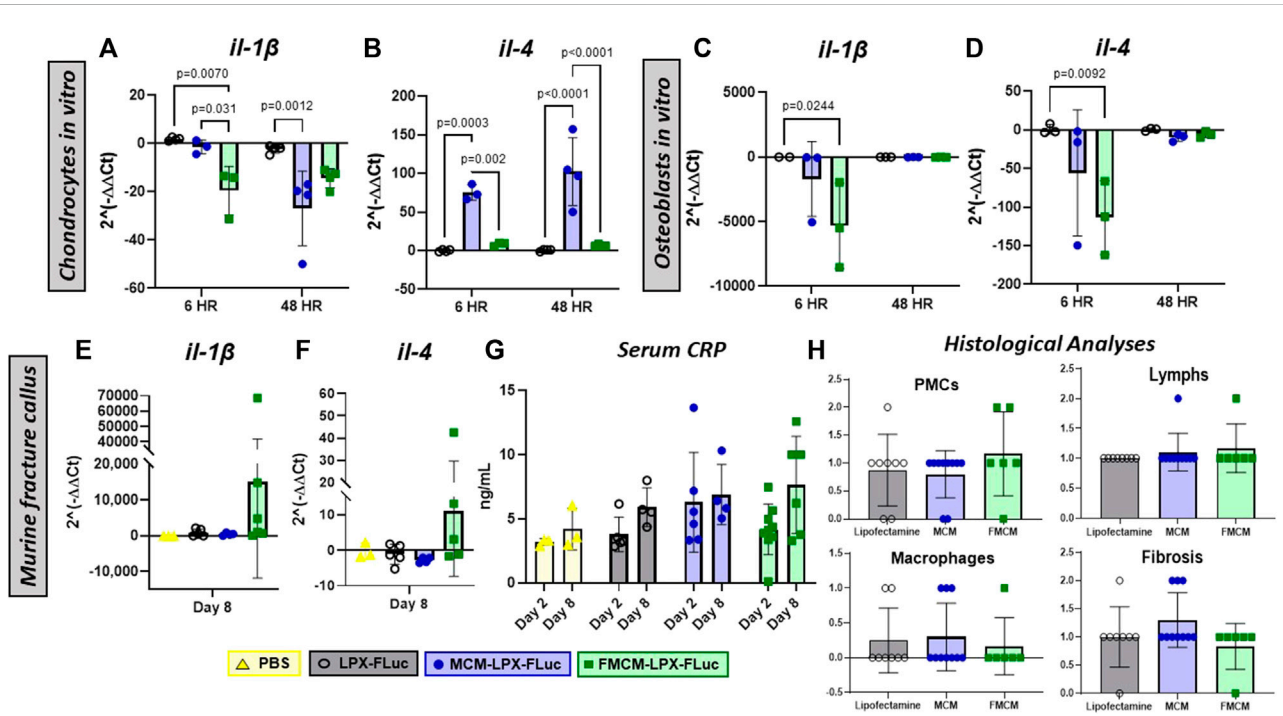

FIGURE 3
Inflammatory responses were measured by using qRT-PCR for pro-inflammatory marker, il-1β, **(A,C and E)** and anti-inflammatory marker, il-4, **(B,D and F)** both *in vitro* and within the fracture callus to measure localized inflammatory response following treatments. Systemic inflammation was tested by quantifying C-reactive protein within the serum both 2 and 8 days after local injections **(G)**. Additionally, H&E sections of the fracture callus were scored by a pathologist for peripheral mononuclear cells, lymphocytes, macrophages and fibrosis, 2 days after treatments **(H)**.

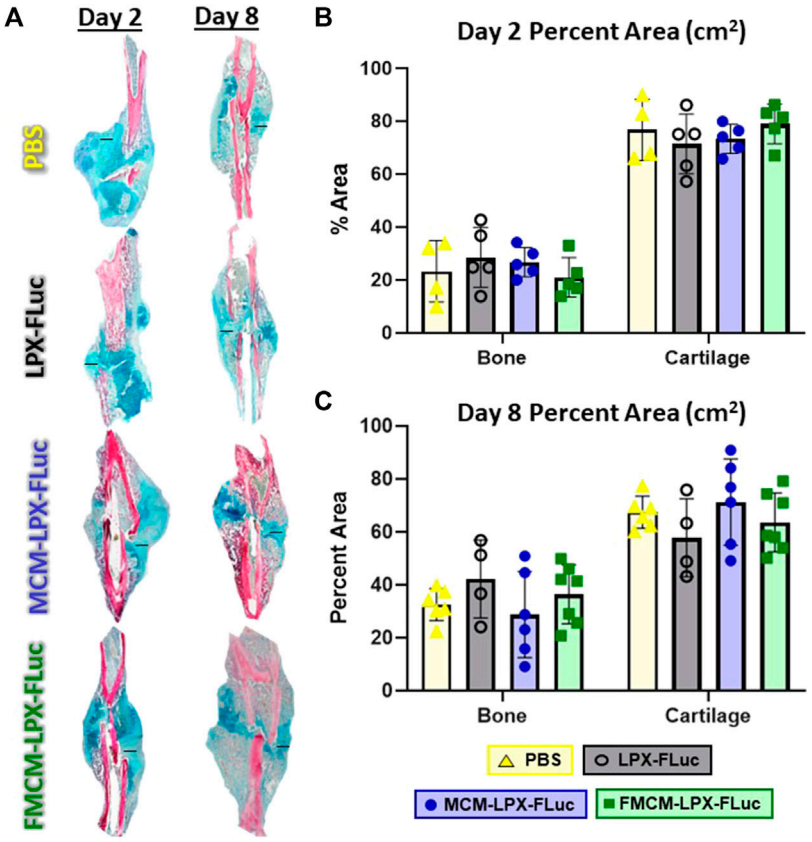

FIGURE 4
Fractured limbs were harvested, processed for histological analyses and stained with Hall Brundt's Quadruple (HBQ) stain, where bone is stained red and cartilage is stained blue, scale bars represent 500 μm **(A)**. Histomorphometric principles were used to quantify tissue composition both 2 days after treatment **(B)** and 8 days after treatment **(C)**.

Thrasher, 2013; Ramunas et al., 2015; Sultana et al., 2017; Shirley et al., 2020; Watson-Levings et al., 2022). Specifically, the considerable success of the SARS-CoV-2 vaccine has catalyzed research efforts in developing mRNA-based technologies as safety and efficacy have been established with mRNA therapeutics (Altawalah, 2021; Ward et al., 2022; Watson-Levings et al., 2022). mRNA-based therapy in orthopedics remains a nascent field, and specifically for skeletal tissues as these are prone to clinical challenges such as multifactorial pathologies and complex healing mechanisms (Evans et al., 2021; Watson-Levings et al., 2022). Recent work pioneering mRNA therapies to promote bone regeneration through coding for BMP2/9 has shown considerable promise, yet all studies use a biomimetic scaffold requiring surgical implantation (Balmayor et al., 2016; Khorsand et al., 2017; De La Vega et al., 2022). We propose that the ideal mRNA delivery platform to promote fracture repair should include a localized and injectable therapeutic, mitigating the need for additional surgeries in impaired fracture healing cases.

Effective mRNA delivery to cells requires the use of delivery carriers to protect the nucleic acids from degradation from nucleases (Kowalski et al., 2019; Nitika et al., 2022). Currently liposomal complexes are the most commonly utilized delivery vehicles for mRNA based therapeutics, including lipid nanoparticles and liposomes (Kowalski et al., 2019; Nitika et al., 2022). However, lipoplexes can induce immunogenic reactions and are rapidly cleared by the mononuclear phagocytic system (MPS) through the kidney, liver, and spleen (Kowalski et al., 2019). Alternative strategies have been employed to mitigate these limitations and more effectively transport genes important in bone repair. β-tricalcium phosphate mineral coated microparticles (Alluri et al., 2019; Fontana et al., 2019; Kang et al., 2021) (MCM) which consist of a bioresorbable core material coated with calcium phosphate resulting in microparticles 5–8 μm in diameter with a thin, plate-like mineral coating on their surface (Choi and Murphy, 2010; Yu and Murphy, 2014; Fontana et al., 2019). Recently published studies demonstrate that MCMs can enhance mRNA transfection when combined with lipoplexes and mitigate cytotoxicity resulting from high *in vitro* mRNA concentrations (Dang et al., 2016; Khalil et al., 2017; Fontana et al., 2019).

In this study, we have developed and tested an MCM-mRNA delivery platform for its capacity to effectively deliver a reporter mRNA in a fracture healing setting. The biomimetic mineral coating localizes the delivery of lipoplexes to cells and has been found to prolong the biological function of various biomolecules

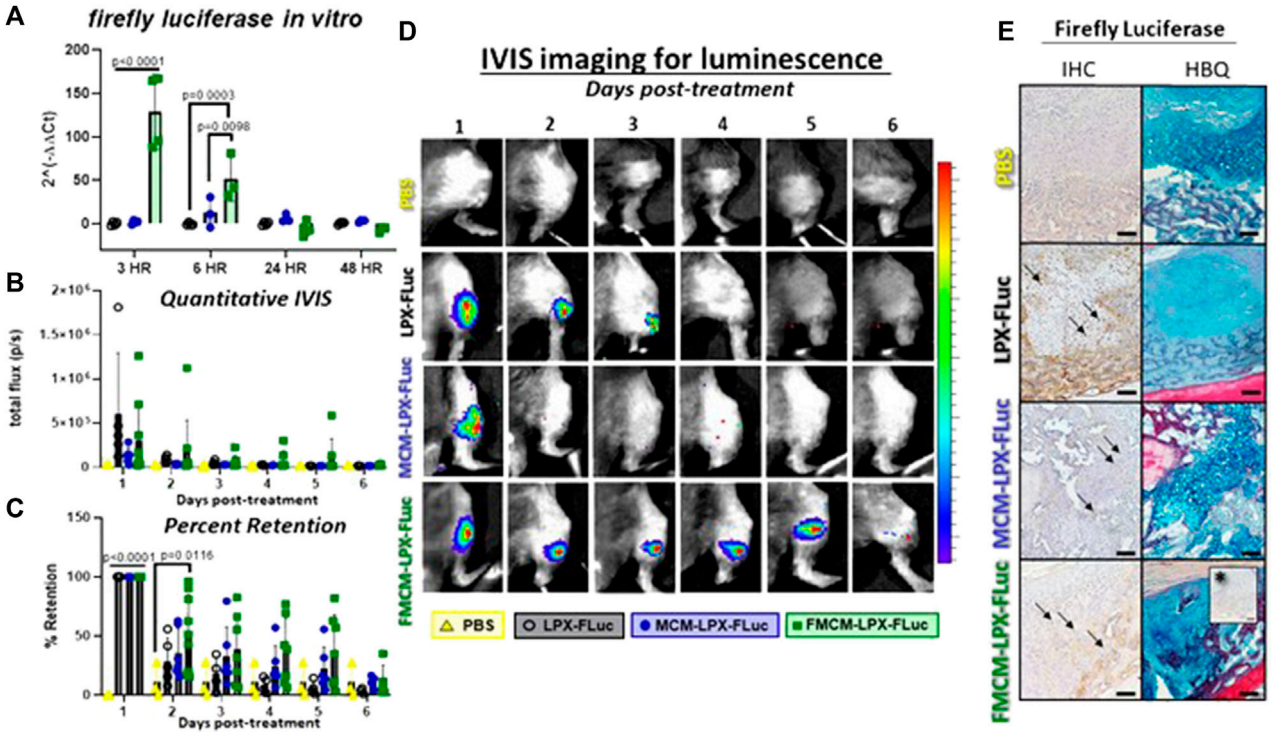

FIGURE 5
Transfection efficacy and kinetics were tested using firefly luciferase as a reporter gene to track and measure transfection. *In vitro* analysis was first measured in chondrocytes to determine transfection efficiency by testing firefly luciferase gene expression **(A)**. IVIS imaging was used for *in vivo* analysis to quantify luciferase signal and view expression **(B, D)**. Percent of luciferase signal retained within each mouse was measured for each treatment group **(C)**. IHC for firefly luciferase was used to qualitatively assess cells expressing the FLuc mRNA 2 days after local injections using adjacent slides stained with HBQ to determine cell lineage **(E)**. Arrows represent examples of positively stained cells for firefly luciferase protein. *Represents IgG negative control. Scale bars represent 100 μm.

being delivered *in vivo* testing various applications, such as for spinal cord injuries (Khalil et al., 2017; Fontana et al., 2019; Khalil et al., 2020; Khalil et al., 2022). The use of MCMs to localize lipoplexed mRNA and improve cell internalization of mRNA at the fracture callus addresses several limitations, including the immunogenicity associated with liposomal carriers. Here we show that mRNA transfection is enhanced, prolonged, and does not interfere with fracture healing when using MCMs as a transfection platform in a murine tibial fracture healing model.

Methods and materials

Synthesis of mineral coated microparticles and fluoride-doped MCM and microparticle characterization

Mineral coated microparticles were made from β-tricalcium phosphate (β-TCP) 2 μm powder (Cambioceramics, Amsterdam, Netherlands) as the microparticle core and incubated in modified simulated body fluid (mSBF) at 1 mg/mL for 7 days. The mSBF was prepared by using 141 mM NaCl, 4 mM KCl, 0.5 mM MgSO4, 1 mM MgCl2, 4.2 mM NaHCO3, 20 mM HEPES, 5 mM CaCl2, and 2 mM KH2PO4. For Fluoride-doped MCM (FMCM) we introduced 1 mM NaF to the standard mSBF. All microparticles were maintained in suspension at 37°C with rotation. The microparticles were centrifuged at 2,000 x g for 5 min every 24 h over 7 days. The supernatant was discarded and replenished with fresh mSBF. Post 7 days, the MCMs were rinsed three times using 50 mL deionized water and filtered using a 40 μm pore cell strainer. Finally, the MCMs were concentrated and subjected them to lyophilization for 48 h (Fontana et al., 2019). Dry MCMs were placed on carbon tape and sputter coated with 10 nm of platinum (ACE600, Leica Microsystems, Morrisville, NC, United States). MCMs were imaged at 5.0 KV using a Gemini 450 scanning electron microscope (Zeiss, Jena, Germany).

Cell culture maintenance and cytotoxicity experiments

The chondrogenic cell line (ATDC5, Sigma Aldrich, Cat # 99072806) was used for all *in vitro* studies. Cells were used at passage 5 and under for all experiments. ATDC5 cells were maintained using media DMEM/F12 (Thermo Fisher, Cat# 11320033), 5% fetal bovine serum (FBS, Thermo Fisher, Cat# 16000044) and 1% penicillin/streptomycin (P/S, Thermo Fisher, Cat# 15140122). For all *in vitro* experiments, ATDC5 cells were plated at 20,000 cells/well in 12 well plates. Prior to transfection experiments, chondrocytes underwent serum starvation using basal

media OPTI-MEM (Thermo Fisher, Cat# 31985070) 0.5% FBS and 1% P/S for 24 h. All transfection protocols were executed using serum-free media, OPTI-MEM supplemented with 1% P/S. The cytotoxic effects were assessed using PrestoBlue™ Cell Viability Reagent (Thermo Fisher, Cat# A13261) according to the manufacturer's protocol. To quantify the number of metabolically active cells, a standard curve of ATDC5 cells was created and the absorbance values were related back to the number of cells for quantitation. The plate was read at 570 nm with a reference wavelength at 600 nm using a plate reader (TECAN infinite M200 Pro).

Mineral coated microparticles and fluoride-doped MCM formulations with lipoplexes

MCM and FMCM were used as a platform to deliver lipid vesicles encapsulating mRNA to the chondrocytes *in vitro* and to the site of the fracture callus *in vivo*. To determine transfection protocols and concentrations for effective delivery of mRNA, firefly luciferase (FLuc) mRNA was used as a reporter transcript (TriLink Biotech, Cat# L-7202) for all experiments. Lipoplexes (LPX), liposomes complexed with mRNA, were generated using Lipofectamine™ MessengerMAX (ThermoFisher, Cat# LMRNA001) and firefly luciferase mRNA according to manufacturer's protocol. To combine the LPXs with MCM and FMCM, the LPX solution was added to MCM or FMCM in OPTI-MEM for *in vitro* studies or sterile filtered 1X phosphate buffer solution (PBS, Thermo Fisher, Cat # 10010023) for *in vivo* studies, with shaking for 30 min at RT. All *in vitro* experiments used 0.25 µg of firefly luciferase mRNA/well, 2 µL of Lipofectamine™/well, and 100 µg of MCM or FMCM per well. *In vivo* analysis of transfection reagents used firefly luciferase mRNA at a concentration of 10 µg/mouse, Lipofectamine™ at 15 µL/mouse, and MCM/FMCM at 100 µg/mouse. Firefly luciferase expression in MCM-Lipofectamine™-FLuc mRNA platform (MCM-LPX-FLuc) and FMCM-Lipofectamine™-FLuc mRNA (FMCM-LPX-FLuc) was compared to the luciferase expression from Lipofectamine™-FLuc mRNA (LPX-FLuc).

Tibial fracture and stabilization procedure in mice

In vivo experiments were approved by and conducted in compliance with the Institutional Animal Care and Use Committee at Colorado State University (CSU). Mid-shaft tibial fractures were created in adult (12–14 weeks), male C57BL/6J mice (Charles River # 027). All animals received a pre-surgical analgesic, Buprenorphine SR (ZooPharm), at a dose of 0.6–1.0 mg/kg. Mice were placed under general anesthesia using inhaled 1%–5% isoflurane to effect. Left hind limbs were shaved and sterilely prepared using 70% alcohol wipes and Chlorhexidine surgical scrub solution, repeated for a total of 3 times. Lubrication was provided for the eyes of each mouse using artificial tears ointment (Bausch and Lomb) and mice were then transferred to a heated operating table. Using aseptic technique, an incision was made along the tibia, and a hole was made at the top of the tibial plateau using a 23-gauge needle. An intermedullary pin (sterilized insect pin) was inserted through the hole made from the tibial plateau through the tibial cavity and into the distal tibia. Two to three small holes were created in the mid-shaft of the tibia using a Dremel and pressure was applied to both proximal and distal ends to fracture the tibia (Hu et al., 2017; Wong et al., 2020). The surgical incision was then sutured using 5–0 Biosyn Sutures (Covidien, Cat #5687) and one surgical skin staple was applied over the skin incision to protect against chewing. A local anesthetic, 0.25% Bupivicaine Hydrochloride (NovaPlus, cat # RL-7562), was applied topically after the initial staple was placed. Mice were then allowed to recover individually in a heated cage before being transferred back to their original cage. Mice were socially housed throughout the in-life period, and permitted free ambulation. Mice were closely monitored for pain and signs of infections for 72 h following the surgery. All treatments were suspended in 25 µL sterile PBS and vortexed before injecting. All experimental and control groups were injected on day 6 post-fracture into the fracture callus using a Hamilton syringe 1800 series (Sigma Aldrich, Cat # 21397). Localized treatments consisted of experimental groups (MCM-LPX and FMCM-LPX), negative and positive control groups (PBS and LPX respectively). Serum was collected 2 days following treatment via tail vein blood draw and lastly at time of harvest using a cardiac puncture. Animals were sacrificed according to approved euthanasia protocols after 2 or 8 days following localized treatments. At euthanasia, serum, fractured tibia, kidneys, liver spleen and lung were harvested for later analysis. Harvested tibias were either fixed in 4% paraformaldehyde for histological analysis or flash-frozen in liquid nitrogen for RNA analysis. Tissues and serum were flash frozen by immediately placing in liquid nitrogen and stored at −80°C.

In vitro and *in vivo* RNA isolation and qRT-PCR

RNA was isolated using TRIzol™ Reagent (ThermoFisher, Cat# 15596026) according to the manufacturer's guidelines. To isolate RNA from all frozen tissues, the tissues were minced and placed in 1 mL of TRIzol Reagent and were homogenized using IKA Tissue Homogenizer (IKA, Cat# 0003737001) using a speed of 5 for 3 min, or at least until all large chunks were broken down. Specifically, the fracture callus was isolated from the surrounding muscle and bone tissues prior to homogenization. RNA was then quantified by reading the absorbance values at 260 and 280 nm. 1 µg of RNA was then synthesized into cDNA using qScript cDNA SuperMix (QuantaBio, Cat# 95048-025). Primers were designed and are listed below. Quality measurements were used to confirm primer specificity and appropriate reaction temperatures by running PCR using DreamTaq Green PCR Master Mix (2X) (ThermoFisher, Cat# K1081) using a 3-step method with denaturation at 95°C for 30 s, annealing at 60°C for 30 and extension at 72°C for 1 min. The bands were analyzed on a 1.5% agarose gel with 2 µL GelStar Nucleic Acid Stain (Lonza, Cat # 50535) run at 150V for 25 min. Quantitative real-time PCR was run using SYBR Green Master Mix (Bio-Rad, Cat#1725270) to detect the amplified DNA. qRT-PCR was performed on a StepOnePlus™ instrument (Applied Biosystems). To analyze

Gene	Forward	Reverse
β-2-modulin	ATACGCCTGCAGAGTTAAGCA	TCACATGTCTCGATCCCAGT
collagen 10a1 (colX)	TTCTGCTGCTAATGTTCTTGACC	GGGATGAAGTATTGTGTCTTGGG
axin2	GTGAGCTGGTTGTCACCTACTT	GCAAATTCGTCACTCGCCTTC
runt-related transcription factor 2 (runx2)	ACTCTTCTGGAGCCGTTTATG	GTGAATCTGGCCATGTTTGTG
osterix (osx)	TGCGCCAGGAGTAAAGAATAG	CCTGACCCGTCATCATAACTTAG
osteocalcin (ocn)	CGCTCTGTCTCTCTGACCTC	TCACAAGCAGGGTTAAGCTC
interleukin-1β (il-1β)	TGGACCTTCCAGGATGAGGACA	GTTCATCTCGGAGCCTGTAGTG
interleukin-4 (il-4)	GGTCTCAACCCCCAGCTAGT	GCCGATGATCTCTCTCAAGTGAT
firefly luciferase (fluc)	GTGGTGTGCAGCGAGAATAG	CGCTCGTTGTAGATGTCGTTAG

the output Ct values, the reference housekeeping gene (β-2-modulin) was used to determine ΔCt values. The value of 2-(ΔΔCt) was calculated for all graphs and to determine statistical significance. All 2(−ΔΔCt) values less than 1.0, were calculated as −1/(2(−ΔΔCt)) as followed and described in Schmittgen and Livak, 2008.

In vitro and *in vivo* immunogenicity, osteostimulatory and transfection efficacy testing

Analysis of transfection formulations for all *in vitro* studies was measured after collecting RNA at 3, 6, 24, and 48 h after treatments and for *in vivo* studies, RNA was collected 8 days after treatments. To measure *in vitro* and *in vivo* immune responses, qRT-PCR was used testing for pro-inflammatory marker, *interleukin-1β (il-1β),* and anti-inflammatory marker, *interleukin-4 (il-4)*. Local inflammatory response was measured using qRT-PCR and histopathology while systemic inflammation was tested using a C-Reactive Protein (CRP) ELISA kit (R&D Systems, Cat# MCRP00) according to manufacturer's instructions on the serum collected at day 2 and 8 post-treatment (Morioka et al., 2019). Osteostimulatory characterization was determined by using qRT-PCR for osteogenic markers *osterix* (*osx*), *osteocalcin* (*ocn*), *collagen 10a1* (*colX*) and downstream canonical Wnt markers, *axis inhibition protein 2* (*axin2)* and *runt-related transcription factor* (*runx2)*. Firefly luciferase primers were used to measure luciferase expression to determine magnitude of luciferase signal and kinetics of transfection.

Histopathological scoring

Tibias of treated mice were collected 48 h post treatment, immersion fixed in 4% paraformaldehyde, and decalcified using 19% ethylenediaminetetraacetic acid (EDTA). Formalin-fixed tibial samples were embedded in paraffin, sectioned at 8 μm thickness, and mounted onto glass slides. Two serial sections of each sample were cut and stained with hematoxylin and eosin using routine methods. Semiquantitative histopathologic analysis was performed by a board-certified veterinary pathologist (D.P.R.) who was blinded to the treatment arm. For analysis, slides were scanned on low magnification and the fracture callus region-of-interest identified and histological scoring performed based on the average cellular response across this callus region-of-interest. Semi-quantitative scoring was performed using a modification of ISO10993-6 Annex E: Biological evaluation of medical devices–Part 6: Tests for local effects after implantation (Supplementary Table S1). Cellular and host tissue response parameters assessed included the inflammatory cell types of polymorphonuclear cells (PMNs), lymphocytes (lymphs), plasma cells, macrophages, and giant cells, as well as necrosis, edema, hemorrhage, neovascularization and fibrosis. Responses were scored based on a 0–4 scale where 0 represents "none," 1 represents "rare/minimal," 2 represents "mild," 3 represents "heavy infiltrate/moderate" and 4 represents "packed/severe."

Real-time bioluminescent imaging

IVIS imaging was performed daily to quantitatively assess the magnitude and duration of luciferase expression from the time of delivery of reporter mRNA until signal dissipated. All mice were anesthetized using isoflurane and injected with 100 μL of firefly luciferase substrate, D-luciferin, subcutaneously at 10 mg/mL in PBS. Continued isoflurane was maintained at 1%–5% and mice were imaged 5 min following subcutaneous injection of D-luciferin. Bioluminescence was acquired using the "Auto" setting and regions of interest were measured for bioluminescence using LivingImage software (PerkinElmer, version). Percent retention was calculated using the following equation for each animal:

$$\%\text{Retention} = 100\%-\left[\left((A-B_x)/A\right)\text{x}\,100\%\right]$$

where A = IVIS output from day 1, and B_x = IVIS output from day x.

Histological and histomorphometric analysis

Bilateral tibias were decalcified for 14–18 days using 19% EDTA, pH 7.4. The tissues were then processed in increased ethanol solutions (50%, 70%, 95%, and 100%), processed in xylene (x2) and then placed in paraffin for 1.5 h each. Tissues were then paraffin embedded and sectioned at 8 μm. Immunohistochemistry (IHC) was performed to identify transfected cells within the fracture callus using previously published methods (Bahney et al., 2014; Hu et al., 2017). Antigen labeling was performed using a primary anti-luciferase (Novus Biologicals, Cat# NM600-307) antibody.

Negative control mouse IgG monoclonal antibody (ThermoFisher, Cat# 10400C) was used in replace of firefly luciferase antibody to determine non-specific stain. Cell morphology was used as the primary tool to identify specific immunopositive cell types, using Hall Brundt's Quadruple (HBQ) Stain on adjacent slides (Hall, 1986). The following kits were used for IHC detection: Mouse on Mouse Immunodetection Kit (Vector Laboratories, Cat# BMK2202), VectaStain Elite ABC-HRP Kit (Vector Laboratories, Cat# PK-6200) and DAB Substrate Kit, Peroxidase (HRP) (Vector Laboratories, Cat# SK-4100). All kits were used according to manufacturer's protocol. Sections were counterstained using Hematoxylin, dehydrated and mounted in a xylene-based mounting medium.

To perform quantitative histomorphometry, serial sections were obtained using the first section beginning in the fracture callus and every 10th section afterwards. Standard histomorphometry principles were used as previously described and quantification of the fracture callus components including bone and cartilage tissues were determined (Hu et al., 2017; Rivera et al., 2021). HBQ stain was used to identify the dense collagenous fibrils of bone, stained red by direct red, and proteoglycans in the cartilage matrix, stained by alcian blue. Quantification of callus composition was determined using the Trainable Weka Segmentation2 add-on in Fiji ImageJ (version 1.54f; NIH, Maryland, United States) (Malhan et al., 2018). Volume of specific tissue types was determined by summing the individual compositions relative to the whole fracture callus compositions. Tissues were imaged using a Nikon Eclipse Ti microscope. Additionally, photoshop (version 24.7.0, Adobe) was used to isolate fractured tissue from the adjacent muscle and skin tissues.

Statistical design

Animal sample size was determined *a priori* using the mean and standard deviation from our preliminary data, where a power analysis was conducted using G*Power to determine that 5 mice/group/time are required for IVIS imaging to achieve a power level >80% with an effect size d = 1.5 and a significance level of 5%. Statistical analysis was performed using Graph Pad Prism 8. Data were plotted so that each sample represented a single dot on each graph. The bar indicates the mean with error bars representing standard deviation. Statistical difference was determined by ANOVAs and all *post hoc* comparison performed using Tukey's HSD test.

Results

Mineral coated microparticles and fluoride-doped MCM characterization and metabolic testing

A schematic depicting the generation of MCM-LPX-FLuc and FMCM-LPX-FLuc can be viewed in Figure 1A, beginning with the synthesis of MCM and FMCM from a β-TCP core, and finally complexed with LPXs. All injections were performed locally to the site of the fracture callus (Figure 1B), where the MCM-LPX-FLuc and FMCM-LPX-FLuc are not endocytosed by the cell, but act as a carrier for the LPX-FLuc, which undergo endocytosis. mRNA is then expressed as protein using the cell's internal machinery (Figure 1C). MCM and FMCM were characterized using scanning electron microscopy (SEM) to visualize the outer morphology of the microparticles (Figure 1D). MCM were found to have a plate-like outer coating where FMCM had a more needle-like structure. The cytotoxic effects of the microparticles were evaluated and were found to have no significant *in vitro* chondrocyte cytotoxicity at any dose tested (12.5 μg–250 μg) (Figure 1E). Based on this data, 100 μg of MCM or FMCM was chosen to use in all *in vitro* and *in vivo* experiments, as this concentration did not promote cytotoxic effects when *in vitro* and additionally, this concentration has previously shown success in a murine spinal cord injury model (Khalil et al., 2022). All animal experiments were conducted according to the timeline outlined in Figure 1F, where injections of test article or control were performed 6 days following the fracture.

Mineral coatings stimulate osteogenesis

As it has previously been shown that mineral coatings have some osteogenic characteristics *in vitro* using various cell types, such as progenitor osteoblasts and mesenchymal and embryonic stem cells, we tested whether there was any osteostimulatory effect in chondrocytes and osteoblasts (Murphy et al., 2004; Chou et al., 2005; Choi and Murphy, 2010; Choi et al., 2013; Dang et al., 2016; Wang et al., 2016). When probing for osteogenic markers *in vitro*, MCM-LPX-FLuc was found to have more *ocn* expression at every time point tested in chondrocytes as compared to FMCM-LPX-FLuc (Figure 2B), yet FMCM-LPX-FLuc and MCM-LPX-FLuc both exhibited significant *axin2* expression at later time points in chondrocytes (Figure 2A). Osteogenic markers, *axin2* and *ocn*, were significantly downregulated in osteoblasts following treatment with FMCM-LPX-FLuc after 6 h, yet this significance dissipated by 48 h (Figures 2C,D). Within the tibia fracture callus, both earlier osteogenic genes, *collagen 10a1*, *axin2,* and *runx2,* and late osteogenic genes, *osterix* and *osteocalcin,* were tested for a more robust analysis of MCM-LPX-FLuc and FMCM-LPX-FLuc osteogenic potential. While no statistical significance was found *in vivo*, a trend of higher expression of osteogenic genes was observed with the FMCM-LPX-FLuc group (Figures 2E–I).

MCM-LPX-FLuc and FMCM-LPX-FLuc do not stimulate an inflammatory response

We aimed to test localized and systemic inflammatory responses following treatments with MCM-LPX-FLuc and FMCM-LPX-FLuc. Overall, both FMCM-LPX-FLuc and MCM-LPX-FLuc were found to have less *il-1β* expression at all time points in both chondrocytes and osteoblasts. Specifically, FMCM-LPX-FLuc was found to have significantly less *il-1β* at earlier time points tested in both chondrocytes and osteoblasts as compared to the LPX-FLuc group alone (Figures 3A,C). The MCM-LPX-FLuc was found to

have significantly less *il-1β* when tested in chondrocytes at 48 h compared to the LPX-FLuc group (Figure 3A). Additionally, MCM-LPX-FLuc was found to have significantly more *il-4* in chondrocytes at all time points as compared to both LPX-FLuc and FMCM-LPX-FLuc groups (Figure 3B), yet no significant differences with MCM-LPX-FLuc group were found when tested in osteoblasts (Figure 3D). FMCM-LPX-FLuc group was found to have significantly less *il-4* expression at 6 h in osteoblasts as compared to LPX-FLuc, yet this significance dissipated by 48 h (Figure 3D).

While no significance was found, modulation of inflammatory markers *in vivo* showed FMCM-LPX-FLuc to trend higher in *il-1β* and *il-4* as compared to both MCM-LPX-FLuc and LPX-FLuc groups (Figures 3E,F). Additionally, systemic inflammation was measured by testing the serum for CRP on days 2 and 8 following the injection of the various treatments. No significant differences were found between the treatment groups in CRP values on either of the days tested (Figure 3G). H&E slides 2 days following injections were scored by a blinded pathologist for peripheral mononuclear cells, lymphocytes, macrophages and fibrosis, to reveal no differences between any of the groups nor within any inflammatory cell type (Figure 3H).

MCM-LPX-FLuc and FMCM-LPX-FLuc do not inhibit fracture healing

To test whether MCM-LPX-FLuc or FMCM-LPX-FLuc interfered with bone healing when delivered locally following fracture and stabilization, histomorphometry was performed 2 and 8 days following treatments. No significant differences were found between any of the groups tested in bone or cartilage tissue composition within the fracture callus at day 2 (Figure 4B) or day 8 (Figure 4C) following treatment.

FMCM-LPX-FLuc prolongs transfection kinetics in a murine tibia fracture model

MCM-LPX-FLuc and FMCM-LPX-FLuc were tested for their capacity to regulate lipoplex encapsulation and release dynamics. FMCM-LPX-FLuc was found to significantly enhance transfection to chondrocytes *in vitro* at 3 and 6 h following treatment compared to both LPX-FLuc and MCM-LPX-FLuc groups (Figure 5A). IVIS images show representative luciferase expression over time within each group (Figure 5D) along with the corresponding quantification of the regions of interest within each individual animal (Figure 5B). Interestingly, while FMCM-LPX-FLuc had the highest amount of luciferase expression *in vitro*, LPX-FLuc ($n = 5$) had the highest luciferase signal on the first day following treatment *in vivo*. In calculating the percent of luciferase signal retained within each mouse, FMCM-LPX-FLuc maintained significantly more luciferase signal over the PBS control 2 days after injections, when all other treatment groups lost significance (Figure 5C). The MCM-LPX-FLuc group showed an average sustained signal of only 1 day after treatment, with some mice in this group having no detected signal. For qualitative assessment, immunohistochemistry was performed for firefly luciferase 2 days after treatment to determine the cell type expressing FLuc mRNA (Figure 5E). The cell lineage was determined using adjacent slides stained with HBQ, revealing firefly luciferase expression within cartilage, and specifically within hypertrophic chondrocytes, and mesenchyme tissues. Arrows show examples of cells positive for expressing firefly luciferase.

Discussion

Limited treatment options are available to facilitate fracture healing in non-union or delayed union cases. Most current treatments require additional surgeries which are often associated with long recovery times and increased work absences. Protein-based therapeutics, including the only FDA-approved osteoanabolic recombinant BMP-2, are the traditional approach to promoting fracture healing. However, proteins are typically delivered using supraphysiological doses as recombinant proteins are frequently challenged with low physiologic activity (Shields et al., 2006; Mumcuoglu et al., 2017; Khalil et al., 2020). Specifically, delivering high doses of recombinant BMP-2 results in high complication rates ranging from 20%–70% of all cases with complications ranging from mild to severe and potentially catastrophic (Shields et al., 2006; James et al., 2016). As an alternative, recombinant BMP-7 with collagen carrier was FDA approved in the past for impaired fracture healing cases, yet has since been removed from market (White et al., 2007; Gillman and Jayasuriya, 2021).

As an alternative to traditional protein based therapeutics, gene therapy proves to be an emerging field in bone regeneration with studies investigating genes encoding growth factors, transcription factors, and hormones involved in osteogenesis (De la Vega et al., 2021; Evans et al., 2021; Watson-Levings et al., 2022). De la Vega et al., 2021 has thoroughly reviewed preclinical studies which delivered BMP-2 cDNA using vector systems, like adenovirus and lentivirus. It was found that use of viral platforms to deliver gene encoding BMP-2 provoked an immune response and consequently impeded bone healing when tested *in vivo* (Lieberman et al., 1998; Musgrave et al., 1999; Egermann et al., 2006; Müller et al., 2017; Bougioukli et al., 2019). New strategies in gene therapy for bone regeneration involve use of mRNA, yet this approach is still challenged with short-half life and immunogenicity (Balmayor, 2022; Balmayor, 2023). To combat these challenges, other approaches have focused on modifying the mRNA sequence to maximize transfection while minimizing an immune reaction (Zhang et al., 2019; Balmayor, 2022). Despite these modifications, when testing chemically modified BMP-2 mRNA in various models, the use of liposomes in addition with a collagen sponge have frequently been employed as a delivery mechanism (Geng et al., 2021; De La Vega et al., 2022). Thus, it is imperative to develop biomaterials for mRNA therapeutics that facilitate an injectable application with effective transfection of cells, while minimizing immunogenicity.

In this study, we used a mineral coated microparticle (MCM) based platform to deliver mRNA encapsulated liposomes to a fracture site to evaluate their ability to effectively prolong mRNA delivery without promoting inflammation or inhibiting bone healing. Protein expression following transient transfection from

mRNA is sustained for only a limited time, making it an ideal platform for bone repair, as stable transfection is more suited for chronic or genetic diseases (Agholme et al., 2010). Further, this transient gene expression necessitates the enhancement of mRNA stability from endonuclease-mediated decay (DR and Schoenberg, 2011). Until recently, the use of mRNA therapeutic platforms have been limited due to challenges associated with mRNA stability, cytotoxicity of the delivery platform, and induction of innate inflammation (Mockey et al., 2006; Zohra et al., 2007; Ramunas et al., 2015; Sultana et al., 2017). Cationic lipid vesicles such as Lipofectamine™, are frequently used *in vitro* to enhance mRNA stability, yet the cytotoxicity associated with this reagent limits clinical translation (Guo et al., 2019; Inglut et al., 2020). MCMs are comprised of calcium phosphate and biomimetic fluids, creating a mineral coating originally designed for controlled and localized delivery of growth factors (Choi and Murphy, 2010; Dang et al., 2016; Khalil et al., 2017). Recently, MCM lipoplexes have been utilized to enhance mRNA and cDNA stability, resulting in an increased transfection efficiency, enhanced cell internalization, and reduced cytotoxicity seen from cationic lipid vectors (Fontana et al., 2019). Additionally, it has previously been shown that mineral coatings display an osteogenic potential, but also can enhance transfection of plasmid DNA in bone marrow stem cells (Choi and Murphy, 2010; Choi et al., 2013).

Building on previous engineering efforts to develop the MCM platform for gene delivery, this platform was tuned to further advance mRNA delivery by the inclusion of a chemical dopant. Incorporating fluoride in the mineral coating has been shown to decelerate mineral dissolution which subsequently affected the protein binding and release kinetics for BMP2 (Yu and Murphy, 2014; Khalil et al., 2017). Fluoride has also been associated with activation of the canonical Wnt pathway, a critical pathway in bone formation (Guo et al., 2011; Pan et al., 2014; Nelson et al., 2022). Specifically, fluoride prevents the destruction complex from sending β-catenin to be proteolytically degraded, thereby increasing the nuclear localization of β-catenin (Pan et al., 2014). The transcription factor β-catenin modulates the expression of bone-associated genes, specifically *runt-related transcription factor 2* (*Runx2*) and *Osterix* (*Osx*) (Zhang et al., 2008; Cai et al., 2016). Importantly, while fluoride has frequently been tested as a treatment for osteoporosis and to enhance osseointegration, minimal efforts have focused on fluoride's efficacy in fracture repair (SAVCHUCK, 1957; de Gubareff and Platt, 1969; Shteyer et al., 1977).

In this study, we evaluated the effects of FMCM-LPX on canonical Wnt activation and further osteogenic potential by probing for bone-related genes *Axin2*, *Runx2*, *Osx* and *Ocn* following treatment. While FMCM-LPX significantly activated the canonical Wnt pathway in chondrocytes *in vitro*, there was no significant upregulation of Wnt *in vivo*. While the same increased osteogenic effect was not observed in differentiated osteoblasts as in the progenitor chondrocytes, this may be due to the FMCM-LPX platform having more influence on cells in a less differentiated state, like progenitor cells. Multiple cell lineages comprise a fracture callus, all with varied states of differentiation, including both progenitor chondrocytes and osteoblasts. The *in vivo* gene expression data trended higher in osteogenic markers yet did not reach significance, suggesting more resemblance to that of the less differentiated cell type, progenitor chondrocytes. Additionally, the higher amount of cartilage composition, as evidenced through histomorphometry, confirms that more progenitor chondrocytes reside within the fracture as compared to osteoblasts at this time point. Thus, this heterogeneous cell population within a fracture callus may have hindered the osteogenic gene expression from reaching statistical significance. While fluoride has been heavily implicated in therapies that enhance bone mass, an adverse and deleterious effect at high doses (>8 mg/day) has been observed with chronic exposure (Grynpas et al., 2000; Du et al., 2022). Thus, only moderate amounts of FMCM-LPX-FLuc were tested *in vitro,* showing no cytotoxic effect on metabolic activity at any of the concentrations tested. Additionally, the concentration chosen for *in vivo* studies was previously used in a murine spinal cord injury model and was shown to not only effectively deliver mRNA, but also improve motor function (Khalil et al., 2022).

Since viral platforms delivering BMP-2 gene have been found to impede fracture healing due to an immunogenic response, it was important to determine whether immunogenicity was found using non-viral platforms (Egermann et al., 2006; De la Vega et al., 2021). Robust testing of localized and systemic inflammation revealed that delivery of FMCM-LPX-FLuc did not provoke a significant immunogenic response at either level. While this group did have the least pro-inflammatory effect *in vitro*, no significant differences were found when testing pro- or anti-inflammatory cytokines within the fracture callus. Interestingly, De La Vega et al., 2022 reported elevated levels of both pro-and anti-inflammatory cytokines in animals treated with synthetic RNA, yet were not elevated in animals treated with sham or protein groups. In this study, robust testing of localized and systemic inflammation revealed no acute inflammatory response found even 2 days after treatment with FMCM-LPX-FLuc or any treatment tested. This lack of immunogenicity may be due in part to a modest amount of mRNA being delivered (10 μg) in comparison to other reports (50 μg) (De La Vega et al., 2022).

This study had several limitations including use of Lipofectamine™ at various times within the shelf-life range, which impacts the transfection potency of cells as the reagent diminishes in potency with increased time on the shelf. To mitigate this variance, all experiments were executed using the same Lipofectamine™ vial so that all treatment groups were comparable. Additionally, only one of the concentrations of MCM-LPX-FLuc and FMCM-LPX-FLuc was tested *in vivo* for enhanced osteogenic markers and for stimulation of bone. Since there was a minimal osteogenic response using FMCM-LPX-FLuc, future work will include testing a functional mRNA sequence involved in promoting bone, such as BMP-2 or BMP-7 (Gao et al., 2014; Gao et al., 2022). One last limitation of the study includes the lack of biodistribution tested following treatment. While a localized delivery may only minimize biodistribution of the mRNA lipoplexes, this should be further examined through analysis of main organs including liver, lung, spleen, kidney and heart tissues.

The mRNA delivery platform developed in this study, FMCM-LPX-FLuc, was found to prolong the transfection kinetics of luciferase, without provoking immunogenicity nor interfering with fracture repair. This data proves to be consistent with prior data showing fluoride dopant to decrease mineral dissolution in MCM and to prolong delivery of growth factors and nucleic acids (Khalil et al., 2017; Fontana et al., 2019). In this manuscript, we explored the safety and efficacy of this novel mRNA delivery

platform prior to administering a therapeutic gene. The decision to utilize the luciferase reporter system was based on its well-established detection methods, which enable accurate and non-invasive monitoring of transfection efficiency and kinetics. Furthermore, it provided us with the means to confirm the absence of any cytotoxic or adverse immune reactions, which are crucial factors to consider prior to introducing osteoinductive mRNAs, especially in a fracture healing application. We think that the osteogenic potential of this platform could be maximized through addition of a functional mRNA transcript like BMP-2, or BMP-7.

Scope

The scope of this manuscript is to test biomimetic mineral coated microparticles (MCM) as an mRNA delivery platform for fracture healing applications. MCM and additionally a fluoride-doped MCM (FMCM) were tested in its osteogenic potential and capacity to provoke a robust inflammatory response in a murine fracture healing model. Bone formation was then quantified histologically and finally, reporter gene, Firefly Luciferase, was used to track and measure transfection *in vitro* and *in vivo*. The scope of this work specifically tests an advanced biomaterial for the regeneration of bone and is well suited for Research Topic: Advanced Biomaterials for Hard Tissue Repair and Regeneration.

Data availability statement

The original contributions presented in the study are included in the article/Supplementary Material, further inquiries can be directed to the corresponding authors.

Ethics statement

The animal study was approved by the Institutional Animal Care and Use Committee at Colorado State University. The study was conducted in accordance with the local legislation and institutional requirements.

Author contributions

AN: Conceptualization, Data curation, Investigation, Methodology, Writing–original draft, Writing–review and editing. GF: Conceptualization, Investigation, Methodology, Writing–review and editing. LC: Data curation, Methodology, Writing–review and editing. JC: Data curation, Investigation, Writing–review and editing. KW: Data curation, Writing–review and editing. DR: Data curation, Writing–review and editing. JH: Funding acquisition, Resources, Supervision, Writing–review and editing. WM: Conceptualization, Methodology, Resources, Writing–review and editing. NE: Conceptualization, Funding acquisition, Investigation, Resources, Supervision, Writing–original draft, Writing–review and editing. CB: Conceptualization, Funding acquisition, Investigation, Resources, Supervision, Writing–original draft, Writing–review and editing.

Funding

The author(s) declare financial support was received for the research, authorship, and/or publication of this article. This manuscript was supported in part by the National Institutes of Health through NIAMS (R01-AR077761 to CB) and an ON Kickstarter Grant (20–166). Philanthropic support for this project was also generously provided by Mary-Sue and Mike Shannon. The content is solely the responsibility of the authors and does not represent the official views of the National Institutes of Health or any other funding source. JAC was also supported by the National Institute on Aging of the National Institutes of Health under Award Number F30AG077748 and the University of Wisconsin–Madison Medical Scientist Training Program: T32GM140935. The content is solely the responsibility of the authors and does not necessarily represent the official views of the National Institutes of Health.

Acknowledgments

The authors gratefully acknowledge the use of facilities and instrumentation at the UW-Madison Wisconsin Centers for Nanoscale Technology (wcnt.wisc.edu) partially supported by the NSF through the University of Wisconsin Materials Research Science and Engineering Center (DMR-1720415).

Conflict of interest

The authors declare that the research was conducted in the absence of any commercial or financial relationships that could be construed as a potential conflict of interest.

Publisher's note

Supplementary material

The Supplementary Material for this article can be found online at: https://www.frontiersin.org/articles/10.3389/fbioe.2023.1295313/full#supplementary-material

References

Agholme, F., Li, X., Isaksson, H., Ke, H. Z., and Aspenberg, P. (2010). Sclerostin antibody treatment enhances metaphyseal bone healing in rats. *J. Bone Min. Res.* 25 (11), 2412–2418. doi:10.1002/jbmr.135

Alluri, R., Song, X., Bougioukli, S., Pannell, W., Vakhshori, V., Sugiyama, O., et al. (2019). Regional gene therapy with 3D printed scaffolds to heal critical sized bone defects in a rat model. *J. Biomed. Mater Res. A* 107 (10), 2174–2182. doi:10.1002/jbm.a.36727

Altawalah, H. (2021). Antibody responses to natural SARS-CoV-2 infection or after COVID-19 vaccination. *Vaccines (Basel)* 9 (8), 910. doi:10.3390/vaccines9080910

Bahney, C. S., Hu, D. P., Taylor, A. J., Ferro, F., Britz, H. M., Hallgrimsson, B., et al. (2014). Stem cell-derived endochondral cartilage stimulates bone healing by tissue transformation. *J. Bone Min. Res.* 29 (5), 1269–1282. doi:10.1002/jbmr.2148

Balmayor, E. R. (2022). Synthetic mRNA - emerging new class of drug for tissue regeneration. *Curr. Opin. Biotechnol.* 74, 8–14. doi:10.1016/j.copbio.2021.10.015

Balmayor, E. R. (2023). Bringing gene therapy to regenerative medicine. *Mol. Ther. Methods Clin. Dev.* 30, 81–82. doi:10.1016/j.omtm.2023.05.021

Balmayor, E. R., Geiger, J. P., Aneja, M. K., Berezhanskyy, T., Utzinger, M., Mykhaylyk, O., et al. (2016). Chemically modified RNA induces osteogenesis of stem cells and human tissue explants as well as accelerates bone healing in rats. *Biomaterials* 87, 131–146. doi:10.1016/j.biomaterials.2016.02.018

Bisignano, C., James, S. L., Abady, G. G., Abedi, A., Abu-Gharbieh, E., et al. (2021). Global, regional, and national burden of bone fractures in 204 countries and territories, 1990–2019: a systematic analysis from the Global Burden of Disease Study 2019. *Lancet Healthy Longev.* 2 (9), E580–E592. doi:10.1016/s2666-7568(21)00172-0

Bougioukli, H., Sofia, A., Ram, P., William, S., Osamu, V., Andrew, T., et al. (2019). Ex vivo gene therapy using human bone marrow cells overexpressing BMP-2:"Next-day" gene therapy versus standard "two-step" approach. *Bone* 128, 115032. doi:10.1016/j.bone.2019.08.005

Cai, T., Sun, D., Duan, Y., Wen, P., Dai, C., Yang, J., et al. (2016). WNT/β-catenin signaling promotes VSMCs to osteogenic transdifferentiation and calcification through directly modulating Runx2 gene expression. *Exp. Cell. Res.* 345 (2), 206–217. doi:10.1016/j.yexcr.2016.06.007

Cauley, J. A. (2021). The global burden of fractures. *Lancet Healthy Longev.* 2 (9), e535–e536. doi:10.1016/s2666-7568(21)00183-5

Choi, S., and Murphy, W. L. (2010). Sustained plasmid DNA release from dissolving mineral coatings. *Acta Biomater.* 6 (9), 3426–3435. doi:10.1016/j.actbio.2010.03.020

Choi, S., Yu, X., Jongpaiboonkit, L., Hollister, S. J., and Murphy, W. L. (2013). Inorganic coatings for optimized non-viral transfection of stem cells. *Sci. Rep.* 3, 1567. doi:10.1038/srep01567

Chou, Y. F., Huang, W., Dunn, J. C., Miller, T. A., and Wu, B. M. (2005). The effect of biomimetic apatite structure on osteoblast viability, proliferation, and gene expression. *Biomaterials* 26 (3), 285–295. doi:10.1016/j.biomaterials.2004.02.030

Colón-Emeric, C., and Saag, K. (2006). Osteoporotic fractures in older adults. *Best. Pract. Res. Clin. Rheumatol.* 20 (4), 695–706. doi:10.1016/j.berh.2006.04.004

Dang, P. N., Dwivedi, N., Yu, X., Phillips, L., Bowerman, C., Murphy, W. L., et al. (2016). Guiding chondrogenesis and osteogenesis with mineral-coated hydroxyapatite and BMP-2 incorporated within high-density hMSC aggregates for bone regeneration. *ACS Biomater. Sci. Eng.* 2 (1), 30–42. doi:10.1021/acsbiomaterials.5b00277

De La Vega, Rodolfo, E., van Griensven, Martijn, Zhang, Wen, C., et al. (2022). Efficient healing of large osseous segmental defects using optimized chemically modified messenger RNA encoding BMP-2. *Sci. Adv.* 8 (7), eabl6242. doi:10.1126/sciadv.abl6242

de Gubareff, N., and Platt, W. R. (1969). Influence of sodium fluoride on healing of experimental fractures. *Archives Environ. Health Int. J.* 19 (1), 22–31. doi:10.1080/00039896.1969.10666800

De la Vega, R. E., Atasoy-Zeybek, A., Panos, J. A., Griensven, M. V. A. N., Evans, C. H., and Balmayor, E. R. (2021). Gene therapy for bone healing: lessons learned and new approaches. *Transl. Res.* 236, 1–16. doi:10.1016/j.trsl.2021.04.009

DR, Schoenberg (2011). Mechanisms of endonuclease-mediated mRNA decay. *Wiley Interdiscip. Rev. RNA* 2 (4), 582–600. doi:10.1002/wrna.78

Du, C., Xiao, P., Gao, S., Chen, S., Chen, B., Huang, W., et al. (2022). High fluoride ingestion impairs bone fracture healing by attenuating M2 macrophage differentiation. *Front. Bioeng. Biotechnol.* 10, 791433. doi:10.3389/fbioe.2022.791433

Egermann, M., Lill, C. A., Griesbeck, K., Evans, C. H., Robbins, P. D., Schneider, E., et al. (2006). Effect of BMP-2 gene transfer on bone healing in sheep. *Gene Ther.* 13 (17), 1290–1299. doi:10.1038/sj.gt.3302785

Ekegren, C. L., Edwards, E. R., de Steiger, R., and Gabbe, B. J. (2018). Incidence, costs and predictors of non-union, delayed union and mal-union following long bone fracture. *Int. J. Environ. Res. Public Health* 15 (12), 2845. doi:10.3390/ijerph15122845

Evans, C. H., Ghivizzani, S. C., and Robbins, P. D. (2021). Orthopaedic gene therapy: twenty-five years on. *JBJS Rev.* 9 (8). doi:10.2106/jbjs.rvw.20.00220

Fontana, G., Martin, H. L., Lee, J. S., Schill, K., Hematti, P., and Murphy, W. L. (2019). Mineral-coated microparticles enhance mRNA-based transfection of human bone marrow cells. *Mol. Ther. Nucleic Acids* 18, 455–464. doi:10.1016/j.omtn.2019.09.004

Gaebler, C., Berger, U., Schandelmaier, P., Greitbauer, M., Schauwecker, H., Applegate, B., et al. (2001). Rates and odds ratios for complications in closed and open tibial fractures treated with unreamed, small diameter tibial nails: a multicenter analysis of 467 cases. *J. Orthop. Trauma* 15, 415–423. doi:10.1097/00005131-200108000-00006

Gao, X., Hwang, M. P., Wright, N., Lu, A., Ruzbarsky, J. J., Huard, M., et al. (2022). The use of heparin/polycation coacervate sustain release system to compare the bone regenerative potentials of 5 BMPs using a critical sized calvarial bone defect model. *Biomaterials* 288, 121708. doi:10.1016/j.biomaterials.2022.121708

Gao, X., Usas, A., Tang, Y., Lu, A., Tan, J., Schneppendahl, J., et al. (2014). A comparison of bone regeneration with human mesenchymal stem cells and muscle-derived stem cells and the critical role of BMP. *Biomaterials* 35 (25), 6859–6870. doi:10.1016/j.biomaterials.2014.04.113

Geng, Y., Duan, H., Xu, L., Witman, N., Yan, B., Yu, Z., et al. (2021). BMP-2 and VEGF-A modRNAs in collagen scaffold synergistically drive bone repair through osteogenic and angiogenic pathways. *Commun. Biol.* 4 (1), 82. doi:10.1038/s42003-020-01606-9

Gillman, C. E., and Jayasuriya, A. C. (2021). FDA-approved bone grafts and bone graft substitute devices in bone regeneration. *Mater Sci. Eng. C Mater Biol. Appl.* 130, 112466. doi:10.1016/j.msec.2021.112466

Gruber, R., Koch, H., Doll, B. A., Tegtmeier, F., Einhorn, T. A., and Hollinger, J. O. (2006). Fracture healing in the elderly patient. *Exp. Gerontol.* 41 (11), 1080–1093. doi:10.1016/j.exger.2006.09.008

Grynpas, M. D., Chachra, D., and Limeback, H. (2000). The action of fluoride on bone. *Osteoporos. Primer*, 318–330. doi:10.1017/cbo9780511545795.024

Guo, X., Wang, H., Li, Y., Leng, X., Huang, W., Ma, Y., et al. (2019). Transfection reagent Lipofectamine triggers type I interferon signaling activation in macrophages. *Immunol. Cell. Biol.* 97 (1), 92–96. doi:10.1111/imcb.12194

Guo, X., Wu, S., He, Y., Zhang, Z., and Sun, G. (2011). Effect of subchronic fluoride exposure on pathologic change and beta-catenin expression in rat bone tissue. *Wei Sheng yan jiu= J. Hyg. Res.* 40 (3), 304–307.

Hall, B. K. (1986). The role of movement and tissue interactions in the development and growth of bone and secondary cartilage in the clavicle of the embryonic chick. *J. Embryol. Exp. Morph.* 93, 133–152. doi:10.1242/dev.93.1.133

Hu, D. P., Ferro, F., Yang, F., Taylor, A. J., Chang, W., Miclau, T., et al. (2017). Cartilage to bone transformation during fracture healing is coordinated by the invading vasculature and induction of the core pluripotency genes. *Development* 144 (2), 221–234. doi:10.1242/dev.130807

Inglut, C. T., Sorrin, A. J., Kuruppu, T., Vig, S., Cicalo, J., Ahmad, H., et al. (2020). Immunological and toxicological considerations for the design of liposomes. *Nanomater. (Basel)* 10 (2), 190. doi:10.3390/nano10020190

James, A. W., LaChaud, G., Shen, J., Asatrian, G., Nguyen, V., Zhang, X., et al. (2016). A review of the clinical side effects of bone morphogenetic protein-2. *Tissue Eng. Part B Rev.* 22 (4), 284–297. doi:10.1089/ten.teb.2015.0357

Kang, H. P., Ihn, H., Robertson, D. M., Chen, X., Sugiyama, O., Tang, A., et al. (2021). Regional gene therapy for bone healing using a 3D printed scaffold in a rat femoral defect model. *J. Biomed. Mater Res. A* 109 (11), 2346–2356. doi:10.1002/jbm.a.37217

Khalil, A. S., Hellenbrand, D., Reichl, K., Umhoefer, J., Filipp, M., Choe, J., et al. (2022). A localized materials-based strategy to non-virally deliver chondroitinase ABC mRNA improves hindlimb function in a rat spinal cord injury model. *Adv. Healthc. Mater* 11 (19), e2200206. doi:10.1002/adhm.202200206

Khalil, A. S., Yu, X., Umhoefer, J. M., Chamberlain, C. S., Wildenauer, L. A., Diarra, G. M., et al. (2020). Single-dose mRNA therapy via biomaterial-mediated sequestration of overexpressed proteins. *Sci. Adv.* 6 (27), eaba2422. doi:10.1126/sciadv.aba2422

Khalil, A. S., Yu, X., Xie, A. W., Fontana, G., Umhoefer, J. M., Johnson, H. J., et al. (2017). Functionalization of microparticles with mineral coatings enhances non-viral transfection of primary human cells. *Sci. Rep.* 7 (1), 14211. doi:10.1038/s41598-017-14153-x

Khorsand, B., Elangovan, S., Hong, L., Dewerth, A., Kormann, M. S., and Salem, A. K. (2017). A comparative study of the bone regenerative effect of chemically modified RNA encoding BMP-2 or BMP-9. *AAPS J.* 19 (2), 438–446. doi:10.1208/s12248-016-0034-8

Kowalski, P. S., Rudra, A., Miao, L., and Anderson, D. G. (2019). Delivering the messenger: advances in technologies for therapeutic mRNA delivery. *Mol. Ther.* 27 (4), 710–728. doi:10.1016/j.ymthe.2019.02.012

Lieberman, J. R., Lu, Q., Wu, L., Finerman, G. A. M., Berk, A., et al. (1998). Regional gene therapy with a BMP-2-producing murine stromal cell line induces heterotopic and orthotopic bone formation in rodents. *J. Orthop. Res.* 16 (3), 330–339. doi:10.1002/jor.1100160309

Malhan, D., Muelke, M., Rosch, S., Schaefer, A. B., Merboth, F., Weisweiler, D., et al. (2018). An optimized approach to perform bone histomorphometry. *Front. Endocrinol.* 9, 666. doi:10.3389/fendo.2018.00666

Mockey, M., Goncalves, C., Dupuy, F. P., Lemoine, F. M., Pichon, C., and Midoux, P. (2006). mRNA transfection of dendritic cells: synergistic effect of ARCA mRNA capping with Poly(A) chains in cis and in trans for a high protein expression level. *Biochem. Biophys. Res. Commun.* 340 (4), 1062–1068. doi:10.1016/j.bbrc.2005.12.105

Morioka, K., Marmor, Y., Sacramento, J. A., Lin, A., Shao, T., Miclau, K. R., et al. (2019). Differential fracture response to traumatic brain injury suggests dominance of neuroinflammatory response in polytrauma. *Sci. Rep.* 9 (1), 12199. doi:10.1038/s41598-019-48126-z

Mukherjee, S., and Thrasher, A. J. (2013). Gene therapy for PIDs: progress, pitfalls and prospects. *Gene* 525 (2), 174–181. doi:10.1016/j.gene.2013.03.098

Müller, C. W., Hildebrandt, K., Gerich, T., Krettek, C., and Rosado Balmayor, E. (2017). BMP-2-transduced human bone marrow stem cells enhance neo-bone formation in a rat critical-sized femur defect. *J. Tissue Eng. Regen. Med.* 11 (4), 1122–1131. doi:10.1002/term.2015

Mumcuoglu, D., Siverino, C., Tabisz, B., Kluijtmans, B., and Nickel, J. (2017). How to use BMP-2 for clinical applications? A review on pros and cons of existing delivery strategies. *J. Transl. Sci.* 3 (5). doi:10.15761/jts.1000195

Murphy, W. L., Simmons, C. A., Kaigler, D., and Mooney, D. J. (2004). Bone regeneration via a mineral substrate and induced angiogenesis. *J. Dent. Res.* 83 (3), 204–210. doi:10.1177/154405910408300304

Musgrave, D. S., Bosch, P., Ghivizzani, S., Robbins, P. D., Evans, C. H., and Huard, J. (1999). Adenovirus-mediated direct gene therapy with bone morphogenetic protein-2 produces bone. *Bone* 24 (6), 541–547. doi:10.1016/s8756-3282(99)00086-1

Nelson, A. L., Fontana, G., Miclau, E., Rongstad, M., Murphy, W., Huard, J., et al. (2022). Therapeutic approaches to activate the canonical Wnt pathway for bone regeneration. *J. Tissue Eng. Regen. Med.* 16 (11), 961–976. doi:10.1002/term.3349

Nitika, H., Wei, J., and Hui, A. M. (2022). The delivery of mRNA vaccines for therapeutics. *Life (Basel)* 12 (8), 1254. doi:10.3390/life12081254

Pan, L., Shi, X., Liu, S., Guo, X., Zhao, M., Cai, R., et al. (2014). Fluoride promotes osteoblastic differentiation through canonical Wnt/β-catenin signaling pathway. *Toxicol. Lett.* 225 (1), 34–42. doi:10.1016/j.toxlet.2013.11.029

Papakostidis, C., Kanakaris, N. K., Pretel, J., Faour, O., Morell, D. J., and Giannoudis, P. V. (2011). Prevalence of complications of open tibial shaft fractures stratified as per the Gustilo-Anderson classification. *Injury* 42 (12), 1408–1415. doi:10.1016/j.injury.2011.10.015

Ramunas, J., Yakubov, E., Brady, J. J., Corbel, S. Y., Holbrook, C., Brandt, M., et al. (2015). Transient delivery of modified mRNA encoding TERT rapidly extends telomeres in human cells. *FASEB J.* 29 (5), 1930–1939. doi:10.1096/fj.14-259531

Rivera, K. O., Cuylear, D. L., Duke, V., O'Hara, K. M., Kharbikar, B. N., Kryger, A. N., et al. (2021). Localized delivery of β-NGF via injectable microrods accelerates endochondral fracture repair. *bioRxiv* 2021, 468864. doi:10.1101/2021.11.16.468864

Savchuck, WILLIAM B. (1957). Effects of strontium and fluoride on the repair of unreduced humeral fractures in the adult rat. *J. Bone and Jt. Surg.* 39 (1), 140–152. doi:10.2106/00004623-195739010-00013

Schmittgen, T. D., and Livak, K. J. (2008). Analyzing real-time PCR data by the comparative C(T) method. *Nat. Protoc.* 3 (6), 1101–1108. doi:10.1038/nprot.2008.73

Shields, L. B. E., Raque, G. H., Glassman, S. D., Campbell, M., Vitaz, T., Harpring, J., et al. (2006). Adverse effects associated with high-dose recombinant human bone morphogenetic protein-2 Use in anterior cervical spine fusion. *Spine* 31 (5), 542–547. doi:10.1097/01.brs.0000201424.27509.72

Shirley, J. L., de Jong, Y. P., Terhorst, C., and Herzog, R. W. (2020). Immune responses to viral gene therapy vectors. *Mol. Ther.* 28 (3), 709–722. doi:10.1016/j.ymthe.2020.01.001

Shteyer, A., Liberman, R., Simkin, A., and Gedalia, I. (1977). Effect of local application of fluoride on healing of experimental bone fractures in rabbits. *Calcif. Tissue Res.* 22 (1), 297–302. doi:10.1007/bf02010368

Su, C. A., Vopat, M. L., Jildeh, T. R., Day, H. K., Philippon, M. J., and Huard, J. (2022). Biologic therapies in orthopaedic surgery. *Operative Tech. Orthop.* 32 (2), 100963. doi:10.1016/j.oto.2022.100963

Sultana, N., Magadum, A., Hadas, Y., Kondrat, J., Singh, N., Youssef, E., et al. (2017). Optimizing cardiac delivery of modified mRNA. *Mol. Ther.* 25 (6), 1306–1315. doi:10.1016/j.ymthe.2017.03.016

Wang, Y., Yu, X., Baker, C., Murphy, W. L., and McDevitt, T. C. (2016). Mineral particles modulate osteo-chondrogenic differentiation of embryonic stem cell aggregates. *Acta biomater.* 29, 42–51. doi:10.1016/j.actbio.2015.10.039

Ward, H., Whitaker, M., Flower, B., Tang, S. N., Atchison, C., Darzi, A., et al. (2022). Population antibody responses following COVID-19 vaccination in 212,102 individuals. *Nat. Commun.* 13 (1), 907. doi:10.1038/s41467-022-28527-x

Watson-Levings, R. S., Palmer, G. D., Levings, P. P., Dacanay, E. A., Evans, C. H., and Ghivizzani, S. C. (2022). Gene therapy in orthopaedics: progress and challenges in pre-clinical development and translation. *Front. Bioeng. Biotechnol.* 10, 901317. doi:10.3389/fbioe.2022.901317

Weiss, R. J., Montgomery, S. M., Ehlin, A., Al Dabbagh, Z., Stark, A., and Jansson, K. A. (2008). Decreasing incidence of tibial shaft fractures between 1998 and 2004: information based on 10,627 Swedish inpatients. *Acta Orthop.* 79 (4), 526–533. doi:10.1080/17453670710015535

White, A. P., Vaccaro, A. R., Hall, J. A., Whang, P. G., Friel, L., Brian, C., et al. (2007). Clinical applications of BMP-7/OP-1 in fractures, nonunions and spinal fusion. *Int. Orthop.* 31, 735–741. doi:10.1007/s00264-007-0422-x

Wong, S. A., Hu, D., Shao, T., Niemi, E., Barruet, E., Morales, B. M., et al. (2020). Beta-catenin signaling regulates cell fate decisions at the transition zone of the chondro-osseous junction during fracture healing. *bioRxiv*. doi:10.1101/2020.03.11.986141

Yu, X., and Murphy, W. L. (2014). 3-D scaffold platform for optimized non-viral transfection of multipotent stem cells. *J. Mater Chem. B* 2 (46), 8186–8193. doi:10.1039/c4tb00957f

Zhang, C., Cho, K., Huang, Y., Lyons, J. P., Zhou, X., Sinha, K., et al. (2008). Inhibition of Wnt signaling by the osteoblast-specific transcription factor Osterix. *Proc. Natl. Acad. Sci.* 105 (19), 6936–6941. doi:10.1073/pnas.0710831105

Zhang, W., De La Vega, Rodolfo, E., Coenen, M. J., Müller, Sebastian, A., et al. (2019). An improved, chemically modified RNA encoding BMP-2 enhances osteogenesis *in vitro* and *in vivo*. *Tissue Eng. Part A* 25 (1-2), 131–144. doi:10.1089/ten.tea.2018.0112

Zohra, F. T., Chowdhury, E. H., Tada, S., Hoshiba, T., and Akaike, T. (2007). Effective delivery with enhanced translational activity synergistically accelerates mRNA-based transfection. *Biochem. Biophys. Res. Commun.* 358 (1), 373–378. doi:10.1016/j.bbrc.2007.04.059

frontiers | Frontiers in Bioengineering and Biotechnology

TYPE Original Research
PUBLISHED 10 January 2024
DOI 10.3389/fbioe.2023.1339912

OPEN ACCESS

EDITED BY
Xiaoxiao Cai,
Sichuan University, China

REVIEWED BY
Zhule Wang,
Radboud University Medical Centre, Netherlands
Xin Li,
The University of Hong Kong, Hong Kong SAR, China

*CORRESPONDENCE
Ya Shen,
yashen@dentistry.ubc.ca
Jian Yu,
yujiandoctor@whu.edu.cn

†These authors have contributed equally to this work and share first authorship

RECEIVED 17 November 2023
ACCEPTED 29 December 2023
PUBLISHED 10 January 2024

CITATION
Wang D, Yue Y, Liu H, Zhang T, Haney EF, Hancock REW, Yu J and Shen Y (2024), Antibiofilm peptides enhance the corrosion resistance of titanium in the presence of *Streptococcus mutans*.
Front. Bioeng. Biotechnol. 11:1339912.
doi: 10.3389/fbioe.2023.1339912

Antibiofilm peptides enhance the corrosion resistance of titanium in the presence of *Streptococcus mutans*

Dan Wang[1,2†], Yingying Yue[3†], He Liu[2], Tian Zhang[4], Evan F. Haney[5], Robert E. W. Hancock[5], Jian Yu[2,6*] and Ya Shen[2*]

[1]Department of Stomatology, Tongji Hospital, Tongji Medical College, Huazhong University of Science and Technology, Wuhan, China, [2]Division of Endodontics, Department of Oral Biological and Medical Sciences, Faculty of Dentistry, University of British Columbia, Vancouver, BC, Canada, [3]Liaoning Institute of Science and Technology, Benxi, China, [4]School of Medicine, Vanderbilt University, Nashville, TN, United States, [5]Centre for Microbial Diseases and Immunity Research, Department of Microbiology and Immunology, University of British Columbia, Vancouver, BC, Canada, [6]State Key Laboratory of Oral and Maxillofacial Reconstruction and Regeneration, Key Laboratory of Oral Biomedicine Ministry of Education, Hubei Key Laboratory of Stomatology, School and Hospital of Stomatology, Wuhan University, Wuhan, China

Titanium alloys have gained popularity in implant dentistry for the restoration of missing teeth and related hard tissues because of their biocompatibility and enhanced strength. However, titanium corrosion and infection caused by microbial biofilms remains a significant clinical challenge leading to implant failure. This study aimed to evaluate the effectiveness of antibiofilm peptides 1018 and DJK-5 on the corrosion resistance of titanium in the presence of *Streptococcus mutans*. Commercially pure titanium disks were prepared and used to form biofilms. The disks were randomly assigned to different treatment groups (exposed to *S. mutans* supplied with sucrose) including a positive control with untreated biofilms, peptides 1018 or DJK-5 at concentrations of 5 μg/mL or 10 μg/mL, and a negative control with no *S. mutans*. Dynamic biofilm growth and pH variation of all disks were measured after one or two treatment periods of 48 h. After incubation, the dead bacterial proportion, surface morphology, and electrochemical behaviors of the disks were determined. The results showed that peptides 1018 and DJK-5 exhibited significantly higher dead bacterial proportions than the positive control group in a concentration dependent manner ($p < 0.01$), as well as far less defects in microstructure. DJK-5 at 10 μg/mL killed 84.82% of biofilms and inhibited biofilm growth, preventing acidification due to *S. mutans* and maintaining a neutral pH. Potential polarization and electrochemical impedance spectroscopy data revealed that both peptides significantly reduced the corrosion and passive currents on titanium compared to titanium surfaces with untreated biofilms, and increased the resistance of the passive film ($p < 0.05$), with 10 μg/mL of DJK-5 achieving the greatest effect. These findings demonstrated that antibiofilm peptides are effective in promoting corrosion resistance of titanium against *S. mutans*, suggesting a promising strategy to enhance the stability of dental implants by endowing them with antibiofilm and anticorrosion properties.

KEYWORDS

biofilm, corrosion, implant, peptide, titanium

1 Introduction

On account of its excellent biocompatibility, mechanical strength, and low modulus of elasticity, titanium has been extensively applied in implant dentistry for the restoration of missing teeth and hard tissues in recent decades (López-Píriz et al., 2019). However, oral bacteria from dental tissue inflammatory sites can adhere to any surface of materials placed in the oral cavity, including titanium. As a result, bacterial biofilm formation on titanium remains a significant clinical challenge, leading to peri-implantitis and the failure of dental implantation (Daubert and Weinstein, 2019; Dhaliwal et al., 2021; Siddiqui et al., 2022). When exposed to fermentable carbohydrates, acid-producing bacteria within biofilms, such as *Streptococcus mutans*, can generate a low pH microenvironment via bacterial metabolism, and electrochemical circuits via a potential difference (Pitts et al., 2017; Yu et al., 2022). This facilitates the deterioration of protective passive oxide film of titanium via a bio-corrosion process, and the demineralization of dental hard tissues (Prestat and Thierry, 2021; Weller et al., 2022). Titanium corrosion is likely to result in the release of titanium ions, causing an inflammatory reaction in the surrounding tissues, which is regarded as another critical risk factor for implant failure (Curtin and Wang, 2017; Prestat and Thierry, 2021; Alhamad et al., 2023). Accordingly, effective strategies are necessary to improve the antibacterial ability and corrosion resistance of titanium, thereby prolonging its stability and service life.

Controlling the inflammation process is the main purpose and principle for the treatment of titanium corrosion and peri-implant diseases. To address this issue, either surgical or nonsurgical approaches are generally employed in clinical practice (Hasan et al., 2022). Noninvasive strategies provide nonsurgical therapy with enormous potential for the treatment of implant-associated infections. However, owing to implant design, it is unlikely to completely remove the biofilms by nonsurgical mechanical therapy alone (Renvert et al., 2008). The adjunctive application of antimicrobials, including chemical agents and antibiotics, is therefore considered a promising strategy to alleviate microbial burden (Patil et al., 2022; López-Valverde et al., 2023). The past few years have witnessed a variety of antimicrobial agents for use in implant disinfection (Malheiros et al., 2023). Nevertheless, due to heterogeneous microbial community organization, as well as existing extracellular polymeric substances and differentiated gene expression, dental biofilms are recalcitrant to most antibiotics and difficult to treat (Kim et al., 2014; Wang et al., 2015). In this regard, microbial overgrowth is likely to increase the corrosion risk of titanium and affect the homeostasis of normal oral flora.

Recent studies have suggested that cationic antimicrobial peptides (host defense peptides) are effective as potential alternatives in treating biofilm-associated infections (Gera et al., 2022; Shao et al., 2023). By specifically targeting microbial biofilms with these peptides, pre-existing biofilms can be dissolved and biofilm formation can be prevented (de la Fuente-Núñez et al., 2012). Their unique additional ability to modulate the immune system contributes significantly to microbial killing and reducing local inflammation (Mansour et al., 2014). Recently, broad-spectrum antibiofilm peptides 1018 and DJK-5 (Supplementary Figure S1) have been shown to act by promoting guanosine tetraphosphate (ppGpp) degradation, which is crucial for biofilm growth (de la Fuente-Núñez et al., 2014; de la Fuente-Núñez et al., 2015). While peptide 1018 comprises natural L-amino acids, peptide DJK-5 contains D-amino acids that alter the peptide stereochemistry and confers proteolytic stability (de la Fuente-Núñez et al., 2015). Both oral single-species and multispecies biofilms formed on dental substrates have been shown to be killed by these two peptides in our previous investigations (Wang et al., 2018; Huang et al., 2019). These advantages imply that antibiofilm peptides might be promising for application in preventing titanium corrosion caused by microbial biofilms. No published data has reported the effects of peptides 1018 and DJK-5 on the corrosion behaviors of titanium against biofilms at present.

The objective of this study was to evaluate the effectiveness of antibiofilm peptides 1018 and DJK-5 on the corrosion resistance of titanium exposed to *S. mutans*. The null hypotheses were that (i) peptides 1018 and DJK-5 cannot kill *S. mutans* biofilm on titanium surfaces in one or two 48-h periods; (ii) peptides 1018 and DJK-5 cannot enhance the corrosion resistance of titanium in one or two 48-h periods; and (iii) there is no difference in the efficacy of peptides 1018 and DJK-5 on biofilm killing and corrosion resistance.

2 Materials and methods

2.1 Preparation of titanium disks

Commercial pure titanium (cp-Ti, grade 2, Baoji Titanium Industry Co., Ltd., Baoji, China) was used to prepare titanium disks with a diameter of 12 mm and a thickness of 1.5 mm. All disks were uniformly polished with silicon carbide sandpapers ranging from 400 to 1,200 grit in sequence and then cleaned by ultrasonic bathing in deionized water, acetone, 75% ethanol, and deionized water for 10 min, respectively. After drying overnight at 60°C, these disks were sterilized by UV light for 6 h on each side and placed in sterile 24-well plates.

2.2 Energy dispersive X-ray spectroscopy (EDS) analysis of titanium disks

The elemental analysis of titanium disks was detected by EDS (Helios Nanolab 650, FEI, Eindhoven, Netherlands) to inspect their purity. Three titanium disks were randomly selected, and three random areas on each disk were recorded and measured by EDS at a voltage of 10 kV.

2.3 Synthesis of the peptides

As described in previous studies (Yang et al., 2019; Hu et al., 2023), peptides DJK-5 and 1018 were synthesized in the method of solid-phase 9-fluorenylmethoxy carbonyl (Fmoc) chemistry by CPC Scientific (Sunnyvale, United States). The synthesized peptides were identified by amino acid analysis, and reverse-phase high-performance liquid chromatography was utilized to achieve at least 95% purity. One hundred μg/mL stock solutions of both peptides were then prepared by dissolving lyophilized powders in sterile deionized water and keeping them sterile over time.

2.4 Bacterial strain and culture condition

S. mutans (ATCC 25175) was grown anaerobically on plates with 32 g/L of brain-heart infusion (BHI) agar (Becton-Dickinson, Sparks, United States) at 37°C and subcultured on a new agar plate for 48–72 h. After that, the bacteria were picked up and transferred into BHI broth (Becton-Dickinson, Sparks, United States) for 24 h of incubation at 37°C. Amplified bacteria were harvested by centrifugation (5,000 rpm) at 4°C for 5 min and washed twice with PBS. The collected *S. mutans* were suspended in BHI to achieve an optical density (OD) at 0.05 as determined by a microplate reader (ELx808, BioTek, Winooski, United States) at the wavelength of 405 nm.

2.5 Biofilm formation on titanium disks

Titanium disks were placed in 24-well plates (one disk in each well) and randomly distributed into different groups in accordance with the following treatments: 1) the positive control (untreated biofilm) group: bacterial suspension (200 μL) and BHI (1,800 μL) containing sucrose (222.22 g/L) were added to each well; 2) 5 μg/mL of peptide treatment groups (DJK-5 or 1018): peptide stock solution (100 μL), bacterial suspension (200 μL), and BHI (1,700 μL) containing sucrose (235.29 g/L) were added to each well; 3) 10 μg/mL of peptide treatment groups (DJK-5 or 1018): peptide stock solution (200 μL), bacterial suspension (200 μL), and BHI (1,600 μL) containing sucrose (250 g/L) were added to each well; and 4) the negative control group: each well only added with BHI (2,000 μL) containing sucrose (200 g/L). Each group of bacteria received the same amount of sucrose (200 g/L as the final concentration (Souza et al., 2010; Souza et al., 2013).

Two different incubation times were tested separately for each experiment condition. In the 48 h group, titanium disks were removed from each well after 48 h and rinsed three times with sterile deionized water, followed by a 5-min ultrasonic bath in 100% ethanol and air drying. In the two 48-h treatments group, the consumed solution was removed after incubation for the first 48 h, and the corresponding fresh peptide solution and BHI medium were supplied for another 48 h. Following that, titanium disks were rinsed and dried as previously stated.

2.6 Dynamic monitoring of biofilm development and pH value

To monitor the dynamic growth of *S. mutans* biofilms on titanium disks treated with or without peptides DJK-5 and 1018, biofilms were detached at designated time intervals (0, 2, 4, 6, 8, 10, 12, 18, 24, 30, 36, 48, 72, and 96 h) and dispersed by pipetting to obtain an even bacterial suspension. Subsequently, 150 μL of the suspension was aspirated into 96-well plates and read by the microplate reader at OD_{405nm}. Three parallel wells were replicated at each time interval for each group. Then, the pH of the remaining suspension in each well was measured by a pH Meter (Accumet Basic AB 15 Plus, Thermo Fisher Scientific, Waltham, United States). For each group, three parallel wells were tested and recorded.

2.7 Determination of dead bacterial proportion

After incubation for one or two 48-h periods, titanium disks coated with biofilms were gently washed with PBS and stained with a fresh mixture of SYTO-9 and propidium iodide (BacLight live/dead bacterial viability kit, Molecular Probes, Eugene, United States) based on the manufacturer's instruction. And observed by confocal laser scanning microscopy (CLSM, FV10i-LIV, Olympus, Canada) (Yu et al., 2021; Liu et al., 2022). The wavelength of excitation/emission light detected for SYTO-9 and propidium iodide was set 480/500 nm and 490/635 nm, respectively. For each group, three disks were selected, and five areas for each disk were scanned from the bottom to the top of the biofilm with a 2 μm step. An Imaris 7.2 software (Bitplane, Switzerland) was employed to convert the two-dimension images into three-dimensional volume stacks. The obtained green and red fluorescence intensity was analyzed as the total volume of live and dead bacteria, and the dead bacteria proportion was calculated using red fluorescence in relation to total fluorescence (green + red) (Guo et al., 2021).

2.8 Scanning electron microscopy (SEM) of corrosion characters

The characteristics of corrosive titanium surfaces exposed to *S. mutans* (treated with or without peptides DJK-5 and 1018) were inspected through SEM (SU3500, Hitachi, Toronto, Canada). After one or two 48-h periods of incubation, titanium disks were taken out from the wells and washed three times using sterile deionized water to detach the biofilms before being ultrasonically cleaned for 5 min in sterile deionized water and 100% ethanol, respectively. After drying in the air, randomly selected areas from SEM images (at ×3,000) were captured at 3 kV for each disk.

2.9 Electrochemical tests in artificial saliva

The electrochemical experiments were carried out to investigate the effects of DJK-5 and 1018 on the corrosion resistance of titanium after exposure to *S. mutans*. A Princeton Applied Research (PAR) VersaSTAT 4 potentiostat (AMETEK, Berwyn, United States) was employed in this study. The electrochemical setup consisted of a conventional three-electrode cell with a platinum net as a counter electrode (CE) and an Ag/AgCl [(KCl) = 4 M] electrode as a reference electrode (RE) introduced into the cell through a Luggin probe. All potential values are used according to the Ag/AgCl reference electrode (0.197 V vs. SHE). The working electrode (WE) was set in a special mould with an exposed area of 1 cm^2 as the working area. The schematic diagram of the mould and the electrochemical setup are presented in Figures 1A, B. The biofilm-coated disks were connected to the PAR via a copper sheet. The solutions were purged with nitrogen for at least 30 min before introducing the working electrode, and the purging lasted throughout the experiment. Each test was repeated at least three times to ensure reproducibility.

The electrochemical tests were performed in a modified Fusayama's artificial saliva solution (0.4 g/L NaCl, 0.4 g/L

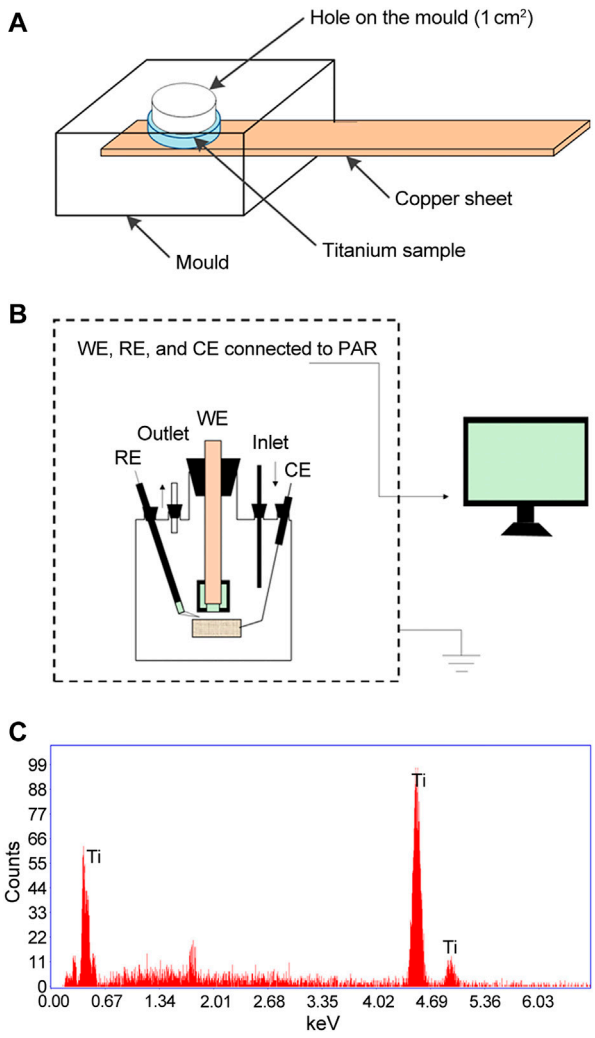

FIGURE 1
Schematic diagrams of **(A)** The mould and **(B)** The electrochemical setup used in the present study. **(C)** EDS analysis of titanium disks used prior to corrosion exposure. CE, counter electrode; RE, reference electrode; WE, working electrode.

KCl, 0.795 g/L $CaCl_2{\cdot}2H_2O$, 0.005 g/L $Na_2S{\cdot}9H_2O$, 0.69 g/L $NaH_2PO4{\cdot}H_2O$, 1.0 g/L urea, pH = 6.0) at 37°C ± 0.5°C as previously reported (Souza et al., 2013; Fukushima et al., 2018). The potential dynamic polarization (PDP) curves and electrochemical impedance spectroscopy (EIS) tests were determined to evaluate the corrosion resistance of titanium in the Fusayama's artificial saliva after different treatments (Zhang et al., 2007). Prior to the tests, the open circuit potential (OCP) measurements were carried out for at least 1 h until it reached a quasi-steady state value (deviation in OCP from its 5 min value within 2%). PDP measurements were conducted from −0.5 V vs. OCP to 1.5 V vs. OCP at a scan rate of 1 mV/s. The electrochemical parameters, including the corrosion potential (E_{corr}), corrosion current density (I_{corr}), pitting potential (E_{pit}), and passive current density ($I_{passive}$), were determined. EIS measurements were conducted at OCP with a sinusoidal potential wave as a disturbing signal. The amplitude of sinusoidal potential was 10 mV, and the scan frequency ranged from 0.01 to 105 Hz. The EIS results were analyzed with ZSimpWin software (AMETEK, Berwyn, United States). All experiments were performed with at least three independent tests.

2.10 Statistical analysis

All data obtained were presented as means ± standard deviations for statistical analysis. One-way analysis of variance (ANOVA) was performed by SPSS 22.0 software (IBM, Armonk, United States), and *post hoc* Fisher's LSD multiple comparison tests were then examined. The significance level was set at $p < 0.05$.

3 Results

3.1 EDS analysis

The elemental content of titanium disks used in this study was examined by EDS. As shown in Figure 1C, almost all of the typical titanium element peaks were detected. The results of the EDS analysis revealed that titanium had a purity of more than 99.9%, as measured by the atomic percentage of the Ti element.

3.2 Dynamic determination of biofilm development and pH value

The dynamic growth of *S. mutans* biofilm on titanium disks in each group was plotted in Figure 2A. In the first 2 h, there was no discernible increase in bacteria. Then, *S. mutans* proliferation in the positive control group accelerated and reached ~9-fold the initial level after 12 h, followed by a gradual increase up to 48 h and then levels plateaued. *S. mutans* exposed to 5 μg/mL of peptide 1018 or DJK-5 showed similar but delayed kinetics with a longer lag phase, beginning to thrive after 4 h and lower growth by 6–7 fold in the first 8 h. Bacterial growth was stabilized between 12 and 48 h and reached a plateau within 96 h. Overall, there were more bacteria in the 1018 group (5 μg/mL) than in the DJK-5 group (5 μg/mL) at each time interval. The kinetics of growth was much more dramatically affected at 10 μg/mL of peptide. Treatment with 10 μg/mL of 1018 led to much slower proliferation of *S. mutans* in the group between 12 and 48 h, but its eventual optical density after 48 h value was higher than in the 5 μg/mL of DJK-5 group. The biofilm development of *S. mutans* exposed to 10 μg/mL of DJK-5 was substantially and effectively inhibited during the first 72-h, but increased slightly by 96 h.

S. mutans is known acidify the medium. The pH of the medium in the untreated *S. mutans* control decreased to around 4 within 18 h, due to biofilm growth (Figure 2B). The decrease in pH values in each group at the designated time intervals corresponded to the increase in OD values. Specifically, in the positive control group, pH values dropped rapidly from 7.0 at 0 h to 4.48 within 10 h, then to 4.02 by 18 h, and then remained stable. The pH values of the medium with 5 μg/mL of 1018 and DJK-5 added revealed the same declining trend. They maintained a slower decline in pH than the

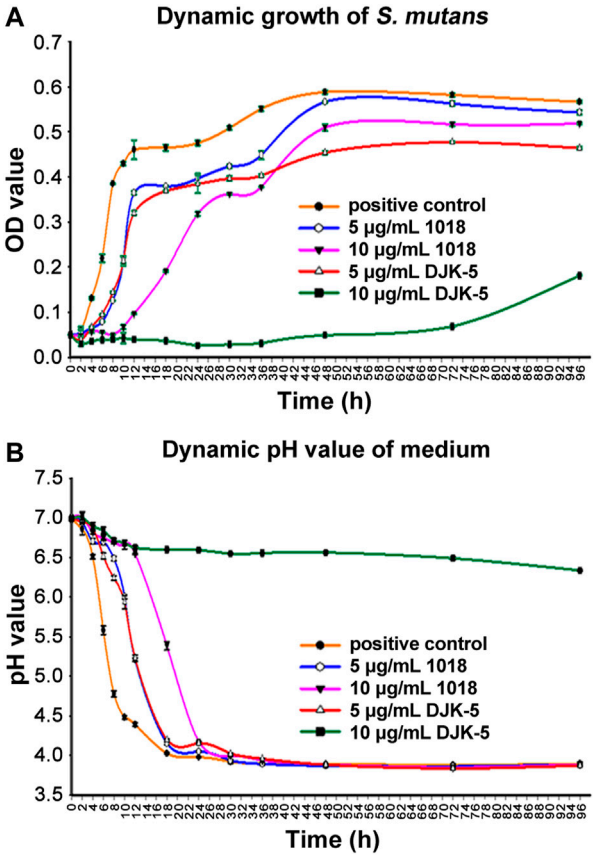

FIGURE 2
The dynamic determination of *S. mutans* in BHI medium supplemented with sucrose (200 g/L) from 0 to 96 h for each group: **(A)** The dynamic growth of *S. mutans* biofilms on titanium disks as measured by optical density at 405 nm; and **(B)** The dynamic variation of the pH of the culture medium. Data are shown as means ± standard deviations (no statistical analysis was carried out).

positive control group but still reached a pH of around 4 by 18 h. Ten μg/mL of 1018 delayed the pH drop for the first 12 h, but it still went down to 4.17 at 24 h. Remarkably, 10 μg/mL of DJK-5 was able to maintain the pH around neutrality with only a 0.5 unit decrease during the 96-h incubation period.

3.3 Biofilm killing

The dead bacterial proportions and live/dead bacteria CLSM images of *S. mutans* biofilms on titanium surfaces after incubation with or without peptides for one or two 48-h periods are shown in Figures 3A, B. Both peptides 1018 and DJK-5 (at 5 and 10 μg/mL) killed the majority of bacteria over 48 h (from 53.95% to 84.82%) with significant differences compared to the positive control group ($p < 0.01$), and the most bacterial killing was found in the 10 μg/mL of DJK-5 group. Peptide DJK-5 was more effective in killing *S. mutans* than peptide 1018 at the same concentration, and higher concentrations (10 μg/mL) of peptide led to a higher proportion of dead bacteria than lower concentrations (5 μg/mL) did ($p < 0.05$). Except for DJK-5 at 10 μg/mL, more *S. mutans* were killed in the peptide-treated groups after two 48-h treatments than a single 48-h treatment. Ten μg/mL of DJK-5 (48 + 48 h) induced approximately 73.88% of bacterial cell death and had a higher killing proportion than the 5 μg/mL of DJK-5 and the positive control groups ($p < 0.05$).

3.4 SEM of corrosive titanium surfaces

The SEM surface microstructures of titanium disks (after biofilm removal) from each group incubated with *S. mutans* for two 48-h treatments are shown in Figure 4. In the negative control group (no bacteria), the disks retained their smooth and even surface morphology, with the presence of longitudinal grooves as a consequence of the polishing process. In the positive control group, the titanium surface colonized by *S. mutans* from the beginning of immersion was rich in irregular micro-pits of various sizes and shapes along the longitudinal grooves, as indicated by red arrows in SEM images. In the case of titanium disks exposed to bacteria and 5 μg/mL of peptides 1018 and DJK-5, corrosion pits on their surfaces appeared to decrease. Ten μg/mL of peptide DJK-5 had the greatest ability to prevent material degradation, followed by 10 μg/mL of peptide 1018, with only a few visible randomly-scattered micro-pits.

3.5 Electrochemical results of PDP curves

To assess electrochemical corrosion resistance, PDP curves of titanium were examined in artificial saliva at 37°C after incubation with bacteria and peptides. As shown in Figures 5A, B, titanium disks demonstrated moderate corrosion resistance in the test environment because a typical passive plateau of 10^{-7} A·cm^{-2} was observed, followed by the $I_{passive}$ ranging from 10^{-6} to 10^{-7} A·cm^{-2}. This phenomenon reflected that a relatively protective passive film of titanium dioxide remained on the disks. The E_{corr} and I_{corr} in the active region were measured using the Tafel extension method. The passive film was broken down as the applied potential was increased above 10^{-6} A·cm^{-2}, leading to a sharp increase in the current density. The specific electrochemical data of PDP are depicted in Figures 5C–F. The E_{corr} of the positive control group was lower than that of the other groups ($p < 0.05$), whereas the I_{corr} of the positive control group was higher than that of the other groups ($p < 0.05$). With the addition of peptides DJK-5 and 1018, the E_{corr} shifted to a less negative value while the E_{pit} showed significantly higher values than the positive control group ($p < 0.05$), and the I_{corr} and $I_{passive}$ were significantly lower ($p < 0.05$).

After 48 h, the I_{corr} and $I_{passive}$ had increased in the following order: negative control <10 μg/mL DJK-5 < 10 μg/mL 1018 < 5 μg/mL 1018 < 5 μg/mL DJK-5 < positive control. The OCP and E_{pit} decreased in the following order: negative control >10 μg/mL DJK-5 > 10 μg/mL 1018 > 5 μg/mL DJK-5 > 5 μg/mL 1018 > positive control. Treatment with 10 μg/mL of peptides 1018 and DJK-5 showed improved corrosion resistance of titanium when compared to 5 μg/mL of these peptides, with 10 μg/mL of DJK-5 achieving the greatest effect. A similar trend was observed for titanium disks after two treatments for 48 h of immersion, and the I_{corr} in each group after two 48-h treatments was lower than those after one treatment, except in the case of the positive control.

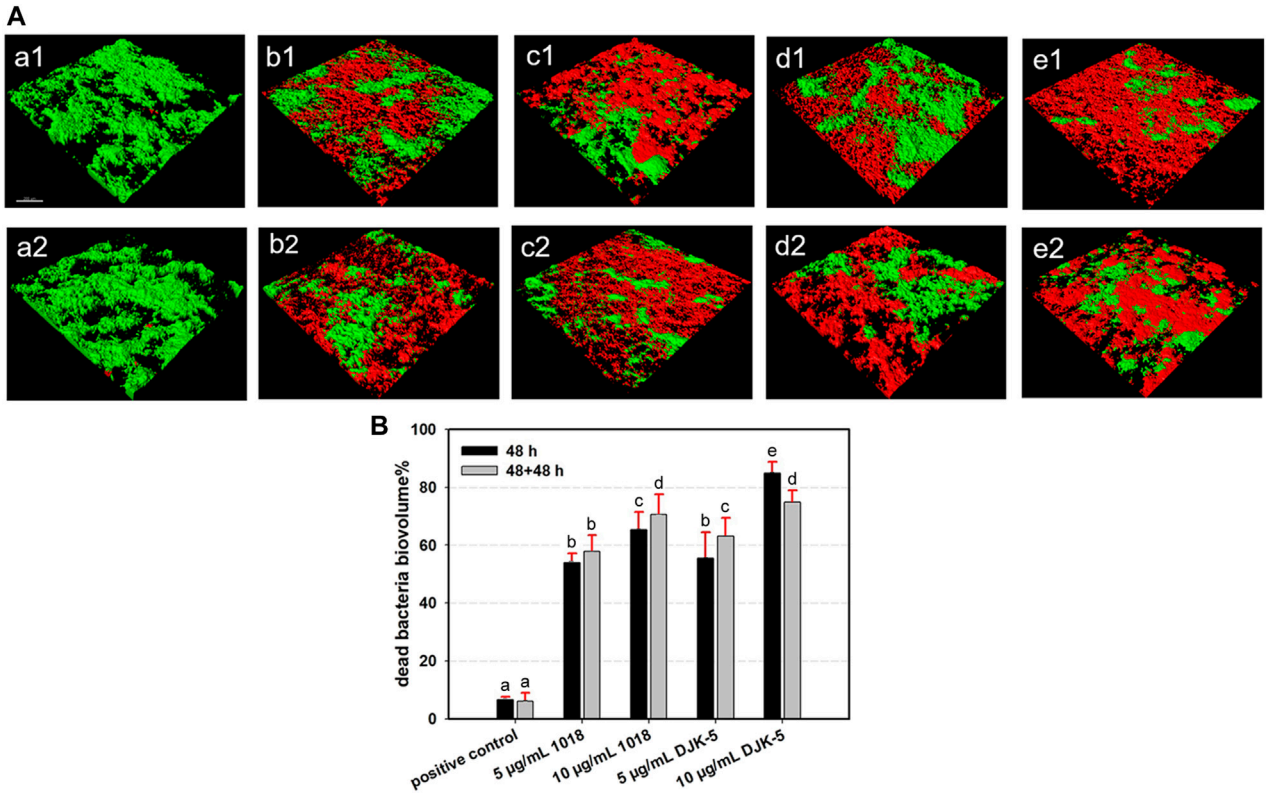

FIGURE 3
(A) Representative CLSM images (green, live bacteria; red, dead bacteria) and **(B)** Dead bacterial biovolume percentages of *S. mutans* biofilms for each group after 48 and 48 + 48 h of incubation. Images of (a1 and a2) positive control, (b1 and b2) 5 μg/mL 1018, (c1 and c2) 10 μg/mL 1018, (d1 and d2) 5 μg/mL DJK-5, and (e1 and e2) 10 μg/mL DJK-5 groups. Images of (a1–e1) 48 h and (a2–e2) 48 + 48 h. Data are shown as means ± standard deviations [groups with the same lowercase letters are not statistically significant ($p > 0.05$)].

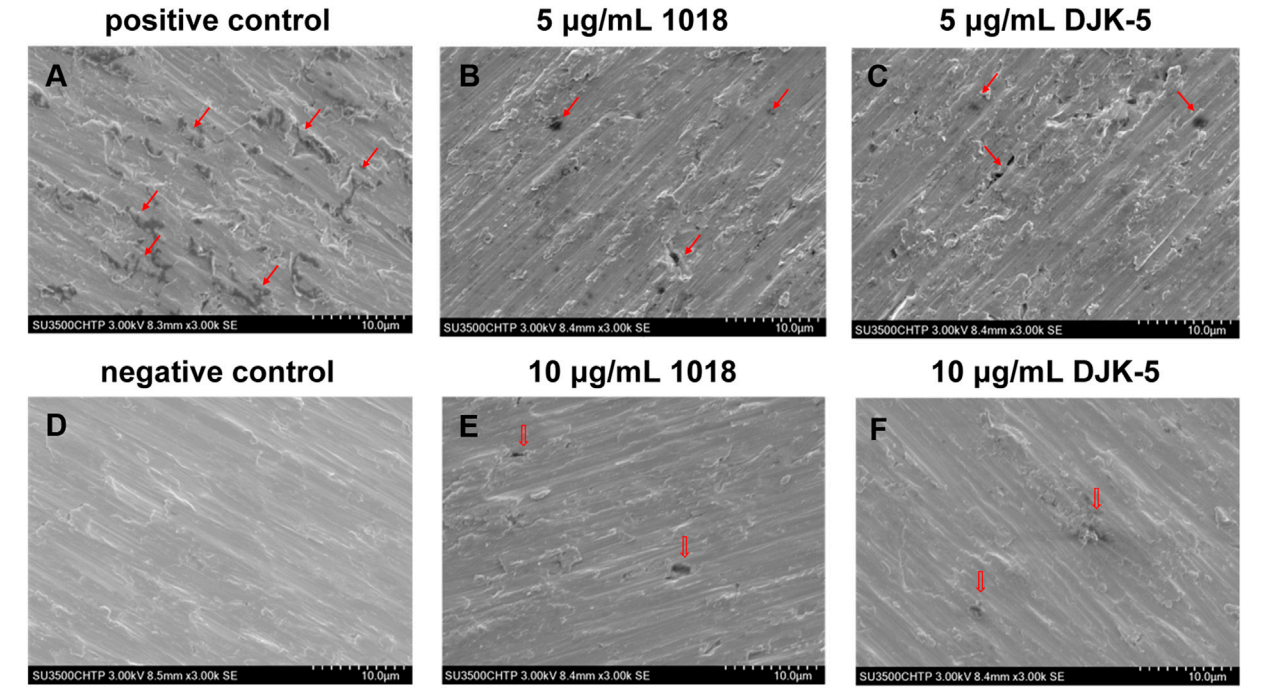

FIGURE 4
SEM images **(A–F)** of corrosion of titanium surfaces exposed to *S. mutans* in BHI medium supplemented with sucrose (200 g/L) for 48 + 48 h from each group (after biofilm removal). Red arrows indicate the corroded areas.

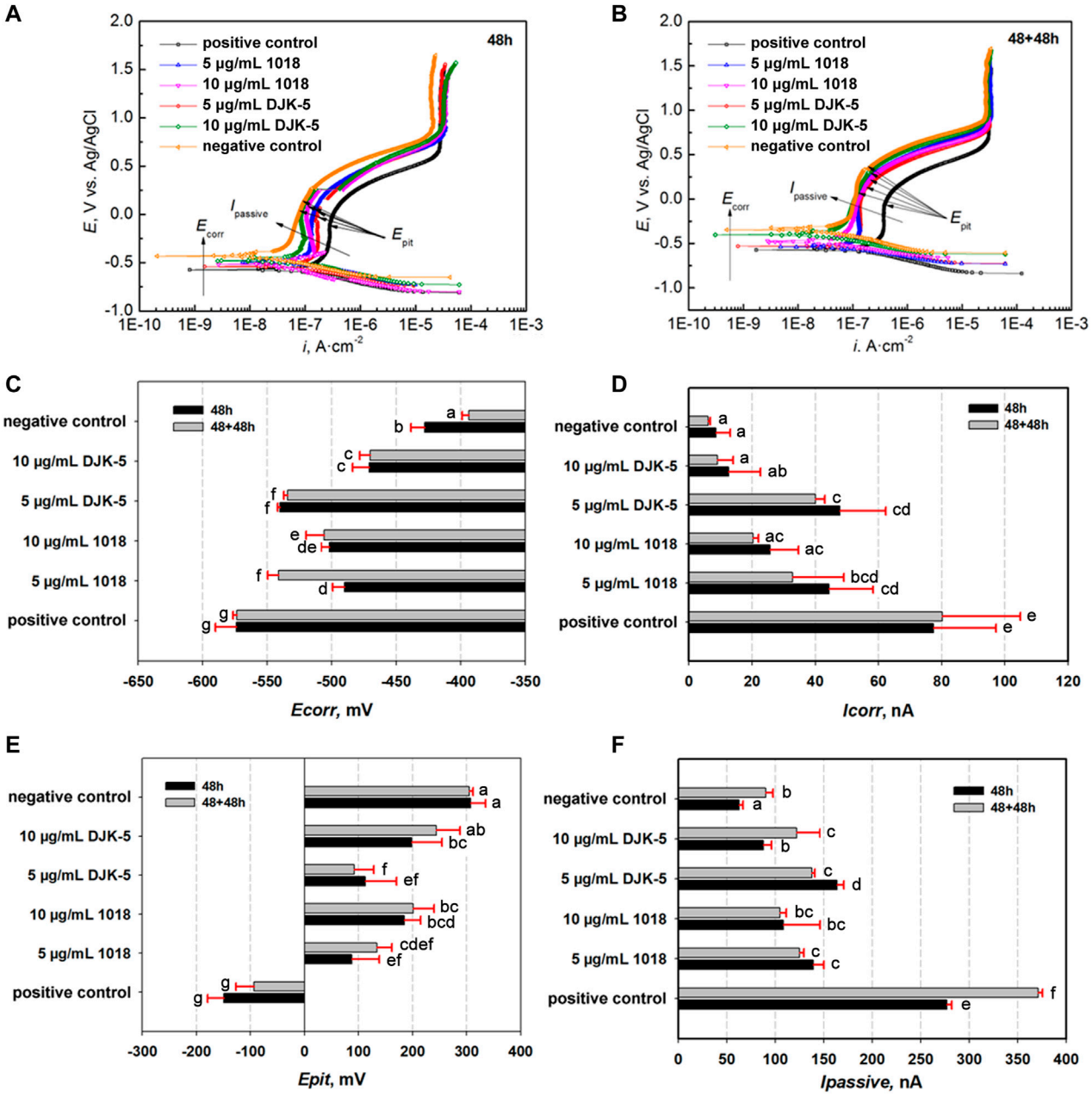

FIGURE 5
Potential dynamic polarization (PDP) curves of titanium disks after exposure to *S. mutans* with or without peptides for **(A)** 48 h and **(B)** 48 + 48 h, as well as **(C–F)** relative electrochemical parameters (E_{corr}, I_{corr}, E_{pit}, and $I_{passive}$). Data are shown as means ± standard deviations [groups with the same lowercase letters are not statistically significant ($p > 0.05$)].

3.6 EIS measurements

The EIS tests were performed to characterize the stability of the passive film on titanium after different treatments, with the Nyquist and Bode plots for each group in artificial saliva at 37°C are shown in Figures 6A–D. The Nyquist plots (Figures 6A, C) revealed a capacitive loop, whereas the Bode plots (Figures 6B, D) revealed only a one-time constant, suggesting that the corrosion process of titanium was controlled by charge transfer. The impedance values were in the order of 10^6 Ω·cm^{-2}, indicating that the titanium was covered by a protective passive film. The most commonly used electrical equivalent circuit (EEC) of titanium's passive film is R_s {Q_{ou} [R_{ou} ($R_{in}Q_{in}$)]}. R_s denotes the solution resistance, Q_{ou} and Q_{in} refer to the constant phase element (Q) of the outer porous film and inner barrier film, respectively, and R_{ou} and R_{in} represent the outer and inner film resistance. The resistance of the passive film (R_T) equals R_{ou} + R_{in}. The corresponding fitting data are listed in Table 1, with chi-square (χ^2) values in the order of 10^{-4}. The fitting curves, fitting results, and experimental data showed great agreement. Thus, the R_s {Q_{ou} [R_{ou} ($R_{in}Q_{in}$)]} of EEC was appropriate to describe the passive film in this study.

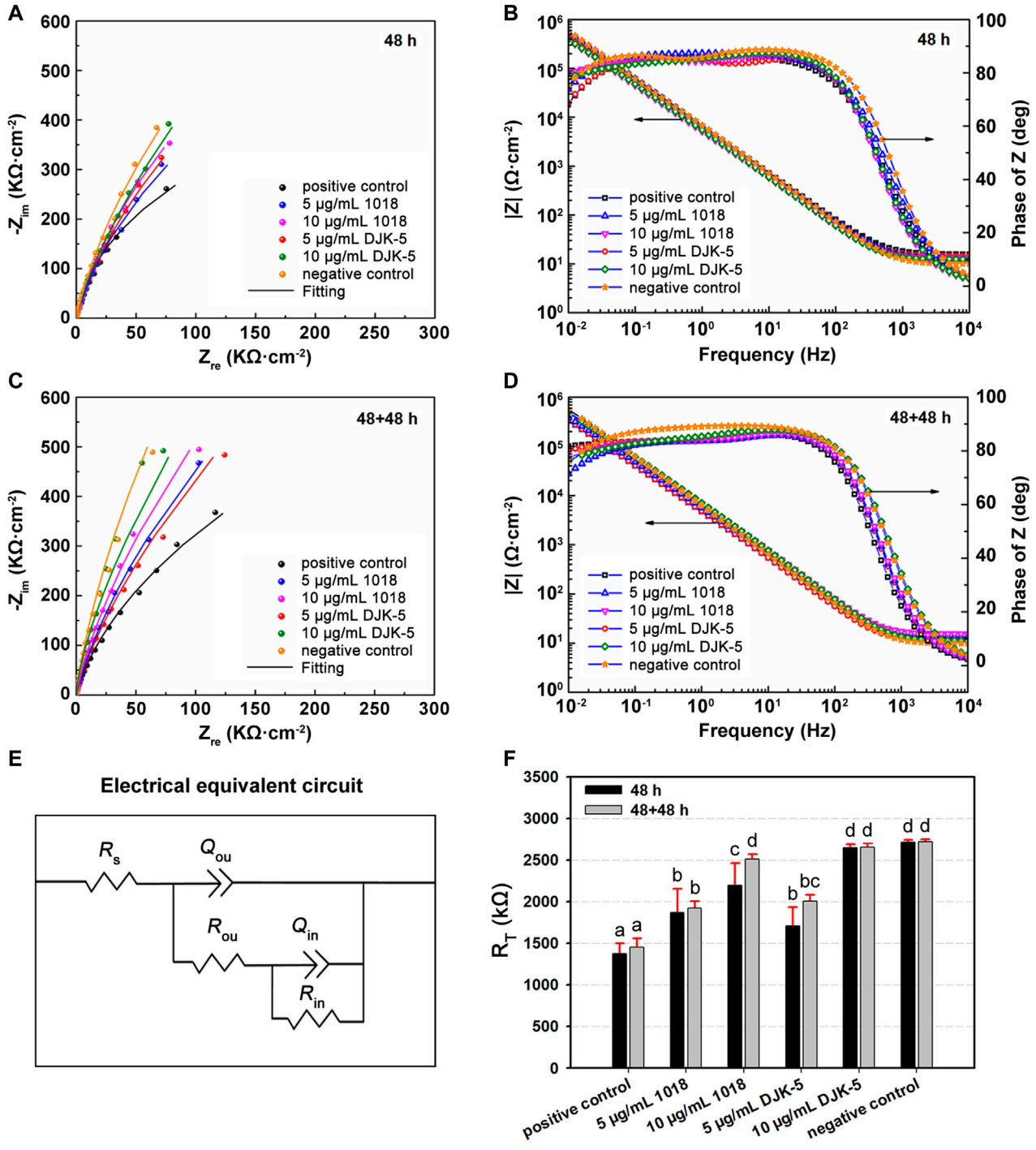

FIGURE 6
(A,C) Nyquist and **(B,D)** Bode plots from EIS measurements for titanium disks in each group after incubation with *S. mutans* for **(A,B)** 48 h and **(C,D)** 48 + 48 h. **(E)** Electrical equivalent circuit used for fitting the impedance data. **(F)** R_T values of titanium disks for each group. Data are shown as means ± standard deviations [groups with the same lowercase letters are not statistically significant ($p > 0.05$)].

Figure 6E exhibits the equivalent circuit fitting the experimental impedance data. The Q represents the non-ideal behavior of the capacitor, and there is a positive correlation between Q and capacitance (C). The capacity was related to the property of the passive film's metal/solution interface based on the following equation: $C = \varepsilon\varepsilon_0 A/d$, where C denotes the capacitance of a film, ε_0 (8.854×10^{-14} F·cm^{-1}) is the vacuum permittivity, ε is the dielectric constant, and A and d are the area and thickness of the film, respectively. According to Table 1, Q_{ou} is one order of magnitude greater than Q_{in}, and R_{ou} is two orders of magnitude less than R_{in}. The ε of the outer layer was estimated to be greater than that of the inner layer, indicating that the inner layer is more compact and protective. The corrosion resistance of the passive film (R_T) for each group is manifested in Figure 6F. The R_T values of

TABLE 1 Means and (standard deviations) of electrochemical parameters determined by electrical equivalent circuit models for titanium disks from each group.

Time	Groups	R_s ($\Omega \cdot cm^2$)	$Q_{ou} \times 10^5$ ($s^{-n} \cdot \Omega^{-1} \cdot cm^{-2}$)	n_1	R_{ou} ($k\Omega \cdot cm^2$)	$Q_{in} \times 10^5$ ($s^{-n} \cdot \Omega^{-1} \cdot cm^{-2}$)	n_2	R_{in} ($k\Omega \cdot cm^2$)	R_T ($k\Omega \cdot cm^2$)
48 h	Positive control	12.15 ± 3.85	2.73 ± 0.56	1.00 ± 0.00	36.38 ± 20.92	0.72 ± 0.13	0.84 ± 0.13	1,339.67 ± 141.29	1,376.05 ± 122.71
	5 μg/mL 1018	12.04 ± 0.88	2.55 ± 0.34	1.00 ± 0.00	24.14 ± 14.53	2.42 ± 2.77	0.89 ± 0.07	1,847.00 ± 281.09	1,871.14 ± 286.18
	10 μg/mL 1018	10.10 ± 0.73	2.57 ± 0.34	1.00 ± 0.00	34.51 ± 31.23	0.69 ± 0.26	0.88 ± 0.07	2,163.67 ± 242.44	2,198.18 ± 266.59
	5 μg/mL DJK-5	13.05 ± 3.85	2.55 ± 0.67	1.00 ± 0.00	19.97 ± 14.02	0.82 ± 0.18	0.84 ± 0.03	1,689.67 ± 223.25	1,709.64 ± 227.40
	10 μg/mL DJK-5	11.51 ± 0.81	2.39 ± 0.27	0.99 ± 0.01	20.51 ± 14.96	0.84 ± 0.30	0.86 ± 0.11	2,627.00 ± 37.64	2,647.51 ± 39.83
	Negative control	15.27 ± 1.92	3.28 ± 0.75	1.00 ± 0.00	17.26 ± 12.87	1.15 ± 0.59	0.80 ± 0.03	2,698.33 ± 22.55	2,715.59 ± 30.34
48 + 48 h	Positive control	11.72 ± 2.95	2.30 ± 0.08	1.00 ± 0.00	18.24 ± 10.10	0.73 ± 0.14	0.84 ± 0.03	1,436.67 ± 106.93	1,454.91 ± 103.58
	5 μg/mL 1018	8.77 ± 2.17	2.83 ± 0.65	1.00 ± 0.00	31.66 ± 7.22	0.84 ± 0.25	0.83 ± 0.04	1,893.33 ± 77.67	1,924.99 ± 81.08
	10 μg/mL 1018	10.13 ± 3.01	2.39 ± 0.44	0.97 ± 0.00	22.15 ± 22.85	1.02 ± 0.50	0.85 ± 0.02	2,486.67 ± 80.83	2,508.82 ± 60.88
	5 μg/mL DJK-5	11.62 ± 3.45	2.67 ± 0.54	1.00 ± 0.00	21.15 ± 4.44	0.85 ± 0.19	0.83 ± 0.05	1,983.33 ± 76.38	2,004.48 ± 76.40
	10 μg/mL DJK-5	10.39 ± 3.81	2.78 ± 0.67	0.99 ± 0.02	29.71 ± 12.56	0.76 ± 0.41	0.85 ± 0.08	2,622.67 ± 42.44	2,652.37 ± 48.00
	Negative control	14.35 ± 1.76	2.89 ± 0.12	1.00 ± 0.00	16.67 ± 12.51	0.95 ± 0.13	0.80 ± 0.03	2,703.33 ± 25.17	2,720.00 ± 27.40

titanium treated with peptides (in 48 h) were higher than those of the positive control group ($p < 0.05$), demonstrating that 1018 and DJK-5 could prevent *S. mutans* from deteriorating the passive film. Furthermore, the RT values of titanium treated with 10 μg/mL of DJK-5 were close to the negative control group, denoting a significant anticorrosion efficacy. In the case of two 48 h treatments, the R_T of titanium treated with peptides increased slightly. This trend was consistent with the results of PDP experiments.

4 Discussion

In this work, the effects of peptides 1018 and DJK-5 on the biofilm killing and corrosion behaviors of titanium exposed to *S. mutans* were evaluated. The results demonstrated that peptides 1018 and DJK-5 (at 5 and 10 μg/mL) killed the majority of the bacteria (from 53.95% to 84.82%) in one and two 48-h treatments. Ten μg/mL of DJK-5 inhibited *S. mutans* growth the most and kept the pH neutral. Furthermore, the two peptides exhibited less negative $E_{corr,}$ significantly lower I_{corr}, and higher R_T than the positive control after one and two 48-h treatments, with 10 μg/mL of DJK-5 showing the greatest effects. These findings suggest that antibiofilm peptides were effective in improving the corrosion resistance of titanium with biofilm-killing ability. Hence, the null hypotheses have to be rejected.

As an opportunistic bacterium known to facilitate the corrosion of dental implants, *S. mutans* has been extensively selected *in vitro* and *in vivo* studies to evaluate the biofilm formation and electrochemical behaviors of titanium (Souza et al., 2018; Chai et al., 2021; Lu et al., 2022). The growth of *S. mutans* in the positive control group remained stable after 48 h, indicating a mature biofilm characteristic (Costa et al., 2020) (which was used as the observation time point in subsequent experiments), and the bacteria were largely alive after one or two 48-h periods of incubation. As the biofilm develops and the pH rises, the accumulation of microbial metabolic byproducts, including lactic acid, and the acidic environment are expected to trigger titanium corrosion. The colonization of oral microbes in both the early and late stages of SLA titanium surface corrosion has been reported in previous investigations (Rodrigues et al., 2016; Siddiqui et al., 2019). Severe corrosive characteristics, such as discoloration and pitting, were discovered after analyzing these retrieved titanium samples. Apart from acid production, recent studies have suggested that the metabolism of viable microbial cells and oxygen consumption contribute to titanium corrosion as well (Zhang et al., 2013; Fukushima et al., 2014). The non-uniform distribution of oxygen contents generated by reactions between oxygen around microbes and their metabolites most likely creates a local potential difference, and thus electrochemically corrosive properties may appear.

Treatment with peptides 1018 and DJK-5 (at 5 and 10 μg/mL) inhibited *S. mutans* growth and killed the biofilms on the titanium

surface to varying degrees, and DJK-5 (10 μg/mL) displayed the highest ability among all groups to maintain a neutral pH, prevent microbial growth, and induce cell death within biofilms. These results confirm that bacterial growth inhibition and biofilm killing (with pH stabilization) on titanium can be obtained by antimicrobial peptides, implying an effective strategy for preventing biofilm-induced implant infection and corrosion. The mechanism behind this could be elucidated as follows. In general, the integrity or functioning of bacterial cell membranes can be destroyed by positively charged antimicrobial peptides because of the presence of negatively charged bacterial lipids (Bechinger and Gorr, 2017). Both peptides have been shown to be effective against a variety of Gram-negative and Gram-positive bacteria in terms of killing and decomposing preformed biofilms (Pletzer et al., 2016; Pletzer and Hancock, 2016). In addition to the promotion of ppGpp degradation involved in biofilm development, biofilm killing may be enhanced through immune cell activation, autophagy, and apoptosis mediation (Hancock et al., 2016). Interestingly, peptide DJK-5 outperformed peptide 1018 in terms of antibiofilm capability. In this regard, DJK-5 possesses improved *in vitro* biological activities and is less likely to be recognized by host or bacterial proteases during infections, as well as being more resistant to degradation by host proteases (de la Fuente-Núñez et al., 2016). Furthermore, following an extra 48 h of bacterial growth in a medium with 10 μg/mL of DJK-5, the ratio of dead bacteria to total bacteria dropped in comparison to the initial 48 h. This may be due to the fact that the growth of live bacteria might outpace the prolonged bactericidal effect of DJK-5. However, it is encouraging that DJK-5 was able to kill nearly 80% of the bacterial biofilms after 96 h. Even so, future studies are demanded to explore the long-term biofilm killing efficacy of these peptides.

SEM was used to observe the surface morphology of corrosive titanium disks exposed to *S. mutans* and peptides. Irregular micro-pits of varying were manifested along the grooves in the positive control group (contained *S. mutans* without peptides) after 48 + 48 h, which was consistent with the findings of Souza et al. (2018) and Siddiqui et al. (2019). On the contrary, micro-pits decreased on surfaces treated with peptides 1018 and DJK-5, indicating that the addition of peptides had the potential to prevent titanium corrosion. The inhibitory effects with applied potentials was further assessed by PDP curves. Generally, the electrochemical corrosion of titanium alloys can arise from several modes of attack, each with its unique mechanisms (Nyby et al., 2021). Therefore, multiple parameters are available for assessing the salient features of corrosion events, such as E_{corr}, I_{corr}, E_{pit}, and $I_{passive}$. While the passive film slows down the rate of uniform corrosion, it can also accelerate localized corrosion, which is linked to the local breakdown of passive films. The persistence of titanium-based implant may fail as a result of these corrosion mechanisms. The electrochemical data in the positive control group showed the lowest E_{corr} and the highest I_{corr} and $I_{passive}$ among all groups, denoting that the electrochemical properties of titanium can be changed by the grown biofilms. This could be ascribed to the effect of *S. mutans* growth and metabolism at high sucrose concentrations on acid production, which lowers the pH value of the culture medium (Souza et al., 2013; Costa et al., 2021). As a result, the stability of the passive film on titanium deteriorated, and the corrosion and degradation rate of the film in saliva was accelerated. Notably, peptides 1018 and DJK-5 shifted the E_{corr} and E_{pit} in a more positive direction and displayed significantly lower I_{corr} and $I_{passive}$ than the positive control (in 48 and 48 + 48 h), with 10 μg/mL of DJK-5 achieving the greatest effects. Thus, the use of peptides effectively reduced the corrosion susceptibility of titanium in the presence of biofilms, which supports the results of biofilm-killing experiments.

The resistance properties of peptides applied to titanium exposed to *S. mutans* were assessed by EIS measurements. The resistance (R_T) of titanium treated with peptides 1018 and DJK-5 (at 5 and 10 μg/mL) in *S. mutans* medium for 48 and 48 + 48 h was significantly increased, and the anticorrosion trend corresponded to the antibiofilm trend. From a clinical standpoint, titanium corrosion and passive film dissolution induced by biofilm challenge are considered the primary causes of titanium ion release (Noronha Oliveira et al., 2018). Such ions, along with debris and particles released by titanium-based dental implants, are harmful to the surrounding oral tissues, triggering inflammatory responses and bone loss (Messous et al., 2021; Barrak et al., 2022). In the present study, the application of peptides was shown to increase the electrochemical stability of titanium. When combined with the results from the PDP, EIS, and antibiofilm experiments, the improved corrosion resistance might relate to their effectiveness in *S. mutans* growth inhibition and biofilm killing. In this regard, the pH of the local environment was kept neutral, and the decrease in the generation of acids and the formation of differential oxygen slowed the corrosive processes. With the reduction of metal dissolution and surface deterioration, the passive film of titanium can be protected to maintain the stability of the implants (Hancock et al., 2021).

The use of antibiofilm peptides was successful in enhancing the corrosion resistance of titanium surfaces against microbial biofilms. The effectiveness of peptides 1018 and DJK-5 on biofilm killing on titanium surfaces at an initial stage was confirmed to reflect clinical situations of early implant infection and treatment. In terms of form, peptides could be applied as functional components to be incorporated into mouthwash or irrigants, preventing and/or treating biofilm-associated implant infection and corrosion to reduce the risk of failure. Despite the encouraging results, it should be noted that there is a complex relationship between microorganisms, corrosion, osseointegration, and surrounding tissues of titanium-based implants. Moreover, it could be a slow process for the deterioration of the passive film caused by microbial accumulation and acid production, and a model system that can mimic more realistic *in vivo* situations should be developed. Thus, further studies, including clinical trials, are needed to explore the detailed mechanism of antibiofilm peptides interacting with titanium and microbial biofilm, as well as their long-term efficacy in overcoming dental implant corrosion.

5 Conclusion

This study evaluated the effects of antibiofilm peptides on the corrosion resistance of titanium against *S. mutans* biofilms. The results suggested that the application of antibiofilm peptides effectively killed *S. mutans* biofilms and reduced the corrosion reaction on titanium. Furthermore, 10 μg/mL of DJK-5 can achieve the greatest effects and lead to a pH neutral

environment. Therefore, antibiofilm peptides offer promising benefits for promoting the anticorrosion performance of titanium against microbial biofilm to enhance the stability of dental implants and prevent peri-implant infections.

Data availability statement

The original contributions presented in the study are included in the article/Supplementary Material, further inquiries can be directed to the corresponding authors.

Author contributions

DW: Formal Analysis, Investigation, Methodology, Writing–original draft. YY: Formal Analysis, Investigation, Writing–original draft. HL: Investigation, Writing–original draft. TZ: Validation, Writing–original draft. EH: Validation, Writing–original draft. RH: Writing–review and editing. JY: Data curation, Formal Analysis, Writing–review and editing. YS: Conceptualization, Supervision, Writing–review and editing.

Funding

The author(s) declare financial support was received for the research, authorship, and/or publication of this article. This work was supported by the Canadian Institutes for Health Research (CIHR) FDN-154287 to RH, the S. Wah Leung Endowment Fund (2023) of UBC Faculty of Dentistry, and the Liaoning Basic Applied Research Youth Program (2023JH2/101600066). JY's research conducted at the UBC Faculty of Dentistry was supported by China Scholarship Council (202006275049).

Conflict of interest

RH is a co-inventor of a patent application on the use of antibiofilm peptides 1018 and DJK-5 that is assigned to his employer, University of British Columbia, Vancouver, BC, Canada, and has been licensed to ABT Innovations Inc., which is partially owned by RH.

The remaining authors declare that the research was conducted in the absence of any commercial or financial relationships that could be construed as a potential conflict of interest.

Publisher's note

All claims expressed in this article are solely those of the authors and do not necessarily represent those of their affiliated organizations, or those of the publisher, the editors and the reviewers. Any product that may be evaluated in this article, or claim that may be made by its manufacturer, is not guaranteed or endorsed by the publisher.

Supplementary material

The Supplementary Material for this article can be found online at: https://www.frontiersin.org/articles/10.3389/fbioe.2023.1339912/full#supplementary-material

References

Alhamad, M., Barão, V. A., Sukotjo, C., Yerokhin, A., and Mathew, M. T. (2023). Unpredictable electrochemical processes in Ti dental implants: the role of Ti ions and inflammatory products. *ACS Appl. Bio Mat.* 6, 3661–3673. doi:10.1021/acsabm.3c00235

Barrak, F., Li, S., Muntane, A., Bhatia, M., Crossthwaite, K., and Jones, J. (2022). Particle release from dental implants immediately after placement - an *ex vivo* comparison of different implant systems. *Dent. Mat.* 38, 1004–1014. doi:10.1016/j.dental.2022.04.003

Bechinger, B., and Gorr, S. U. (2017). Antimicrobial peptides: mechanisms of action and resistance. *J. Dent. Res.* 96, 254–260. doi:10.1177/0022034516679973

Chai, M., An, M., and Zhang, X. (2021). Construction of a TiO2/MoSe2/CHI coating on dental implants for combating Streptococcus mutans infection. *Mat. Sci. Eng. C Mat. Biol. Appl.* 129, 112416. doi:10.1016/j.msec.2021.112416

Costa, R. C., Abdo, V. L., Mendes, P. H., Mota-Veloso, I., Bertolini, M., Mathew, M. T., et al. (2021). Microbial corrosion in titanium-based dental implants: how tiny bacteria can create a big problem? *J. Bio. Tribo. Corros.* 7, 136. doi:10.1007/s40735-021-00575-8

Costa, R. C., Souza, J. G. S., Cordeiro, J. M., Bertolini, M., de Avila, E. D., Landers, R., et al. (2020). Synthesis of bioactive glass-based coating by plasma electrolytic oxidation: untangling a new deposition pathway toward titanium implant surfaces. *J. Colloid Interface Sci.* 579, 680–698. doi:10.1016/j.jcis.2020.06.102

Curtin, J. P., and Wang, M. (2017). Are clinical findings of systemic titanium dispersion following implantation explained by available *in vitro* evidence? An evidence-based analysis. *J. Biol. Inorg. Chem.* 22, 799–806. doi:10.1007/s00775-017-1464-1

Daubert, D. M., and Weinstein, B. F. (2019). Biofilm as a risk factor in implant treatment. *Periodontol. 2000* 81, 29–40. doi:10.1111/prd.12280

de la Fuente-Núñez, C., Cardoso, M. H., de Souza Cândido, E., Franco, O. L., and Hancock, R. E. (2016). Synthetic antibiofilm peptides. *Biochim. Biophys. Acta* 1858, 1061–1069. doi:10.1016/j.bbamem.2015.12.015

de la Fuente-Núñez, C., Korolik, V., Bains, M., Nguyen, U., Breidenstein, E. B., Horsman, S., et al. (2012). Inhibition of bacterial biofilm formation and swarming motility by a small synthetic cationic peptide. *Antimicrob. Agents Chemother.* 56, 2696–2704. doi:10.1128/AAC.00064-12

de la Fuente-Núñez, C., Reffuveille, F., Haney, E. F., Straus, S. K., and Hancock, R. E. (2014). Broad-spectrum anti-biofilm peptide that targets a cellular stress response. *PLoS Pathog.* 10, e1004152. doi:10.1371/journal.ppat.1004152

de la Fuente-Núñez, C., Reffuveille, F., Mansour, S. C., Reckseidler-Zenteno, S. L., Hernández, D., Brackman, G., et al. (2015). D-enantiomeric peptides that eradicate wild-type and multidrug-resistant biofilms and protect against lethal *Pseudomonas aeruginosa* infections. *Chem. Biol.* 22, 196–205. doi:10.1016/j.chembiol.2015.01.002

Dhaliwal, J. S., Abd Rahman, N. A., Ming, L. C., Dhaliwal, S. K. S., Knights, J., and Albuquerque Junior, R. F. (2021). Microbial biofilm decontamination on dental implant surfaces: a mini review. *Front. Cell Infect. Microbiol.* 11, 736186. doi:10.3389/fcimb.2021.736186

Fukushima, A., Mayanagi, G., Nakajo, K., Sasaki, K., and Takahashi, N. (2014). Microbiologically induced corrosive properties of the titanium surface. *J. Dent. Res.* 93, 525–529. doi:10.1177/0022034514524782

Fukushima, A., Mayanagi, G., Sasaki, K., and Takahashi, N. (2018). Corrosive effects of fluoride on titanium under artificial biofilm. *J. Prosthodont. Res.* 62, 104–109. doi:10.1016/j.jpor.2017.08.004

Gera, S., Kankuri, E., and Kogermann, K. (2022). Antimicrobial peptides - unleashing their therapeutic potential using nanotechnology. *Pharmacol. Ther.* 232, 107990. doi:10.1016/j.pharmthera.2021.107990

Guo, R., Peng, W., Yang, H., Yao, C., Yu, J., and Huang, C. (2021). Evaluation of resveratrol-doped adhesive with advanced dentin bond durability. *J. Dent.* 114, 103817. doi:10.1016/j.jdent.2021.103817

Hancock, R. E., Haney, E. F., and Gill, E. E. (2016). The immunology of host defence peptides: beyond antimicrobial activity. *Nat. Rev. Immunol.* 16, 321–334. doi:10.1038/nri.2016.29

Hancock, R. E. W., Alford, M. A., and Haney, E. F. (2021). Antibiofilm activity of host defence peptides: complexity provides opportunities. *Nat. Rev. Microbiol.* 19, 786–797. doi:10.1038/s41579-021-00585-w

Hasan, J., Bright, R., Hayles, A., Palms, D., Zilm, P., Barker, D., et al. (2022). Preventing peri-implantitis: the quest for a next generation of titanium dental implants. *ACS Biomater. Sci. Eng.* 8, 4697–4737. doi:10.1021/acsbiomaterials.2c00540

Hu, J., Yu, J., Liu, H., Wang, Z., Haapasalo, M., Haney, E. F., et al. (2023). Dynamic killing effectiveness of mouthrinses and a D-enantiomeric peptide on oral multispecies biofilms grown on dental restorative material surfaces. *J. Dent.* 134, 104552. doi:10.1016/j.jdent.2023.104552

Huang, X., Haapasalo, M., Wang, Z., Hancock, R. E. W., Wei, X., and Shen, Y. (2019). Effect of Long-term exposure to peptides on mono- and multispecies biofilms in dentinal tubules. *J. Endod.* 45, 1522–1528. doi:10.1016/j.joen.2019.09.003

Kim, Y. S., Lee, E. S., Kwon, H. K., and Kim, B. I. (2014). Monitoring the maturation process of a dental microcosm biofilm using the Quantitative Light-induced Fluorescence-Digital (QLF-D). *J. Dent.* 42, 691–696. doi:10.1016/j.jdent.2014.03.006

Liu, H., Li, H., Zhang, L., Wang, Z., Qian, J., Yu, M., et al. (2022). *In vitro* evaluation of the antibacterial effect of four root canal sealers on dental biofilms. *Clin. Oral Investig.* 26, 4361–4368. doi:10.1007/s00784-022-04399-9

López-Píriz, R., Cabal, B., Goyos-Ball, L., Fernández, A., Bartolomé, J. F., Moya, J. S., et al. (2019). Current state-of-the-art and future perspectives of the three main modern implant-dentistry concerns: aesthetic requirements, mechanical properties, and peri-implantitis prevention. *J. Biomed. Mat. Res. A* 107, 1466–1475. doi:10.1002/jbm.a.36661

López-Valverde, N., López-Valverde, A., and Blanco-Rueda, J. A. (2023). Efficacy of adjuvant metronidazole therapy on peri-implantitis: a systematic review and meta-analysis of randomized clinical studies. *Front. Cell Infect. Microbiol.* 13, 1149055. doi:10.3389/fcimb.2023.1149055

Lu, S., Li, R., Chai, M., Wang, J., Duan, W., Yao, X., et al. (2022). Nanostructured Cu-doped TiO2 with photothermal effect for prevention of implant-associated infection. *Colloids Surf. B Biointerfaces* 217, 112695. doi:10.1016/j.colsurfb.2022.112695

Malheiros, S. S., Nagay, B. E., Bertolini, M. M., de Avila, E. D., Shibli, J. A., Souza, J. G. S., et al. (2023). Biomaterial engineering surface to control polymicrobial dental implant-related infections: focusing on disease modulating factors and coatings development. *Expert Rev. Med. Devices* 20, 557–573. doi:10.1080/17434440.2023.2218547

Mansour, S. C., Pena, O. M., and Hancock, R. E. (2014). Host defense peptides: front-line immunomodulators. *Trends Immunol.* 35, 443–450. doi:10.1016/j.it.2014.07.004

Messous, R., Henriques, B., Bousbaa, H., Silva, F. S., Teughels, W., and Souza, J. C. M. (2021). Cytotoxic effects of submicron- and nano-scale titanium debris released from dental implants: an integrative review. *Clin. Oral Investig.* 25, 1627–1640. doi:10.1007/s00784-021-03785-z

Noronha Oliveira, M., Schunemann, W. V. H., Mathew, M. T., Henriques, B., Magini, R. S., Teughels, W., et al. (2018). Can degradation products released from dental implants affect peri-implant tissues? *J. Periodontal. Res.* 53, 1–11. doi:10.1111/jre.12479

Nyby, C., Guo, X., Saal, J. E., Chien, S. C., Gerard, A. Y., Ke, H., et al. (2021). Electrochemical metrics for corrosion resistant alloys. *Sci. Data* 8, 58. doi:10.1038/s41597-021-00840-y

Patil, C., Agrawal, A., Abullais, S. S., Arora, S., Khateeb, S. U., and Fadul A Elagib, M. (2022). Effectiveness of different chemotherapeutic agents for decontamination of infected dental implant surface: a systematic review. *Antibiot. (Basel)* 11, 593. doi:10.3390/antibiotics11050593

Pitts, N. B., Zero, D. T., Marsh, P. D., Ekstrand, K., Weintraub, J. A., Ramos-Gomez, F., et al. (2017). Dental caries. *Nat. Rev. Dis. Prim.* 3, 17030. doi:10.1038/nrdp.2017.30

Pletzer, D., Coleman, S. R., and Hancock, R. E. (2016). Anti-biofilm peptides as a new weapon in antimicrobial warfare. *Curr. Opin. Microbiol.* 33, 35–40. doi:10.1016/j.mib.2016.05.016

Pletzer, D., and Hancock, R. E. (2016). Antibiofilm peptides: potential as broad-spectrum agents. *J. Bacteriol.* 198, 2572–2578. doi:10.1128/JB.00017-16

Prestat, M., and Thierry, D. (2021). Corrosion of titanium under simulated inflammation conditions: clinical context and *in vitro* investigations. *Acta Biomater.* 136, 72–87. doi:10.1016/j.actbio.2021.10.002

Renvert, S., Roos-Jansåker, A. M., and Claffey, N. (2008). Non-surgical treatment of peri-implant mucositis and peri-implantitis: a literature review. *J. Clin. Periodontol.* 35, 305–315. doi:10.1111/j.1600-051X.2008.01276.x

Rodrigues, D. C., Sridhar, S., Gindri, I. M., Siddiqui, D. A., Valderrama, P., Wilson, T. G., et al. (2016). Spectroscopic and microscopic investigation of the effects of bacteria on dental implant surfaces. *RSC Adv.* 6, 48283–48293. doi:10.1039/C6RA07760A

Shao, H., Zhou, J., Lin, X., Zhou, Y., Xue, Y., Hong, W., et al. (2023). Bio-inspired peptide-conjugated liposomes for enhanced planktonic bacteria killing and biofilm eradication. *Biomaterials* 300, 122183. doi:10.1016/j.biomaterials.2023.122183

Siddiqui, D. A., Fidai, A. B., Natarajan, S. G., and Rodrigues, D. C. (2022). Succession of oral bacterial colonizers on dental implant materials: an *in vitro* biofilm model. *Dent. Mat.* 38, 384–396. doi:10.1016/j.dental.2021.12.021

Siddiqui, D. A., Guida, L., Sridhar, S., Valderrama, P., Wilson, T. G., and Rodrigues, D. C. (2019). Evaluation of oral microbial corrosion on the surface degradation of dental implant materials. *J. Periodontol.* 90, 72–81. doi:10.1002/JPER.18-0110

Souza, J. C., Henriques, M., Oliveira, R., Teughels, W., Celis, J. P., and Rocha, L. A. (2010). Do oral biofilms influence the wear and corrosion behavior of titanium? *Biofouling* 26, 471–478. doi:10.1080/08927011003767985

Souza, J. C., Ponthiaux, P., Henriques, M., Oliveira, R., Teughels, W., Celis, J. P., et al. (2013). Corrosion behaviour of titanium in the presence of Streptococcus mutans. *J. Dent.* 41, 528–534. doi:10.1016/j.jdent.2013.03.008

Souza, J. G. S., Beline, T., Matos, A. O., Costa Oliveira, B. E., Ricomini-Filho, A. P., and Barão, V. A. R. (2018). Electrochemical behavior of titanium exposed to a biofilm supplemented with different sucrose concentrations. *J. Prosthet. Dent.* 120, 290–298. doi:10.1016/j.prosdent.2017.10.012

Wang, D., Haapasalo, M., Gao, Y., Ma, J., and Shen, Y. (2018). Antibiofilm peptides against biofilms on titanium and hydroxyapatite surfaces. *Bioact. Mat.* 3, 418–425. doi:10.1016/j.bioactmat.2018.06.002

Wang, Z., de la Fuente-Núñez, C., Shen, Y., Haapasalo, M., and Hancock, R. E. (2015). Treatment of oral multispecies biofilms by an anti-biofilm peptide. *PLoS One* 10, e0132512. doi:10.1371/journal.pone.0132512

Weller, J., Vasudevan, P., Kreikemeyer, B., Ekat, K., Jackszis, M., Springer, A., et al. (2022). The role of bacterial corrosion on recolonization of titanium implant surfaces: an *in vitro* study. *Clin. Implant Dent. Relat. Res.* 24, 664–675. doi:10.1111/cid.13114

Yang, Y., Xia, L., Haapasalo, M., Wei, W., Zhang, D., Ma, J., et al. (2019). A novel hydroxyapatite-binding antimicrobial peptide against oral biofilms. *Clin. Oral Investig.* 23, 2705–2712. doi:10.1007/s00784-018-2701-x

Yu, J., Bian, H., Zhao, Y., Guo, J., Yao, C., Liu, H., et al. (2022). Epigallocatechin-3-gallate/mineralization precursors co-delivery hollow mesoporous nanosystem for synergistic manipulation of dentin exposure. *Bioact. Mat.* 23, 394–408. doi:10.1016/j.bioactmat.2022.11.018

Yu, J., Yi, L., Guo, R., Guo, J., Yang, H., and Huang, C. (2021). The stability of dentin surface biobarrier consisting of mesoporous delivery system on dentinal tubule occlusion and Streptococcus mutans biofilm inhibition. *Int. J. Nanomedicine* 16, 3041–3057. doi:10.2147/IJN.S290254

Zhang, S. M., Qiu, J., Tian, F., Guo, X. K., Zhang, F. Q., and Huang, Q. F. (2013). Corrosion behavior of pure titanium in the presence of Actinomyces naeslundii. *J. Mat. Sci. Mat. Med.* 24, 1229–1237. doi:10.1007/s10856-013-4888-3

Zhang, X. P., Zhao, Z. P., Wu, F. M., Wang, Y. L., and Wu, J. (2007). Corrosion and wear resistance of AZ91D magnesium alloy with and without microarc oxidation coating in Hank's solution. *J. Mat. Sci.* 42, 8523–8528. doi:10.1007/s10853-007-1738-z

frontiers | Frontiers in Bioengineering and Biotechnology

TYPE Original Research
PUBLISHED 12 January 2024
DOI 10.3389/fbioe.2024.1350024

OPEN ACCESS

EDITED BY
Hongye Yang,
Wuhan University, China

REVIEWED BY
Longquan Shao,
Southern Medical University, China
Yingliang Song,
The Fourth Military Medical University, China

*CORRESPONDENCE
Wen-yun Zhang,
drwenyun@qq.com

RECEIVED 05 December 2023
ACCEPTED 04 January 2024
PUBLISHED 12 January 2024

CITATION
Zhao Y, Su J, Xu C-y, Li Y-b, Hu T, Li Y, Yang L, Zhao Q and Zhang W-y (2024), Establishment of a mandible defect model in rabbits infected with multiple bacteria and bioinformatics analysis. *Front. Bioeng. Biotechnol.* 12:1350024. doi: 10.3389/fbioe.2024.1350024

Establishment of a mandible defect model in rabbits infected with multiple bacteria and bioinformatics analysis

Yuan Zhao[1,2], Jun Su[1], Chong-yan Xu[1,2], Yan-bo Li[2], Tong Hu[1,2], Yi Li[1,2], Li Yang[1], Qiang Zhao[1] and Wen-yun Zhang[1]*

[1]Department of Stomatology, 920th Hospital of Joint Logistics Support Force of People's Liberation Army of China, Kunming, China, [2]Postgraduate Research Institute, Kunming Medical University, Kunming, China

Objective: A model of chronic infectious mandibular defect (IMD) caused by mixed infection with *Staphylococcus aureus* and *Pseudomonas aeruginosa* was established to explore the occurrence and development of IMD and identify key genes by transcriptome sequencing and bioinformatics analysis.

Methods: *S. aureus* and *P. aeruginosa* were diluted to 3×10^8 CFU/mL, and 6 × 3 × 3 mm defects lateral to the Mandibular Symphysis were induced in 28 New Zealand rabbits. Sodium Morrhuate (0.5%) and 50 μL bacterial solution were injected in turn. The modeling was completed after the bone wax closed; the effects were evaluated through postoperative observations, imaging and histological analyses. Gene Ontology (GO), Kyoto Encyclopedia of Genes and Genomes (KEGG) pathway, and protein–protein interaction (PPI) network analyses were performed to investigate the function of the differentially expressed genes (DEGs).

Results: All rabbits showed characteristics of infection. The bacterial cultures were positive, and polymerase chain reaction (PCR) was used to identify *S. aureus* and *P. aeruginosa*. Cone beam CT and histological analyses showed inflammatory cell infiltration, pus formation in the medullary cavity, increased osteoclast activity in the defect area, and blurring at the edge of the bone defect. Bioinformatics analysis showed 1,804 DEGs, 743 were upregulated and 1,061 were downregulated. GO and KEGG analyses showed that the DEGs were enriched in immunity and osteogenesis inhibition, and the core genes identified by the PPI network were enriched in the Hedgehog pathway, which plays a role in inflammation and tissue repair; the MEF2 transcription factor family was predicted by IRegulon.

Conclusion: By direct injection of bacterial solution into the rabbit mandible defect area, the rabbit chronic IMD model was successfully established. Based on the bioinformatics analysis, we speculate that the Hedgehog pathway and the MEF2 transcription factor family may be potential intervention targets for repairing IMD.

KEYWORDS

animal model, mixed bacterial solution, infectious mandible defects, bioinformatics analysis, the hedgehog pathway

1 Introduction

The incidence of infectious mandibular defects (IMD) caused by war trauma and traffic injuries is increasing (Cicuendez et al., 2018), and these infections often result from a variety of bacteria; furthermore, traditional treatments are not effective, which seriously impacts the patient's quality of life and the advances in implant restoration. The mechanism of mandible infection and the clinical problems caused by it have not yet been clarified, and a large part of this lack of knowledge is due to the lack of suitable animal models. For ethical reasons, it is difficult to carry out research on IMD in humans, so a suitable animal model of IMD is urgently needed to simulate clinical incidence and find key genes and pathways related to the development of IMD to provide a good research basis for addressing clinical problems.

There are many methods for preparing animal models of infectious bone defects. Lei MG et al. (Lei et al., 2017) implanted a stainless-steel tube soaked with bacterial fluid in the shin bone marrow cavity of rats and confirmed the signs of bone infection by testing. Tao J and Pearson JJ et al. (Pearson et al., 2020; Tao et al., 2020) first established defects in the shin and femur of rabbits, injected bacteria into the defect site, and successfully established a model of infectious bone defects. However, at present, the selected body parts for modeling are mainly conducted in limb bones, and the infection is usually caused by one bacterium. Furthermore, the osteogenic mechanism of the limb bones is different from that of the craniofacial bone, the traditional animal models of bone defect do not accurately simulate the clinically complex mandible infection, and there is still not an ideal animal model of compound bacterial infection in mandible defects.

In studying the occurrence and development of infectious bone defects, the effect of genetic polymorphisms on susceptibility to bone infection has been reported, which includes their effects on TNF-α, IL-1β, and IL-6; (Wang et al., 1985; Frangiamore et al., 2015; Hofmann et al., 2016a); these studies also showed the correlation between specific genes and bone infection. However, these studies only propose correlations at the genetic level and do not further investigate specific mechanisms. With the development of high-throughput technology, technologies such as DNA microarrays or transcriptome sequencing have become powerful tools for screening disease-causing genes by studying the differences in gene expression profiles between experimental and control groups, and the molecular function (MF), biological process (BP), cellular component (CC) and signaling pathways enriched in genes related to the occurrence and development of diseases have been identified.

In this study, to simulate IMD caused by war injuries, a mixture of *S. aureus* and *Pseudomonas aeruginosa* was used to establish IMD by animal experiments. And bioinformatics methods were used to analyze transcriptome data from animal models, identify DEGs, and analyze the functions, related pathways, core modules and core genes related to IMD (Figure 1); these results provide a direction for future research to repair IMD.

2 Materials and methods

2.1 Materials

A total of 28 New Zealand white rabbits (male and female, Conventional Animal) aged 3 months and weighing 2–2.5 kg were selected for the experiment (Kunming Chu Shang Technology Co., LTD. License Number [SCXK (Yunnan) K2019-0003]). The animals were raised in the Medical Animal Experimental Center of the 920th Hospital of the Joint Logistic Support Force [SYXK (Yunnan) K2020-0006], reared separately and given free access to feed and water for 1 week. All animals were handled in accordance with ethical regulations and were examined and allowed by the 920th Hospital Ethics Review Committee of the PLA Joint Logistic Support Force [2023–127 (Section) –01]. *S. aureus* (ATCC 29213), and *P. aeruginosa* (ATCC 27853, Luwei Technology Co., LTD. Shanghai, China) strains were obtained, as well as 5% sodium morrhuate (Xinyi Jinzhu Pharmaceutical Co., LTD. Shanghai, China, specification: 2 ML, 0.1 g/branch).

2.2 Methods

2.2.1 Bacterial cultivation

S. aureus and *P. aeruginosa* were inoculated on Luria-Bertani (LB) culture plates (Solarbio, Beijing, China), incubated in a constant temperature incubator at 37°C for 36 h, and then removed. An appropriate amount of colonies were selected in 15 mL of LB culture medium (Solarbio, Beijing, China) for larger cultures. The mixture was incubated in a constant temperature incubator at 37°C for 36 h and diluted with sterile normal saline. The concentration of bacteria was adjusted to 3×10^8 CFU/mL, and the two bacterial solutions were mixed and used immediately.

2.2.2 Surgery

The experimental rabbits were weighed, and 3 wt% pentobarbital (Tengshan Biotechnology Co., Ltd. Kunming, China) was extracted and injected into the auricular vein for general anesthesia. After the anesthesia took effect, the head was fixed, and the skin of the mandible was prepared on both sides to facilitate follow-up observation of hair growth. In the iodoprene disinfection area, a 3–4 cm incision was made along the lower margin near the median union of the mandible, and the lateral bone surface of the mandible was exposed by blunt separation layer by layer. A circular bone drill with a diameter of 3 mm was used to drill holes, and a ball drill was used to trim the shape of a rectangular bone defect of 6 × 3 × 4 mm. A total of 0.1 mL of 5% sodium maphuate was injected into the bone defect, and after 5 min, normal saline was used for rinsing, 50 μL of 3×10^8 CFU/mL mixed bacterial solution was injected, bone wax (Johnson & Johnson, Shanghai, China) was used to seal the defect, sterile normal saline was used for rinsing, and the wound was sutured layer by layer (Figure 2). After the operation, the rabbits were fed in cages without antibiotics. After the operation, rabbits were divided into two groups, and samples were collected at 14 and 28 days. Healthy rabbits fed conventionally for 1 month without any treatment were used as the blank group.

2.2.3 Evaluation methods

Serious infection outside the experimental area, systemic blood-borne infection, extremely altered mental state, and difficulty eating were used as humane endpoints, and the experimental rabbits were

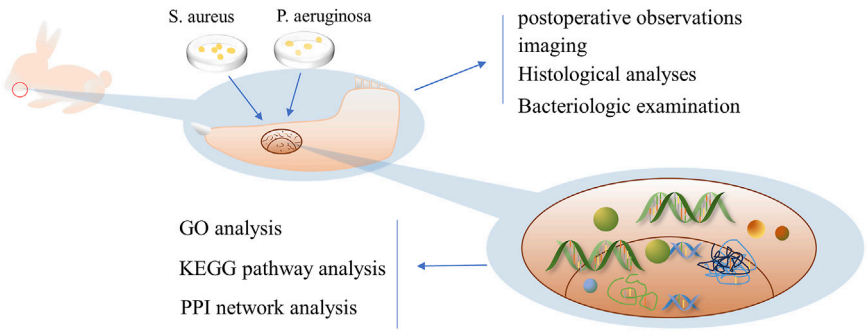

FIGURE 1
Schematic diagram of the research process Legend: In this study, the mandibular bone defect of rabbits was first established, and then the prepared bacterial solution was injected to successfully establish the IMD model, and bioinformatics analysis was conducted by transcriptomic sequencing.

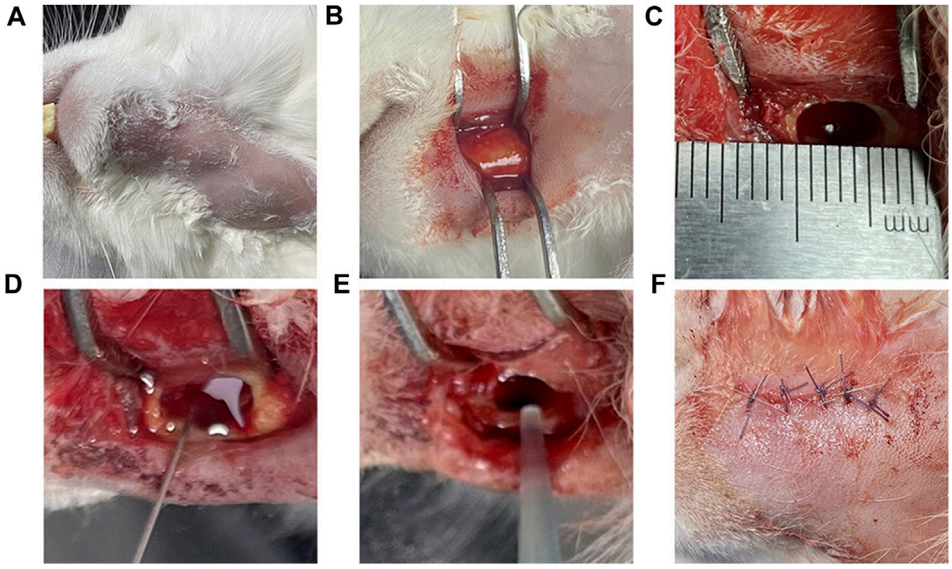

FIGURE 2
Model of the surgical procedure Legend: **(A)** Skin preparation and iodophor disinfection of the operative area. **(B)** The surgical area was dissected and separated the lateral surface of the mandible. **(C)** A 6 × 3 × 4 mm rectangular bone defect was prepared; and **(D)** 0.1 mL 5% sodium morate was injected and maintained for 5 min. **(E)** After rinsing with normal saline, 0.1 mL of 3×10^8 CFU/mL mixed bacterial solution was injected; and **(F)** the bone wax was used for closure and the area was sutured layer by layer.

selected for modeling. The experiment was conducted using a before-after study with the same samples.

2.2.3.1 Temperature and food intake

The anal temperature of rabbits from 5 days before surgery to 5 days after surgery was measured at 9 a.m. every day, and the food intake during the same period was determined; the changes before and after surgery were analyzed.

2.2.3.2 Wound healing

Skin healing at the incision was observed to determine whether there was sinus formation after modeling.

2.2.3.3 Imaging examination

On the 14th and 28th day after modeling, a CBCT (Bondent, Shanghai, China) scan was performed on rabbits under anesthesia to observe the bone defect at the modeling site.

2.2.3.4 Gross specimens

The rabbits were sacrificed by excessive anesthesia on the 14th and 28th days after modeling. The mandible on the modeling side was removed, and the soft tissues were removed to observe whether there was pus and new bone formation in the defect area. Animal carcasses were handled uniformly according to laboratory requirements.

TABLE 1 Histological parameters and scoring system.

Score	Scoring rules
Intraosseous acute inflammation	
0	Not present
1	Minimal to mild inflammation with no intramedullary abscess
2	Moderate to severe inflammation with no intramedullary abscess
3	Minimal to mild inflammation with intramedullary abscess
4	Moderate to severe inflammation with intramedullary abscess
Intraosseous chronic inflammation	
0	Not present
1	Minimal to mild chronic inflammation with no significant intramedullary fibrosis
2	Moderate to severe chronic inflammation with no significant intramedullary fibrosis
3	Minimal to mild chronic inflammation with significant intramedullary fibrosis
4	Moderate to severe chronic inflammation with significant intramedullary fibrosis
Periosteal inflammation	
0	Not present
1	Minimal to mild inflammation with no subperiosteal abscess formation
2	Moderate to severe inflammation with no subperiosteal abscess formation
3	Minimal to mild inflammation with subperiosteal abscess formation
4	Moderate to severe inflammation with subperiosteal abscess formation
Bone necrosis	
0	No evidence of necrosis
1	Single focus of necrosis without sequestrum formation
2	Multiple foci of necrosis without sequestrum formation
3	Single focus of sequestrum
4	Multiple foci of sequestra

2.2.3.5 Histological analysis

The mandible was fixed with 4% paraformaldehyde (Solarbio, Beijing, China) and then decalcified in EDTA (Solarbio, Beijing, China) decalcification solutionuntil a fine needle was inserted into the bone cortex without resistance; then, paraffin-embedded sections were cut. Hematoxylin and eosin staining, Goldner's tricolor staining (Source leaf, Shanghai, China) and tartrate acid fast phosphatase (TRAP) staining (Solarbio, Beijing, China) were performed and sections were viewed under a microscope. Goldner staining procedures were as follows: First, paraffin sections were dewaxed to water, and then Goldner staining solution A was mixed with Goldner staining solution B in equal proportion for nuclear staining. The sections were then stained with Goldner dye C, Goldner dye D, Goldner dye C, and Goldner dye E in turn. Finally, neutral gum sealed the section. TRAP staining procedures were as follows: First, paraffin sections were dewaxed to water. The slices were fixed using TRAP fixative. After rinsing sections with distilled water, add TRAP incubation solution and re-stain with hematoxylin. Finally, the sections were sealed with water-based sealer. Improved smelter scoring (Smeltzer et al., 1997) (Table 1) was used for the quantitative analysis of the HE section. The minimum score for each section was 0 points, the highest score was 4 points, and the total score was 16 points. Areas of the same size in TRAP-stained sections were randomly selected to count osteoclasts.

2.2.3.6 Bacteriological analysis

Secretions from the defect were mixed in normal saline aseptically and coated on LB culture plates to observe whether there was colony growth. Afterward, specific primers (Table 2) were selected for different colonies for PCR (Solarbio, Beijing, China) detection to identify whether the infection was caused by the inoculated bacteria.

2.2.4 Transcriptomic sequencing

Healthy rabbits were fed in the same environment for 1 month, and then a mandible defect model of rabbits infected with complex bacteria was established according to the described method. Fourteen days after the operation, 3 rabbits in the complex bacterial infection group and 4 rabbits in the healthy blank control group were sacrificed,

TABLE 2 List of specific primers.

GENE		Sequence (5,→3′)	Length	Tm	GC%
S. aureus	Forward Primer	GGGATGGCTATCAGTAA	17	43.88	47
S. aureus	Reverse Primer	TGAATCAGCGTTGTCTT	17	45.73	41
P. aeruginosa	Forward Primer	TACCTTCCTGTTTTGAG	17	43.95	41
P. aeruginosa	Reverse Primer	ATCCAACTTGCTGAACCAG	19	51.1	47

TABLE 3 Number of DEGs.

SampleID	Total	UP_num	DOWN_num
INF_vs._NC	1804	743	1,061

and the mandibles were removed and stored in liquid nitrogen for quick freezing. Afterward, RNA libraries were constructed and sequenced to determine gene expression.

2.2.5 Differential expression analysis

To compare the differences in gene expression between different samples, we used the R package edgeR (Robinson et al., 2010), which allowed for the identification of DEGs between the experimental group and the control group. The screening threshold was set as an adjusted *p*-value (adj.p) < 0.05, and genes whose fold change (FC) absolute value was greater than 2 were considered significant DEGs. The significant DEG expression levels of all samples were determined, and a heatmap of DEGs was drawn using pheatmap.

2.2.6 GO term and KEGG pathway enrichment analysis of DEGs

For GO annotation for DEGs, the genes corresponding to a specific GO annotation were counted and then classified and plotted according to MF, CC, and BP (Ashburner et al., 2000). The genes corresponding to GO annotation were enriched, and the significant enrichment results were screened according to the threshold *p*-value < 0.05. All GO enrichment results were sorted according to *p*-value from smallest to largest, and the top 20 GO enrichment terms were depicted in bubble maps. The biological pathway information from the pathway analysis was derived from KEGG. First, KEGG annotation was performed for DEGs; then, the number of genes corresponding to KEGG annotation was statistically analyzed (Kanehisa and Goto, 2000), and functional classification was performed. The genes corresponding to the map number annotated by KEGG were enriched, and the significant enrichment results were screened according to the threshold *p*-value < 0.05. All KEGG enrichment results were sorted according to *p*-value from small to large, and the top 20 enrichment pathways were depicted in bubble maps.

2.2.7 PPI network and module analysis

The DEGs were imported into the STRING database to convert protein names, and then the PPI network diagram and interaction information were obtained. Information on protein interactions were imported into Cytoscape software to create visual networks. Then, the nodes, degrees, betweenness centrality and edges in the visual network were analyzed. Using the MCODE plug-in to filter modules, the analysis parameters were set to node score cutoff = 0.2, degree cutoff = 2, K-core≥2, and max. depth = 100. The key nodes in the PPI network were identified using cytoHubba plug-ins. The cytoHubba plug-in uses the DMNC analysis strategy to predict and evaluate important nodes, and the nodes with the top 10 scores were considered core genes.

2.2.8 Predicting transcription factors

Transcription factors were predicted using the iRegulon plug-in in Cytoscape software. The plug-in used the normalized enrichment score (NES) to assess the confidence of the predicted results. The greater the NES value is, the higher the confidence. In this study, transcription factors with NES>4.5 were used establish the network.

2.2.9 Statistical analysis

The mapping software Image-Pro Plus, GraphPad Prism 9.0 (Graphpad software, Lajolla, CA, United States) and the statistical software SPSS 29.0 (IBM corporation, Armonk,NY, United States)were used for analysis. Data are expressed as x ± s. We used Paired T tests and one-way analysis of variance for preoperative and postoperative comparisons, and $p < 0.05$ was considered a significant difference.

3 Results

The mental state of animals was altered after modeling, and no death or loss occurred within 4 weeks. All 28 rabbits were observed during the experiment.

3.1 Changes in body temperature and food intake

The mean value of the measured data was determined, and statistical analysis showed that the body temperature was 38.5°C ± 0.1°C before modeling and 39.6°C ± 0.2°C after modeling, and the food intake decreased from 146.3 ± 8.5 g before to 93.1 ± 8.4 after modeling; the differences were significant ($p < 0.001$) (Figures 3A,B). The changes in body temperature reverted over time (Figure 3C).

3.2 Wound healing

All rabbits had local skin redness 3 days after modeling, subcutaneous swelling of different degrees and purulent secretions at the incision on day 14 (Figure 3D). The local condition of the rabbits improved somewhat before day 28, but there were still abscesses and sinus, and there was no significant increase in body hair when compared with the contralateral hair (Figure 3E).

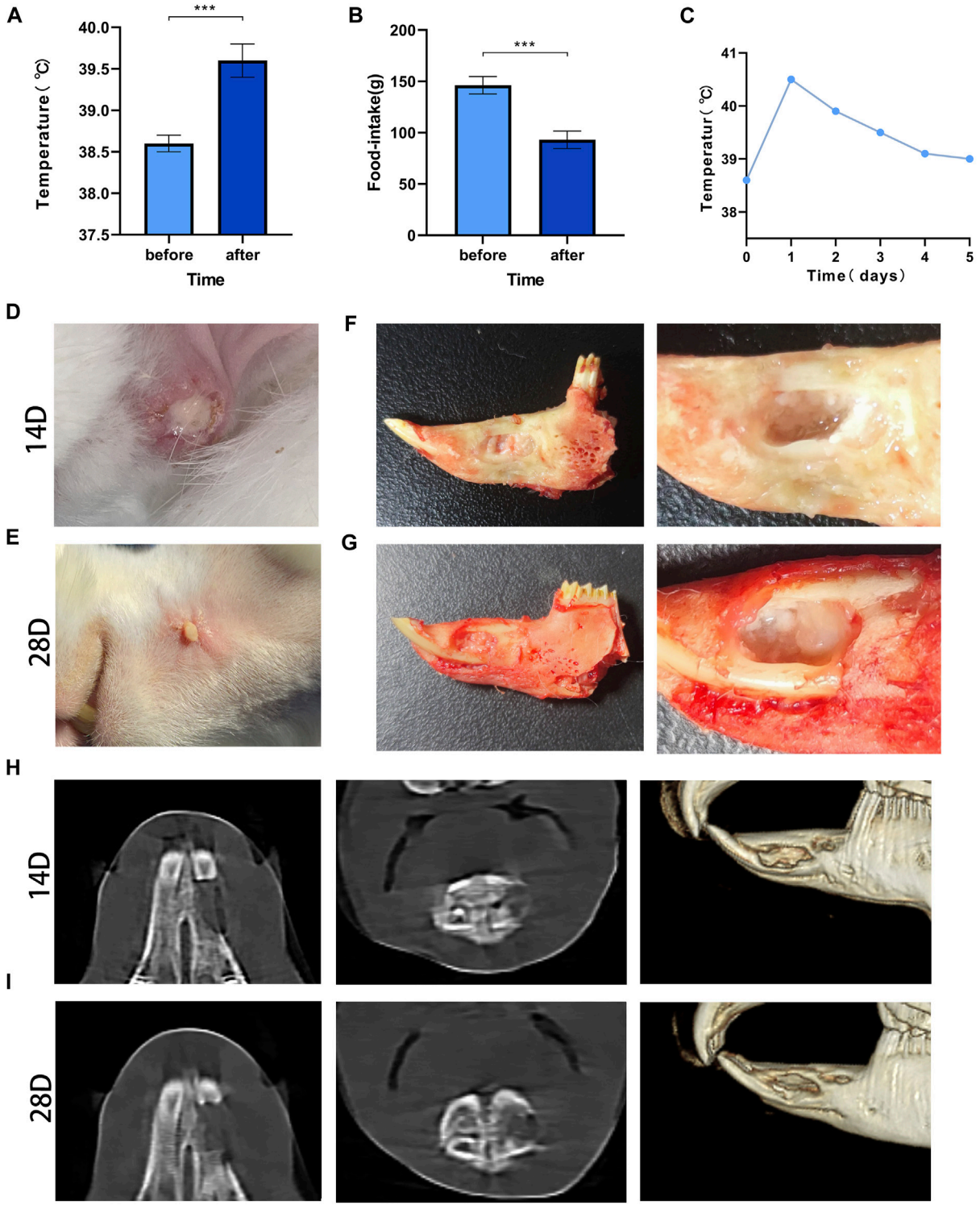

FIGURE 3
Post-modeling monitoring results and imaging results Legend: **(A)**. The difference in body temperature before and after modeling. **(B)**. The difference in food intake before and after modeling. **(C)**. The temperature changes before and after modeling. *** means $p < 0.001$ (n = 28). **(D)**. The result of wound healing at 14 days after surgery; **(E)**. The result of wound healing at 28 days after surgery. **(F)**. Gross specimens at 14 days after modeling. **(G)**. Gross specimens at 28 days after modeling. **(H)**. The results of imaging changes at 14 days. **(I)**. The results of imaging changes at 28 days.

3.3 Imaging changes

On day 14, the edges of the bone defect were blurred, and there were signs of bone destruction. Osteolysis, mainly manifested by decreased bone density, appeared in the bone marrow cavity, and the bone trabeculae's number were decreased (Figure 3H). At 28 days, erosion at the edge of the defect was observed, the bone density at the distal end of the defect was significantly

10.3389/fbioe.2024.1350024

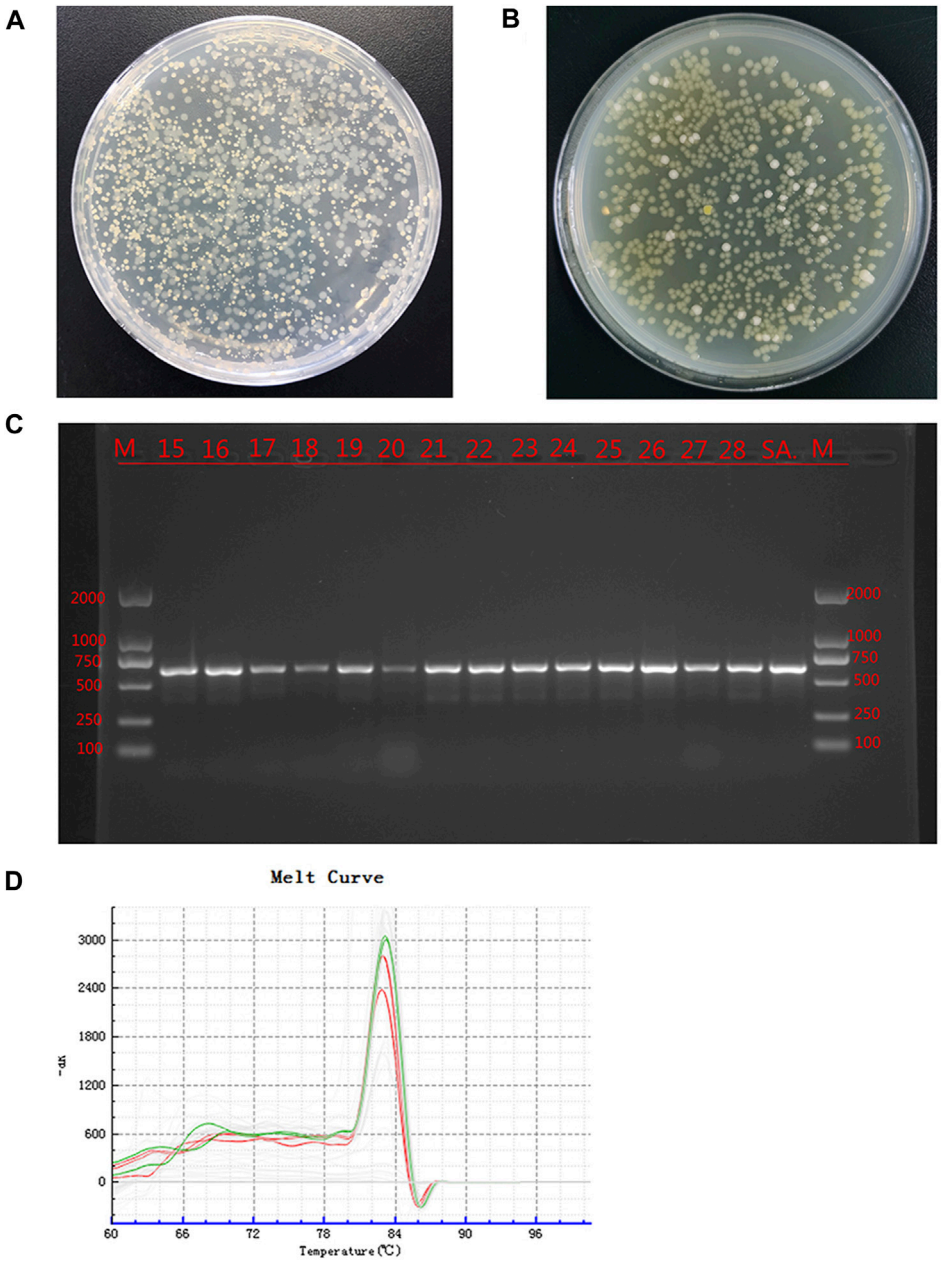

FIGURE 4
Bacterial culture and identification Legend: **(A)**. The bacterial culture of the secretions of defects at 14 days. **(B)**. The bacterial culture of the secretions of defects at 28 days. **(C)**. PCR results of the suspected SA sample and the SA standard strain, where M is the standard band, SA is the standard *Staphylococcus aureus* band, and the rest are the suspected *Staphylococcus aureus* samples. **(D)**. qPCR results of suspected PA samples and PA standard strains. Green is the dissolution curve of PA standard bacteria, and red is the dissolution curve of suspected PA. The curve trend and peak value were consistent.

reduced, and the normal structure of the bone trabecula was disrupted (Figure 3I).

3.4 Gross specimens

The rabbits were sacrificed by excessive anesthesia at 14 and 28 days. After incision of the skin, fistulas were found, and small pus cavities were found in the soft tissue of the wound. After the soft tissue was removed, yellow–white pus filled the bone defect area, the defect was not healed, and the pus was aspirated sterilely for bacterial culture (Figures 3F,G).

3.5 Bacteriological results

The bacterial culture of secretions from the defects of all experimental animals were positive on day 14, and two types of colonies with different forms were visible; the cultures were still positive on day 28 (Figures 4A, B). The two colonies were selected

10.3389/fbioe.2024.1350024

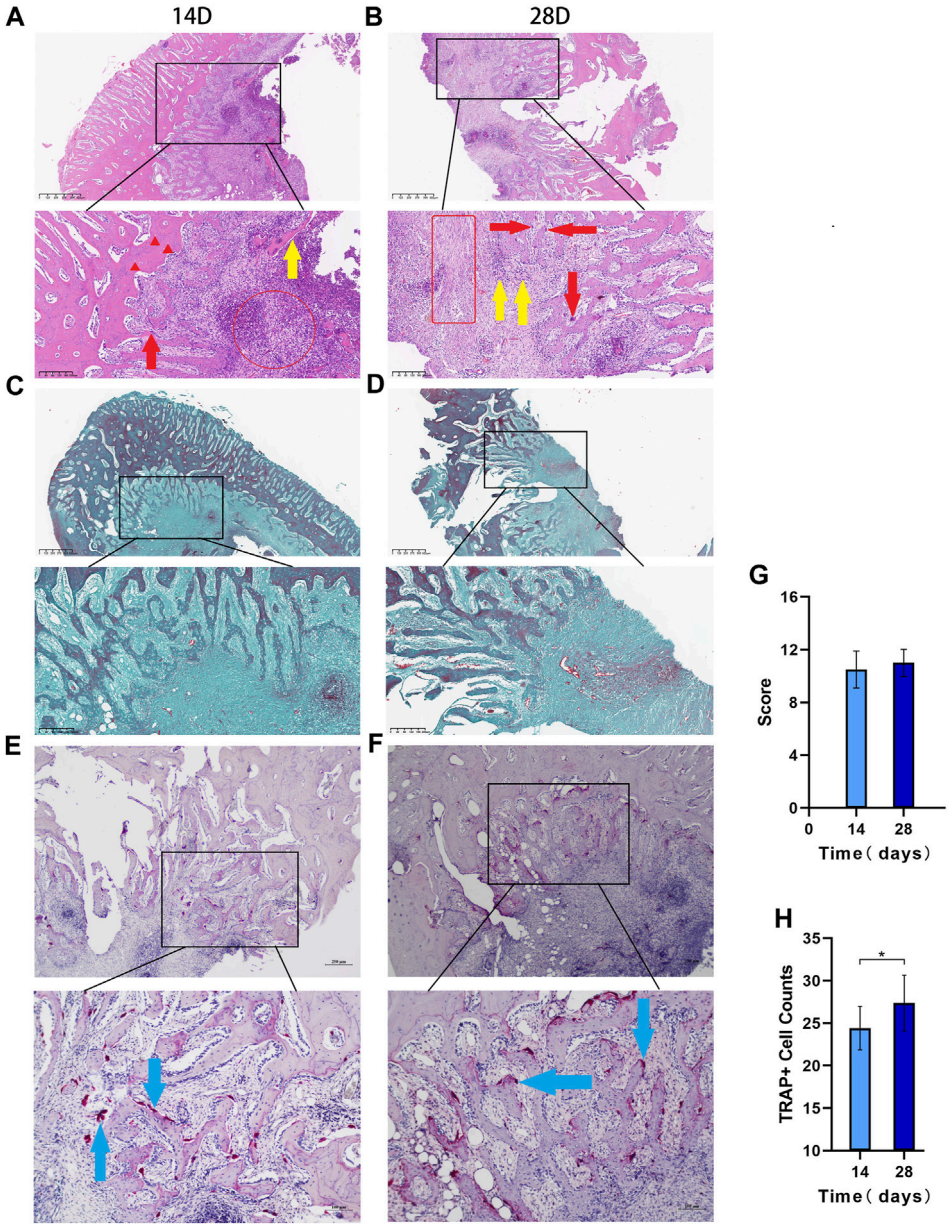

FIGURE 5
The histopathological results Legend: **(A)**. HE 14 days after modeling and **(B)**. 28 days after modeling, and the red circles in a and bindicate acute inflammation. The red box indicates chronic inflammation, the red arrows indicate macrophages, the red triangle indicates the loss of bone nucleus, and the yellow arrow shows free dead bone. **(C)**. Goldner staining at 14 days after modeling; **(D)**. Goldner staining at 28 days after modeling. **(E)**. TRAP staining results at 14 days and **(F)**. TRAP staining results at 28 days. **(G)**. Differences in the Smeltzer score were determined according to the Smeltzer scoring rules; the pathological changes between the two groups have no significant difference ($p > 0.05$, n = 14). **(H)**. Analysis of osteoclast count per unit area in the two groups. The blue arrows are osteoclast-positive areas (* indicates $p < 0.05$ and n = 14).

aseptically for qualitative detection, and the suspected *S. aureus* samples and *S. aureus* standards were amplified by PCR using specific primers. The results showed that all samples and standard strains were amplified with clear bands of 618 bp (Figure 4C). At the same time, the suspected *P. aeruginosa* samples and *P. aeruginosa* standards were tested by qPCR, and the results showed that all the samples were positive (Figure 4D); the CT value was 24.34 ± 2.28. The above results showed that SA and PA were the bacteria found in the culture of secretions from bone defects.

3.6 Histopathological results

3.6.1 HE staining results

HE staining showed that on day 14, there was inflammatory cell infiltration, the bone trabecular structure was destroyed, abscesses were formed around the lesion, and osteolysis was manifested by disappearance of the bone nucleus (Figure 5A). On day 28, bone destruction became more obvious, and many inflammatory cells infiltrated the bone marrow cavity; furthermore, the number of macrophages increased and necrosis and abscesses formed,

indicating aggravation of the bone infection. According to Smeltzer scoring rules (Table 1), the pathological changes between the two groups have no significant difference ($p > 0.05$, Figures 5B,G).

3.6.2 Goldner staining results

Goldner staining showed that the bone cancellous around the defect was reduced on day 14 (Figure 5C), and bone cancellous damage in the medullary cavity was serious on day 28, which was consistent with the HE results. The trabecular structure of the bone at the edge of the defect was seriously damaged, the infection showed signs of spreading, and some new bone had formed (Figure 5D).

3.6.3 TRAP staining results

The TRAP staining results showed that the osteoclast-positive areas were mainly clustered near the defect on day 14 (Figure 5E), and osteoclast activity and function were significantly increased on day 28 (Figure 5F). The number of osteoclasts per unit area significantly differed between the two groups ($p < 0.05$, Figure 5H).

3.7 Results of differential expression analysis

Based on the criteria of adj. $p < 0.05$ and FC absolute value greater than 2, 1804 DEGs were identified after comparing the infected group and the control group,; among these, 743 were upregulated and 1,061 were downregulated (Table 3; Figure 6A). A heatmap was used to cluster DEGs and show the dynamic change in DEGs expression; red indicates upregulated expression and blue indicates downregulated expression. The expression changes and clustering results of DEGs in the test and control group are shown (Figure 6B).

3.8 The results of GO analysis of DEGs

GO cluster analysis showed that there were 1,615 DEGs clusters related to BP, 1,584 related to CC, and 1,397 related to MF (Figure 7A). The results of GO enrichment analysis showed that in terms of BP, DEGs were enriched in the response to stimulus, the immune response, the regulation of vasculature development, cell migration, skeletal system development, the regulation of vasculature development, cell migration, and animal organ morphogenesis. In terms of CC, DEGs were enriched in the ribonucleoprotein complex, the chromosome centromeric region, condensed chromosomes, extracellular spaces, the cell surface, etc. In terms of MF, DEGs were enriched in structural constituents of the ribosome, RNA binding, Wnt protein binding, and the combination of growth factor receptors (Figure 7B).

3.9 The results of KEGG clustering and enrichment of DEGs

To further study the clustering and enrichment pathways of DEGs, we performed KEGG analysis. The pathways of DEGs were mainly enriched in brite hierarchies, cellular processes, environmental information processing, and genetic information processing and metabolism (Figure 7C). The DEGs were mainly enriched in pathways in cancer, the PI3K-AKT signaling pathway, the AGE-RAGE signaling pathway, *S. aureus* infection, the P53 signaling pathway,etc. (Figure 7D).

3.10 PPI network establishment and core module and gene identification

To determine which genes and proteins play key central roles in infection, PPI analysis of DEGs was performed using the String database. After infection, the PPI network had a total of 62 nodes and 220 functional relationships between nodes (Figure 8).

MCODE plug-in analysis showed that core module 1 with the highest score in the PPI network included the Hedgehog signaling pathway (Figure 9A). Further analysis by the cytoHubba plug-in showed that the core genes that met the screening criteria were

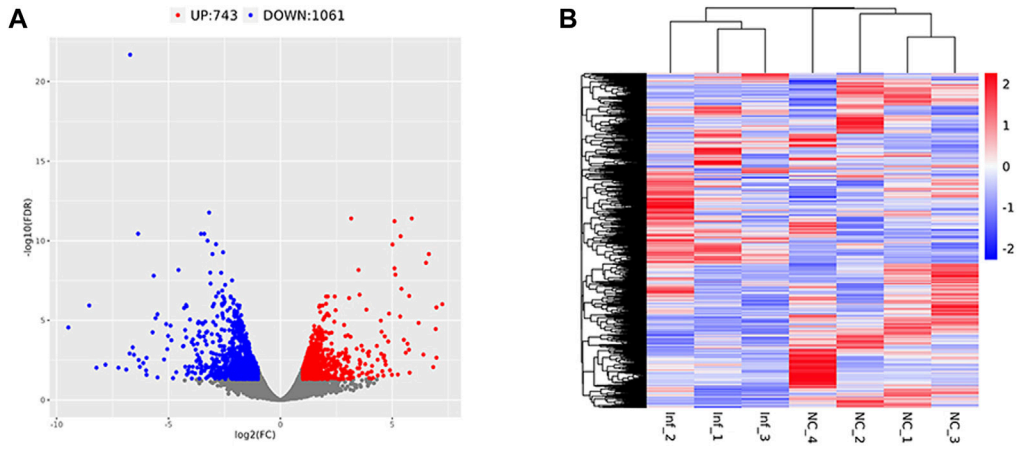

FIGURE 6
Differentially expressed gene volcano plot and heatmap Legend: Red represents upregulated genes, blue represents downregulated genes, and gray represents non-differentially expressed genes. **(A)** The differentially expressed gene volcano plot. **(B)** The differentially expressed gene heatmap.

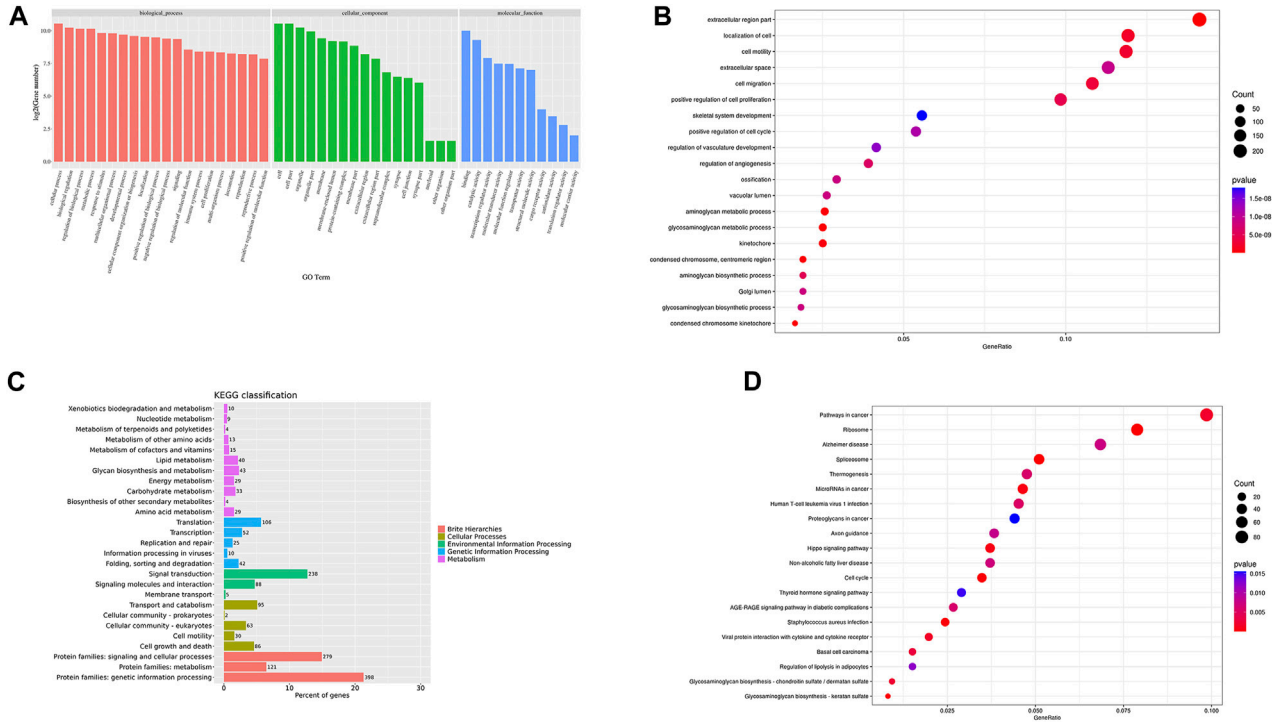

FIGURE 7
GO/KEGG cluster histogram and enrichment analysis bubble diagram Legend: **(A)**. The DEGs GO cluster histogram. **(B)**. The DEGs GO enrichment bubble diagram. **(C)**. The KEGG cluster histogram of DEGs. **(D)**. The KEGG enrichment bubble diagram of DEGs; the darker the color, the more significant the enrichment, and the larger the bubble, the larger the GeneRatio.

patched 1, 2 (PTCH1&2), hedgehog interacting protein (HHIP), GLI1, GLI-Kruppel family member, sonic hedgehog signaling molecule (SHH), myosin heavy chain 1&7&8 (MYH1&7&8), tenascin N (TNN), and actin alpha cardiac muscle 1 (ACTC1) (Figure 9B). Among them, PTCH1&2, HHIP, GLI1 and SHH were in the first module.

3.11 Prediction of transcription factors and the establishment of regulatory networks

According to iRegulon predictions, transcription factors with NES>4.5 were myocyte enhancer factor 2A, 2B gene (MEF2A, MEF2B), serum response factor gene (SRF), engrailed homeobox 1 gene (EN1) and paired-like homeodomain 3 gene (PITX3), which regulated 21, 33, 31, 11, and 15 DEGs, respectively (Figure 9C).

4 Discussion

To explore the mechanism of mandibular infection and evaluate the effect of bone repair materials on mandibular repair, it is necessary to select a suitable animal model. Animal experiments can avoid the risks of experiments in humans; in these experiments, the conditions are controllable and reliable data can be obtained. The use of experimental animals to simulate IMD is helpful to understand the mechanism of mandibular infection and the characteristics and properties of osteogenic materials.

Beagle dogs, miniature pigs, monkeys and other large animals, whose teeth and mandible structure are similar to humans, are ideal experimental animals for modeling the dental alveolar bone and mandible (Pieri et al., 2009; Ruehe et al., 2009; Tatić et al., 2010; Hwang et al., 2019). However, large animals are more expensive, they require more specific environments, and there are few canine models, most likely due to the ethical issues associated with using animals that are typically family pets. Rabbits and mice are small and medium-sized animals that are low cost and convenient and can be used to simulate many diseases in a short period of time; thus, these are important animal models in scientific research (Freilich et al., 2009; Munhoz et al., 2011; Bayar et al., 2012; Wang et al., 2018). However, the mouse mandible is small and difficult to manipulate, and mise are often used as a model of periodontitis (de Molon et al., 2014; Liu et al., 2021). Compared with rats, rabbits have larger mandibles and thicker bone walls, which can be used to simulate IMD. X-rays showed that the mandibular ascending branch of rabbits was very thin, and the defect here could not guarantee the stability of subsequent implant materials. The root of the molar in the mandibular body is longer, which can easily damage the root when the mandibular defect is made, and the front-end edentulous jaw area will not be disturbed; thus, this model does not affect rabbit eating and is more in line with ethical guidelines. Therefore, we chose to model the edentulous jaw region of rabbits.

In war trauma, bone infection is often caused by a variety of bacteria, among which, *S. aureus* and *P. aeruginosa* have a high detection rate (Ghieh et al., 2023). Clinically, *S. aureus* infection is the most common form of bone infection, so *S. aureus* is often the

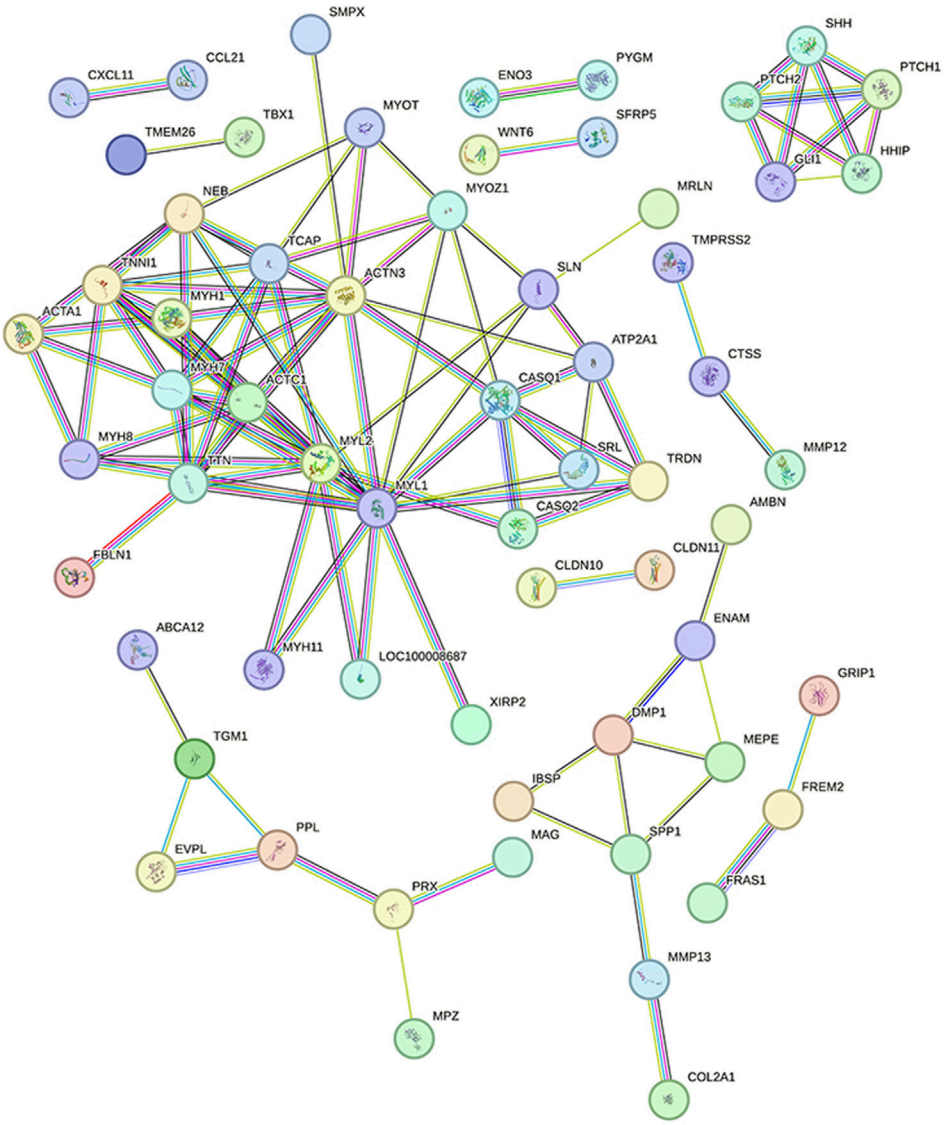

FIGURE 8
Protein interaction network diagram Legend: Each node represents the proteins produced by a single, protein-coding gene locus. The lines between nodes represent the interactions between proteins.

first choice for the establishment of an infectious bone defect model (Lüthje et al., 2020; Watson et al., 2020; Karau et al., 2022). *P. aeruginosa* can also be found in the infections of patients with bone infection. However, most bone infection models use a single bacterial strain (Norden and Keleti, 1980), so we chose these two types of bacteria to make our model. For the amount of bacteria, domestic and foreign scholars often use 10^6~10^8 CFU/mL to make the model (Wu et al., 2020; Wu et al., 2022). Due to the limitation of the scope of the defect area, we chose to inject 50 μL of a 3 × 10^8 CFU/mL bacterial mixture. Obvious pathological changes in bone infection appeared after 14 and 28 days, and the success rate reached 100%. There was no animal death during the observation period, indicating that 3 × 10^8 CFU/mL was the appropriate modeling concentration for the bacterial mixture. For bacterial implantation methods, most scholars utilize direct injection (Hriouech et al., 2020; Li et al., 2022; Yin et al., 2022). When the research involves implants, such as titanium implants and titanium nails, some scholars first implant bacteria on the surface of the implants and then put implants into the modeling area (Karau et al., 2022; Yang et al., 2022). Considering that the modeling simulates IMD caused by war trauma, we chose the method of directly injecting bacterial solution after the inducing mandible defects.

We used 5% sodium morrhuate as a vascular hardener, which blocks microcirculation, helps prevent systemic blood-borne infection, and simulates local blood circulation necrosis (Inzana et al., 2016), which occurs on the battlefield. Some people think that the use of vascular hardeners interferes with the establishment of infection models, but most people think that 5% sodium cod liver oleate, as an important treatment factor in the experiment, does not affect the modeling of bone infection and can prevent the failure of modeling due to macrophage phagocytosis of bacteria (Li et al., 2022; Wang et al., 2022).

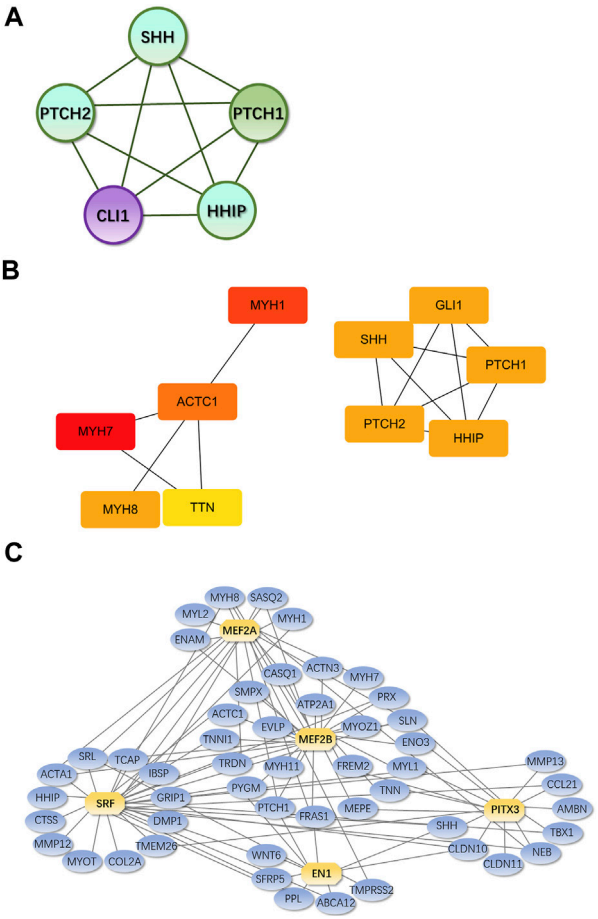

FIGURE 9
Core genes and modules and iRegulon predictions from PPI Legend: **(A)**. Core module 1. **(B)**. Core genes from cytoHubba; the darker the color, the higher the score and ranking; circles represent genes in the core module and lines represent the mutual regulation of genes. **(C)**. Transcription factors and their regulatory networks; Yellow indicates the predicted transcription factor, blue indicates DEGs, and the lines show the regulatory relationship between transcription factors and DEGs.

There are many ways to evaluate bone infection, such as gross observation, phenotypic evaluation and histological evaluation. For this model, we observed the general condition of rabbits at 9:00 a.m. every day before and after surgery, which was consistent with what was done in previous reports. The normal body temperature of rabbits at room temperature was 38.6°C (Kasa and Thwaites, 1990). After modeling, the rabbits' body temperature increased, food intake decreased, and local skin redness and swelling were the most intuitive signs of infection (Atkins, 1964). After modeling, the skin was red and swollen, the sinus was still present at 28 days, and pus could be seen flowing out of the sinus, proving that the infection persisted.

CBCT is one of the imaging devices that is commonly used in stomatology. Compared with X-ray, CBCT can be used to detect changes in the jaw in multiple dimensions. To dynamically observe the manifestations of bone tissue infection, we used CBCT for noninvasive detection after anesthetizing rabbits in different time. Due to the short observation time, serious symptoms such as bone malformations and pathological fractures did not appear in this model. The imaging observations were similar to the clinical findings and included osteolysis and decreased bone density (Lew and Waldvogel, 2004).

Some scholars conduct sampling and testing at 6–8 weeks (Odekerken et al., 2013; Bilgili et al., 2015), while others conduct testing at 3–4 weeks (Hwang et al., 2019; Zhang et al., 2019). The selection of model testing time depends on the type of model and the purpose of modeling. We chose 2–4 weeks because the histopathological scores at the two time points in the model have no significant difference, and the purpose of our modeling was to explore the pathogenesis of IMD to find appropriate treatment methods for early intervention. During the sampling process, pus lesions of varying degrees were found in the soft tissues around the site. After sampling, there was no periosteum covering the defect area, the bone surface was exposed, and the color was normal. The defect was filled with yellowish-white pus. This is consistent with the symptoms of animal bone limb infection models (Afzelius et al., 2022; Li et al., 2022).

Due to the influence of various factors, such as sampling site, surgical operation and bacterial virulence, there are many patients with bone infection that have negative bacterial cultures in clinical practice; thus, positive bacterial cultures are not necessary for the diagnosis of every bone infection. However, we used LB medium to culture bacteria from pus at the defect, and the results were positive. However, there was no significant change in the bacterial quantity at 28 days of infection or the ratio at 14 days of infection, indicating that the bacteria were stable in the middle and later stages, which was consistent with the findings of previous research reports (Vitko and Richardson, 2013). For the identification of bacterial species, traditional methods include observing the morphology of bacteria under an electron microscope and mass spectrometry identification. However, the observation error when using electron microscopy is large, and mass spectrometry analysis takes a long time (Alharbi et al., 2021). Existing biofluorescence imaging techniques can prevents animal sacrifice, but bacteria with fluorescent labels need to be constructed, and there is sometimes differences between the fluorescence intensity and the actual bacterial population (Kadurugamuwa et al., 2003). In recent years, PCR technology and high-throughput sequencing have emerged as strategies to detect bacteria, and these methods can accelerate the qualitative analysis of bacteria (Watts et al., 2017). We used PCR technology to compare the cultured bacteria with standard bacteria and demonstrated that the infection was caused by the two bacteria used in the modeling; furthermore, there was no interference from other bacteria during the operation and postoperative observation period.

Histopathological diagnosis is essential for bone infection, and appropriate scoring criteria are needed for complex histological changes. Smeltzer systematically proposed histopathological scoring criteria for rabbit tibial bone infection in the early stage; these criteria include aspects such as intramedullary inflammatory infiltration, intramedullary abscesses and osteonecrosis (Smeltzer et al., 1997). Currently, these aspects are used as evaluation criteria for the histopathological diagnosis of bone infection (Tiemann et al., 2014). After staining the bone tissue sections in the defect area, we used the Smeltzer score to distinguish the histopathological severity of the infection model; these results were consistent with the imaging results, and pathological changes such as inflammatory cell

infiltration, bone cell disappearance, and dead bone formation occurred in the model. Goldner tricolor staining results also indicated that the number of cancellous bone trabeculae around the defect was significantly reduced, and these changes verified that this model was consistent with the clinical pathological changes seen in bone infection (Tiemann et al., 2014; Jiang et al., 2019). In our results, the pathological tissue scores between the 14-day group and the 28-day group have no significant difference, which may indicate that the infection entered a chronic stage as a result of process stabilization.

As a specific marker enzyme that stains osteoclasts, TRAP staining can be applied to observe the distribution of osteoclasts over time and determine the osteoclast count per unit area to monitor the progression of bone destruction. The results showed that osteoclasts mainly appeared and gathered around the defect, and the number of osteoclasts increased with time. Some scholars believe that bacteria can contact osteoblasts after infecting bone tissue and be internalized in cells for long-term survival, during which they cause serious damage to bone tissue (Foster et al., 2014). Although the specific mechanism of the changes in bone mass caused by complex bacteria has not been fully elucidated, the experimental results suggest that, under the condition of infection, the intramedullary cancellous bone structure may be caused by the direct action of bacteria and the induction of proinflammatory factors, which promote the function of osteoclasts and inhibit osteoblasts; this action results in the gradual absorption of cancellous bone and causes further bone loss.

Infectious bone defects have become a research hot issue in recent years, but current studies focus on the role of specific genes (Evans et al., 1998; Scianaro et al., 2014; Delsing et al., 2015; Hofmann et al., 2016b; Van Asten et al., 2017). However, the response of patients with infectious jaw defects to pathogens is systematic, and we should pay attention not only to the immune response to bacteria but also to other aspects of the response, especially bone metabolism. Many patients have a risk of bone nonunion and pathological fracture due to bone infection throughout the course of this disease. Therefore, we need to further explore the overall transcriptomic changes in bone tissue during bone infection and search for key genes to provide ideas for the early diagnosis, systematic treatment and prevention of infectious jaw defects.

Through high-throughput transcriptomic sequencing analysis, we identified 1804 DEGs when comparing the experimental group and healthy rabbits 14 days after surgery. The DEGs were enriched in BPs including immune response, the response to stimulation, the development of the bone and vascular system and the regulation of cell movement. The same trends were seen for CC and MF. According to these results, the biological function of the body after infection includes the stimulation and immune response to pathogens. Meanwhile, the expression of genes contained in angiogenesis, osteogenesis and cell migration is downregulated, and bone metabolism is inhibited.

Similar to GO analysis, KEGG pathway analysis showed that the DEGs were enriched in tumor-related pathways, the PI3k-AKT pathway, the AGE-RAGE signaling pathway, etc. Cytokines produced by chronic inflammation cause abnormal inflammatory signaling pathway activation by inducing gene mutations and altering the expression and transformation of oncogenes and tumor suppressor genes. Meanwhile, chronic inflammation promotes the establishment of an immunosuppressive tumor microenvironment by recruiting a variety of immunosuppressive cells, which promotes the occurrence and development of tumors (Guthrie et al., 2013; Schaue et al., 2015). The PI3K-AKT and AGE-RAGE signaling pathways are closely related to inflammation (Stark et al., 2015). Akt is involved in inflammation and is a key protein downstream of PI3K signaling (Testa and Tsichlis, 2005). Lipopolysaccharides (LPS) stimulate human innate immune cells, and the expression of the proinflammatory factors IL-12, TNF-α and IL-6 increases after the administration of PI3K or Akt inhibitors, while the expression of the anti-inflammatory factor IL-10 decreases (Yin et al., 2016). Studies have shown that Akt activation can inhibit LPS-induced inflammation in mice and rabbits with sepsis (Wang et al., 2013). In some patients with type II diabetes, AGEs in periodontal tissues are elevated due to increased blood glucose, and AGEs bind to RAGE on the surface of immune cells, inducing the release of inflammatory factors, and ultimately accelerating the destruction of periodontal tissues (Blasco-Baque et al., 2017; Figueredo et al., 2019). Pathway enrichment analysis showed that pathways associated with the immune system and bone destruction were activated after infection, as well as pathways associated with anti-inflammatory activity.

In the PPI network constructed based on DEGs, the modules with the top 1 scores based on the MCODE plug-in were regarded as core modules; these modules were enriched in the Hedgehog signaling pathway. It is speculated that these molecular events are related to the pathogenesis of IMD. The core genes identified by the cytoHubba plug-in were SHH GLI1, PTCH1&2, HHIP, MYH1&7&8, ACTC1 and TNN, which were all located in the center of the PPI network and were concentrated in core modules; thus, we speculate that these genes may be intervention targets for repairing IMD.

Among the identified core genes, SHH, PTCH1&2, HHIP, and GLI1 are components of the Hedgehog signaling pathway, which is closely related to inflammation and tissue repair. Lowrey et al. (Lowrey et al., 2002) showed that when exogenous SHH peptide is added to the Hedgehog signaling pathway, and the proliferation of anti-CD3/CD28-activated peripheral blood $CD4^+$ T cells significantly increased. Kim JH et al. (Kim et al., 2010) showed that *Helicobacter pylori* can activate NF-kB and induce SHH expression in a CAGa-dependent manner, and SHH can be used as a chemical inducer of macrophages to recruit macrophages to the inflammatory region (Schumacher et al., 2012). In addition, SHH is also a chemical inducer of BMSCS in chronic inflammation (Warzecha et al., 2006). Circulatory signals (such as TGF-β) released during H. pylori-mediated gastritis can induce HH/GLI signaling in bone marrow-derived stromal cells and enable BMSCS recruitment to the inflammatory region. Cai et al. (Cai et al., 2012) interfered with rat BMSCs using rShh-N and found that rShh-N increased the proportion of cells in the S phase and the G2/M phase, enhanced ALP activity and matrix mineralization ability, and increased the expression of osteogenic genes, indicating that SHH promotes the proliferation and osteogenic differentiation of BMSCs. Baht et al. (Baht et al., 2014) used the mouse tibial fracture model and found that the expression of the Hedgehog target genes (GLI1 and PTC1) gradually increased 7, 14, and 21 days after fracture repair in wild-type mice, indicating that the activation of Hedgehog signaling plays a role in regulating fracture healing. In conclusion, the Hedgehog signaling pathway is involved in regulating the immune system during infection and can recruit

BMSCS cells to accelerate repair in the body. Therefore, the intervention of this pathway is expected to control infection and promote the repair of mandibular defects.

In this study, the MEF2 family was the transcription factor family whose prediction results were of the highest confidence in the IRegulon, which is consistent with the results of Zhang RK (Zhang et al., 2018). MEF2A is a component of the MEF2 transcription factor family (Pon and Marra, 2016). Chen C's (Chen et al., 2023) study indicated that Mef2A may upregulate the expression of the collagen X gene (Col10a1) by interacting with its cis-enhancer, and changes in MEF2A levels affect the chondrogenic marker gene's expression, such as Runx2 and Sox9. Blixt N (Blixt et al., 2020) showed that the loss of Mef2A inhibited the differentiation and activity of osteoclasts by altering the expression of key proteins that regulate the expression of osteoclast genes, and the ability of osteoclasts to differentiate was almost completely inhibited. The regulation of this transcription factor is expected to inhibit the activity of osteoclasts and prevent further expansion of bone defects.

In summary, we successfully established an infection defect animal model of the mandibular, which was formed by directly injecting bacterial solution into the defect area. The establishment process for this model was relatively simple, the production cost was low, the method has strong repeatability, and this model can simulate the histopathological changes seen in clinical bone infections. This model is a basic tool for the study of mandibular defects infected with complex bacteria. Subsequently, we screened and identified susceptibility genes, transcription factors and related signaling pathways associated with IMD by transcriptome sequencing and bioinformatics analysis. A total of 1804 DEGs related to IMD were found, including 11 core genes and 1 key transcription factor family. The above signaling pathways involved in the occurrence of IMD include immune regulation, promoting osteogenesis and regulating osteoclast differentiation. The treatment of infectious mandibular defects requires not only infection control, but also restoration of mandibular defects caused by infection. Therefore, further study of these molecules and their pathways will help to elucidate the specific mechanism of IMD and discover the target of repair IMD related to the regulation of immunity, the promotion of osteogenesis and the inhibition of osteoclast.

Data availability statement

The datasets presented in this study can be found in online repositories. The names of the repository/repositories and accession number(s) can be found below: https://www.ncbi.nlm.nih.gov/, GSE248915.

Ethics statement

The animal study was approved by the 920th Hospital Ethics Review Committee of the PLA Joint Logistic Support Force. The study was conducted in accordance with the local legislation and institutional requirements.

Author contributions

YZ: Writing–original draft, Writing–review and editing, Conceptualization, Investigation, Methodology, Supervision, Visualization. JS: Writing–original draft, Writing–review and editing, Data curation, Resources. CX: Writing–review and editing, Data curation, Formal Analysis. YaL: Writing–review and editing, Supervision. TH: Writing–review and editing, Formal Analysis. YiL: Writing–review and editing. LY: Writing–review and editing. QZ: Writing–review and editing. WZ: Writing–original draft, Writing–review and editing, Conceptualization, Funding acquisition, Methodology, Supervision.

Funding

The author(s) declare financial support was received for the research, authorship, and/or publication of this article. This work was supported by the Joint Special Fund for Applied Basic Research of the Yunnan Provincial Department of Science and Technology and Kunming Medical University (202101AY070001-028), the Scientific Research Fund of Yunnan Provincial Department of Education (2023Y0826), and the Yunnan Academician (Expert) Workstation (202305AF150120).

Acknowledgments

We would like to thank Li-jia He, Li-mei Shao, Qing Liu and Cheng LY from the Department of Stomatology of 920th Hospital of Joint Logistics Support Force of People's Liberation Army of China, for their assistance in the experiment. We thank the associate editor and the reviewers for their useful feedback that improved this paper and for the funding provided by the Yunnan Provincial Department of Education.

Conflict of interest

The authors declare that the research was conducted in the absence of any commercial or financial relationships that could be construed as a potential conflict of interest.

Publisher's note

References

Afzelius, P., Morsing, M. K., Nielsen, O. L., Alstrup, A. K. O., Jensen, S. B., and Jødal, L. (2022). Lymph nodes draining infections investigated by PET and immunohistochemistry in a juvenile porcine model. *Molecules* 27 (9), 2792. doi:10.3390/molecules27092792

Alharbi, A., Al-Dubaib, M., Elhassan, M. A. S., and Elbehiry, A. (2021). Comparison of MALDI-TOF mass spectrometry with phenotypic methods for identification and characterization of *Staphylococcus aureus* causing mastitis. *Trop. Biomed.* 38 (2), 9–24. doi:10.47665/tb.38.2.032

Ashburner, M., Ball, C. A., Blake, J. A., Botstein, D., Butler, H., Cherry, J. M., et al. (2000). Gene Ontology: tool for the unification of biology. *Nat. Genet.* 25 (1), 25–29. doi:10.1038/75556

Atkins, E. (1964). Elevation of body temperature in disease. *Ann. N. Y. Acad. Sci.* 121, 26–30. doi:10.1111/j.1749-6632.1964.tb13681.x

Baht, G. S., Silkstone, D., Nadesan, P., Whetstone, H., and Alman, B. A. (2014). Activation of hedgehog signaling during fracture repair enhances osteoblastic-dependent matrix formation. *J. Orthop. Res.* 32 (4), 581–586. doi:10.1002/jor.22562

Bayar, G. R., Gunaydin, Y., Ortakoglu, K., Gunhan, O., Aydintug, Y. S., and Sencimen, M. (2012). Histomorphometric analysis of new bone obtained by osteogenic periosteal distraction in ovariectomized rabbits. *Oral Surg. Oral Med. Oral Pathol. Oral Radiol.* 113 (4), 472–479. doi:10.1016/j.tripleo.2011.04.012

Bilgili, F., Balci, H. I., Karaytug, K., Sariyilmaz, K., Atalar, A. C., Bozdag, E., et al. (2015). Can normal fracture healing Be achieved when the implant is retained on the basis of infection? An experimental animal model. *Clin. Orthop. Relat. Res.* 473 (10), 3190–3196. doi:10.1007/s11999-015-4331-9

Blasco-Baque, V., Garidou, L., Pomié, C., Escoula, Q., Loubieres, P., Le Gall-David, S., et al. (2017). Periodontitis induced by Porphyromonas gingivalis drives periodontal microbiota dysbiosis and insulin resistance via an impaired adaptive immune response. *Gut* 66 (5), 872–885. doi:10.1136/gutjnl-2015-309897

Blixt, N., Norton, A., Zhang, A., Aparicio, C., Prasad, H., Gopalakrishnan, R., et al. (2020). Loss of myocyte enhancer factor 2 expression in osteoclasts leads to opposing skeletal phenotypes. *Bone* 138, 115466. doi:10.1016/j.bone.2020.115466

Cai, J. Q., Huang, Y. Z., Chen, X. H., Xie, H., Zhu, H., Tang, L., et al. (2012). Sonic hedgehog enhances the proliferation and osteogenic differentiation of bone marrow-derived mesenchymal stem cells. *Cell Biol. Int.* 36 (4), 349–355. doi:10.1042/cbi20110284

Chen, C., Wu, X., Han, T., Chen, J., Bian, H., Hei, R., et al. (2023). Mef2a is a positive regulator of Col10a1 gene expression during chondrocyte maturation. *Am. J. Transl. Res.* 15 (6), 4020–4032.

Cicuendez, M., Doadrio, J. C., Hernandez, A., Portolés, M. T., Izquierdo-Barba, I., and Vallet-Regí, M. (2018). Multifunctional pH sensitive 3D scaffolds for treatment and prevention of bone infection. *Acta Biomater.* 65, 450–461. doi:10.1016/j.actbio.2017.11.009

Delsing, C. E., Becker, K. L., Simon, A., Kullberg, B. J., Bleeker-Rovers, C. P., van de Veerdonk, F. L., et al. (2015). Th17 cytokine deficiency in patients with Aspergillus skull base osteomyelitis. *BMC Infect. Dis.* 15, 140. doi:10.1186/s12879-015-0891-2

de Molon, R. S., de Avila, E. D., Boas Nogueira, A. V., Chaves de Souza, J. A., Avila-Campos, M. J., de Andrade, C. R., et al. (2014). Evaluation of the host response in various models of induced periodontal disease in mice. *J. Periodontol.* 85 (3), 465–477. doi:10.1902/jop.2013.130225

Evans, C. A., Jellis, J., Hughes, S. P., Remick, D. G., and Friedland, J. S. (1998). Tumor necrosis factor-α, interleukin-6, and interleukin-8 secretion and the acute-phase response in patients with bacterial and tuberculous osteomyelitis. *J. Infect. Dis.* 177 (6), 1582–1587. doi:10.1086/515313

Figueredo, C. M., Lira-Junior, R., and Love, R. M. (2019). T and B Cells in periodontal disease: new functions in A complex scenario. *Int. J. Mol. Sci.* 20 (16), 3949. doi:10.3390/ijms20163949

Foster, T. J., Geoghegan, J. A., Ganesh, V. K., and Höök, M. (2014). Adhesion, invasion and evasion: the many functions of the surface proteins of *Staphylococcus aureus*. *Nat. Rev. Microbiol.* 12 (1), 49–62. doi:10.1038/nrmicro3161

Frangiamore, S. J., Saleh, A., Kovac, M. F., Grosso, M. J., Zhang, X., Bauer, T. W., et al. (2015). Synovial fluid interleukin-6 as a predictor of periprosthetic shoulder infection. *J. Bone JointSurg. Am.* 97A (1), 63–70. doi:10.2106/JBJS.N.00104

Freilich, M., Shafer, D., Wei, M., Kompalli, R., Adams, D., and Kuhn, L. (2009). Implant system for guiding a new layer of bone. Computed microtomography and histomorphometric analysis in the rabbit mandible. *Clin. Oral Implants Res.* 20 (2), 201–207. doi:10.1111/j.1600-0501.2008.01615.x

Ghieh, F., Bizri, A. R., Beaineh, P., Chalhoub, R., and Abu Sittah, G. (2023). Systematic review of the microbiology of osteomyelitis associated with war injuries in the Middle East and North Africa. *Med. Confl. Surviv* 39, 150–161. doi:10.1080/13623699.2023.2193862

Guthrie, G. J., Charles, K. A., Roxburgh, C. S., Horgan, P. G., McMillan, D. C., and Clarke, S. J. (2013). The systemic inflammation-based neutrophil-lymphocyte ratio: experience in patients with cancer. *Crit. Rev. Oncol. Hematol.* 88 (1), 218–230. doi:10.1016/j.critrevonc.2013.03.010

Hofmann, S. R., Kubasch, A. S., Range, U., Laass, M. W., Morbach, H., Girschick, H. J., et al. (2016b). Serum biomarkers for the diagnosis and monitoring of chronic recurrent multifocal osteomyelitis (CRMO). *Rheumatol. Int.* 36 (6), 769–779. doi:10.1007/s00296-016-3466-7

Hofmann, S. R., Schnabel, A., Rösen-Wolff, A., Morbach, H., Girschick, H. J., and Hedrich, C. M. (2016a). Chronic nonbacterial osteomyelitis: pathophysiological concepts and current treatment strategies. *J. Rheumatol.* 43 (11), 1956–1964. doi:10.3899/jrheum.160256

Hriouech, S., Akhmouch, A. A., Mzabi, A., Chefchaou, H., Tanghort, M., Oumokhtar, B., et al. (2020). The antistaphylococcal activity of amoxicillin/clavulanic acid, gentamicin, and 1,8-cineole alone or in combination and their efficacy through a rabbit model of methicillin-resistant *Staphylococcus aureus* osteomyelitis. *Evid. Based Complement. Altern. Med.* 2020, 1–9. doi:10.1155/2020/4271017

Hwang, S. C., Hwang, D. S., Kim, H. Y., Kim, M. J., Kang, Y. H., Byun, S. H., et al. (2019). Development of bone regeneration strategies using human periosteum-derived osteoblasts and oxygen-releasing microparticles in mandibular osteomyelitis model of miniature pig. *J. Biomed. Mater Res. A* 107 (10), 2183–2194. doi:10.1002/jbm.a.36728

Inzana, J. A., Schwarz, E. M., Kates, S. L., and Awad, H. A. (2016). Biomaterials approaches to treating implant-associated osteomyelitis. *Biomaterials* 81, 58–71. doi:10.1016/j.biomaterials.2015.12.012

Jiang, N., Wang, B. W., Chai, Y. M., Wu, X. B., Tang, P. F., Zhang, Y. Z., et al. (2019). Chinese expert consensus on diagnosis and treatment of infection after fracture fixation. *Injury* 50 (11), 1952–1958. doi:10.1016/j.injury.2019.08.002

Kadurugamuwa, J. L., Sin, L., Albert, E., Yu, J., Francis, K., DeBoer, M., et al. (2003). Direct continuous method for monitoring biofilm infection in a mouse model. *Infect. Immun.* 71 (2), 882–890. doi:10.1128/iai.71.2.882-890.2003

Kanehisa, M., and Goto, S. (2000). KEGG: kyoto encyclopedia of genes and genomes. *Nucleic Acids Res.* 28 (1), 27–30. doi:10.1093/nar/28.1.27

Karau, M., Schmidt-Malan, S., Mandrekar, J., Lehoux, D., Schuch, R., Cassino, C., et al. (2022). Locally delivered antistaphylococcal lysin exebacase or CF-296 is active in methicillin-resistant *Staphylococcus aureus* implant-associated osteomyelitis. *J. Bone Jt. Infect.* 7 (4), 169–175. doi:10.5194/jbji-7-169-2022

Kasa, W., and Thwaites, C. J. (1990). The effects of elevated temperature and humidity on rectal temperature and respiration rate in the New Zealand white rabbit. *Int. J. Biometeorol.* 34 (3), 157–160. doi:10.1007/bf01048713

Kim, J. H., Choi, Y. J., Lee, S. H., Shin, H. S., Lee, I. O., Kim, Y. J., et al. (2010). Effect of *Helicobacter pylori* infection on the sonic hedgehog signaling pathway in gastric cancer cells. *Oncol. Rep.* 23, 1523–1528. doi:10.3892/or_00000791

Lei, M. G., Gupta, R. K., and Lee, C. Y. (2017). Proteomics of *Staphylococcus aureus* biofilm matrix in a rat model of orthopedic implant-associated infection. *PLoS One* 12, e0187981. doi:10.1371/journal.pone.0187981

Lew, D. P., and Waldvogel, F. A. (2004). Osteomyelitis. *Lancet.* 364 (9431), 369–379. doi:10.1016/s0140-6736(04)16727-5

Li, Y., Chen, L., Lin, M., Wang, C., Zhang, R., Li, Y., et al. (2022). Micro-CT analysis of osteomyelitis of rabbit tibial for model establishment and biomaterials application in tissue engineering. *Heliyon* 8 (12), e12471. doi:10.1016/j.heliyon.2022.e12471

Liu, H., Zhang, X., Yang, Q., Zhu, X., Chen, F., Yue, J., et al. (2021). Knockout of NRAGE promotes autophagy-related gene expression and the periodontitis process in mice. *Oral Dis.* 27 (3), 589–599. doi:10.1111/odi.13575

Lowrey, J. A., Stewart, G. A., Lindey, S., Hoyne, G. F., Dallman, M. J., Howie, S. E., et al. (2002). Sonic hedgehog promotes cell cycleprogression in activated peripheral CD4(+) T lymphocytes. *J. Immunol.* 169, 1869–1875. doi:10.4049/jimmunol.169.4.1869

Lüthje, F. L., Skovgaard, K., Jensen, H. E., Blirup-Plum, S. A., Henriksen, N. L., Aalbæk, B., et al. (2020). Receptor activator of nuclear factor kappa-B ligand is not regulated during chronic osteomyelitis in pigs. *J. Comp. Pathol.* 179, 7–24. doi:10.1016/j.jcpa.2020.06.010

Munhoz, E. A., Bodanezi, A., Cestari, T. M., Taga, R., Ferreira Junior, O., and de Carvalho, P. S. (2011). Biomechanical and microscopic response of bone to titanium implants in the presence of inorganic grafts. *J. Oral Implantol.* 37 (1), 19–25. doi:10.1563/aaid-joi-d-09-00086

Norden, C. W., and Keleti, E. (1980). Experimental osteomyelitis caused by *Pseudomonas aeruginosa*. *J. Infect. Dis.* 141 (1), 71–75. doi:10.1093/infdis/141.1.71

Odekerken, J. C., Arts, J. J., Surtel, D. A., Walenkamp, G. H., and Welting, T. J. (2013). A rabbit osteomyelitis model for the longitudinal assessment of early post-operative implant infections. *J. Orthop. Surg. Res.* 8, 38. doi:10.1186/1749-799x-8-38

Pearson, J. J., Gerken, N., Bae, C., Lee, K. B., Satsangi, A., McBride, S., et al. (2020). *In vivo* hydroxyapatite scaffold performance in infected bone defects. *J. Biomed. Mater Res. B Appl. Biomater.* 108 (3), 1157–1166. doi:10.1002/jbm.b.34466

Pieri, F., Lucarelli, E., Corinaldesi, G., Fini, M., Aldini, N. N., Giardino, R., et al. (2009). Effect of mesenchymal stem cells and platelet-rich plasma on the healing of standardized bone defects in the alveolar ridge: a comparative histomorphometric study in minipigs. *J. Oral Maxillofac. Surg.* 67 (2), 265–272. doi:10.1016/j.joms.2008.06.036

Pon, J. R., and Marra, M. A. (2016). MEF2 transcription factors: developmental regulators and emerging cancer genes. *Oncotarget* 7 (3), 2297–2312. doi:10.18632/oncotarget.6223

Robinson, M. D., McCarthy, D. J., and Smyth, G. K. (2010). edgeR: a Bioconductor package for differential expression analysis of digital gene expression data. *Bioinformatics* 26 (1), 139–140. doi:10.1093/bioinformatics/btp616

Ruehe, B., Niehues, S., Heberer, S., and Nelson, K. (2009). Miniature pigs as an animal model for implant research: bone regeneration in critical-size defects. *Oral Surg. Oral Med. Oral Pathol. Oral Radiol. Endod.* 108 (5), 699–706. doi:10.1016/j.tripleo.2009.06.037

Schaue, D., Micewicz, E. D., Ratikan, J. A., Xie, M. W., Cheng, G., and McBride, W. H. (2015). Radiation and inflammation. *Semin. Radiat. Oncol.* 25 (1), 4–10. doi:10.1016/j.semradonc.2014.07.007

Schumacher, M. A., Donnelly, J. M., Engevik, A. C., Xiao, C., Yang, L., Kenny, S., et al. (2012). Gastric Sonic Hedgehog acts as a macrophage chemoattractant during the immune response to *Helicobacter pylori*. *Gastroenterology* 142, 1150–1159.e6. doi:10.1053/j.gastro.2012.01.029

Scianaro, R., Insalaco, A., Bracci Laudiero, L., De Vito, R., Pezzullo, M., Teti, A., et al. (2014). Deregulation of the IL-1β axis in chronic recurrent multifocal osteomyelitis. *Pediatr. Rheumatol. Online J.* 12, 30. doi:10.1186/1546-0096-12-30

Smeltzer, M. S., Thomas, J. R., Hickmon, S. G., Skinner, R. A., Nelson, C. L., Griffith, D., et al. (1997). Characterization of a rabbit model of staphylococcal osteomyelitis. *J. Orthop. Res.* 15 (3), 414–421. doi:10.1002/jor.1100150314

Stark, A. K., Sriskantharajah, S., Hessel, E. M., and Okkenhaug, K. (2015). PI3K inhibitors in inflammation, autoimmunity and cancer. *Curr. Opin. Pharmacol.* 23, 82–91. doi:10.1016/j.coph.2015.05.017

Tao, J., Zhang, Y., Shen, A., Yang, Y., Diao, L., Wang, L., et al. (2020). Injectable chitosan-based thermosensitive hydrogel/nanoparticle-loaded system for local delivery of vancomycin in the treatment of osteomyelitis. *Int. J. Nanomedicine* 15, 5855–5871. doi:10.2147/ijn.s247088

Tatić, Z., Stamatović, N., Bubalo, M., Jancić, S., Racić, A., Miković, N., et al. (2010). Histopathological evaluation of bone regeneration using human resorbable demineralized membrane. *Vojnosanit. Pregl.* 67 (6), 480–486. doi:10.2298/vsp1006480t

Testa, J. R., and Tsichlis, P. N. (2005). AKT signaling in normal and malignant cells. *Oncogene* 24 (50), 7391–7393. doi:10.1038/sj.onc.1209100

Tiemann, A., Hofmann, G. O., Krukemeyer, M. G., Krenn, V., and Langwald, S. (2014). Histopathological Osteomyelitis Evaluation Score (HOES) - an innovative approach to histopathological diagnostics and scoring of osteomyelitis. *GMS Interdiscip. Plast. Reconstr. Surg. DGPW* 3, Doc08. doi:10.3205/iprs000049

Van Asten, S. A., Nichols, A., La Fontaine, J., Bhavan, K., Peters, E. J., and Lavery, L. A. (2017). The value of inflammatory markers to diagnose and monitor diabetic foot osteomyelitis. *Int. Wound J.* 14 (1), 40–45. doi:10.1111/iwj.12545

Vitko, N. P., and Richardson, A. R. (2013). Laboratory maintenance of methicillin-resistant Staphylo-coccus aureus (MRSA). *Curr. Protoc. Microbiol.* 28, Unit 9C.2. doi:10.1002/9780471729259.mc09c02s28

Wang, A. M., Creasey, A. A., Ladner, M. B., Lin, L. S., Strickler, J., Van Arsdell, J. N., et al. (1985). Molecular cloning of the complementary DNA for human tumor necrosis factor. *Science* 228, 149–154. doi:10.1126/science.3856324

Wang, L., Lu, Y., Zhang, X., Zhang, Y., Jiang, D., Dong, X., et al. (2013). Mindin is a critical mediator of ischemic brain injury in an experimental stroke model. *Exp. Neurol.* 247, 506–516. doi:10.1016/j.expneurol.2013.01.022

Wang, S., Ye, L., Li, M., Zhan, H., Ye, R., Li, Y., et al. (2018). Effects of growth hormone and functional appliance on mandibular growth in an adolescent rat model. *Angle Orthod.* 88 (5), 624–631. doi:10.2319/120417-829.1

Wang, Y., Zhao, Z., Liu, S., Luo, W., Wang, G., Zhu, Z., et al. (2022). Application of vancomycin-impregnated calcium sulfate hemihydrate/nanohydroxyapatite/carboxymethyl chitosan injectable hydrogels combined with BMSC sheets for the treatment of infected bone defects in a rabbit model. *BMC Musculoskelet. Disord.* 23 (1), 557. doi:10.1186/s12891-022-05499-z

Warzecha, J., Gottig, S., Bruning, C., Lindhorst, E., Arabmothlagh, M., and Kurth, A. (2006). Sonic hedgehog protein promotes proliferation and chondrogenic differentiation of bone marrow-derived mesenchymal stem cells *in vitro*. *J. Orthop. Sci.* 11, 491–496. doi:10.1007/s00776-006-1058-1

Watson, E., Smith, B. T., Smoak, M. M., Tatara, A. M., Shah, S. R., Pearce, H. A., et al. (2020). Localized mandibular infection affects remote *in vivo* bioreactor bone generation. *Biomaterials* 256, 120185. doi:10.1016/j.biomaterials.2020.120185

Watts, G. S., Youens-Clark, K., Slepian, M. J., Wolk, D. M., Oshiro, M. M., Metzger, G. S., et al. (2017). 16S rRNA gene sequencing on a benchtop sequencer: accuracy for identification of clinically important bacteria. *J. Appl. Microbiol.* 123 (6), 1584–1596. doi:10.1111/jam.13590

Wu, W. J., Xia, C. L., Ou, S. J., Yang, Y., Zhou, X. Z., Ma, Y. F., et al. (2020). Sustainable release of vancomycin from micro-arc oxidised 3D-printed porous Ti6Al4V for treating methicillin-resistant *Staphylococcus aureus* bone infection and enhancing osteogenesis in a rabbit tibia osteomyelitis model. *Biomater. Sci.* 8 (11), 3106–3115. doi:10.1039/c9bm01968e

Wu, W. J., Xia, C. L., Ou, S. J., Yang, Y., Zhou, X. Z., Ma, Y. F., et al. (2022). Prophylactic effects of NFκB essential modulator-binding domain peptides on bone infection: an experimental study in a rabbit model. *J. Inflamm. Res.* 15, 2745–2759. doi:10.2147/jir.s346627

Yang, Y., Li, M., Zhou, B., Jiang, X., Zhang, D., and Luo, H. (2022). Graphene oxide/gallium nanoderivative as a multifunctional modulator of osteoblastogenesis and osteoclastogenesis for the synergistic therapy of implant-related bone infection. *Bioact. Mater* 25, 594–614. doi:10.1016/j.bioactmat.2022.07.015

Yin, H., Zhou, H., Kang, Y., Zhang, X., Duan, X., Alnabhan, R., et al. (2016). Syk negatively regulates TLR4-mediated IFNβ and IL-10 production and promotes inflammatory responses in dendritic cells. *Biochim. Biophys. Acta* 1860 (3), 588–598. doi:10.1016/j.bbagen.2015.12.012

Yin, X., Fang, Z., Fang, Y., Zhu, L., Pang, J., Liu, T., et al. (2022). Antimicrobial photodynamic therapy involving a novel photosensitizer combined with an antibiotic in the treatment of rabbit tibial osteomyelitis caused by drug-resistant bacteria. *Front. Microbiol.* 13, 876166. doi:10.3389/fmicb.2022.876166

Zhang, D., Liu, W., Wu, X. D., He, X., Lin, X., Wang, H., et al. (2019). Efficacy of novel nano-hydroxyapatite/polyurethane composite scaffolds with silver phosphate particles in chronic osteomyelitis. *J. Mater Sci. Mater Med.* 30 (6), 59. doi:10.1007/s10856-019-6261-7

Zhang, R. K., Li, G. W., Jiang, D., Zhang, D. W., Yu, B., and Yang, L. K. (2018). Transcription factors analysis of subchondral bone in early experimental osteoarthritis based on gene expression profiles. *Zhongguo Gu Shang* 31 (2), 165–169. doi:10.3969/j.issn.1003-0034.2018.02.014

frontiers | Frontiers in Bioengineering and Biotechnology

TYPE Original Research
PUBLISHED 12 January 2024
DOI 10.3389/fbioe.2023.1329752

OPEN ACCESS

EDITED BY
Jian Yu,
University of British Columbia, Canada

REVIEWED BY
Xiaopei Wu,
Wuhan University of Technology, China
Milad Fathi,
Middle East Technical University, Türkiye

*CORRESPONDENCE
Janis Locs,
Janis.Locs@rtu.lv

RECEIVED 29 October 2023
ACCEPTED 13 December 2023
PUBLISHED 12 January 2024

CITATION
Indurkar A, Kudale P, Rjabovs V, Heinmaa I, Demir Ö, Kirejevs M, Rubenis K, Chaturbhuj G, Turks M and Locs J (2024), Small organic molecules containing amorphous calcium phosphate: synthesis, characterization and transformation.
Front. Bioeng. Biotechnol. 11:1329752.
doi: 10.3389/fbioe.2023.1329752

Small organic molecules containing amorphous calcium phosphate: synthesis, characterization and transformation

Abhishek Indurkar[1,2], Pawan Kudale[3], Vitālijs Rjabovs[4], Ivo Heinmaa[5], Öznur Demir[1,2], Matvejs Kirejevs[1], Kristaps Rubenis[1,2], Ganesh Chaturbhuj[3], Māris Turks[4] and Janis Locs[1,2]*

[1]Rudolfs Cimdins Riga Biomaterials Innovations and Development Centre of RTU, Institute of General Chemical Engineering, Faculty of Materials Science and Applied Chemistry, Riga Technical University, Riga, Latvia, [2]Baltic Biomaterials Centre of Excellence, Headquarters at Riga Technical University, Riga, Latvia, [3]Department of Pharmaceutical Sciences and Technology, Institute of Chemical Technology, Mumbai, India, [4]Institute of Technology of Organic Chemistry, Faculty of Materials Science and Applied Chemistry, Riga Technical University, Riga, Latvia, [5]National Institute of Chemical Physics and Biophysics, Tallinn, Estonia

As the primary solid phase, amorphous calcium phosphate (ACP) is a pivotal precursor in cellular biomineralization. The intrinsic interplay between ACP and Howard factor underscores the significance of understanding their association for advancing biomimetic ACP development. While organic compounds play established roles in biomineralization, this study presents the synthesis of ACP with naturally occurring organic compounds (ascorbate, glutamate, and itaconate) ubiquitously found in mitochondria and vital for bone remodeling and healing. The developed ACP with organic compounds was meticulously characterized using XRD, FTIR, and solid-state ^{13}C and ^{31}P NMR. The morphological analysis revealed the characteristic spherical morphology with particle size close to 20 nm of all synthesized ACP variants. Notably, the type of organic compound strongly influences true density, specific surface area, particle size, and transformation. The *in vitro* analysis was performed with MC3T3-E1 cells, indicating the highest cell viability with ACP_ASC (ascorbate), followed by ACP_ITA (itaconate). The lowest cell viability was observed with 10 %w/v of ACP_GLU (glutamate); however, 1 %w/v of ACP_GLU was cytocompatible. Further, the effect of small organic molecules on the transformation of ACP to low crystalline apatite (Ap) was examined in Milli-Q® water, PBS, and α-MEM.

KEYWORDS

amorphous calcium phosphate, organic compounds, ascorbate, itaconate, glutamate, biomaterials, bone tissue engineering, biomimetics

1 Introduction

Amorphous calcium phosphate (ACP) has attracted much attention since it is the first calcium phosphate (CaP) phase synthesized and stabilized by cells and acts as a precursor of hydroxyapatite (HAp) (Combes and Rey, 2010). ACP provides a reservoir of calcium and phosphate ions that can be utilized for bone growth and regeneration. It is formed in the early stages of mineralization, which gradually crystallizes to HAp (Barrère et al., 2006). Naturally, ACP is stabilized by an organic compound known as the "Howard factor," whose exact chemical properties are unknown (Howard and Thomas, 1968; Lehninger, 1970). The association of Howard factor with ACP occurs in mitochondria, indicating that ACP forms a complex natural composite of inorganic CaP associated with an organic compound. In literature, synthetic ACP was prepared via numerous routes; however, the biogenic organic additives were not considered (Combes and Rey, 2010). The prerequisite for developing biomimetic ACP is the association of organic compounds present in mitochondria.

Considering this, numerous attempts have been undertaken in the development of ACP composite materials using macromolecules such as osteopontin, osteocalcin, dentin matrix protein, bone sialoprotein, dentin phosphoprotein, matrix extracellular protein, connexin 43, casein phospho-peptide, α_2HS-glycoproteins, fibrin, and albumin (Reynolds, 1998; Makowski and Ramsby, 2001; Gajjeraman et al., 2007; Yang et al., 2010; Yarbrough et al., 2010; Syed-Picard et al., 2013; Padovano et al., 2015; Zhao et al., 2018; Iline-Vul et al., 2020; Erceg and Dutour Sikirić, 2022; Nakamura et al., 2022; Indurkar et al., 2023a). However, *Becher et al.* have identified that many biological ubiquitous small organic molecules can inhibit the conversion of ACP to HAp at their respective tissue concentration (Becker, 1977). Considering these findings, ACP composites were developed using small organic molecules of polycarboxylate (such as citrate, succinate, acetate, and several amino acids), pyrophosphate, phosphocitric acid, polyphosphates as well as di-and-triphosphate nucleotide (Ikawa et al., 2009; Chinopoulos and Adam-Vizi, 2010; Grover et al., 2013; Stipniece et al., 2016; Feng et al., 2020; Indurkar et al., 2023b).

Mitochondria, which is the epicenter of numerous biochemical cycles, result in the formation of many small organic molecules (Scheffler, 2002; Osellame et al., 2012). Considering that ACP was associated with organic compounds in mitochondria, we have screened molecules based on their functions in bone remodeling and regeneration, such as ascorbate, glutamate, and itaconate, as shown in Figure 1.

Ascorbate (ascorbic acid or vitamin C) is crucial in collagen synthesis and is a vital organic compound in connective tissues and bone (Murad et al., 1981). Collagen provides structure and flexibility to the bone, enabling it to withstand mechanical stress. Without sufficient ascorbate, collagen synthesis is impaired, weakening the bone structure and increasing susceptibility to bone fractures (Gunson et al., 2013). Furthermore, osteogenic cell differentiation depends on ascorbate (Aghajanian et al., 2015; Thaler et al., 2022). Despite human's incapability of ascorbate synthesis, a specific mitochondrial uptake mechanism obtains vitamins from the diet. The vitamin carrier dehydroascorbic acid enters the mitochondria, where it is reduced and accumulated as ascorbic acid (Chen et al., 2022). Human studies have shown a positive relationship between ascorbic acid and biomineralization, emphasizing its importance in maintaining bone health (Chin and Ima-Nirwana, 2018).

Glutamate is an amino acid that plays a significant role in bone remodeling and healing processes. The glutamate receptors are expressed on the osteoblasts, osteoclasts, and bone marrow cells.

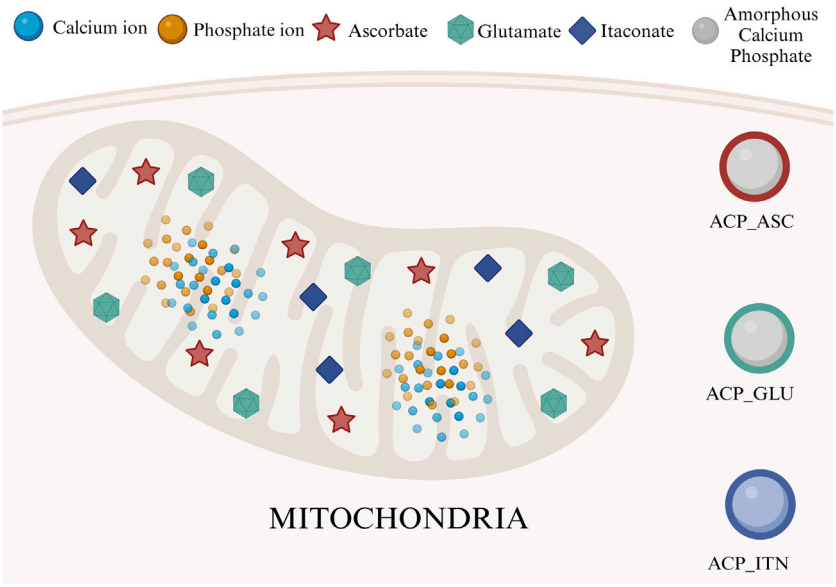

FIGURE 1
Mitochondria is an epicenter of various small organic compounds and ACP synthesis. In this study, we have utilized ascorbate, glutamate, and itaconate to develop composite ACP nanoparticles.

Activation of glutamate receptors controls the phenotype of osteoblasts and osteoclasts *in vitro* and bone mass *in vivo* (Brakspear and Mason, 2012). Moreover, glutamate has attained the nitrogen balance in a fractured bone, thus accelerating the bone healing process (Polat et al., 2007).

Itaconate is a metabolite that has gained much attention in recent years due to its role in immune regulation and inhibiting the production of proinflammatory molecules (Wang et al., 2022). Inflammation occurs in various bone disorders, such as rheumatoid arthritis and osteoporosis (Shi et al., 2022). Itaconate controls the immune response, thus indirectly controlling bone health. It also affects the function of macrophages, impacting the bone remodeling process (Peace and O'Neill, 2022). Itaconate interferes with the Krebs cycle, and changes in metabolism influences cell function and overall bone health (Yang et al., 2020).

Mitochondrial molecules such as acetate, citrate, ascorbate, glutamate, and itaconate play a major role in bone regeneration and are linked closely to mitochondrial function. As mitochondria are abundant in bone cells, the dysfunction of these organelles can lead to bone-related disorders (Kalani et al., 2014). The novel direction of incorporation of mitochondrial organic molecules in ACP offers a unique strategy to address bone-related disorders, potentially leading to innovative therapeutic interventions. Previously, we have developed ACP and its composite with citrate (ACP_CIT) and acetate (ACP_ACE) (Indurkar et al., 2023b). In this study, the ACP was synthesized with ascorbate (ACP_ASC), glutamate (ACP_GLU), and itaconate (ACP_ITN), were thoroughly characterized, and their cytocompatibility was evaluated. Additionally, transformation rate of ACP containing small organic molecules in different media were assessed.

The mechanism behind the transformation of ACP to low crystalline apatite (Ap) is a subject of ongoing debate. Several proposed mechanisms include dissolution reprecipitation, cluster reorganization, and solution-mediated solid-solid transformation. It is plausible that multiple processes may coincide during transformation (Jin et al., 2021). Previous studies have explored the transformation of ACP in aqueous solutions and have revealed the influence of factors such as pH, temperature, presence of foreign ions, and additives (polyelectrolyte, phospholipids, polyglycols, proteins, etc.), all of which can affect the transformation rate of ACP (Chatzipanagis et al., 2016). In this context, the role of small organic molecules containing ACP has received relatively less attention, with only a few reports available in the literature (Tsuji et al., 2008; Ikawa et al., 2009; Chatzipanagis et al., 2016; Sun et al., 2020).

In this study, we have also explored the transformation of ACP containing small organic molecules (acetate, glutamate, itaconate, ascorbate, and citrate) in three different mediums: Milli-Q® water, phosphate buffer saline (PBS), and alpha-modified minimum essential eagle medium with 10% fetal bovine serum (FBS) and 1% penicillin and streptomycin (α-MEM). The transformation of ACP was studied using X-ray diffraction (XRD) and Fourier-transformed infrared spectroscopy (FTIR) analysis performed at various time points. The results uncover how incorporation of small organic molecules into the ACP affects its crystallization rate in different media.

2 Material and methods

Calcium chloride (CAS 10043-52-4), trisodium phosphate (CAS 7601-54-9), sodium hydroxide (CAS 1301-73-2), and itaconic anhydride (CAS 2170-03-8) were procured from Sigma Aldrich, Germany. Calcium glutamate (CAS 19238-49-4) was obtained from BenchChem, United States, and ascorbic acid (CAS 50-81-7) was procured from Enola, Latvia.

2.1 Synthesis

To synthesize ACP_GLU, 150 mM calcium glutamate solution was prepared in Milli-Q® water. For the synthesis of ACP_ITN and ACP_ASC, a similar procedure was followed, starting with the preparation of 150 mM calcium chloride was prepared in Milli-Q® water, followed by the addition of 150 mM itaconic acid (ACP_ITN) and ascorbic acid (ACP_ASC) respectively. Afterwards, the pH of the calcium precursor solution was carefully adjusted to 11.5 using 3 M NaOH solution.

Following the pH adjustment, an equal amount (150 mL) of 100 mM of trisodium phosphate solution was added rapidly to the respective calcium salt solution (total volume 300 mL). Throughout the process, continuous stirring was maintained. Immediately after precipitation, the suspension underwent centrifugation at 3,000 rpm for 5 min, and the resulting precipitate was washed thrice with Milli-Q® water. Later, the centrifuge tube containing the precipitate was immersed in liquid nitrogen for 15 min, followed by freeze-drying for 72 h. The obtained power was stored in airtight containers until further characterization. Similarly, pure ACP, ACP_ACE and ACP_CIT were synthesized and characterized previously (Indurkar et al., 2023b).

2.2 Characterization

The phase composition of synthesized ACP variants were determined using X-ray diffraction, performed with a PANalytical Aeris diffractometer (Netherlands). The diffraction data were collected at 40 kV and 15 mA in a step mode with a step size of 0.04°, in the 2θ range from 10° to 60°.

The Fourier-transformed infrared spectroscopy (FTIR) analysis was performed using a Nicolet iS50 FT-IR spectrometer (Thermo Scientific, Waltham, MA, United States). Experiments were performed in transmission mode from the wavenumber ranging from 4,000 to 400 cm^{-1} with a resolution of 4 cm^{-1} (64 scans).

Solid-state CP MAS ^{13}C NMR spectra were recorded on Bruker AVANCE-II spectrometer at 14.1 T magnetic field using a home-built double resonance magic-angle-spinning probe for 4 x 25 mm Si_3N_4 rotors. The spinning speed of the sample was 12.5 kHz, the duration of the ramped polarization transfer pulse was 1 ms, and the relaxation delay between accumulations was 5 s. From 15,000 to 32,000, scans were accumulated for the spectra. The intensities were normalized to the number of scans and the sample's weight. Solid-state ^{31}P NMR spectra were recorded on JOEL, ECZR 600 NMR spectrometer. The experiment was performed with a 90° single pulse at a MAS frequency of 10 Hz with 2048 scans and a relaxation delay of 3 s.

The morphology and particle size of synthesized ACPs were evaluated by FEG-TEM (Tecnai G2 F30, United States) operated at 300 kV. The sample preparation was as follows: a small amount of powder was dispersed in isopropyl alcohol and sonicated in an ultrasonic bath. Further, the samples were placed on a carbon-coated grid and dried before analysis.

The true density of ACPs was analyzed by a helium pycnometer Micro UltraPyc 1200e (Quantachrome instruments, Boynton, FL, United States). Initially, the calibration was performed using a stainless-steel calibration sphere. It was followed by adding a known amount of ACP powder into the sample holder and purging it with helium gas in pulse mode (30 pulses). Subsequently, the sample volume was analyzed by pressurizing it at 10 psi with helium gas. The true density was calculated using sample weight and the analyzed sample volume. The analysis of each ACP was performed in triplicate.

The specific surface area (SSA) of the synthesized powder was analyzed using a nitrogen adsorption system Quadrasorb S1 (Quantachrome instruments, Boynton, FL, United States) by Brunauer-Emmett-Taylor (BET) method. Before analysis, the samples were degassed at room temperature for 24 h.

2.3 *In vitro* cytocompatibility

The preosteoblast (MC3T3-E1) cell line, obtained from ATCC, United States, was used in this study. Cells were grown in α-MEM (alpha-modified minimum essential medium eagle) with 10% fetal bovine serum (FBS) and 1% penicillin and streptomycin (pen-strep). The cells were cultured in 75 cm^2 flasks and maintained under 5% CO_2 at 37°C until the cell confluency reached 70%. The medium was replaced every 2 days.

For cellular analysis, suspensions were prepared by adding 10 %w/v ACP precipitate in α-MEM medium and incubated at 37°C in a humidified atmosphere of 95% air and 5% CO_2 for 24 h. The extracts were collected by centrifugation at 350 rpm for 5 min and filtered to eliminate solid particles. The extracts were diluted with α-MEM medium to get the desired concentration of 1 %w/v. Therefore, the total sample concentration comprises 10 %w/v and 1 %w/v of each ACP. The extracts were then added to MC3T3-E1 cells containing well plates and incubated for 48 h. The α-MEM medium was added as a positive control, whereas the α-MEM medium with 6 %vol DMSO (dimethyl sulfoxide) was utilized as a negative control. Each sample was prepared in triplicate, and the same procedure was performed for all ACP variants.

Cell viability was measured by Cell counting kit-8 (CCK-8) (Sigma Aldrich, United States). Briefly, cells at a density of 1×10^4 per well were seeded in a 96-well plate and pre-incubated at 37°C under 5% CO_2 for 24 h. After 24 h, the cell culture medium was replaced with various concentrations of ACP extracted medium [0 (as positive control), 10 %w/v, and 1 %w/v] and was further incubated for 48 h. CCK-8 was performed following the manufacturer's protocol to determine cell viability. Cell viability (in percent) was determined as the absorbance ratio between cells grown in the presence and absence of extracted solutions. The average values and standard deviations were calculated from six replicate samples. 6 %v/v DMSO was used as a negative control. The experiments were performed in triplicate, and cytocompatibility was evaluated by calculating cell viability using Eq. 1:

$$Cell\ viability\ (\%) = \frac{(Absorbance\ of\ sample - Absorbance\ of\ blank)}{(Absorbance\ of\ positive\ control - Absorbance\ of\ blank)} \times 100 \quad (1)$$

2.4 *In vitro* biomineralization

The *invitro* biomineralization experiments were performed with six types of ACP (pure ACP, ACP_ACE, ACP_GLU, ACP_ITN, ACP_ASC, and ACP_CIT). The ACP variants, such as pure ACP, ACP with citrate (ACP_CIT), and acetate (ACP_ACE), were synthesized, and characterization was reported in our previous study (Indurkar et al., 2023b). On the other hand, ACP variants such as ACP_GLU, ACP_ITN, and ACP_ASC were synthesized and characterized in the current study.

Experiments were performed in batch mode. To analyze the effect of small organic molecules containing ACP on transformation to Ap, 100 mg of ACP was added into 5 mL of media (Milli-Q® water, PBS, and α-MEM) preheated at 37°C. Further, the samples were incubated at 37°C and removed after specific time points (15, 30, 60, 120, 240, 1,440, 2,880, and 4,320 min) followed by centrifugation, freezing in liquid nitrogen for 15 min and freeze-drying for 72 h. The obtained powders were used for characterization as shown in Figure 2.

The obtained powders after freeze drying were analyzed using X-ray diffraction, performed with a Malvern Panalytical Aeris diffractometer (Netherlands). The diffraction data were collected at 40 kV and 15 mA in a step mode with a step size of 0.04°, in the 2θ range from 10° to 60°. This was followed by Fourier-transformed infrared spectroscopy (FTIR) analysis performed using a Nicolet iS50 FT-IR spectrometer (Thermo Scientific, Waltham, MA, United States). Experiments were performed in transmission mode in the range from 4,000 to 400 cm^{-1} with a resolution of 4 cm^{-1} (64 scans).

2.5 Statistical analysis

GraphPad Prism (GraphPad Software, San Diego, United States) was utilized to perform statistical analysis by two-way ANOVA and Tukey's multiple comparisons. Probability (P) values $*p < 0.05$ $**p < 0.01$ were considered the statistically significant differences. The results were expressed in mean ± standard deviation (S.D.).

3 Results and discussion

3.1 Synthesis and characterization

The synthesis of ACP_ASC and ACP_ITN showed color changes during the reaction. For instance, a colorless solution was formed when ascorbic acid was added to calcium chloride. However, as the pH of the solution increased to 11.5 using 3 M NaOH, a light-yellow solution was obtained. Therefore, the resultant ACP_ASC powder was light-yellow. Similarly, the color change was observed during the synthesis of ACP_ITN; when the itaconic anhydride was added to the calcium chloride, a colorless solution was formed, which changes to light brown when pH was increased to

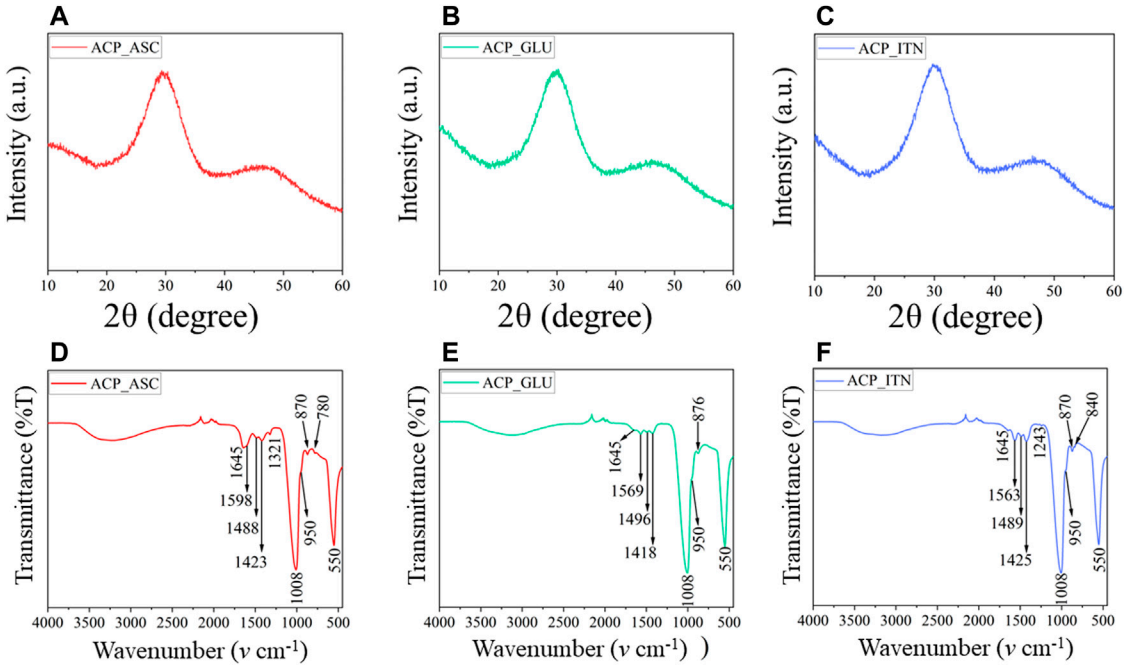

FIGURE 2
XRD **(A–C)** analysis confirms the amorphous nature of synthesized ACP with respective small compounds. The functional groups of ACP and the small compounds were revealed by FTIR **(D–F)** analysis.

11.5 using 3 M NaOH. Therefore, the resultant ACP_ITN powder had a brownish tinge. No color change was observed during the synthesis of ACP_GLU; therefore, a white powder was obtained.

3.1.1 XRD and FTIR analysis

The lack of crystalline order was observed in Figures 2A–C, confirming the formation of X-ray amorphous ACP. The FTIR spectra are shown in Figures 2D–F. The broad band of water observed between 3,000 cm^{-1} and 3,700 cm^{-1} corresponds to asymmetric and symmetric vibrations, and the band detected at 1,645 cm^{-1} represents the bending mode of water. These bands were observed in all the synthesized ACPs. In FTIR, the phosphate group shows four vibrational domains: *v1* (~950 cm^{-1}), *v2* (400–470 cm^{-1}), *v3* (1,000–1,150 cm^{-1}), and *v4* (500–620 cm^{-1}). The phosphate vibrational peaks at *v1, v3,* and *v4* were observed in all the synthesized ACP variants (Indurkar et al., 2023a).

The ascorbate bands in ACP_ASC were observed at ~3,000 cm^{-1} attributed to C-H vibrations. The bands between 1,500 cm^{-1} and 1,660 cm^{-1} indicate the presence of C=O and C-O vibrations (Williams and Rogers, 1937). The band at 1,488 cm^{-1} represents the CH bending, 1,423 cm^{-1} (CH_2 scissoring), 1,321 cm^{-1} (CH bending), 871 cm^{-1} (C-C ring stretching), and 780 cm^{-1} (OH out of plane deformation) (Yohannan Panicker et al., 2006; Bichara et al., 2010; Dabbagh et al., 2014).

The glutamate bands in ACP_GLU were observed between 3,000 cm^{-1} and 3,700 cm^{-1}, which also corresponds to -NH_2 vibrations (Cárdenas-Triviño et al., 2020). The bands at 1,569 cm^{-1} and 1,418 cm^{-1} correspond to the asymmetric and symmetric vibration of C=O (Barth, 2000). The bands observed in 1,496 cm^{-1} were attributed to symmetric and asymmetric stretching of C-O of carboxylate ion (De Castro and Cassella, 2016). The band observed at 876 cm^{-1} represents C-C vibration of glutamate (Sumayya et al., 2008).

The itaconate bands in ACP_ITN were observed at 1,645 cm^{-1} and attributed to C=C vibrations. The band at 1,563 and 1,425 cm^{-1} corresponds to the asymmetric and symmetric vibration of C=O (Damilola Olawale et al., 2020). Moreover, the band observed at 1,489 cm^{-1} and 1,243 cm^{-1} corresponds to O-C-O and C-O stretching (Loginova et al., 2016; Wibowo et al., 2018). The band observed at 870 cm^{-1} and 840 cm^{-1} indicates CH stretching vibrations (Uhanov et al., 2020).

3.1.2 NMR analysis

The solid-state ^{13}C and ^{31}P NMR analysis of synthesized ACPs is shown in Figures 3A, B. The ascorbate signals in ^{13}C NMR analysis of ACP_ASC show the lactone ring and β-carbon carbonyl groups in the range of 170–180 ppm, corresponding to C=O of the carbonyl group. The carbon atoms at γ-,δ-, and ε-positions of ascorbate appeared at 72 and 64 ppm (Tajmir-Riahi, 1991). The interaction of ACP resulted in the shifted peaks of ascorbate.

Glutamate signals in ^{13}C NMR analysis of ACP_GLU were observed at 183 and 169 ppm correspond to the carboxylate signals. The signal observed at 58 and 36 ppm was assigned to the carbon atom of the methine group bonded to the amino and carboxyl group (C2) and those branches in the alkyl chain (C3 and C4), respectively. The peak of the C4 carbon was shifted by the disordered conformation of the methylene group due to the association of ACP (Ikawa et al., 2009; Sannelli et al., 2023).

Itaconate signals in ^{13}C NMR analysis of ACP_ITN were observed at 183 and 163 ppm, corresponding to the carboxyl

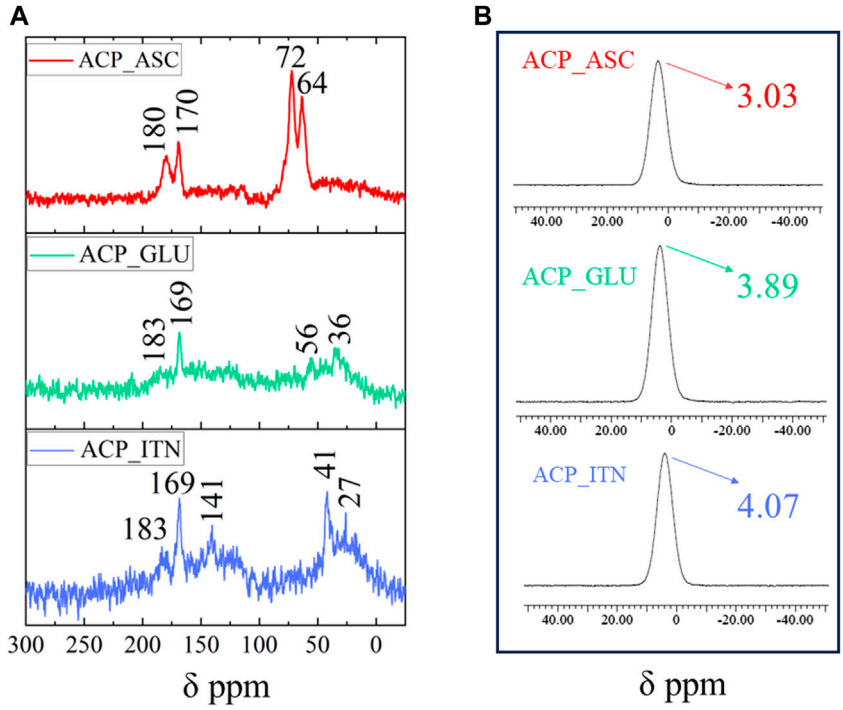

FIGURE 3
Solid-state NMR analysis of synthesized ACP with respective organic compounds **(A)** ^{13}C NMR and **(B)** ^{31}P NMR.

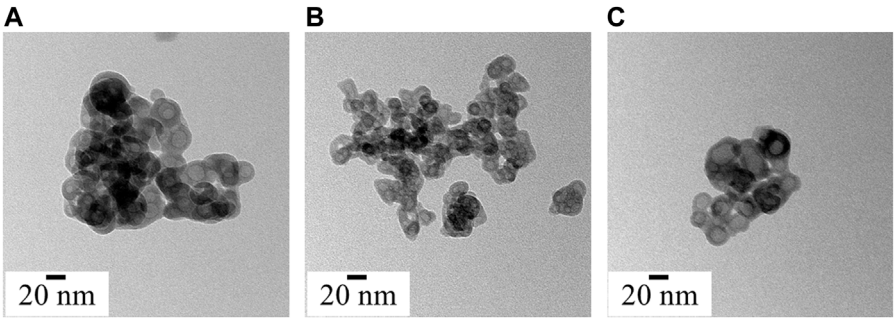

FIGURE 4
Morphology and particle size analysis of synthesized ACP variants **(A)** ACP_ASC, **(B)** ACP_GLU and **(C)** ACP_ITN.

group. The double bond signals were observed at 141 ppm. The carbon atom at the gamma position relative to the carboxyl group in the side chain appeared at 42 ppm, and the carbon atom of the methylene group was observed at 27 ppm (C3) (Strelko et al., 2011; Jahandideh et al., 2018; Vettori et al., 2022). The association with ACP resulted in peaks shifting in all the organic compounds.

The ^{31}P NMR spectra of ACP show characteristic broad Gaussian peaks between −15 and 15 ppm centered from 2.2 to 6.5 ppm (Indurkar et al., 2023b). As shown in Figure 4B, the broad peak was observed in all the synthesized ACPs centered at 3.03 ppm (ASP_ASC), 3.89 ppm (ACP_GLU), and 4.07 ppm (ACP_ITN) respectively. The NMR analysis has confirmed the formation of ACP in the presence of the respective organic compounds (ascorbate, glutamate, and itaconate).

3.1.3 Density and Brauner-Emmette-Teller (B.E.T.) analysis

The density and the specific surface area (SSA) of the synthesized ACP are shown in Table 1. The difference in density and SSA was observed, indicating the effect of the type of carboxyl ions on the synthesized ACP. One or several of the possible mechanisms can facilitate the interaction of ACP with organic compounds: 1) surface adsorption of organic compounds by chelating action of calcium ions of ACP and the carboxyl groups

TABLE 1 The density and specific surface area of the synthesized ACP.

Sample	Density (g/cm^3)	SSA (m^2/g)
ACP_ASC	2.82	115.2
ACP_GLU	2.64	92.4
ACP_ITN	2.43	130.3

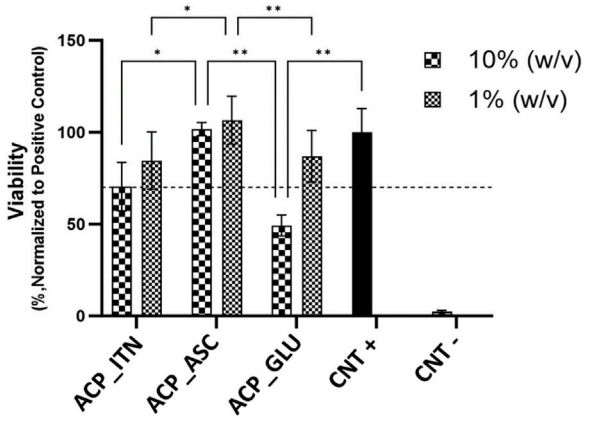

FIGURE 5
Relative cell viabilities of MC3T3-E1 cells cultured with extracts of ACP variants (10% and 1% w/v) prepared in α-MEM medium. All the samples were analyzed in triplicate, and data is presented in average and standard deviation. The CNT + and CNT−were positive and negative controls.

of organic compounds (Gorbunoff, 1984; Zong et al., 2023); 2) Organic compounds bearing two carboxylate ions ($^{-}$O(O)C-R-C(O)O^{-}) can substitute the hydrogen phosphate ion (HPO_4^{2-}) during the precipitation of ACP (Yokoi et al., 2022); 3) interaction between phosphates and carboxylates groups (P-O···H-O-C or P-O-H···O-C) (Corbridge, 1971). 4) Interaction of ascorbate anion can interact with calcium and/or phosphate group (Xu et al., 2019). However, more advanced analysis is required to evaluate the exact interaction of ACP with the organic compound.

3.1.4 Morphological analysis

Under electron microscopy, the morphological appearance of ACP shows spherical particles of a few tenths of the nanometre scale (Zhao et al., 2012). All the synthesized ACPs show the characteristic spherical morphology, as shown in Figure 4. Numerous research groups have consistently identified the biomimetic size range of ACP, typically falling between 10 and 50 nm (Niu et al., 2014; Hoeher et al., 2023). Interestingly, the ascorbate, glutamate, and itaconate ACP variants show spherical hollow particles that align with the biomimetic size range. Moreover, ACP is highly sensitive to the electron beam and crystalizes on high electron beam exposure (Lotsari et al., 2018). The crystallization of synthesized ACP under a high electron beam is presented in Supplementary Figure S1.

3.1.5 Cell culture analysis

The cytocompatibility was evaluated by analyzing the cell viability of MC3T3-E1 cells in the presence of synthesized ACP extracts (10% and 1% w/v) prepared in α-MEM medium, as shown in Figure 5. The absorbance recorded for the cells cultured in the plain cell culture medium was normalized to 100% and termed positive control (CNT+). The cells cultured in 10% w/v ACP_GLU showed the lowest cell viability compared to other groups. The higher glutamate concentration can lead to excitotoxicity and or oxidative glutamate toxicity (Schubert and Piasecki, 2001; Kritis et al., 2015). However, reducing the concentration to 1% w/v, ACP_GLU enhanced the cell viability. The concentration of 10% w/v ACP_ITN and 10% w/v ACP_ASC was better than 10% w/v ACP_GLU. A similar trend was found in 1% w/v ACP_ITN and 1% w/v ACP_ASC. The cell viability of 10% and 1% w/v ACP_ASC was better than CNT+. Ascorbate is critical for the differentiation of the preosteoblast, and this may be the reason for the higher cell viability (Hadzir et al., 2014; Hwang and Horton, 2019). The preliminary analysis has confirmed the cytocompatibility of ACP_ASC (10% and 1% w/v), ACP_ITN (10% and 1% w/v), and ACP_GLU (1% w/v).

3.1.6 *In vitro* biomineralization

The first *in vitro* biomineralization was investigated by Boskey and Posner by examining the impact of pH on the conversion of ACP to Ap. Their finding has provided critical insights revealing that transformation rate increases with higher pH levels. Furthermore, it was also discovered that the conversion pathways remain unaffected by the following factors: a) the nature of the buffer system used, b) the presence of a different type of univalent ions, and c) whether the material was in contact with mother liquor or filtered, dried, or added to the fresh buffer. Additionally, the transformation rate exhibited dependency on several factors, including smaller particle size, faster stirring rate, and higher ACP concentration (Boskey and Posner, 1973). Temperature also emerged as a significant variable affecting the conversion of ACP. For instance, at pH of 7.5, ACP converts five times more rapidly at 37°C than at 25°C. The synthesis condition of ACP was also found to influence the transformation rate (Eanes, 1998). Given the focus of our study on the application of ACP and its variants in tissue engineering, we consistently maintained 37°C in all the transformation experiments.

XRD analysis was employed to track alteration in long-range structural order as samples underwent successive progressive crystallization in different solvents, as shown in Supplementary Figure S2. In the analysis of CaP material, it is conventionally assumed that any part of the diffractogram not corresponding to the crystalline phase is amorphous. Nonetheless, there is ambiguity between non-coherent diffraction domains and genuinely separated amorphous phases. In the case of CaP (except hydroxyapatite), various ionic substitutions, defects, and vacancies can disrupt the regularity of the atomic array. This can significantly increase background diffraction patterns without necessarily implying the presence of any amorphous phase or domain (Combes and Rey, 2010). Therefore, FTIR analysis was also employed to provide additional insights. The FTIR spectra of all the ACP variants are shown in Supplementary Figure S3. The characteristic bands of ACP and the respective small organic molecules are shown in Supplementary Table S1).

FTIR spectral examination of ACP variants exhibits a distinct short order evident through absorbance band related to phosphate absorption bands. Notably, the ACP spectrum displays a broader band with no evident splitting in the ν_4 PO_4^{3-} vibration region. The highlights distinction between XRD, which primarily detects specific

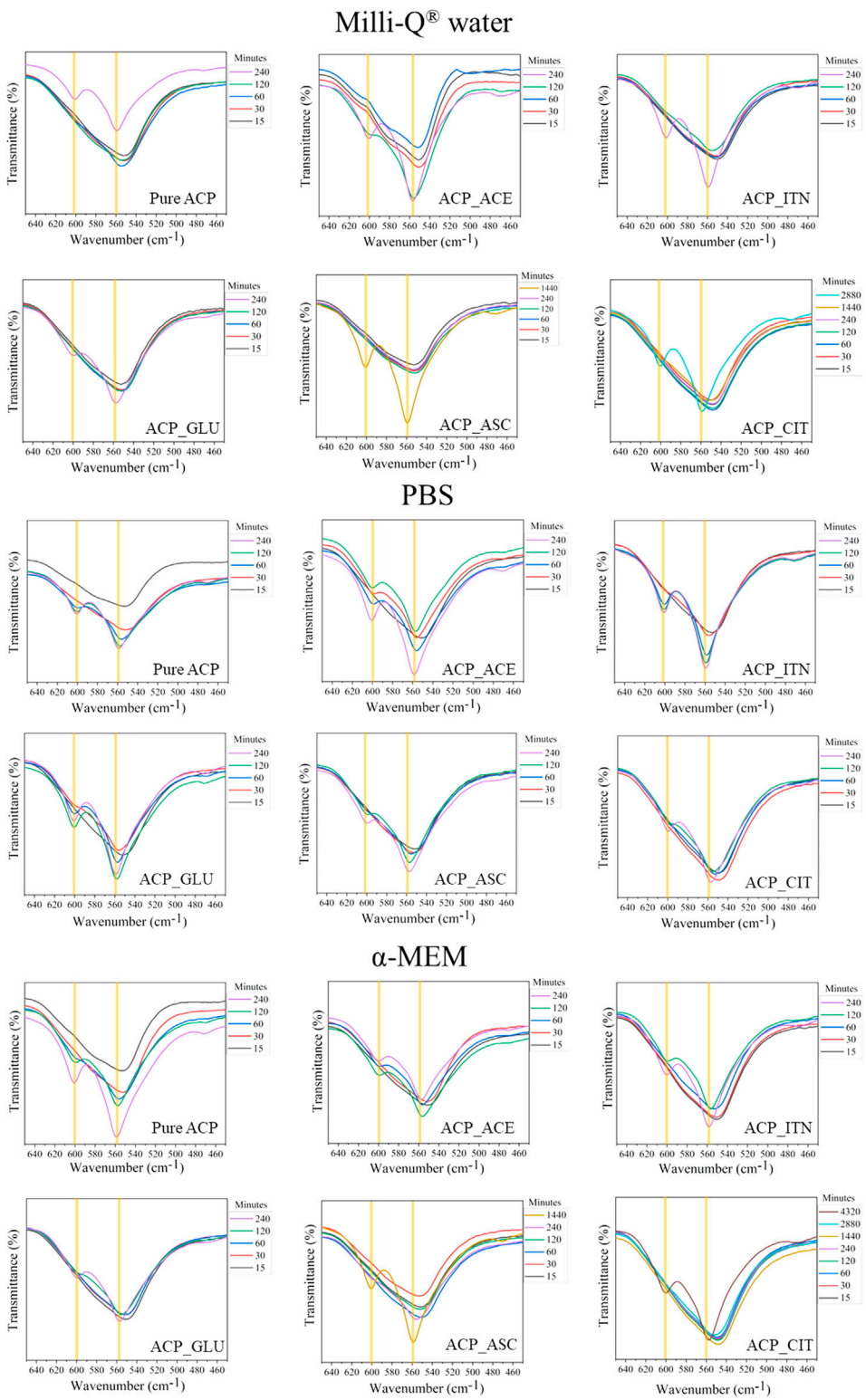

FIGURE 6
The stability of ACP in the different mediums was evaluated based on v_4 PO_4^{3-} vibration region. The samples that did not show evident splitting in the v_4 PO_4^{3-} vibration region was termed amorphous; on the contrary, the samples that showed splitting of v_4 PO_4^{3-} vibration region were termed crystalline.

TABLE 2 Time required for transformation of ACP to Ap evaluated from peak formation in XRD and splitting of the v_4 PO_4^{3-} vibration observed in FTIR spectra.

Samples	Milli-Q® water (min)	PBS (min)	α-MEM (min)
Pure ACP	120	30	60
ACP_ACE	60	15	30
ACP_ITN	120	30	60
ACP_GLU	120	30	60
ACP_ASC	240	60	120
ACP_CIT	1,440	120	2,880

peaks associated with crystalline phases, and FTIR, which detects absorbances originating from both amorphous and crystalline components (Querido et al., 2020). The splitting of the v_4 PO_4^{3-} vibration region confirms the crystallization of ACP, as shown in Figure 6. XRD analysis was utilized to complement the data obtained from FTIR analysis, and the stability time of the ACP variant in the respective medium is presented in Table 2.

The inorganic contentment in the respective solvents is presented in Supplementary Table S2. The inorganic ions were absent in Milli-Q® water; therefore, the transformation rates of ACP variants (except ACP_CIT) were slower compared to PBS and α-MEM medium. In PBS, all the synthesized ACP variants underwent a rapid transformation, aligning perfectly with findings from the literature (Zhao et al., 2012).

Previous studies have revealed that in the presence of PBS solution, the organic molecules are released from the surface of ACP, likely due to ionic exchange with the phosphate groups in the medium. This leads to an elevated concentration of phosphate in ACP, thus reducing stability and resulting in rapid transformation to low crystalline apatite (Chatzipanagis et al., 2016). This outcome was consistently observed for all the synthesized ACP variants. The phosphate content in α-MEM medium was less compared to PBS; therefore, the transformation rates were slower (except ACP_CIT). In the case of ACP_CIT, the highest stability of 2,880 min was observed in α-MEM medium. Previous studies have shown the interaction of serum albumin with citrate-stabilized gold nanoparticles forming protein corona (Dominguez-Medina et al., 2012; Zhang et al., 2014; Szekeres and Kneipp, 2018). Similarly, the delayed transformation of ACP_CIT may be due to the interaction of negatively charged citrate with FBS present in α-MEM medium. However, in-depth analysis is required to confirm this phenomenon.

The organic molecules such as acetate, itaconate, glutamate, and citrate contain carboxyl groups, as shown in Figure 7. Both the carboxyl and ascorbate anion have the potential to interact with both calcium and phosphate ions present in ACP (Winand et al., 1961; Corbridge, 1971; Ancillotti et al., 1977; Chatzipanagis et al., 2016). Due to the combination of these factors, the interaction between these organic compounds and ACP is complex and demands a sophisticated analysis to fully comprehend the precise nature of these interactions.

To investigate the effect of small organic molecules on transformation rate, pure ACP was used for comparison as shown in Figure 8. The variations in the transformation rate can be attributed to the changes in the physiochemical properties of ACP, such as particle size, morphology, specific surface area (SSA), and density induced by different functional groups from the respective small organic molecules, as illustrated in Supplementary Table S3.

The fastest conversion rate was observed in ACP_ACE in all the respective mediums compared to other ACP variants. Acetate consists of one carboxyl group (COO^-) representing a negative charge of −1. Monocarboxylic ions can interact with calcium ions but are not capable of bridging two calcium ions. The incompatible charge of −1 promotes the formation of HAp (Yamada et al., 2021). A similar phenomenon is observed in the case of fluoride-doped ACP. Fluoride ions also have a negative charge of −1; therefore, the transformation of ACP to Ap was faster in the presence of fluoride-doped ACP than in pure ACP (Ten Cate and Featherstone, 1991; Iafisco et al., 2018).

Pure ACP, ACP_GLU, and ACP_ITN represent similar conversion rates in respective medium. Our previous study observed presence of carbonate (CO_3^{2-}) in pure ACP. The presence of carbonate ions in ACP is known to retard its conversion to Ap (Combes and Rey, 2010; Edén, 2021). Similarly, itaconate and

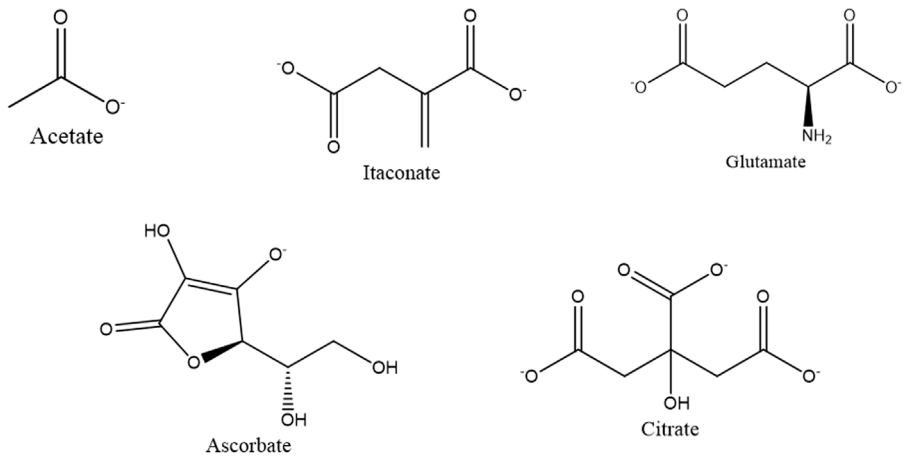

FIGURE 7
Small organic compounds are utilized for the synthesis of ACP variants.

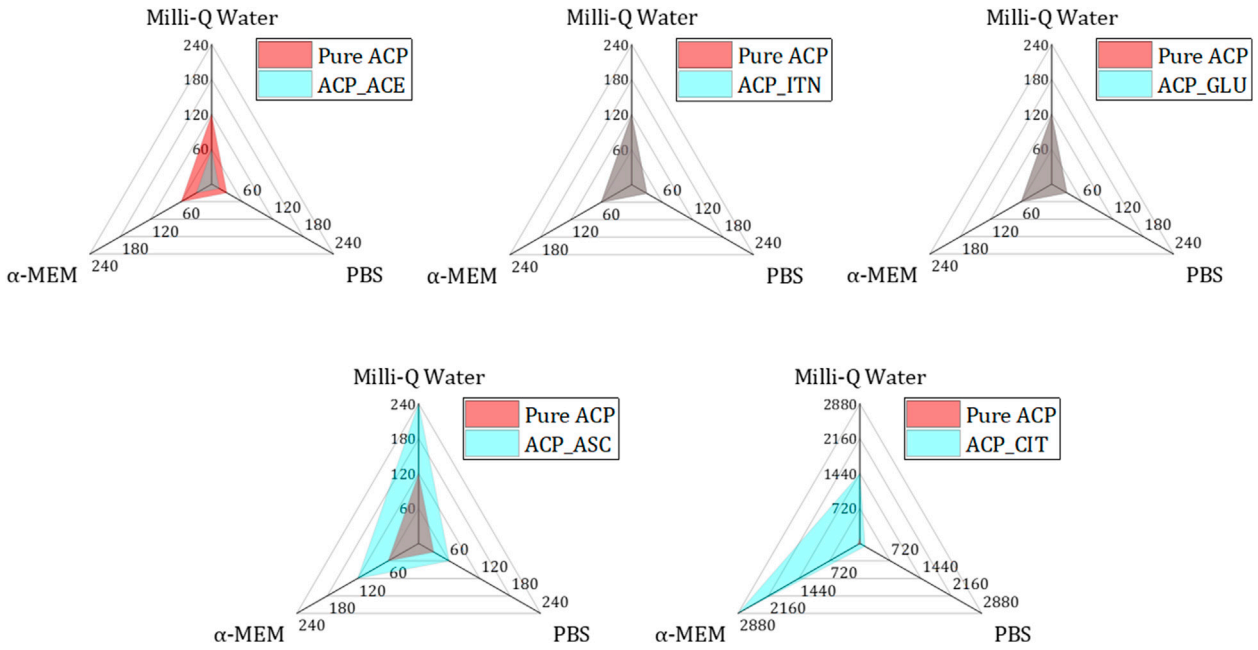

FIGURE 8
Analysing the transformation rates of small organic molecules containing ACP (blue) in comparison to pure ACP (red) across different mediums (Milli-Q® water, PBS, and α-MEM) reveals distinct patterns. Specifically, ACP_ACE exhibited accelerated transformation rates in all mediums compared to pure ACP (both represented in grey colour by combination of blue and red). Conversely, ACP_ITN and ACP_GLU demonstrated similar transformation rates to pure ACP. Notably, ACP_GLU and ACP_CIT displayed slower transformation rates compared to their pure ACP counterpart.

glutamate are dicarboxylic compounds with a negative charge of −2 and may behave similarly to carbonate-substituted ACP. Therefore, the transformation rate of pure ACP, ACP_ITN and ACP_GLU was the same.

In the case of ascorbate containing ACP, the conversion was slower than that of other ACP variants (except ACP_CIT). The presence of the ascorbate anion can interact with ACP, thus retarding its conversion to Ap. Previous studies have shown delayed struvite crystallization in the presence of ascorbate due to a decrease in pH (Manzoor et al., 2018). Additionally, ascorbate in the bloodstream has been shown to prevent struvite stone formation in urine (Flannigan et al., 2014). Similarly, delayed sugar crystallization was observed in the presence of ascorbic acid (Zhou and Roos, 2012). Likewise, a delayed transformation was observed in ACP_ASC despite its higher surface area (115.2 m^2/g). However, a more comprehensive analysis is required to confirm the exact behavior.

The highest stability was observed in ACP_CIT. Citrate is a tricarboxylic acid that can interact in four ways with ACP: a). The carboxyl group can interact with calcium ions of ACP. B) $HCit^{3-}$ can substitute PO_4^{3-} of ACP. c) The hydroxy group of citrates can interact with phosphate ions and/or d) The phosphate ions can interact with the carboxyl group of citrates (Indurkar et al., 2023b). Previous reports have also shown citrate's efficacy in stabilizing ACP (Chen et al., 2014; Sakhno et al., 2023).

The ACP variants displayed a generally spherical and hollow morphology, except for ACP citrate, which exhibited a dense spherical structure. Differences in the morphologies may also contribute to the transformation rate. However, more detailed analysis is required to confirm this phenomenon.

4 Discussion

The synthesis reactions of ACP are known for their rapid nature and are typically performed under alkaline conditions. However, owing to the triprotic nature of phosphate ions, fluctuations in pH, temperature, and precursor concentration play a crucial role in determining the efficiency of precipitation and particle size of the synthesized product (ACP) (Mekmene et al., 2009).

To address these inherent challenges, we have devised a straightforward and effective method to synthesize ACP, aiming to minimize pH variations. Based on this approach, we have previously achieved successful ACP synthesis with citrate and acetate (Indurkar et al., 2023b). Inspired by this successful strategy, we have extended our efforts to synthesize ACP with other organic compounds such as ascorbate, glutamate, and itaconate. The schematic representation of our synthesis method is outlined in Figure 9. These methods have broadened the scope of ACP synthesized by incorporating diverse organic compounds, thus showcasing its versatility and potential for further exploration in developing novel ACP composites.

Our prior study also synthesized two pristine ACPs devoid of organic compounds (Indurkar et al., 2023b). The ACP particles exhibited an SSA of 105 m^2/g and particle size of less than 20 nm. In that investigation, acetate and citrate have shown distinct effects on the properties of ACP. The surface area and particle size were affected when ACP was linked with acetate and citrate. Building on these findings, our current study investigated the effect of other organic compounds, ascorbate, glutamate, and

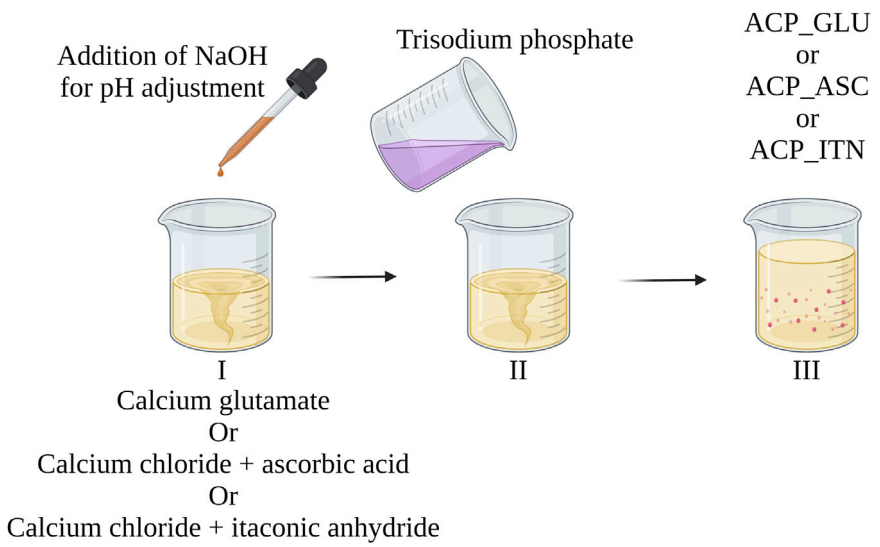

FIGURE 9
Illustrating the systematic approach to achieve controlled ACP (with organic compounds) synthesis with minimal pH variations. The approach was previously reported in developing pure ACP and ACP with citrate and acetate (Indurkar et al., 2023b).

itaconate, on the properties of ACP. Interestingly, introducing these compounds impacted the SSA and particle size. Moreover, an effect on cytocompatibility was also observed, wherein the 10% w/v ACP_GLU represented a toxic effect on MC3T3-E1 cells.

Glutamate is a versatile molecule with a potential role in influencing cellular processes and viability in bone tissue (Skerry and Taylor, 2005). It has been suggested that glutamate can impact cell proliferation and differentiation through group III metabotropic glutamate receptors expressed in mouse calvaria osteoblasts. Furthermore, previous investigations have revealed that specific concentrations within 50 μM to 1 mM enhance survival rates of human primary osteoblasts when exposed to tumor necrosis factor-α and interferon-γ. However, it is essential to note that a cytotoxic effect was observed when glutamate concentration exceeded 10 mM (Genever and Skerry, 2001).

The cytotoxicity resulting from elevated glutamate levels is attributed to the induction of oxidative stress. This occurs because of triggering the release of reactive oxygen species and nitric oxide. Consequently, excess glutamate concentration leads to oxidative damage to MC3T3-E1 cells, resulting in apoptosis (Fatokun et al., 2006). A similar behavior may be responsible for 10% w/v ACP_GLU samples resulting in cell death. However, further advanced analysis and experiments are required to confirm this phenomenon and gain a deeper understanding of the underlying mechanism.

Examination into *in vitro* biomineralization has revealed a significant influence of small organic molecules on the transformation rate of ACP. By aligning ACP with small organic molecules and solvents, transformation necessities can be tuned based on the applications. FTIR analysis has confirmed that the resulting Ap retained characteristics of the respective small organic molecules. This observation suggests the potential utilization of transformed Ap as an advanced bone substitute material.

5 Conclusion

The study introduces a promising avenue for biomimetic ACP developed by leveraging mitochondrial (ascorbate, glutamate, and itaconate) small organic molecules. Synthesized ACP variants were characterized using XRD, FTIR, and NMR, which confirmed the presence of respective organic compounds and the amorphous nature of ACP. Advanced analysis is required to understand the exact interaction of the organic compounds with ACP. *In vitro* analysis using MC3T3-E1 cells has provided primary evidence of cytocompatibility of compositions obtained. *In vitro* biomineralization studies have shown differences in the transformation rate of small organic molecules containing ACP. The variations in the transformation rate can be induced by different functional groups from the respective small organic molecules. The research contributes to the expanding field of biomaterial science by bridging the gap between the biomineralization process and synthetic material, thus opening the door to innovative tissue engineering strategies and bone therapeutic interventions.

Data availability statement

The raw data supporting the conclusion of this article will be made available by the authors, without undue reservation.

Author contributions

AI: Conceptualization, Data curation, Formal Analysis, Investigation, Methodology, Writing–original draft. PK: Data curation, Validation, Writing–review and editing. VR: Software, Validation, Writing–review and editing. IH: Resources, Writing–review and editing. ÖD: Data curation, Formal Analysis,

Writing–review and editing. MK: Data curation, Writing–review and editing. KR: Formal Analysis, Validation, Writing–review and editing. GC: Formal Analysis, Investigation, Resources, Software, Validation, Writing–review and editing. MT: Formal Analysis, Resources, Validation, Writing–review and editing. JL: Formal Analysis, Funding acquisition, Project administration, Resources, Supervision, Validation, Writing–review and editing.

Funding

The author(s) declare financial support was received for the research, authorship, and/or publication of this article. The authors acknowledge financial support from the European Union' Horizon 2020 research and innovation program under grant agreement No. 857287 (BBCE) and Baltic Research Programme Project No. EEA-RESEARCH-85"Waste-to-resource: eggshells as a source for next-generation biomaterials for bone regeneration (EGGSHELL)" under the EEA Grant of Iceland, Liechtenstein and Norway No. EEZ/BPP/VIAA/2021/1. The authors are grateful for generous funding from the Mahatma Jyotiba Phule Research Fellowship, Govt. of Maharashtra, India (MAHAJYOTI/2022/PhD Fellowship/1002(624)).

Conflict of interest

The authors declare that the research was conducted in the absence of any commercial or financial relationships that could be construed as a potential conflict of interest.

Publisher's note

Supplementary material

The Supplementary Material for this article can be found online at: https://www.frontiersin.org/articles/10.3389/fbioe.2023.1329752/full#supplementary-material

References

Aghajanian, P., Hall, S., Wongworawat, M. D., and Mohan, S. (2015). The roles and mechanisms of actions of vitamin C in bone: new developments. *J. Bone Min. Res.* 30, 1945–1955. doi:10.1002/JBMR.2709

Ancillotti, F., Boschi, G., Perego, G., and Zazzetta, A. (1977). Calcium binding capacity of carboxylic acids with an ethereal function. Crystal and molecular structure of calcium ethylenedioxydiacetate. *J. Chem. Soc. Dalt. Trans.* 1977, 901–905. doi:10.1039/DT9770000901

Barrère, F., van Blitterswijk, C. A., and de Groot, K. (2006). Bone regeneration: molecular and cellular interactions with calcium phosphate ceramics. *Int. J. Nanomedicine* 1, 317–332.

Barth, A. (2000). The infrared absorption of amino acid side chains. *Prog. Biophys. Mol. Biol.* 74, 141–173. doi:10.1016/S0079-6107(00)00021-3

Becker, G. L. (1977). Calcification mechanisms: roles for cells and mineral. *J. Oral Pathol.* 6, 307–315. doi:10.1111/J.1600-0714.1977.TB01653.X

Bichara, L. C., Lanús, H. E., Nieto, C. G., and Brandán, S. A. (2010). Density functional theory calculations of the molecular force field of L -ascorbic acid, vitamin C. *J. Phys. Chem. A* 114, 4997–5004. doi:10.1021/jp912251g

Boskey, A. L., and Posner, A. S. (1973). Conversion of amorphous calcium phosphate to microcrystalline hydroxyapatite. A pH-dependent, solution-mediated, solid-solid conversion. *J. Phys. Chem.* 77, 2313–2317. doi:10.1021/j100638a011

Brakspear, K. S., and Mason, D. J. (2012). Glutamate signaling in bone. *Front. Endocrinol. (Lausanne).* 3, 97. doi:10.3389/FENDO.2012.00097

Cárdenas-Triviño, G., Soto-Seguel, R., Cárdenas-Triviño, G., and Soto-Seguel, R. (2020). CHITOSAN COMPOSITES PREPARATION AND CHARACTERIZATION OF GUIDE TUBES FOR NERVE REPAIR. *J. Chil. Chem. Soc.* 65, 4870–4878. doi:10.4067/S0717-97072020000204870

Chatzipanagis, K., Iafisco, M., Roncal-Herrero, T., Bilton, M., Tampieri, A., Kröger, R., et al. (2016). Crystallization of citrate-stabilized amorphous calcium phosphate to nanocrystalline apatite: a surface-mediated transformation. *CrystEngComm* 18, 3170–3173. doi:10.1039/C6CE00521G

Chen, M. M., Li, Y., Deng, S. L., Zhao, Y., Lian, Z. X., and Yu, K. (2022). Mitochondrial function and reactive oxygen/nitrogen species in skeletal muscle. *Front. Cell Dev. Biol.* 10, 826981. doi:10.3389/fcell.2022.826981

Chen, Y., Gu, W., Pan, H., Jiang, S., and Tang, R. (2014). Stabilizing amorphous calcium phosphate phase by citrate adsorption. *CrystEngComm* 16, 1864–1867. doi:10.1039/C3CE42274G

Chin, K.-Y., and Ima-Nirwana, S. (2018). Vitamin C and bone health: evidence from cell, animal and human studies. *Curr. Drug Targets* 19, 439–450. doi:10.2174/1389450116666150907100838

Chinopoulos, C., and Adam-Vizi, V. (2010). Mitochondrial Ca2+ sequestration and precipitation revisited. *FEBS J.* 277, 3637–3651. doi:10.1111/J.1742-4658.2010.07755.X

Combes, C., and Rey, C. (2010). Amorphous calcium phosphates: synthesis, properties and uses in biomaterials. *Acta Biomater.* 6, 3362–3378. doi:10.1016/J.ACTBIO.2010.02.017

Corbridge, D. E. C. (1971). The structural chemistry of phosphates. *Bull. Minéralogie* 94, 271–299. doi:10.3406/BULMI.1971.6534

Dabbagh, H. A., Azami, F., Farrokhpour, H., and Chermahini, A. N. (2014). UV-VIS, NMR AND FT-IR SPECTRA OF TAUTOMERS OF VITAMIN C. EXPERIMENTAL AND DFT CALCULATIONS. *J. Chil. Chem. Soc.* 59, 2588–2594. doi:10.4067/S0717-97072014000300013

Damilola Olawale, M., Obaleye, J., Olawale, M. D., Obaleye, J. A., and Oladele, E. O. (2020). ITACONIC ACID BASED COORDINATION POLYMER: MECHANOCHEMICAL SYNTHESIS, CHARACTERIZATION AND VAPOCHROMIC STUDY. *Niger. Res. J. Chem. Sci.* 8, 2020. Available at: http://repository.elizadeuniversity.edu.ng/jspui/handle/20.500.12398/887 (Accessed August 15, 2023).

De Castro, E. D. S. G., and Cassella, R. J. (2016). Direct determination of sorbitol and sodium glutamate by attenuated total reflectance Fourier transform infrared spectroscopy (ATR-FTIR) in the thermostabilizer employed in the production of yellow-fever vaccine. *Talanta* 152, 33–38. doi:10.1016/J.TALANTA.2016.01.054

Dominguez-Medina, S., McDonough, S., Swanglap, P., Landes, C. F., and Link, S. (2012). *In situ* measurement of bovine serum albumin interaction with gold nanospheres. *Langmuir* 28, 9131–9139. doi:10.1021/LA3005213

Eanes, E. D. (1998). Amorphous calcium phosphate: thermodynamic and kinetic considerations. *Calcium Phosphates Biol. Ind. Syst.* 1998, 21–39. doi:10.1007/978-1-4615-5517-9_2

Edén, M. (2021). Structure and formation of amorphous calcium phosphate and its role as surface layer of nanocrystalline apatite: implications for bone mineralization. *Materialia* 17, 101107. doi:10.1016/J.MTLA.2021.101107

Erceg, I., and Dutour Sikirić, M. (2022). Influence of biomacromolecules on calcium phosphate formation on TiO2 nanomaterials. *Minerals* 12, 1557. doi:10.3390/min12121557

Fatokun, A. A., Stone, T. W., and Smith, R. A. (2006). Hydrogen peroxide-induced oxidative stress in MC3T3-E1 cells: the effects of glutamate and protection by purines. *Bone* 39, 542–551. doi:10.1016/J.BONE.2006.02.062

Feng, W., Feng, C., Wang, B., Jing, A., Li, G., Xia, X., et al. (2020). An amorphous calcium phosphate for drug delivery: ATP provides a phosphorus source and microwave-assisted hydrothermal synthesis. *Mat. Today Commun.* 25, 101455. doi:10.1016/J.MTCOMM.2020.101455

Flannigan, R., Choy, W. H., Chew, B., and Lange, D. (2014). Renal struvite stones-pathogenesis, microbiology, and management strategies. *Nat. Rev. | Urol.* 11, 333–341. doi:10.1038/nrurol.2014.99

Gajjeraman, S., Narayanan, K., Hao, J., Qin, C., and George, A. (2007). Matrix macromolecules in hard tissues control the nucleation and hierarchical assembly of hydroxyapatite. *J. Biol. Chem.* 282, 1193–1204. doi:10.1074/JBC.M604732200

Genever, P. G., and Skerry, T. M. (2001). Regulation of spontaneous glutamate release activity in osteoblastic cells and its role in differentiation and survival: evidence for intrinsic glutamatergic signaling in bone. *FASEB J.* 15, 1586–1588. doi:10.1096/FJ.00-0594FJE

Gorbunoff, M. J. (1984). The interaction of proteins with hydroxyapatite. *Anal. Biochem.* 136, 433–439. doi:10.1016/0003-2697(84)90240-9

Grover, L. M., Wright, A. J., Gbureck, U., Bolarinwa, A., Song, J., Liu, Y., et al. (2013). The effect of amorphous pyrophosphate on calcium phosphate cement resorption and bone generation. *Biomaterials* 34, 6631–6637. doi:10.1016/J.BIOMATERIALS.2013.05.001

Gunson, D., Gropp, K. E., and Varela, A. (2013). Bone and joints. *Haschek Rousseaux's Handb. Toxicol. Pathol.* 1-3, 2761–2858. doi:10.1016/B978-0-12-415759-0.00063-7

Hadzir, S. N., Ibrahim, S. N., Abdul Wahab, R. M., Zainol Abidin, I. Z., Senafi, S., Ariffin, Z. Z., et al. (2014). Ascorbic acid induces osteoblast differentiation of human suspension mononuclear cells. *Cytotherapy* 16, 674–682. doi:10.1016/J.JCYT.2013.07.013

Hoeher, A. J., Mergelsberg, S. T., Borkiewicz, O. J., and Michel, F. M. (2023). Impacts of initial Ca/P on amorphous calcium phosphate. *Cryst. Growth Des.* 7, 3736–3745. doi:10.1021/acs.cgd.1c00058

Howard, J. E., and Thomas, W. C. (1968). Control of crystallization in urine. *Am. J. Med.* 45, 693–699. doi:10.1016/0002-9343(68)90205-2

Hwang, P. W., and Horton, J. A. (2019). Variable osteogenic performance of MC3T3-E1 subclones impacts their utility as models of osteoblast biology. *Sci. Rep.* 9, 8299. doi:10.1038/s41598-019-44575-8

Iafisco, M., Degli Esposti, L., Ramírez-Rodríguez, G. B., Carella, F., Gómez-Morales, J., Ionescu, A. C., et al. (2018). Fluoride-doped amorphous calcium phosphate nanoparticles as a promising biomimetic material for dental remineralization. *Sci. Rep.* 8, 17016. doi:10.1038/S41598-018-35258-X

Ikawa, N., Kimura, T., Oumi, Y., and Sano, T. (2009). Amino acid containing amorphous calcium phosphates and the rapid transformation into apatite. *J. Mat. Chem.* 19, 4906–4913. doi:10.1039/B815154G

Iline-Vul, T., Nanda, R., Mateos, B., Hazan, S., Matlahov, I., Perelshtein, I., et al. (2020). Osteopontin regulates biomimetic calcium phosphate crystallization from disordered mineral layers covering apatite crystallites. *Sci. Rep.* 101 (10), 15722–15816. doi:10.1038/s41598-020-72786-x

Indurkar, A., Choudhary, R., Rubenis, K., and Locs, J. (2023a). Role of carboxylic organic molecules in interfibrillar collagen mineralization. *Front. Bioeng. Biotechnol.* 11, 1150037. doi:10.3389/FBIOE.2023.1150037

Indurkar, A., Choudhary, R., Rubenis, K., Nimbalkar, M., Sarakovskis, A., Boccaccini, A. R., et al. (2023b). Amorphous calcium phosphate and amorphous calcium phosphate carboxylate: synthesis and characterization. *ACS Omega* 8, 26782–26792. doi:10.1021/ACSOMEGA.3C00796

Jahandideh, A., Esmaeili, N., and Muthukumarappan, K. (2018). Facile synthesis and characterization of activated star-shaped itaconic acid based thermosetting resins. *Polym. Degrad. Stab.* 153, 201–209. doi:10.1016/J.POLYMDEGRADSTAB.2018.04.035

Jin, B., Liu, Z., Shao, C., Chen, J., Liu, L., Tang, R., et al. (2021). Phase transformation mechanism of amorphous calcium phosphate to hydroxyapatite investigated by liquid-cell transmission electron microscopy. *Cryst. Growth Des.* 21, 5126–5134. doi:10.1021/acs.cgd.1c00503

Kalani, A., Kamat, P. K., Voor, M. J., Tyagi, S. C., and Tyagi, N. (2014). Mitochondrial epigenetics in bone remodeling during hyperhomocysteinemia. *Mol. Cell. Biochem.* 395, 89–98. doi:10.1007/S11010-014-2114-3

Kritis, A. A., Stamoula, E. G., Paniskaki, K. A., and Vavilis, T. D. (2015). Researching glutamate – induced cytotoxicity in different cell lines: a comparative/collective analysis/study. *Front. Cell. Neurosci.* 9, 91. doi:10.3389/fncel.2015.00091

Lehninger, A. L. (1970). Mitochondria and calcium ion transport. *Biochem. J.* 119, 129–138. doi:10.1042/bj1190129

Loginova, E. V., Mikheev, I. V., Volkov, D. S., and Proskurnin, M. A. (2016). Quantification of copolymer composition (methyl acrylate and itaconic acid) in polyacrylonitrile carbon-fiber precursors by FTIR-spectroscopy. *Anal. Methods* 8, 371–380. doi:10.1039/C5AY02264A

Lotsari, A., Rajasekharan, A. K., Halvarsson, M., and Andersson, M. (2018). Transformation of amorphous calcium phosphate to bone-like apatite. *Nat. Commun.* 91 (9), 4170–4211. doi:10.1038/s41467-018-06570-x

Makowski, G. S., and Ramsby, M. L. (2001). Interaction of amorphous calcium phosphate with fibrin *in vitro* causes decreased fibrinolysis and altered protease profiles: implications for atherosclerotic disease. *Inflammation* 25, 319–329. doi:10.1023/a:1012831900153

Manzoor, M. A. P., Duwal, S. R., Mujeeburahiman, M., and Rekha, P. D. (2018). Vitamin C inhibits crystallization of struvite from artificial urine in the presence of *Pseudomonas aeruginosa*. *Int. Braz. J. Urol. Off. J. Braz. Soc. Urol.* 44, 1234–1242. doi:10.1590/S1677-5538.IBJU.2017.0656

Mekmene, O., Quillard, S., Rouillon, T., Bouler, J. M., Piot, M., and Gaucheron, F. (2009). Effects of pH and Ca/P molar ratio on the quantity and crystalline structure of calcium phosphates obtained from aqueous solutions. *Dairy Sci. Technol.* 89, 301–316. doi:10.1051/DST/2009019

Murad, S., Grove, D., Lindberg, K. A., Reynolds, G., Sivarajah, A., and Pinnell, S. R. (1981). Regulation of collagen synthesis by ascorbic acid. *Proc. Natl. Acad. Sci. U. S. A.* 78, 2879–2882. doi:10.1073/PNAS.78.5.2879

Nakamura, K., Isoyama, N., Nakayama, Y., Hiroyoshi, T., Fujikawa, K., Miura, Y., et al. (2022). Association between amorphous calcium-phosphate ratios in circulating calciprotein particles and prognostic biomarkers in hemodialysis patients. *Sci. Rep.* 121 (12), 13030–13038. doi:10.1038/s41598-022-17405-7

Niu, L. N., Zhang, W., Pashley, D. H., Breschi, L., Mao, J., Chen, J. H., et al. (2014). Biomimetic remineralization of dentin. *Dent. Mat.* 30, 77–96. doi:10.1016/J.DENTAL.2013.07.013

Osellame, L. D., Blacker, T. S., and Duchen, M. R. (2012). Cellular and molecular mechanisms of mitochondrial function. *Best. Pract. Res. Clin. Endocrinol. Metab.* 26, 711–723. doi:10.1016/J.BEEM.2012.05.003

Padovano, J. D., Ravindran, S., Snee, P. T., Ramachandran, A., Bedran-Russo, A. K., and George, A. (2015). DMP1-derived peptides promote remineralization of human dentin. *J. Dent. Res.* 94, 608–614. doi:10.1177/0022034515572441

Peace, C. G., and O'Neill, L. A. J. (2022). The role of itaconate in host defense and inflammation. *J. Clin. Invest.* 132, e148548. doi:10.1172/JCI148548

Polat, O., Kilicoglu, S. S., and Erdemli, E. (2007). A controlled trial of glutamine effects on bone healing. *Adv. Ther.* 24, 154–160. doi:10.1007/BF02850003

Querido, W., Shanas, N., Bookbinder, S., Oliveira-Nunes, M. C., Krynska, B., and Pleshko, N. (2020). Fourier transform infrared spectroscopy of developing bone mineral: from amorphous precursor to mature crystal. *Analyst* 145, 764–776. doi:10.1039/C9AN01588D

Reynolds, E. C. (1998). Anticariogenic complexes of amorphous calcium phosphate stabilized by casein phosphopeptides: a review. *Spec. Care Dent.* 18, 8–16. doi:10.1111/j.1754-4505.1998.tb01353.x

Sakhno, Y., Degli Esposti, L., Adamiano, A., Borgatta, J., Cahill, M., Vaidya, S., et al. (2023). Citrate-stabilized amorphous calcium phosphate nanoparticles doped with micronutrients as a highly efficient nanofertilizer for environmental sustainability. *ACS Agric. Sci. Technol.* 3, 845–854. doi:10.1021/acsagscitech.3c00117

Sannelli, F., Jensen, P. R., and Meier, S. (2023). In-cell NMR approach for real-time exploration of pathway versatility: substrate mixtures in nonengineered yeast. *Anal. Chem.* 95, 7262–7270. doi:10.1021/acs.analchem.3c00225

Scheffler, I. E. (2002). Metabolic pathways inside mitochondria. *Mitochondria* 2002, 246–272. doi:10.1002/0471223891.CH6

Schubert, D., and Piasecki, D. (2001). Oxidative glutamate toxicity can Be a component of the excitotoxicity cascade. *J. Neurosci.* 21, 7455–7462. doi:10.1523/JNEUROSCI.21-19-07455.2001

Shi, X., Zhou, H., Wei, J., Mo, W., Li, Q., and Lv, X. (2022). The signaling pathways and therapeutic potential of itaconate to alleviate inflammation and oxidative stress in inflammatory diseases. *Redox Biol.* 58, 102553. doi:10.1016/J.REDOX.2022.102553

Skerry, T., and Taylor, A. (2005). Glutamate signalling in bone. *Curr. Pharm. Des.* 7, 737–750. doi:10.2174/1381612013397771

Stipniece, L., Salma-Ancane, K., Rjabovs, V., Juhnevica, I., Turks, M., Narkevica, I., et al. (2016). Development of functionalized hydroxyapatite/poly(vinyl alcohol) composites. *J. Cryst. Growth* 444, 14–20. doi:10.1016/J.JCRYSGRO.2016.03.029

Strelko, C. L., Lu, W., Dufort, F. J., Seyfried, T. N., Chiles, T. C., Rabinowitz, J. D., et al. (2011). Itaconic acid is a mammalian metabolite induced during macrophage activation. *J. Am. Chem. Soc.* 133, 16386–16389. doi:10.1021/ja2070889

Sumayya, A., Panicker, Cy., and Tresa Varghese, H. (2008). VIBRATIONAL SPECTROSCOPIC STUDIES AND *ab initio* CALCULATIONS OF L-GLUTAMIC ACID 5-AMIDE. *Rasayan J. Chem.* 1, 548–555.

Sun, R., Åhlén, M., Tai, C. W., Bajnóczi, É. G., de Kleijne, F., Ferraz, N., et al. (2020). Highly porous amorphous calcium phosphate for drug delivery and bio-medical applications. *Nanomaterials* 10, 20. doi:10.3390/NANO10010020

Syed-Picard, F. N., Jayaraman, T., Lam, R. S. K., Beniash, E., and Sfeir, C. (2013). Osteoinductivity of calcium phosphate mediated by connexin 43. *Biomaterials* 34, 3763–3774. doi:10.1016/J.BIOMATERIALS.2013.01.095

Szekeres, G. P., and Kneipp, J. (2018). Different binding sites of serum albumins in the protein corona of gold nanoparticles. *Analyst* 143, 6061–6068. doi:10.1039/C8AN01321G

Tajmir-Riahi, H. A. (1991). Coordination chemistry of vitamin C. Part II. Interaction of L-ascorbic acid with Zn(II), Cd(II), Hg(II), and Mn(II) ions in the solid state and in aqueous solution. *J. Inorg. Biochem.* 42, 47–55. doi:10.1016/0162-0134(91)80031-C

Ten Cate, J. M., and Featherstone, J. D. B. (1991). Mechanistic aspects of the interactions between fluoride and dental enamel. *Crit. Rev. Oral Biol. Med.* 2, 283–296. doi:10.1177/10454411910020030101

Thaler, R., Khani, F., Sturmlechner, I., Dehghani, S. S., Denbeigh, J. M., Zhou, X., et al. (2022). Vitamin C epigenetically controls osteogenesis and bone mineralization. *Nat. Commun.* 131 (13), 5883–5918. doi:10.1038/s41467-022-32915-8

Tsuji, T., Onuma, K., Yamamoto, A., Iijima, M., and Shiba, K. (2008). Direct transformation from amorphous to crystalline calcium phosphate facilitated by

motif-programmed artificial proteins. *Proc. Natl. Acad. Sci. U. S. A.* 105, 16866–16870. doi:10.1073/PNAS.0804277105

Uhanov, A. S., Klepov, V. V., Vologzhanina, A. V., Zubavichus, Y. V., Savchenkov, A. V., Pushkin, D. V., et al. (2020). New itaconate-containing uranyl complex unit and coordination modes of itaconate ions. *Comptes Rendus Chim.* 23, 117–126. doi:10.5802/crchim.8

Vettori, I., Macchiagodena, M., Pagliai, M., Bassu, G., Fratini, E., and Baglioni, P. (2022). Conformational and solvent effects in structural and spectroscopic properties of 2-hydroxyethyl methacrylate and acrylic acid. *J. Mol. Liq.* 360, 119428. doi:10.1016/j.molliq.2022.119428

Wang, Y., Li, S., Zhao, L., Cheng, P., Liu, J., Guo, F., et al. (2022). Aging relevant metabolite itaconate inhibits inflammatory bone loss. *Front. Endocrinol. (Lausanne)* 13, 885879. doi:10.3389/fendo.2022.885879

Wibowo, A. H., Hasanah, Y. I. F., Firdaus, M., Widjonarko, D. M., and Cepeda, J. (2018). Efficient CO2 adsorption by Cu(II) acetate and itaconate bioproduct based MOF. *J. Environ. Chem. Eng.* 6, 2910–2917. doi:10.1016/J.JECE.2018.04.031

Williams, D., and Rogers, L. H. (1937). The infrared absorption spectrum of vitamin C. *J. Am. Chem. Soc.* 59, 1422–1423. doi:10.1021/ja01287a005

Winand, L., Dallemagne, M. J., and Duyckaerts, G. (1961). Hydrogen bonding in apatitic calcium phosphates. *Nat* 190, 164–165. doi:10.1038/190164a0

Xu, X., Urlaub, J., Woźniczka, M., Wynendaele, E., Herman, K., Schollmayer, C., et al. (2019). Zwitterionic-hydrophilic interaction liquid chromatography for l-ascorbic acid 2-phosphate magnesium, a raw material in cell therapy. *J. Pharm. Biomed. Anal.* 165, 338–345. doi:10.1016/J.JPBA.2018.12.010

Yamada, I., Galindo, T. G. P., Noda, D., and Tagaya, M. (2021). Effect of orotic acid addition on hydrolysis conversion of α-tricalcium phosphate to hydroxyapatite. *Int. J. Ceram. Eng. Sci.* 3, 267–271. doi:10.1002/CES2.10109

Yang, C., Liu, T., and Shi, G. P. (2020). Therapeutic potential of tricarboxylic acid cycle metabolite itaconate in cardiovascular diseases. *EBioMedicine* 59, 102938. doi:10.1016/j.ebiom.2020.102938

Yang, Y., Cui, Q., and Sahai, N. (2010). How does bone sialoprotein promote the nucleation of hydroxyapatite? A molecular dynamics study using model peptides of different conformations. *Langmuir* 26, 9848–9859. doi:10.1021/LA100192Z

Yarbrough, D. K., Hagerman, E., Eckert, R., He, J., Choi, H., Cao, N., et al. (2010). Specific binding and mineralization of calcified surfaces by small peptides. *Calcif. Tissue Int.* 86, 58–66. doi:10.1007/S00223-009-9312-0

Yohannan Panicker, C., Tresa Varghese, H., and Philip, D. (2006). FT-IR, FT-Raman and SERS spectra of Vitamin C. *Spectrochim. Acta Part A Mol. Biomol. Spectrosc.* 65, 802–804. doi:10.1016/J.SAA.2005.12.044

Yokoi, T., Shimabukuro, M., and Kawashita, M. (2022). Octacalcium phosphate with incorporated carboxylate ions: a review. *Sci. Technol. Adv. Mat.* 23, 434–445. doi:10.1080/14686996.2022.2094728

Zhang, S., Moustafa, Y., and Huo, Q. (2014). Different interaction modes of biomolecules with citrate-capped gold nanoparticles. *ACS Appl. Mat. Interfaces* 6, 21184–21192. doi:10.1021/am506112u

Zhao, J., Liu, Y., Sun, W. B., and Yang, X. (2012). First detection, characterization, and application of amorphous calcium phosphate in dentistry. *J. Dent. Sci.* 7, 316–323. doi:10.1016/J.JDS.2012.09.001

Zhao, W., Wang, Z., Xu, Z., and Sahai, N. (2018). Osteocalcin facilitates calcium phosphate ion complex growth as revealed by free energy calculation. *Phys. Chem. Chem. Phys.* 20, 13047–13056. doi:10.1039/C8CP01105B

Zhou, Y., and Roos, Y. H. (2012). Stability and plasticizing and crystallization effects of vitamins in amorphous sugar systems. *J. Agric. Food Chem.* 60, 1075–1083. doi:10.1021/JF204168F

Zong, C., Wang, Y., and Jiang, S. (2023). Toward the understanding of poly (Acrylic Acid) on amorphous calcium phosphate mediated collagen intrafibrillar Mineralization: surface adsorption versus bulk incorporation. *J. Cryst. Growth* 616, 127304. doi:10.1016/J.JCRYSGRO.2023.127304

frontiers | Frontiers in Bioengineering and Biotechnology

TYPE Original Research
PUBLISHED 15 January 2024
DOI 10.3389/fbioe.2024.1354241

OPEN ACCESS

EDITED BY
Hongye Yang,
Wuhan University, China

REVIEWED BY
Libang He,
Sichuan University, China
Sema Belli,
Selçuk University, Türkiye

*CORRESPONDENCE
Jiale Fu,
fullers@126.com

RECEIVED 12 December 2023
ACCEPTED 04 January 2024
PUBLISHED 15 January 2024

CITATION
Hu Y, Gao J, Huang X, Li Y, Chen Z, Zhan D, Sano H, Carvalho RM and Fu J (2024), The possibility of clinical bonding between metal/ceramic brackets to zirconia: *in vitro* study. *Front. Bioeng. Biotechnol.* 12:1354241. doi: 10.3389/fbioe.2024.1354241

The possibility of clinical bonding between metal/ceramic brackets to zirconia: *in vitro* study

Yichun Hu[1], Jiayang Gao[1], Xinyue Huang[1], Yutong Li[1], Ziyi Chen[1], Desong Zhan[2], Hidehiko Sano[3], Ricardo M. Carvalho[4] and Jiale Fu[2]*

[1]School and Hospital of Stomatology, China Medical University, Shenyang, China, [2]Department of Dental Materials Science, The Second Department of Prosthodontics, School and Hospital of Stomatology, China Medical University, Shenyang, China, [3]Department of Restorative Dentistry, Division of Oral Health Science, Faculty of Dental Medicine, Hokkaido University, Sapporo, Japan, [4]Department of Oral Biological and Medical Sciences, Division of Biomaterials, Faculty of Dentistry, University of British Columbia, Vancouver, BC, Canada

Objective: The present study aimed to assess the bond strength and durability of six bonding agents concerning their application to metal or ceramic brackets and zirconia.

Materials and Methods: Six resin cement bonding agents (XT, XTS, RSBU, RGBU, SBPM, and GMP) were chosen for this investigation. Specimens were either stored in distilled water at 37°C for 24 h or subjected to 5,000 thermocycles before conducting a Shear Bond Strength (SBS) test. Statistical analysis of the SBS data was performed using three-way ANOVA and Games-Howell tests ($\alpha = 0.05$). The Adhesive Remnant Index was examined, and the debonding surface details on brackets and zirconia were observed.

Results: For metal brackets, all groups demonstrated clinically acceptable bond strength, irrespective of storage conditions, except for the XT group. Regarding ceramic brackets, all groups displayed acceptable bond strength after 24 h of water storage. However, following thermocycling, a significant decrease in SBS was noted across all groups ($p < 0.05$), with SBPM exhibiting a higher bond strength. Three-way ANOVA analysis indicated that SBS values were notably influenced by each factor, and an interaction among the three independent variables was observed ($p = 0.000$).

Conclusion: The reliable bond strength between ceramic brackets and zirconia was significantly lower after thermocycling compared to that of metal brackets and zirconia. SBPM exhibited consistent and robust bond strength between ceramic/metal brackets and zirconia across various storage conditions. Furthermore, the HEMA-free adhesive demonstrated a potentially more consistent bonding performance compared to the HEMA-containing adhesive employed in this study.

KEYWORDS

shear bond strength (SBS), ceramic bracket, zirconia, resin cement, metal bracket, storage condition

1 Introduction

Zirconia (ZrO2) has gained widespread use in dentistry for fixed dental prostheses (FDPs), single crowns, bridge restorations, and implant abutments (Ju et al., 2020). Its exceptional mechanical strength sets it apart from other conventional ceramic materials (Zhang and Lawn, 2018). Additionally, Zirconia exhibits favorable biocompatibility, aesthetic properties, and high resistance to corrosion (Gautam et al., 2016; Zarone et al., 2019). The popularity of zirconia restorations has surged due to their convenient milling from prefabricated disks using CAD/CAM devices (Ju et al., 2019; Goracci et al., 2022).

Zirconia crystals exist in various patterns: monoclinic (M), cubic (C), and tetragonal (T) structures (Nistor et al., 2019). At ambient temperature, the monoclinic phase is most stable but transforms into tetragonal and cubic phases upon heating (Hanawa, 2020). Yttrium-stabilized zirconia (YSZ), also known as tetragonal zirconia polycrystal (TZP), achieves enhanced molecular stability by combining ZrO2 with Y2O3(Nistor et al., 2019; Hanawa, 2020). The typical yttria content in dental YSZ ranges between 3 and 5 mol % (Vult von Steyern et al., 2022). Increasing the yttria content enhances zirconia's translucency for anterior teeth restoration, but it compromises strength and toughness (Vult von Steyern et al., 2022). In clinical practice, zirconia is predominantly used for porcelain-fused-to-zirconia crowns in anterior teeth, while full zirconia crowns are favored for posterior teeth (Makhija et al., 2016; Rauch et al., 2021). Despite zirconia's microstructural characteristics, chemical inertness, and biocompatibility, establishing reliable bonding between zirconia and resin cement remains challenging (Lima et al., 2019). Silica-based porcelains are preferred due to superior translucency and their ability to be acid-etched and silanized, enhancing adhesion and reinforcing resin bonding (Zhang and Lawn, 2018).

The rising demand for dental aesthetics has led to an increased number of individuals seeking orthodontic treatment, including adults with a history of fixed prosthetic treatments (Babaee Hemmati et al., 2022). Orthodontic brackets are categorized as metal or ceramic brackets. Ceramic brackets were developed to meet the demand for improved aesthetics (Urichianu et al., 2022). Despite their aesthetic appeal, ceramic brackets exhibit lower bond strength to enamel, acrylic, and porcelain surfaces compared to traditional metal brackets (Pinho et al., 2020). Moreover, ceramic brackets are prone to fracture and may cause irreversible tooth damage during debonding (Alexopoulou et al., 2020). The demographic of adult patients seeking orthodontic treatment is on the rise (Jawad et al., 2015; Hellak et al., 2016).

As ceramic restorations, including zirconia restorations, are frequently performed in adults, the bonding strategy for different brackets and restoration surfaces becomes a pertinent concern (Pinho et al., 2020). Numerous chair-side challenges can arise when orthodontic brackets are bonded to zirconia ceramic surfaces. These challenges include insufficient familiarity with bonding techniques, lack of knowledge about resin cement or bonding products, and inconvenient treatment methods. For instance, clinicians may suggest replacing a ceramic crown with a CAD/CAM resin crown during orthodontic treatment to achieve better bonding performance, subsequently remaking the ceramic crown (Blakey and Mah, 2010). Enhancing the bonding performance between zirconia and metal or ceramic brackets to cater to orthodontic treatment needs could significantly benefit patients. However, scarce previous studies have explored the durability of various bonding agents between different brackets and zirconia.

Hence, this study aims to evaluate the bonding performance and durability of six different bonding agents concerning their application to metal or ceramic brackets and zirconia. The null hypotheses were as follows: (1) no significant difference exists in the bond strength of different bonding agents; (2) the storage condition does not affect the bond strength of the six bonding agents; and (3) metal/ceramic brackets achieve equivalent bonding durability on zirconia.

2 Materials and methods

2.1 Bonding agents and brackets

CAD/CAM-produced zirconia cube specimens (48 in total, Aidite Technology, Qinhuangdao, China) with a length of 2 cm were acquired for the study. These zirconia samples were randomly divided into six experimental groups based on the use of specific bonding agents:

- Group 1 (XT): Transbond™ XT Light Cure adhesive paste (XTL) + Transbond™ XT Light Cure Orthodontic Adhesive Primer (XTP)
- Group 2 (XTS): Transbond™ XT Light Cure adhesive paste (XTL) + Single Bond Universal (SBU)
- Group 3 (RSBU): Rely X™ Ultimate Clicker Adhesive Resin Cement (RUC) + Single Bond Universal (SBU)
- Group 4 (RGBU): Rely X™ Ultimate Clicker Adhesive Resin Cement (RUC) + Gluma Bond Universal (GBU)
- Group 5 (SBPM): Superbond C&B (SB) + Porcelain liner M (PLM)
- Group 6 (GMP): GC G-CEM ONE (GCO) + G-Multi Primer (MP)

Please refer to Table 1 for detailed information on the chemical composition and application procedures of the bonding agents and cleaning paste used in this study.

The zirconia cube specimens in each group were divided into two subgroups, each accommodating two types of brackets: metal brackets (Victory Series, 3M Unitek, United States) and ceramic brackets (Maia Series, Protect, Zhejiang, China). A total of 216 metal brackets and 216 ceramic brackets were utilized. The mean base surface areas of the metal and ceramic brackets were 11.94 mm^2 and 14.82 mm^2.

2.2 Surface preparation

To prepare the bonding surfaces on the zirconia cube, sandblasting with 125 μm aluminum oxide particles was conducted for 60 s at a distance of 1 cm and 2.8 bar pressure. Subsequently, all specimens underwent ultrasonic cleaning in distilled water for 5 min and gentle air drying for 15 s. The application of Ivoclean (IVO) followed the manufacturer's instructions.

TABLE 1 The chemical composition and application procedure of the bonding agents and cleaning paste used in present study.

Code	Materials (Manufacturer/ Lot No)	Chemical formulation	Application procedure
XTP	Transbond™ XT Light Cure Orthodontic Adhesive Primer (3M Unitek, Monrovia, CA, United States/NE66698)	Bis-GMA and TEGDMA, triphenylantimony, CQ, DMAEMA	1. Place 1 drop of primer on the surface of zirconia
			2. Gently blow dry the primer for 15 s to a thin uniform coat
			3. Light curing for 20 s
XTL	Transbond™ XT Light Cure adhesive paste (3M Unitek/NE79372)	Bis-GMA, TEGDMA, Bis-EMA quartz, silicon dioxide, canforquinone, DMAEMA	1. Apply appropriate amount of paste to the bracket base with syringe
			2. Lightly place the bracket onto zirconia surface
			3. Remove excess adhesive and light curing for 20 s on each side of the bracket at a distance of approximately 5 mm from the surface
SBU	Single Bond Universal (3M ESPE, St. Paul, MN, United States/11220A)	10-MDP, dimethacrylate resins, HEMA, polyalkenoic acid copolymer, filler, ethanol, water, initiators, silane	1. Apply the adhesive to the zirconia surface and brackets base
			2. Gently blow dry the adhesive for 15 s to a thin uniform coat
			3. Light cure for 20 s
GBU	Gluma Bond Universal (Kulzer, Hanau, Germany/K010046)	10-MDP, 4-META, Methacrylates, acetone and water	1. Apply the adhesive to the zirconia surface and brackets base
			2. Gently blow dry the adhesive for 15 s to a thin uniform coat
			3. Light cure for 20 s
RUC	Rely X™ Ultimate Clicker Adhesive Resin Cement (3M ESPE/9037935)	Base paste: methacrylate monomers, radiopaque, silanated fillers, initiator components, stabilizers, rheological additives	1. Apply appropriate amount of paste to the bracket base with syringe
		Catalyst paste: methacrylate monomers, radiopaque, alkaline (basic) fillers, initiator components, stabilizers, pigments, rheological additives, fluorescence dye, dual-cure activator for single bond universal adhesive	2. Immediately after applying adhesive, lightly place the bracket onto zirconia surface
			3. Remove excess adhesive and light cure for 20 s on each side of the bracket at a distance of approximately 5 mm from the surface
PLM	Porcelain liner M (Sun Medical Company, Kyoto, Japan/VF1F, VR1)	liquid A: MMA,4-META; liquid B: MMA, MPTS	1. Apply 1 drop of liquid A and liquid B into mixing plate which was cooled in the refrigerator in advance. Gently mixed A and B together
			2. Apply the Liner M mixture to the zirconia surface and ceramic bracket base
			3. Gently blow dry the primer for 15 s to a thin uniform coat
SB	Superbond C&B (Sun Medical Company/ EV12)	TBB, MMA, 4-META, red treatment agent (65% phosphoric acid), green treatment agent (10%citric acid, 3%Ferric chloride), PMMA	1. Gently mixed the base material, catalyzer and L-type Radiopaque in the proportion of 4:1:1
			2. Apply appropriate amount of mixture to the bracket base. 3. Place the bracket onto zirconia surface and fix it
			3. Place the bracket onto zirconia surface and fix it
			4. Gently remove the excess cement around the bracket base without disturbing the bracket.
MP	G-Multi PRIMER (GC, Tokyo, Japan/ 2207081)	MPTMS, 10-MDP, MDTP, BisGMA, TEGDMA, ethanol	1. Apply the primer to the zirconia surface and brackets base respectively
			2. Gently blow dry the adhesive for 15 s to a thin uniform coat
GCO	G-CEM ONE (GC/2202182)	A: Silicate glass powder, 3-Methacryloxypropyltrimethoxysilane, 2-Propenoic-3,3,3-d3 acid, methyl ester, Silicon dioxide	1. Apply appropriate amount of cement to the bracket after hand-mixing
		B: Silicon dioxide, 3-Methacryloxypropyltrimethoxysilane, 2-Propenoic-3,3,3-d3 acid, methyl ester, 12-Methacryloyldodeylphosphate, Cumyl hydroperoxide	2. Lightly place the bracket onto zirconia surface and fix it
			3. Remove excess adhesive and light cure for 20 s on each side of the bracket at a distance of approximately 5 mm from the surface
IVO	Ivoclean (Ivoclar-Vivadent, Schaan, Liechtenstein/Y49501)	Zirconium oxide, water, polyethylene glycol, sodium hydroxide, pigments, additives	1. Apply ivoclean to prepared zirconia surface for 60 s
			2. Rinse with distilled water for 15 s and gently blow dry

HEMA, 2-hydroxyethyl methacrylate; TEGDMA, triethyleneglycol dimethacrylate; Bis-GMA, bisphenol A-diglycidyl methacrylate; Bis-EMA, bisphenol A ethoxylated dimethacrylate; 10-MDP, 10-methacryloyloxydecyl dihydrogen phosphate; CQ, camphorquinone; DMAEMA, dimethylaminoethyl methacrylate; MPTS, (3-Mercaptopropyl) trimethoxysilane; 4-META, 4-methacryloxyethyl trimellitate anhydride; MMA, methyl methacrylate; TBB, tributylborane; PMMA, poly (methyl methacrylate); MDTP, methacryloyloxydecyl dihydrogen thiophosphate; MPTMS, γ-methacryloxypropyl trimethoxysilane.

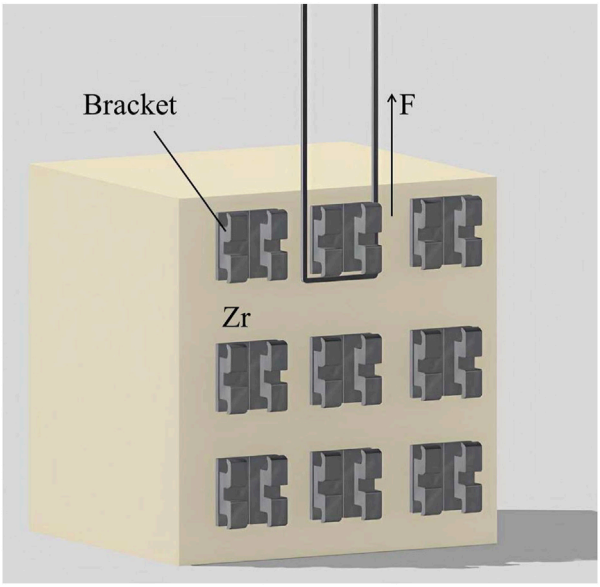

FIGURE 1
Diagram of specimen setting for SBS Test.

2.3 Application procedure

The same pressure (5 N) was applied to each bracket using a consistent clamp across all groups. The application procedures for light curing (Kerr Demi Plus, Orange, CA, United States) and cement removal were standardized and detailed in Table 1.

Each group comprised a total of 72 bracket specimens, divided into two subgroups (metal and ceramic brackets) with 36 specimens each.

2.4 Shear bond strength (SBS) test

Half of the brackets in each subgroup were tested after storing in distilled water at 37°C for 24 h, while the rest underwent 5,000 cycles of thermocycling between 5°C and 55°C in a thermocycling device (SD Mechatronik, Feldkirchen-Westerham, Germany). The SBS test was conducted using a universal testing machine (WD-200 Weidu, Wenzhou, China) with a crosshead speed of 1 mm/min (Figure 1). The SBS formula used was P (MPa) = F (N)/S (mm^2). Out of 18 results in each group, the highest 4 and lowest 4 data points were discarded, and the remaining 10 were considered for analysis (n = 10).

2.5 Adhesive remnant index (ARI) score

The ARI scoring was performed based on the amount of remaining cement on the zirconia surface with the help of a dental digital camera (EyeSpecial C-IV, shofu, Koyoto, Japan). The score is represented by a scale with 5 levels (Score A to Score E) as follows:

Score A: almost all the cement remained on the zirconia surface;

Score B: more than 90% of the cement remained on the zirconia surface;

Score C: more than 10% but less than 90% of the cement remained on the zirconia surface;

Score D: less than 10% of the cement remained on the zirconia surface;

Score E: no cement remained on the zirconia surface.

Images were scored by three calibrated examiners, and a majority opinion was adopted in cases of disagreement. Figure 2 demonstrates the ARI score on the samples.

2.6 Statistical analysis

Statistical analysis involved three-way ANOVA (bonding agents, storage conditions, and brackets) and the Games-Howell test using SPSS version 26.0, with a significance level of $\alpha = 0.05$.

2.7 Surface evaluation

The debonding bracket base surface was analyzed using field emission scanning electron microscopy (FE-SEM) and energy dispersive X-ray spectrometry (EDS; Phenom Pharos G2, Netherlands) to determine elemental composition and distribution.

3 Results

3.1 Shear bond strength (SBS)

The SBS mean values and standard deviations for each group are summarized in Table 2. Notably, RSBU, SBPM, and GMP exhibited higher SBS for metal bracket groups after 24 h of water storage, with no significant difference among these groups ($p > 0.05$). However, RSBU's SBS decreased significantly after thermocycling, while SBPM and GMP remained unchanged.

For ceramic brackets, SBPM displayed higher SBS after 24 h of water storage but significantly declined post-thermocycling, akin to other bonding agents ($p < 0.05$). Comparatively, ceramic brackets demonstrated a more significant decrease in SBS after thermocycling in contrast to metal brackets. Generally, the SBS of ceramic brackets was lower than that of metal brackets after both 24 h of water storage ($p > 0.05$) and thermocycling ($p < 0.05$), except for XTS group results ($p > 0.05$) post-24 h of water storage and XT group outcomes under both storage conditions ($p < 0.05$).

SBPM showcased higher SBS values after thermocycling, irrespective of bracket type, while XT exhibited the lowest SBS in the metal bracket group. XTS displayed a significant increase in SBS for metal brackets post-thermocycling ($p < 0.05$).

The SPSS analysis (Table 3) revealed significant influences on SBS values by brackets, bonding agents, and storage conditions ($p < 0.001$). Interactions were observed among brackets, bonding agents, and storage conditions ($p < 0.001$).

Regarding the SBS results in Tables 4, 5, metal brackets displayed significantly higher SBS than ceramic brackets after thermocycling ($p < 0.05$). Also, RSBU, RGBU, SBPM, and GMP exhibited significantly higher SBS after 24 h of water storage compared to XT and XTS ($p < 0.05$). XT demonstrated notably lower SBS than other groups post-thermocycling ($p < 0.05$). SBPM

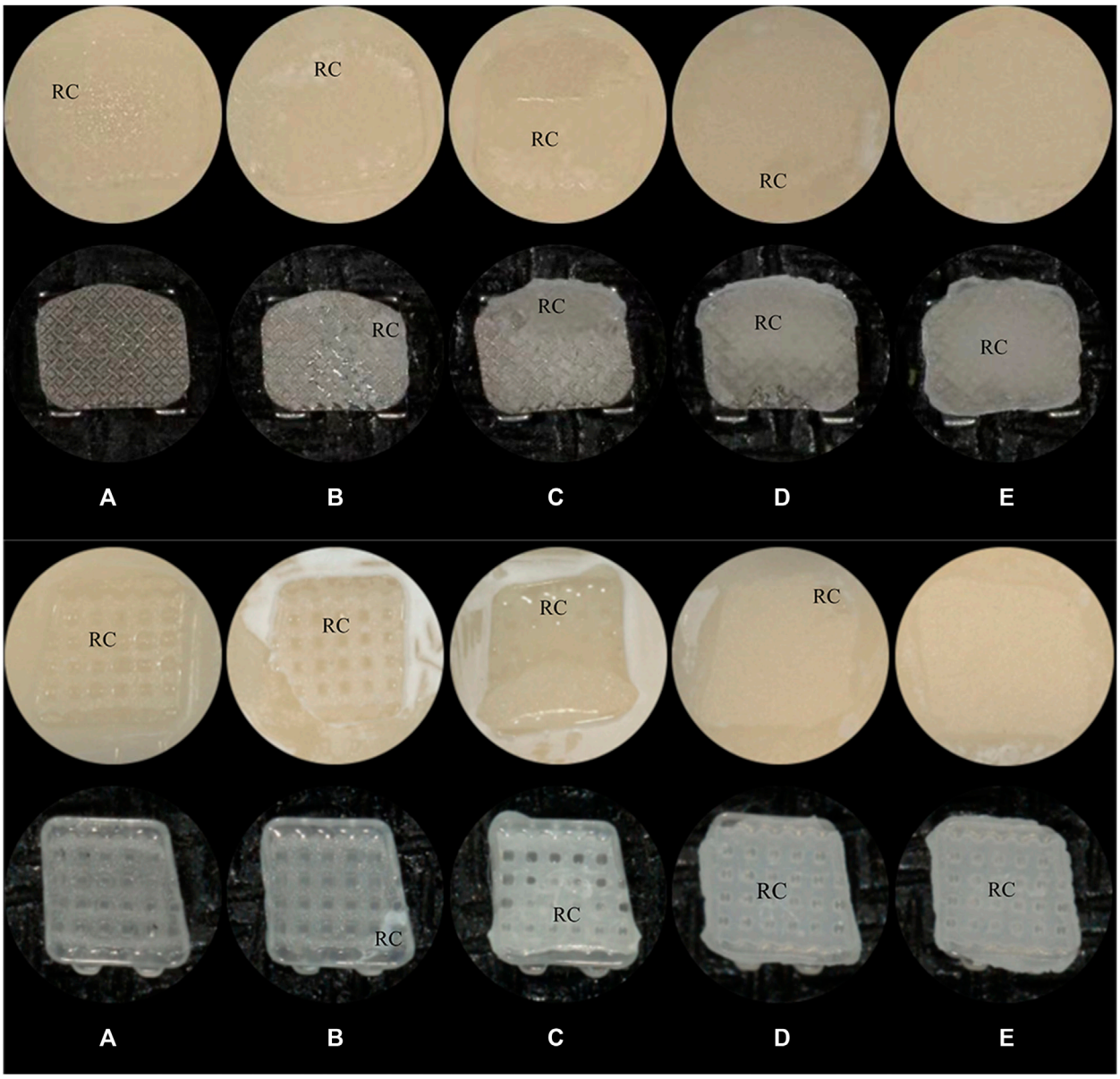

FIGURE 2
The ARI scores**(A)**: score A; **(B)**: score B; **(C)**: score C; **(D)**: score D; **(E)**: score E; RC: Resin Cement. **(A)** Metal Brackets **(B)** Ceramic Brackets.

consistently demonstrated higher SBS irrespective of storage conditions.

3.2 Failure modes

The distribution of failure modes for metal and ceramic bracket groups are visualized in Figures 3, 4, respectively. Under 24 h water storage, ARI scores for various groups were concentrated within different categories. After thermocycling, shifts in ARI scores were observed across groups.

For ceramic brackets under both conditions, XT showed a tendency toward E in ARI scores, while GMP and SBPM exhibited a notable increase in A and a decrease to 0 in C after thermocycling.

Typical bracket fractures were observed in ceramic bracket groups after 24 h water storage, except for XT, predominantly in bracket wings with fewer base fractures in RGBU and GMP. After thermocycling, fractures were observed only in SBPM and GMP, with SBPM showing bracket base fractures. Figure 5 displays the two modes of bracket fractures.

3.3 Surface characterization

FE-SEM images (Figure 6) and EDS results (Figures 7, 8) indicated the presence of Si on bracket bases of XT, XTS, RSBU, RGBU, and GMP groups. Zr particles were detected in RSBU and RGBU metal bracket bases. SBPM showed Zr particles in both

TABLE 2 SBS values (MPa) for six bonding agents using different brackets in two different storage conditions (mean ± SD).

Bracket	Storage	XT	XTS	RSBU	RGBU	SBPM	GMP
Metal brackets	24H	3.91 ± 0.81^{1,A}	6.61 ± 1.49^{1,B}	15.62 ± 1.19^{1,C}	12.36 ± 1.01^{1,D}	16.31 ± 2.67^{1,C}	15.62 ± 1.60^{1,C}
		$p < 0.05$	$p < 0.05$	$p < 0.05$	*NS*	*NS*	*NS*
	5,000 cycles	0.25 ± 0.44^{3,A}	12.64 ± 1.28$^{3,\ BC}$	12.44 ± 0.59^{3,B}	12.71 ± 1.84$^{3,\ BC}$	14.91 ± 1.96$^{3,\ CD}$	14.93 ± 0.93^{3,D}
Ceramic brackets	24H	6.82 ± 1.17^{2,A}	6.64 ± 2.03^{1,A}	8.37 ± 1.44$^{2,\ AB}$	10.69 ± 2.57$^{1,\ BC}$	14.89 ± 1.54^{1,D}	10.81 ± 1.7^{2,C}
		$p < 0.05$	$p < 0.05$	$p < 0.05$	$p < 0.05$	$p < 0.05$	$p < 0.05$
	5,000 cycles	0.61 ± 0.12^{4,A}	2.33 ± 0.91^{4,B}	2.78 ± 0.90^{4,B}	2.58 ± 0.87^{4,B}	10.65 ± 1.69^{4,C}	2.36 ± 0.95^{4,B}

NS indicates no significance between storage periods for each type of bracket ($p > 0.05$).
Identical capital letters indicate no significant differences among materials for each storage period ($p > 0.05$).
Identical numbers indicate no significant differences between brackets for each storage condition ($p > 0.05$).

TABLE 3 Three-way ANOVA analysis result.

Source	df	Mean square	F	P
Corrected model	23	288.012	135.007	0.000
Intercept	1	19770.251	9267.415	0.000
Brackets	1	1439.375	674.715	0.000
Bonding agents	5	581.216	272.448	0.000
Storage conditions	1	649.15	304.293	0.000
Bonding agents * Brackets	5	149.857	70.246	0.000
Storage conditions * Brackets	1	491.491	230.389	0.000
Bonding agents * Storage conditions	5	46.589	21.839	0.000
Bonding agents * Storage conditions * Brackets	5	31.189	14.62	0.000

TABLE 4 The mean SBS values (MPa) of all six bonding agents in the different experimental groups (mean ± SD).

Storage	Metal brackets	Ceramic brackets
24H	11.74 ± 5.08^{a}	9.70 ± 3.36^{a}
5,000 cycles	11.31 ± 5.25^{a}	3.55 ± 3.42^{b}

Identical lower case letters indicate no significant differences between values ($p > 0.05$).

ceramic and metal bracket bases. Fe and Al were detected on metal bracket bases, whereas Fe was absent on ceramic bracket bases.

These observations provide insights into the elemental composition and characteristics of the bracket bases across different bonding agents and brackets used in the study.

4 Discussion

4.1 Comparison of bonding agents

The study aimed to evaluate the bond strength and durability of six bonding agents with metal or ceramic brackets on zirconia. Table 5 highlighted significant differences in shear bond strength (SBS) among bonding agents, rejecting the null hypothesis that no significant difference exists in the bond strength of different bonding agents. Typically, for optimal orthodontic efficacy, the bond strength of orthodontic brackets should ideally be within the range of 6–8 MPa at least (Uysal et al., 2004; Tecco et al., 2005). According to Table 5, except for the XT group, all metal bracket groups achieved long-term bond strengths deemed clinically acceptable. In contrast, among the ceramic bracket groups, while acceptable strength was achieved in the short term by all groups, only the SBPM group exhibited sustained durability.

Using XT as a control group for bonding brackets to enamel, it demonstrated higher SBS in ceramic brackets after 24 h of water storage compared to metal brackets. This outcome suggests the potential influence of ceramic translucence in enhancing XT resin polymerization, contributing to improved short-term bonding (Al-Hity et al., 2012; Reginato et al., 2013). However, XT's SBS significantly decreased after thermocycling, potentially due to mismatched coefficients of shrinkage/expansion between XT resin and brackets, failing to meet the required clinical bond strength.

The XTS group, employing SBU, an universal adhesive, exhibited improved bonding performance attributed to 10-MDP's presence, facilitating chemical bonding to zirconia via phosphate groups (Khan et al., 2017; Nagaoka et al., 2017). This bond was indicated by ARI scores concentrated on A, consistent with SBU's ability to strengthen XTL resin-zirconia bonds.

TABLE 5 The mean shear bond strength values (MPa) of all brackets in the different experimental groups (mean ± SD).

Storage	XT	XTS	RSBU	RGBU	SBPM	GMP
24H	5.36 ± 1.78^{A}	6.63 ± 1.73^{A}	11.99 ± 3.94^{B}	11.53 ± 2.08^{B}	15.60 ± 2.24^{C}	13.21 ± 2.97^{BC}
	$p < 0.05$	*NS*	$p < 0.05$	$p < 0.05$	$p < 0.05$	$p < 0.05$
5000cycles	0.43 ± 0.37^{A}	7.48 ± 5.40^{B}	7.61 ± 5.01^{B}	7.65 ± 5.38^{B}	12.78 ± 2.82^{C}	8.65 ± 6.51^{BC}

NS indicates no significance in SBS, between storage periods for each material ($p > 0.05$).
Identical capital letters indicate no significant differences in SBS among materials for each storage period ($p > 0.05$).

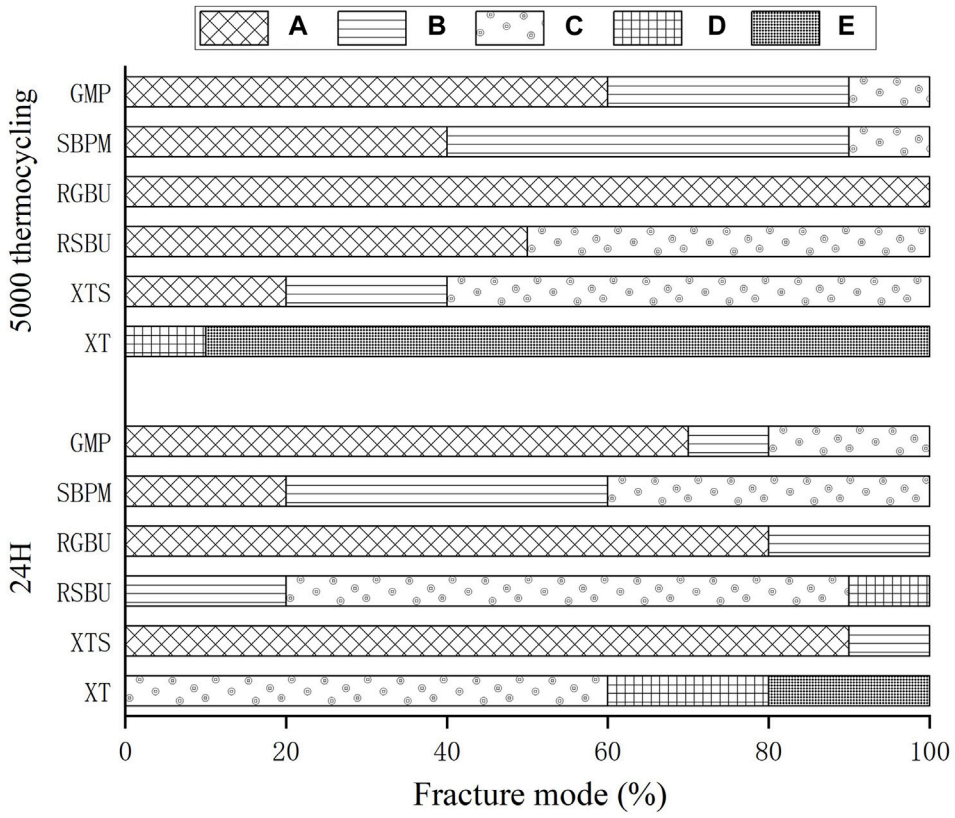

FIGURE 3
Percentages (%) of the different failure modes after SBS test of metal brackets bonded to zirconia. A to E correspond to Score A to Score E.

4.2 Hydrophilic monomer HEMA's effect

The absence of HEMA in GBU aimed to evaluate HEMA's impact on bracket-zirconia bonding. RSBU (containing HEMA) for metal brackets demonstrated significantly higher SBS than HEMA-free RGBU after 24 h water storage. HEMA's role in enhancing component miscibility and forming a uniform adhesive layer could explain RSBU's superiority (Toledano et al., 2001; Moszner et al., 2005; Van Landuyt et al., 2005), despite its decreased SBS post-thermocycling. However, RGBU's hydrophobic nature prevented water absorption, resulting in more stable bonding durability, aligning with earlier findings (Hu et al., 2022).

4.3 Impact of resin water absorption on durability

Studies have shown that HEMA-containing adhesives, due to continuous water absorption, lead to decreased bond strength post-polymerization (Ito et al., 2005; Takahashi et al., 2011). RSBU demonstrated significant SBS reduction after 5,000 cycles of thermocycling, attributed to water absorption. Conversely, RGBU's SBS remained stable in metal brackets group, indicating its resistance to water-induced degradation. Therefore, Three-way ANOVA demonstrated a statistically significant interaction among bonding agents, storage conditions and brackets ($p < 0.001$), which was not detected in previous experiment (Hu et al., 2022).

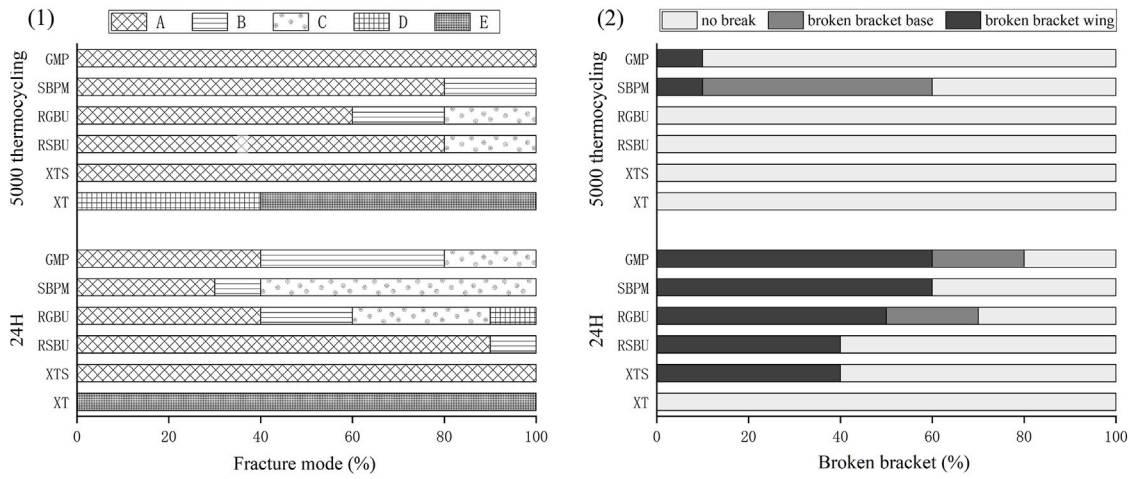

FIGURE 4
Results of ARI and breakage of ceramic brackets. (1) Percentages (%) of the different failure modes after shear bond strength test of ceramic brackets bonded to zirconia. (2) Percentages (%) of breakage of different ceramic brackets.

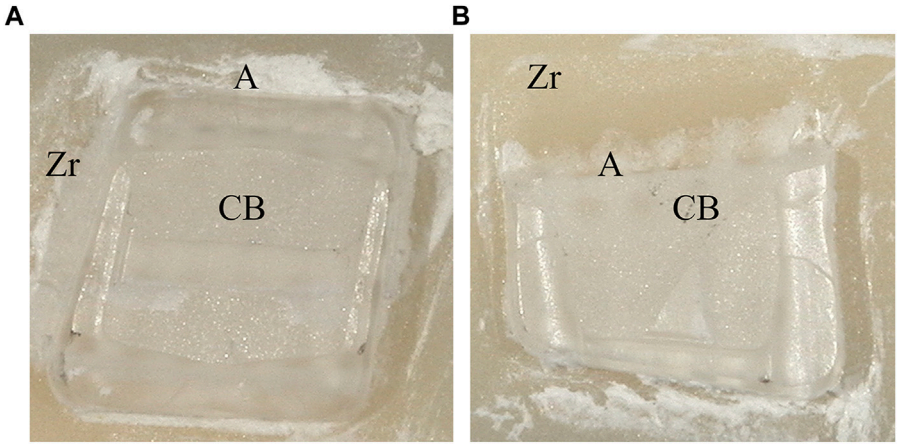

FIGURE 5
Typical bracket fractures including wings breakage **(A)** and base breakage **(B)**: Zr (zirconia), A (Adhesive), CB (ceramic bracket base).

4.4 Specific bonding agents' performance

GMP, containing a self-adhesive resin cement, showed comparable SBS to SBPM in the metal bracket group after 5,000 thermocycles, suggesting GMP's stability post-thermal stress.

SBPM exhibited significantly higher SBS for ceramic brackets, despite a notable 60% bracket breakage rate. This could be attributed to MMA resin's water resistivity (Ikemura and Endo, 2010; Aoki et al., 2011) and the absence of silicon components in EDS analysis. Due to the absence of inorganic fillers, SBPM is typically polymerized in a linear form, resulting in better toughness compared to cross-linked polymers. On the other hand, SBPM can promote free radical polymerization of the resin using oxygen and water in the presence of TBB, a polymerization initiator, which can significantly improve the bond strength and long-term durability of ceramic brackets to zirconia porcelain (Tanaka et al., 2004; Meguro et al., 2006; Shinagawa et al., 2019). The presence of Zr in the EDS results also reveals the viewpoint. This finding is consistent with those of Shimoe et al., who also observed an increase in the [C] and [O] intensity peaks when the zirconia surface was treated with 4-META, indicating that 4-META chemically adheres to the zirconia surface effectively (Shimoe et al., 2018).

4.5 Influence of storage conditions

While most groups demonstrated decreased SBS after thermocycling, XTS displayed a significant SBS increase, possibly due to radical mobility enhancement in high-temperature conditions during resin solidification (Al Jabbari et al., 2014). This variance partially rejected the null

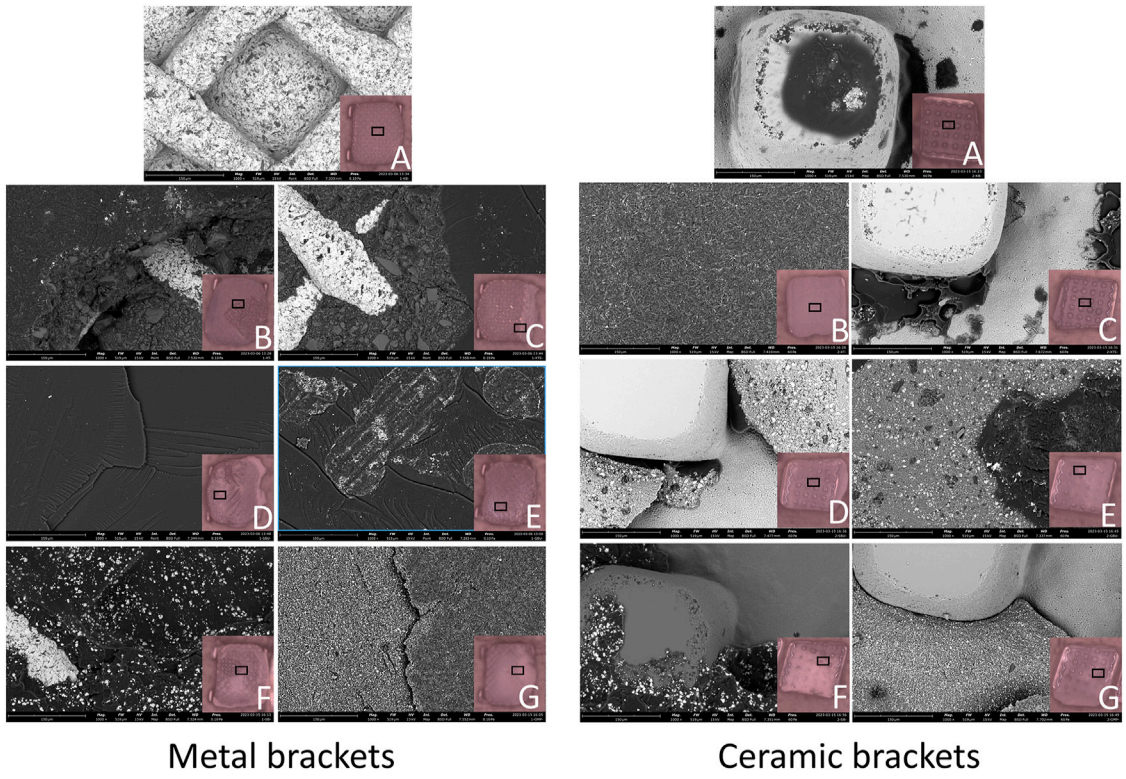

FIGURE 6
SEM photographs (1,000 × original magnification) of bracket bases: **(A)** Control Group; **(B)** XT Group; **(C)** XTS Group; **(D)** RSBU Group; **(E)** RGBU Group; **(F)** SBPM Group; **(G)** GMP Group.

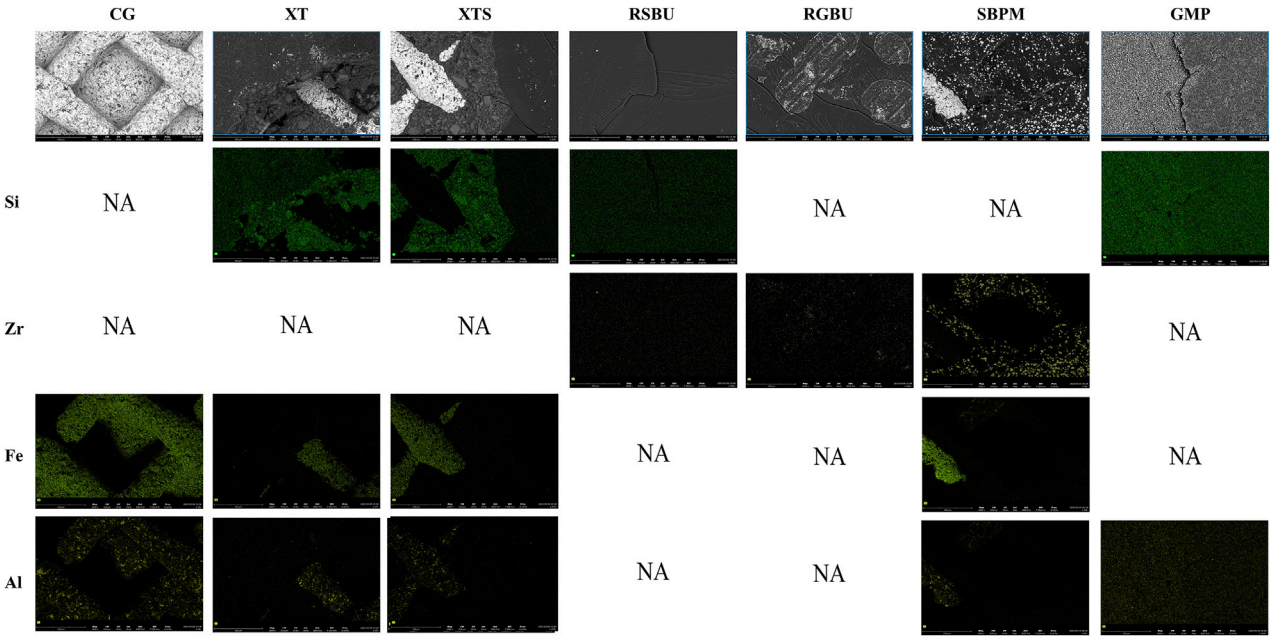

FIGURE 7
Distribution of elemental composition on the debonding base of metal brackets and ceramic brackets. CG indicates Control Group; NA indicates no applicable.

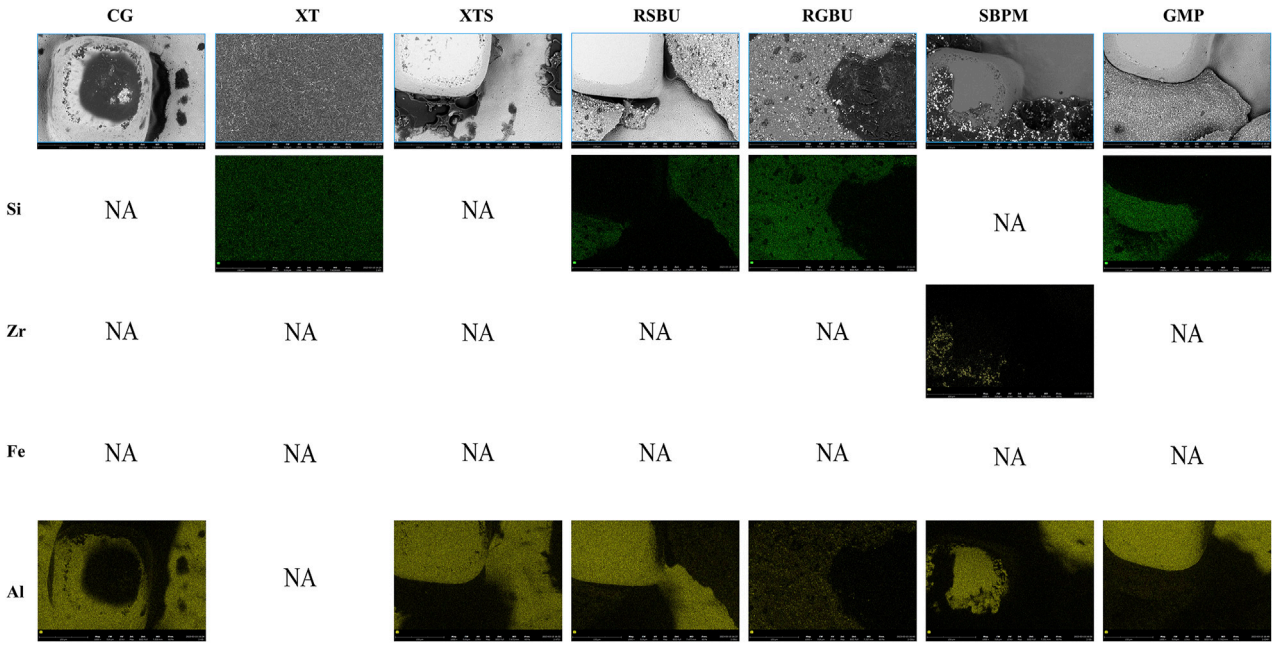

FIGURE 8
Distribution of elemental composition on the debonding base of ceramic brackets.

hypothesis of storage conditions not affecting bonding agents' strength.

4.6 Comparison of metal vs. ceramic brackets

Metal and ceramic brackets showcased comparable SBS after 24 h water storage, but ceramic brackets exhibited significantly lower SBS post-thermocycling, rejecting the null hypothesis of similar bonding durability between metal and ceramic brackets on zirconia.

4.7 Discussion limitations

Limitations include *in vitro* conditions not entirely mimicking oral temperatures, potentially impacting XTS's clinical bond strength, and bracket fractures affecting measured SBS accuracy in ceramic brackets. Meanwhile, the study solely applied sandblasting treatment to zirconia surfaces, without comprehensive assessment of other factors capable of zirconia surface modification, such as laser treatment (Hou et al., 2020) and silica coating (Galvão Ribeiro et al., 2018), which have been demonstrated to have a positive impact on the bonding efficacy between zirconia and resin. The subsequent phase of research may encompass the effects of diverse surface modification treatments between orthodontic brackets and zirconia and investigate their clinical practicality.

5 Conclusion

1. Ceramic brackets displayed significantly lower bond strength on zirconia compared to metal brackets after thermocycling.
2. SBPM exhibited stable and sufficient bond strength between ceramic/metal brackets and zirconia under diverse storage conditions.
3. HEMA-free adhesive presented more stable bonding performance compared to HEMA-containing adhesive used in the study.

Data availability statement

The raw data supporting the conclusions of this article will be made available by the authors, without undue reservation.

Author contributions

YH: Formal Analysis, Investigation, Project administration, Visualization, Writing–original draft. JG: Investigation, Supervision, Writing–original draft. XH: Investigation, Visualization, Writing–original draft. YL: Investigation, Writing–original draft. ZC: Investigation, Writing–original draft. DZ: Supervision, Writing–review and editing. HS: Supervision, Writing–review and editing. RC: Funding acquisition, Supervision, Writing–review and editing. JF: Conceptualization, Methodology, Resources, Writing–original draft, Writing–review and editing.

Funding

The author(s) declare that no financial support was received for the research, authorship, and/or publication of this article.

Acknowledgments

The authors would like to acknowledge the support of Minnesota Mining and Manufacturing Company (3M, St.Paul, MN, United States) and Zhejiang Protect Medical Equipment Co., Ltd. (Protect, Zhejiang, China) for providing Unitek Gemini™ metal brackets (2022-ISR-000369) and Maia ceramic brackets (KYHZ20221212-1). The support of Research and Development Center, Aidite (Qinhuangdao) Technology Co., Ltd. during the surface evaluation stages of this research is also appreciated. Additionally, this research was organized and carried out by the Student Innovation and Entrepreneurship Training Program of China Medical University.

Conflict of interest

The authors declare that the research was conducted in the absence of any commercial or financial relationships that could be construed as a potential conflict of interest.

Publisher's note

All claims expressed in this article are solely those of the authors and do not necessarily represent those of their affiliated organizations, or those of the publisher, the editors and the reviewers. Any product that may be evaluated in this article, or claim that may be made by its manufacturer, is not guaranteed or endorsed by the publisher.

References

Alexopoulou, E., Polychronis, G., Konstantonis, D., Sifakakis, I., Zinelis, S., and Eliades, T. (2020). A study of the mechanical properties of as-received and intraorally exposed single-crystal and polycrystalline orthodontic ceramic brackets. *Eur. J. Orthod.* 42, 72–77. doi:10.1093/ejo/cjz024

Al-Hity, R., Gustin, M.-P., Bridel, N., Morgon, L., and Grosgogeat, B. (2012). *In vitro* orthodontic bracket bonding to porcelain. *Eur. J. Orthod.* 34, 505–511. doi:10.1093/ejo/cjr043

Al Jabbari, Y. S., Al Taweel, S. M., Al Rifaiy, M., Alqahtani, M. Q., Koutsoukis, T., and Zinelis, S. (2014). Effects of surface treatment and artificial aging on the shear bond strength of orthodontic brackets bonded to four different provisional restorations. *Angle Orthod.* 84, 649–655. doi:10.2319/090313-649.1

Aoki, K., Kitasako, Y., Ichinose, S., Burrow, M. F., Ariyoshi, M., Nikaido, T., et al. (2011). Ten-year observation of dentin bonding durability of 4-META/MMA-TBB resin cement--a SEM and TEM study. *Dent. Mater J.* 30, 438–447. doi:10.4012/dmj.2011-003

Babaee Hemmati, Y., Neshandar Asli, H., Falahchai, M., and Safary, S. (2022). Effect of different surface treatments and orthodontic bracket type on shear bond strength of high-translucent zirconia: an *in vitro* study. *Int. J. Dent.* 2022, 1–8. doi:10.1155/2022/9884006

Blakey, R., and Mah, J. (2010). Effects of surface conditioning on the shear bond strength of orthodontic brackets bonded to temporary polycarbonate crowns. *Am. J. Orthod. Dentofac. Orthop.* 138, 72–78. doi:10.1016/j.ajodo.2008.08.030

Galvão Ribeiro, B. R., Galvão Rabelo Caldas, M. R., Almeida, A. A., Fonseca, R. G., and Adabo, G. L. (2018). Effect of surface treatments on repair with composite resin of a partially monoclinic phase transformed yttrium-stabilized tetragonal zirconia. *J. Prosthet. Dent.* 119, 286–291. doi:10.1016/j.prosdent.2017.02.014

Gautam, C., Joyner, J., Gautam, A., Rao, J., and Vajtai, R. (2016). Zirconia based dental ceramics: structure, mechanical properties, biocompatibility and applications. *Dalton Trans.* 45, 19194–19215. doi:10.1039/c6dt03484e

Goracci, C., Di Bello, G., Franchi, L., Louca, C., Juloski, J., Juloski, J., et al. (2022). Bracket bonding to all-ceramic materials with universal adhesives. *Mater. (Basel)* 15, 1245. doi:10.3390/ma15031245

Hanawa, T. (2020). Zirconia versus titanium in dentistry: a review. *Dent. Mater J.* 39, 24–36. doi:10.4012/dmj.2019-172

Hellak, A., Ebeling, J., Schauseil, M., Stein, S., Roggendorf, M., and Korbmacher-Steiner, H. (2016). Shear bond strength of three orthodontic bonding systems on enamel and restorative materials. *Biomed. Res. Int.* 2016, 1–10. doi:10.1155/2016/6307107

Hou, Y., Yi, J., Huang, Y., Gao, J., Chen, Y., and Wang, C. (2020). Effect of Er:YAG laser etching on the shear bond strength and microleakage of self-glazed zirconia ceramics. *Photobiomodul Photomed. Laser Surg.* 38, 289–294. doi:10.1089/photob.2019.4658

Hu, B., Hu, Y., Li, X., Gao, J., Sun, R., Zhan, D., et al. (2022). Shear bond strength of different bonding agents to orthodontic metal bracket and zirconia. *Dent. Mater J.* 41, 749–756. doi:10.4012/dmj.2022-028

Ikemura, K., and Endo, T. (2010). A review of our development of dental adhesives--effects of radical polymerization initiators and adhesive monomers on adhesion. *Dent. Mater J.* 29, 109–121. doi:10.4012/dmj.2009-057

Ito, S., Hashimoto, M., Wadgaonkar, B., Svizero, N., Carvalho, R. M., Yiu, C., et al. (2005). Effects of resin hydrophilicity on water sorption and changes in modulus of elasticity. *Biomaterials* 26, 6449–6459. doi:10.1016/j.biomaterials.2005.04.052

Jawad, Z., Bates, C., and Hodge, T. (2015). Who needs orthodontic treatment? Who gets it? And who wants it? *Br. Dent. J.* 218, 99–103. doi:10.1038/sj.bdj.2015.51

Ju, G.-Y., Lim, B.-S., Moon, W., Park, S.-Y., Oh, S., and Chung, S. H. (2020). Primer-treated ceramic bracket increases shear bond strength on dental zirconia surface. *Mater. (Basel)* 13, 4106. doi:10.3390/ma13184106

Ju, G.-Y., Oh, S., Lim, B.-S., Lee, H.-S., and Chung, S. H. (2019). Effect of simplified bonding on shear bond strength between ceramic brackets and dental zirconia. *Mater. (Basel)* 12, 1640. doi:10.3390/ma12101640

Khan, A. A., Al Kheraif, A. A. A., Jamaluddin, S., Elsharawy, M., and Divakar, D. D. (2017). Recent trends in surface treatment methods for bonding composite cement to zirconia: a reveiw. *J. Adhes. Dent.* 19, 7–19. doi:10.3290/j.jad.a37720

Lima, R. B. W., Barreto, S. C., Alfrisany, N. M., Porto, T. S., De Souza, G. M., and De Goes, M. F. (2019). Effect of silane and MDP-based primers on physico-chemical properties of zirconia and its bond strength to resin cement. *Dent. Mater* 35, 1557–1567. doi:10.1016/j.dental.2019.07.008

Makhija, S. K., Lawson, N. C., Gilbert, G. H., Litaker, M. S., McClelland, J. A., Louis, D. R., et al. (2016). Dentist material selection for single-unit crowns: findings from the national dental practice-based research network. *J. Dent.* 55, 40–47. doi:10.1016/j.jdent.2016.09.010

Meguro, D., Hayakawa, T., Kawasaki, M., and Kasai, K. (2006). Shear bond strength of calcium phosphate ceramic brackets to human enamel. *Angle Orthod.* 76, 301–305. doi:10.1043/0003-3219(2006)076[0301:SBSOCP]2.0.CO;2

Moszner, N., Salz, U., and Zimmermann, J. (2005). Chemical aspects of self-etching enamel-dentin adhesives: a systematic review. *Dent. Mater* 21, 895–910. doi:10.1016/j.dental.2005.05.001

Nagaoka, N., Yoshihara, K., Feitosa, V. P., Tamada, Y., Irie, M., Yoshida, Y., et al. (2017). Chemical interaction mechanism of 10-MDP with zirconia. *Sci. Rep.* 7, 45563. doi:10.1038/srep45563

Nistor, L., Grădinaru, M., Rîcă, R., Mărășescu, P., Stan, M., Manolea, H., et al. (2019). Zirconia use in dentistry - manufacturing and properties. *Curr. Health Sci. J.* 45, 28–35. doi:10.12865/CHSJ.45.01.03

Pinho, M., Manso, M. C., Almeida, R. F., Martin, C., Carvalho, Ó., Henriques, B., et al. (2020). Bond strength of metallic or ceramic orthodontic brackets to enamel, acrylic, or porcelain surfaces. *Mater. (Basel)* 13, 5197. doi:10.3390/ma13225197

Rauch, A., Schrock, A., Schierz, O., and Hahnel, S. (2021). Material selection for tooth-supported single crowns-a survey among dentists in Germany. *Clin. Oral Investig.* 25, 283–293. doi:10.1007/s00784-020-03363-9

Reginato, C. F., Oliveira, A. S., Kaizer, M. R., Jardim, P. S., and Moraes, R. R. (2013). Polymerization efficiency through translucent and opaque fiber posts and bonding to root dentin. *J. Prosthodont Res.* 57, 20–23. doi:10.1016/j.jpor.2012.05.003

Shimoe, S., Hirata, I., Otaku, M., Matsumura, H., Kato, K., and Satoda, T. (2018). Formation of chemical bonds on zirconia surfaces with acidic functional monomers. *J. Oral Sci.* 60, 187–193. doi:10.2334/josnusd.17-0160

Shinagawa, J., Inoue, G., Nikaido, T., Ikeda, M., Burrow, M. F., and Tagami, J. (2019). Early bond strengths of 4-META/MMA-TBB resin cements to CAD/CAM resin composite. *Dent. Mater J.* 38, 28–32. doi:10.4012/dmj.2017-438

Takahashi, M., Nakajima, M., Hosaka, K., Ikeda, M., Foxton, R. M., and Tagami, J. (2011). Long-term evaluation of water sorption and ultimate tensile strength of HEMA-containing/-free one-step self-etch adhesives. *J. Dent.* 39, 506–512. doi:10.1016/j.jdent.2011.04.008

Tanaka, Y., Sugaya, T., Tanaka, S., and Kawanami, M. (2004). Long-term durability of root-end sealing with 4-MEtA/MMA-TBB resin. *Dent. Mater J.* 23, 453–456. doi:10.4012/dmj.23.453

Tecco, S., Traini, T., Caputi, S., Festa, F., de Luca, V., and D'Attilio, M. (2005). A new one-step dental flowable composite for orthodontic use: an *in vitro* bond strength study. *Angle Orthod.* 75, 672–677. doi:10.1043/0003-3219(2005)75[672:ANODFC]2.0.CO;2

Toledano, M., Osorio, R., de Leonardi, G., Rosales-Leal, J. I., Ceballos, L., and Cabrerizo-Vilchez, M. A. (2001). Influence of self-etching primer on the resin adhesion to enamel and dentin. *Am. J. Dent.* 14, 205–210.

Urichianu, M., Makowka, S., Covell, D., Warunek, S., and Al-Jewair, T. (2022). Shear bond strength and bracket base morphology of new and rebonded orthodontic ceramic brackets. *Mater. (Basel)* 15, 1865. doi:10.3390/ma15051865

Uysal, T., Sari, Z., and Demir, A. (2004). Are the flowable composites suitable for orthodontic bracket bonding? *Angle Orthod.* 74, 697–702. doi:10.1043/0003-3219(2004)074<0697:ATFCSF>2.0.CO;2

Van Landuyt, K. L., De Munck, J., Snauwaert, J., Coutinho, E., Poitevin, A., Yoshida, Y., et al. (2005). Monomer-solvent phase separation in one-step self-etch adhesives. *J. Dent. Res.* 84, 183–188. doi:10.1177/154405910508400214

Vult von Steyern, P., Bruzell, E., Vos, L., Andersen, F. S., and Ruud, A. (2022). Sintering temperature accuracy and its effect on translucent yttria-stabilized zirconia: flexural strength, crystal structure, tetragonality and light transmission. *Dent. Mater* 38, 1099–1107. doi:10.1016/j.dental.2022.04.023

Zarone, F., Di Mauro, M. I., Ausiello, P., Ruggiero, G., and Sorrentino, R. (2019). Current status on lithium disilicate and zirconia: a narrative review. *BMC Oral Health* 19, 134. doi:10.1186/s12903-019-0838-x

Zhang, Y., and Lawn, B. R. (2018). Novel zirconia materials in dentistry. *J. Dent. Res.* 97, 140–147. doi:10.1177/0022034517737483

frontiers | Frontiers in Bioengineering and Biotechnology

TYPE Correction
PUBLISHED 15 May 2024
DOI 10.3389/fbioe.2024.1423030

OPEN ACCESS

EDITED AND REVIEWED BY
Hongye Yang,
Wuhan University, China

*CORRESPONDENCE
Jiale Fu,
fullers@126.com

RECEIVED 25 April 2024
ACCEPTED 02 May 2024
PUBLISHED 15 May 2024

CITATION
Hu Y, Gao J, Huang X, Li Y, Chen Z, Zhan D, Sano H, Carvalho RM and Fu J (2024), Corrigendum: The possibility of clinical bonding between metal/ceramic brackets to zirconia: *in vitro* study.
Front. Bioeng. Biotechnol. 12:1423030.
doi: 10.3389/fbioe.2024.1423030

Corrigendum: The possibility of clinical bonding between metal/ceramic brackets to zirconia: *in vitro* study

Yichun Hu[1], Jiayang Gao[1], Xinyue Huang[1], Yutong Li[1], Ziyi Chen[1], Desong Zhan[2], Hidehiko Sano[3], Ricardo M. Carvalho[4] and Jiale Fu[2]*

[1]School and Hospital of Stomatology, China Medical University, Shenyang, China, [2]Department of Dental Materials Science, The Second Department of Prosthodontics, School and Hospital of Stomatology, China Medical University, Shenyang, China, [3]Department of Restorative Dentistry, Division of Oral Health Science, Faculty of Dental Medicine, Hokkaido University, Sapporo, Japan, [4]Department of Oral Biological and Medical Sciences, Division of Biomaterials, Faculty of Dentistry, University of British Columbia, Vancouver, BC, Canada

KEYWORDS

shear bond strength (SBS), ceramic bracket, zirconia, resin cement, metal bracket, storage condition

A Corrigendum on
The possibility of clinical bonding between metal/ceramic brackets to zirconia: *in vitro* study

by Hu Y, Gao J, Huang X, Li Y, Chen Z, Zhan D, Sano H, Carvalho RM and Fu J (2024). Front. Bioeng Biotechnol. 12:1354241. doi: 10.3389/fbioe.2024.1354241

In the published article, there was an error. A sentence was included which inaccurately describes **Figures 3 and 4**.

A correction has been made to **3.2 Failure modes**, Paragraph 2. This sentence previously stated:

> "For ceramic brackets under both conditions, XT showed a tendency toward E in ARI scores, while SBPM shifted toward C after thermocycling. Other groups displayed varied tendencies across scores."

The corrected sentence appears below:

> "For ceramic brackets under both conditions, XT showed a tendency toward E in ARI scores, while GMP and SBPM exhibited a notable increase in A and a decrease to 0 in C after thermocycling."

The authors apologize for this error and state that this does not change the scientific conclusions of the article in any way. The original article has been updated.

Publisher's note

frontiers | Frontiers in Bioengineering and Biotechnology

TYPE Original Research
PUBLISHED 02 February 2024
DOI 10.3389/fbioe.2024.1356412

OPEN ACCESS

EDITED BY
Hongye Yang,
Wuhan University, China

REVIEWED BY
Xi Ding,
First Affiliated Hospital of Wenzhou Medical University, China
Mengjiao Zhou,
Stomatological Hospital of Chongqing Medical University, China

*CORRESPONDENCE
Weimin Weng,
wengweimin31@126.com
Chun Xu,
imxuchun@163.com

†These authors have contributed equally to this work

RECEIVED 15 December 2023
ACCEPTED 19 January 2024
PUBLISHED 02 February 2024

CITATION
Wang Y, Cao X, Shen Y, Zhong Q, Wu Z, Wu Y, Weng W and Xu C (2024), Evaluate the effects of low-intensity pulsed ultrasound on dental implant osseointegration under type II diabetes. *Front. Bioeng. Biotechnol.* 12:1356412. doi: 10.3389/fbioe.2024.1356412

Evaluate the effects of low-intensity pulsed ultrasound on dental implant osseointegration under type II diabetes

Yingying Wang[1,2,3,4†], Ximeng Cao[1,2,3,4†], Yingyi Shen[1,2,3,4], Qi Zhong[1,2,3,4], Ziang Wu[1,2,3,4], Yaqin Wu[1,2,3,4], Weimin Weng[1,2,3,4*] and Chun Xu[1,2,3,4*]

[1]Department of Prosthodontics, Shanghai Ninth People's Hospital, Shanghai Jiao Tong University School of Medicine, Shanghai, China, [2]College of Stomatology, Shanghai Jiao Tong University, Shanghai, China, [3]National Center for Stomatology and National Clinical Research Center for Oral Diseases, Shanghai, China, [4]Shanghai Key Laboratory of Stomatology, Shanghai Research Institute of Stomatology, Shanghai, China

Objective: The objective of this study is to assess the impact of low-intensity pulsed ultrasound (LIPUS) therapy on the peri-implant osteogenesis in a Type II diabetes mellitus (T2DM) rat model.

Methods: A total of twenty male Sprague-Dawley (SD) rats were randomly allocated into four groups: Control group, T2DM group, Control-LIPUS group, and T2DM-LIPUS group. Implants were placed at the rats' bilateral maxillary first molar sites. The LIPUS treatment was carried out on the rats in Control-LIPUS group and T2DM-LIPUS group, immediately after the placement of the implants, over three consecutive weeks. Three weeks after implantation, the rats' maxillae were extracted for micro-CT, removal torque value (RTV), and histologic analysis.

Results: Micro-CT analysis showed that T2DM rats experienced more bone loss around implant cervical margins compared with the non-T2DM rats, while the LIPUS treated T2DM rats showed similar bone heights to the non-T2DM rats. Bone-implant contact ratio (BIC) were lower in T2DM rats but significantly improved in the LIPUS treated T2DM rats. Bone formation parameters including bone volume fraction (BV/TV), trabecular thickness (Tb.Th), bone mineral density (BMD) and RTV were all positively influenced by LIPUS treatment. Histological staining further confirmed LIPUS's positive effects on peri-implant new bone formation in T2DM rats.

Conclusion: As an effective and safe treatment in promoting osteogenesis, LIPUS has a great potential for T2DM patients to attain improved peri-implant osteogenesis. To confirm its clinical efficacy and to explore the underlying mechanism, further prospective cohort studies or randomized controlled trials are needed in the future.

KEYWORDS

low-intensity pulsed ultrasound, implantation, type II diabetes mellitus, osteogenesis, osseointegration

1 Introduction

Low-intensity pulsed ultrasound (LIPUS) is a noninvasive therapy that harnesses acoustic pulsed energy to provide physical stimulation. The research on LIPUS has been ongoing for approximately two decades. Ultrasound has been found to promote various biological processes, including the formation of bone matrix by osteoblasts, the synthesis of collagen by fibroblasts, the synthesis of aggrecan in chondrocytes, and the differentiation of bone mesenchymal stem cells (BMSC) into osteoblasts on titanium surfaces (An et al., 2018). LIPUS treatment increased the number of mineralization nodules of microfilaments, pseudopods of the cells and the amount of extracellular matrix (An et al., 2018).

With the development of the materials and technologies, dental implants emerged as a popular solution for restoring missing teeth in patients. Osseointegration, a crucial aspect for successful implant fixation (Chauvel-Picard et al., 2022), was first conceptualized by Brånemark in 1965 (Brånemark et al., 1977). It refers to the direct contact between a biomaterial and bone tissue without the presence of fibrous tissue in between.

Several factors might influence the establishment of osseointegration, one of which is Type II diabetes mellitus (T2DM) condition. Bone re-modelling disorders resulting from diabetes poses significant risks to the overall success of dental implant treatments (Hua et al., 2018; Ding et al., 2019; Meza Maurício et al., 2019). T2DM has a high prevalence especially in the elderly, while among which the need for restoring the missing teeth is high (Petersmann et al., 2018). Studies have showed that T2DM can exert detrimental effects on various organs and tissues (Ren et al., 2019; Guo et al., 2020). Human blood carries a substantial amount of oxygen and active proteins, which can influence the proliferation and differentiation of bone-derived cells surrounding the implant. Previous studies have indicated that patients with diabetes mellitus exhibit diminished proliferation and osteogenic differentiation capabilities of osteoblasts compared to individuals without diabetes (Li et al., 2015; Graves et al., 2020). Furthermore, the presence of elevated blood glucose levels (Li et al., 2015; Przekora et al., 2016) and disruptions in calcium or phosphorus metabolism, commonly observed in individuals with T2DM, can significantly impact bone tissue remodeling and interfere with the bonding between implants and bone, particularly within the first three weeks following implant placement (Wang et al., 2021).

For achieving a high-quality implant fixation, it is essential to have a rapid and successful osseointegration (Ustun et al., 2008; Meng et al., 2016). Various methods have been developed to stimulate osteogenesis. Among these approaches, ultrasounds, specifically LIPUS, have been proven to be effective in stimulating bone, cartilage, tendon and mucosal regeneration (Khanna et al., 2009; Lavandier et al., 2009; Hsu et al., 2011; Padilla et al., 2016; Chauvel-Picard et al., 2021). Multiple studies have investigated the potential benefits of LIPUS in promoting the osseointegration of dental implants using animal models (Park et al., 2007; Suh et al., 2007; Ustun et al., 2008; Mathieu et al., 2011; Liu et al., 2012; Wang et al., 2023a). However, whether LIPUS could promote osteogenesis around dental implant under T2DM condition has not been reported.

Drawing from these studies on the use of LIPUS in facilitating bone regeneration around implants, it is reasonable to speculate that LIPUS could serve as a valuable supplementary treatment approach to enhance implant osseointegration in individuals with diabetes. Therefore, this study evaluated the effects of LIPUS treatment on osteogenesis around dental implant in a T2DM rat model, by which to provide a reference for future studies to achieve better prognosis of implant treatment in T2DM patients.

2 Materials and methods

The entire process followed the guidelines specified in the Animal Research: Reporting *In Vivo* Experiments (ARRIVE protocol) (Percie du Sert et al., 2020). Approval for this study was obtained from the Experimental Animal Ethics Committee of the Ninth People's Hospital, affiliated with Shanghai Jiao Tong University School of Medicine (reference number: SH9H-2022-A84-1).

2.1 Animals

Male Sprague-Dawley (SD) rats, aged 7 weeks, were acquired and subsequently housed at room temperature around 20°C with a 12-hour light/dark cycle.

2.2 Group assignment

Following Mead's resource equation and considering outcome variance and various treatments, the estimated sample size remained consistent with that employed in previous studies (Ganzorig et al., 2015; Ruppert et al., 2019; Sun et al., 2020). The SD rats were randomly divided into 4 groups, 5 rats in each group, as follows: (a) Control group, (b) T2DM group: with experimentally induced T2DM before implantation surgery, (c) Control-LIPUS: after implantation surgery, the implant sites were treated with LIPUS for 3 consecutive weeks, and (d) T2DM-LIPUS group: with experimentally induced T2DM before implantation surgery, and the implant sites were treated with LIPUS for 3 consecutive weeks after implantation surgery. The group assignment and the entire clinical procedure are depicted in Figure 1.

2.3 Induction of T2DM

The rats were provided with a high-fat diet for a duration of 4 weeks. Following the high-fat diet regimen, the rats received an intraperitoneal injection of 35 mg/kg streptozotocin (STZ) to induce a state of T2DM (Li et al., 2020; Chen et al., 2021; Khater et al., 2021). Rats with fasting blood glucose (FBG) levels exceeding 16.7 mmol/L 3 days after the STZ injection were considered successfully established T2DM models.

2.4 Implantation surgery

This implantation surgery in rats maxillae has been reported and evaluated in our previous study (Wang, 2023b), and the procedure

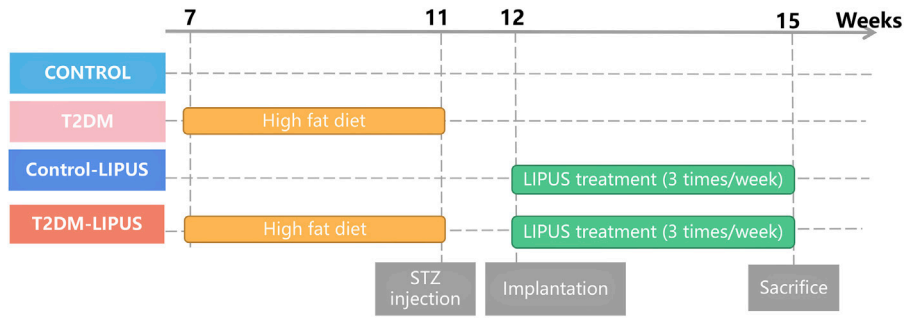

FIGURE 1
Group assignment. T2DM, type II diabetes mellitus; LIPUS, low-intensity pulsed ultrasound; STZ, streptozotocin.

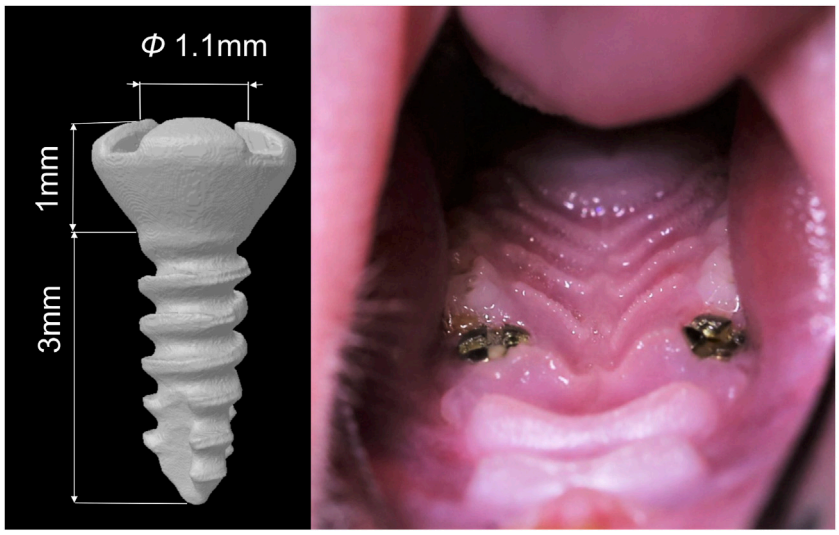

FIGURE 2
Diagram of the dental implant used in the study and the intra-oral photographs of the rat after implantation surgery.

was as follows. One week before the surgery, the rats were administered daily antibiotics through oral infusion, with a dosage of 100 μL, including 20 mg of kanamycin and 20 mg of ampicillin. After the rats were anesthetized by administering ketamine (85–90 mg/kg body weight) and xylazine (5–10 mg/kg body weight) intraperitoneally, the bilateral maxillary first molars were extracted. Sockets were rinsed with saline. After socket rinsing, a low-speed handpiece was utilized, operating at a drill diameter of 1 mm and a speed of 1,000 rpm, with continuous irrigation of cooled saline solution to prepare the implant sites in the palatal root socket area of the extraction site. Subsequently, a titanium alloy self-tapped implant (Ti-6Al-4V with an anodized surface, Baiortho™, China) was inserted and allowed to heal transmucosally (Figure 2). Throughout the initial week of the healing period, the rats received a daily antibiotic dose (consistent with the previous dosage). Their oral and overall health was regularly monitored. At the conclusion of the experiment (3 weeks post-implantation surgery), the rats were humanely euthanized using an anesthesia overdose.

2.5 Insonification

The rats were anesthetized through intraperitoneal administration of ketamine (85–90 mg/kg body weight) and xylazine (5–10 mg/kg body weight). The implant placement site received LIPUS (Osteotron IV, Ito Co., Ltd, Japan) for a duration of 20 min per day, 3 days per week, over a period of 3 consecutive weeks after the implantation surgery, with a 60 mW/cm^2 average temporal and spatial intensity and a 1.5 MHz operation frequency (Figure 3). The parameters of LIPUS treatment were taken from our previous study results (Wang et al., 2023a).

2.6 Removal torque test

At the conclusion of the experiment (3 weeks post-implantation surgery), the rats' maxillae were collected, and the Removal Torque Value (RTV) was assessed. RTV was defined as the maximum rotational force applied in the reverse direction until the implant became horizontally rotatable.

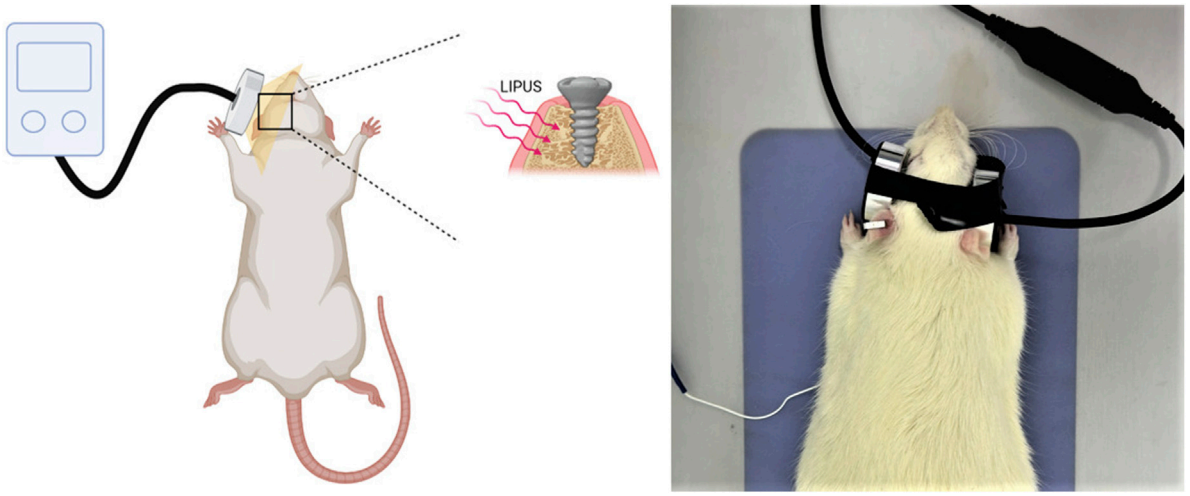

FIGURE 3
LIPUS treatment. LIPUS, low-intensity pulsed ultrasound.

2.7 Micro-CT analysis

The maxillae of the rats were collected and subjected to scanning using a micro-CT (Skyscan 1076, Belgium) with a resolution of 9 μm. A Volume of Interest (VOI) was the area within a 500 μm radius around the implants, covering the peri-implant region. The 3D reconstructions of the maxillae with the placed dental implants were established from the micro-CT scanning and the marginal bone heights around the implants in the rats of different groups were marked. Subsequently, the bone tissue evaluation script generated the final segmented bone image, encompassing the following parameters: marginal bone loss, trabecular thickness (Tb.Th), trabecular number (Tb.N), trabecular separation (Tb.Sp), bone volume fraction (BV/TV), bone mineral density (BMD), bone-implant contact ratio (BIC), and bone surface density (BS/TV). The measurement method of marginal bone loss is to select the section along the long axis of the implant and also including the central axis of the implant. According to the above section and the implant actual length, the marginal bone loss = (4 - the length of the intraosseous implant/4) mm (Sun et al., 2020).

2.8 Histologic processing

Three weeks after surgery, the animals were euthanized with an overdose of anesthesia. The specimens underwent fixation, decalcification, dehydration, and embedding. Subsequently, all specimens were sectioned parallel to the long axis of the implant. The hematoxylin and eosin (H&E) staining and Masson staining were applied to detect the new bone formation around the implant. Images were taken under a microscope (CX33, Olympus, Japan).

2.9 Statistical analysis

The data expressed as mean ± standard deviation was analyzed using SPSS version 26.0 (IBM, Chicago, IL, USA). The differences among the three groups were compared using a one-way ANOVA and the following LSD test. The statistical significance was when the *p*-value was less than 0.05.

3 Results

3.1 Implant survival rate

Three weeks after the implant surgery, the implant survival rate was recorded as showed in Table 1 (implant survival rate = number of final residual implants/number of placed implants). The implant survival rate was 80% in all four groups.

3.2 Evaluation of T2DM rats

Our findings indicated that all rats induced by a high-fat diet and STZ exhibited T2DM. Illustrated in Figure 4A, the rats in the T2DM group exhibited lower body weight than those in the control group, indicative of typical T2DM symptoms. As presented in Figure 4B, a week post-STZ injection, the T2DM group showed a significantly elevated blood glucose level compared to the control group, maintaining levels more than 16.7 mmol/L throughout the experiment. These results indicated the successful establishment of T2DM rat models with hyperglycemia.

3.3 Analysis of the micro-CT

The 3D reconstructions of the maxillae with the placed dental implants were shown in Figure 5, demonstrating the marginal bone height around the implants of the rats in different groups. There was significantly more bone loss at the implant cervical margin area in T2DM groups, but T2DM-LIPUS group showed similar marginal bone height with Control group, as showed in Figure 6A. BIC ratio was presented in Figure 6B, showing that T2DM group had significant

TABLE 1 The implant number and implant survival rates of different groups.

	Control	Control-LIPUS	T2DM	T2DM-LIPUS
Number of rats	5	5	5	5
Number of placed implants	10	10	10	10
Number of final residual implants	8	8	8	8
Implant survival rate	80%	80%	80%	80%

LIPUS, low-intensity pulsed ultrasound; T2DM, type II diabetes mellitus.

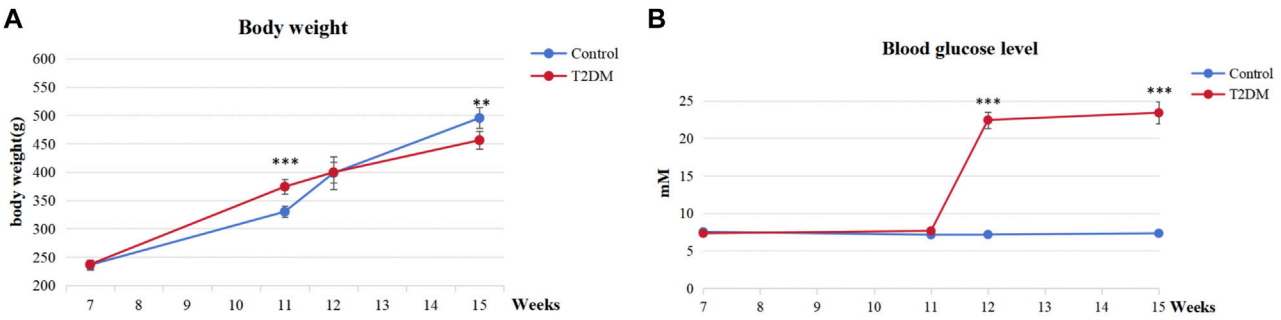

FIGURE 4
Evaluation of T2DM rats. **(A)** Body weight at various time points. **(B)** Blood glucose levels at various time points. ***$p < 0.001$, **$p < 0.01$.

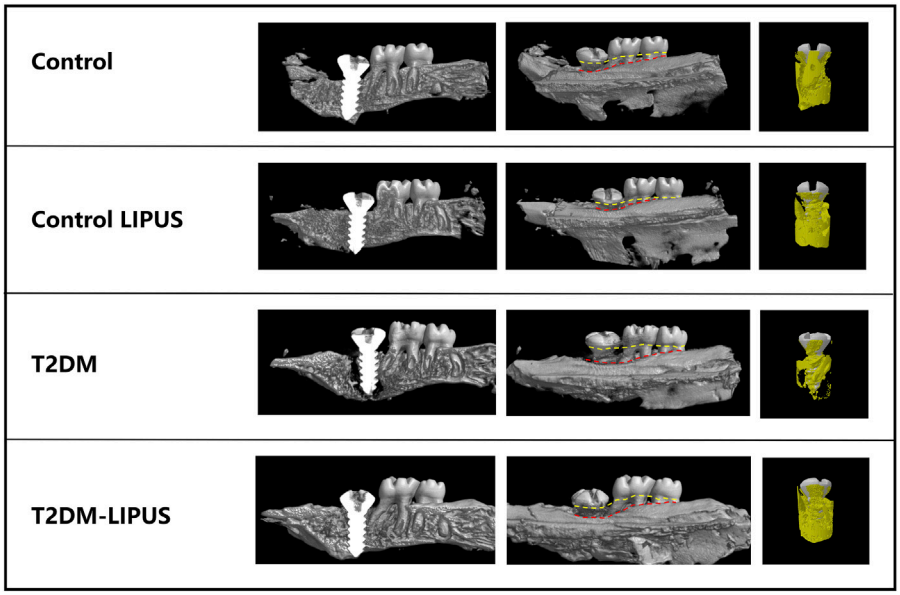

FIGURE 5
Three-dimensional visualization of the dental implant using Micro-CT technology. The marginal bone loss is assessed by the distance between the yellow and red line in the long axis direction of implants. Yellow line refers to the top of implant and cemento-enamel junction of the second and third molars. Red line refers to the marginal bone level. T2DM group showed significantly more marginal bone loss than other groups. T2DM, type II diabetes mellitus; LIPUS, low-intensity pulsed ultrasound.

lower BIC ratio than Control group. T2DM-LIPUS group had significant higher BIC ratio than T2DM group. BS/TV ratio was presented in Figure 6C, showing that LIPUS treatment increased BS/TV ratio of control and T2DM groups significantly. Tb.Sp was presented in Figure 6D, which showed that T2DM group had significant higher Tb.Sp than other three groups. Tb.N was presented in Figure 6E, which showed that T2DM group had significant lower Tb.N than other three groups. Tb.Th was

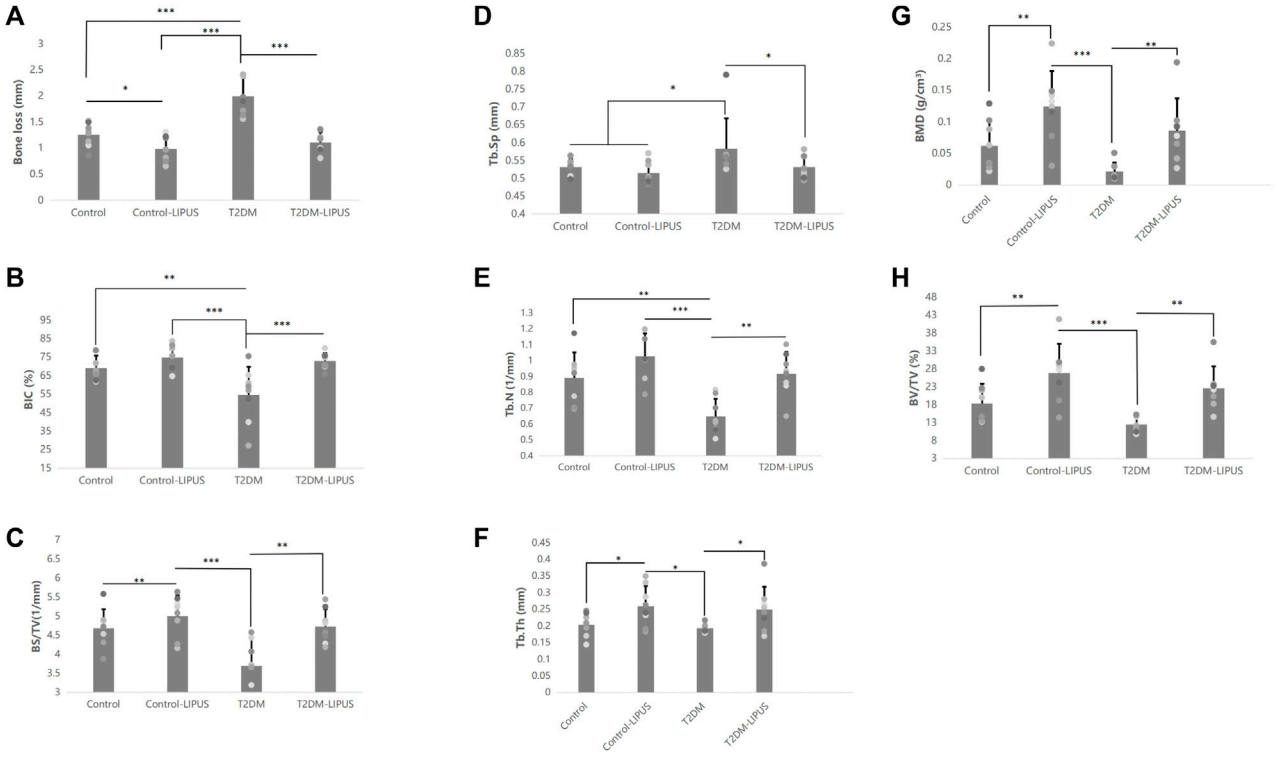

FIGURE 6
Results of the Micro-CT analysis of marginal bone loss, BIC, BS/TV, Tb.Sp, Tb.N, Tb.Th, BMD, and BV/TV. **(A)** Results of the micro-CT analysis of marginal bone loss; **(B)** Results of the micro-CT analysis of BIC; **(C)** Results of the micro-CT analysis of BS/TV; **(D)** Results of the micro-CT analysis of Tb.Sp; **(E)** Results of the micro-CT analysis of Tb.N; **(F)** Results of the micro-CT analysis of Tb.Th; **(G)** Results of the micro-CT analysis of BMD; **(H)** Results of the micro-CT analysis of BV/TV. The results showed that T2DM group had significant lower BIC ratio and Tb.N than control group, and significant higher Tb.Sp and greater marginal bone loss than control group. LIPUS treatment significantly increased BIC, Tb.N, Tb.Th, BMD, BV/TV and BS/TV, and significantly decreased marginal bone loss and Tb. Sp of T2DM rats. LIPUS treatment also significantly increased Tb.Th, BMD, BV/TV and BS/TV, and significantly decreased marginal bone loss of healthy rats. There was no difference between Control and T2DM-LIPUS groups in all the above indexes. *: $p < 0.05$, **: $p < 0.01$,***:$p < 0.001$. Tb.N, trabecular number; Tb.Th, trabecular thickness; Tb.Sp, trabecular separation; BV/TV, bone volume fraction; BMD, bone mineral density; BIC, bone-implant contact ratio; BS/TV, bone surface density; LIPUS, low-intensity pulsed ultrasound; T2DM, type II diabetes mellitus.

presented in Figure 6F, which showed that LIPUS treatment increased Tb.Th of control and T2DM groups significantly. BMD was presented in Figure 6G, showing that LIPUS treatment increased BMD of control and T2DM groups significantly. BV/TV ratio was presented in Figure 6H, which showed that LIPUS treatment increased BV/TV ratio of control and T2DM groups significantly.

3.4 Analysis of the RTV

RTV was presented in Figure 7, showing that Control-LIPUS group had significant higher RTV than other three groups.

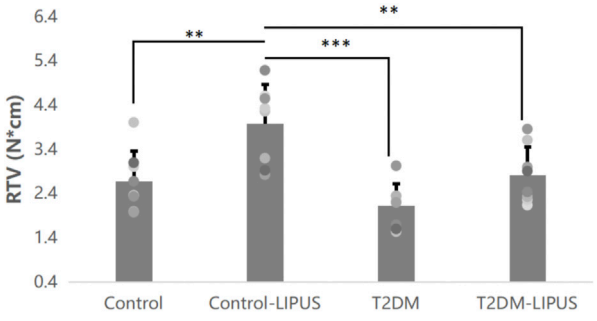

FIGURE 7
Results of the RTV analysis. LIPUS treatment also significantly increased RTV of healthy rats. There was no difference between Control and T2DM-LIPUS groups. *: $p < 0.05$, **: $p < 0.01$,***:$p < 0.001$. RTV, removal torque value; LIPUS, low-intensity pulsed ultrasound; T2DM, type II diabetes mellitus.

3.5 Characterization of the peri-implant H&E and Masson staining

The H&E staining and Masson staining were applied to observe the new bone formation around the implant. As shown in Figure 8A, there were more osteoid tissues around implant in Control-LIPUS group than others stained by H&E stain, and LIPUS played a positive role in osteogenic response of peri-implant bone for T2DM rats. In the Masson staining samples, as shown in Figure 8B, the new bone was shown by blue, while the mature bone was shown by red. Mature

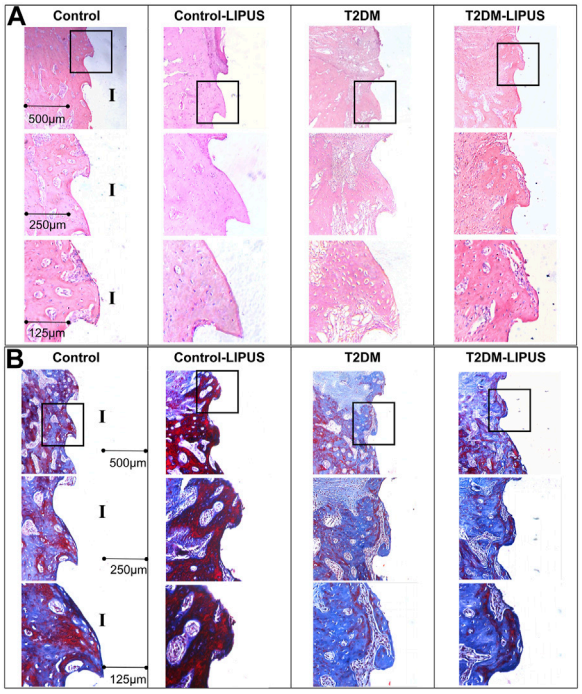

FIGURE 8
Representative images of H&E and Masson staining in mid-sagittal section of peri-implant bone tissue. **(A)** H&E staining results. **(B)** Masson staining results. The formation of new bone around the implant was more prominent in the LIPUS treated groups, notably the Control-LIPUS group. H&E, hematoxylin and eosin; LIPUS, low-intensity pulsed ultrasound; I, implant area.

trabecular bone area was obviously bigger in Control-LIPUS group than others both in T2DM and normal models. What is more, LIPUS treatment improved bone formation in T2DM models. The histologic results were in agreement with the micro-CT evaluation.

4 Discussion

Previous studies about the effects of LIPUS on dental implantation have not focused on its effects under T2DM condition. In the present study, the researchers conducted the first evaluation of the effectiveness of LIPUS in stimulating osteogenesis around dental implants in a T2DM rat model. The findings of the study demonstrated a significant and positive impact of LIPUS treatment on promoting osseointegration of dental implants under T2DM conditions.

Though studies have shown that dental implants have a high long-term survival rates and a favorable prognosis (Klokkevold et al., 2007; Chen et al., 2013), it is important to acknowledge that systemic diseases, such as diabetes mellitus, remain significant risk factors that can negatively influence the success rate of dental implantation (Chen et al., 2013). With advancements in implant surface treatment technology, diabetes mellitus with well-managed blood glucose levels is no longer considered an absolute contraindication for implant surgery (Buser et al., 2000). However, several studies have reported that patients with these diseases still pose a potentially high risk of implant failure (Liu et al., 2017; Tang et al., 2021).

T2DM is often associated with various degrees of bone remodeling disorders, which can impede the process of osseointegration during the healing period following implant placement (Liang et al., 2022). Many animal studies have provided confirmation that rats with T2DM exhibit significantly lower osteogenesis level around the implant compared to normal rats (Wang et al., 2010; Hashiguchi et al., 2014; Zhang et al., 2016b), which is also confirmed by the present study's Micro-CT analysis results, showing that rats in T2DM group had greater cervical marginal bone loss, significant lower BIC ratio, Tb.N, and significant higher Tb.Sp around the implant, compared with those in Control group. Moreover, cellular studies have demonstrated that the high-glucose microenvironment characteristic of T2DM can substantially hinder the osteogenic differentiation and proliferation capacity of BMSCs. It can also decrease the expression of genes related to osteogenesis and slowdown *in vitro* mineralization processes (Gopalakrishnan et al., 2006; Wang et al., 2013; Zhang et al., 2016a).

One clinical study showed statistically significant differences in probing depth ($p < .00001$), marginal bone loss ($p < .00001$), and peri-implant bleeding ($p < .00001$) around the dental implants between the diabetic and non-preexisting disease patients (Jiang et al., 2021). And the incidence of complications with implants was lower in the non-preexisting diseases group (Jiang et al., 2021). Therefore, current clinical researches focus on identifying effective and simple methods to enhance the osseointegration of implants under T2DM condition while also to reduce the duration of the healing process.

LIPUS has been applied in clinical treatment for more than 20 years. LIPUS received approval from the US Food and Drug Administration (FDA) as early as 1994 and 2000 for its use in facilitating the reconstitution of bone nonunion and accelerating the healing process of fresh fractures (Rubin et al., 2001). In recent years, LIPUS has gained widespread recognition as an effective and convenient method for promoting the repairment of bone defects and fracture healing (Harrison and Alt, 2021).

In dentistry, LIPUS has been found effective in promoting periodontal bone defect repairing and bone regeneration after oral maxillofacial surgery (Kim and Hong, 2010; Shiraishi et al., 2011). Besides, clinical studies in orthodontics showed that LIPUS could shorten the whole procedure time of orthodontic treatment (Kaur and El-Bialy, 2020). Some animal experiments have suggested that LIPUS has the potential to influence the osseointegration process and enhance the stability of implants inserted into the femur or tibia of these animals (Ustun et al., 2008; Zhou et al., 2011; Miura et al., 2014; Jiang et al., 2020). Based on the different anatomy, function, and osteogenesis procedure of the long bone from those of alveolar bone (Son et al., 2020), the present study chose maxillae as the implantation site. The implant survival rates in all groups 3 weeks after surgery were 80%, which is similar to the result of a delayed implantation study in rats' maxillae (He et al., 2022). In the present study, it was found that rats in Control-LIPUS group showed better peri-implant osteogenesis (Tb.Th, BMD, BV/TV, BS/TV, RTV, H&E staining and Masson staining) and lower marginal bone loss than those in Control group, suggesting the positive effect of LIPUS on promoting osteogenesis around the implants.

However, to date, there has been limited clinical research on the application of LIPUS in dental implantation. Only one clinical study conducted by Abdulhameed et al. applied LIPUS to patients with dental implants specifically in the premolar region (Akram et al., 2017). Their findings demonstrated that LIPUS effectively enhanced

implant osseointegration and reduced the healing duration. However, as of now, no relevant *in vivo* or clinical studies have reported the effect of LIPUS on osseointegration of implants specifically under diabetic condition and the underlying mechanism. This preliminary *in vivo* study for the first time confirmed that LIPUS promoted osteogenesis around dental implant placed in rats' maxilla under T2DM condition, as LIPUS treatment significantly increased BIC, Tb.N, Tb.Th, BMD, BV/TV and BS/TV, and significantly decreased marginal bone loss and Tb.Sp of T2DM rats. The present study also showed that LIPUS treatment was able to restore the peri-implant osteogenesis level of the T2DM rats back to the normal level, as confirmed by the same level marginal bone loss, BIC, BS/TV, Tb.Sp, Tb.N, Tb.Th, BMD, BV/TV and RTV of the implants in the LIPUS-treated T2DM rats and the healthy rats.

The potential mechanisms by which LIPUS enhances osteogenesis around dental implants can involve various cellular and molecular processes. Firstly, LIPUS has been shown to stimulate the proliferation and differentiation of osteoblasts through upregulating the expression of key osteogenic genes, including osteocalcin (OCN), runt-related transcription factor 2 (RUNX2), and bone morphogenetic proteins (BMPs) the cells responsible for bone formation (Garg et al., 2017; Liu et al., 2020). This could lead to an increased number of bone-forming cells around dental implants. Besides, LIPUS may enhance the synthesis of extracellular matrix proteins, such as collagen, which are essential for the structural integrity of bone (Kang et al., 2019). LIPUS also has angiogenic effects, promoting the formation of new blood vessels (Kang et al., 2019). Adequate blood supply is crucial for the delivery of nutrients and oxygen to cells involved in bone regeneration, facilitating the overall healing process. Study also showed that LIPUS modulate various signaling pathways involved in bone metabolism, such as the Wnt/β-catenin pathway (Liao et al., 2021). Activation of these pathways can positively influence bone formation and remodeling. Another important function of LIPUS is its anti-inflammatory effects by reducing pro-inflammatory cytokines (Zhang et al., 2020). Lastly, the mechanical forces generated by LIPUS may induce micro-mechanical stress on bone cells, mimicking the physiological loading conditions (Tian et al., 2023). This mechanical stimulation is known to be an important factor in bone remodeling and adaptation. These mechanisms have been observed in various studies, but the exact processes may vary depending on specific experimental conditions. Further research is needed to fully elucidate the intricate mechanisms underlying the beneficial effects of LIPUS on osteogenesis around dental implants.

LIPUS has the advantages of low immunogenicity, low toxicity, high targeting selectivity, noninvasiveness, and repeatability. Based on the reports of clinical studies examining the application of LIPUS, no abnormal reactions or discomfort-related symptoms, such as swelling, redness, or inflammation, have been observed in patients receiving the intervention (Tanaka et al., 2015; Jiang et al., 2019; Tanaka et al., 2020). Moreover, the portable nature of the LIPUS device, which is small and powered by a mobile unit, allows for flexible application without space limitations. Consequently, in the future, LIPUS has the potential to become a safe, effective, and comfortable physical therapy method. It may pave the way for chair-side or at-home treatments for patients with T2DM, ultimately leading to enhanced bone regeneration around the implant, improved implant osseointegration, and even the prevention of marginal bone loss. This, in turn, can significantly enhance the long-term success of dental implant treatment.

Indeed, it is crucial to conduct more prospective cohort studies or randomized controlled trials in the future to further investigate the potential benefits and efficacy of LIPUS in promoting implant osseointegration, especially in patients with T2DM. These studies would provide valuable insights into the optimal treatment protocols, the long-term effects, and the underlying mechanisms of LIPUS therapy.

5 Conclusion

This preliminary *in vivo* study showed that LIPUS promoted peri-implant osteogenesis in rats under T2DM condition and found that after LIPUS treatment, the peri-implant osteogenesis level of the T2DM rats increased to the level of normal rats. LIPUS as an effective and safe method has a great potential for T2DM patients in promoting bone regeneration around the implant and achieving higher-quality implant osseointegration. However, in order to validate its clinical function and to investigate its underlying mechanism, further prospective cohort studies or randomized controlled trials are required in the future.

Data availability statement

The original contributions presented in the study are included in the article, further inquiries can be directed to the corresponding authors.

Ethics statement

The animal study was approved by Experimental Animal Ethics Committee of the Ninth People's Hospital Affiliated to Shanghai Jiao Tong University School of Medicine. The study was conducted in accordance with the local legislation and institutional requirements.

Author contributions

YW: Data curation, Formal Analysis, Investigation, Methodology, Software, Writing–original draft, Writing–review and editing. XC: Investigation, Methodology, Writing–original draft. YS: Methodology, Writing–original draft. QZ: Data curation, Methodology, Writing–original draft. ZW: Software, Validation, Writing–original draft. YW: Investigation, Methodology, Writing–original draft. WW: Conceptualization, Writing–review and editing. CX: Conceptualization, Funding acquisition, Project administration, Resources, Supervision, Writing–review and editing.

Funding

The author(s) declare financial support was received for the research, authorship, and/or publication of this article. This work was supported by National Natural Science Foundation (grant number 82071157); and Original Exploration Project of Shanghai

Ninth People's Hospital, Shanghai Jiao Tong University School of Medicine (grant number JYYC002).

Conflict of interest

The authors declare that the research was conducted in the absence of any commercial or financial relationships that could be construed as a potential conflict of interest.

Publisher's note

References

Akram, A. E., Hammad, E. H., Marzuki, O., Atsuo, K., Sugita, Y., Hegazy, F. A., et al. (2017). The effect of low intensity pulsed ultrasound therapy on osseointegration and marginal bone loss around dental implants. *J. Hard Tissue Biol.* 26, 323–330. doi:10.2485/jhtb.26.323

An, Y., Song, Y., Wang, Z., Wang, J., Wu, G., Zhu, G., et al. (2018). Effect of low-intensity pulsed ultrasound on the biological behaviors of bone marrow mesenchymal stem cells on titanium with different surface topographies. *Am. J. Transl. Res.* 10, 67–76.

Brånemark, P. I., Hansson, B. O., Adell, R., Breine, U., Lindström, J., Hallén, O., et al. (1977). Osseointegrated implants in the treatment of the edentulous jaw. Experience from a 10-year period. *Scand. J. Plast. Reconstr. Surg. Suppl.* 16, 1–132.

Buser, D., von Arx, T., ten Bruggenkate, C., and Weingart, D. (2000). Basic surgical principles with ITI implants [Note]. *Clin. Oral Implants Res.* 11, 59–68. Suppl 1. doi:10.1034/j.1600-0501.2000.011s1059.x

Chauvel-Picard, J., Gourmet, R., Vercherin, P., Béra, J. C., and Gleizal, A. (2022). Stimulation of dental implant osseointegration by low-Intensity pulsed ultrasound: an *in vivo* preliminary study in a porcine model. *J. Prosthodont Res.* 66, 639–645. doi:10.2186/jpr.JPR_D_21_00115

Chauvel-Picard, J., Korn, P., Corbin, S., Brosset, S., Bera, J. C., and Gleizal, A. (2021). Stimulation of oral mucosal regeneration by low intensity pulsed ultrasound: an *in vivo* study in a porcine model. *J. Prosthodont Res.* 65, 46–51. doi:10.2186/jpr.JPOR_2019_345

Chen, H., Liu, N., Xu, X., Qu, X., and Lu, E. (2013). Smoking, radiotherapy, diabetes and osteoporosis as risk factors for dental implant failure: a meta-analysis. *PLoS One* 8, e71955. doi:10.1371/journal.pone.0071955

Chen, R., Zeng, Y., Xiao, W., Zhang, L., and Shu, Y. (2021). LC-MS-Based untargeted metabolomics reveals early biomarkers in STZ-induced diabetic rats with cognitive impairment. *Front. Endocrinol. (Lausanne)* 12, 665309. doi:10.3389/fendo.2021.665309

Ding, X., Yang, L., Hu, Y., Yu, J., Tang, Y., Luo, D., et al. (2019). Effect of local application of biphosphonates on improving peri-implant osseointegration in type-2 diabetic osteoporosis. *Am. J. Transl. Res.* 11, 5417–5437.

Ganzorig, K., Kuroda, S., Maeda, Y., Mansjur, K., Sato, M., Nagata, K., et al. (2015). Low-intensity pulsed ultrasound enhances bone formation around miniscrew implants. *Arch. Oral Biol.* 60, 902–910. doi:10.1016/j.archoralbio.2015.02.014

Garg, P., Mazur, M. M., Buck, A. C., Wandtke, M. E., Liu, J., and Ebraheim, N. A. (2017). Prospective review of mesenchymal stem cells differentiation into osteoblasts. *Orthop. Surg.* 9, 13–19. doi:10.1111/os.12304

Gopalakrishnan, V., Vignesh, R. C., Arunakaran, J., Aruldhas, M. M., and Srinivasan, N. (2006). Effects of glucose and its modulation by insulin and estradiol on BMSC differentiation into osteoblastic lineages. *Biochem. Cell Biol.* 84, 93–101. doi:10.1139/o05-163

Graves, D. T., Ding, Z., and Yang, Y. (2020). The impact of diabetes on periodontal diseases. *Periodontol* 82, 214–224. doi:10.1111/prd.12318

Guo, Y., Huang, Z., Sang, D., Gao, Q., and Li, Q. (2020). The role of nutrition in the prevention and intervention of type 2 diabetes. *Front. Bioeng. Biotechnol.* 8, 575442. doi:10.3389/fbioe.2020.575442

Harrison, A., and Alt, V. (2021). Low-intensity pulsed ultrasound (LIPUS) for stimulation of bone healing - a narrative review. *Injury* 52, S91–s96. Suppl 2. doi:10.1016/j.injury.2021.05.002

Hashiguchi, C., Kawamoto, S., Kasai, T., Nishi, Y., and Nagaoka, E. (2014). Influence of an antidiabetic drug on biomechanical and histological parameters around implants in type 2 diabetic rats. *Implant Dent.* 23, 264–269. doi:10.1097/id.0000000000000021

He, Q., Mu, Z., Shrestha, A., Wang, C., Wang, S., Tang, H., et al. (2022). Development of a rat model for type 2 diabetes mellitus peri-implantitis: a preliminary study. *Oral Dis.* 28, 1936–1946. doi:10.1111/odi.13845

Hsu, S. K., Huang, W. T., Liu, B. S., Li, S. M., Chen, H. T., and Chang, C. J. (2011). Effects of near-field ultrasound stimulation on new bone formation and osseointegration of dental titanium implants *in vitro* and *in vivo*. *Ultrasound Med. Biol.* 37, 403–416. doi:10.1016/j.ultrasmedbio.2010.12.004

Hua, Y., Bi, R., Zhang, Y., Xu, L., Guo, J., and Li, Y. (2018). Different bone sites-specific response to diabetes rat models: bone density, histology and microarchitecture. *PLoS One* 13, e0205503. doi:10.1371/journal.pone.0205503

Jiang, X., Savchenko, O., Li, Y., Qi, S., Yang, T., Zhang, W., et al. (2019). A review of low-intensity pulsed ultrasound for therapeutic applications. *IEEE Trans. Biomed. Eng.* 66, 2704–2718. doi:10.1109/tbme.2018.2889669

Jiang, X., Zhu, Y., Liu, Z., Tian, Z., and Zhu, S. (2021). Association between diabetes and dental implant complications: a systematic review and meta-analysis. *Acta Odontol. Scand.* 79, 9–18. doi:10.1080/00016357.2020.1761031

Jiang, Y., Yuan, Y., Xiong, Y., Wang, B., Guo, Y., Gong, P., et al. (2020). Low-intensity pulsed ultrasound improves osseointegration of dental implant in mice by inducing local neuronal production of αCGRP. *Arch. Oral Biol.* 115, 104736. doi:10.1016/j.archoralbio.2020.104736

Kang, P. L., Huang, H. H., Chen, T., Ju, K. C., and Kuo, S. M. (2019). Angiogenesis-promoting effect of LIPUS on hADSCs and HUVECs cultured on collagen/hyaluronan scaffolds. *Mater Sci. Eng. C Mater Biol. Appl.* 102, 22–33. doi:10.1016/j.msec.2019.04.045

Kaur, H., and El-Bialy, T. (2020). Shortening of overall orthodontic treatment duration with low-intensity pulsed ultrasound (LIPUS). *J. Clin. Med.* 9, 1303. doi:10.3390/jcm9051303

Khanna, A., Nelmes, R. T., Gougoulias, N., Maffulli, N., and Gray, J. (2009). The effects of LIPUS on soft-tissue healing: a review of literature. *Br. Med. Bull.* 89, 169–182. doi:10.1093/bmb/ldn040

Khater, S. I., Mohamed, A. A., Arisha, A. H., Ebraheim, L. L. M., El-Mandrawy, S. A. M., Nassan, M. A., et al. (2021). Stabilized-chitosan selenium nanoparticles efficiently reduce renal tissue injury and regulate the expression pattern of aldose reductase in the diabetic-nephropathy rat model. *Life Sci.* 279, 119674. doi:10.1016/j.lfs.2021.119674

Kim, S. H., and Hong, K. S. (2010). Histologic evaluation of low-intensity pulsed ultrasound effects on bone regeneration in sinus lift. *J. Periodontal Implant Sci.* 40, 271–275. doi:10.5051/jpis.2010.40.6.271

Klokkevold, P. R., and Han, T. J. (2007). How do smoking, diabetes, and periodontitis affect outcomes of implant treatment? *Int. J. Oral Maxillofac. Implants* 22, 173–202. Suppl.

Lavandier, B., Gleizal, A., and Béra, J. C. (2009). Experimental assessment of calvarial bone defect re-ossification stimulation using low-intensity pulsed ultrasound. *Ultrasound Med. Biol.* 35, 585–594. doi:10.1016/j.ultrasmedbio.2008.10.002

Li, J., Liu, C. Y., Jiang, Y. F., Wei, X. Z., and Li, J. U. (2015). Proliferation and differentiation of human osteoblasts from a type 2 diabetic patient *in vitro*. *Genet. Mol. Res.* 14, 11292–11299. doi:10.4238/2015.September.22.23

Li, W., Zhu, C., Liu, T., Zhang, W., Liu, X., Li, P., et al. (2020). Epigallocatechin-3-gallate ameliorates glucolipid metabolism and oxidative stress in type 2 diabetic rats. *Diab Vasc. Dis. Res.* 17, 1479164120966998. doi:10.1177/1479164120966998

Liang, C., Liu, X., Yan, Y., Sun, R., Li, J., and Geng, W. (2022). Effectiveness and mechanisms of low-intensity pulsed ultrasound on osseointegration of dental implants and biological functions of bone marrow mesenchymal stem cells. *Stem Cells Int.* 2022, 1–16. doi:10.1155/2022/7397335

Liao, B., Guan, M., Tan, Q., Wang, G., Zhang, R., Huang, J., et al. (2021). Low-intensity pulsed ultrasound inhibits fibroblast-like synoviocyte proliferation and reduces synovial fibrosis by regulating Wnt/β-catenin signaling. *J. Orthop. Transl.* 30, 41–50. doi:10.1016/j.jot.2021.08.002

Liu, J., Wu, Z., He, H., Cai, K., Zhang, H., and Xu, L. (2017). Gallium and silicon synergistically promote osseointegration of dental implant in patients with osteoporosis. *Med. Hypotheses* 103, 35–38. doi:10.1016/j.mehy.2017.02.018

Liu, Q., Liu, X., Liu, B., Hu, K., Zhou, X., and Ding, Y. (2012). The effect of low-intensity pulsed ultrasound on the osseointegration of titanium dental implants. *Br. J. Oral Maxillofac. Surg.* 50, 244–250. doi:10.1016/j.bjoms.2011.03.001

Liu, S., Zhou, M., Li, J., Hu, B., Jiang, D., Huang, H., et al. (2020). LIPUS inhibited the expression of inflammatory factors and promoted the osteogenic differentiation

capacity of hPDLCs by inhibiting the NF-κB signaling pathway. *J. Periodontal Res.* 55, 125–140. doi:10.1111/jre.12696

Mathieu, V., Anagnostou, F., Soffer, E., and Haïat, G. (2011). Ultrasonic evaluation of dental implant biomechanical stability: an *in vitro* study. *Ultrasound Med. Biol.* 37, 262–270. doi:10.1016/j.ultrasmedbio.2010.10.008

Meng, H. W., Chien, E. Y., and Chien, H. H. (2016). Dental implant bioactive surface modifications and their effects on osseointegration: a review. *Biomark. Res.* 4, 24. doi:10.1186/s40364-016-0078-z

Meza Maurício, J., Miranda, T. S., Almeida, M. L., Silva, H. D., Figueiredo, L. C., and Duarte, P. M. (2019). An umbrella review on the effects of diabetes on implant failure and peri-implant diseases. *Braz Oral Res.* 33, e070. doi:10.1590/1807-3107bor-2019.vol33.0070

Miura, K., Motoyoshi, M., Inaba, M., Iwai, H., Karasawa, Y., and Shimizu, N. (2014). A preliminary study of the effects of low-intensity pulsed ultrasound exposure on the stability of orthodontic miniscrews in growing rats. *Eur. J. Orthod.* 36, 419–424. doi:10.1093/ejo/cjt066

Padilla, F., Puts, R., Vico, L., Guignandon, A., and Raum, K. (2016). Stimulation of bone repair with ultrasound. *Adv. Exp. Med. Biol.* 880, 385–427. doi:10.1007/978-3-319-22536-4_21

Park, J. W., Park, K. B., and Suh, J. Y. (2007). Effects of calcium ion incorporation on bone healing of Ti6Al4V alloy implants in rabbit tibiae. *Biomaterials* 28, 3306–3313. doi:10.1016/j.biomaterials.2007.04.007

Percie du Sert, N., Hurst, V., Ahluwalia, A., Alam, S., Avey, M. T., Baker, M., et al. (2020). The ARRIVE guidelines 2.0: updated guidelines for reporting animal research. *PLoS Biol.* 18, e3000410. doi:10.1371/journal.pbio.3000410

Petersmann, A., Nauck, M., Müller-Wieland, D., Kerner, W., Müller, U. A., Landgraf, R., et al. (2018). Definition, classification and diagnosis of diabetes mellitus. *Exp. Clin. Endocrinol. Diabetes* 126, 406–410. doi:10.1055/a-0584-6223

Przekora, A., Benko, A., Blazewicz, M., and Ginalska, G. (2016). Hybrid chitosan/β-1,3-glucan matrix of bone scaffold enhances osteoblast adhesion, spreading and proliferation via promotion of serum protein adsorption. *Biomed. Mater* 11, 045001. doi:10.1088/1748-6041/11/4/045001

Ren, W., Pu, F., Luan, H., Duan, Y., Su, H., Fan, Y., et al. (2019). Effects of local vibration with different intermittent durations on skin blood flow responses in diabetic people. *Front. Bioeng. Biotechnol.* 7, 310. doi:10.3389/fbioe.2019.00310

Rubin, C., Bolander, M., Ryaby, J. P., and Hadjiargyrou, M. (2001). The use of low-intensity ultrasound to accelerate the healing of fractures. *J. Bone Jt. Surg. Am.* 83, 259–270. doi:10.2106/00004623-200102000-00015

Ruppert, D. S., Harrysson, O., Marcellin-Little, D. J., Bollenbecker, S., and Weinhold, P. S. (2019). Osteogenic benefits of low-intensity pulsed ultrasound and vibration in a rodent osseointegration model. *J. Musculoskelet. Neuronal Interact.* 19, 150–158.

Shiraishi, R., Masaki, C., Toshinaga, A., Okinaga, T., Nishihara, T., Yamanaka, N., et al. (2011). The effects of low-intensity pulsed ultrasound exposure on gingival cells. *J. Periodontol.* 82, 1498–1503. doi:10.1902/jop.2011.100627

Son, C., Choi, M. S., and Park, J. C. (2020). Different responsiveness of alveolar bone and long bone to epithelial-mesenchymal interaction-related factor. *JBMR Plus* 4, e10382. doi:10.1002/jbm4.10382

Suh, J. Y., Jeung, O. C., Choi, B. J., and Park, J. W. (2007). Effects of a novel calcium titanate coating on the osseointegration of blasted endosseous implants in rabbit tibiae. *Clin. Oral Implants Res.* 18, 362–369. doi:10.1111/j.1600-0501.2006.01323.x

Sun, J., Eberhard, J., Glage, S., Held, N., Voigt, H., Schwabe, K., et al. (2020). Development of a peri-implantitis model in the rat. *Clin. Oral Implants Res.* 31, 203–214. doi:10.1111/clr.13556

Tanaka, E., Kuroda, S., Horiuchi, S., Tabata, A., and El-Bialy, T. (2015). Low-intensity pulsed ultrasound in dentofacial tissue engineering. *Ann. Biomed. Eng.* 43, 871–886. doi:10.1007/s10439-015-1274-y

Tanaka, E., Liu, Y., Xia, L., Ogasawara, N., Sakamaki, T., Kano, F., et al. (2020). Effectiveness of low-intensity pulsed ultrasound on osteoarthritis of the temporomandibular joint: a review. *Ann. Biomed. Eng.* 48, 2158–2170. doi:10.1007/s10439-020-02540-x

Tang, D., Wang, E., Xu, Y., Liang, C., Liu, C., Lin, X., et al. (2021). Is hyperglycemia the only risk factor for implant in type 2 diabetics during the healing period? *Oral Dis.* 27, 1551–1563. doi:10.1111/odi.13685

Tian, C., Liu, H., Zhao, C., Zhang, C., and Wang, W. (2023). A numerical study on mechanical effects of low-intensity pulsed ultrasound on trabecular bone and osteoblasts. *J. Biomech. Eng.* 145, 051010. doi:10.1115/1.4056658

Ustun, Y., Erdogan, O., Kurkcu, M., Akova, T., and Damlar, I. (2008). Effects of low-intensity pulsed ultrasound on dental implant osseointegration: a preliminary report. *Eur. J. Dent.* 2, 254–262. doi:10.1055/s-0039-1697389

Wang, F., Song, Y. L., Li, D. H., Li, C. X., Wang, Y., Zhang, N., et al. (2010). Type 2 diabetes mellitus impairs bone healing of dental implants in GK rats. *Diabetes Res. Clin. Pract.* 88, e7–e9. doi:10.1016/j.diabres.2010.01.017

Wang, J., Wang, B., Li, Y., Wang, D., Lingling, E., Bai, Y., et al. (2013). High glucose inhibits osteogenic differentiation through the BMP signaling pathway in bone mesenchymal stem cells in mice. *Excli J.* 12, 584–597.

Wang, L., Gao, Z., Liu, C., and Li, J. (2021). Potential biomarkers of abnormal osseointegration of implants in type II diabetes mellitus. *BMC Oral Health* 21, 583. doi:10.1186/s12903-021-01939-9

Wang, Y., Cao, X., Shen, Y., Zhong, Q., Huang, Y., Zhang, Y., et al. (2023a). Osteogenic effect of low-intensity pulsed ultrasound on peri-implant bone: a systematic review and meta-analysis. *J. Prosthodont Res.* doi:10.2186/jpr.JPR_D_23_00068

Wang, Y. C. X., Shen, Y., Zhong, Q., Huang, Y., Zhang, Y., Wang, S., et al. (2023b). Initial development of an immediate implantation model in rats and assessing the prognostic impact of periodontitis on immediate implantation. *Bioengineering* 10, 896. doi:10.3390/bioengineering10080896

Zhang, B., Chen, H., Ouyang, J., Xie, Y., Chen, L., Tan, Q., et al. (2020). SQSTM1-dependent autophagic degradation of PKM2 inhibits the production of mature IL1B/IL-1β and contributes to LIPUS-mediated anti-inflammatory effect. *Autophagy* 16, 1262–1278. doi:10.1080/15548627.2019.1664705

Zhang, B., Liu, N., Shi, H., Wu, H., Gao, Y., He, H., et al. (2016a). High glucose microenvironments inhibit the proliferation and migration of bone mesenchymal stem cells by activating GSK3β. *J. Bone Min. Metab.* 34, 140–150. doi:10.1007/s00774-015-0662-6

Zhang, J., Shirai, M., Yamamoto, R., Yamakoshi, Y., Oida, S., Ohkubo, C., et al. (2016b). Effect of nerve growth factor on osseointegration of titanium implants in type 2 diabetic rats. *Int. J. Oral Maxillofac. Implants* 31, 1189–1194. doi:10.11607/jomi.4455

Zhou, H. B., Hou, Y. F., Chen, W. C., Shen, J. F., Wang, J., and Zhu, Z. M. (2011). The acceleration of titanium implant osseointegration by low intensity pulsed ultrasound: an experimental study in rats. *Zhonghua Kou Qiang Yi Xue Za Zhi* 46, 425–430.

frontiers | Frontiers in Bioengineering and Biotechnology

TYPE Original Research
PUBLISHED 08 February 2024
DOI 10.3389/fbioe.2024.1343329

OPEN ACCESS

EDITED BY
Jian Yu,
University of British Columbia, Canada

REVIEWED BY
Ollie Yiru Yu,
The University of Hong Kong, Hong Kong SAR, China
Yuanjing Zhu,
Hunan Clinical Research Center of Oral Major Diseases and Oral Health, China

*CORRESPONDENCE
Hao Yu,
haoyu-cn@hotmail.com

†These authors have contributed equally to this work

RECEIVED 23 November 2023
ACCEPTED 26 January 2024
PUBLISHED 08 February 2024

CITATION
Chen J-M, Cheng Y-L, Yang M-H, Su C and Yu H (2024), Enhancing the inhibition of dental erosion and abrasion with quercetin-encapsulated hollow mesoporous silica nanocomposites.
Front. Bioeng. Biotechnol. 12:1343329.
doi: 10.3389/fbioe.2024.1343329

Enhancing the inhibition of dental erosion and abrasion with quercetin-encapsulated hollow mesoporous silica nanocomposites

Jia-Min Chen[1†], Yi-Ling Cheng[1†], Meng-Hui Yang[1], Chen Su[1] and Hao Yu[1,2,3,4*]

[1]Fujian Key Laboratory of Oral Diseases and Fujian Provincial Engineering Research Center of Oral Biomaterial and Stomatological Key Laboratory of Fujian College and University, School and Hospital of Stomatology, Fujian Medical University, Fuzhou, China, [2]Department of Prosthodontics, School and Hospital of Stomatology, Fujian Medical University, Fuzhou, China, [3]Clinic for Conservative and Preventive Dentistry, Center of Dental Medicine, University Zurich, Zurich, Switzerland, [4]Department of Applied Prosthodontics, Graduate School of Biomedical Sciences, Nagasaki University, Nagasaki, Japan

Introduction: Dental erosion and abrasion pose significant clinical challenges, often leading to exposed dentinal tubules and dentine demineralization. The aim of this study was to analyse the efficacy of quercetin-encapsulated hollow mesoporous silica nanocomposites (Q@HMSNs) on the prevention of dentine erosion and abrasion.

Method: Q@HMSNs were synthesized, characterized, and evaluated for their biocompatibility. A total of 130 dentine specimens (2 mm × 2 mm × 2 mm) were prepared and randomly distributed into 5 treatment groups (n = 26): DW (deionized water, negative control), NaF (12.3 mg/mL sodium fluoride, positive control), Q (300 μg/mL quercetin), HMSN (5.0 mg/mL HMSNs), and Q@HMSN (5.0 mg/mL Q@HMSNs). All groups were submitted to *in vitro* erosive (4 cycles/d) and abrasive (2 cycles/d) challenges for 7 days. The specimens in the DW, NaF, and Q groups were immersed in the respective solutions for 2 min, while treatment was performed for 30 s in the HMSN and Q@HMSN groups. Subsequently, the specimens were subjected to additional daily erosion/abrasion cycles for another 7 days. The effects of the materials on dentinal tubule occlusion and demineralized organic matrix (DOM) preservation were examined by scanning electron microscopy (SEM). The penetration depth of rhodamine B fluorescein into the etched dentine was assessed using confocal laser scanning microscopy (CLSM). The erosive dentine loss (EDL) and release of type I collagen telopeptide (ICTP) were measured. The data were analysed by one-way analysis of variance (ANOVA) with *post hoc* Tukey's test (α = 0.05).

Results: Q@HMSNs were successfully synthesized and showed minimal toxicity to human dental pulp stem cells (HDPSCs) and gingival fibroblasts (HGFs). Q@HMSNs effectively occluded the dentinal tubules, resulting in a thicker DOM in the Q@HMSN group. The CLSM images showed more superficial penetration in the HMSN and Q@HMSN groups than in the quercetin, NaF, and DW groups. The Q@HMSN group exhibited a significantly lower EDL and reduced ICTP levels compared to the other groups ($p < 0.05$).

Conclusion: Q@HMSNs hold promise for inhibiting dentine erosion and abrasion by promoting tubule occlusion and DOM preservation.

KEYWORDS

abrasion, demineralized organic matrix, erosion, hollow mesoporous silica, quercetin, tubule occlusion

1 Introduction

Oral diseases pose substantial public health challenges worldwide, with significant negative impacts on individuals and communities (Peres et al., 2019). Dental erosion, characterized by the chronic loss of dental hard tissues due to acid exposure and mechanical influences without bacterial involvement, has become prevalent, affecting a significant proportion of the population (Wiegand and Attin, 2007; Schlueter et al., 2011). Recent studies have indicated that dental erosion has affected 57.1% of European adults (Bartlett et al., 2013), with a global prevalence in permanent teeth of approximately 20% in children and 45% in adults (Schlueter and Luka, 2018), and this trend continues to grow (Vered et al., 2014). In the later stages of dental erosion, the opening of dentine tubules facilitates hypersensitivity and pulp infection (Aminoshariae and Kulid, 2021).

Dentine, which is primarily composed of collagen, plays a crucial role in dental structure, and preserving its demineralized organic matrix (DOM) is essential for preventing erosion (Mazzoni et al., 2015). However, the DOM is vulnerable to dissolution due to the presence of matrix metalloproteinases (MMPs) (Zarella et al., 2015). The application of MMP inhibitors has been demonstrated to effectively prevent and slow the disintegration of the DOM (Kato et al., 2010). Compounds such as quercetin, epigallocatechin gallate (EGCG), chlorhexidine (CHX), and proanthocyanidin (PA) have proven to be effective inhibitors of MMPs in dentine, protecting dental hard tissue against erosion (Balalaie et al., 2018). In particular, quercetin has demonstrated superior mechanical reinforcement after being crosslinked with collagen, emphasizing its potential clinical significance (Hong et al., 2022). However, the timing of inhibitor application was found to significantly affect the efficacy in terms of protecting against dentine erosion (Lapinska et al., 2018). In our previous study, the application of quercetin before acid attack resulted in a significantly thicker DOM compared to the application of well-known MMP inhibitors such as EGCG and CHX. However, when quercetin was applied after erosion, its effectiveness was notably reduced, and it could not protect the dentine tubule from exposure (Li et al., 2022). This reduced effectiveness is likely due to the surface targeting of collagen degradation and dissolution of the MMP inhibitors by the low pH environment following erosive attacks (Barbosa et al., 2019). Nevertheless, patients experiencing erosion often visit dental offices when the dentine has already been affected. Therapeutic interventions for treating dentine erosion frequently begin with treatment of the eroded tooth hard tissues, which usually involve exposed tubules. Consequently, appropriately managing quercetin on eroded tooth hard tissues may hold greater clinical significance than the pretreatment of intact dentine.

In recent decades, mesoporous silica nanoparticles (MSNs) have garnered attention for their well-structured framework, as they have a stable structure, chemical and thermal stability, a high pore volume, a large surface area, and excellent biocompatibility. MSNs have versatile applications as nanocarriers for drugs, proteins, genes, and enzymes (Izquierdo-Barba et al., 2009; Lee et al., 2016; Ni et al., 2018; Kankala et al., 2020; Zhang et al., 2021; Wang et al., 2022). In addition, the valuable role MSNs have in dental materials has been demonstrated by a growing body of literature, particularly in applications related to tubule occlusion and acid resistance (Chiang et al., 2014; Yu et al., 2016). Hollow MSNs (HMSNs) are of particular interest due to their mesoporous shells and hollow interiors (Li et al., 2017). The hollow cavities within HMSNs make them ideal carriers for drug delivery, particularly for compounds such as quercetin. In this context, using quercetin-encapsulated HMSNs (Q@HMSNs) presents a novel approach for addressing tooth erosion, showing the potential to block dentinal tubules after erosion and prevent dentine organic matrix breakdown. To our knowledge, no prior report is available on Q@HMSNs in the context of dental erosion, making this area an intriguing focus for research.

Therefore, the aim of the present study was to test the following null hypotheses: (1) Q@HMSNs have no effect on erosive dentine loss (EDL) after erosion and abrasion; (2) Q@HMSNs have no effect on dentine tubule occlusion after erosion and abrasion; and (3) Q@HMSNs have no effect on DOM preservation after erosion and abrasion.

2 Materials and methods

2.1 HMSNs synthesis

Silica nanoparticles (NPs) were synthesized using a modified Stöber method (Bai et al., 2019). Briefly, 6.28 mL of ammonium hydroxide solution (25%–28%; Aladdin, China), 42.8 mL of absolute ethanol (Xilong Scientific, China), and 20 mL of deionized water were mixed for 15 min under constant stirring, while 12 mL of tetraethyl orthosilicate (TEOS; Sigma, United States) was dissolved in 100 mL of ethanol. The latter solution was poured into the former solution under continuous stirring for 2 h (Mutlu et al., 2021). The SiO_2 NPs were collected by centrifugation, deionized water was used to wash the sediment one time, and then the NPs were washed three times with ethanol. Subsequently, the SiO_2 NPs was dried in an oven at 60°C overnight.

The SiO_2 NPs were transformed into HMSNs using a self-templating strategy (Fang et al., 2013; Yu et al., 2021a). Five hundred milligrams of the SiO_2 NPs were dispersed ultrasonically

in 250 mL of deionized water. Then, 750 mg of cetyltrimethylammonium bromide (CTAB; Sigma, United States of America), 150 mL of ethanol, and 2.75 mL of ammonium hydroxide (25%–28%) were added, and the mixture was stirred continuously for 30 min at ambient temperature, after which TEOS (6 mL) was added and stirring continued for 6 h. After centrifugation, the sediment was redispersed in 100 mL of deionized water. Subsequently, 2.12 g of sodium bicarbonate (Na_2CO_3; Aladdin, China) was added, and the mixture was continuously stirred at 65°C for 24 h to, etch the hollow core. After centrifugation, the precipitate was washed twice with deionized water and ethanol, and the collected particles were calcined at 550°C for 6 h.

2.2 Q@HMSNs fabrication

One hundred milligrams of HMSNs was dispersed ultrasonically in 10 mL of ethanol. Then, 20 mg of quercetin (Sigma, United States) was added to the HMSNs solution with constant stirring at 400 rpm for 24 h. The mixture was then shaken at 150 rpm for an additional 24 h in the dark to achieve maximum quercetin loading. The suspension was washed with deionized water twice (Sapino et al., 2015; Saputra et al., 2022).

2.3 Q@HMSNs characterization

The morphologies of the HMSNs and Q@HMSNs were observed using transmission electron microscopy (TEM; JEM-F200, JEOL, Japan). Scanning TEM equipped with energy dispersive spectroscopy (EDS) was employed to examine the mapping patterns of elements. The crystalline phase was determined by applying X-ray diffraction (XRD; Smartlab 9KW, Rigaku, Japan). Small-angle and wide-angle XRD patterns were scanned from 0.5° to 10° and 10°–70°, respectively, and recorded in the 2θ range with a scanning speed of 1°/min. The functional groups in the sample were detected by Fourier transform infrared (FTIR) spectroscopy (iN10, Thermo Scientific, United States of America). The nitrogen adsorption–desorption isotherm was studied by an ASAP 2460M gas adsorption analyser (Micromeritics, United States of America) at 77 K. The pore size distribution, pore volume and surface area were calculated by the Brunauer–Emmett–Teller and Barrett–Joyner–Halenda (BET/BJH) methods. A Zetasizer Nano ZSP system (ZS90, Malvern Instruments, United Kingdom) was used to determine the size distribution. The effective amount of quercetin loaded into the HMSNs was determined using thermogravimetric analysis (TGA; TG 209 F3 Tarsus, NETZSCH, Germany) from 30°C to 1,000°C with a heating speed of 15°C/min.

2.4 Quercetin release from the Q@HMSNs

One hundred milligrams of Q@HMSNs was dispersed in 10 mL of phosphate-buffered saline (PBS; Xilong Scientific, China), and then the mixture was shaken at 120 rpm in the dark. The release of quercetin was measured at 0.5, 1, 2, 4, 8, 12, 24, 48, 72, 120 and 168 h. At each time point, the Q@HMSNs solution was centrifuged at 4,200 rpm for 4 min, and 1 mL of the liquid supernatant was collected for UV–Vis measurement (SpectraMax iD3, Molecular Devices, United States of America). The solution was then replenished with 1 mL of fresh PBS. The content of released quercetin was determined by measuring the absorbance at 377 nm (Yu et al., 2021b; Saputra et al., 2022).

2.5 Cytotoxicity evaluation

Human dental pulp stem cells (HDPSCs) and human gingival fibroblasts (HGFs) were taken from the pulp and peridental membranes of healthy adults who had given informed consent for third molar extraction, as approved by the Biomedical Research Ethics Committee of Local University (FMUSS 2018–20). α-Modified essential medium (α-MEM; HyClone, United States of America) with 1% penicillin/streptomycin (PS; Beyotime, China) and 10% foetal bovine serum (FBS; Gibco, Australia) were applied to culture the HDPSCs and HGFs in a humidified atmosphere of 5% CO_2 at 37 °C. Subculturing was performed when the cells reached confluence. The HDPSCs and HGFs were collected at third passage and seeded in 96-well plates (2000 cells/well). After 24 h, the cells were cultured with complete medium containing Q@HMSNs extract solutions at concentrations of 1.0, 2.5, and 5.0 mg/mL. A control group without Q@HMSNs was included in the experiment. After an additional 1, 4, and 7 days of incubation, cell counting kit-8 (CCK-8; Dojindo Japan) (10 μL) was added to each well. Incubation was continued at 37°C for 2 h. Then, the absorbance at 450 nm was measured (SpectraMax iD3, Molecular Devices, United States). Each test was performed in triplicate, the relative viability rates of the HDPSCs and HGFs were calculated using the following equation (Xing et al., 2022).

$$\text{Relative cell viability } (\%) = \frac{OD_{Sample} - OD_{Medium}}{OD_{Control} - OD_{Medium}} \times 100\,\%$$

In addition, calcein/propidium iodide (PI) live/dead fluorescent dye (Beyotime, China) was utilized to stain the cells for 30 min on day 7. Images of cell morphology and proliferation were recorded by an inverted fluorescence microscope (Axio Observer A1, Carl Zeiss, Germany) (Huang et al., 2020).

2.6 Specimen preparation and experimental design

The study protocol was approved by the Institutional Review Board of the local university (2020QH2045), and all teeth were obtained after donors provided signed informed consent.

Seventy intact fresh human third molars were collected. All molars were immersed in a 0.5% thymol solution and stored at 4°C within 1 month of extraction prior to use. A low-speed saw (Buehler; Lake Bluff, IL, United States of America) was used to slice the molar to 145 dentine specimens (each 2 mm × 2 mm × 2 mm, the mid-crown portions beneath the enamel–dentinal junction) under water cooling. The dentine blocks were distributed for various analyses: 50 were taken for surface profile measurements (n = 10); 20 for surface morphology observations (n = 4); 25 for rhodamine B

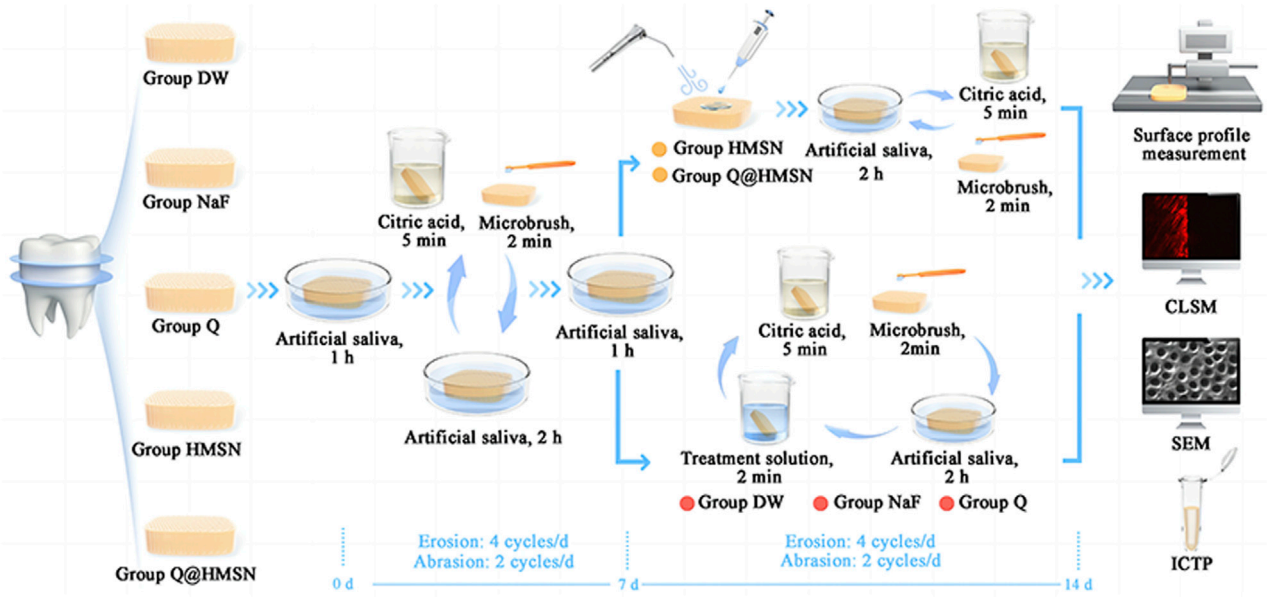

FIGURE 1
Flow chart of the study.

fluorescein evaluations (n = 5); and 50 for type I collagen telopeptide (ICTP) assessment (n = 10).

The dentine blocks were coupled to a customed silicone mould, embedded with acrylic resin (New century, China) and wet polished using silicon carbide sandpapers (#320, #600, #800, #1000, #1200, and #2000; Matador, Germany) for 60 s each. Subsequently, ultrasound was used to clean the surface of each specimen. The final dimensions of the specimens were as follows: 4 mm × 4 mm for the top surface, 5 mm × 5 mm for the bottom surface, and a thickness of 3 mm. Each specimen was covered on both sides with nail varnish (Top Speed; Revlon, United States), leaving a 1 mm × 1 mm area exposed as the erosion region (Jiang et al., 2020).

All samples were subjected to erosive and abrasive challenges (4 cycles/d) for 7 days to simulate an eroded tooth (Wiegand and Attin, 2011). In each erosion cycle, specimens were first immersed in artificial saliva (containing 0.795 g/L $CaCl_2{\cdot}H_2O$, 0.4 g/L NaCl, 0.005 g/L $Na_2S{\cdot}9H_2O$, 0.4 g/L KCl, 0.3 g/L KSCN, 1 g/L urea, and 0.69 g/L $NaH_2PO_4{\cdot}H_2O$, pH = 6.8) for 1 h (O Toole et al., 2015). Afterwards, the specimens were soaked in citric acid (pH = 2.45; Sigma, United States of America) for 5 min (Shellis et al., 2011), followed by a 10 s water rinse. Subsequently, the specimens were stored in renewed artificial saliva for 2 h before the next erosive challenge. Additionally, the specimens were brushed with a toothbrush for 2 min after the first and final daily erosive attacks (a total of 2 cycles per day) over a 7 days period, as previously described (Hong et al., 2020).

After the initial 7 days of erosive and abrasive challenges, the specimens were randomly divided into 5 groups (n = 26): DW (deionized water, negative control), NaF (12.3 mg/mL sodium fluoride, positive control), Q (300 μg/mL quercetin), HMSN (5.0 mg/mL HMSNs), and Q@HMSN (5.0 mg/mL Q@HMSNs).

The samples in the DW, NaF, and Q groups were immersed in their respective solutions for 2 min each day, while the samples in the HMSN and Q@HMSN groups were treated as follows. First, 0.2 mL of the appropriate suspension was gently applied to the surface of the specimen, and then the surface was blown dry using a dental air–water syringe for 30 s. Following these treatments, the specimens were placed in renewed artificial saliva for 2 h before undergoing daily cycles of erosion (4 cycles/d) and abrasion (2 cycles/d). The abrasion procedure, as described previously, was performed after the first and last erosive attacks over 7 days (2 cycles/d). However, unlike the DW, NaF and Q groups, the HMSN and Q@HMSN groups did not received additional treatment with HMSNs or Q@HMSNs during the subsequent 6 days of erosive and abrasive challenges (Figure 1).

2.7 Dentine morphology observations

Scanning electron microscopy (SEM; EM8000, KYKY, China) was employed to observe the morphology of the dentine surface after 7 and 14 days of erosive and abrasive challenges. Twenty specimens were placed in the freeze dryer for desiccation for 24 h and coated with gold via a sputter-coating process. Observations were made with both surface and cross-sectional views, with central site of each segment being examined at a ×5,000 magnification (Yu et al., 2017).

2.8 Surface profile measurements

The surface profiles of the specimens were measured after the 14 days experimental period using a contact profilometer (SEF680, Kosaka Laboratory, Japan) (Capalbo et al., 2022). Before evaluation, a scalpel blade was used to carefully remove the nail varnish. The EDL was calculated by determining the difference in height between

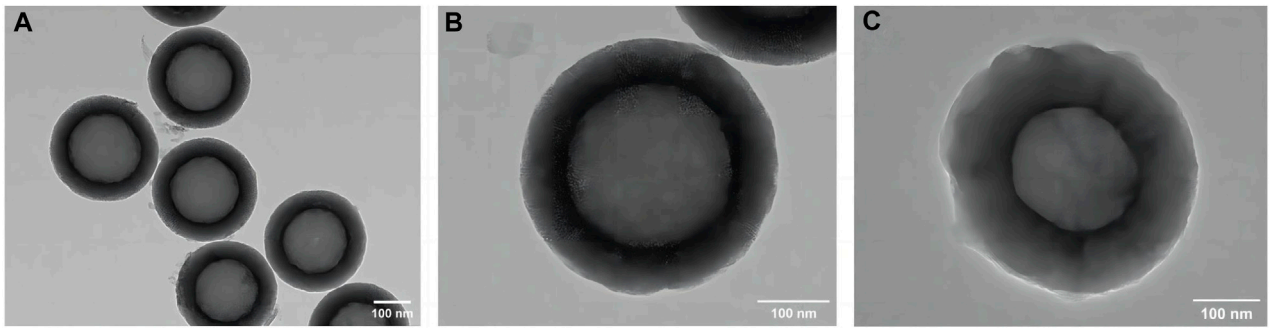

FIGURE 2
TEM images of **(A,B)** HMSNs and **(C)** quercetin-encapsulated HMSNs. HMSNs, hollow mesoporous silica nanocomposites.

the eroded surface and the reference surface. The surface of each sample was scanned with a stylus, and the mean value of 5 height difference measurements was recorded (in μm) as the EDL (Hannas et al., 2016).

2.9 Dentine permeability evaluation

Ten dentine specimens from each group (n = 2) were selected. Rhodamine B (0.1% (w/v)) was applied to the dentine surfaces of the specimens using a microbrush for 1 min. Afterwards, the specimens were washed with PBS three times. Subsequently, the specimens were longitudinally sectioned into slices, and confocal laser scanning microscopy (CLSM; FV3000, Olympus, Japan) was applied to observe the penetration depth of the specimens using laser excitation at 523 nm (Park et al., 2019).

2.10 Collagen degradation assessment

To evaluate the effect of the Q@HMSNs on the DOM, the release of ICTP was measured. The remaining 50 dentine specimens were demineralized with 10% phosphoric acid (pH = 1.0) (Aladdin, China) for 12 h at 25°C. Subsequently, the samples were rinsed in deionized water with continuous stirring at 4°C for 72 h, followed by drying in 60°C oven for 8 h. The specimens were then immersed in tubes contained 500 μL of artificial saliva at 37°C for 1 week. After centrifugation, the supernatants from each tube were collected, and an ELISA kit (MBbio, China) was used to analyse the release of ICTP (Osorio et al., 2011).

2.11 Statistical analysis

The data were analysed using the SPSS statistical software package (IBM, SPSS 19, United States of America). The equal variances and normality of the data were confirmed using the Levene test and the Kolmogorov–Smirnov test, respectively. For the CCK-8, EDL, and ICTP release assays, one-way analysis of variance (ANOVA) with *post hoc* Tukey's test was used for data analysis. A value of $p < 0.05$ was considered to indicate statistical significance.

3 Results

3.1 Characterization of the Q@HMSNs

The TEM image of the HMSNs in Figures 2A, B revealed spherical NPs with an approximate diameter of 400 nm and a well-ordered channel framework shell structure with a cavity. After loading quercetin, the mesoporous structure remained intact, albeit slightly obscured, indicating that quercetin had been successfully incorporated into the HMSNs with maintenance of the overall morphology (Figure 2C). The mapping pattern of scanning TEM/EDS was used to identify the element distribution. The presence of Si and O signals was demonstrated in both the HMSNs and Q@HMSNs, with the intensity of C in Q@HMSNs being further highlighted (Supplementary Figure S1).

The mesoporous crystalline phase and structure were analysed using XRD. For the small-angle pattern (Figure 3A), the XRD analysis of the HMSNs displayed a characteristic diffraction peak at $2\theta = 1.9^{\circ}$ (100), consistent with a mesoporous structure. Notably, the intensity of this diffraction peak decreased after quercetin loading. In the wide-angle pattern (Supplementary Figure S2), both the HMSNs and Q@HMSNs presented a broad band of non-crystalline scattering around $2\theta = 22^{\circ}$. The Q@HMSNs did not exhibit any crystalline peaks in the observed 2-theta range. This could be explained by the quercetin changing into a non-crystalline state (Yu et al., 2023).

Additionally, in the FTIR spectrum of the HMSNs, distinctive peaks at 968 cm^{-1} (Si–OH bending vibration), 1,096 cm^{-1} (Si–O–Si vibration), 800 cm^{-1}, 470 cm^{-1} (Si–O stretching and bending vibration), and 1,632 cm^{-1} (H–O–H bending vibration) were observed. When compared to the HMSNs spectrum, the spectrum of the Q@HMSNs exhibited changes due to quercetin loading at 1,635 cm^{-1} (C=O stretching vibration), 1,559 cm^{-1}, 1,384 cm^{-1} (C=C stretching vibrations) and 3,442 cm^{-1} (OH stretching) (Elmowafy et al., 2022). The presence of these functional groups confirmed the successful loading of quercetin (Figure 3B).

Nitrogen absorption-desorption isotherms were used to characterize the mesoporous characteristics of both the undoped HMSNs and Q@HMSNs. Both the HMSNs and Q@HMSNs presented type IV isotherms, and their mesoporous structure

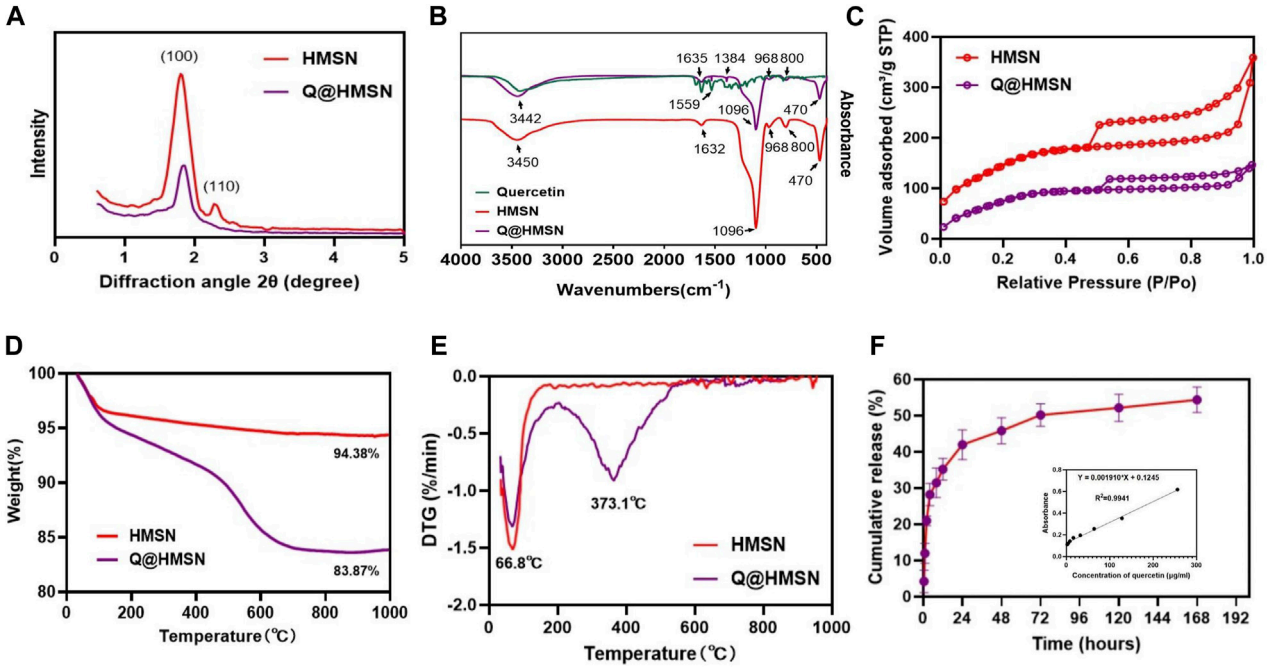

FIGURE 3
Characterization of the HMSNs and Q@HMSNs. **(A)** Small-angle XRD, **(B)** FTIR spectra, **(C)** nitrogen adsorption–desorption isotherms, **(D)** thermogravimetric analysis, **(E)** derivative thermogravimetric analysis, and **(F)** release profile of quercetin from the Q@HMSNs. HMSNs, hollow mesoporous silica nanocomposites; Q@HMSNs, quercetin-encapsulated hollow mesoporous silica nanocomposites.

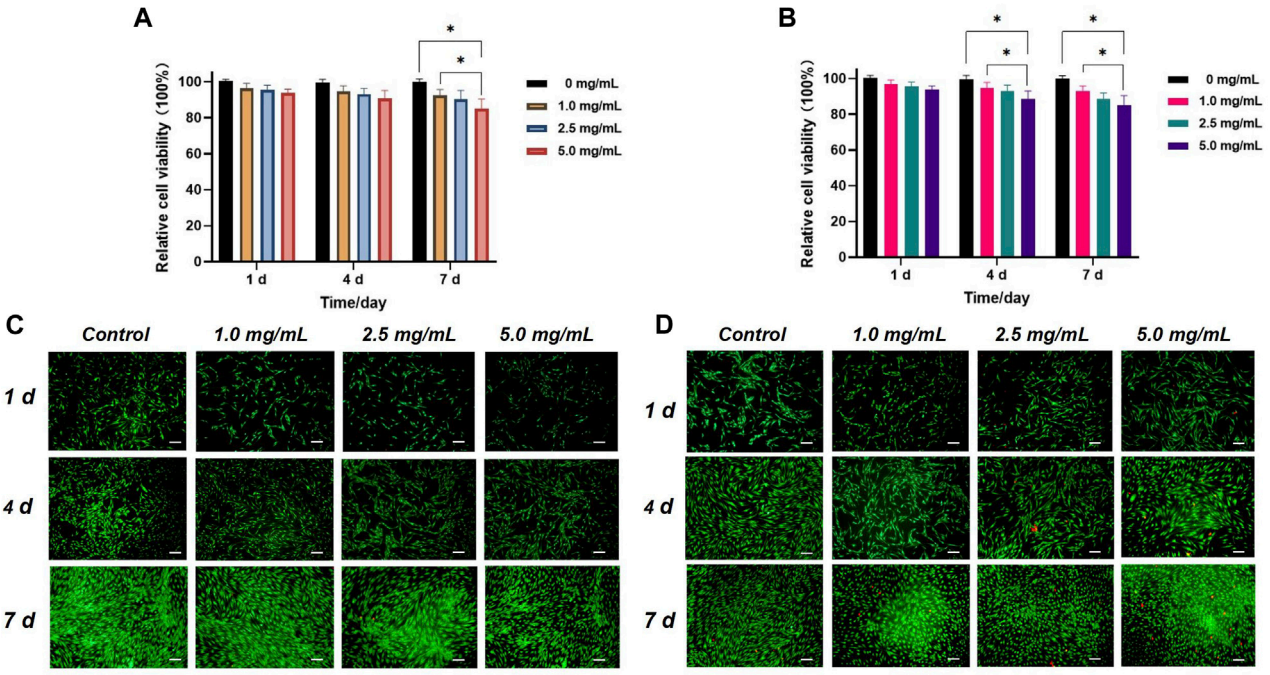

FIGURE 4
In vitro biocompatibility evaluation of the Q@HMSNs. **(A)** Results of the CCK-8 assay with human gingival fibroblasts at 1, 4, and 7 d $*p < 0.05$. **(B)** Results of the CCK-8 assay with human dental pulp stem cells at 1, 4, and 7 d $*p < 0.05$. **(C)** Calcein/PI live/dead fluorescence staining images of human gingival fibroblasts incubated with different concentrations of Q@HMSNs. **(D)** Calcein/PI live/dead fluorescence staining images of human dental pulp stem cells incubated with different concentrations of Q@HMSNs. The data are presented as means and standard deviations. Scale bar: 20 μm. HMSNs, hollow mesoporous silica nanocomposites; Q@HMSNs, quercetin-encapsulated hollow mesoporous silica nanocomposites.

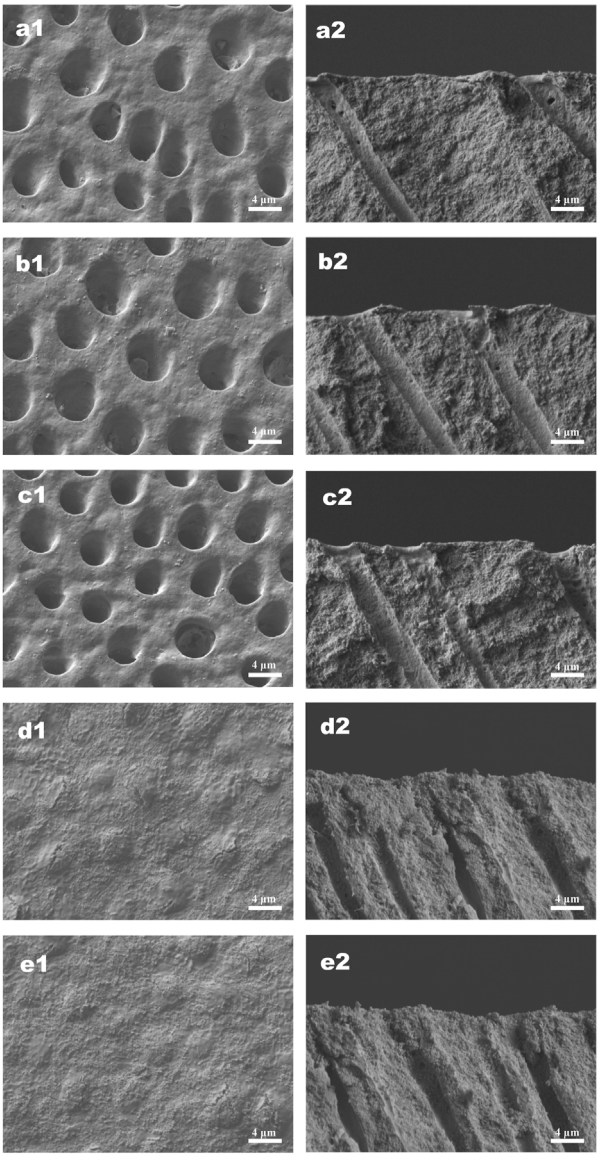

FIGURE 5
Representative SEM images (×5,000 magnification) of specimens treated with the respective solutions immediately after 7 days of erosion and abrasion. **(a1–e1)** Corresponding surface-section SEM images of specimens. **(a2–e2)** Corresponding cross-section SEM images of specimens. **(a1,a2)** Specimens treated with deionized water. **(b1,b2)** Specimens treated with NaF. **(c1,c2)** Specimens treated with quercetin. **(d1,d2)** Specimens treated with HMSNs. **(e1,e2)** Specimens treated with Q@HMSNs. The images in d1, d2, e1, and e2 show that the dentine tubules were occluded by HMSNs and Q@HMSNs. HMSNs, hollow mesoporous silica nanocomposites; Q@HMSNs, quercetin-encapsulated hollow mesoporous silica nanocomposites.

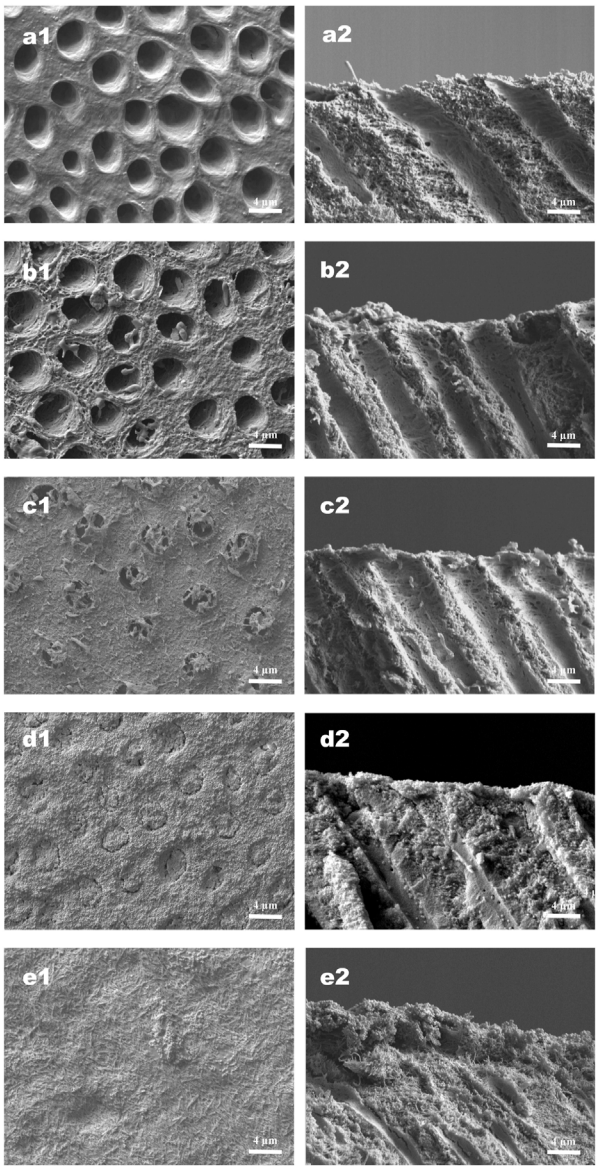

FIGURE 6
Representative SEM images (×5,000 magnification) of specimens under continuous erosive and abrasive challenge for 14 d **(a1–e1)** Corresponding surface-section SEM images of specimens. **(a2–e2)** Corresponding cross-section SEM images of specimens. **(a1,a2)** Specimens treated with deionized water. **(b1,b2)** Specimens treated with NaF. **(c1,c2)** Specimens treated with quercetin. **(d1,d2)** Specimens treated with HMSNs once. **(e1,e2)** Specimens treated with Q@HMSNs once. The images in d1, d2, e1, and e2 show clear dentine tubule occlusion, and the images in e1 and e2 show a notably distinct and thick DOM surface. HMSNs, hollow mesoporous silica nanocomposites; Q@HMSNs, quercetin-encapsulated hollow mesoporous silica nanocomposites.

curves were in accordance with the TEM images and XRD analysis. The specific surface area (SBET), pore volume (V_P), and pore diameter (D_P) of the HMSNs, calculated using the BET/BJH method, were found to be 597.5 m^2/g, 0.567 cm^3/g, and 3.93 nm, respectively. After quercetin loading, the SBET and V_P decreased to 391.8.9 m^2/g and 0.242 cm^3/g, respectively. This reduction indicated the successful loading of quercetin into the mesopores of the silica NPs (Figure 3C; Supplementary Figures S3, S4; Supplementary Table S1).

TGA and derivative thermogravimetric analysis (DTG) were employed to assess the quantity and thermal stability of the quercetin loaded into the HMSNs. TGA revealed a weight loss of 5.62 wt% for the HMSNs and 16.13 wt% for the Q@HMSNs (Figure 3D). The prominent downwards peak at 66.8°C in the DTG curve corresponds to the evaporation of physically adsorbed water, while another significant downwards peak at

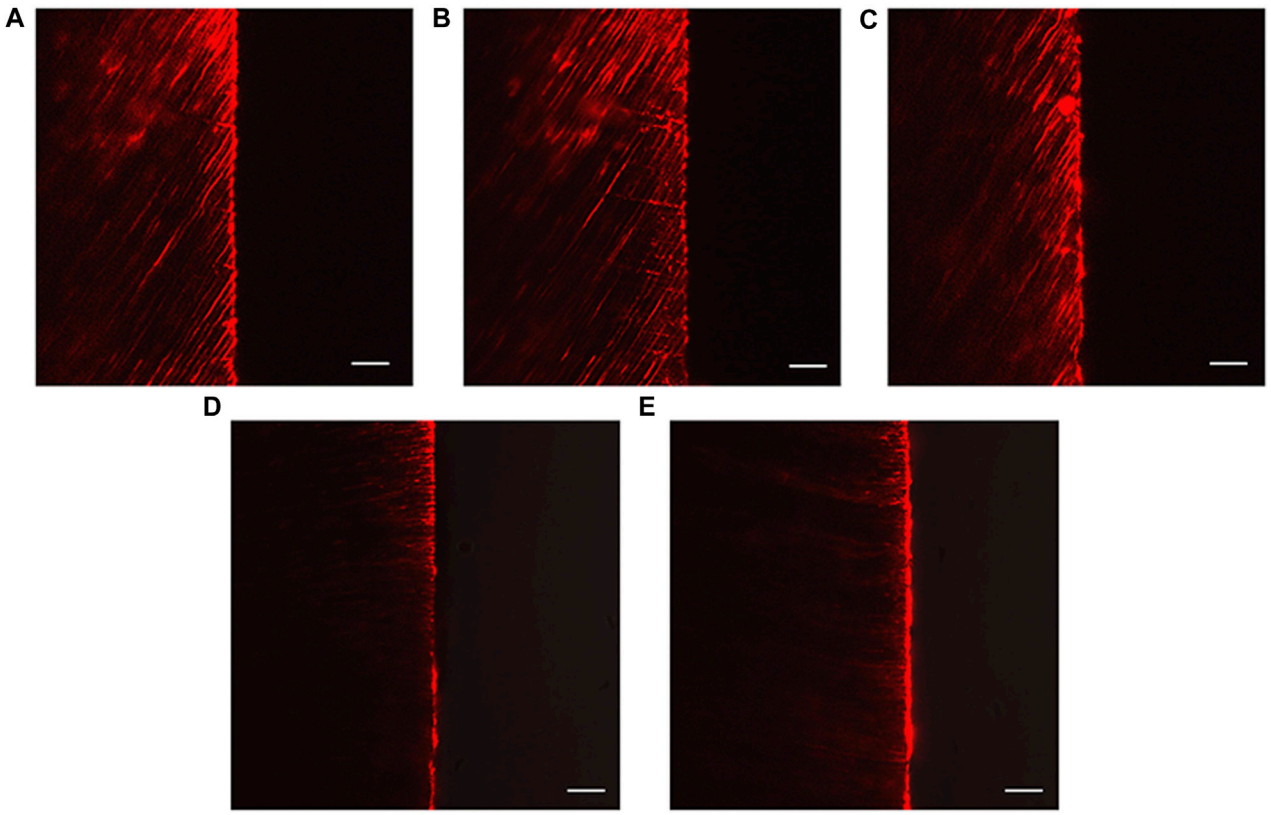

FIGURE 7
Confocal images of vertically sectioned specimens that were treated with the respective solutions after 14 days of erosion and abrasion. **(A)** Specimens treated with deionized water. **(B)** Specimens treated with NaF. **(C)** Specimens treated with quercetin. **(D)** Specimens treated with HMSNs. **(E)** Specimens treated with Q@HMSNs (magnification, ×40, scale bar: 20 μm). HMSNs, hollow mesoporous silica nanocomposites; Q@HMSNs, quercetin-encapsulated hollow mesoporous silica nanocomposites.

373.1°C indicates the decomposition of the organic substance quercetin. These results confirmed the encapsulation of quercetin into the HMSNs, with a calculated loading amount of 10.51 wt% (Figure 3E; Supplementary Figure S5).

Figure 3F; Supplementary Figure S6 illustrates the drug release profile from the Q@HMSNs, which indicated an initial burst release during the first 8 h, followed by a gradual slowing of the release rate, finally resulting in sustained release over 7 days.

3.2 Biocompatibility evaluation

Figures 4A, B depict the relative viabilities of HGFs and HDPSCs after exposure to different concentrations of Q@HMSNs (1.0, 2.5, and 5.0 mg/mL) for 1, 4, and 7 days. These figures illustrate that even at the highest concentration of 5.0 mg/mL, the viabilities of HDPSCs and HGFs exceeded 80% after 7 days of incubation. The live/dead fluorescence staining results of HGFs and HDPSCs in Figures 4C, D further illustrate the substantial cell proliferation at each concentration, with minimal induction of cell death by Q@HMSNs compared to the other groups. These results provide strong evidence that Q@HMSNs induced relatively negligible toxicity to HGFs and HDPSCs.

3.3 Tubule occlusion and DOM preservation

The effects of different treatments on tubule occlusion and DOM preservation are presented in Figures 5, 6. After the application of HMSNs and Q@HMSNs, the dentinal tubules in the HMSN and Q@HMSN groups were completely obstructed. The cross-sectional images confirmed that these tubes were effectively sealed by the NPs. In contrast, the tubules in the DW, NaF, and Q groups were exposed due to acid attack (Figure 5). After 14 days of erosion and abrasion, the DW and NaF groups showed mostly exposed tubules. Moreover, narrower tubules were observed in group Q, while the tubules were blocked in the HMSN group. In contrast, the specimens treated with Q@HMSNs demonstrated well-defined dentine tubule occlusion with integration of the DOM and microparticles. Moreover, the cross-sectional view shows a notably distinct and thick DOM in the Q@HMSN group compared with the other groups (Figure 6).

3.4 Dentine tubule permeability

The CLSM images revealed the penetration depth of rhodamine B in each group. The DW, NaF, and Q groups showed extensive rhodamine B penetration into the dentinal tubules (Figures 7A–C).

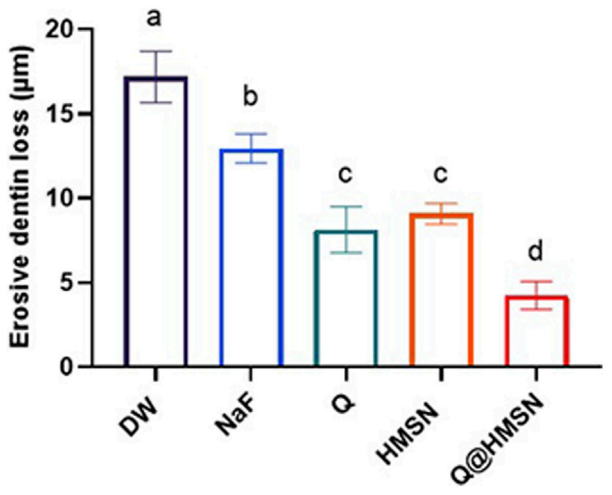

FIGURE 8
Means and standard deviations of the erosive dentine loss values in each group. Values marked with the same superscript letter were not significantly different ($p > 0.05$).

In contrast, superficial fluorescent bands were observed in the HMSN and Q@HMSN groups (Figures 7D, E).

3.5 Effect of Q@HMSNs on EDL

Figure 8 shows the EDL of the specimens treated with different solutions. Significantly less EDL was observed in the NaF, Q, HMSN and Q@HMSN groups than in the DW group ($p < 0.05$). The Q@HMSN group had the lowest EDL among the tested groups ($p < 0.05$).

3.6 Effect of Q@MSNs on collagen release

The results from ICTP analysis revealed that 44.34 ± 3.37, 40.13 ± 4.38, and 43.35 ± 3.43 g/L ICTP were released in the DW, NaF, and HMSN groups, respectively, with no significant differences among these values ($p > 0.05$). In contrast, ICTP release was significantly reduced in the Q and Q@HMSN groups (19.37 ± 4.38 and 12.36 ± 2.49 g/L, respectively) ($p < 0.05$).

4 Discussion

In this study, the potential of using Q@HMSNs as dentinal tubule sealing agents and their efficacy to inhibit dentine erosion and abrasion were investigated. The findings supported effective dentinal tubule sealing, DOM preservation, and reduced EDL following acid erosion and abrasion and treatment with Q@HMSNs, leading to the rejection of all three null hypotheses. The erosion challenge model was utilized to simulate the impact of dietary soft drinks, with 4 erosion cycles/d and 2 abrasion cycles/d (Shellis et al., 2011). A concentration of 12.3 mg/mL sodium fluoride (NaF), a widely studied treatment for tooth erosion, was chosen as the positive control (Magalhaes et al., 2010). Moreover, 300 μg/mL quercetin was chosen based on established protocols (Jiang et al., 2020). Based on previous studies (Hong et al., 2022), the effects of quercetin on dentin erosion may be related to the inhibition of dentin-derived MMPs and the enhancement in the mechanical properties of dentin collagen fibre. In the present study, collagen degradation was performed using ICTP ELISA kits. The present results showed that Q@HMSNs significantly affected the activation of dentin-derived MMPs. The primary inhibitory mechanism of Q@HMSNs on MMPs can be attributed to the inefficiency of MMPs due to the quercetin blocking their bonding with Zn^{2+}/Ca^{2+} (Saragusti et al., 2010). Additionally, the phenolic hydroxyl groups in quercetin can form stable hydrogen bonds with hydroxyl group in collagen (Zhai et al., 2010).

Historically, various approaches, such as calcium-containing pastes (Pei et al., 2013), sodium fluoride (Anderson et al., 2020), and laser treatment (Meng et al., 2023), have been used for tubule obstruction, but limitations persist, including shallow infiltration and the susceptibility to re-exposure during acid attack (Wang et al., 2010). Beltrame et al. (2018) reported a 28% reduction in EDL with phosphorylated chitosan after 5 days of acid erosion. Li et al. (2022) reported that the EDL decreased by 45% after quercetin was applied after acid attacks. Schlueter et al. (2009) reported that the EDL was reduced approximately 29% after the application of NaF and 7 days of citric acid demineralization compared to the placebo. In the present study, the effects of HMSNs and Q@HMSNs surpassed these results, with HMSNs providing a 47% reduction in EDL and Q@HMSNs delivering a 75% reduction.

Considering its unique tubular structure, mesoporous silica has been employed as an effective biomimetic vehicle for dentine (Yu et al., 2021a). TEM images of the Q@HMSNs confirmed their stable framework and the successful incorporation of quercetin into the MSNs. Nitrogen adsorption–desorption analysis demonstrated a type IV isotherm for the HMSNs and Q@HMSNs, indicating a mesoporous structure. The *in vitro* release profiles demonstrated that the HMSNs served as a reservoir and carrier for sustained quercetin delivery. The CCK-8 assay results revealed the low cytotoxicity of the Q@HMSNs, ensuring their suitability for gingival fibroblast and dental pulp cell proliferation. The dentine permeability assessments and SEM observations indicated enhanced erosion and abrasion resistance 14 days after treatment with the HMSNs and Q@HMSNs. Q@HMSNs showed potential as a durable system against acid attacks, with hollow mesoporous silica exhibiting a superior loading capacity compared to traditional mesoporous silica (Elmowafy et al., 2022). Additionally, the quercetin loaded into the HMSNs may be more resistant to degradation inside the tubules than on the dentine surface. Even after a single application to the dentine specimens, the Q@HMSNs demonstrated significant tubule occlusion and DOM preservation capabilities.

Due to the advantageous properties of NPs, such as MSNs and bioactive glass NPs (BGNs), these materials have been widely employed to efficiently occlude dentinal tubules and maintain stability against everyday acid erosion (Li et al., 2018; Zhang et al., 2018; Jung et al., 2019a; Jung et al., 2019b). However, few studies have explored the combined effect of MSNs with MMP inhibitors on the DOM. In this study, Q@HMSNs demonstrated dual functionality by occluding tubules and protecting the DOM from acid erosion. The EDL results indicated that using Q@HMSNs

was more effective than applying HMSNs separately. In a study by Vertuan et al. (2021), preservation of the DOM reduced the EDL by 28% compared to conditions without the DOM. Viana et al. (2020) used β-tricalcium phosphate (β-TCP) NPs to combat dental erosion, resulting in an approximately 50% reduction in the EDL compared to the control group. While the HMSN group in our study showed a 47% reduction in EDL, the Q@HMSN group demonstrated a higher reduction (75%). This suggests that the presence of Q@MSNs may lead to favourable tubule occlusion, providing enhanced protection for quercetin against acid attack. With the dissolution of dentine mineralization and release of quercetin, the remaining dentine organic matrix combines with Q@HMSNs to form a membrane-like layer (Figures 6e1, e2). Based on the present findings, we assume that the main mechanism of action for inhibiting dentine erosion and abrasion is that Q@MSNs could efficiently occlude the dentinal tubules and protect DOM. Theoretically, the HMSNs, as antiacid inorganic contents on the surface dentin, will prevent the further exposure of dentine tubules and demineralization of dentine. Beyond that, quercetin holds inhibitory activity against MMPs, strengthens the mechanical properties of dentin collagen, and maintains the organic matrix on the erosion surface. Moreover, the Q@HMSNs demonstrated high biocompatibility and the potential for use in *in vivo* applications. The continuous quercetin release over 7 days and sustained anti-erosion ability highlight the clinical potential of Q@HMSNs.

This study has a few limitations. Firstly, the efficacy of the Q@HMSNs was observed *in vitro*, and further studies are needed to explore its *in situ*/*in vivo* applications. Additionally, this study did not include CHX, EGCG, or other MMP inhibitors. Future studies should assess and compare the effectiveness of other MMP inhibitors encapsulated in HMSNs.

5 Conclusion

Despite these limitations, the results here suggest that Q@HMSNs could effectively inhibit dentine erosion and abrasion through tubule occlusion and DOM preservation. Q@HMSNs hold promise as an innovative measure for treating dentine erosion and abrasion in future *in vivo* applications.

Data availability statement

The raw data supporting the conclusion of this article will be made available by the authors, without undue reservation.

Ethics statement

The studies involving humans were approved by the Biomedical Research Ethics Committee of the School and Hospital of Stomatology, Fujian Medical University. The studies were conducted in accordance with the local legislation and institutional requirements. The participants provided their written informed consent to participate in this study.

Author contributions

J-MC: Conceptualization, Data curation, Formal Analysis, Investigation, Methodology, Writing–original draft. Y-LC: Formal Analysis, Investigation, Validation, Writing–original draft. M-HY: Methodology, Software, Writing–review and editing. CS: Data curation, Formal Analysis, Methodology, Software, Validation, Writing–review and editing. HY: Conceptualization, Funding acquisition, Project administration, Supervision, Writing–review and editing.

Funding

The author(s) declare financial support was received for the research, authorship, and/or publication of this article. This research project was supported by the Natural Science Foundation of Fujian Province (2023J01714 and 2022J01269) and the Startup Fund for Scientific Research, Fujian Medical University (2020QH1135).

Acknowledgments

We wish to recognize and thank Minxia Wu, Linying Zhou, and Xi Lin from the Public Technology Service Center of Fujian Medical University for their technical assistance.

Conflict of interest

The authors declare that the research was conducted in the absence of any commercial or financial relationships that could be construed as a potential conflict of interest.

Publisher's note

Supplementary material

The Supplementary Material for this article can be found online at: https://www.frontiersin.org/articles/10.3389/fbioe.2024.1343329/full#supplementary-material

References

Aminoshariae, A., and Kulild, J. C. (2021). Current Concepts of Dentinal Hypersensitivity. *J Endod* 47 (11), 1696–1702. doi:10.1016/j.joen.2021.07.011

Anderson, C. J., Kugel, G., Zou, Y., Ferrari, M., and Gerlach, R. (2020). A randomized, controlled, two-month pilot trial of stannous fluoride dentifrice versus sodium fluoride dentifrice after oxalate treatment for dentinal hypersensitivity. *Clin Oral Investig* 24 (11), 4043–4049. doi:10.1007/s00784-020-03275-8

Bai, Y. M., Mao, J., Li, D. X., Luo, X. J., Chen, J., Tay, F. R., et al. (2019). Bimodal antibacterial system based on quaternary ammonium silane-coupled core-shell hollow mesoporous silica. *Acta Biomater* 85, 229–240. doi:10.1016/j.actbio.2018.12.037

Balalaie, A., Rezvani, M. B., and Mohammadi Basir, M. (2018). Dual function of proanthocyanidins as both MMP inhibitor and crosslinker in dentin biomodification: A literature review. *Dent Mater J* 37 (2), 173–182. doi:10.4012/dmj.2017-062

Barbosa, A. I., Costa Lima, S. A., and Reis, S. (2019). Application of pH-Responsive Fucoidan/Chitosan Nanoparticles to Improve Oral Quercetin Delivery. *Molecules* 24 (2), 346. doi:10.3390/molecules24020346

Bartlett, D. W., Lussi, A., West, N. X., Bouchard, P., Sanz, M., and Bourgeois, D. (2013). Prevalence of tooth wear on buccal and lingual surfaces and possible risk factors in young European adults. *J Dent* 41 (11), 1007–1013. doi:10.1016/j.jdent.2013.08.018

Beltrame, A., Suchyta, D., Abd Alraheam, I., Mohammed, A., Schoenfisch, M., Walter, R., et al. (2018). Effect of Phosphorylated Chitosan on Dentin Erosion: An *in vitro* Study. *Caries Res* 52 (5), 378–386. doi:10.1159/000486521

Capalbo, L. C., Delbem, A. C. B., Dal-Fabbro, R., Inacio, K. K., de Oliveira, R. C., and Pessan, J. P. (2022). Effect of sodium hexametaphosphate and quercetin, associated or not with fluoride, on dentin erosion *in vitro*. *Arch Oral Biol* 143, 105541. doi:10.1016/j.archoralbio.2022.105541

Chiang, Y. C., Lin, H. P., Chang, H. H., Cheng, Y. W., Tang, H. Y., Yen, W. C., et al. (2014). A mesoporous silica biomaterial for dental biomimetic crystallization. *ACS Nano* 8 (12), 12502–12513. doi:10.1021/nn5053487

Elmowafy, M., Alruwaili, N. K., Ahmad, N., Kassem, A. M., and Ibrahim, M. F. (2022). Quercetin-Loaded Mesoporous Silica Nanoparticle-Based Lyophilized Tablets for Enhanced Physicochemical Features and Dissolution Rate: Formulation, Optimization, and *In Vitro* Evaluation. *AAPS PharmSciTech* 24 (1), 6. doi:10.1208/s12249-022-02464-w

Fang, X., Zhao, X., Fang, W., Chen, C., and Zheng, N. (2013). Self-templating synthesis of hollow mesoporous silica and their applications in catalysis and drug delivery. *Nanoscale* 5 (6), 2205–2218. doi:10.1039/c3nr34006f

Hannas, A. R., Kato, M. T., Cardoso Cde, A., Magalhaes, A. C., Pereira, J. C., Tjaderhane, L., et al. (2016). Preventive effect of toothpastes with MMP inhibitors on human dentine erosion and abrasion *in vitro*. *J Appl Oral Sci* 24 (1), 61–66. doi:10.1590/1678-775720150289

Hong, D. W., Chen, L. B., Lin, X. J., Attin, T., and Yu, H. (2022). Dual function of quercetin as an MMP inhibitor and crosslinker in preventing dentin erosion and abrasion: An *in situ*/*in vivo* study. *Dent Mater* 38 (12), e297–e307. doi:10.1016/j.dental.2022.09.019

Hong, D. W., Lin, X. J., Wiegand, A., and Yu, H. (2020). Does delayed toothbrushing after the consumption of erosive foodstuffs or beverages decrease erosive tooth wear? A systematic review and meta-analysis. *Clin Oral Investig* 24 (12), 4169–4183. doi:10.1007/s00784-020-03614-9

Huang, C., Zhang, C., Yang, P., Chao, R., Yue, Z., Li, C., et al. (2020). Eldecalcitol Inhibits LPS-Induced NLRP3 Inflammasome-Dependent Pyroptosis in Human Gingival Fibroblasts by Activating the Nrf2/HO-1 Signaling Pathway. *Drug Des Devel Ther* 14, 4901–4913. doi:10.2147/DDDT.S269223

Izquierdo-Barba, I., Vallet-Regi, M., Kupferschmidt, N., Terasaki, O., Schmidtchen, A., and Malmsten, M. (2009). Incorporation of antimicrobial compounds in mesoporous silica film monolith. *Biomaterials* 30 (29), 5729–5736. doi:10.1016/j.biomaterials.2009.07.003

Jiang, N. W., Hong, D. W., Attin, T., Cheng, H., and Yu, H. (2020). Quercetin reduces erosive dentin wear: Evidence from laboratory and clinical studies. *Dent Mater* 36 (11), 1430–1436. doi:10.1016/j.dental.2020.08.013

Jung, J. H., Kim, D. H., Yoo, K. H., Yoon, S. Y., Kim, Y., Bae, M. K., et al. (2019a). Dentin sealing and antibacterial effects of silver-doped bioactive glass/mesoporous silica nanocomposite: an *in vitro* study. *Clin Oral Investig* 23 (1), 253–266. doi:10.1007/s00784-018-2432-z

Jung, J. H., Park, S. B., Yoo, K. H., Yoon, S. Y., Bae, M. K., Lee, D. J., et al. (2019b). Effect of different sizes of bioactive glass-coated mesoporous silica nanoparticles on dentinal tubule occlusion and mineralization. *Clin Oral Investig* 23 (5), 2129–2141. doi:10.1007/s00784-018-2658-9

Kankala, R. K., Han, Y. H., Na, J., Lee, C. H., Sun, Z., Wang, S. B., et al. (2020). Nanoarchitectured Structure and Surface Biofunctionality of Mesoporous Silica Nanoparticles. *Adv Mater* 32 (23), e1907035. doi:10.1002/adma.201907035

Kato, M. T., Leite, A. L., Hannas, A. R., and Buzalaf, M. A. (2010). Gels containing MMP inhibitors prevent dental erosion *in situ*. *J Dent Res* 89 (5), 468–472. doi:10.1177/0022034510363248

Lapinska, B., Klimek, L., Sokolowski, J., and Lukomska-Szymanska, M. (2018). Dentine Surface Morphology after Chlorhexidine Application-SEM Study. *Polymers (Basel)* 10 (8), 905. doi:10.3390/polym10080905

Lee, J. H., El-Fiqi, A., Jo, J. K., Kim, D. A., Kim, S. C., Jun, S. K., et al. (2016). Development of long-term antimicrobial poly(methyl methacrylate) by incorporating mesoporous silica nanocarriers. *Dent Mater* 32 (12), 1564–1574. doi:10.1016/j.dental.2016.09.001

Li, X., Li, X., Wang, S., Leung, K. C., Zhang, C., and Jin, L. (2018). Infiltration and Profiles of Mesoporous Silica Nanoparticles in Dentinal Tubules. *ACS Biomater Sci Eng* 4 (4), 1428–1436. doi:10.1021/acsbiomaterials.7b00919

Li, X. Y., Lin, X. J., Zhong, B. J., and Yu, H. (2022). Effects of the application timing of anti-erosive agents on dentin erosion. *J Mech Behav Biomed Mater* 136, 105512. doi:10.1016/j.jmbbm.2022.105512

Li, Y., Li, N., Pan, W., Yu, Z., Yang, L., and Tang, B. (2017). Hollow Mesoporous Silica Nanoparticles with Tunable Structures for Controlled Drug Delivery. *ACS Appl Mater Interfaces* 9 (3), 2123–2129. doi:10.1021/acsami.6b13876

Magalhaes, A. C., Levy, F. M., Rios, D., and Buzalaf, M. A. (2010). Effect of a single application of TiF(4) and NaF varnishes and solutions on dentin erosion *in vitro*. *J Dent* 38 (2), 153–157. doi:10.1016/j.jdent.2009.09.015

Mazzoni, A., Tjaderhane, L., Checchi, V., Di Lenarda, R., Salo, T., Tay, F. R., et al. (2015). Role of dentin MMPs in caries progression and bond stability. *J Dent Res* 94 (2), 241–251. doi:10.1177/0022034514562833

Meng, Y., Huang, F., Wang, S., Huang, X., Lu, Y., Li, Y., et al. (2023). Evaluation of dentinal tubule occlusion and pulp tissue response after using 980-nm diode laser for dentin hypersensitivity treatment. *Clin Oral Investig* 27 (8), 4843–4854. doi:10.1007/s00784-023-05114-y

Mutlu, N., Beltran, A. M., Nawaz, Q., Michalek, M., Boccaccini, A. R., and Zheng, K. (2021). Combination of Selective Etching and Impregnation toward Hollow Mesoporous Bioactive Glass Nanoparticles. *Nanomaterials (Basel)* 11 (7), 1846. doi:10.3390/nano11071846

Ni, D., Jiang, D., Ehlerding, E. B., Huang, P., and Cai, W. (2018). Radiolabeling Silica-Based Nanoparticles via Coordination Chemistry: Basic Principles, Strategies, and Applications. *Acc Chem Res* 51 (3), 778–788. doi:10.1021/acs.accounts.7b00635

Osorio, R., Yamauti, M., Osorio, E., Ruiz-Requena, M. E., Pashley, D., Tay, F., et al. (2011). Effect of dentin etching and chlorhexidine application on metalloproteinase-mediated collagen degradation. *Eur J Oral Sci* 119 (1), 79–85. doi:10.1111/j.1600-0722.2010.00789.x

O Toole, S., Mistry, M., Mutahar, M., Moazzez, R., and Bartlett, D. (2015). Sequence of stannous and sodium fluoride solutions to prevent enamel erosion. *J Dent* 43 (12), 1498–1503. doi:10.1016/j.jdent.2015.10.003

Park, S. H., Lee, Y. S., Lee, D. S., Park, J. C., Kim, R., and Shon, W. J. (2019). CPNE7 Induces Biological Dentin Sealing in a Dentin Hypersensitivity Model. *J Dent Res* 98 (11), 1239–1244. doi:10.1177/0022034519869577

Pei, D., Liu, S., Huang, C., Du, X., Yang, H., Wang, Y., et al. (2013). Effect of pretreatment with calcium-containing desensitizer on the dentine bonding of mild self-etch adhesives. *Eur J Oral Sci* 121 (3 Pt 1), 204–210. doi:10.1111/eos.12047

Peres, M. A., Macpherson, L. M. D., Weyant, R. J., Daly, B., Venturelli, R., Mathur, M. R., et al. (2019). Oral diseases: a global public health challenge. *Lancet* 394 (10194), 249–260. doi:10.1016/S0140-6736(19)31146-8

Sapino, S., Ugazio, E., Gastaldi, L., Miletto, I., Berlier, G., Zonari, D., et al. (2015). Mesoporous silica as topical nanocarriers for quercetin: characterization and *in vitro* studies. *Eur J Pharm Biopharm* 89, 116–125. doi:10.1016/j.ejpb.2014.11.022

Saputra, O. A., Lestari, W. A., Kurniansyah, V., Lestari, W. W., Sugiura, T., Mukti, R. R., et al. (2022). Organically surface engineered mesoporous silica nanoparticles control the release of quercetin by pH stimuli. *Sci Rep* 12 (1), 20661. doi:10.1038/s41598-022-25095-4

Saragusti, A. C., Ortega, M. G., Cabrera, J. L., Estrin, D. A., Marti, M. A., and Chiabrando, G. A. (2010). Inhibitory effect of quercetin on matrix metalloproteinase 9 activity molecular mechanism and structure-activity relationship of the flavonoid-enzyme interaction. *Eur J Pharmacol* 644 (1-3), 138–145. doi:10.1016/j.ejphar.2010.07.001

Schlueter, N., Hara, A., Shellis, R. P., and Ganss, C. (2011). Methods for the measurement and characterization of erosion in enamel and dentine. *Caries Res* 45 (Suppl 1), 13–23. doi:10.1159/000326819

Schlueter, N., Klimek, J., and Ganss, C. (2009). Efficacy of an experimental tin-F-containing solution in erosive tissue loss in enamel and dentine *in situ*. *Caries Res* 43 (6), 415–421. doi:10.1159/000252974

Schlueter, N., and Luka, B. (2018). Erosive tooth wear - a review on global prevalence and on its prevalence in risk groups. *Br Dent J* 224 (5), 364–370. doi:10.1038/sj.bdj.2018.167

Shellis, R. P., Ganss, C., Ren, Y., Zero, D. T., and Lussi, A. (2011). Methodology and models in erosion research: discussion and conclusions. *Caries Res* 45 (Suppl 1), 69–77. doi:10.1159/000325971

Vered, Y., Lussi, A., Zini, A., Gleitman, J., and Sgan-Cohen, H. D. (2014). Dental erosive wear assessment among adolescents and adults utilizing the basic erosive wear examination (BEWE) scoring system. *Clin Oral Investig* 18 (8), 1985–1990. doi:10.1007/s00784-013-1175-0

Vertuan, M., Souza, B. M., Mosquim, V., Silva, C. V., Freitas, P. M., Borges, A. F. S., et al. (2021). Effect of TiF(4) varnish after pre-treatment with proanthocyanidin or chlorhexidine on the progression of erosive dentin loss in the presence or absence of the demineralized organic matrix. *J Mech Behav Biomed Mater* 115, 104287. doi:10.1016/j.jmbbm.2020.104287

Viana, I. E. L., Lopes, R. M., Silva, F. R. O., Lima, N. B., Aranha, A. C. C., Feitosa, S., et al. (2020). Novel fluoride and stannous -functionalized β-tricalcium phosphate nanoparticles for the management of dental erosion. *J Dent* 92, 103263. doi:10.1016/j.jdent.2019.103263

Wang, J., Liu, Y., Cai, Q., Dong, A., Yang, D., and Zhao, D. (2022). Hierarchically Porous Silica Membrane as Separator for High-Performance Lithium-Ion Batteries. *Adv Mater* 34 (3), e2107957. doi:10.1002/adma.202107957

Wang, Z., Sa, Y., Sauro, S., Chen, H., Xing, W., Ma, X., et al. (2010). Effect of desensitising toothpastes on dentinal tubule occlusion: a dentine permeability measurement and SEM *in vitro* study. *J Dent* 38 (5), 400–410. doi:10.1016/j.jdent.2010.01.007

Wiegand, A., and Attin, T. (2007). Occupational dental erosion from exposure to acids: a review. *Occup Med (Lond).* 57 (3), 169–176. doi:10.1093/occmed/kql163

Wiegand, A., and Attin, T. (2011). Design of erosion/abrasion studies--insights and rational concepts. *Caries Res* 45 (Suppl 1), 53–59. doi:10.1159/000325946

Xing, X., Su, J., Liu, Y., Lin, H., Wang, Y., and Cheng, H. (2022). A novel visible light-curing chitosan-based hydrogel membrane for guided tissue regeneration. *Colloids Surf B Biointerfaces* 218, 112760. doi:10.1016/j.colsurfb.2022.112760

Yu, J., Bian, H., Zhao, Y., Guo, J., Yao, C., Liu, H., et al. (2023). Epigallocatechin-3-gallate/mineralization precursors co-delivery hollow mesoporous nanosystem for synergistic manipulation of dentin exposure. *Bioact Mater* 23, 394–408. doi:10.1016/j.bioactmat.2022.11.018

Yu, J., Yang, H., Li, K., Lei, J., Zhou, L., and Huang, C. (2016). A novel application of nanohydroxyapatite/mesoporous silica biocomposite on treating dentin hypersensitivity: An *in vitro* study. *J Dent* 50, 21–29. doi:10.1016/j.jdent.2016.04.005

Yu, J., Yang, H., Li, K., Ren, H., Lei, J., and Huang, C. (2017). Development of Epigallocatechin-3-gallate-Encapsulated Nanohydroxyapatite/Mesoporous Silica for Therapeutic Management of Dentin Surface. *ACS Appl Mater Interfaces* 9 (31), 25796–25807. doi:10.1021/acsami.7b06597

Yu, J., Yi, L., Guo, R., Guo, J., Yang, H., and Huang, C. (2021a). The Stability of Dentin Surface Biobarrier Consisting of Mesoporous Delivery System on Dentinal Tubule Occlusion and Streptococcus Mutans Biofilm Inhibition. *Int J Nanomedicine* 16, 3041–3057. doi:10.2147/IJN.S290254

Yu, J., Zhang, Z., Guo, R., Peng, W., Yang, H., and Huang, C. (2021b). Epigallocatechin-3-gallate/nanohydroxyapatite platform delivery approach to adhesive-dentin interface stability. *Mater Sci Eng C Mater Biol Appl* 122, 111918. doi:10.1016/j.msec.2021.111918

Zarella, B. L., Cardoso, C. A., Pela, V. T., Kato, M. T., Tjaderhane, L., and Buzalaf, M. A. (2015). The role of matrix metalloproteinases and cysteine-cathepsins on the progression of dentine erosion. *Arch Oral Biol* 60 (9), 1340–1345. doi:10.1016/j.archoralbio.2015.06.011

Zhai, W., Lu, X., Chang, J., Zhou, Y., and Zhang, H. (2010). Quercetin-crosslinked porcine heart valve matrix: mechanical properties, stability, anticalcification and cytocompatibility. *Acta Biomater* 6 (2), 389–395. doi:10.1016/j.actbio.2009.07.035

Zhang, L., Sun, H., Yu, J., Yang, H., Song, F., and Huang, C. (2018). Application of electrophoretic deposition to occlude dentinal tubules *in vitro*. *J Dent* 71, 43–48. doi:10.1016/j.jdent.2018.01.012

Zhang, T., Liu, H., Li, L., Guo, Z., Song, J., Yang, X., et al. (2021). Leukocyte/platelet hybrid membrane-camouflaged dendritic large pore mesoporous silica nanoparticles co-loaded with photo/chemotherapeutic agents for triple negative breast cancer combination treatment. *Bioact Mater* 6 (11), 3865–3878. doi:10.1016/j.bioactmat.2021.04.004

frontiers | Frontiers in Bioengineering and Biotechnology

TYPE Original Research
PUBLISHED 19 April 2024
DOI 10.3389/fbioe.2024.1390337

OPEN ACCESS

EDITED BY
Jian Yu,
University of British Columbia, Canada

REVIEWED BY
Abdorreza Mesgar,
University of Tehran, Iran
Amit Kumar Jaiswal,
VIT University, India
Lin Wang,
Southern University of Science and Technology, China
Zhen Geng,
Shanghai University, China

*CORRESPONDENCE
Lijia Cheng,
chenglijia@cdu.edu.cn
Zheng Shi,
drshiz1002@hotmail.com

†These authors share first authorship

RECEIVED 23 February 2024
ACCEPTED 11 April 2024
PUBLISHED 19 April 2024

CITATION
Liu L, Hou S, Xu G, Gao J, Mu J, Gao M, He J, Su X, Yang Z, Liu Y, Chen T, Dong Z, Cheng L and Shi Z (2024), Evaluation of osteogenic properties of a novel injectable bone-repair material containing strontium *in vitro* and *in vivo*.
Front. Bioeng. Biotechnol. 12:1390337.
doi: 10.3389/fbioe.2024.1390337

Evaluation of osteogenic properties of a novel injectable bone-repair material containing strontium *in vitro* and *in vivo*

Lishuang Liu†, Sha Hou†, Guangya Xu†, Jingjing Gao, Junyu Mu, Min Gao, Jianrong He, Xiaoyu Su, Zheng Yang, Yi Liu, Tengzhuo Chen, Zhihong Dong, Lijia Cheng* and Zheng Shi*

Clinical Medical College, Affiliated Hospital, School of Basic Medical Sciences of Chengdu University, Chengdu, China

Objective: This study aims to develop and evaluate the biocompatibility and osteogenic potential of a novel injectable strontium-doped hydroxyapatite bone-repair material.

Methods: The properties of strontium-doped hydroxyapatite/chitosan (Sr-HA/CS), hydroxyapatite/chitosan (HA/CS) and calcium phosphate/chitosan (CAP/CS) were assessed following their preparation via physical cross-linking and a one-step simplified method. Petri dishes containing *Escherichia coli* and *Staphylococcus epidermidis* were inoculated with the material for *in vitro* investigations. The material was also co-cultured with stem cells derived from human exfoliated deciduous teeth (SHEDs), to assess the morphology and proliferation capability of the SHEDs, Calcein-AM staining and the Cell Counting Kit-8 assay were employed. Osteogenic differentiation of SHEDs was determined using alkaline phosphatase (ALP) staining and Alizarin Red staining. For *in vivo* studies, Sr-HA/CS was implanted into the muscle pouch of mice and in a rat model of ovariectomy-induced femoral defects. Hematoxylin-eosin (HE) staining was performed to determine the extent of bone formation and defect healing. The formation of new bone was determined using Masson's trichrome staining. The osteogenic mechanism of the material was investigated using Tartrate-resistant acid phosphatase (TRAP) staining and immunohistochemical studies.

Results: X-ray diffraction (XRD) and energy-dispersive spectroscopy (EDS) showed that strontium was successfully doped into HA. The Sr-HA/CS material can be uniformly squeezed using a syringe with a 13% swelling rate. Sr-HA/CS had a significant antibacterial effect against both *E. coli* and *S. epidermidis* ($p < 0.05$), with a stronger effect observed against *E. coli*. The Sr-HA/CS significantly improved cell proliferation and cell viability *in vitro* studies ($p < 0.05$). Compared to CAP/CS and CS, Sr-HA/CS generated a substantially greater new bone area during osteoinduction experiments ($p < 0.05$, $p < 0.001$). The Sr-HA/CS material demonstrated a significantly higher rate of bone repair in the

bone defeat studies compared to the CAP/CS and CS materials ($p < 0.01$). The OCN-positive area and TRAP-positive cells in Sr-HA/CS were greater than those in control groups ($p < 0.05$).

Conclusion: A novel injectable strontium-doped HA bone-repair material with good antibacterial properties, biocompatibility, and osteoinductivity was successfully prepared.

KEYWORDS

hydroxyapatite, strontium, chitosan, bone regeneration, osteoporosis

1 Introduction

Osteoporosis, a prevalent global health concern, affects millions of individuals worldwide and poses a significant medical challenge. This systemic skeletal disorder is characterized by reduced bone mass, compromised microstructural integrity leading to increased bone fragility, and heightened susceptibility to fractures. Consequently, the management of osteoporosis often necessitates the utilization of bone repair materials for the treatment of pathological fractures across diverse anatomical sites. Autogenous bone transplantation is considered the most effective method for the treatment of large-scale bone defects resulting from trauma, infection, tumor, or ischemic osteonecrosis (Silva Filho et al., 2013; Ahn et al., 2014). However, the clinical application of autogenous bone is greatly limited due to limited sources and the risk of infections and immune rejection (Myeroff and Archdeacon, 2011). Therefore, there is an urgent need for bone tissue–engineering materials in clinical settings as an alternative to implant materials. Traditional biomaterials such as hydroxyapatite (HA) and calcium phosphate (CAP) have been extensively investigated because of their superior bone conductivity, biocompatibility, and biodegradability (Gao et al., 2014). However, these materials have certain drawbacks, including limited biological activity and poor mechanical properties that prevent them from adapting to the shape of the defect (Rezwan et al., 2006; Mercado-Pagán et al., 2015). Furthermore, the majority of calcium phosphate-containing materials lack antibacterial activity. This limitation restricts their use in bone repair (Campoccia et al., 2006; Yuan et al., 2014).

Fortunately, the discovery of strontium (Sr) has invoked renewed interest in conventional calcium phosphate–containing materials. Sr is a trace element found in humans' body in amounts ranging from 0.008% to 0.01%, which is widely distributed in human hard tissues, such as bones and teeth. Due to the similar ionic radius of strontium ions (Sr^{2+}) and calcium ions (Ca^{2+}) (0.12 nm vs. 0.099 nm), Sr^{2+} can frequently displace calcium ions Ca^{2+} in HA (Boanini et al., 2010). Geng et al.demonstrated that Sr could completely replace Ca and that the addition of Sr increased the lattice parameters of HA and enhanced the biological activity (Geng et al., 2016; Geng et al., 2018). In addition to being an essential constituent of bone tissue, Sr regulates the physiological environment of cells and promotes bone healing (Glenske et al., 2018). It is recognized for its distinctive dual mechanism of action, which simultaneously promotes bone formation and hinders bone resorption (Bonnelye et al., 2008). Clinically, Sr ranelate has been utilized for the treatment of osteoporosis in postmenopausal women (Meunier et al., 2004; Meunier et al., 2009). However, it may increase the incidence of side effects such as heart disease and thromboembolism, leading to its restriction by the European Medicines Agency in 2014 (Diepenhorst et al., 2018). Studies have indicated that Sr can stimulate calcium-sensitive receptors, MAPK ERK1/2, NFATc/Maf, and the Wnt pathway, which in turn enhances the process of osteoblast differentiation (Chattopadhyay et al., 2007; Saidak et al., 2012). Moreover, it can reduce osteoclast differentiation by inhibiting the NF-κB pathway (Caudrillier et al., 2010). Therefore, considering the effects of Sr on the physiological process of bone remodeling, a viable safe approach to enhance osseointegration could involve the combination of Sr with implants to stimulate bone differentiation properties (Li et al., 2010; Zhang et al., 2016; Wang et al., 2019). However, limited studies have been reported on Sr-doped compounds or related materials for bone regeneration.

In addition, it is necessary for the implanted biomaterials to have excellent biocompatibility and antibacterial activity, because the implanted biomaterials may trigger a dependent inflammatory response followed by infection, thereby leading to surgical failure. Fortunately, in many studies, chitosan (CS) has gradually been discovered to have excellent performance. CS is a naturally occurring polysaccharide with exceptional biocompatibility, biodegradability, and antibacterial properties, finds extensive application in bone tissue engineering (Madihally and Matthew, 1999; Di Martino et al., 2005; Venkatesan and Kim, 2010; Croisier and Jérôme, 2013). CS binds and combines with negatively charged substances on the bacterial surface, forming an impermeable layer that obstructs the transport of important solutes, due to the presence of multiple positively charged amine groups in its molecular structure (Khattak et al., 2019). Another method involves the ability of low-molecular-weight CS to enter cells, alter the structure of DNA, and hinder the production of RNA and proteins in bacteria (Li et al., 2022).

After the incorporation of Sr into HA, Sr^{2+} can replace the Ca^{2+} in HA and become Sr/HA. Moreover, the difference in ionic radius and properties between Sr^{2+} and Ca^{2+} will distort the crystal lattice of the original HA, thus changing the crystal structure and biodegradability of HA, so that it can better match and integrate with natural bone. CS hydrogels can enhance the biocompatibility and antibacterial properties of the materials, and can be used as scaffolds. The addition of Sr/HA microspheres not only enhanced the mechanical properties of hydrogel, but also effectively promoted the healing of bone defects. A simplified one-step approach was used in this study to prepare Sr-doped HA (Sr-HA) to enhance the osteogenic capabilities of the material. A composite CS/medical polyvinyl alcohol gel was prepared using a physical cross-linking approach to make it suitable for injection. Finally, the modified Sr-

FIGURE 1
One-step simplified method and physical cross-linking were used to prepare Sr-HA/CS. (1) 98% phosphocreatine was mixed with 96% NaOH and heated followed by the addition of $SrCl_2$ to obtain strontium-doped hydroxyapatite (Sr-HA); (2) KOH, urea, chitosan, and 5wt% medical PVA were added separately and the gel was prepared after thawing and freezing cycle; (3) Finally, a specific proportion of the two substances were mixed to produce Sr-HA/CS.

HA was incorporated into the CS gel to develop the novel Sr-HA/CS. The material characterization experiments, *in vitro* antibacterial tests, cellular experiments, and *in vivo* experiments were used to determine the characteristics of the synthesized materials and assess their clinical viability for the treatment of osteoporotic bone defect. It is anticipated that this composite material can enhance the potential for bone regeneration applications.

2 Materials and methods

2.1 Fabrication of the Sr-HA/CS

A 50 mL solution of phosphocreatine (98%, Hefei Bomei Biotechnology, Anhui, China) was added dropwise into a 50 mL solution of calcium chloride (99%) to prepare a mixed solution. The resulting solution was then stirred using a magnetic stirrer (WH220-HT, WIGGENS, Germany) for 30 min at 1,200 r/min. The pH of the solution was adjusted to 10 using a NaOH solution. After that, 0.525 g of $SrCl_2$ (99% purity, Macklin, Shanghai, China) was added to the solution, which was then subjected to heating in an oil bath at 120°C for 30 min. The solution was subsequently cooled to room temperature, allowed to precipitate, filtered using a filter paper, washed twice with phosphate-buffered saline (PBS), and freeze-dried in a vacuum freeze drier (FDU-2100, EYELA, Japan) to obtain Sr-HA microspheres. Simultaneously, CS hydrogel was made using the following procedure: 16 g KOH and 8 g urea were accurately measured in a balance and added to 71 mL distilled water. The solution was decanted into a 150-mL flask, stirred slowly with a glass rod, and cooled to 20°C in a refrigerator. Then, 5 g of CS (degree of deacetylation ≥95%, Macklin, Shanghai, China) was introduced into the solution and stirred at 1,200 r/min for 1 h using a magnetic stirring to produce a transparent CS solution. Following this, 100 g of medical polyvinyl alcohol (5%, Evoh, Japan) was added to the CS solution, which was stirred at 25°C for 30 min at 1,200 r/min with a magnetic heating agitator. The CS/medical polyvinyl alcohol solution was heated in a water bath at 50°C for 1 h. The solution was frozen at −20°C for 12 h and thawed at room temperature (25°C). The freeze-thaw cycle was repeated three times. The resulting solution was dialyzed in distilled water for 5 days and then filtered to remove the residue to get the CS hydrogel. Finally, the CS gel and HA microspheres were mixed in a specific solid-liquid ratio (0.05–0.2 g/mL) and stirred for 1 h with a magnetic stirrer at 1,200 r/min to produce a homogenous, milky composite hydrogel of the Sr-HA/CS composite (Figure 1). Furthermore, control trials were conducted using HA/CS and CAP/CS materials without Sr. All materials were exposed to 250 nm UV light (Chuangu Lighting Technology Co., Ltd.) for an hour before implantation.

2.2 Characterization of materials

2.2.1 Surface and composition analyses of Sr-HA and HA

To evaluate surface morphology of Sr-HA and HA, the sample was sprayed with gold in a vacuum for 10 min and then examined using scanning electron microscopy (SEM, Regulus8100, Hitachi, Japan). After gold plating, the elements of the material were identified using energy dispersive spectroscopy (EDS, Regulus8100, Hitachi, Japan). The sample was analyzed using X-ray diffractometry (XRD, D8 ADVANCE, Bruker, Germany).

2.2.2 Swelling of Sr-HA/CS and HA/CS

To evaluate the swelling rate (SR), the Sr-HA/CS and HA/CS hydrogel was dried at 60°C in a constant temperature vacuum dryer (DZF6020, China). A specific amount of the dried hydrogel was weighed (W1). Then, the hydrogel was soaked in PBS for 12 h. The

liquid on the surface of the sample was removed and the sample was measured using an electronic balance (W2). The formula used to calculate SR is as follows: SR = (W2–W1)/W1.

2.2.3 Injectability of Sr-HA/CS

The hydrogel was loaded in a 5-mL syringe and squeezed into a Petri dish containing PBS. The criteria for judgment were the ability of the gel to be squeezed out uniformly and the retention of its shape in solution.

2.3 Antibacterial effect of Sr-HA/CS hydrogel

The bacteriostatic effect of the Sr-HA/CS hydrogel was determined. First, 0.1 mL of *E. coli* (*Escherichia coli*) and *S. epidermidis* (*Staphylococcus epidermidis*) at a density of 2×10^6 cells/mL was uniformly spread onto agar plates using a sterile swab. Four holes were punched in the agar plates using a pipette tip and the plugs in the medium were removed from the holes using a sterile needle. The plates were sealed to prevent contamination and incubated at a temperature of 37°C and then examined 18 h later. The diameters of the bacteriostatic circles were quantitatively measured with a Vernier caliper and the effects of bacteriostasis and colony growth were observed and recorded.

2.4 *In vitro* studies

2.4.1 Cell culture

Following the sterilization of the two material groups (Sr-HA/CS and HA/CS), 2 mg/mL rat tail glue (Solarbio, China) was introduced and distributed across a 24-well plate (Nest, America). The plate was then subjected to ultraviolet gel. Next, 5×10^4 stem cells derived from human exfoliated deciduous teeth (SHEDs) were placed on the Sr-HA/CS and HA/CS bioceramics in 24-well plates, and the culture medium was replaced after 24 h. The Dulbecco's Modified Eagle Medium (high glucose) was supplemented with 1% penicillin-streptomycin and 10% standard fetal bovine serum.

2.4.2 Cell proliferation

Cell proliferation was assessed using the Cell Counting Kit-8 (CCK-8, Biyuntian, China). Briefly, 2×10^4 SHEDs were inoculated on samples in 48-well plates. The samples were then cultured for 1, 4, and 7 days, respectively, and incubated in CCK-8 working solution for 2 h. The culture medium was replaced every 2 days. Then, 100 μL of the sample solution was transferred to a 96-well plate and the absorbance was measured at 450 nm. The relative growth rate (RGR) was calculated using the following equation: RGR (%) = $OD_{test}/OD_{control} \times 100\%$.

In morphological studies, cells were treated for 15–30 min with a Calcein-AM fluorescent dye kit (HR0444, Baiaolaibo, China) after 7 days of cell culture. The Calcein-AM staining solution was removed and the cells were washed twice with a serum-free medium. Following the preparation of Hoechst working solution (C1017, Biyuntian, China) at a concentration of 20 μg/mL, the cells were further incubated for 10–20 min. The cells were then washed twice with PBS before being examined under inverted fluorescence microscopy (IX73, Olympus, Japan). RGR was calculated using $OD_{control}$ represents the absorption of the sample at 12 h.

2.4.3 Alkaline phosphatase (ALP) activity

The cells were inoculated into each well at a density of 3×10^4 cells. Osteoinduction commenced as the cells cultivated on the tissue culture plate achieved 80% confluence, the materials were added in the cell to induce cell osteogenic differentiation. The samples were transferred to a new well plate and washed with PBS after 7 and 14 days. The cells on the sample were lysed in 200 μL of 0.1% polyethylene glycol octyl phenyl ether (Tritonx-100) buffer for 30 min, and the lysate was collected in a 1.5-mL microcentrifuge tube. The ALP activity in the supernatant was measured using an ALP assay kit (YX-W-B002, Ainobestbio, China). The total protein content was evaluated using a bicinchoninic acid assay kit, following the instructions provided by the manufacturer. The ALP activity was determined and calibrated using the total protein content (U/g).

2.4.4 Extracellular matrix mineralization

After 21 days of osteogenic induction, Alizarin Red staining was performed to evaluate the surface mineralization level of samples. Briefly, the samples were fixed in 4% paraformaldehyde for 30 min, washed with PBS, and then stained with Alizarin Red staining solution (Jiayuan Biotechnology, Guangzhou, China) for 15 min. The samples were then thoroughly rinsed with distilled water and images were captured with a stereoscopic microscope (Leica, Germany). After 15 min of elution in 1 mL of 10% cetylpyridinium chloride (Sinopharm Chemical Reagent, China), the mineralized body was transferred to a 96-well plate at 37°C and its absorbance at 562 nm was measured using semi-quantitative analysis. In general, materials with good biocompatibility exhibited more mineralized nodules.

2.5 *In vivo* studies

2.5.1 Bone induction surgery in mice

All animal experimental protocols were approved by the Animal Ethics Committee of Chengdu University. Surgery was conducted on animals after 1 week of adaptive housing. Twenty-four 8-week-old female ICR mice (Chengdu Dashuo Experimental Animal Co., Ltd., China) were randomly divided into the following four groups ($n = 6$ each): 0.01 mL of CS, 0.01 mL of Sr-HA/CS, 10 μg of calcium phosphate (CAP), and 0.01 mL of CAP/CS. Calcium phosphate-based materials are very similar to the inorganic components of human bone, both in terms of chemical composition and biological properties, and are therefore widely used in bone tissue engineering and clinical medicine. In our study, we chose to increase the CAP group for comparison, thus better demonstrating the advantages of our prepared materials. Before implantation, CAP, an amorphous powder, was moistened with sterile PBS and thereafter underwent natural drying and solidification. The ratio of Sr HA/CAP: CS hydrogel was 0.05 g: 10 mL. The mice were anesthetized using isoflurane gas (Shenzhen Reward Life Science and Technology Co., Ltd.). After complete anesthesia, the hair on both outer thighs of mice was clipped, the skin was sterilized with ethanol, and a 10-mm long incision was made in the skin. Subsequently, a longitudinal muscle pocket measuring approximately 8 mm in length was promptly prepared along the skin incision. Finally, the four kinds of materials were implanted, and the muscles and skin were sutured sequentially. Normal postoperative feeding was performed and penicillin was injected for 3 consecutive days to

prevent postoperative infection. Following the CO_2-inhalation-induced execution of mice at 8 and 10 weeks, the tissues were fixed for 72 h in 4% paraformaldehyde.

2.5.2 Bone-defect surgery in OVX rats

Thirty 3-month-old female Sprague Dawley rats weighing >200 g (Chengdu Dashuo Experimental Animal Co., Ltd., China) were bilaterally ovariectomized after 1 week of acclimatization. After 8 weeks, OVX rats were placed in a supine position on a heating pad to ensure their body temperature was maintained at 36°C–37°C after anesthesia and skin preparation. The hind limbs of OVX rats were shaved and disinfected, and an incision of approximately 1.5 cm in length was made in the skin of the distal femur to expose the muscle. After a blunt dissection of the muscle to expose the femoral condyles, a circular bone defect of about 3 mm in diameter was drilled perpendicular to the median axis with a medical DC drill at a low speed of 3,000 rpm. To prevent thermal necrosis of cells and tissues, 0.9% saline was continuously flushed during drilling. After drilling, bone fragments were removed from the cavity by rinsing with saline solution. The skin was then sutured using each of the four materials filled into the hole. To avoid infection, penicillin was administered intraperitoneally in three consecutive injections postoperatively. The execution method and time points were similar to those used for mice.

2.5.3 Histological staining

Specimens were decalcified in 10% ethylenediaminetetraacetic acid for 3 weeks at room temperature while being subjected to agitation on a shaker. Specimens were dehydrated in a series of ethanol solutions with concentrations ranging from 75% to 100%, embedded in a paraffin-embedding machine (TKD-BMC, Hubei, China), and sliced into 5-μm-thick posterior sections using a microtome (RM2235, Leica, Germany). Following that, hematoxylin-eosin (HE) staining, Masson's trichrome staining, saffron-solid green (S&G) staining, and tartrate-resistant acid phosphatase (TRAP) staining were performed separately according to the manufacturer's instructions. The images were scanned using a NanoZoomer digital pathology scanner (NDP; Hamamatsu, Japan). Three slices were randomly selected based on HE staining, and new bone areas were automatically measured and calculated using Image-Pro Plus 6.0 (IPP). The formula used to calculate new bone area is as follows: New bone area (%) = new bone area/tissue area × 100%.

2.5.4 Immunohistochemistry

The paraffin sections were deparaffinized, washed, and incubated in antigen repair solution before being treated with hydrogen peroxide. The prepared primary antibody [OCN (1:100, Servicebio)] was added dropwise and incubated overnight at 4°C. The secondary antibody, specifically horseradish peroxidase–labeled rabbit anti-goat IgG (1:200, Servicebio), was introduced and allowed to incubate for 50 min at room temperature. This was followed by the gradual addition of the DAB color development solution and hematoxylin. Positive staining was then quantified using IPP and represented as a percentage of positive area.

2.6 Statistical analysis

Data are expressed as mean ± standard deviation ($\bar{x}$ ± s) and analyzed using SPSS 26.0. The differences between multiple groups were analyzed using a one-way analysis of variance, while the differences between two groups were analyzed using an independent samples *t*-test. A $p < 0.05$ was considered statistically significant (*$p < 0.05$, **$p < 0.01$, ***$p < 0.001$).

3 Results

3.1 Characterization of materials

3.1.1 Surface morphology and composition analysis of Sr-HA/CS

Figure 2 illustrates the morphology and EDS element mapping of Sr-HA powder. SEM analysis revealed the presence of large spheroidal structures on the surface of the powder, which differed from the typical HA structure (Figure 2A). Sr was successfully incorporated into the powder, as evidenced by EDS mapping (Figure 2B). The phase composition of the sample was analyzed using XRD and the most similar HA PDF card was searched using Jade 9.0. Compared to the standard card, in our analysis, the HA and Sr-HA generated showed similar characteristic peaks of HA, specifically at 211, 401, and 313. HA and Sr-HA powders had similar peaks at 31.6°, 45.4°, 56.4°, 66.2°, and 75.2°. However, the peak intensity of Sr-HA was lower, which may be related to the incorporation of Sr (Figure 2C).

3.1.2 Injectability assay

The hydrogel was filled in a 5-mL syringe and squeezed evenly into a Petri dish containing PBS. The squeezed gel was observed in the Petri dish and it retained its original shape (Figure 3A).

3.1.3 Swelling assay

The weight change of the hydrogel before and after 12 h was measured using an electronic balance, and the histogram of the swelling rate was calculated using the formula SR = (W2-W1)/W1. Through statistical analysis, we found that there was no significant difference in swelling rate between Sr-HA/CS and HA/CS ($p > 0.05$, Figure 3B), and the inclusion of Sr may not change the water absorption of the material.

3.2 Evaluation of the antibacterial activity of Sr-HA/CS

To assess the ability of the synthesized materials to inhibit bacterial growth, 0.3 mL of saline (NS) was injected into Petri dishes containing *E. coli* and *S. epidermidis* as control samples. Simultaneously, 0.3 mL of Sr-HA/CS in the ratios of 0.05 g/10 mL (0.05), 0.10 g/10 mL (0.10), and 0.15 g/10 mL (0.15) were added. After 18 h of incubation, a noticeable zone of inhibition was observed around the material, in contrast to the control NS (Figure 3C). The statistical analysis of the diameters of the zones of inhibition, measured using the Vernier calipers, demonstrated that the material exhibited greater efficacy against *E. coli* at all ratios, as depicted in Figure 3D. The concentration of Sr-HA powder had a negligible impact on the inhibition effect at ratios of 0.05 and 0.10 groups. However, between 0.05 and 0.15 groups, the former exhibited a more pronounced inhibition effect, suggesting that Sr does not appear to exert an inhibitory effect in this experiment.

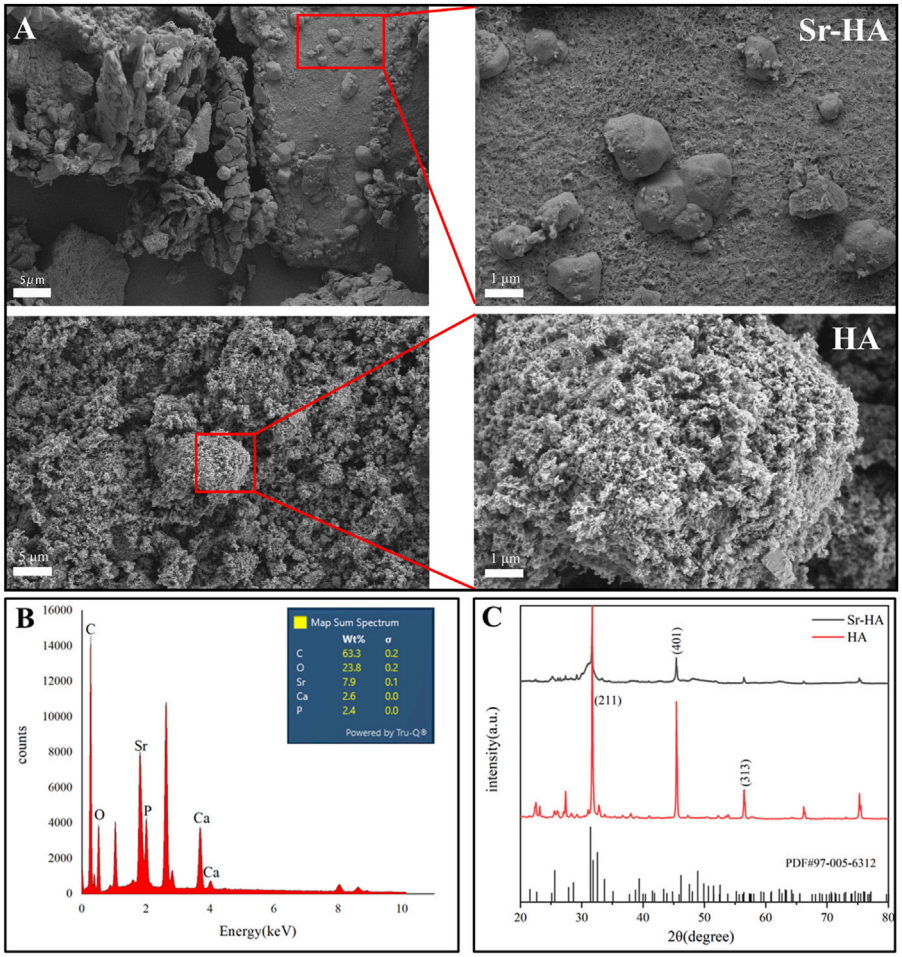

FIGURE 2
Surface morphology and composition analysis of Sr-HA and HA powder. **(A)** SEM images of Sr-HA and HA, **(B)** EDS analysis of Sr-HA, and **(C)** XRD pattern of Sr-HA and HA powder.

3.3 The osteogenic capacity assay of Sr-HA/CS *in vitro*

3.3.1 Cell proliferation

The ideal bone-repair material should possess biocompatibility in addition to effective antimicrobial properties. Therefore, cell viability and proliferation of the materials cultured on days 1, 4, and 7 were assessed using the CCK-8 assay. The results of the CCK-8 assay indicated that there was no statistically significant difference in cell proliferation between the groups ($p > 0.05$) on day 1. However, the Sr-HA/CS group exhibited greater cell viability than the HA/CS group on days 4 and 7 ($p < 0.05$, Figure 4A). There was a noticeable upward trend in cell proliferation for both groups on days 1, 4, and 7. However, the Sr-HA/CS group exhibited a higher level of cell proliferation compared to the HA/CS group ($p < 0.05$, Figure 4B). Calcein-AM staining revealed that SHEDs could proliferated normally on the surface of the hydrogel (Figure 4C).

3.3.2 ALP activity

ALP staining is indicative of the impact of early osteogenic differentiation on cells, while Alizarin Red staining can be used to assess the level of mineralization in late osteogenic cells. After 7 days of culture, ALP staining was darker in the Sr-HA/CS group than in the HA/CS group (Figure 4D). Additionally, the Sr-HA/CS group exhibited higher ALP activity than the HA/CS group. The results of ALP staining and activity on day 14 were in line with the pattern observed on day 7.

3.3.3 Extracellular matrix mineralization

Following a 21-day incubation period, the mineralized bodies underwent treatment. The absorbance at 562 nm in the Sr-HA/CS group (Figure 4E) was higher, however, there was no significant difference between the two groups ($p > 0.05$).

3.4 Ectopic bone formation of Sr-HA/CS *in vivo*

3.4.1 Histological analysis

To investigate the osteoinductive ability of Sr-HA/CS, HE staining was performed on samples obtained from mice at 8 and 10 weeks after implantation. At 8 weeks, immature bone tissue was observed, whereas at 10 weeks, newly formed bone tissue was observed. Additionally, a part of the bone marrow tissue could be observed in the Sr-HA/CS group (Figure 5A). The new bone area of Sr-HA/CS, CAP/CS, and CAP

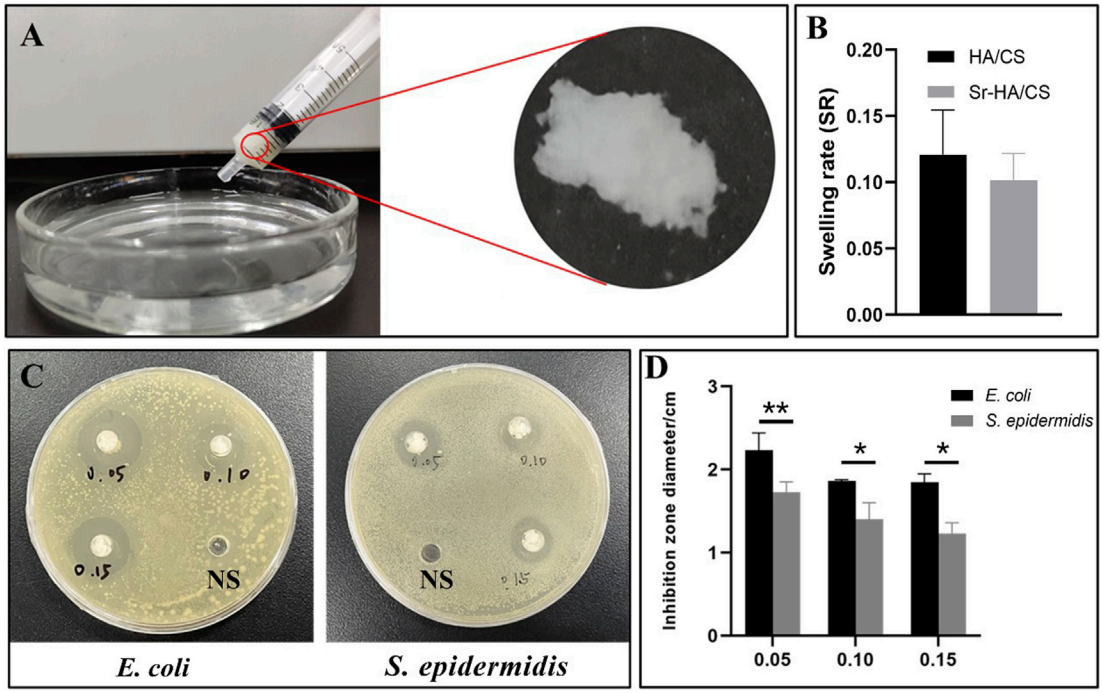

FIGURE 3
The tests on injectability, swelling and antibacterial properties of Sr-HA/CS gel. **(A)** Injectability of Sr-HA/CS. **(B)** Swelling experiments of Sr-HA/CS and HA/CS (n = 3). **(C)** The inhibitory impact of varying concentrations of Sr HA/CS against *E. coli* and *S. epidermidis*. **(D)** Inhibition zone of varying concentrations of Sr-HA/CS against *E. coli* and *S. epidermidis* (n = 3, *p < 0.05, **p < 0.01, upon comparison with HA/CS group).

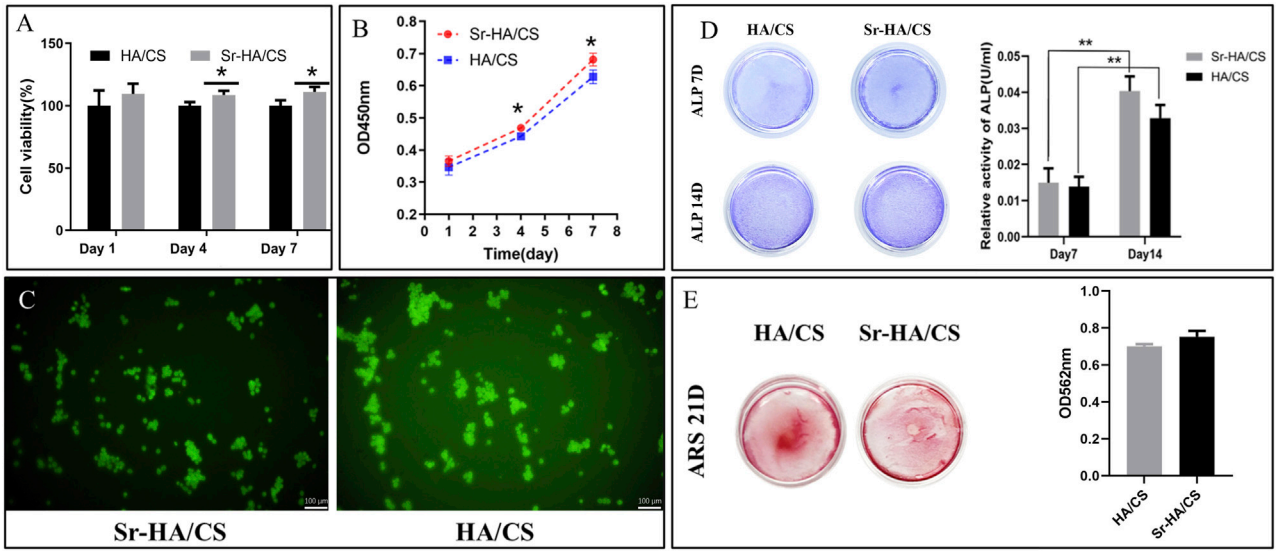

FIGURE 4
(A) Cell viability of Sr-HA/CS and HA/CS (n = 3) on days 1, 4, and 7. **(B)** CCK-8 assay revealing the proliferation capability of SHEDs of the two groups (n = 3). **(C)** Calcein-AM staining following 7 days and inverted fluorescence microscopy for the visualization of cell fluorescence. **(D)** ALP staining of SHEDs after 7 and 14 days of osteoinduction, and quantitative results of ALP staining (n = 3). **(E)** Alizarin Red staining of SHEDs after 21 days of osteoinduction, and quantitative results of Alizarin Red staining (n = 3). (ALP, alkaline phosphatase; *p < 0.05, **p < 0.01; compared with the HA/CS group).

all were greater than that of CS (p < 0.001), but did not differ significantly at 8 weeks (p > 0.05). At 10 weeks, the Sr-HA/CS group exhibited a greater new bone area compared to the other two groups (p < 0.05, p < 0.001). Furthermore, there was no significant difference in bone formation between the CAP/CS and CAP groups (p > 0.05, Figure 5B).

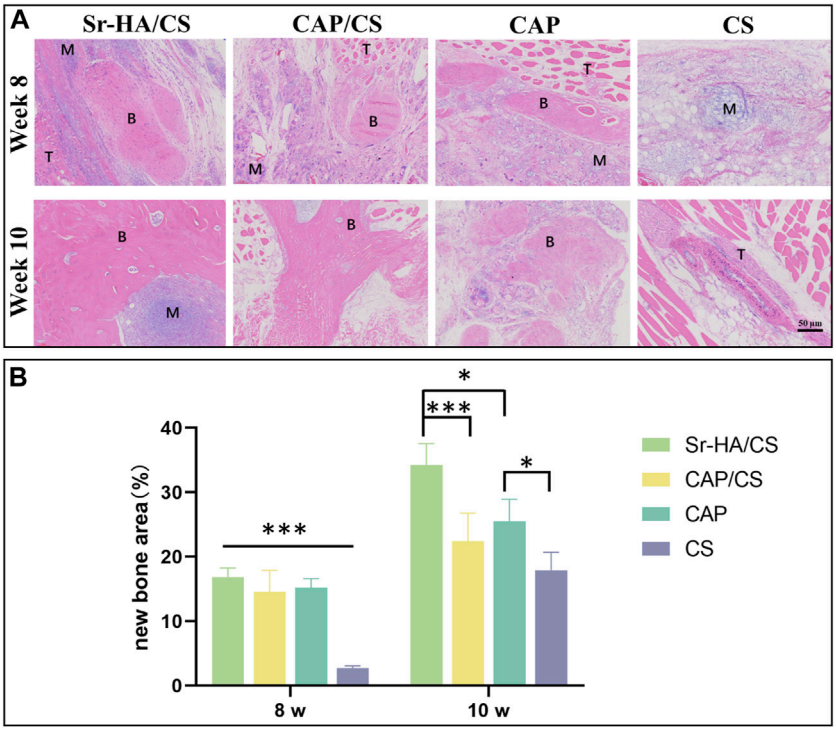

FIGURE 5
Histological analysis of osteoinduction in mice at weeks 8 and 10. **(A)** HE staining (M: material, T: tissue, B: bone; scale bar: 50 μm); **(B)** Quantitative analysis of the ratio of new bone area (n = 3, *p < 0.05, **p < 0.01, ***p < 0.001).

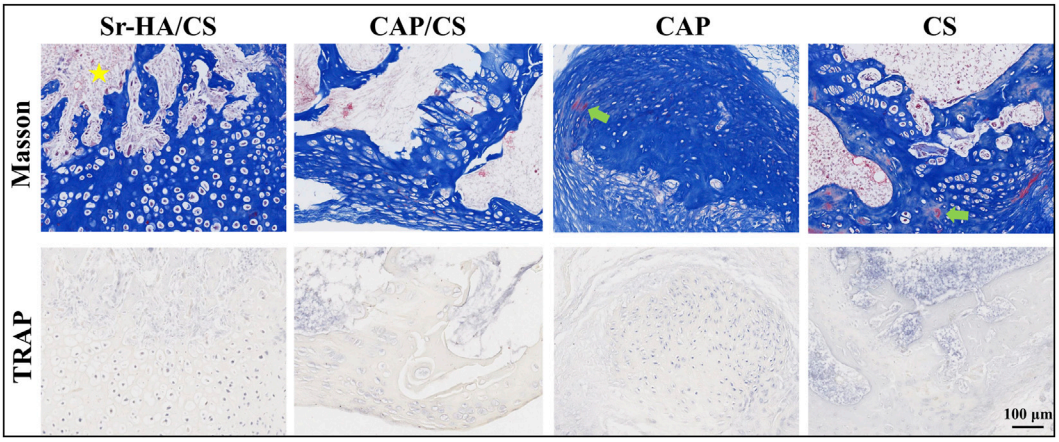

FIGURE 6
Masson's staining and TRAP analysis in mice at week 10. Yellow pentagram: bone marrow tissue; green arrow: red staining, mature bone tissue; scale bar: 100 μm.

3.4.2 Masson's staining and TRAP analysis

Serial sections of 10-week specimens were stained with Masson's and TRAP to more clearly observe the development of new bone. At 10 weeks, the new bone was more mature and showed bone marrow tissue (Figure 6). Figure 6 illustrates that the absence of osteoclasts during TRAP staining suggests that the bone was in the early osteogenesis stage.

3.5 Repairing of bone defects with Sr-HA/CS in OVX rats

3.5.1 Histological analysis

To assess the degree of osteoporosis and observe the healing process at the site of the bone defect, HE staining was applied. The Sr-HA/CS and CAP groups had superior healing as observed by the

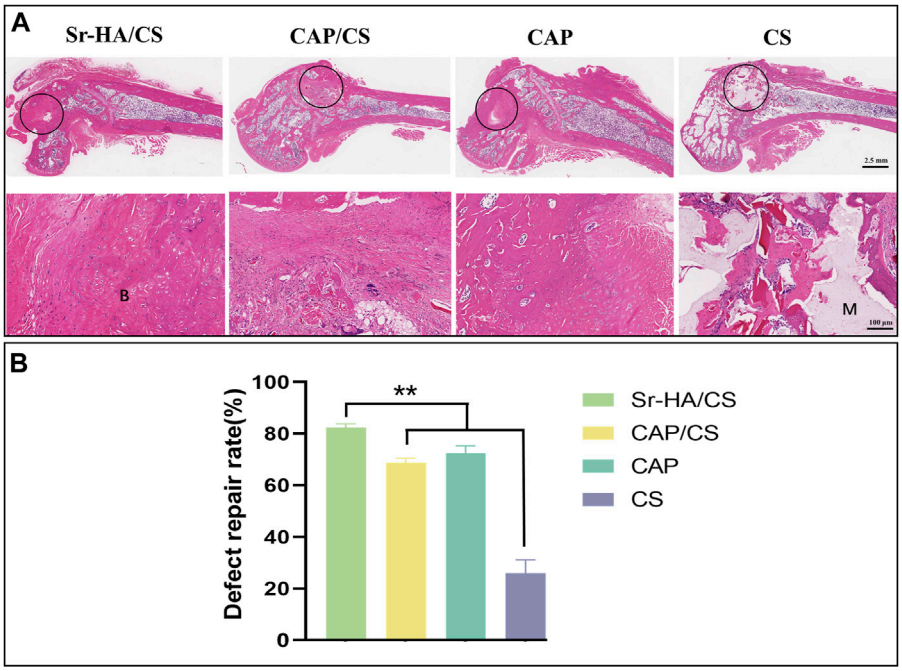

FIGURE 7
Histological analysis of bone defects in OVX rats at week 8. **(A)** HE staining (M: material, B: bone, black circle: bone-defect site; scale bar: 2.5 mm and 100 μm); **(B)** Quantitative analysis of defect repair rate (n = 3, $^{**}p < 0.01$).

naked eye (Figure 7A), which was further confirmed by quantitative analysis (Figure 7B). Meanwhile, the trabeculae of the femoral epiphysis of CS were broken and sparsely arranged (Figure 7A). The remaining three groups displayed superior conditions. The sections exhibited significant growth in which a substantial amount of new bone tissue was generated, including bone marrow tissue. A large number of osteoblasts were seen, including in the CS (Figure 7A). The bone-repair rates of the four groups were as follows: 82.28% ± 1.43%, 69.11% ± 1.59%, 74.61% ± 4.91%, and 24.53% ± 5.11%. The repair rate of the Sr-HA/CS group showed a statistically significant increase compared to both the CAP/CS and CS groups ($p < 0.01$), but was comparable to that of the CAP group ($p > 0.05$).

3.5.2 Masson's staining and S&G staining

Masson's staining and S&G staining of serial sections of the specimens were used to visualize the new bone. Masson's staining demonstrated the presence of distinct blue new bone, and the defects were replaced with lamellar bone and bone marrow. In comparison to the latter two groups, the Sr-HA/CS and CAP/CS groups had more area of new bone formation (Figure 8). The red portion (cartilage) observed in S&G staining suggested that the osteogenic process originated from the cartilage and progressed to the mature bone tissue; however, the defects were predominantly green (Figure 8), suggesting that the bone tissues were more mature at this time. In line with the findings of the Masson's staining analysis, the Sr-HA/CS group showed the most pronounced osteogenesis, whereas the CS group did not demonstrate any obvious or substantial bone formation.

3.5.3 Immunohistochemical and TRAP analyses

To elucidate the mechanism of osteogenesis, serial sections were stained with TRAP and OCN. During the 8-week, OCN-positive areas were observed both at the edges of the defect and in the central region of the newly formed bone (Figure 9A). The Sr-HA/CS group had the highest levels of positive staining, which were found to be considerably greater than those in the CAP and CS groups ($p < 0.05$, Figure 9B). Additionally, the TRAP staining of the multinucleate osteoblasts revealed that osteoblasts were considerably more abundant in the Sr-HA/CS group over the other three groups (Figure 9C), and these osteoblasts were found to be multinucleated (Figure 9A).

4 Discussion

Sr is not only a common component of bone, but also an essential trace element that plays a role in various physiological and biochemical processes in the human body (Pilmane et al., 2017). Recently, Sr has been extensively included in bioactive materials due to its exceptional bone-inducing capability and reduced adverse effects. For example, Cheng et al. (Cheng et al., 2023) prepared strontium ion-functionalized nano-hydroxyapatite/chitosan composite microspheres. The slow release of strontium ions from these microspheres facilitates the osteogenic differentiation of mesenchymal stem cells and the vascularization of endothelial cells, thereby promoting bone regeneration in defect areas. Geng et al. prepared titanium-based implants containing Sr. Through *in vitro* and *in vivo* experiments, they demonstrated that the incorporation of Sr promoted osteoblast

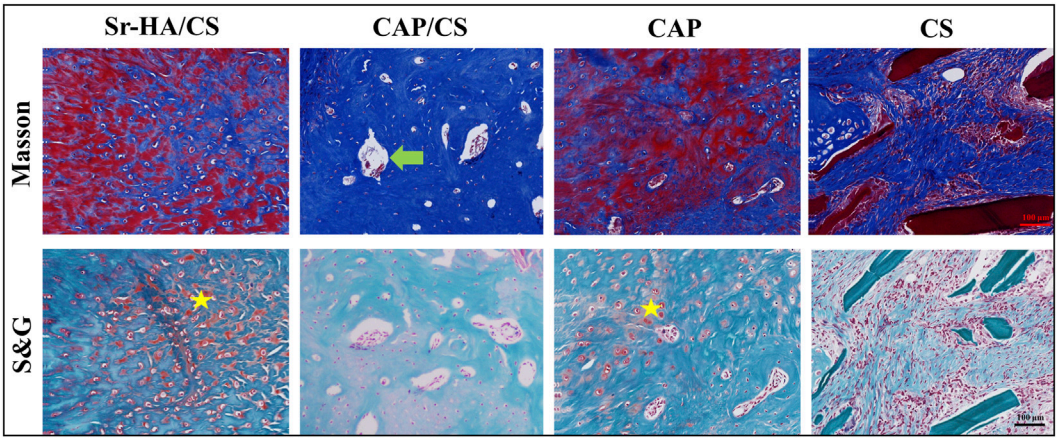

FIGURE 8
Masson's and S&G staining of bone defects in OVX rats. Green arrow: bone marrow tissue; yellow pentagram: cartilage; scale bar: 100 μm.

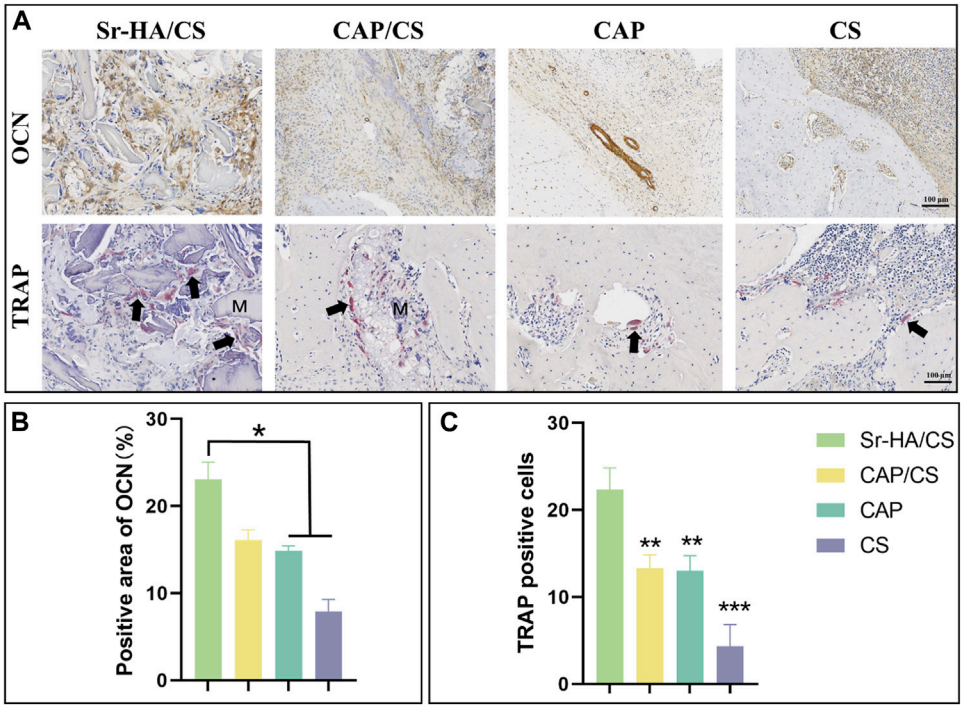

FIGURE 9
Immunohistochemical and TRAP analysis of bone defects in OVX rats. **(A)** OCN and TRAP staining (M: material, black arrow: osteoclast; scale bar: 100 μm); **(B)** Quantitative analysis of the positive area of OCN; **(C)** Quantitative analysis of TRAP-positive cells ($n = 3$, $^{*}p < 0.05$, $^{**}p < 0.01$, $^{***}p < 0.001$).

adhesion and osteogenesis, inhibited osteoclastogenesis, increased bone formation and mineralization, and enhanced the bonding strength of bone implants (Geng et al., 2021; Geng et al., 2022). Studies have shown that Sr-doped biomaterials have superior safety and can induce bone formation and remodeling (Baron and Tsouderos, 2002; Marie et al., 2011; Neves et al., 2017).

The SEM analysis revealed that the Sr-HA powder showed a spheroid structure, while the XRD and EDS peaks confirmed the successful doping of Sr. Injectable biomaterials can provide better filling of defect shapes and therefore achieve better bone-to-material contact even for irregular defects (Kretlow et al., 2007). Furthermore, the XRD pattern demonstrated that the HA and Sr-HA prepared in this investigation exhibit comparable peaks associated with HA, which aligns with the findings reported by Hu et al. (Hu et al., 2020), and strontium doping does not significantly change the crystal structure of HA. Injectability experiments, which demonstrated that the material could be injected with a syringe, allowing the material to pass through

the syringe into the bone-defect site in patients. In a clinical setting, injectable bone-repair materials may lessen the severity of surgically induced tissue fibrosis, reduce treatment expenses, and reduce patient discomfort (Cui et al., 2017). Furthermore, it would be beneficial to conduct additional research into the possibilities of improving mechanical properties through material ratio adjustments and minimizing solidification time *in vivo*.

The cell viability of the material is greater than 100% in all groups, suggesting exceptional biocompatibility of the material. Moreover, no significant cytotoxicity was observed, probably due to the excellent biocompatibility of CS and HA (Tetteh et al., 2014; Hao et al., 2020). Notably, at 4 and 7 days, cell viability was higher in the Sr-HA group, indicating a positive effect with Sr-HA and highlighting the beneficial effect of Sr ions (Pontremoli et al., 2022) in improving the biocompatibility of the material. Furthermore, extracellular ALP activity is an important parameter for determining osteogenic potential in both *in vivo* and *in vitro* (Prins et al., 2014). The ratio of inorganic phosphate (Pi) to inorganic pyrophosphate (Ppi) is crucial in the process of bone mineralization. ALP catalyzes the hydrolysis of Ppi into Pi. Additionally, Ppi inhibits the formation of HA. Therefore, ALP can be considered a reliable marker of bone mineralization (Vimalraj, 2020). At week 2, despite the lack of statistical significance of the results, ALP activity was higher in the Sr-HA group compared to the control group, which indicated Sr-HA had excellent osteogenic potential.

After the occurrence of a bone defect, the presence of a bacterial infection would inevitably impede the process of bone healing during treatment and implantation of biomaterials. Therefore, the implanted biomaterials may exhibit poor performance due to the inflammatory reactions at the site of the defect (Tenti et al., 2014; Neves et al., 2017). Therefore, biomaterials with excellent antibacterial efficacy and biocompatibility can effectively prevent inflammation resulting from bacterial infections. As previously mentioned in the introduction, numerous research has indicated that CS possesses antibacterial properties and can effectively inhibit the growth of several common pathogens. Germicidal efficacy against *E. coli* and *S. epidermidis* was significantly enhanced in this investigation with Sr-HA/CS, particularly against *E. coli*. Furthermore, the release of Sr^{2+} has the potential to impede bacterial activity, including processes such as growth and reproduction, cell wall formation, cell metabolism, and chromosomal replication (Enright et al., 2002; Brauer et al., 2013; Ranga et al., 2019). However, there is controversy regarding the antibacterial capabilities of Sr^{2+} (Sampath Kumar et al., 2015). The present study observed a decline in inhibition as the ratio of Sr-HA increased. This finding aligns with the research conducted by Kumar et al. (Sampath Kumar et al., 2015), which reported that calcium phosphate nanoparticles doped with Sr^{2+} exhibited limited antimicrobial activity against *S. epidermidis* and exhibited no effect against *E. coli*, even at a high concentration of 300 μg/μL. Moreover, Anastasiou et al. (Anastasiou et al., 2019) demonstrated that the antibacterial activity was reduced upon Sr^{2+} addition.

HA is an extremely biocompatible and essential mineral constituent of teeth and bone (Campana et al., 2014). The ability of HA to stimulate osteogenesis in muscle pouches of mice has been previously reported (He et al., 2022). Since calcium phosphate is also capable of inducing bone formation, it was utilized as a positive control while Sr-HA/CS was implanted into the muscle pouches of mice. HE staining revealed that the newborn bone of Sr-HA/CS was substantially different from that of the other three groups at 10 weeks, indicating that it exhibits a favorable osteoinductive property. In contrast, osteoclastogenesis was not detected using TRAP staining during a period of predominant new bone formation and when osteoclasts were not temporarily involved in bone remodeling.

Osteoporosis comprises a collection of bone metabolism disorders characterized by decreased bone mass and increased bone fragility (Wu et al., 2022), which may have a serious effect on the daily life of patients. OVX rats were used for bone-defect experiments. HE staining showed denser bone and more intact bone trabeculae in the Sr-HA/CS group. The Sr-HA/CS group had a significantly higher OCN positive area and TRAP cell count at week 8 compared to the other three groups, but the difference with respect to TRAP was more significant ($p < 0.01$). This could be attributed to the fact that Sr-HA/CS stimulates osteoclasts that promote bone formation during the phase of bone remodeling (Chen et al., 2022). OCN, a calcium-binding protein dependent on vitamin K, is a characteristic biomarker of osteoblasts (Liu et al., 2019). Therefore, it was anticipated that Sr-HA/CS might induce new bone formation via two stages: (1) Initial stage (0–8 weeks): It inhibits osteoclast formation and stimulates osteogenic differentiation of MSCs, thereby promoting OCN secretion; (2) In the late stage of implantation (≥8 weeks): By promoting bone remodeling, Sr-HA/CS facilitated the development of a substantial quantity of mature bone tissues enriched with active osteoclasts (Ranga et al., 2019). Additionally, various studies revealed the potential of Sr^{2+} to promote the proliferation and differentiation of mMSCs through the activation of membrane-bound calcium-sensitive receptors and Wnt/β-linker protein signaling pathways (Yang et al., 2011; Bose et al., 2013). Activation of the Wnt/β-linker protein pathway by Sr^{2+} ions liberated from Sr-HA/CS could potentially account for the enhanced secretion of proteins associated with osteogenesis. Furthermore, an *in vitro* study conducted by Lee et al. (Lee et al., 2021) showed that the incorporation of Sr^{2+} reduced the immune response to the material, thereby promoting bone regeneration *in vitro*. However, further research is required to comprehensively explain the mechanism through which Sr promotes osteogenic differentiation.

5 Conclusion

The current study reported the synthesis of novel injectable Sr-HA/CS with remarkable antibacterial properties against *E. coli* and *S. epidermidis*. *In vitro* studies including cell proliferation, CCK-8 assay, ALP activity, and extracellular matrix mineralization experiments demonstrated that Sr-HA/CS exhibits favorable characteristics for cell proliferation. Moreover, it was found to be non-toxic with the capability to promote osteogenesis. *In vivo* experiments provided evidence regarding the remarkable osteoinductive characteristics exhibited by Sr-HA/CS, as well as its potential in the treatment of osteoporosis and bone defects. Overall, the current findings revealed the potential of Sr-HA/CS to be used as a promising implant to repair bone defects at various sites through minimally invasive surgery.

Data availability statement

The raw data supporting the conclusion of this article will be made available by the authors, without undue reservation.

Ethics statement

All animal experimental protocols were approved by the Animal Ethics Committee of Chengdu University.

Author contributions

LL: Conceptualization, Data curation, Writing–original draft, Writing–review and editing, Formal Analysis, Project administration, Software. SH: Investigation, Supervision, Writing–original draft, Writing–review and editing, Funding acquisition, Validation, Visualization. GX: Formal Analysis, Investigation, Methodology, Resources, Writing–original draft, Writing–review and editing, Funding acquisition, Validation. JG: Methodology, Validation, Visualization, Writing–original draft, Writing–review and editing. JM: Funding acquisition, Investigation, Resources, Validation, Writing–original draft, Writing–review and editing. MG: Conceptualization, Project administration, Supervision, Writing–original draft, Writing–review and editing. JH: Investigation, Visualization, Writing–original draft, Writing–review and editing. XS: Resources, Validation, Writing–original draft, Writing–review and editing. ZY: Data curation, Formal Analysis, Writing–original draft, Writing–review and editing. YL: Conceptualization, Formal Analysis, Funding acquisition, Writing–original draft, Writing–review and editing. TC: Funding acquisition, Validation, Writing–original draft, Writing–review and editing, Investigation. ZD: Investigation, Writing–original draft, Writing–review and editing, Visualization. LC: Funding acquisition, Resources, Supervision, Writing–original draft, Writing–review and editing. ZS: Funding acquisition, Resources, Validation, Writing–original draft, Writing–review and editing.

Funding

The author(s) declare that financial support was received for the research, authorship, and/or publication of this article. This work was supported by the Natural Science Foundation of Sichuan Province, China (2022NSFSC1510), the Medical Scientific Research Project of Chengdu City, China (2021043), the Higher Education Talent Training Quality and Teaching reform project of the Education Department of Sichuan Province, China (JG 2021-1102), Innovation team project of Clinical Medical college and Affiliated hospital of Chengdu University (CDFYCX202208), and Sichuan Provincial Science and Technology Foundation (22NZZH0031).

Conflict of interest

The authors declare that the research was conducted in the absence of any commercial or financial relationships that could be construed as a potential conflict of interest.

Publisher's note

All claims expressed in this article are solely those of the authors and do not necessarily represent those of their affiliated organizations, or those of the publisher, the editors and the reviewers. Any product that may be evaluated in this article, or claim that may be made by its manufacturer, is not guaranteed or endorsed by the publisher.

References

Ahn, K. J., Kim, Y. K., and Yun, P. Y. (2014). Reconstruction of defect after treatment of bisphosphonate-related osteonecrois of the jaw with staged iliac bone graft. *Maxillofac. plastic Reconstr. Surg.* 36 (2), 57–61. doi:10.14402/jkamprs.2014.36.2.57

Anastasiou, A. D., Nerantzaki, M., Gounari, E., Duggal, M. S., Giannoudis, P. V., Jha, A., et al. (2019). Antibacterial properties and regenerative potential of Sr(2+) and Ce(3+) doped fluorapatites; a potential solution for peri-implantitis. *Sci. Rep.* 9 (1), 14469. doi:10.1038/s41598-019-50916-4

Baron, R., and Tsouderos, Y. (2002). *In vitro* effects of S12911-2 on osteoclast function and bone marrow macrophage differentiation. *Eur. J. Pharmacol.* 450 (1), 11–17. doi:10.1016/s0014-2999(02)02040-x

Boanini, E., Gazzano, M., and Bigi, A. (2010). Ionic substitutions in calcium phosphates synthesized at low temperature. *Acta biomater.* 6 (6), 1882–1894. doi:10.1016/j.actbio.2009.12.041

Bonnelye, E., Chabadel, A., Saltel, F., and Jurdic, P. (2008). Dual effect of strontium ranelate: stimulation of osteoblast differentiation and inhibition of osteoclast formation and resorption *in vitro*. *Bone* 42 (1), 129–138. doi:10.1016/j.bone.2007.08.043

Bose, S., Fielding, G., Tarafder, S., and Bandyopadhyay, A. (2013). Understanding of dopant-induced osteogenesis and angiogenesis in calcium phosphate ceramics. *Trends Biotechnol.* 31 (10), 594–605. doi:10.1016/j.tibtech.2013.06.005

Brauer, D. S., Karpukhina, N., Kedia, G., Bhat, A., Law, R. V., Radecka, I., et al. (2013). Bactericidal strontium-releasing injectable bone cements based on bioactive glasses. *J. R. Soc. Interface* 10 (78), 20120647. doi:10.1098/rsif.2012.0647

Campana, V., Milano, G., Pagano, E., Barba, M., Cicione, C., Salonna, G., et al. (2014). Bone substitutes in orthopaedic surgery: from basic science to clinical practice. *J. Mater. Sci. Mater. Med.* 25, 2445–2461. doi:10.1007/s10856-014-5240-2

Campoccia, D., Montanaro, L., and Arciola, C. R. (2006). The significance of infection related to orthopedic devices and issues of antibiotic resistance. *Biomaterials* 27 (11), 2331–2339. doi:10.1016/j.biomaterials.2005.11.044

Caudrillier, A., Hurtel-Lemaire, A.-S., Wattel, A., Cournarie, F., Godin, C., Petit, L., et al. (2010). Strontium ranelate decreases receptor activator of nuclear factor-κB ligand-induced osteoclastic differentiation *in vitro*: involvement of the calcium-sensing receptor. *Mol. Pharmacol.* 78 (4), 569–576. doi:10.1124/mol.109.063347

Chattopadhyay, N., Quinn, S. J., Kifor, O., Ye, C., and Brown, E. M. (2007). The calcium-sensing receptor (CaR) is involved in strontium ranelate-induced osteoblast proliferation. *Biochem. Pharmacol.* 74 (3), 438–447. doi:10.1016/j.bcp.2007.04.020

Chen, F., Tian, L., Pu, X., Zeng, Q., Xiao, Y., Chen, X., et al. (2022). Enhanced ectopic bone formation by strontium-substituted calcium phosphate ceramics through regulation of osteoclastogenesis and osteoblastogenesis. *Biomaterials Sci.* 10 (20), 5925–5937. doi:10.1039/d2bm00348a

Cheng, D., Ding, R., Jin, X., Lu, Y., Bao, W., Zhao, Y., et al. (2023). Strontium ion-functionalized nano-hydroxyapatite/chitosan composite microspheres promote osteogenesis and angiogenesis for bone regeneration. *ACS Appl. Mater. interfaces* 15 (16), 19951–19965. doi:10.1021/acsami.3c00655

Croisier, F., and Jérôme, C. (2013). Chitosan-based biomaterials for tissue engineering. *Eur. Polym. J.* 49 (4), 780–792. doi:10.1016/j.eurpolymj.2012.12.009

Cui, X., Huang, W., Zhang, Y., Huang, C., Yu, Z., Wang, L., et al. (2017). Evaluation of an injectable bioactive borate glass cement to heal bone defects in a rabbit femoral condyle model. *Mater. Sci. Eng. C* 73, 585–595. doi:10.1016/j.msec.2016.12.101

Diepenhorst, N. A., Leach, K., Keller, A. N., Rueda, P., Cook, A. E., Pierce, T. L., et al. (2018). Divergent effects of strontium and calcium-sensing receptor positive allosteric

modulators (calcimimetics) on human osteoclast activity. *Br. J. Pharmacol.* 175 (21), 4095–4108. doi:10.1111/bph.14344

Di Martino, A., Sittinger, M., and Risbud, M. V. (2005). Chitosan: a versatile biopolymer for orthopaedic tissue-engineering. *Biomaterials* 26 (30), 5983–5990. doi:10.1016/j.biomaterials.2005.03.016

Enright, M. C., Robinson, D. A., Randle, G., Feil, E. J., Grundmann, H., and Spratt, B. G. (2002). The evolutionary history of methicillin-resistant *Staphylococcus aureus* (MRSA). *Proc. Natl. Acad. Sci.* 99 (11), 7687–7692. doi:10.1073/pnas.122108599

Gao, C., Deng, Y., Feng, P., Mao, Z., Li, P., Yang, B., et al. (2014). Current progress in bioactive ceramic scaffolds for bone repair and regeneration. *Int. J. Mol. Sci.* 15 (3), 4714–4732. doi:10.3390/ijms15034714

Geng, Z., Cheng, Y., Ma, L., Li, Z., Cui, Z., Zhu, S., et al. (2018). Nanosized strontium substituted hydroxyapatite prepared from egg shell for enhanced biological properties. *J. biomaterials Appl.* 32 (7), 896–905. doi:10.1177/0885328217748124

Geng, Z., Li, X., Ji, L., Li, Z., Zhu, S., Cui, Z., et al. (2021). A novel snail-inspired bionic design of titanium with strontium-substituted hydroxyapatite coating for promoting osseointegration. *J. Mater. Sci. Technol.* 79, 35–45. doi:10.1016/j.jmst.2020.11.041

Geng, Z., Sang, S., Wang, S., Meng, F., Li, Z., Zhu, S., et al. (2022). Optimizing the strontium content to achieve an ideal osseointegration through balancing apatite-forming ability and osteogenic activity. *Biomater. Adv.* 133, 112647. doi:10.1016/j.msec.2022.112647

Geng, Z., Wang, R., Li, Z., Cui, Z., Zhu, S., Liang, Y., et al. (2016). Synthesis, characterization and biological evaluation of strontium/magnesium-co-substituted hydroxyapatite. *J. biomaterials Appl.* 31 (1), 140–151. doi:10.1177/0885328216633892

Glenske, K., Donkiewicz, P., Köwitsch, A., Milosevic-Oljaca, N., Rider, P., Rofall, S., et al. (2018). Applications of metals for bone regeneration. *Int. J. Mol. Sci.* 19 (3), 826. doi:10.3390/ijms19030826

Hao, R., Peng, X., Zhang, Y., Chen, J., Wang, T., Wang, W., et al. (2020). Rapid hemostasis resulting from the synergism of self-assembling short peptide and O-carboxymethyl chitosan. *ACS Appl. Mater. interfaces* 12 (50), 55574–55583. doi:10.1021/acsami.0c15480

He, Y., Peng, Y., Liu, L., Hou, S., Mu, J., Lan, L., et al. (2022). The relationship between osteoinduction and vascularization: comparing the ectopic bone formation of five different calcium phosphate biomaterials. *Materials* 15 (10), 3440. doi:10.3390/ma15103440

Hu, B., Meng, Z. D., Zhang, Y. Q., Ye, L. Y., Wang, C. J., and Guo, W. C. (2020). Sr-HA scaffolds fabricated by SPS technology promote the repair of segmental bone defects. *Tissue Cell.* 66, 101386. doi:10.1016/j.tice.2020.101386

Khattak, S., Wahid, F., Liu, L. P., Jia, S. R., Chu, L. Q., Xie, Y. Y., et al. (2019). Applications of cellulose and chitin/chitosan derivatives and composites as antibacterial materials: current state and perspectives. *Appl. Microbiol. Biotechnol.* 103, 1989–2006. doi:10.1007/s00253-018-09602-0

Kretlow, J. D., Klouda, L., and Mikos, A. G. (2007). Injectable matrices and scaffolds for drug delivery in tissue engineering. *Adv. drug Deliv. Rev.* 59 (4-5), 263–273. doi:10.1016/j.addr.2007.03.013

Lee, N. H., Kang, M. S., Kim, T. H., Yoon, D. S., Mandakhbayar, N., Jo, S. B., et al. (2021). Dual actions of osteoclastic-inhibition and osteogenic-stimulation through strontium-releasing bioactive nanoscale cement imply biomaterial-enabled osteoporosis therapy. *Biomaterials* 276, 121025. doi:10.1016/j.biomaterials.2021.121025

Li, D., Liu, P., Hao, F., Lv, Y., Xiong, W., Yan, C., et al. (2022). Preparation and application of silver/chitosan-sepiolite materials with antimicrobial activities and low cytotoxicity. *Int. J. Biol. Macromol.* 210, 337–349. doi:10.1016/j.ijbiomac.2022.05.015

Li, Y., Li, Q., Zhu, S., Luo, E., Li, J., Feng, G., et al. (2010). The effect of strontium-substituted hydroxyapatite coating on implant fixation in ovariectomized rats. *Biomaterials* 31 (34), 9006–9014. doi:10.1016/j.biomaterials.2010.07.112

Liu, Z., Yu, Z., Chang, H., Wang, Y., Xiang, H., Zhang, X., et al. (2019). Strontium-containing α-calcium sulfate hemihydrate promotes bone repair via the TGF-β/Smad signaling pathway. *Mol. Med. Rep.* 20 (4), 3555–3564. doi:10.3892/mmr.2019.10592

Madihally, S. V., and Matthew, H. W. (1999). Porous chitosan scaffolds for tissue engineering. *Biomaterials* 20 (12), 1133–1142. doi:10.1016/S0142-9612(99)00011-3

Marie, P., Felsenberg, D., and Brandi, M. L. (2011). How strontium ranelate, via opposite effects on bone resorption and formation, prevents osteoporosis. *Osteoporos. Int.* 22, 1659–1667. doi:10.1007/s00198-010-1369-0

Mercado-Pagán, Á. E., Stahl, A. M., Shanjani, Y., and Yang, Y. (2015). Vascularization in bone tissue engineering constructs. *Ann. Biomed. Eng.* 43, 718–729. doi:10.1007/s10439-015-1253-3

Meunier, P., Roux, C., Ortolani, S., Diaz-Curiel, M., Compston, J., Marquis, P., et al. (2009). Effects of long-term strontium ranelate treatment on vertebral fracture risk in postmenopausal women with osteoporosis. *Osteoporos. Int.* 20, 1663–1673. doi:10.1007/s00198-008-0825-6

Meunier, P. J., Roux, C., Seeman, E., Ortolani, S., Badurski, J. E., Spector, T. D., et al. (2004). The effects of strontium ranelate on the risk of vertebral fracture in women with postmenopausal osteoporosis. *N. Engl. J. Med.* 350 (5), 459–468. doi:10.1056/NEJMoa022436

Myeroff, C., and Archdeacon, M. (2011). Autogenous bone graft: donor sites and techniques. *J. bone Jt. Surg.* 93 (23), 2227–2236. doi:10.2106/JBJS.J.01513

Neves, N., Linhares, D., Costa, G., Ribeiro, C., and Barbosa, M. (2017). *In vivo* and clinical application of strontium-enriched biomaterials for bone regeneration: a systematic review. *Bone and Jt. Res.* 6 (6), 366–375. doi:10.1302/2046-3758.66.BJR-2016-0311.R1

Pilmane, M., Salma-Ancane, K., Loca, D., Locs, J., and Berzina-Cimdina, L. (2017). Strontium and strontium ranelate: historical review of some of their functions. *Mater. Sci. Eng. C* 78, 1222–1230. doi:10.1016/j.msec.2017.05.042

Pontremoli, C., Boffito, M., Laurano, R., Iviglia, G., Torre, E., Cassinelli, C., et al. (2022). Mesoporous bioactive glasses incorporated into an injectable thermosensitive hydrogel for sustained Co-release of Sr^{2+} ions and N-acetylcysteine. *Pharmaceutics* 14 (9), 1890. doi:10.3390/pharmaceutics14091890

Prins, H. J., Braat, A. K., Gawlitta, D., Dhert, W. J., Egan, D. A., Tijssen-Slump, E., et al. (2014). *In vitro* induction of alkaline phosphatase levels predicts *in vivo* bone forming capacity of human bone marrow stromal cells. *Stem Cell. Res.* 12 (2), 428–440. doi:10.1016/j.scr.2013.12.001

Ranga, N., Poonia, E., Jakhar, S., Sharma, A. K., Kumar, A., Devi, S., et al. (2019). Enhanced antimicrobial properties of bioactive glass using strontium and silver oxide nanocomposites. *J. Asian Ceram. Soc.* 7 (1), 75–81. doi:10.1080/21870764.2018.1564477

Rezwan, K., Chen, Q., Blaker, J. J., and Boccaccini, A. R. (2006). Biodegradable and bioactive porous polymer/inorganic composite scaffolds for bone tissue engineering. *Biomaterials* 27 (18), 3413–3431. doi:10.1016/j.biomaterials.2006.01.039

Saidak, Z., Haÿ, E., Marty, C., Barbara, A., and Marie, P. J. (2012). Strontium ranelate rebalances bone marrow adipogenesis and osteoblastogenesis in senescent osteopenic mice through NFATc/Maf and Wnt signaling. *Aging Cell.* 11 (3), 467–474. doi:10.1111/j.1474-9726.2012.00804.x

Sampath Kumar, T. S., Madhumathi, K., Rubaiya, Y., and Doble, M. (2015). Dual mode antibacterial activity of ion substituted calcium phosphate nanocarriers for bone infections. *Front. Bioeng. Biotechnol.* 3, 59. doi:10.3389/fbioe.2015.00059

Silva Filho, O. G. d., Ozawa, T. O., Bachega, C., and Bachega, M. A. (2013). Reconstruction of alveolar cleft with allogenous bone graft: clinical considerations. *Dent. press J. Orthod.* 18, 138–147. doi:10.1590/s2176-94512013000600021

Tenti, S., Cheleschi, S., Guidelli, G. M., Galeazzi, M., and Fioravanti, A. (2014). What about strontium ranelate in osteoarthritis? Doubts and securities. *Mod. Rheumatol.* 24 (6), 881–884. doi:10.3109/14397595.2014.888156

Tetteh, G., Khan, A., Delaine-Smith, R., Reilly, G., and Rehman, I. (2014). Electrospun polyurethane/hydroxyapatite bioactive Scaffolds for bone tissue engineering: the role of solvent and hydroxyapatite particles. *J. Mech. Behav. Biomed. Mater.* 39, 95–110. doi:10.1016/j.jmbbm.2014.06.019

Venkatesan, J., and Kim, S.-K. (2010). Chitosan composites for bone tissue engineering—an overview. *Mar. drugs* 8 (8), 2252–2266. doi:10.3390/md8082252

Vimalraj, S. (2020). Alkaline phosphatase: structure, expression and its function in bone mineralization. *Gene* 754, 144855. doi:10.1016/j.gene.2020.144855

Wang, S., Yang, Y., Li, Y., Shi, J., Zhou, J., Zhang, L., et al. (2019). Strontium/adiponectin co-decoration modulates the osteogenic activity of nano-morphologic polyetheretherketone implant. *Colloids Surfaces B Biointerfaces* 176, 38–46. doi:10.1016/j.colsurfb.2018.12.056

Wu, Q., Hu, L., Yan, R., Shi, J., Gu, H., Deng, Y., et al. (2022). Strontium-incorporated bioceramic scaffolds for enhanced osteoporosis bone regeneration. *Bone Res.* 10 (1), 55. doi:10.1038/s41413-022-00224-x

Yang, F., Yang, D., Tu, J., Zheng, Q., Cai, L., and Wang, L. (2011). Strontium enhances osteogenic differentiation of mesenchymal stem cells and *in vivo* bone formation by activating Wnt/catenin signaling. *Stem cells* 29 (6), 981–991. doi:10.1002/stem.646

Yuan, K., Chan, Y. J., Kung, K. C., and Lee, T. M. (2014). Comparison of osseointegration on various implant surfaces after bacterial contamination and cleaning: a rabbit study. *Int. J. Oral Maxillofac. Implants* 29 (1), 32–40. doi:10.11607/jomi.2436

Zhang, W., Cao, H., Zhang, X., Li, G., Chang, Q., Zhao, J., et al. (2016). A strontium-incorporated nanoporous titanium implant surface for rapid osseointegration. *Nanoscale* 8 (9), 5291–5301. doi:10.1039/c5nr08580b

frontiers | Frontiers in Bioengineering and Biotechnology

TYPE Original Research
PUBLISHED 19 April 2024
DOI 10.3389/fbioe.2024.1372636

OPEN ACCESS

EDITED BY
Hongye Yang,
Wuhan University, China

REVIEWED BY
Dana Akilbekova,
Nazarbayev University, Kazakhstan
Guowen Qian,
Jiangxi University of Science and Technology, China
Zhengwei You,
Donghua University, China

*CORRESPONDENCE
Xiaowu Li,
xwli@mail.neu.edu.cn
Xing Zhang,
xingzhang@imr.ac.cn

RECEIVED 18 January 2024
ACCEPTED 08 April 2024
PUBLISHED 19 April 2024

CITATION
Xu Q, Bai Y, Li S, Hou W, Hao Y, Yang R, Li X and Zhang X (2024), Enhancing osteogenesis and angiogenesis functions for Ti-24Nb-4Zr-8Sn scaffolds with methacrylated gelatin and deferoxamine.
Front. Bioeng. Biotechnol. 12:1372636.
doi: 10.3389/fbioe.2024.1372636

Enhancing osteogenesis and angiogenesis functions for Ti-24Nb-4Zr-8Sn scaffolds with methacrylated gelatin and deferoxamine

Qian Xu[1,2], Yun Bai[2,3], Shujun Li[2,3], Wentao Hou[2,3], Yulin Hao[2,3], Rui Yang[2,3], Xiaowu Li[1]* and Xing Zhang[2,3]*

[1]Department of Materials Physics and Chemistry, School of Materials Science and Engineering, Key Laboratory for Anisotropy and Texture of Materials, Ministry of Education, Northeastern University, Shenyang, Liaoning, China, [2]Institute of Metal Research, Chinese Academy of Sciences, Shenyang, Liaoning, China, [3]School of Materials Science and Engineering, University of Science and Technology of China, Hefei, Anhui, China

Repair of large bone defects remains challenge for orthopedic clinical treatment. Porous titanium alloys have been widely fabricated by the additive manufacturing, which possess the elastic modulus close to that of human cortical bone, good osteoconductivity and osteointegration. However, insufficient bone regeneration and vascularization inside the porous titanium scaffolds severely limit their capability for repair of large-size bone defects. Therefore, it is crucially important to improve the osteogenic function and vascularization of the titanium scaffolds. Herein, methacrylated gelatin (GelMA) were incorporated with the porous Ti-24Nb-4Zr-8Sn (Ti2448) scaffolds prepared by the electron beam melting (EBM) method (Ti2448-GelMA). Besides, the deferoxamine (DFO) as an angiogenic agent was doped into the Ti2448-GelMA scaffold (Ti2448-GelMA/DFO), in order to promote vascularization. The results indicate that GelMA can fully infiltrate into the pores of Ti2448 scaffolds with porous cross-linked network (average pore size: 120.2 ± 25.1 μm). Ti2448-GelMA scaffolds facilitated the differentiation of MC3T3-E1 cells by promoting the ALP expression and mineralization, with the amount of calcium contents ~2.5 times at day 14, compared with the Ti2448 scaffolds. Impressively, the number of vascular meshes for the Ti2448-GelMA/DFO group (~7.2/mm^2) was significantly higher than the control group (~5.3/mm^2) after cultivation for 9 h, demonstrating the excellent angiogenesis ability. The Ti2448-GelMA/DFO scaffolds also exhibited sustained release of DFO, with a cumulative release of 82.3% after 28 days. Therefore, Ti2448-GelMA/DFO scaffolds likely provide a new strategy to improve the osteogenesis and angiogenesis for repair of large bone defects.

KEYWORDS

Ti2448, GelMA, bone scaffolds, deferoxamine, angiogenesis

1 Introduction

The large bone defect repair remains challenging for orthopedic clinical treatment (Vidal et al., 2020; Zhang et al., 2023). With the advances of 3D printing technology, porous titanium alloys have been widely developed as bone scaffolds, due to good osteoconductivity and osteointegration (Niinomi et al., 2016; Chen et al., 2023; Yuan et al., 2023). Previous studies have found that 3D printed Ti-24Nb-4Zr-8Sn (Ti2448) showed the good biocompatibility and low elastic modulus, close to that of the human bone (Nune et al., 2017a; Tang et al., 2021). Nevertheless, the bare scaffolds lack the bioactive components that are critical for stimulating osteogenesis (Jahr et al., 2021). Moreover, the growth of blood vessels inside the bone scaffold remains great challenge for large bone defect repair. (Koons et al., 2020). Thus, the development of porous titanium alloys with improved bioactivity is of particular interest.

The vascularization is crucially important for repair of large bone defects (Wang et al., 2018). After the bone fracture, the inflammation and hematoma are immediately established, following by the formation of blood clots at ~1–5 days (Yang and Xiao, 2020). During the soft callus formation at ~5–16 days, the endothelial cells from the blood vessels provide angiocrine factors such as BMP-2, Noggin and IL-33 to the osteoprogenitor cells or mesenchymal stem cells (MSCs), leading to the cell differentiation to osteoblasts and further ossification (Chen et al., 2020; Salhotra et al., 2020). During the hard callus formation at ~16–21 days, osteoblasts can secrete angiogenic factors such as VEGF and FGF, which act on endothelial cells and further promote the vascular growth (Raines et al., 2019; Hendriks and Ramasamy, 2020; Chen et al., 2021). During the remodeling stage at ~21–35 days, blood vessels can also participate in clearing the bone metabolites and improve the repair effects. Thus, blood vessel formation and bone regeneration occur in a coupled manner (Liu and Castillo, 2018; Ha et al., 2022). Sufficient blood vessels distributed in distance ~100–300 μm are critical to ensure the sufficient supply of oxygen and nutrients, as well as removal of waste products (Marrella et al., 2018). While the number of blood vessels is not enough, cell death, inadequate and delayed blood circulation may occur, ultimately causing inner bone tissue necrosis (Kang et al., 2016; Liu et al., 2017; Marrella et al., 2018). For example, the 3D-printed porous Ti6Al4V scaffolds were implanted in the longitudinal axis of rabbit radius (1.5 cm in length) (Ma et al., 2021). Post surgery for 12 weeks, only a few newly formed bone tissues were found inside the porous Ti6Al4V scaffolds with sparse blood vessels (Ma et al., 2021). The collagen modified titanium-based implants induced angiogenic activity via *in vitro* tubule formation as compared to bared titanium-based implants, but no differences were noticed in angiogenesis and osteointegration *in vivo*. However, by incorporating the vascular endothelial growth factors (VEGF) into the collagen modified titanium-based implants, both bone growth and vascular regeneration were significantly improved (Li J et al., 2021). Therefore, achieving effective vascular regeneration during the repair of large bone defects remains a great challenge.

DFO is a commonly used drug, which can activate the HIF-1α pathway by chelating Fe^{3+}, thereby promoting the expression of downstream signaling molecule VEGF, and facilitating vascular regeneration (Ran et al., 2018; Cheng et al., 2020; Xue et al., 2020). However, DFO can be easily filtered and cleared by kidneys, resulting in a relatively short drug residence time in the human body ($t_{1/2}$ = 5 min, in mice) (Park et al., 2022). Therefore, suitable carriers are necessitate to sustained release of DFO with extended life time. For example, DFO-gelatin microspheres loaded with type I collagen and fibronectin were prepared and dispersed in 10 mL PBS at 37°C, which showed a long sustained release of DFO up to 20 days (Zeng et al., 2022). Herein, the biocompatible methacryloyl group-grafted gelatin denoted as GelMA has been selected for DFO loading, which can be incorporated into the porous Ti2448 scaffolds, which may promote internal vascularization and further bone regeneration.

In this study, 3D printed Ti2448 scaffolds with low elastic modulus have been selected as the loading-bearing part (Liu et al., 2016; Li et al., 2019). Ti2448-GelMA scaffolds are further prepared. DFO is then doped into the Ti2448-GelMA scaffold as the angiogenic agent. The chemical composition and micro-structures of Ti2448-GelMA and Ti2448-GelMA/DFO scaffolds are characterized. The proliferation, adhesion, and differentiation of MC3T3-E1 cells cultured on these scaffolds are evaluated. Additionally, the angiogenic effects of DFO are investigated by culturing human umbilical vascular endothelial cells (HUVECs) on the Ti2448-GelMA/DFO scaffolds. The release of DFO from the Ti2448-GelMA/DFO scaffolds has also been investigated. The Ti2448-GelMA/DFO scaffolds as prepared can obviously enhance the osteogenic differentiation ability and vascular regeneration, demonstrating great potential application or large bone defect repair.

2 Experimental procedure

2.1 The synthesis and characterization of GelMA

Type A porcine skin gelatin (Sigma, St. Louis, USA) was fully dissolved in phosphate buffer saline (PBS) solution at 50°C (10% w/v). The methacrylic anhydride (MAA, 8% v/v) was then added and stirred at 200 rpm for 24 h. Dulbecco's phosphate-buffered saline (DPBS) was preheated to 50°C under the same volume with PBS. The preheated DPBS was then mixed with the above mixed solution at 50°C for 10 min. The final solution was dialyzed against distilled water at 40°C for 5 days, using a dialysis membrane with 12–14 kDa cutoff (Fisher Scientific, Waltham, USA), then lyophilized for 5 days to yield the purified gelatin methacrylate (GelMA).

2.2 The fabrication of Ti2448-GelMA and Ti2448-GelMA/DFO scaffolds

The 3D-printed porous Ti2448 scaffolds were prepared by an Arcam A1 EBM system (Arcam, Gothenburg, Sweden), following the same method as previously reported (Xu et al., 2022). In brief, the scaffold models (9.50 mm × 9.50 mm × 2.50 mm) with a nominal 70% porosity were created. The Ti2448 powders (particle size ~45–106 μm) were preheated to 773 K before melting. The samples were produced with a scan speed of 130 mm/s, a voltage of 60 kV, and a vacuum of 2×10^{-3} mbar.

The lithium phenyl-2,4,6-trimethylbenzoylphosphinate (LAP) photoinitiator (0.1% w/v) was added to the GelMA solution in PBS (5% w/v), and then filtered through 0.22 μm membrane filter. 100 μL GelMA solution was added to the Ti2448 scaffolds, which was exposed to the UV light (365 nm) both top and bottom sides for 2 min. The samples were then lyophilized for 24 h, denoted as Ti2448-GelMA. The DFO powder was added to the above 5% w/v GelMA solution, with the final DFO concentration of 0.5 wt%, and LAP was then added. Following the same procedure as Ti2448-GelMA preparation, Ti2448-GelMA scaffolds loaded with DFO are acquired and denoted as Ti2448-GelMA/DFO.

2.3 The characterization of GelMA and Ti2448-GelMA scaffolds

The chemical structure of gelatin and GelMA was characterized by ^{1}H nuclear magnetic resonance spectrometer (^{1}H-NMR) with a Bruker Avance Neo 400 spectrometer (Bruker, Bremen, Germany) using D_2O as the solvent.

Fourier transform infrared spectrometry (FTIR, Agilent Technologies, California, USA) was conducted in the range of 400–4,000 cm^{-1}. The crystal information was measured by X-ray diffraction (Rigaku, Tokyo, Japan) using the radiation of Cu Kα radiation (λ = 1.5418 Å). The surface morphology and elemental analysis was investigated by a scanning electron microscope (SEM, Carl Zeiss AG, Jena, Germany) equipped with energy dispersive spectroscopy (EDS, Oxford Instruments, Abingdon, UK). The mean pore size of GelMA network was evaluated by the ImageJ software based on SEM images.

2.4 Cell viability and proliferation

MC3T3-E1 cells were purchased from the Cell Bank of the Chinese Academy of Sciences (Shanghai, China), and incubated in the α-MEM medium (Hyclone, GE Healthcare, Chicago, USA) supplemented with 10% FBS (Lonsera, Uruguay) and 1% antibiotic/antimycotic (Gen-View Scientific Inc., Calimesa, USA). MC3T3-E1 cells (3×10^4 cells/scaffolds) were seeded on both Ti2448 and Ti2448-GelMA scaffolds in a 48-well plate for 1, 3, and 5 days. The cytotoxicity was evaluated by the CCK-8 reagent (Gen-View Scientific Inc., Calimesa, USA). Briefly, the 100 μL mixture (10 μL CCK-8 and 90 μL culture medium) was added to each well for 3 h and the OD value was measured with a microplate reader (Multiskan Go, Thermo Fisher Scientific, Waltham, USA) under 450 nm.

MC3T3-E1 cells (3×10^4 cells/scaffolds) were seeded on Ti2448, Ti2448-GelMA and Ti2448-GelMA/DFO scaffolds. After culturing for 24 h, cells on the scaffold were gently rinsed by PBS, and immobilized in 4% paraformaldehyde for 2 h, following by dehydration in a graded series of ethanol solutions (50%, 70%, 90%, 95% and 100%) for 10 min each and dried with hexamethyldisilane for 20 min. The morphology was observed by SEM.

2.5 Osteogenic differentiation of MC3T3-E1 cells

Alkaline phosphatase (ALP) activities of MC3T3-E1 cells cultured on both Ti2448 and Ti2448-GelMA scaffolds were evaluated. MC3T3-E1 cells were seeded on the scaffolds (3×10^4 cells/scaffold) for 7 and 14 days, which were lysed in 100 μL of Triton X-100 (1% v/v) for 5 min. The ALP activity was determined by ALP quantification kit (Beyotime, Shanghai, China) and the OD value was measured at 520 nm.

Alizarin Red S (ARS) staining was used to evaluate the biomineralization level. After cultured for 7 and 14 days, cells were fixed with 4% paraformaldehyde for 15 min. The fixed samples were stained with ARS solution (Beijing Solarbio Science and Technology Co., Ltd., Beijing, China) for 30 min and cleaned with PBS. Finally, the cells are observed utilizing a confocal microscope (Olympus Corporation, Tokyo, Japan). For quantification analysis, 10% hexadecyl pyridinium chloride monohydrate (Sigma-Aldrich, St. Louis, USA) was used to dissolve the mineralized nodules and the OD value was measured at 562 nm.

2.6 *In vitro* tube formation experiment

In vitro angiogenesis of Ti2448-GelMA and Ti2448-GelMA/DFO scaffolds was investigated by the tube formation assay. The pipette tips, 96-well plates and Matrigel matrix (ABW, Shanghai, China) were first placed at 4°C overnight. 50 μL Matrigel matrix were then added to the plates for 30 min Ti2448-GelMA and Ti2448-GelMA/DFO scaffolds were first immersed into 2 mL serum-free α-MEM at 100 rpm for 24 h. The serum-free α-MEM was incorporated into the extracts to generate a range of diluted extracts (1/2, 1/4 and 1/8 concentrations). The serially diluted extraction medium was prepared by supplemention with 10% FBS and 1% antibiotic/antimycotic, hereafter referred to as 1, 1/2, and 1/4 dilution group. Cells (3×10^4 cells/scaffold) with different diluted extraction were seeded on the Matrigel coated plate for 3, 6 and 9 h. The morphology of HUVEC cells were observed by an Eclipse Ti inverted fluorescent microscope (Nikon Instruments Inc., Tokyo, Japan). Quantitative analysis for the number of vascular meshes were calculated by ImageJ software.

The release of DFO from the Ti2448-GelMA/DFO scaffolds was evaluated by a mould incubator (Shanghai Longyue Instrument Equipment Co., Ltd, Shanghai, China). The Ti2448-GelMA/DFO scaffolds were first incubated in the centrifuge tube at 37°C under 100% humidity. After 1, 3, 7 and 14 days, the scaffolds were removed and rinsed with deionized water. Then more deionized water was collected and supplied in the centrifuge tube until the final volume is 2 mL. The obtained solution was then chelated with $FeCl_3$ (10 mg/mL) at a 9:1 volumetric ratio for 5 min. The OD value was measured at 485 nm. The amount of DFO released was calculated according to the standard DFO calibration curve. The drug release rate is calculated using the amount of released drug divided by the total drug content.

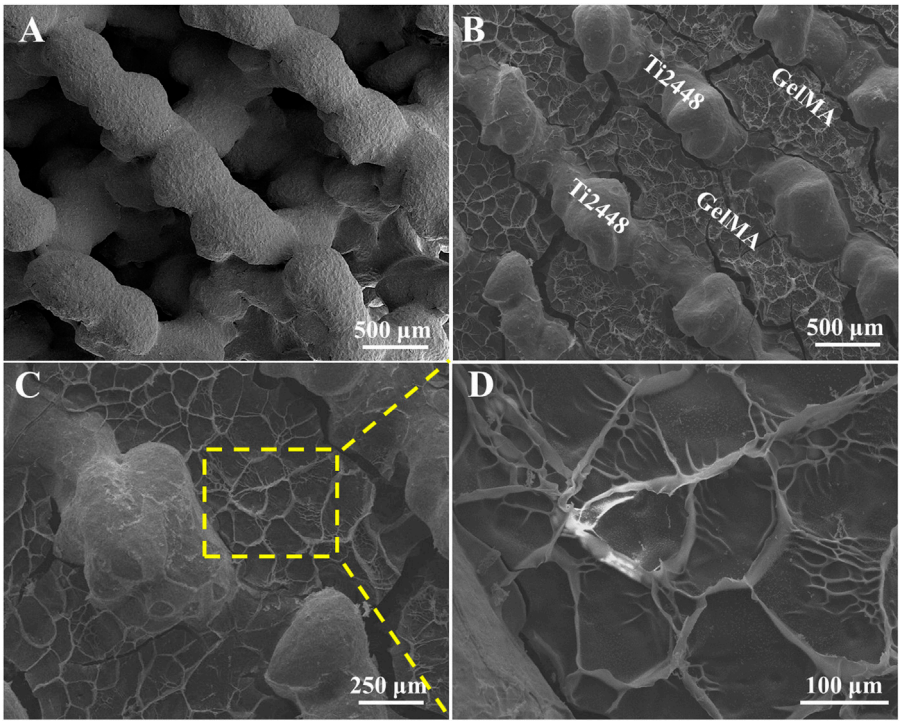

FIGURE 1
The morphology of **(A)** Ti2448 and **(B–D)** Ti2448-GelMA scaffolds.

2.7 Statistical analysis

All data were expressed as means ± standard deviation. One-way analysis of variance (ANOVA) was conducted for multiple samples with varying time points. Statistical significance was determined by $p < 0.05$.

3 Results and discussion

3.1 The characterization of GelMA

GelMA was first fabricated by the reaction between the MAA and the functional groups of lysine and hydroxyl lysine in gelatin (Supplementary Figure S1A). GelMA was further photo crosslinked to form three-dimensional network structures. The ^{1}H spectra of gelatin and GelMA were conducted to confirm the synthesis of GelMA (Supplementary Figure S1B). Two new peaks were found at 5.45 ppm and 5.68 ppm, corresponding to vinyl from the methacrylate group. However, both peaks were not present in the gelatin sample. The peak at 2.81 ppm represented the methylene proton (2H) of lysine, which showed high intensity peak of the unmodified gelatin and low intensity peak of the GelMA, consistent with previous findings (Cao et al., 2021; He et al., 2023). Supplementary Figure S2 showed that GelMA as prepared was amorphous. FTIR results (Supplementary Figure S1C) revealed the characteristic peaks of gelatin and GelMA. The peak at 1,543 cm^{-1} from the amide bond was related to N-H bending. Furthermore, the peak at 1,641 cm^{-1} for gelatin was associated with the C=O stretching of amide bond, while that for GelMA associated with both C=O and C=C stretching exhibited higher intensity, indicating the presence of methacrylate groups in the GelMA sample. The presence of these characteristic peaks again confirmed the successful synthesis of GelMA.

3.2 Preparation and characterization of Ti2448-GelMA scaffolds

Previous study reported that Ti2448 have good biocompatibility and osteoconductivity (Nune et al., 2017b; Liu et al., 2019). Ti2448 scaffolds showed the porous structure with the pore size of ~600 μm (Figure 1A). GelMA, mimicking the extracellular matrix, offered a three-dimensional structure and support the osteogenic differentiation of bone marrow mesenchymal stem cells, leading to further bone regeneration (Piao et al., 2021). For Ti2448-GelMA scaffolds, GelMA was incorporated into the porous interconnected structure of Ti2448 scaffolds (Figure 1B) and formed a porous network with the mean pore size of 120.2 ± 25.1 μm (Figures 1C,D). The interconnectivity and proper pore size (>100 μm) were crucially important for the transportation of oxygen/nutrients, cell attachment as well as the vascular growth, which were beneficial for the bone regeneration (Cimenoglu et al., 2011; Wu et al., 2014; Safaei-Yaraziz et al., 2021; Uiiah et al., 2021; Yao et al., 2021). Taking the advantages of 3D printing technology, the porous Ti2448-GelMA scaffolds provides the good interconnectivity with proper pore size (120.2 ± 25.1 μm), which may enhance the vessel growth and further facilitate the bone regeneration.

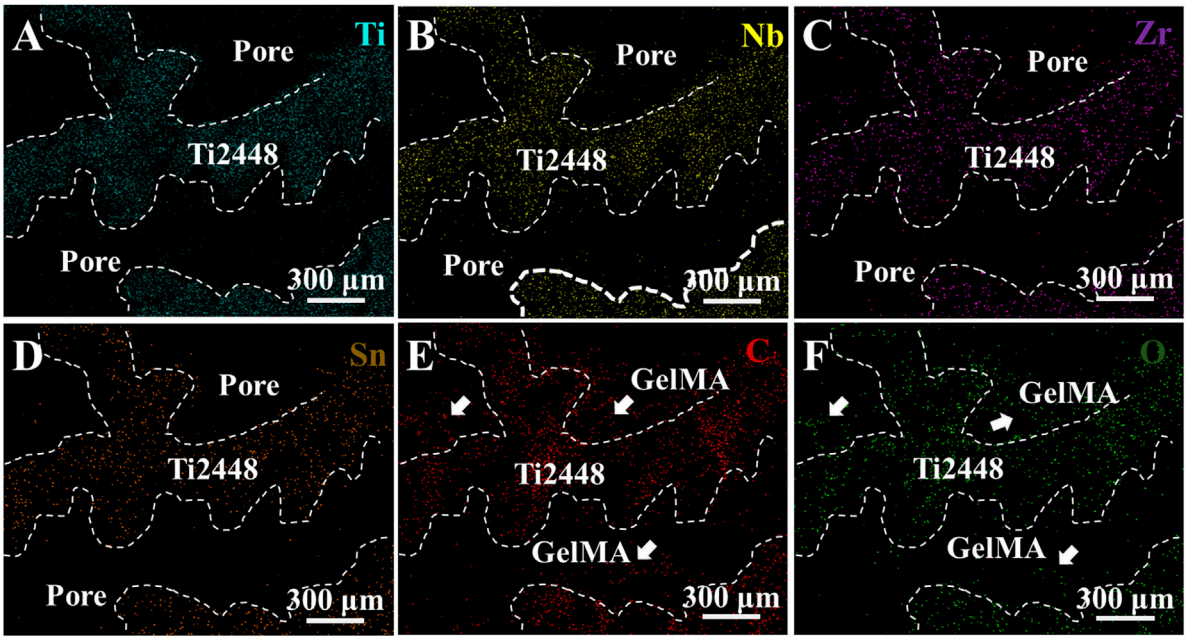

FIGURE 2
EDS mapping of Ti2448-GelMA scaffolds for **(A)** Ti, **(B)** Nb, **(C)** Zr, **(D)** Sn, **(E)** C and **(F)** O elements.

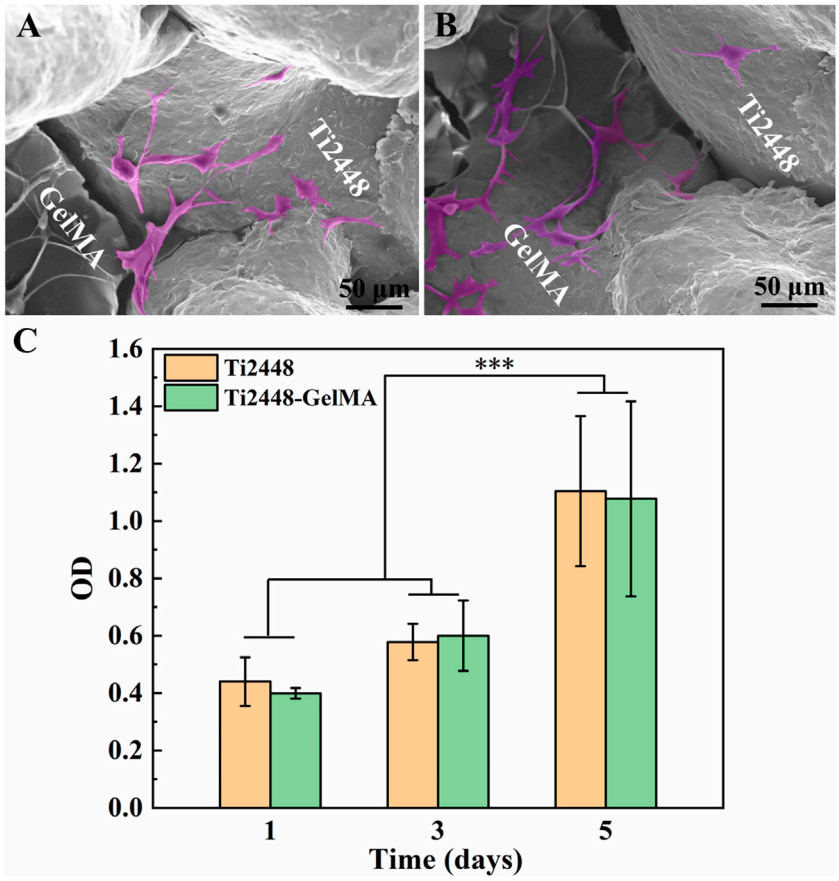

FIGURE 3
(A, B) Cell morphology of MC3T3-E1 cells on Ti2448-GelMA scaffold for 1 day, **(C)** CCK-8 assay of MC3T3-E1 cells on Ti2448 and Ti2448-GelMA scaffold surfaces for 1, 3, and 5 days. Cells were highlighted with a pink color based on the gray values of the images. (***$p < 0.001$)

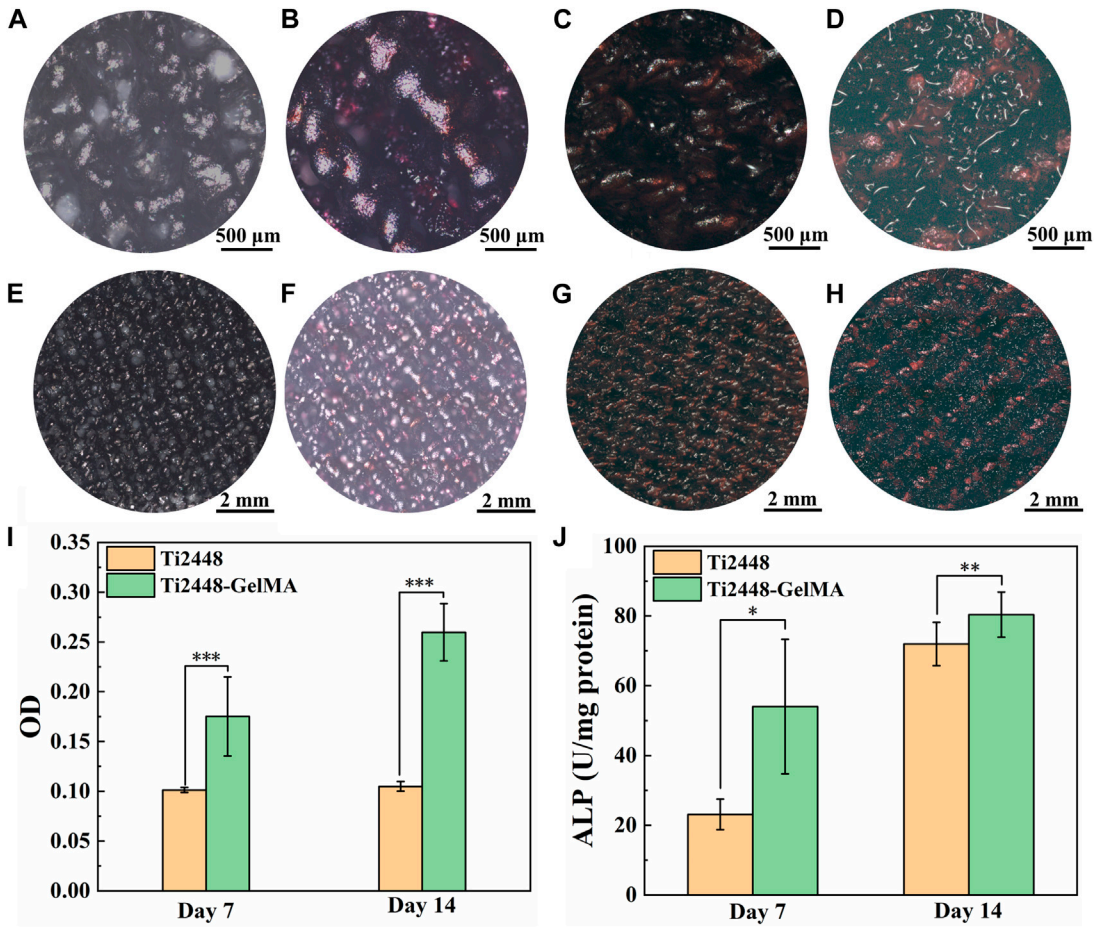

FIGURE 4
(A–H) The Alizarin Red S staining of MC3T3-E1 cells on **(A, E, C, G)** Ti2448, **(B, F, D, H)** Ti2448-GelMA scaffolds for **(A, B, E, F)** seven and **(C, D, G, H)** 14 days. **(I)** OD values for quantitative analysis of Alizarin Red S staining. **(J)** ALP activity of MC3T3-E1 cells cultured on different scaffolds for 7 and 14 days. Statistically significant difference is marked (*$p < 0.05$, **$p < 0.01$, ***$p < 0.001$).

EDS mapping of Ti, Nb, Zr, Sn, C, and O elements in the Ti2448-GelMA scaffold was conducted (Figure 2). The presence of C and O elements further proved the incorporation of GelMA into the Ti2448 scaffolds. Overall, GelMA was successfully loaded into the Ti2448 scaffold.

3.3 *In vitro* cytocompatibility of Ti2448-GelMA scaffolds

The morphology of MC3T3-E1 cells cultured on Ti2448-GelMA scaffolds was evaluated after 1 day culture (Figures 3A, B). Cells spread well with the pseudopodia extending outwards on both Ti2448 and GelMA surfaces. Notably, the cells exhibited unhindered adhesion and traversal across the Ti2448 scaffold and GelMA surfaces simultaneously (Figure 3B). Gelatin retains the key amino acid sequence, such as arginine glycine aspartate (RGD), which is critical to cell adhesion (Ahmady and Abu Samah, 2021). The proliferation of MC3T3-E1 cells was also evaluated (Figure 3C). As the cultivation time increased, the number of cells increased on both Ti2448 and Ti2448-GelMA scaffolds, without significant difference. For the Ti2448 scaffold group, the cell number at day 3 and day 5 was about 1.32 and 2.50 folds of that at day 1, respectively. For the Ti2448-GelMA scaffold group, the cell number at day 3 and day 5 was about 1.50 and 2.75 folds of that at day 1, respectively. There was no significant difference on cell numbers between these two groups at the same time point. Therefore, in our study, Ti2448-GelMA scaffold can support the cell adhesion and proliferation, demonstrating the excellent biocompatibility.

3.4 *In vitro* differentiation of MC3T3-E1 cells on Ti2448-GelMA scaffolds

To evaluate the osteogenic differentiation of MC3T3-E1 cells on Ti2448-GelMA scaffolds, cells were cultured for 7 and 14 days and subsequently performed ARS staining to evaluate biomineralization levels (Figures 4A–H). The results showed a relatively low degree of biomineralization for MC3T3-E1 cells cultured on the Ti2448 scaffold for 7 days, with scarcely noticeable red-stained mineralized nodules. On the other hand, the amount of mineralized nodules in the Ti2448-GelMA group was higher than the Ti2448 group after culture for 7 days. Meanwhile, the ARS staining showed progressive biomineralization with increase of culture time. After cell culture for 14 days, the Ti2448-GelMA group showed a higher amount of

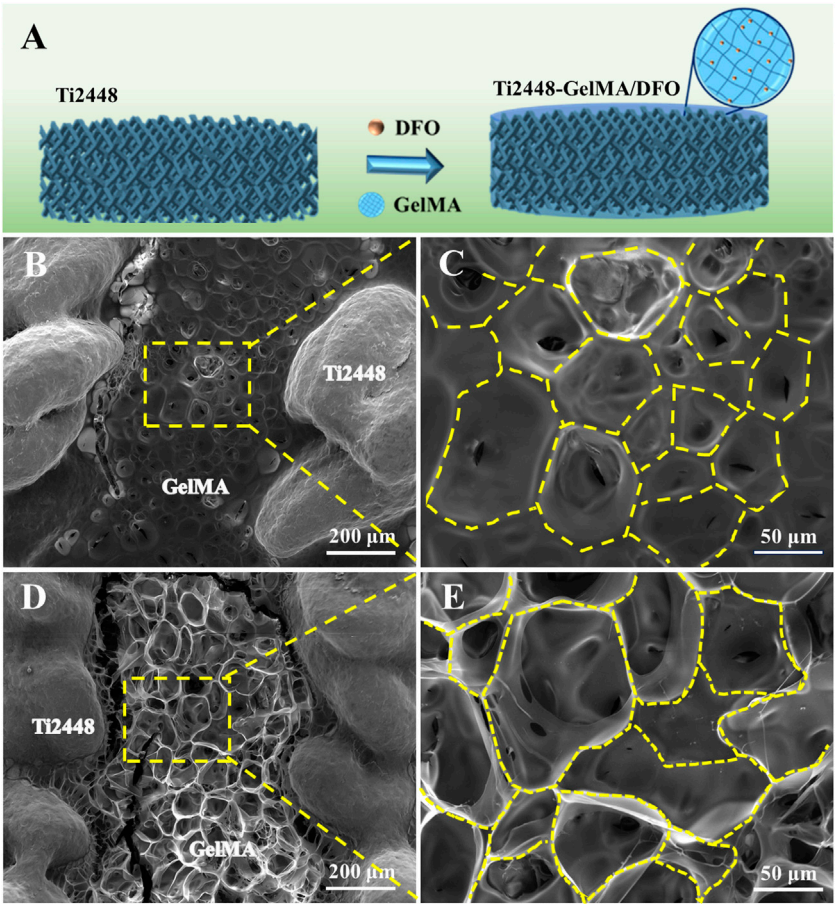

FIGURE 5
(A) Schematic diagram of Ti2448-GelMA/DFO scaffolds. The morphological images of **(B, C)** Ti2448-GelMA scaffold and **(D, E)** Ti2448-GelMA/DFO scaffold.

mineralized nodules than the Ti2448 group. Additionally, quantitative analysis showed that the amount of calcium contents from the Ti2448-GelMA group were 1.8 times and 2.5 times of that from the Ti2448 group after cell culture for 7 and 14 days, respectively (Figure 4I). Compared with the Ti2448 group, MC3T3-E1 cells in the Ti2448-GelMA group also showed significantly higher expressions of ALP activity when cultured for 7 and 14 days (Figure 4J). These results suggest that Ti2448-GelMA scaffolds can facilitate osteogenic differentiation of MC3T3-E1 cells, thereby promoting further biomineralization. GelMA recently attracts more attention, which can be used to mimic the natural bone extracellular matrix and is beneficial to vascular growth and bone regeneration (Dong et al., 2019; Heltmann-Meyer et al., 2021; Li Y et al., 2021). For example, the GelMA scaffolds were prepared by the thermally induced phase separation technique, and the ALP activity of the adipose derived stem cells cultured on the GelMA group was approximate 2 times of the untreated group after 14 and 21 days (Fang et al., 2016). In our previous work, compared with the Ti2448 scaffolds, MC3T3-E1 cells derived ECM modified Ti2448 scaffold can effectively promote osteogenic differentiation of MC3T3-E1 cells, and enhance the bone integration after implantation in rabbit femoral bone defects for 1 month (Xu et al., 2022). Therefore, the Ti2448-GelMA scaffolds were prepared by introducing the three-dimensional GelMA as the bone extracellular matrix and can be beneficial for the osteogenic differentiation of MC3T3-E1 cells.

3.5 Angiogenic effects of Ti2448-GelMA/DFO scaffolds

Vascularization plays an important role on the repair of large bone defects (Li et al., 2023). During bone healing and remodeling, vascular formation and bone tissue regeneration are indeed coupled processes (Ramasamy et al., 2014). Porous titanium alloys demonstrate the good osteoconductivity and osteointegration capabilities, yet the pursuit of effective internal vascularization remains a big challenge. Herein, DFO was incorporated into GelMA to enhance the Ti2448-GelMA vascularization (Figure 5A). SEM morphology revealed that doping of DFO did not change pore structures of Ti2448-GelMA/DFO scaffolds (Figures 5D, E) compared to the Ti2448-GelMA (Figures 5B, C) scaffolds.

The angiogenic effects of Ti2448-GelMA/DFO scaffolds were evaluated by co-culture with HUVEC cells (Figure 6; Supplementary Figure S3). After cell culture for 3 h, no tubes formed on both the Ti2448-GelMA group and control group, while a small amount of tubes formed in the Ti2448-GelMA/DFO group (Supplementary Figure

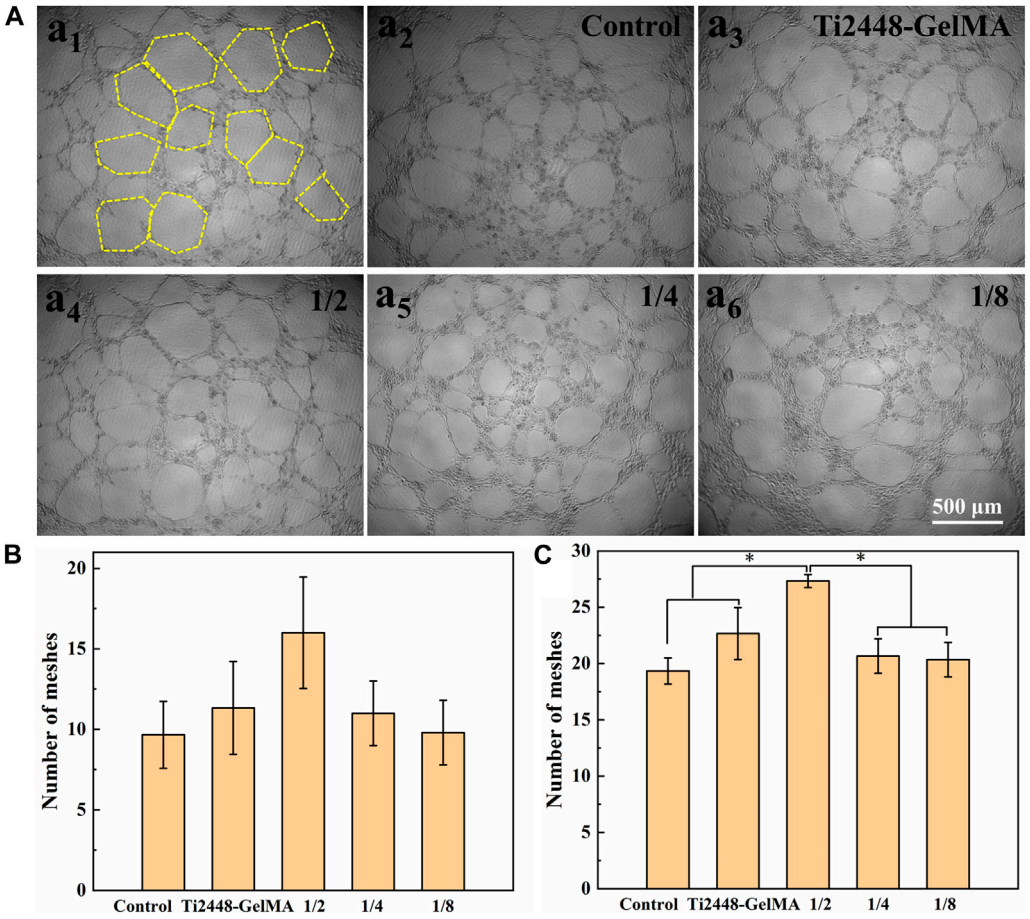

FIGURE 6
(A) The morphology of HUVEC cells (a_1) on the Ti2448-GelMA/DFO extraction at 1/2 concentration for 9 h. The yellow dash lines represent the vascular meshes. The morphology of HUVEC cells on (a_2) the control group, (a_3) Ti2448-GelMA extraction and Ti2448-GelMA/DFO extractions at (a_4) 1/2 concentration, (a_5) 1/4 concentration, (a_6) 1/8 concentration after 9 h, the number of vascular meshes at **(B)** 6 h and **(C)** 9 h. (*$p < 0.05$).

S3A). With increase of the cultivation time, the number and size of vascular tubes increased for all groups. After cultivation for 6 h, large tubes (~300 μm) were observed in the Ti2448-GelMA/DFO group, compared to the Ti2448-GelMA group and control group (Supplementary Figure S3B). After culture for 9 h, a greater number of small vascular tubes consolidated into large tubes, and there were much more uniform large tubes in the Ti2448-GelMA/DFO group than the other two groups (Figure 6A). The number of vascular meshes represented the closed areas delimited by the vascular tubes marked with the yellow dash line in Figure 6A$_1$. The number of vascular meshes were calculated after culture for 6 and 9 h (Figures 6B, C). The results indicated that the number of meshes for all groups increased with increase of culturing time. Additionally, the meshes increased with the increase of DFO concentration, especially for the 1/2 dilution group (7.2/mm^2) with the higher number of vascular meshes than the other two groups (Control group: 5.3/mm^2, Ti2448-GelMA group: 6.2/mm^2). Therefore, HUVECs cultured with Ti2448-GelMA/DFO extractions exhibited more vascular network compared to the Ti2448-GelMA and control groups. As the concentration of DFO increases, the vascularization became more significant, demonstrating the improved vascularization effect in a dose-dependent manner. Hou et al. cultured HUVEC cells with a series of DFO concentrations (5, 20, 100 μM) for 24 h. Results showed that the group with the highest concentration of DFO (100 μM) exhibited the largest tube length and the greatest number of tubes, also demonstrating that DFO improved the tube formation of HUVECs in a concentration-dependent manner (Hou et al., 2013). Therefore, the release of DFO can effectively promote the vascularization of the Ti2448-GelMA/DFO scaffolds. Besides, the MC3T3-E1 cells attached well on the Ti2448-GelMA/DFO scaffolds (Supplementary Figure S4), which demonstrated that DFO loading on theTi2448-GelMA scaffold does not affect the cell behavior.

The DFO release profile was shown in Figure 7. At the first day, DFO exhibited the release rate of nearly 14.3%, followed by a constant sustained release. After 7 days, about 42.0% DFO has been released from the Ti2448-GelMA/DFO scaffold and the final cumulative release reaches to 82.3% after 28 days. As such, Ti2448-GelMA/DFO scaffolds exhibited a sustained release of DFO possibly through the hydrogen bonding. In fact, the regeneration of blood vessels runs through the entire process of bone repair from early bone formation, maturation to remodeling (Chen et al., 2020; Simunovic and Finkenzeller, 2021). The new blood vessels infiltrated into the newly formed bone are necessitate to supply of oxygen and nutrients, as well as removal of metabolic wastes (Marenzana and Arnett, 2013). Previous research also studied

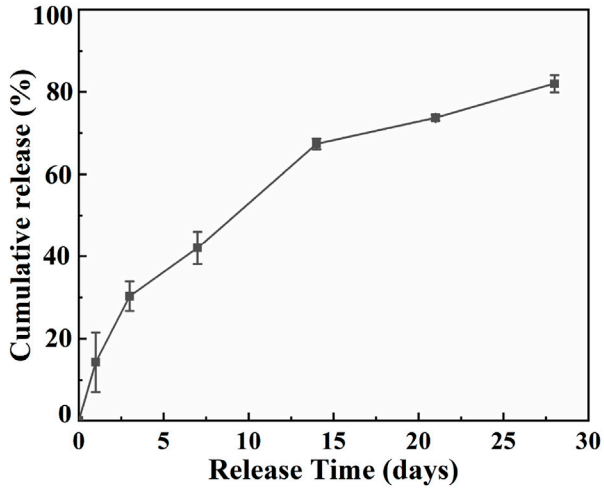

FIGURE 7
The cumulative release of DFO from the Ti2448-GelMA/DFO scaffolds.

the DFO release profiles *in vitro* (Cheng et al., 2018; Ran et al., 2018). For example, DFO loaded titania nanotubes substrates were prepared and then immersed into PBS solution with gently shaking at 37°C. The burst release of DFO (~83.7%) was found in the first 12 h (Ran et al., 2018). However, immersion of the sample in a liquid solution cannot truly simulate the real release behavior of DFO from the implants *in vivo* under a mild and humid environment. Once the scaffolds are implanted in the bone defects, which will be encapsuled by the soft callus under a high humidity environment instead of immersion in a liquid solution (Salhotra et al., 2020). Thus, it is necessary to build a model mimicking the real release profile *in vivo*. Herein, Ti2448-GelMA/DFO scaffold were placed under 100% humidity at 37°C, which can well simulate the environment after implantation. The DFO release profiles in Ti2448-GelMA/DFO scaffolds can effectively achieve the sustained drug release, leading to the better vascularization for the large bone defect repair.

Composite materials have been widely studied in order to improve osteogenic activity of the scaffolds and further vascular growth for large bone defect repair (Li J et al., 2021; Qian et al., 2021; Qian et al., 2024). Herein, the Ti2448 scaffold was chosen as the main part, while GelMA was implemented as the osteogenic component, with DFO loaded as the vascularization factor. This combination will provide good mechanical properties and essential biological functions to the implant materials for large bone defect repair.

4 Conclusion

In this study, novel Ti2448-GelMA/DFO bone scaffolds were prepared by incorporating the GelMA loaded with DFO into porous Ti2448 scaffolds that were fabricated by the EBM method. Ti2448-GelMA scaffolds exhibited the porous network with the mean pore size of 120.2 ± 25.1 μm, and promoted the differentiation of MC3T3-E1 cells with enhanced ALP activity and mineralization. Additionally, the Ti2448-GelMA/DFO scaffolds facilitated the angiogenesis in a dose-dependent manner. Impressively, the number of vascular meshes from the Ti2448-GelMA/DFO group (7.2/mm^2) was significantly higher than the control group (5.3/mm^2) after cultivation of HUVECs for 9 h. The Ti2448-GelMA/DFO scaffolds also exhibited a sustained release of DFO in a humidified condition. Therefore, the Ti2448-GelMA/DFO scaffolds show great potential for large bone defect repair.

Data availability statement

The raw data supporting the conclusion of this article will be made available by the authors, without undue reservation.

Author contributions

QX: Conceptualization, Methodology, Writing–original draft. YB: Supervision, Writing–original draft, Writing–review and editing. SL: Writing–review and editing. WH: Writing–review and editing. YH: Writing–review and editing. RY: Writing–review and editing. XL: Supervision, Writing–review and editing. XZ: Funding acquisition, Supervision, Writing–review and editing.

Funding

The author(s) declare that financial support was received for the research, authorship, and/or publication of this article. This work was supported by the National Natural Science Foundation of China (52273278) and Liao Ning Revitalization Talents Program (XLYC2007112).

Conflict of interest

The authors declare that the research was conducted in the absence of any commercial or financial relationships that could be construed as a potential conflict of interest.

Publisher's note

Supplementary material

The Supplementary Material for this article can be found online at: https://www.frontiersin.org/articles/10.3389/fbioe.2024.1372636/full#supplementary-material

References

Ahmady, A., and Abu Samah, N. H. (2021). A review: gelatine as a bioadhesive material for medical and pharmaceutical applications. *Int. J. Pharm.* 608, 121037. doi:10.1016/j.ijpharm.2021.121037

Cao, Y., Cheng, P., Sang, S., Xiang, C., An, Y., Wei, X., et al. (2021). 3D printed PCL/GelMA biphasic scaffold boosts cartilage regeneration using co-culture of mesenchymal stem cells and chondrocytes: *in vivo* study. *Mat. Des.* 210, 110065. doi:10.1016/j.matdes.2021.110065

Chen, J., Zhou, H., Fan, Y., Gao, G., Ying, Y., and Li, J. (2023). 3D printing for bone repair: coupling infection therapy and defect regeneration. *Chem. Eng. J.* 471, 144537. doi:10.1016/j.cej.2023.144537

Chen, M., Li, Y., Huang, X., Gu, Y., Li, S., Yin, P., et al. (2021). Skeleton - vasculature chain reaction: a novel insight into the mystery of homeostasis. *Bone Res.* 9, 21. doi:10.1038/s41413-021-00138-0

Chen, M., Zhang, Y., Zhang, W., and Li, J. (2020). Polyhedral oligomeric silsesquioxane - incorporated gelatin hydrogel promotes angiogenesis during vascularized bone regeneration. *ACS Appl. Mat. Interfaces* 12, 22410–22425. doi:10.1021/acsami.0c00714

Cheng, R., Yan, Y., Liu, H., Chen, H., Pan, G., Deng, L., et al. (2018). Mechanically enhanced lipo-hydrogel with controlled release of multi-type drugs for bone regeneration. *Appl. Mat. Today* 12, 294–308. doi:10.1016/j.apmt.2018.06.008

Cheng, W., Ding, Z., Zheng, X., Lu, Q., Kong, X., Zhou, X., et al. (2020). Injectable hydrogel systems with multiple biophysical and biochemical cues for bone regeneration. *Biomater. Sci.* 8, 2537–2548. doi:10.1039/d0bm00104j

Cimenoglu, H., Gunyuz, M., Kose, G. T., Baydogan, M., Uğurlu, F., and Sener, C. (2011). Micro-arc oxidation of Ti6Al4V and Ti6Al7Nb alloys for biomedical applications. *Mat. Charact.* 62, 304–311. doi:10.1016/j.matchar.2011.01.002

Dong, Z., Yuan, Q., Huang, K., Xu, W., Liu, G., and Gu, Z. (2019). Gelatin methacryloyl (GelMA)-based biomaterials for bone regeneration. *RSC Adv.* 9, 17737–17744. doi:10.1039/c9ra02695a

Fang, X., Xie, J., Zhong, L., Li, J., Rong, D., Li, X., et al. (2016). Biomimetic gelatin methacrylamide hydrogel scaffolds for bone tissue engineering. *J. Mat. Chem. B* 4, 1070–1080. doi:10.1039/c5tb02251g

Ha, Y., Ma, X., Li, S., Li, T., Li, Z., Qian, Y., et al. (2022). Bone microenvironment-mimetic scaffolds with hierarchical microstructure for enhanced vascularization and bone regeneration. *Adv. Funct. Mat.* 32, 2200011. doi:10.1002/adfm.202200011

He, J., Sun, Y., Gao, Q., He, C., Yao, K., Wang, T., et al. (2023). Gelatin methacryloyl hydrogel, from standardization, performance, to biomedical application. *Adv. Funct. Mat.* 12, 2300395. doi:10.1002/adhm.202300395

Heltmann-Meyer, S., Steiner, D., Müller, C., Schneidereit, D., Friedrich, O., Salehi, S., et al. (2021). Gelatin methacryloyl is a slow degrading material allowing vascularization and long-term use *in vivo*. *Biomed. Mat.* 16, 065004. doi:10.1088/1748-605x/ac1e9d

Hendriks, M., and Ramasamy, S. K. (2020). Blood vessels and vascular niches in bone development and physiological remodeling. *Front. Cell Dev. Biol.* 8, 602278. doi:10.3389/fcell.2020.602278

Hou, Z., Nie, C., Si, Z., and Ma, Y. (2013). Deferoxamine enhances neovascularization and accelerates wound healing in diabetic rats via the accumulation of hypoxia-inducible factor-1α. *Diabetes Res. Clin. Pr.* 101, 62–71. doi:10.1016/j.diabres.2013.04.012

Jahr, H., Li, Y., Zhou, J., Zadpoor, A. A., and Schröder, K. U. (2021). Additively manufactured absorbable porous metal implants - processing, alloying and corrosion behavior. *Front. Mat.* 8, 628633. doi:10.3389/fmats.2021.628633

Kang, H. W., Lee, S. J., Ko, I. K., Kengla, C., Yoo, J. J., and Atala, A. (2016). A 3D bioprinting system to produce human-scale tissue constructs with structural integrity. *Nat. Biotechnol.* 34, 312–319. doi:10.1038/nbt.3413

Koons, G. L., Diba, M., and Mikos, A. G. (2020). Materials design for bone - tissue engineering. *Nat. Rev. Mat.* 5, 584–603. doi:10.1038/s41578-020-0204-2

Li, X., Ye, S., Yuan, X., and Yu, P. (2019). Fabrication of biomedical Ti-24Nb-4Zr-8Sn alloy with high strength and low elastic modulus by powder metallurgy. *J. Alloys Compd.* 772, 968–977. doi:10.1016/j.jallcom.2018.08.262

Li, Y., Zhu, J., Zhang, X., Li, Y., Zhang, S., Yang, L., et al. (2023). Drug-delivery nanoplatform with synergistic regulation of angiogenesis - osteogenesis coupling for promoting vascularized bone regeneration. *ACS Appl. Mat. Interfaces* 15, 17543–17561. doi:10.1021/acsami.2c23107

Li J, J., Wang, W., Li, M., Song, P., Lei, H., Gui, X., et al. (2021). Biomimetic methacrylated gelatin hydrogel loaded with bone marrow mesenchymal stem cells for bone tissue regeneration. *Front. Bioeng. Biotechnol.* 9, 770049. doi:10.3389/fbioe.2021.770049

Liu, C., and Castillo, A. B. (2018). Targeting osteogenesis-angiogenesis coupling for bone repair. *J. Am. Acad. Orthop. Surg.* 26, e153–e155. doi:10.5435/jaaos-d-17-00918

Liu, C. F., Li, S. J., Hou, W. T., Hao, Y. L., and Huang, H. H. (2019). Enhancing corrosion resistance and biocompatibility of interconnected porous β-type Ti-24Nb-4Zr-8Sn alloy scaffold through alkaline treatment and type I collagen immobilization. *Appl. Surf. Sci.* 476, 325–334. doi:10.1016/j.apsusc.2019.01.084

Liu, W. C., Chen, S., Zheng, L., and Qin, L. (2017). Angiogenesis assays for the evaluation of angiogenic properties of orthopaedic biomaterials - a general review. *Adv. Healthc. Mat.* 6, 1600434. doi:10.1002/adhm.201600434

Liu, Y., Li, S., Hou, W., Wang, S., Hao, Y., Yang, R., et al. (2016). Electron beam melted beta-type Ti-24Nb-4Zr-8Sn porous structures with high strength-to-modulus ratio. *J. Mat. Sci. Technol.* 32, 505–508. doi:10.1016/j.jmst.2016.03.020

Li Y, Y., Liu, Y., Bai, H., Li, R., Shang, J., Zhu, Z., et al. (2021). Sustained release of VEGF to promote angiogenesis and osteointegration of three-dimensional printed biomimetic titanium alloy implants. *Front. Bioeng. Biotechnol.* 9, 757767. doi:10.3389/fbioe.2021.757767

Ma, L., Wang, X., Zhou, Y., Ji, X., Cheng, S., Bian, D., et al. (2021). Biomimetic Ti-6Al-4V alloy/gelatin methacrylate hybrid scaffold with enhanced osteogenic and angiogenic capabilities for large bone defect restoration. *Bioact. Mat.* 6, 3437–3448. doi:10.1016/j.bioactmat.2021.03.010

Marenzana, M., and Arnett, T. R. (2013). The key role of the blood supply to bone. *Bone Res.* 1, 203–215. doi:10.4248/br201303001

Marrella, A., Lee, T. Y., Lee, D. H., Karuthedom, S., Syla, D., Chawla, A., et al. (2018). Engineering vascularized and innervated bone biomaterials for improved skeletal tissue regeneration. *Mat. Today* 21, 362–376. doi:10.1016/j.mattod.2017.10.005

Niinomi, M., Liu, Y., Nakai, M., Liu, H., and Li, H. (2016). Biomedical titanium alloys with Young's moduli close to that of cortical bone. *Regen. Biomater.* 3, 173–185. doi:10.1093/rb/rbw016

Nune, K. C., Misra, R. D. K., Li, S. J., Hao, Y. L., and Yang, R. (2017a). Cellular response of osteoblasts to low modulus Ti-24Nb-4Zr-8Sn alloy mesh structure. *J. Biomed. Mat. Res. A* 105, 859–870. doi:10.1002/jbm.a.35963

Nune, K. C., Misra, R. D. K., Li, S. J., Hao, Y. L., and Yang, R. (2017b). Osteoblast cellular activity on low elastic modulus Ti-24Nb-4Zr-8Sn alloy. *Dent. Mat.* 33, 152–165. doi:10.1016/j.dental.2016.11.005

Park, S. H., Kim, R. S., Stiles, W. R., Jo, M., Zeng, L., Rho, S., et al. (2022). Injectable thermosensitive hydrogels for a sustained release of iron nanochelators. *Adv. Sci.* 9, e2200872. doi:10.1002/advs.202200872

Piao, Y., You, H., Xu, T., Bei, H. P., Piwko, I. Z., Kwan, Y. Y., et al. (2021). Biomedical applications of gelatin methacryloyl hydrogels. *Eng. Regen.* 2, 47–56. doi:10.1016/j.engreg.2021.03.002

Qian, G., Mao, Y., Zhao, H., Zhang, L., Xiong, L., and Long, Z. (2024). pH-Responsive nanoplatform synergistic gas/photothermal therapy to eliminate biofilms in poly (L-lactic acid) scaffolds. *J. Mat. Chem. B* 12, 1379–1392. doi:10.1039/d3tb02600k

Qian, G., Zhang, L., Wang, G., Zhao, Z., Peng, S., and Shuai, C. (2021). 3D printed Zn-doped mesoporous silica-incorporated poly-L-lactic acid scaffolds for bone repair. *Int. J. Bioprint.* 7, 346. doi:10.18063/ijb.v7i2.346

Raines, A. L., Berger, M. B., Schwartz, Z., and Boyan, B. D. (2019). Osteoblasts grown on microroughened titanium surfaces regulate angiogenic growth factor production through specific integrin receptors. *Acta Biomater.* 97, 578–586. doi:10.1016/j.actbio.2019.07.036

Ramasamy, S. K., Kusumbe, A. P., Wang, L., and Adams, R. H. (2014). Endothelial notch activity promotes angiogenesis and osteogenesis in bone. *Nature* 507, 376–380. doi:10.1038/nature13146

Ran, Q., Yu, Y., Chen, W., Shen, X., Mu, C., Yuan, Z., et al. (2018). Deferoxamine loaded titania nanotubes substrates regulate osteogenic and angiogenic differentiation of MSCs via activation of HIF-1α signaling. *Mat. Sci. Eng. C Mat. Biol. Appl.* 91, 44–54. doi:10.1016/j.msec.2018.04.098

Safaei-Yaraziz, A., Akbari-Birgani, S., and Nikfarjam, N. (2021). Porous scaffolds with the structure of an interpenetrating polymer network made by gelatin methacrylated nanoparticle-stabilized high internal phase emulsion polymerization targeted for tissue engineering. *RSC Adv.* 11, 22544–22555. doi:10.1039/d1ra03333f

Salhotra, A., Shah, H. N., Levi, B., and Longaker, M. T. (2020). Mechanisms of bone development and repair. *Nat. Rev. Mol. Cell Biol.* 21, 696–711. doi:10.1038/s41580-020-00279-w

Simunovic, F., and Finkenzeller, G. (2021). Vascularization strategies in bone tissue engineering. *Cells* 10, 1749. doi:10.3390/cells10071749

Tang, Z., Wei, X., Li, T., Wu, H., Xiao, X., Hao, Y., et al. (2021). Three-dimensionally printed Ti2448 with low stiffness enhanced angiogenesis and osteogenesis by regulating macrophage polarization via Piezo1/YAP signaling axis. *Front. Cell Dev. Biol.* 9, 750948. doi:10.3389/fcell.2021.750948

Ullah, I., Cao, L., Cui, W., Xu, Q., Yang, R., Tang, K. l., et al. (2021). Stereolithography printing of bone scaffolds using biofunctional calcium phosphate nanoparticles. *J. Mat. Sci. Technol.* 88, 99–108. doi:10.1016/j.jmst.2021.01.062

Vidal, L., Kampleitner, C., Brennan, M. Á., Hoornaert, A., and Layrolle, P. (2020). Reconstruction of large skeletal defects: current clinical therapeutic strategies and future directions using 3d printing. *Front. Bioeng. Biotechnol.* 8, 61. doi:10.3389/fbioe.2020.00061

Wang, L., Zhu, L. X., Wang, Z., Lou, A. J., Yang, Y. X., Guo, Y., et al. (2018). Development of a centrally vascularized tissue engineering bone graft with the unique

core-shell composite structure for large femoral bone defect treatment. *Biomaterials* 175, 44–60. doi:10.1016/j.biomaterials.2018.05.017

Wu, S. L., Liu, X. M., Yeung, K. W. K., Liu, C. S., and Yang, X. J. (2014). Biomimetic porous scaffolds for bone tissue engineering. *Mat. Sci. Eng. R.* 80, 1–36. doi:10.1016/j.mser.2014.04.001

Xu, Q., Bai, Y., Misra, R. D. K., Hou, W., Wang, Q., Zhang, Z., et al. (2022). Improving biological functions of three-dimensional printed Ti2448 scaffolds by decoration with polydopamine and extracellular matrices. *ACS Appl. Bio. Mat.* 5, 3982–3990. doi:10.1021/acsabm.2c00521

Xue, Y., Yang, J., Luo, J., Ren, L., Shen, Y., Dong, D., et al. (2020). Disorder of iron metabolism inhibits the recovery of unloading-induced bone loss in hypomagnetic field. *J. Bone Min. Res.* 35, 1163–1173. doi:10.1002/jbmr.3949

Yang, Y., and Xiao, Y. (2020). Biomaterials regulating bone hematoma for osteogenesis. *Adv. Healthc. Mat.* 21, e2000726. doi:10.1002/adhm.202000726

Yao, Y. T., Yang, Y., Ye, Q., Cao, S. S., Zhang, X. P., Zhao, K., et al. (2021). Effects of pore size and porosity on cytocompatibility and osteogenic differentiation of porous titanium. *J. Mat. Sci. Mat. Med.* 32, 72. doi:10.1007/s10856-021-06548-0

Yuan, B., Liu, P., Zhao, R., Yang, X., Xiao, Z., Zhang, K., et al. (2023). Functionalized 3D-printed porous titanium scaffold induces *in situ* vascularized bone regeneration by orchestrating bone microenvironment. *J. Mat. Sci. Technol.* 153, 92–105. doi:10.1016/j.jmst.2022.12.033

Zeng, Y., Huang, C., Duan, D., Lou, A., Guo, Y., Xiao, T., et al. (2022). Injectable temperature-sensitive hydrogel system incorporating deferoxamine-loaded microspheres promotes H-type blood vessel-related bone repair of a critical size femoral defect. *Acta Biomater.* 153, 108–123. doi:10.1016/j.actbio.2022.09.018

Zhang, B., Yin, X., Zhang, F., Hong, Y., Qiu, Y., Yang, X., et al. (2023). Customized bioceramic scaffolds and metal meshes for challenging large-size mandibular bone defect regeneration and repair. *Regen. Biomater.* 10, rbad057. doi:10.1093/rb/rbad057

frontiers | Frontiers in Bioengineering and Biotechnology

TYPE Original Research
PUBLISHED 19 April 2024
DOI 10.3389/fbioe.2024.1356158

OPEN ACCESS

EDITED BY
Wenjie Zhang,
Shanghai Jiao Tong University, China

REVIEWED BY
Wei Qiao,
The University of Hong Kong, Hong Kong SAR, China
Shaobao Liu,
Nanjing University of Aeronautics and Astronautics, China
He Xiao-Tao,
Fourth Military Medical University, China

*CORRESPONDENCE
Zhiguo Qu,
zgqu@xjtu.edu.cn
Ang Li,
drliang@xjtu.edu.cn

†These authors have contributed equally to this work and share first authorship

RECEIVED 15 December 2023
ACCEPTED 14 March 2024
PUBLISHED 19 April 2024

CITATION
Sun G, Shu T, Ma S, Li M, Qu Z and Li A (2024), A submicron forest-like silicon surface promotes bone regeneration by regulating macrophage polarization.
Front. Bioeng. Biotechnol. 12:1356158.
doi: 10.3389/fbioe.2024.1356158

A submicron forest-like silicon surface promotes bone regeneration by regulating macrophage polarization

Guo Sun[1,2†], Tianyu Shu[1†], Shaoyang Ma[1], Meng Li[1], Zhiguo Qu[2*] and Ang Li[1*]

[1]Key Laboratory of Shaanxi Province for Craniofacial Precision Medicine Research, College of Stomatology, Xi'an Jiaotong University, Xi'an, China, [2]MOE Key Laboratory of Thermo-Fluid Science and Engineering, School of Energy and Power Engineering, Xi'an Jiaotong University, Xi'an, China

Introduction: Silicon is a major trace element in humans and a prospective supporting biomaterial to bone regeneration. Submicron silicon pillars, as a representative surface topography of silicon-based biomaterials, can regulate macrophage and osteoblastic cell responses. However, the design of submicron silicon pillars for promoting bone regeneration still needs to be optimized. In this study, we proposed a submicron forest-like (Fore) silicon surface (Fore) based on photoetching. The smooth (Smo) silicon surface and photoetched regular (Regu) silicon pillar surface were used for comparison in the bone regeneration evaluation.

Methods: Surface parameters were investigated using a field emission scanning electron microscope, atomic force microscope, and contact angle instrument. The regulatory effect of macrophage polarization and succedent osteogenesis was studied using Raw264.7, MC3T3-E1, and rBMSCs. Finally, a mouse calvarial defect model was used for evaluating the promoting effect of bone regeneration on the three surfaces.

Results: The results showed that the Fore surface can increase the expression of M2-polarized markers (CD163 and CD206) and decrease the expression of inflammatory cytokines, including interleukin-6 (IL-6) and tumor necrosis factor alpha (TNF-α). Fore surface can promote the osteogenesis in MC3T3-E1 cells and osteoblastic differentiation of rBMSCs. Furthermore, the volume fraction of new bone and the thickness of trabeculae on the Fore surface were significantly increased, and the expression of RANKL was downregulated. In summary, the upregulation of macrophage M2 polarization on the Fore surface contributed to enhanced osteogenesis *in vitro* and accelerated bone regeneration *in vivo*.

Discussion: This study strengthens our understanding of the topographic design for developing future silicon-based biomaterials.

KEYWORDS

silicon, submicron, surface topography, bone regeneration, macrophage polarization

1 Introduction

The highly efficient restoration of a bone defect is a major clinical concern. The reason is that human bone tissue often shows limited regenerative capacity and requires proper external intervention for regeneration (Bai et al., 2018; Wang X. et al., 2018). Silicon is a major trace element in humans (Jugdaohsingh et al., 2013; Martin, 2013). Increased dietary silicon intake facilitates human skeletal health (Jugdaohsingh et al., 2004). Orthosilicic acid, biosilica, and silica nanoparticles can stimulate type I collagen synthesis and osteoblast differentiation in human osteoblast-like cells (Sun et al., 2017; Sun et al., 2018; Friguglietti et al., 2020). Silicon nitride surfaces have also shown osteogenic/antibacterial dual properties (Bock et al., 2017; Ishikawa et al., 2017; Du et al., 2022). Therefore, silicon shows some potential in stimulating bone regeneration. To develop new silicon-based biomaterials for bone regeneration, the optimized design of bioactive silicon surfaces should be completely elaborated.

The surface topography of biomaterials plays a vital role in osteogenesis (Bosshardt et al., 2017). Installed biomaterials can trigger innate immune responses and recruit macrophages (Trindade et al., 2016). To establish a suitable microenvironment for bone regeneration, the M2-polarized macrophages are necessary with their anti-inflammatory and pro-healing potential to inhibit the innate immune response (Chen et al., 2016; Zhu G. et al., 2021; Toita et al., 2022). It has been proven that proper surface topography of biomaterials can promote the M2 polarization of macrophages to enhance bone regeneration (Hotchkiss et al., 2016; Abaricia et al., 2020; Zhu Y. Z. et al., 2021). In addition, the surface topography of biomaterials can directly influence osteogenesis. That is, the material surface that mimics natural bone topography can promote protein adsorption, mesenchymal stem cell osteogenic differentiation, and trabecular bone ingrowth (Boyan et al., 2017; Shah et al., 2019; Berger et al., 2022). Thus, it is crucial to clarify the regulatory effect of silicon-based biomaterials on macrophage polarization and succedent osteogenesis.

Recently, it was shown that lithography technology shows potential in precisely tailoring the surface topography of biomaterials (Kooy et al., 2014; Brown et al., 2023). Therefore, the surface submicron pillar has been a potential pro-osteogenesis design. Submicron pillars can modulate cell behavior such as adhesion and migration (Nouri-Goushki et al., 2020; Angeloni et al., 2023). Lithographically formed silicon nanorods promote the osteopontin expression in pre-osteoblasts, which reveals its pro-osteogenesis effect (Ganjian et al., 2022). In addition, the density and height of submicron pillars have shown an immunomodulating effect in regulating M1/M2 polarization of macrophages (Nouri-Goushki et al., 2021). Specific submicron pillars (500 nm in diameter and 2 μm in height) can stimulate macrophage differentiation into osteoclasts (Akasaka et al., 2022). Notably, the submicron silicon pillars in existing studies are dominantly regular. However, the submicron features of human bone (such as lamellae, osteocytes, and the extrafibrillar matrix) are naturally irregular (Shah et al., 2019). The effect of pillar morphology should be considered further when evaluating the biological response of submicron silicon pillars.

Therefore, this study proposes a submicron forest-like (Fore) silicon surface for promoting bone regeneration and compares it with common submicron silicon columns and the smooth (Smo) silicon surface (Figure 1). We investigate the macrophage response and subsequent pro-osteogenesis effect. The *in vivo* bone regeneration is evaluated in the mouse calvarial defect model. The result will enhance the experimental basis for future silicon-based biomaterial designs.

2 Materials and methods

2.1 Sample preparation and characterization

The Smo, regular (Regu), and Fore submicron silicon surfaces were manufactured by Suzhou Research Materials Microtech Co., Ltd. (China). The Smo surface was a 4,000-grit polished silicon wafer. The Regu surface contained repeating photoetched columns (diameter: 400–500 nm; height: 1,000 nm). The Fore surface contained plasma-treated irregular (diameter: 250–500 nm; height: 800–1,000 nm) pillars. The surface topography was characterized using a field emission scanning electronic microscope (FE-SEM; Hitachi S-4800, Japan). Surface roughness parameters (Sa, Sq, and Sz) were detected using an atomic force microscope (AFM; 5500, Agilent, United States) in a 2.5 mm × 2.5-mm area. The surface chemical composition was analyzed using an energy-dispersive X-ray spectrometer (EDS; EDAX, United States). Surface wettability with distilled water in the air was detected using an optical contact angle meter (DSA100, Kruss, Germany). In addition, a solution containing 1% bovine serum albumin (BSA; Sigma-Aldrich, United States) was prepared, and the protein adsorption capacity of the surface of the three samples was measured using MicroBCA assay.

2.2 Macrophage polarization

Raw264.7 cells were seeded on the surface of each sample (1×10^4 cells/well). After 1, 3, and 9 days, macrophages were fixed with the Gluta fixative, dehydrated with graded ethanol, ion sputtered, and then observed using the FE-SEM (Hitachi S-4800, Japan). For each group of samples, 5 fields of view were selected at 3, 6, 9, and 12 o'clock in the center and around the samples. The spread area and longest diameter of the macrophages were measured using ImageJ software. In addition, F-actin was stained using phalloidin-Alexa Fluor 488 (1: 1,000; C2201S, Beyotime, China) and incubated for 30 min, followed by incubation in mounting medium with DAPI (ab104139, Abcam, United States) and was visualized using the Olympus FV3000 confocal microscope. The cell proliferation activity of the three groups of samples was detected using the CCK-8 method.

After 7 days, the expression of M1 markers (*Mhc2*, *Inos*, and *Il-6*) and M2 markers (*Cd163* and *Cd206*) was evaluated using qRT-PCR. Primer sequences are shown in Supplementary Table S1. The TNF-α level in the cell culture was detected using an ELISA kit (EK0527, Boster, China). Meanwhile, the expression of M1 markers (iNOS and CD86) and M2 markers (CD163, CD206, and Arg-1) was evaluated using Western blot. Antibodies and dilutions included anti-CD86 (1: 200; ab112490, Abcam, United States), anti-iNOS (1:1,000; ab178945, Abcam, United States), anti-CD206 (1:1,000; ab64693, Abcam, United States), anti-CD163 (1:1,000; ab182422, Abcam, United States), and anti-ARG1 (1:5,000; ab233548, Abcam, United States). The anti-β-actin antibody (1:5,000, ab6276, Abcam, United States) was used for quantifying the loading amount of the sample. In addition, the expression of M2 polarization markers

(CD206 and CD163) was observed by immunofluorescence. Antibodies and dilutions included anti-CD206 (1:500; ab64693, Abcam, United States) and anti-CD163 (1:1,000; ab182422, Abcam, United States). All stained samples were visualized using the Olympus FV3000 confocal microscope.

2.3 Osteogenesis *in vitro*

To mimic the microenvironment of bone regeneration, the MC3T3-E1 pre-osteoblasts were cultured on the three silicon surfaces and stimulated by the supernatant from macrophages cultured on the corresponding surfaces (Figure 5A). On day 7 after stimulation, the expression of osteogenic genes (*Alpl*, *Col1a1*, and *Runx2*) was detected by qRT-PCR. The alkaline phosphatase (ALP) activity was analyzed using the alkaline phosphatase activity detection kit (Beyotime, P0321S). In addition, tetracycline solution (ML6401, Mlbio, China) was added at a ratio of 1:100 to the culture medium. At 14 days, Ob fixing solution was added after PBS washing, and DAPI staining solution was added. Given that tetracycline can selectively integrate with new borne hydroxyapatite calcium (Wang et al., 2006; Sakai et al., 2010; Sordi et al., 2021), the fluorescence intensity of tetracycline was observed under a fluorescence microscope. At 21 days, 2% Alizarin Red S Staining Solution (C0138, Beyotime, China) was used to quantify deposited mineral nodules. Then, the mineralized matrix stained with Alizarin Red was destained with 10% cetylpyridinium chloride (Sigma-Aldrich) in 10 mM sodium phosphate (pH 7.0; Sigma-Aldrich), and the calcium concentration was determined using a spectrophotometer (Thermo Fisher Scientific) at 562 nm, with a standard calcium curve in the same solution.

In addition, the supernatant of the macrophages cultured on the three silicon surfaces was also used as the stimulant for rat bone marrow mesenchymal stem cells (rBMSCs). On day 3 after stimulation, ALP staining (C3206, Beyotime, China) and the expression of osteogenic proteins (RUNX2, ALPL, and OPN) were detected. Antibodies include anti-RUNX2 (1:1,000; D1L7F, Cell Signaling Technology, United States), anti-ALPL (1:1,000; 11187-1-AP, Proteintech, China), and anti-OPN (1:1,000; 22952-1-AP, Proteintech, China). The anti-β-actin antibody (1:5,000; ab6276, Abcam, United States) was used for quantifying the loading amount of the sample.

2.4 Bone regeneration *in vivo*

The calvaria of mice was selected as the animal model for *in vivo* osteogenesis evaluation (Wancket, 2015). To examine the bone regeneration effect of the Smo, Regu, and Fore surfaces, 54 male mice (8 weeks old) were selected and randomly divided into three groups under the ethical approval of the Biomedical Ethics Committee of Medical College, Xi'an Jiaotong University (No. 2021-1563). A 4-mm diameter critical-sized bone defect was created in the parietal bone of each mouse using an annulated bit. Each defect was subsequently filled with Smo, Regu, or Fore samples. For sample harvesting, the animals were euthanized with a lethal dose of pentobarbital sodium. The mouse craniums were collected and fixed in 10% formaldehyde for 72 h at room temperature. The samples were scanned by micro-CT (Y.Cheetah, YXLON, Germany). Two-dimensional slices with an isotropic resolution of 19 μm were generated and used for three-dimensional reconstruction. First, we reconstructed the three-dimensional images with the whole sample, including the silicon samples and mouse craniums. Next, a threshold was applied to the images to segment the silicon from the background, and the same threshold was used for all samples. A 4.5-mm-diameter round region of interest (ROI) centered around the epicenter of the defect was analyzed. After setting a determinate threshold, the new bone volume fraction (bone volume/total volume, BV/TV) and trabecular thickness (tb.th) were obtained.

After micro-CT analysis, the craniums were decalcified in 9% formic acid, and then, the implants were removed gently from the craniums. The decalcified craniums were dehydrated in gradient ethanol, embedded in paraffin, cut into slices, and stained with H&E. The obtained sections were also dewaxed in xylene, hydrated in gradient ethanol, incubated in 0.3% hydrogen peroxide, blocked with 1% goat serum (Sigma-Aldrich, United States), and incubated with RANKL (anti-RANKL antibody, 1:200, Abcam, ab216484). Examination and analysis were performed in blind.

2.5 Statistical analysis

Data on biological experiments were obtained from at least three parallel experiments and presented as the mean ± standard deviation. The animals were randomly grouped before surgical treatment. Statistical differences were determined using one-way ANOVA with Tukey's *post hoc* test.

3 Results

3.1 Surface characterization

As shown in Figure 2A, the Regu silicon surface presented cylindrical pillars with uniform spacing, while the Fore silicon surface presented pillars with irregular shape and space. No representative submicron feature appeared on the Smo silicon surface. The average top surface area (Figure 2B) and maximum diameter (Figure 2C) of the pillars in Regu and Fore surfaces showed no statistical difference. The dominant element of the three samples was silicon (Figure 2D). Atomic force microscopy (Figure 2E) revealed that the surface roughness parameters (Sa, Sq, and Sz) of the Fore surface were increased compared to the Regu and Smo surfaces (Figures 2F–H). In addition, the Fore surface showed enhanced protein adsorption (Figure 2I) and hydrophilicity (Figure 2J).

3.2 Promoted macrophage M2 polarization on the Fore surface

The morphology of macrophages cultured on the three surfaces was observed first (Figure 3A). At 1 day after seeding, macrophages on the Smo and Fore surfaces fused. After 3 days, these macrophages on the Smo and Fore surfaces elongated and connected *via* pseudopodia. This trend was more notable after 9 days. On the other hand, macrophages on the Regu surface remained relatively round in shape, which implied the characteristics of colonization. Quantifications of the cell length (Figure 3B) and spread area (Figure 3C) showed significant differences

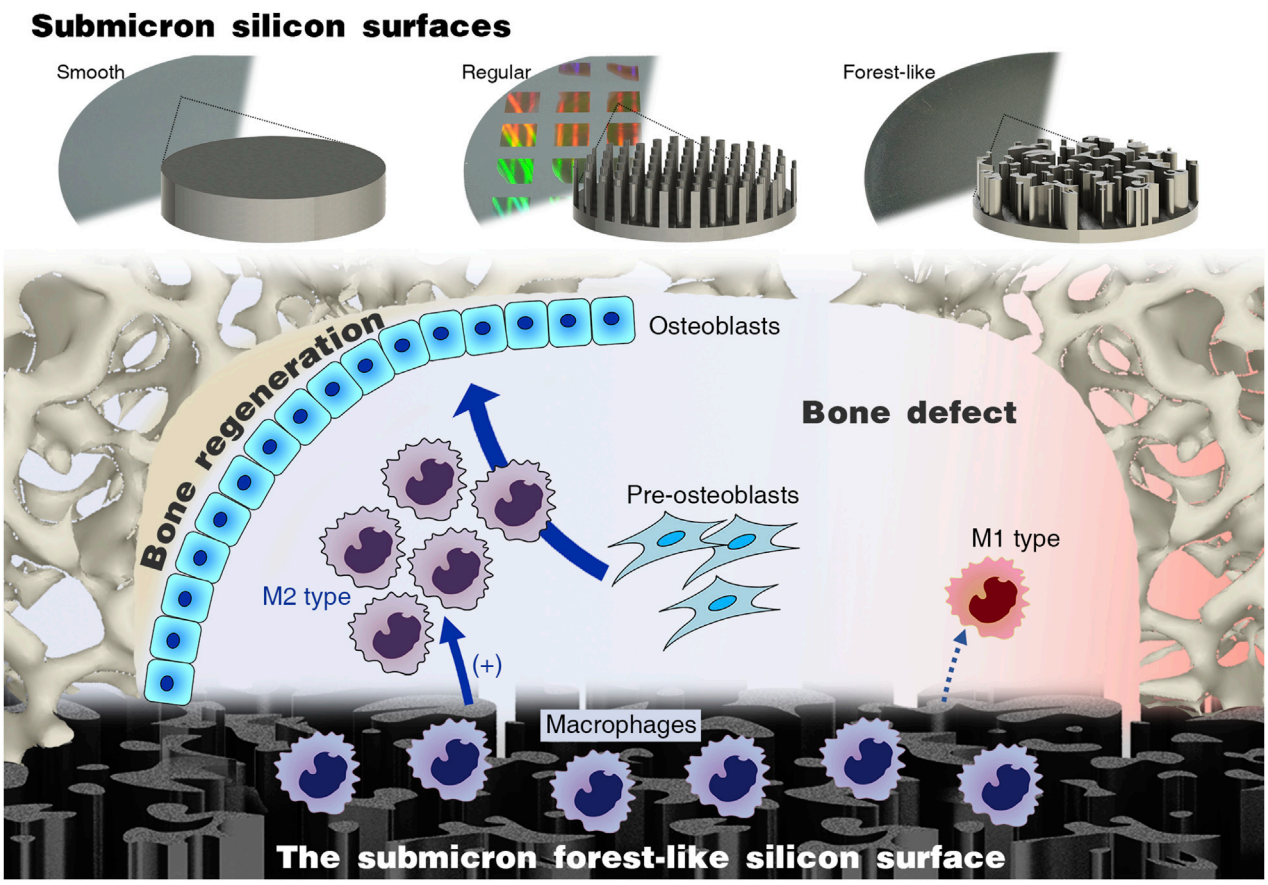

FIGURE 1
Submicron forest-like (Fore) silicon surface promotes M2-type macrophage polarization for bone generation.

between the three groups. Therefore, the Fore surface showed a significantly higher cell length and spread area. The observation obtained by confocal microscopy (Figure 3D) confirmed this trend. Moreover, the proliferation of macrophages cultured on the Fore surface increased 9 days after seeding (Figure 3E).

qRT-PCR showed that the mRNA expression level of M1 polarization markers (*Mhc2*, *Inos*, and *Il-6*) in the Fore group was significantly decreased, while the mRNA expression level of M2 polarization markers (CD163 and CD206) was significantly increased (Figure 4A). At the same time, the levels of TNF-α secreted by Raw264.7 cells on the surface of Fore samples were significantly reduced (Figure 4B). The immunofluorescence intensity of CD163 and CD206 in the Fore group was significantly enhanced, with statistical differences (Figures 4C, D). This trend was also verified using Western blot (Figure 4E) that the protein expression of M2 polarization factors (CD206, CD163, and Arg-1) on the Fore sample increased significantly, and the protein expression of M1 polarization factors (CD86 and iNOS) decreased significantly.

3.3 Enhanced *in vitro* osteogenesis on the Fore surface

After being stimulated by the supernatant from macrophages cultured on corresponding surfaces (Figure 5A), the expression of osteogenic genes (*Alpl*, *Col1a1*, and *Runx2*) of MC3T3-E1 cells in the Fore + RAW group increased significantly on day 7 (Figure 5B). At the same time, the ALP activity in the Fore + RAW group was significantly higher (Figure 5C). The promotion of osteogenesis was also observed by immunofluorescence by tetracycline staining in the Fore + RAW group at 14 days (Figure 5D, E). Similar trends were also found in the staining of Alizarin Red S at 21 days (Figure 5F and Supplementary Figure S1), with more mineral nodules in the Fore + RAW group.

In rBMSCs stimulated by the supernatant from macrophages cultured on the three silicon surfaces (Figure 5G), the alkaline phosphatase activity (Figure 5H) and the expression of RUNX2, ALPL, and OPN (Figure 5I) were increased significantly. Overall, these results proved that the immune microenvironment of the Fore surface could promote bone formation.

3.4 Promoted *in vivo* bone regeneration on the Fore surface

As shown in Figure 6A, the bone regeneration was investigated with a round (Φ 4 mm) bone defect on the mouse calvaria. At 4 weeks post-implantation, a new bone began to form on the edge of the bone defect in all 3 groups, and at 8 weeks and 12 weeks, the new bone on the surface of Fore samples was significantly higher than those in Smo and Regu samples, respectively (Figures 6B–D). Histological analysis

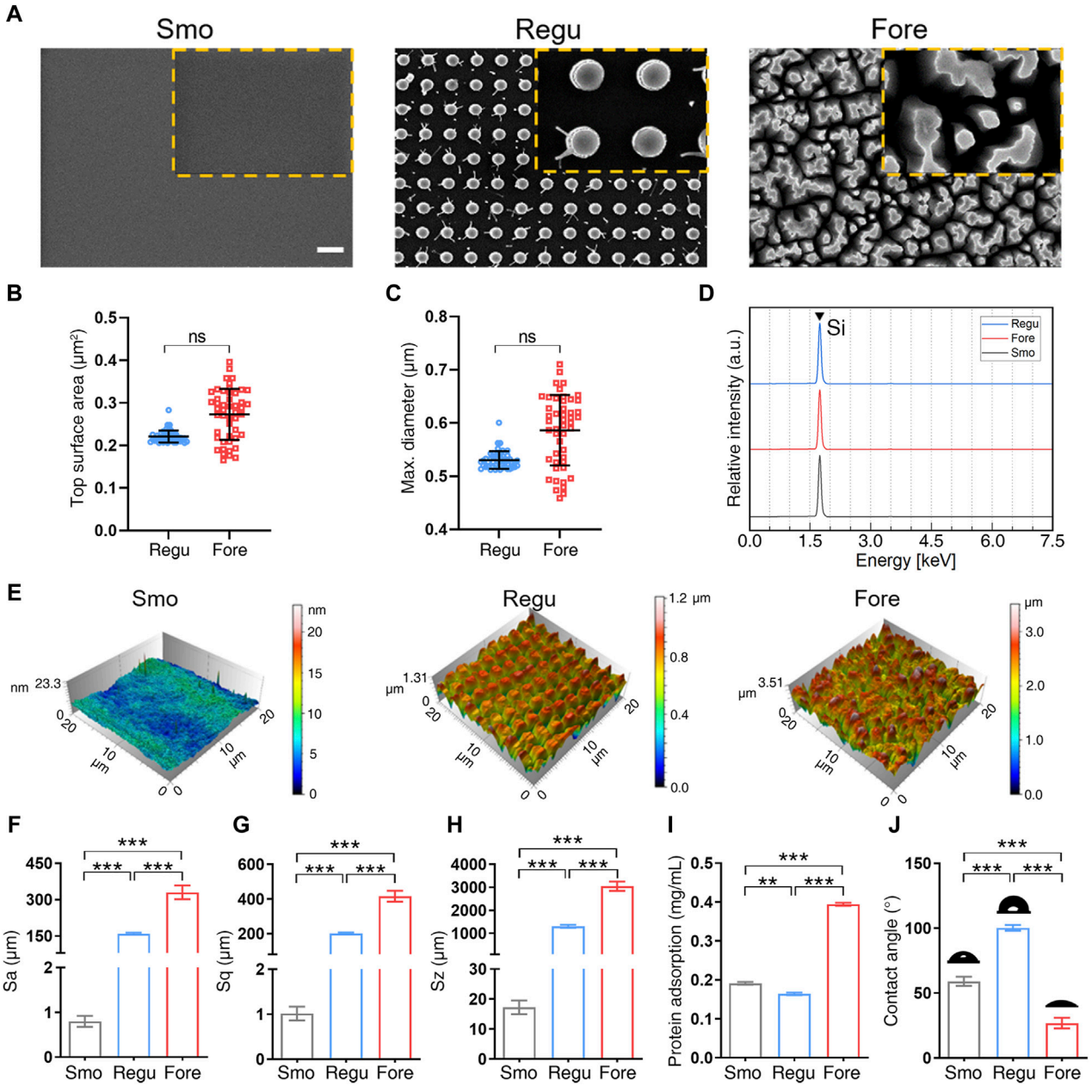

FIGURE 2
Surface characterization. **(A)** Field emission scanning electronic microscope (FE-SEM) images of the three surfaces. Scale bar: 1 μm. **(B)** Top columnar area of regular (Regu) and Fore samples. **(C)** Particle size of Regu and Fore samples. **(D)** Element component of the three surfaces. **(E)** Representative atomic force microscope (AFM) images of the three surfaces. **(F–H)** Surface roughness parameters, including Sa **(F)**, Sq **(G)**, and Sz **(H)**. **(I)** Protein adsorption capacity of the three surfaces. **(J)** Contact angle with deionized water of the three surfaces. One-way ANOVA with Tukey's *post hoc* test was used for statistical analysis. ns: no significance. *$p < 0.05$, **$p < 0.01$, and ***$p < 0.001$.

of the heart, liver, spleen, lung, and kidney at 12 weeks confirmed good biosafety of all Smo, Regu, and Fore specimens (Supplementary Figure S2). At 12 weeks, the expression level of RANKL in the new bone on the Fore surface decreased significantly (Figures 6E, F).

4 Discussion

In this study, a submicron forest-like silicon surface was proposed to verify whether its irregular distribution of silicon pillars on biomaterials can promote bone regeneration. The result showed enhanced macrophage M2 polarization and succedent osteogenesis *in vitro* and promoted bone defect closure *in vivo* compared with the submicron regular and smooth silicon surfaces. Therefore, the irregular forest-like submicron pillar is a potential design for developing silicon-based bone healing biomaterials.

Human bone is a complex multi-scale hierarchical structure (Reznikov et al., 2014). Therefore, varied surface topographies at the micron, submicron, and nano-scales are developed in current intrabony implants (Shah et al., 2019) and are closely related to

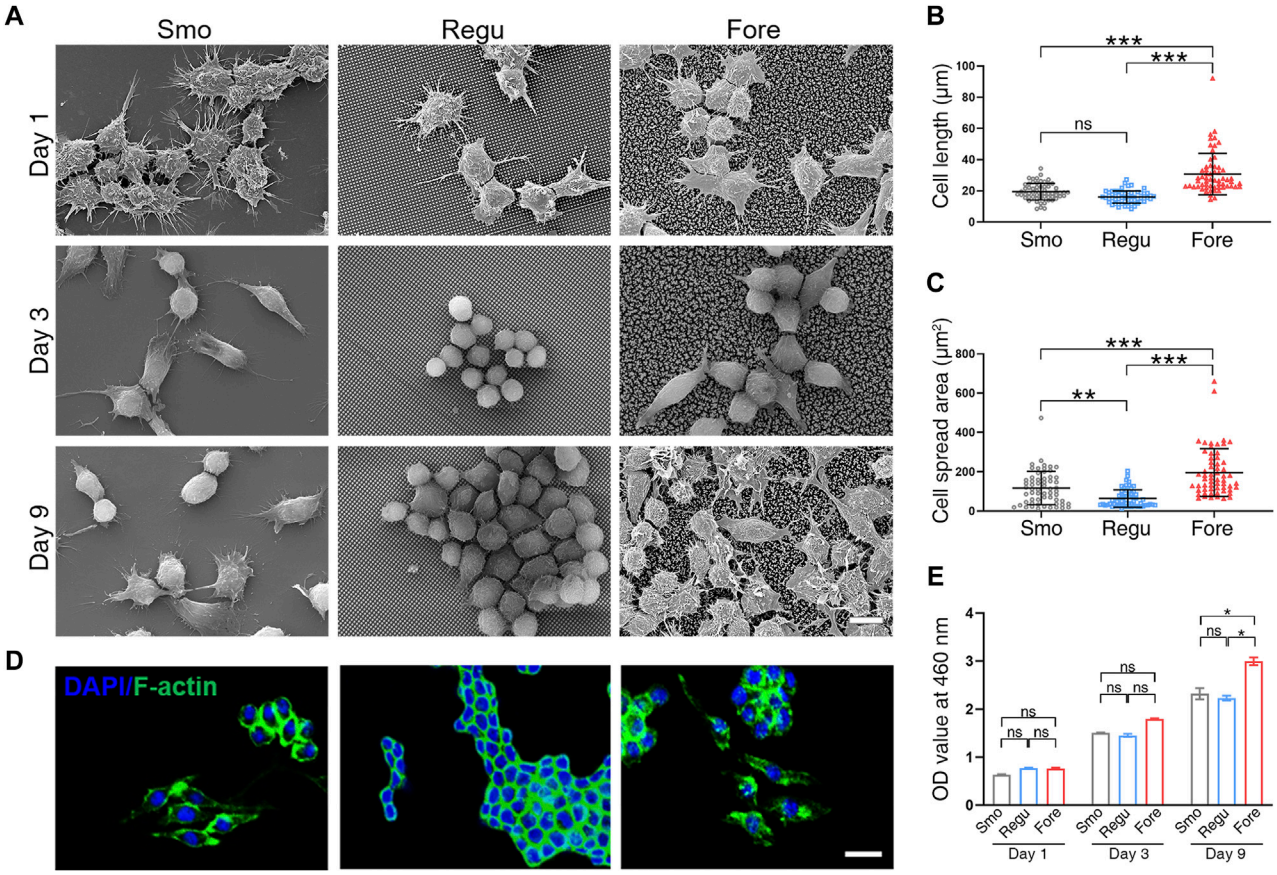

FIGURE 3
Morphological changes in Raw264.7 cells on the three surfaces. **(A)** Representative SEM images of cells on different surfaces. **(B)** Cell elongation and **(C)** cell spreading were measured. **(D)** Representative LSCM images of F-actin distribution in cells. **(E)** Proliferative activity of Raw264.7 cells on the three samples obtained by CCK-8 assay. Scale bar: 10 μm. One-way ANOVA with Tukey's *post hoc* test was used for statistical analysis. ns: no significance. $*p < 0.05$, $**p < 0.01$, and $***p < 0.001$.

bone regeneration. It has been well documented that the micron topography facilitates the mechanical anchorage between bone and biomaterials, while the nano-topography offers more adhesion positions for proteins at the early stage of bone regeneration (Albrektsson and Wennerberg, 2019). However, the significance of submicron topography has not been clearly defined yet. A typical submicron topography is sandblasted and acid-etched (SLA) pits on titanium implants, which is the dominant surface topography in dental implants (Smeets et al., 2016). The SLA implants have shown a less than 5% failure rate at 10 years post-implantation (Albrektsson and Wennerberg, 2019), which implies the positive effect of submicron surface topography in biomaterials on bone regeneration. In this study, the irregularly distributed Fore structure showed higher potential in stimulating the M2 polarization of macrophages and osteogenesis of pre-osteoblasts. This finding is an important supplement to the correlation with surface topography and macrophage polarization. The forest-like silicon surface shows a larger pore size and more abundant porous structure than the regular silicon pillar surface, which may explain the better anti-inflammatory activity and osteogenesis potential (Garg et al., 2013; Rustom et al., 2019). The Fore surface was more hydrophilic than the Regu surface (Figure 2J). Macrophages adhered to a hydrophilic surface tend to enhance the secretion of anti-inflammatory cytokines and M2 surface markers (Hotchkiss et al., 2016; Lv et al., 2018). In addition, it is found that the "topographical effect" plays important roles in macrophage behavior and osteogenesis (Ma et al., 2014; Wang J. et al., 2018). Sa, Sq, and Sz may influence the anti-inflammatory activity and osteogenesis potential. Overall, the result of this study echoes the current opinion that material surfaces resembling the natural bone structure are beneficial to osteogenesis (Boyan et al., 2017; Shah et al., 2019; Berger et al., 2022).

To date, titanium-based implants are holding the largest market share in tooth and bone restoration (Kaur and Singh, 2019). However, the biocompatibility of titanium is gradually being questioned due to inflammatory reactivity or metal hypersensitivity in some patients (Buettner and Valentine, 2012). Further improvement of surface biocompatibility is pivotal in developing the next generation of intrabony implants (Bandyopadhyay et al., 2023). Silicon, as a major trace element in humans (Martin, 2013), shows relatively stable *in vivo* metabolism (Jugdaohsingh et al., 2013). Wang et al. (2023) prepared silicon-deposited coatings on Ti-based implants via electron beam evaporation (Wang et al., 2023), which showed osteoinductive and immunomodulatory capacity. It was found that the burst

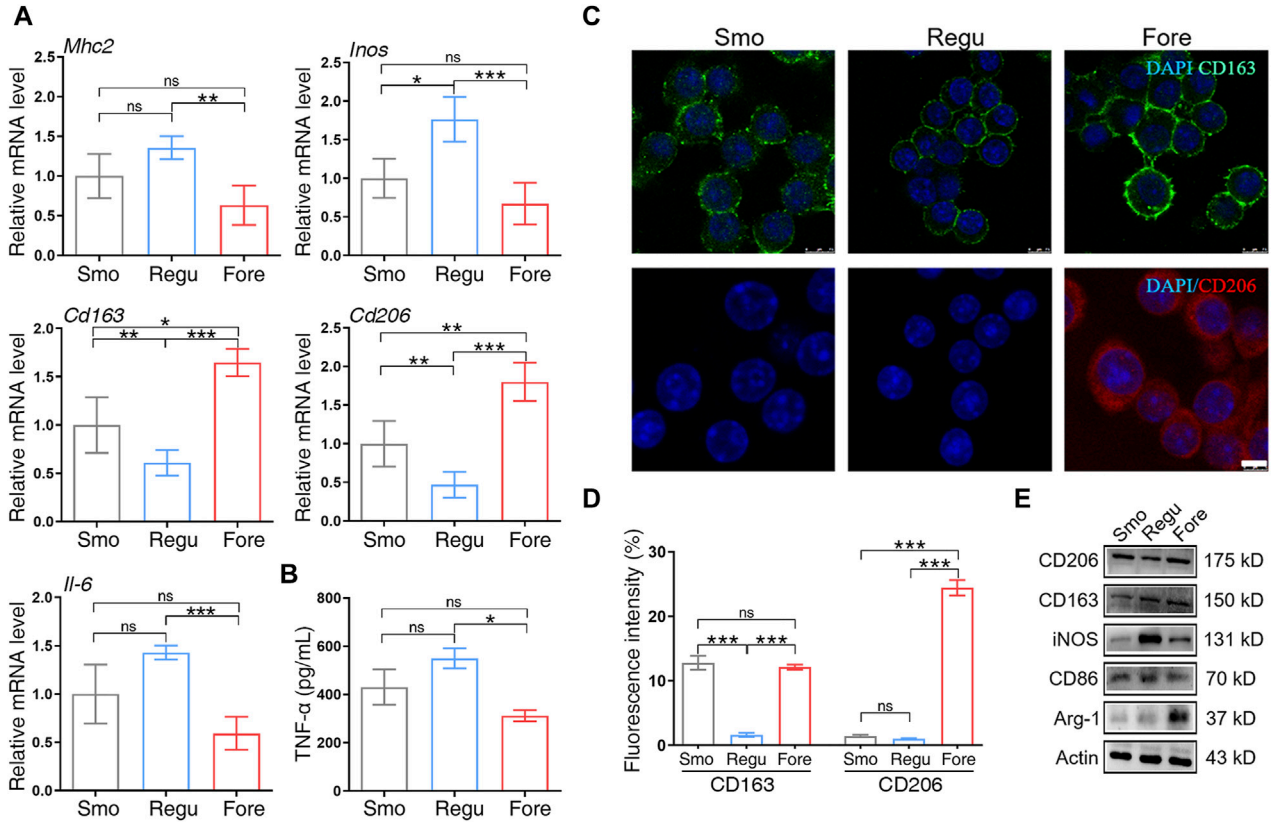

FIGURE 4
Macrophage polarization on the three surfaces. **(A)** Relative gene expression of M1 and M2 polarization markers of macrophages cultured on the three surfaces. **(B)** ELISA detection of tumor necrosis factor alpha (TNF-α) on the three surfaces. **(C, D)** Immunofluorescent staining and semiquantitative analysis for CD163 and CD206. Scale bar: 25 μm. **(E)** Protein expression of M1 and M2 polarization markers of macrophages cultured on the three surfaces. One-way ANOVA with Tukey's *post hoc* test was used for statistical analysis. ns: no significance. *$p < 0.05$, **$p < 0.01$, and ***$p < 0.001$.

release of Si dominated the early stages of implantation to create a favorable osteoimmunomodulatory microenvironment by the timely conversion of macrophages from an M1 to an M2 phenotype that facilitated osteogenic differentiation. In addition, the release of Si also directly activated stem cells and remodeled the extracellular matrix for late osseointegration. For instance, Francesco et al. increased the surface porosity and biological activity of the implants by embedding Si_3N_4 particles on the surface of PEEK implants (Boschetto et al., 2021), which showed the advantages of a low elastic modulus, improved bone integration, and promoted antibacterial effects. At the same time, a porous scaffold based on a Fe–Si alloy was manufactured by 3D printing technology, which could reduce cytotoxicity and improve mechanical stability and bone integration ability (Bondareva et al., 2022). Similar findings have been made in other implants, for example, Edward et al. found that mechanically matched silicone brain implants could potentially improve the long-term functionality and reliability of brain implants by minimizing strain and stress due to movements and swelling of the brain in both lateral and axial directions relative to the implant (E. Zhang D. H. et al., 2021). The result of this study further suggests that irregular submicron silicon surfaces are better than regular submicron silicon surfaces in bone regeneration, which is important for fabricating and optimizing future silicon-based biomaterials.

In addition, the fate of macrophages can be regulated by the surface topography of biomaterials (Hotchkiss et al., 2016; Abaricia et al., 2020; Zhu G. et al., 2021). Existing studies have confirmed that the shape and polarization of macrophages can be influenced by nanotopography of biomaterials (Ma et al., 2014; Neacsu et al., 2014; Wang J. et al., 2018). Nanotubes with a larger diameter are prone to induce M2 polarization of macrophages (Lü et al., 2015; Xu et al., 2019; Yu et al., 2021). The result of this study supports that submicron morphologies at the range of 250–500 nm can also manipulate macrophage polarization, which is an important supplement to current theories.

The control of immune responses after biomaterial implantation in the body has long been a concern in the development of medical implants (Naik et al., 2018). The increase in the number of M2-like macrophages in the damaged tissue has been suggested to be an essential event in tissue healing. Delayed polarization from the inflammatory M1 phenotype into the anti-inflammatory/healing M2 phenotype would lead to compromised stem/progenitor cell response to inhibit the functional regeneration of skin, muscle, heart, nerve, and bone (Zhang E. N. et al., 2021; Li et al., 2021). In this proof-of-concept report using bone as a model tissue, we demonstrate tissue–biomaterial integration in

10.3389/fbioe.2024.1356158

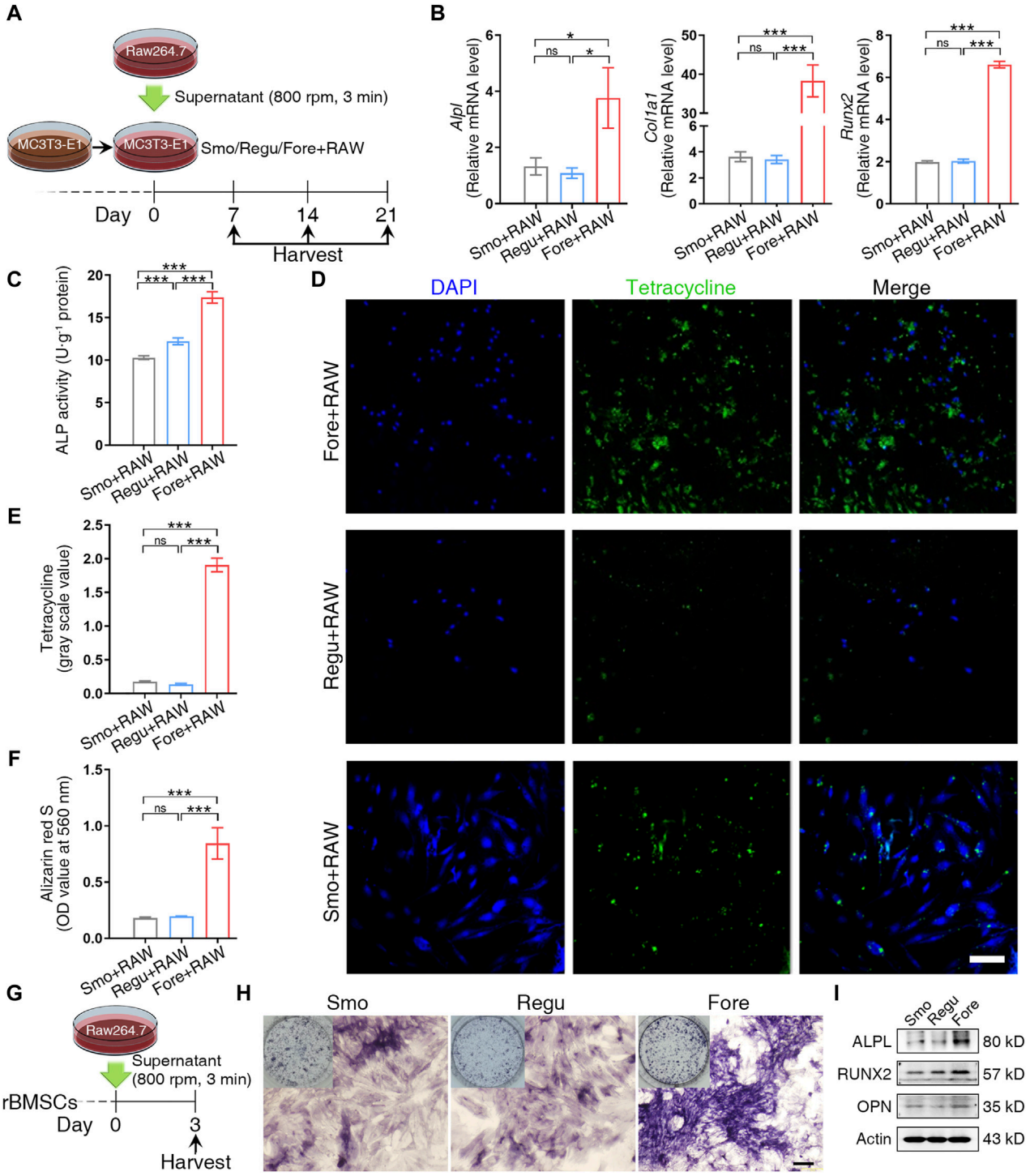

FIGURE 5
Cell osteogenic differentiation on the surface of the three samples. **(A)** Schematic diagram of MC3T3-E1 cell management. **(B)** Relative gene expression of osteogenic genes of MC3T3-E1 cells cultured on the three surfaces on day 7. **(C)** Alkaline phosphatase (ALP) activity of MC3T3-E1 cells cultured on the three surfaces on day 7. **(D, E)** Tetracycline distribution in MC3T3-E1 cells cultured on the three surfaces and semiquantitative analysis on day 14. White scale bar: 100 μm. **(F)** Semiquantification of the calcium nodule formation evaluation by Alizarin Red staining on day 21. **(G)** Schematic diagram of rat bone marrow mesenchymal stem cell (rBMSC) management. **(H)** ALP activity staining. Black scale bar: 200 μm. **(I)** Protein expression of osteogenic markers. One-way ANOVA with Tukey's *post hoc* test was used for statistical analysis. ns: no significance. *$p < 0.05$, **$p < 0.01$, and ***$p < 0.001$.

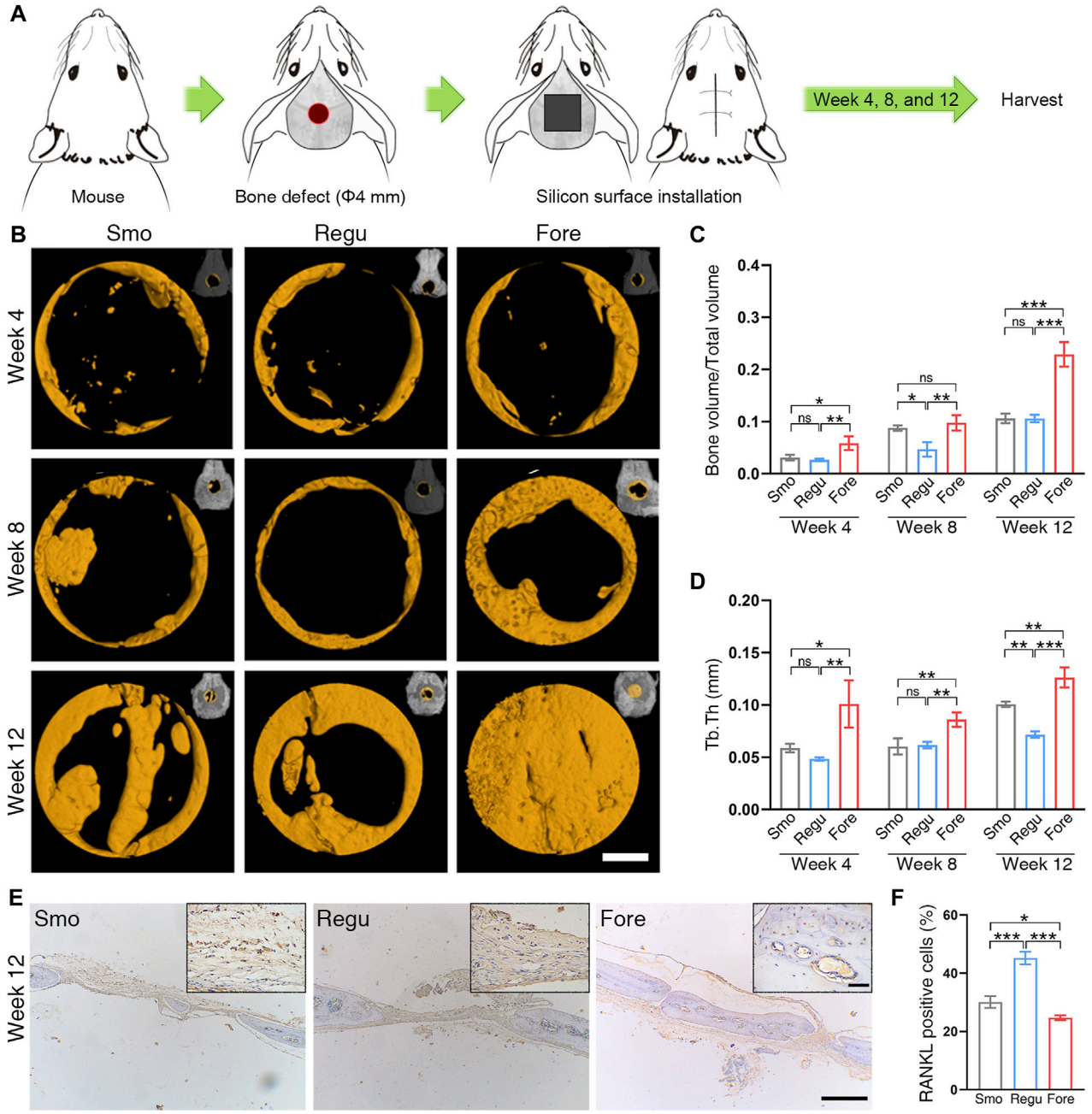

FIGURE 6
Bone regeneration of the mouse calvarial defect. **(A)** Calvarial defect model. **(B)** Bone growth in the calvarial defect at 4, 8, and 12 weeks after surgery revealed by micro-CT. White scale bar: 1.0 mm. **(C)** Quantitative analysis of bone volume/total volume (BV/TV) based on micro-CT. **(D)** Quantitative analysis of trabecular thickness (Tb.Th) based on micro-CT. **(E)** RANKL expression in the calvarial bone revealed by immunohistochemistry at 12 weeks. Long black scale bar: 500 μm. Short black scale bar: 50 μm. **(F)** Quantification of RANKL staining. One-way ANOVA with Tukey's *post hoc* test was used for statistical analysis. ns: no significance. *$p < 0.05$, **$p < 0.01$, and ***$p < 0.001$.

irregular forest-like submicron silicon-based coating with the concurrent modulation of the macrophage response and cytokine profile manifested in the M2-based phenotype. This phenotype switching is pivotal in improving tissue regeneration induced by biomaterials (Huyer et al., 2020; Schlundt et al., 2021). Osteoclasts play a key role in the process of bone regeneration, and RANKL (ligand), expressed by osteoblasts and bone marrow stromal cells, attaches to RANK receptors on mature osteoclasts and osteoclast progenitor cells and promotes their differentiation (Shah et al., 2018; Huntley et al., 2019). In addition to inducing osteoclast activity, RANKL also induces osteoclasts to attach to the bone surface and longevity (Chaparro et al., 2022). In this study, we evaluated the expression of RANKL in the new bone and found that RANKL expression decreased significantly in the Fore group while increased significantly in the Regu group, which was consistent with the results of bone regeneration.

5 Conclusion

In this study, an irregular forest-like submicron silicon surface was proposed as a promising design of biomaterials for bone regeneration. It demonstrated better *in vitro* and *in vivo* biological responses than the regular submicron silicon surface and smooth silicon surface, including promoting macrophage M2 polarization and facilitating bone formation. This finding enriches the research basis for silicon-based biomaterials and highlights the irregular surface design for better bone regeneration performance.

Data availability statement

The datasets presented in this study can be found in online repositories. The names of the repository/repositories and accession number(s) can be found in the article/Supplementary Material.

Ethics statement

The animal study was approved by the Biomedical Ethics Committee of Medical College, Xi'an Jiaotong University. The study was conducted in accordance with the local legislation and institutional requirements.

Author contributions

GS: conceptualization, investigation, methodology, formal analysis, and writing–original draft. TS: funding acquisition, software, visualization, writing–review and editing. SM: writing–review and editing. ML: writing–review and editing ZQ: conceptualization, funding acquisition, resources, project administration, supervision, validation, writing–review and editing. AL: conceptualization, funding acquisition, resources, project administration, supervision, validation, writing–review and editing.

Funding

The author(s) declare that financial support was received for the research, authorship, and/or publication of this article. The author acknowledges the support by the Innovative Research Groups of the National Natural Science Foundation of China (51721004), the National Natural Science Foundation of China (82071078), the Natural Science Foundation of Shaanxi Province (2023-JC-QN-0842), the Fundamental Research Funds for the Central Universities, Xi'an Jiaotong University (xtr012019007, xzy022022071), the Opening Research Fund from the Key Laboratory of Shaanxi Province for Craniofacial Precision Medicine Research, College of Stomatology, Xi'an Jiaotong University (2021LHM-KFKT001), and the Transdisciplinary Support Project for PhD, Xi'an Jiaotong University (IDT1721).

Acknowledgments

The authors acknowledge Suzhou Research Materials Microtech Co., Ltd. for their assistance in the preparation of silicon samples.

Conflict of interest

The authors declare that the research was conducted in the absence of any commercial or financial relationships that could be construed as a potential conflict of interest.

Publisher's note

All claims expressed in this article are solely those of the authors and do not necessarily represent those of their affiliated organizations, or those of the publisher, the editors, and the reviewers. Any product that may be evaluated in this article, or claim that may be made by its manufacturer, is not guaranteed or endorsed by the publisher.

Supplementary material

The Supplementary Material for this article can be found online at: https://www.frontiersin.org/articles/10.3389/fbioe.2024.1356158/full#supplementary-material

References

Abaricia, J. O., Shah, A. H., Chaubal, M., Hotchkiss, K. M., and Olivares-Navarrete, R. (2020). Wnt signaling modulates macrophage polarization and is regulated by biomaterial surface properties. *Biomaterials* 243, 119920. doi:10.1016/j.biomaterials.2020.119920

Akasaka, T., Tamai, M., Yoshimura, Y., Ushijima, N., Numamoto, S., Yokoyama, A., et al. (2022). Different micro/nano-scale patterns of surface materials influence osteoclastogenesis and actin structure. *Nano Res.* 15 (5), 4201–4211. doi:10.1007/s12274-021-4026-3

Albrektsson, T., and Wennerberg, A. (2019). On osseointegration in relation to implant surfaces. *Clin. Implant Dent. Relat. Res.* 21 (Suppl. 1), 4–7. doi:10.1111/cid.12742

Angeloni, L., Popa, B., Nouri-Goushki, M., Minneboo, M., Zadpoor, A. A., Ghatkesar, M. K., et al. (2023). Fluidic force microscopy and atomic force microscopy unveil new insights into the interactions of preosteoblasts with 3D-printed submicron patterns. *Small* 19 (2), e2204662. doi:10.1002/smll.202204662

Bai, X., Gao, M., Syed, S., Zhuang, J., Xu, X., and Zhang, X. Q. (2018). Bioactive hydrogels for bone regeneration. *Bioact. Mat.* 3 (4), 401–417. doi:10.1016/j.bioactmat.2018.05.006

Bandyopadhyay, A., Mitra, I., Goodman, S. B., Kumar, M., and Bose, S. (2023). Improving biocompatibility for next generation of metallic implants. *Prog. Mat. Sci.* 133, 101053. doi:10.1016/j.pmatsci.2022.101053

Berger, M. B., Slosar, P., Schwartz, Z., Cohen, D. J., Goodman, S. B., Anderson, P. A., et al. (2022). A review of biomimetic topographies and their role in promoting bone formation and osseointegration: implications for clinical use. *Biomimetics* 7 (2), 46. doi:10.3390/biomimetics7020046

Bock, R. M., Jones, E. N., Ray, D. A., Sonny Bal, B., Pezzotti, G., and McEntire, B. J. (2017). Bacteriostatic behavior of surface modulated silicon nitride in comparison to polyetheretherketone and titanium. *J. Biomed. Mat. Res. A* 105 (5), 1521–1534. doi:10.1002/jbm.a.35987

Bondareva, J. V., Dubinin, O. N., Kuzminova, Y. O., Shpichka, A. I., Kosheleva, N. V., Lychagin, A. V., et al. (2022). Biodegradable iron-silicon implants produced by additive manufacturing. *Biomed. Mat.* 17 (3), 035005. doi:10.1088/1748-605X/ac6124

Boschetto, F., Marin, E., Ohgitani, E., Adachi, T., Zanocco, M., Horiguchi, S., et al. (2021). Surface functionalization of PEEK with silicon nitride. *Biomed. Mat.* 16 (1), 015015. doi:10.1088/1748-605X/abb6b1

Bosshardt, D. D., Chappuis, V., and Buser, D. (2017). Osseointegration of titanium, titanium alloy and zirconia dental implants: current knowledge and open questions. *Periodontol* 73 (1), 22–40. doi:10.1111/prd.12179

Boyan, B. D., Lotz, E. M., and Schwartz, Z. (2017). <sup/>Roughness and hydrophilicity as osteogenic biomimetic surface properties. *Tissue Eng. Part A* 23 (23-24), 1479–1489. doi:10.1089/ten.TEA.2017.0048

Brown, M. A., Zappitelli, K. M., Singh, L., Yuan, R. C., Bemrose, M., Brogden, V., et al. (2023). Direct laser writing of 3D electrodes on flexible substrates. *Nat. Comm.* 14 (1), 3610. doi:10.1038/s41467-023-39152-7

Buettner, K. M., and Valentine, A. M. (2012). Bioinorganic chemistry of titanium. *Chem. Rev.* 112 (3), 1863–1881. doi:10.1021/cr1002886

Chaparro, A., Beltrán, V., Betancur, D., Sam, Y.-H., Moaven, H., Tarjomani, A., et al. (2022). Molecular biomarkers in peri-implant health and disease: a cross-sectional pilot study. *Int. J. Mol. Sci.* 23 (17), 9802. doi:10.3390/ijms23179802

Chen, Z., Klein, T., Murray, R. Z., Crawford, R., Chang, J., Wu, C., et al. (2016). Osteoimmunomodulation for the development of advanced bone biomaterials. *Mat. Today* 19 (6), 304–321. doi:10.1016/j.mattod.2015.11.004

Du, X., Lee, S. S., Blugan, G., and Ferguson, S. J. (2022). Silicon nitride as a biomedical material: an overview. *Int. J. Mol. Sci.* 23 (12), 6551. doi:10.3390/ijms23126551

Friguglietti, J., Das, S., Le, P., Fraga, D., Quintela, M., Gazze, S. A., et al. (2020). Novel silicon titanium diboride micropatterned substrates for cellular patterning. *Biomaterials* 244, 119927. doi:10.1016/j.biomaterials.2020.119927

Ganjian, M., Modaresifar, K., Rompolas, D., Fratila-Apachitei, L. E. E., and Zadpoor, A. A. A. (2022). Nanoimprinting for high-throughput replication of geometrically precise pillars in fused silica to regulate cell behavior. *Acta Biomater.* 140, 717–729. doi:10.1016/j.actbio.2021.12.001

Garg, K., Pullen, N. A., Oskeritzian, C. A., Ryan, J. J., and Bowlin, G. L. (2013). Macrophage functional polarization (M1/M2) in response to varying fiber and pore dimensions of electrospun scaffolds. *Biomaterials* 34 (18), 4439–4451. doi:10.1016/j.biomaterials.2013.02.065

Hotchkiss, K. M., Reddy, G. B., Hyzy, S. L., Schwartz, Z., Boyan, B. D., and Olivares-Navarrete, R. (2016). Titanium surface characteristics, including topography and wettability, alter macrophage activation. *Acta Biomater.* 31, 425–434. doi:10.1016/j.actbio.2015.12.003

Huntley, R., Jensen, E., Gopalakrishnan, R., and Mansky, K. C. (2019). Bone morphogenetic proteins: their role in regulating osteoclast differentiation. *Bone Rep.* 10, 100207. doi:10.1016/j.bonr.2019.100207

Huyer, L. D., Pascual-Gil, S., Wang, Y. F., Mandla, S., Yee, B., and Radisic, M. (2020). Advanced strategies for modulation of the material-macrophage interface. *Adv. Funct. Mat.* 30 (44), 1909331. doi:10.1002/adfm.201909331

Ishikawa, M., de Mesy Bentley, K. L., McEntire, B. J., Bal, B. S., Schwarz, E. M., and Xie, C. (2017). Surface topography of silicon nitride affects antimicrobial and osseointegrative properties of tibial implants in a murine model. *J. Biomed. Mat. Res. A* 105 (12), 3413–3421. doi:10.1002/jbm.a.36189

Jugdaohsingh, R., Sripanyakorn, S., and Powell, J. J. (2013). Silicon absorption and excretion is independent of age and sex in adults. *Brit. J. Nut.* 110 (6), 1024–1030. doi:10.1017/s0007114513000184

Jugdaohsingh, R., Tucker, K. L., Qiao, N., Cupples, L. A., Kiel, D. P., and Powell, J. J. (2004). Dietary silicon intake is positively associated with bone mineral density in men and premenopausal women of the Framingham Offspring cohort. *J. Bone Min. Res.* 19 (2), 297–307. doi:10.1359/jbmr.0301225

Kaur, M., and Singh, K. (2019). Review on titanium and titanium based alloys as biomaterials for orthopaedic applications. *Mat. Sci. Eng. C* 102, 844–862. doi:10.1016/j.msec.2019.04.064

Kooy, N., Mohamed, K., Pin, L. T., and Guan, O. S. (2014). A review of roll-to-roll nanoimprint lithography. *Nanoscale Res. Lett.* 9, 320. doi:10.1186/1556-276x-9-320

Li, J. H., Jiang, X. Q., Li, H. J., Gelinsky, M., and Gu, Z. (2021). Tailoring materials for modulation of macrophage fate. *Adv. Mat.* 33 (12), 2004172. doi:10.1002/adma.202004172

Lü, W. L., Wang, N., Gao, P., Li, C. Y., Zhao, H. S., and Zhang, Z. T. (2015). Effects of anodic titanium dioxide nanotubes of different diameters on macrophage secretion and expression of cytokines and chemokines. *Cell Prolif.* 48 (1), 95–104. doi:10.1111/cpr.12149

Lv, L., Xie, Y., Li, K., Hu, T., Lu, X., Cao, Y., et al. (2018). Unveiling the mechanism of surface hydrophilicity-modulated macrophage polarization. *Adv. Healthc. Mat.* 7 (19), 1800675. doi:10.1002/adhm.201800675

Ma, Q. L., Zhao, L. Z., Liu, R. R., Jin, B. Q., Song, W., Wang, Y., et al. (2014). Improved implant osseointegration of a nanostructured titanium surface via mediation of macrophage polarization. *Biomaterials* 35 (37), 9853–9867. doi:10.1016/j.biomaterials.2014.08.025

Martin, K. R. (2013). Silicon: the health benefits of a metalloid. *Metall. Ions Life Sci.* 13, 451–473. doi:10.1007/978-94-007-7500-8_14

Naik, S., Larsen, S. B., Cowley, C. J., and Fuchs, E. (2018). Two to tango: dialog between immunity and stem cells in health and disease. *Cell* 175 (4), 908–920. doi:10.1016/j.cell.2018.08.071

Neacsu, P., Mazare, A., Cimpean, A., Park, J., Costache, M., Schmuki, P., et al. (2014). Reduced inflammatory activity of RAW 264.7 macrophages on titania nanotube modified Ti surface. *Int. J. Biochem. Cell Biol.* 55, 187–195. doi:10.1016/j.biocel.2014.09.006

Nouri-Goushki, M., Isaakidou, A., Eijkel, B. I. M., Minneboo, M., Liu, Q., Boukany, P. E., et al. (2021). 3D printed submicron patterns orchestrate the response of macrophages. *Nanoscale* 13 (34), 14304–14315. doi:10.1039/d1nr01557e

Nouri-Goushki, M., Mirzaali, M. J., Angeloni, L., Fan, D., Minneboo, M., Ghatkesar, M. K., et al. (2020). 3D printing of large areas of highly ordered submicron patterns for modulating cell behavior. *ACS Appl. Mat. Interfaces* 12 (1), 200–208. doi:10.1021/acsami.9b17425

Reznikov, N., Shahar, R., and Weiner, S. (2014). Bone hierarchical structure in three dimensions. *Acta Biomater.* 10 (9), 3815–3826. doi:10.1016/j.actbio.2014.05.024

Rustom, L. E., Poellmann, M. J., and Wagoner Johnson, A. J. (2019). Mineralization in micropores of calcium phosphate scaffolds. *Acta Biomater.* 83, 435–455. doi:10.1016/j.actbio.2018.11.003

Sakai, V. T., Zhang, Z., Dong, Z., Neiva, K. G., Machado, M. A. A. M., Shi, S., et al. (2010). SHED differentiate into functional odontoblasts and endothelium. *J. Dent. Res.* 89 (8), 791–796. doi:10.1177/0022034510368647

Schlundt, C., Fischer, H., Bucher, C. H., Rendenbach, C., Duda, G. N., and Schmidt-Bleek, K. (2021). The multifaceted roles of macrophages in bone regeneration: a story of polarization, activation and time. *Acta Biomater.* 133, 46–57. doi:10.1016/j.actbio.2021.04.052

Shah, F. A., Thomsen, P., and Palmquist, A. (2018). A review of the impact of implant biomaterials on osteocytes. *J. Dent. Res.* 97 (9), 977–986. doi:10.1177/0022034518778033

Shah, F. A., Thomsen, P., and Palmquist, A. (2019). Osseointegration and current interpretations of the bone-implant interface. *Acta Biomater.* 84, 1–15. doi:10.1016/j.actbio.2018.11.018

Smeets, R., Stadlinger, B., Schwarz, F., Beck-Broichsitter, B., Jung, O., Precht, C., et al. (2016). Impact of dental implant surface modifications on osseointegration. *Biomed. Res. Int.* 16, 1–16. doi:10.1155/2016/6285620

Sordi, M. B., Curtarelli, R. B., da Silva, I. T., Fongaro, G., Benfatti, C. A. M., de Souza Magini, R., et al. (2021). Effect of dexamethasone as osteogenic supplementation in *in vitro* osteogenic differentiation of stem cells from human exfoliated deciduous teeth. *J. Mat. Sci.* 32 (1), 1. doi:10.1007/s10856-020-06475-6

Sun, J. L., Jiao, K., Niu, L. N., Jiao, Y., Song, Q., Shen, L. J., et al. (2017). Intrafibrillar silicified collagen scaffold modulates monocyte to promote cell homing, angiogenesis and bone regeneration. *Biomaterials* 113, 203–216. doi:10.1016/j.biomaterials.2016.10.050

Sun, J. L., Jiao, K., Song, Q., Ma, C. F., Ma, C., Tay, F. R., et al. (2018). Intrafibrillar silicified collagen scaffold promotes *in-situ* bone regeneration by activating the monocyte p38 signaling pathway. *Acta Biomater.* 67, 354–365. doi:10.1016/j.actbio.2017.12.022

Toita, R., Kang, J. H., and Tsuchiya, A. (2022). Phosphatidylserine liposome multilayers mediate the M1-to-M2 macrophage polarization to enhance bone tissue regeneration. *Acta Biomater.* 154, 583–596. doi:10.1016/j.actbio.2022.10.024

Trindade, R., Albrektsson, T., Tengvall, P., and Wennerberg, A. (2016). Foreign body reaction to biomaterials: on mechanisms for buildup and breakdown of osseointegration. *Clin. Implant Dent. Relat. Res.* 18 (1), 192–203. doi:10.1111/cid.12274

Wancket, L. M. (2015). Animal models for evaluation of bone implants and devices: comparative bone structure and common model uses. *Vet. Pathol.* 52 (5), 842–850. doi:10.1177/0300985815593124

Wang, J., Meng, F., Song, W., Jin, J., Ma, Q., Fei, D., et al. (2018a). Nanostructured titanium regulates osseointegration via influencing macrophage polarization in the osteogenic environment. *Int. J. Nanomedicine* 13, 4029–4043. doi:10.2147/ijn.S163956

Wang, T., Chen, X., Zhang, Y., Ye, T., Liu, Z., Wang, L., et al. (2023). Immunoregulatory silicon-deposited implant promotes osseointegration. *Compos. Part B Eng.* 255, 110618. doi:10.1016/j.compositesb.2023.110618

Wang, X., Wang, G., Zingales, S., and Zhao, B. (2018b). Biomaterials enabled cell-free strategies for endogenous bone regeneration. *Tissue Eng. Part B Rev.* 24 (6), 463–481. doi:10.1089/ten.TEB.2018.0012

Wang, Y. H., Liu, Y., Maye, P., and Rowe, D. W. (2006). Examination of mineralized nodule formation in living osteoblastic cultures using fluorescent dyes. *Biotechnol. Prog.* 22 (6), 1697–1701. doi:10.1021/bp060274b

Xu, W. C., Dong, X., Ding, J. L., Liu, J. C., Xu, J. J., Tang, Y. H., et al. (2019). Nanotubular TiO(2) regulates macrophage M2 polarization and increases macrophage

secretion of VEGF to accelerate endothelialization via the ERK1/2 and PI3K/AKT pathways. *Int. J. Nanomedicine* 14, 441–455. doi:10.2147/ijn.S188439

Yu, W. P., Ding, J. L., Liu, X. L., Zhu, G. D., Lin, F., Xu, J. J., et al. (2021). Titanium dioxide nanotubes promote M2 polarization by inhibiting macrophage glycolysis and ultimately accelerate endothelialization. *Immun. Inflamm. Dis.* 9 (3), 746–757. doi:10.1002/iid3.429

Zhang, D. H., Chen, Q., Shi, C., Chen, M. Z., Ma, K. Q., Wan, J. L., et al. (2021a). Dealing with the foreign-body response to implanted biomaterials: strategies and applications of new materials. *Adv. Funct. Mat.* 31 (6), 2007226. doi:10.1002/adfm.202007226

Zhang, E. N., Clément, J.-P., Alameri, A., Ng, A., Kennedy, T. E., and Juncker, D. (2021b). Mechanically matched silicone brain implants reduce brain foreign body response. *Adv. Mat. Technol.* 6 (3), 2000909. doi:10.1002/admt.202000909

Zhu, G., Zhang, T., Chen, M., Yao, K., Huang, X., Zhang, B., et al. (2021a). Bone physiological microenvironment and healing mechanism: basis for future bone-tissue engineering scaffolds. *Bioact. Mat.* 6 (11), 4110–4140. doi:10.1016/j.bioactmat.2021.03.043

Zhu, Y. Z., Liang, H., Liu, X. M., Wu, J., Yang, C., Wong, T. M., et al. (2021b). Regulation of macrophage polarization through surface topography design to facilitate implant-to-bone osteointegration. *Sci. Adv.* 7 (14), eabf6654. doi:10.1126/sciadv.abf6654

frontiers | Frontiers in Bioengineering and Biotechnology

TYPE Review
PUBLISHED 24 April 2024
DOI 10.3389/fbioe.2024.1380528

OPEN ACCESS

EDITED BY
Dandan Pei,
Xi'an Jiaotong University, China

REVIEWED BY
Jiulong Zhao,
Naval Medical University, China
Tang Ying,
Wuhan University, China

*CORRESPONDENCE
Xing Wang,
40275668@qq.com

RECEIVED 01 February 2024
ACCEPTED 08 April 2024
PUBLISHED 24 April 2024

CITATION
Guo W, Dong H and Wang X (2024), Emerging roles of hydrogel in promoting periodontal tissue regeneration and repairing bone defect. *Front. Bioeng. Biotechnol.* 12:1380528. doi: 10.3389/fbioe.2024.1380528

Emerging roles of hydrogel in promoting periodontal tissue regeneration and repairing bone defect

Wendi Guo[1,2,3], Hongbin Dong[1,2,3] and Xing Wang[1,2,3]*

[1]Department of Prosthodontics and Implant Dentistry, The First Affiliated Hospital of Xinjiang Medical University, Urumqi, China, [2]Affiliated Stomatological Hospital of Xinjiang Medical University, Urumqi, China, [3]Stomatology Research Institute of Xinjiang Uygur Autonomous Region, Urumqi, China

Periodontal disease is the most common type of oral disease. Periodontal bone defect is the clinical outcome of advanced periodontal disease, which seriously affects the quality of life of patients. Promoting periodontal tissue regeneration and repairing periodontal bone defects is the ultimate treatment goal for periodontal disease, but the means and methods are very limited. Hydrogels are a class of highly hydrophilic polymer networks, and their good biocompatibility has made them a popular research material in the field of oral medicine in recent years. This paper reviews the current mainstream types and characteristics of hydrogels, and summarizes the relevant basic research on hydrogels in promoting periodontal tissue regeneration and bone defect repair in recent years. The possible mechanisms of action and efficacy evaluation are discussed in depth, and the application prospects are also discussed.

KEYWORDS

hydrogel, periodontal tissue regeneration, bone tissue engineering, bone defect, repair

1 Introduction

Periodontal disease is a prevalent condition that significantly impacts both dental health and overall wellbeing. Periodontal bone defects, known as a serious consequence of periodontal disease, are challenging to repair, leading to significant impacts on patients' chewing function, aesthetics, and quality of life (Sedghi et al., 2021). Conventional periodontal bone grafting or bone substitute implantation surgery comprises the transplantation of bone or substitute materials to address alveolar bone defects resulting from periodontitis. These surgeries aim to stimulate new bone formation, repair bone defects, restore the anatomical shape of the alveolar bone, and achieve optimal periodontal tissue regeneration (Gao et al., 2024a). Nevertheless, this method is subject to numerous influencing factors and may not consistently yield satisfactory outcomes in periodontal tissue regeneration and bone defect repair. Some bone defects cannot be perfectly repaired. Hydrogels are a new type of functional polymer material that has emerged in recent years. They are cross-linked three-dimensional hydrophilic polymer networks with properties superior to traditional materials, including softness, non-deformability, strong water absorption capacity, intelligence, high drug utilization rate, safety, and convenience (Li et al., 2022a; Li et al., 2024). However, single-component hydrogels have relatively simple structures, generally low mechanical strength, and only basic hydrogel properties,

which cannot fully meet the needs of complex applications and have certain limitations. In recent years, the basic research and clinical applications of hydrogels have become increasingly rich, with great potential and unique therapeutic plasticity in promoting periodontal tissue regeneration and repairing bone defects. Firstly, hydrogels can provide a microenvironment similar to the extracellular matrix, allowing periodontal tissues and bone cells to adhere, proliferate, and differentiate. Secondly, hydrogels can serve as drug release carriers, exerting anti-inflammatory and antibacterial effects, and promoting periodontal tissue regeneration. Additionally, hydrogels can also carry specific bioactive factors such as stromal cell-derived factor-1 (SDF-1) and bone morphogenetic proteins (BMPs), inducing them to differentiate into osteoblasts, thereby accelerating periodontal bone tissue regeneration. Hydrogels are currently one of the hottest research materials, and are expected to provide a new perspective for promoting periodontal tissue regeneration and repairing periodontal bone defects. Therefore, based on the latest literature on hydrogels, this article provides a review of the molecular mechanisms and efficacy evaluation of promoting periodontal tissue regeneration and repairing periodontal bone defects, and looks forward to their clinical application prospects.

2 Periodontal disease and bone defect

Periodontitis is a chronic inflammatory disease affecting the supporting tissues of the teeth, leading some patients to suffer from varying degrees of periodontal bone defects, significantly impacting their physical and mental wellbeing (Dannewitz et al., 2021). The treatment for periodontitis aims not only to remove causative factors and halt disease progression but also to restore damaged periodontal tissues to their original structure and function, achieving the ideal goal of periodontal tissue regeneration. The surgical treatment to promote periodontal tissue regeneration is called regenerative surgery, which mainly includes bone grafting and guided tissue regeneration, or the combination of the two can be used (Bee and Hamid, 2022). Bone grafting is among the most effective methods to repair bone defects caused by periodontitis, traditionally using materials such as autogenous bone, allograft bone, and xenogeneic bone, among others (Smeets et al., 2022). While the efficacy of the mentioned bone graft materials in bone defect repair cannot be entirely dismissed, there are also drawbacks. For instance, autogenous bone necessitates the use of the patients' own bone, resulting in a secondary wound at the donor site, increasing the risk of postoperative complications such as infection, wound dehiscence, and increased bleeding. Additionally, postoperative unpredictable bone resorption may hinder the repair effect and prevent reaching the optimal state. Allogeneic bone carries the risk of immune rejection and requires strict donor screening and immunosuppressive therapy. Xenogeneic bone, due to species differences, has weaker biological activity and mechanical support capabilities (Ajlan et al., 2024). Thus, the clinical demand for bone repair materials with superior biological properties has grown increasingly urgent.

3 Overview of hydrogel

3.1 Basic composition of hydrogel

Hydrogels are three-dimensional hydrophilic polymer networks formed by the crosslinking of hydrophilic polymer chains through various interactions, such as chemical bonds, hydrogen bonds, and van der Waals forces (Hameed et al., 2024). Furthermore, the presence of hydrophilic groups in hydrogels enables rapid water absorption, high water retention capacity, and swelling without dissolution. This unique structure provides hydrogels with flexibility, enabling them to mimic the body's tissue environment. They offer structural support to the defect site, facilitating repair of bone defects through intrinsic healing mechanisms (Li et al., 2022b; Ho et al., 2022; Zhang et al., 2023). The high water content of hydrogels, similar to the permeability of the extracellular matrix, facilitates the transport of oxygen and nutrients (Siddiqui et al., 2021). Owing to their excellent biocompatibility, biodegradability, high water content, adjustable properties, and similarities to the natural extracellular matrix, hydrogels are increasingly recognized as exceptional biomimetic tissue engineering scaffold materials. They are considered the optimal carriers for cells, bioactive factors, and controlled release drugs. It's important to note that injectable hydrogel materials, with their *in situ* cross-linking nature, can fully adapt to and restore the irregular geometric shape of the original bone defect, achieving minimally invasive repair of bone defects (Chen et al., 2022). The relatively low adhesion of hydrogels to proteins and cells ensures that hydrogels in contact with tissues do not interfere with the metabolic processes of living organisms. Additionally, tissue metabolites can easily penetrate the hydrogel (Luo et al., 2022). The scheme illustrating the general composition of hydrogel is displayed in Figure 1.

3.2 Basic physical and chemical properties of hydrogel

3.2.1 Biocompatibility

After the material interacts with the organism, biocompatibility is primarily reflected in two aspects. The material must withstand organismic systems without rejection or damage, and the reactions generated during this process should be non-inflammatory and non-carcinogenic (Crawford et al., 2021). Biocompatibility is crucial for the successful use of hydrogel scaffolds in tissue engineering and regenerative medicine in clinical practice (Zor et al., 2019). Researchers often utilize methods such as synthetic conjugated polymers and the addition of ions to enhance tissue reconstruction and repair and address the poor biocompatibility of hydrogels (Zhang et al., 2022a).

3.2.2 Biodegradability

The biodegradability of hydrogel materials is a significant advantage. The biodegradability of hydrogel involves the gradual decomposition of the material in the body through processes such as dissolution, enzymatic digestion, and cell engulfment. Upon tissue repair, the implanted material is completely replaced by the repaired tissue, without leaving any residual material during the tissue healing process (Xia et al.,

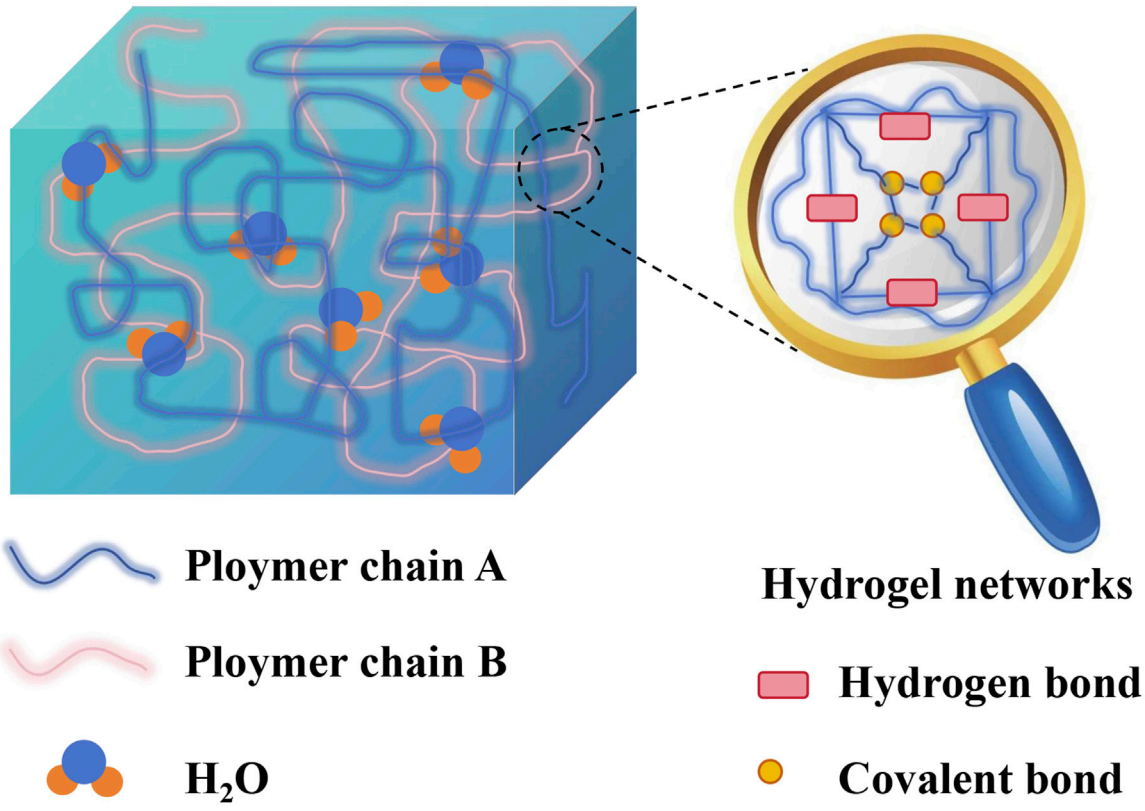

FIGURE 1
The general composition of hydrogel.

2021). Ideally, hydrogel materials should exhibit controllable biodegradability, matching the growth of cells and tissue repair rate. Excessive degradation can result in a loss of mechanical integrity before complete tissue regeneration, whereas slow degradation can lead to delayed tissue healing (Fatahian et al., 2022). Therefore, determining the appropriate degradation rate is a crucial consideration in hydrogel design. Fortunately, there has been significant recent progress by researchers, including the utilization of surface modification, polymer blending, and incorporation of alkaline particles to enhance biodegradability (Gupta et al., 2024).

3.2.3 Mechanical performance

The hydrogel exhibits mechanical properties at both macroscopic and microscopic levels. On the macroscopic scale, the hydrogel scaffold offers stability and volume maintenance (Belgodere et al., 2023). On the microscopic level, cells adhered to the hydrogel matrix can sense mechanical stimuli, converting them into biochemical signals to regulate crucial physiological processes (Li et al., 2022c). Hydrogels offer extensive application potential in bone tissue engineering. Enhancing the mechanical performance of hydrogels is crucial for improving the effectiveness of bone defect repair (Zhao et al., 2022). Inadequate mechanical properties of the hydrogel material can cause the repaired defect to deform easily and fail to offer early-stage support. In order to improve the mechanical performance of hydrogels, researchers have employed diverse methods to enhance the mechanical performance of hydrogels, such as constructing double network structures (Guo et al., 2021), utilizing composite nano-technology (Cui et al., 2019), introducing conductive materials (Arambula-Maldonado et al., 2023), and reinforcing fiber networks (Brusentsev et al., 2023). Studies have demonstrated that biomaterials with mechanical properties matching those of bone can stimulate bone cell proliferation and mineralization, and effectively facilitate bone growth.

4 Classification of polymer-based hydrogels

Polymer-based hydrogels can be classified into two main categories based on their source of materials (Ur Rehman et al., 2020). Naturally derived polymer-based hydrogels are primarily sourced from animals, plants, and microorganisms, exhibiting excellent biocompatibility and biodegradability. Examples include chitosan, sodium alginate, and hyaluronic acid (Sun et al., 2021). Synthetic polymer-based hydrogels are predominantly derived from common chemical raw materials, offering not only good biocompatibility but also enhanced mechanical properties. Common materials used in the preparation of synthetic polymer-based hydrogels include polyethylene glycol (PEG), polyvinyl alcohol (PVA) and polyacrylic acid (PAA). Based on their response to external

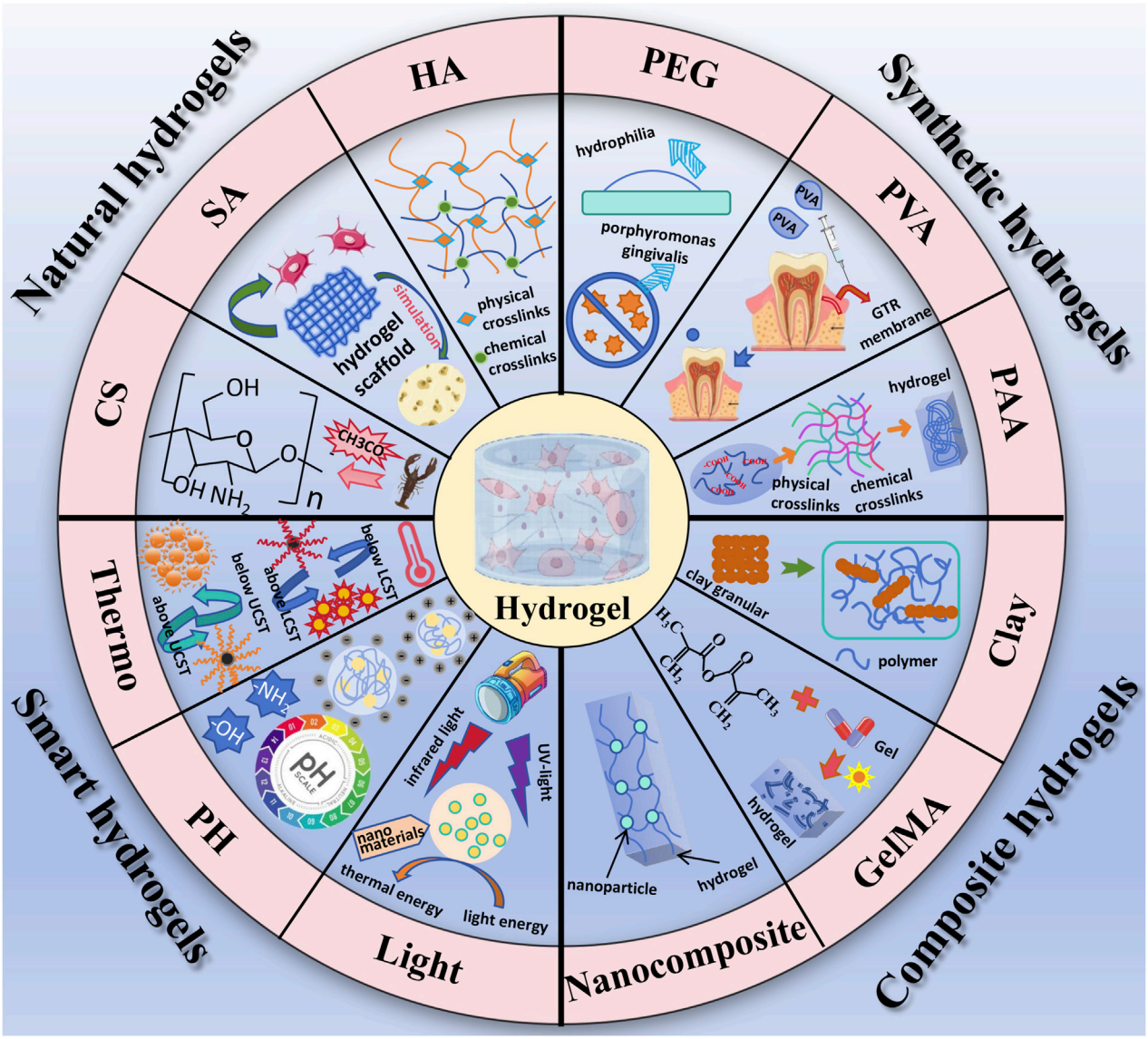

FIGURE 2
The main classification of hydolgel.

stimuli, hydrogels can also be classified as traditional hydrogels and responsive hydrogels, the latter also known as intelligent responsive hydrogels. Intelligent responsive hydrogels exhibit reversible responses to environmental stimuli, with their shape, mechanical, optical, permeation rate, and recognition properties showing acute responses to changes in the surrounding microenvironment (such as temperature, pH, light, and magnetic fields), and reversible changes with the stimulating factors. It is worth mentioning that composite hydrogels, represented by clay hydrogels, have emerged as a new type of hydrogel in recent years. This composite system enhances overall mechanical properties, biocompatibility, and processability through the complementary advantages of different materials. We briefly introduce some representative hydrogel systems and their applications as followed. The main classification of hydolgel is summarized in Figure 2.

4.1 Natural polymer-based hydrogels

4.1.1 Chitosan-based hydrogel

Chitin is usually extracted from natural shells of shrimp, crabs and insects, and part of the acetyl group is removed to obtain chitosan. Chitosan is the sole naturally occurring alkaline polysaccharide that contains free amino groups (Atia et al., 2022). Chitosan-based materials have the capacity to form chemical and physical cross-linked hydrogels through processes like exposure to ultraviolet light, pH alteration, and temperature adjustment (Yu et al., 2016). Its primary characteristic is the capacity to introduce specific functional groups with reactive properties, yielding a range of chitosan derivatives via chemical modification. Chitosan-based hydrogel systems exhibit outstanding biocompatibility, degradability, anti-inflammatory effects, broad-spectrum antibacterial properties, as well as the

ability to facilitate cell adhesion, proliferation, and differentiation (Ma et al., 2022). Gu et al. (2024) used forty-eight male Wistar rats to establish a periodontitis model to detect the effects of chitosan/β-sodium glyceropylate (β-GP)/glycolic acid (GA) hydrogel carrying erythropoietin and FK506 (EPO-FK506-CS/β-GP/GA). The results showed that the hydrogel had drug stability and slow release, could significantly enhance new bone formation in the bone defect area, and had obvious bone induction properties. EPO-FK506-CS/β-GP/GA hydrogel could promote periodontal tissue regeneration. Eshwar et al. (2023) investigated an alginate-chitosan hydrogel, and clinical randomized trials indicated that the hydrogel enhanced the clinical attachment levels and fostered human bone regeneration, thus augmenting its potential in the field of tissue engineering.

4.1.2 Sodium alginate-based hydrogel

Derived from marine algae cell walls and intercellular spaces, sodium alginate is a linear natural anionic polysaccharide (Liu et al., 2023). It is a natural high molecular weight polymer created by linking β-1, 4-D-mannuronic acid (M segment) and α-1, 4-L-guluronic acid (G segment) via (α-1, 4) glycosidic bonds. Due to its non-toxicity, low cost, good biocompatibility, low immunogenicity, and its capability to form gels through crosslinking with divalent or multivalent cations, it has extensive potential applications in oral tissue engineering (Sanchez-Ballester et al., 2021). The three-dimensional network structure of sodium alginate hydrogel offers a novel environment for cell adhesion and proliferation, mimicking the microenvironment of human bone tissue. Furthermore, sodium alginate hydrogel holds significant promise as a scaffold material for bone tissue engineering. It not only offers suitable physical support and biocompatibility but also guides cell proliferation to form specific tissues (Suo et al., 2023). Presently, researchers have started blending sodium alginate with other high molecular weight materials to facilitate cell growth (Ouyang et al., 2024). This blending technique offers a novel approach to develop biomedical materials with outstanding performance and is anticipated to be pivotal in the realm of tissue engineering.

4.1.3 Hyaluronic acid-based hydrogel

One of the main components of the extracellular matrix is hyaluronic acid (HA), which is synthesized into HA hydrogels through physical or chemical crosslinking methods. It has good biocompatibility, does not easily cause immune reactions, and the HA hydrogel has good degradability, gradually degrading into metabolites that exist in the body without burdening the human body (Marinho et al., 2021). HA hydrogels exhibit good biocompatibility and biological activity, which have made them widely used in various fields. In bone tissue repair, HA hydrogels can provide a scaffold structure similar to the bone microenvironment to promote the differentiation of stem cells into bone cells, and promote bone regeneration through the release of growth factors and other bioactive substances (Wang et al., 2021). In tissue engineering, HA hydrogels can serve as cell carriers, providing a suitable environment to support cell adhesion, proliferation, and differentiation, thus achieving tissue regeneration and repair (Fujioka-Kobayashi et al., 2016). Despite the advantages of hyaluronic acid hydrogels including non-toxicity, biodegradability, and biocompatibility, their extremely high water absorption and enzyme degradation make them prone to corrosion and degradation in the body. Thus, combining hyaluronic acid with other smart hydrogels can yield new, environmentally friendly materials with enhanced performance (Liu et al., 2022a). The classification of natural polymer-based hydrogels is summarized in Table 1.

4.2 Synthetic polymer-based hydrogels

4.2.1 Polyethylene glycol-based hydrogels

Polyethylene glycol (PEG) is a linear, neutral polyether polymer that possesses excellent biocompatibility, biodegradability, low immunogenicity, and affordability, making it an important biomaterial in the field of biomedicine. Merrill et al. (1982) first investigated PEG and polyethylene oxide (PEO) as hydrophilic biomaterials, and the results showed that the adsorption of proteins on glass surfaces could be effectively inhibited by the presence of PEO. Since then, various types of PEG have been utilized for different purposes, such as protein surface modification to confer resistance and enhance surface biocompatibility. Fraser and Benoit (2022) found that the presentation of RGD and GFOGER peptides in PEG hydrogels enhanced the functionality of periodontal ligament cells (PDLCs), and this hydrogel system effectively controlled the function and activity of PDLCs, promoting periodontal tissue regeneration. Liu et al. (2021a) studied an intelligent gingival protease-responsive hydrogel loaded with SDF-1 (PEGPD@SDF-1) and observed that the PEGPD@SDF-1 hydrogel exhibited good biocompatibility, promoting the proliferation, migration, and differentiation of periodontal ligament stem cells. Moreover, this hydrogel inhibited the proliferation of porphyromonas gingivalis, creating a low-inflammatory environment and inducing osteogenesis, thus possessing the ability to promote *in situ* regeneration of periodontal tissues.

4.2.2 Polyvinyl alcohol-based hydrogel

Polyvinyl alcohol-based hydrogels, after crosslinking and swelling, form three-dimensional network-like colloidal dispersion. They possess high water absorption, degradability, good biocompatibility, and mechanical properties, making them widely applied in various medical fields (Rivera-Hernández et al., 2021). Due to the relatively simple structure and limited functionality of PVA, reinforcing components and functional materials are often incorporated into PVA hydrogel networks to improve and modify the overall performance of the hydrogel. Xiang et al. (2022) prepared a polyvinyl alcohol/hydroxyapatite/tannic acid (PVA/HA/TA) composite hydrogel, which exhibited high water content, porous structure, and good mechanical properties. *In vitro* cell experiments demonstrated excellent cell compatibility of the PVA/HA/TA composite hydrogel, promoting cell growth and adhesion, making it a promising material for bone tissue engineering. Zhou et al. (2020) developed a novel guided tissue regeneration (GTR) membrane using a composite hydrogel of polyvinyl alcohol (PVA) and fish collagen (Col). By adjusting the ratio of PVA/Col, they achieved control over the adhesion and proliferation of human periodontal ligament fibroblasts (HPDLFs) and human

TABLE 1 Classification of natural polymer-based hydrogels.

Classification	Hydrogel matrix	Research and application	Reference
Chitosan (CS)	Chitosan/quaternized CS/nano-hydroxyapatite	This hydrogel demonstrates excellent biocompatibility and antibacterial properties, and can be utilized for the treatment of bone defects	Tian et al. (2024)
Alginate (Alg)	Alginate/gelatin/freeze-dried bone allograft nanoparticles	The hydrogel enhances cell adhesion, proliferation, and osteogenic differentiation, exhibiting significant potential to augment bone regeneration	Bastami et al. (2024)
Hyaluronic acid (HA)	Fluorenylmethyloxycarbonyl-diphenylalanine (FmocFF)/HA	The fmoff/HA hydrogel is used for acellular, biomimetic, and immunomodulatory bone tissue engineering scaffolds	Halperin-Sternfeld et al. (2023)
Cellulose	Carboxymethyl cellulose-methacrylate/hydroxyapatite	This hydrogel effectively promotes cell proliferation, supports adhesion, upregulates the expression of osteogenesis-related genes, and enhances bone regeneration, thereby increasing the strength of newly formed bone	Qiu et al. (2024)
Gelatin	Zeolitic imidazolate framework-8 (ZIF-8)/gelatin methacryloyl (GelMA)	The hydrogel promotes osteogenic differentiation of bone marrow mesenchymal stem cells and facilitates the regeneration of alveolar bone	Liu et al. (2022b)
Lignin	Lignin-copper sulfide/polyvinyl alcohol	The hydrogel exhibits high-efficiency antimicrobial and anti-biofilm activities, making it suitable for application in wound healing	Xie et al. (2022)
Silk fibroin	MXene nanosheets/regenerated silk fibroin (MXene/RSF)	The MXene/RSF hydrogel can modulate the immune microenvironment and generate new blood vessels, providing a novel strategy for bone regeneration and repair	Hu et al. (2022)

TABLE 2 Classification of synthetic polymer-based hydrogels.

Classification	Hydrogel matrix	Research and application	Reference
Polyethylene glycol (PEG)	Mineral-coated microparticle/bone morphogenetic protein-2/chitosan/polyethylene glycol	This hydrogel can sustainably release growth factors and accelerate bone formation by promoting the activity of bone marrow mesenchymal stem cells	Xu et al. (2023)
Polyvinyl alcohol (PVA)	Polyvinyl alcohol/sodium alginate	PVA/SA hydrogel effectively promotes osteogenic differentiation of cells and is applied in bone tissue engineering	Zhang et al. (2024)
Polyacrylic acid (PAA)	Polyethyleneimine (PEI)/PAA-hydroxyapatite (HA)-Vancomycin (VAN)	The PEI/PAA-HA-VAN hydrogel exhibits effective antibacterial properties and promotes the expression of osteogenic genes	Wang et al. (2022)
Polyacrylamide (PAAM)	Polyurethane (PU)/Polyacrylamide/gelatin (Gel)	The PU/PAAM/Gel hydrogel can stimulate the reconstruction and growth of new bone tissue, exhibiting good osteogenic performance	He et al. (2021)
Polymethyl methacrylate (PMMA)	Gelatin-methacryloyl/polymethyl methacrylate/ polydopamine (GelMA/PMMA/PDA)	The GelMA/PMMA/PDA hydrogel possesses excellent osteogenic capabilities, offering a new perspective for the treatment of bone defects	Wu et al. (2022)

gingival fibroblasts (HGFs). The PVA/Col composite hydrogel exhibited unlimited potential as a GTR membrane for guiding periodontal tissue regeneration.

4.2.3 Polyacrylic acid-based hydrogel

PAA is a type of synthetic polymer with high hydrophilicity and a large number of carboxyl groups. It can form hydrogels through physical or chemical crosslinking. Wen et al. (2023) prepared a novel composite mineral matrix PAA-CMC-TDM hydrogel using amorphous calcium phosphate (ACPs), PAA, carboxymethyl chitosan (CMC), and dentin matrix (TDM) as the matrix. The hydrogel exhibited good biocompatibility and degradability, and its mechanical properties could be adjusted without affecting the functional activity of TDM. The experimental results showed that the hydrogel significantly improved the differentiation ability of mesenchymal stem cells into tooth or bone, and could repair irregular hard tissue defects *in situ*. Fan et al. (2023) combined PAA and sodium alginate (SA) to obtain a double polymer network hydrogel, in which ion crosslinking and SiO2 nanoparticles were introduced as dual reinforcement materials. Compared with standard PAA hydrogel, the hydrogel exhibited enhanced adhesion and shape memory properties, and further improved biocompatibility and osteogenic potential. SA-PAA-SiO2 has great potential in bone tissue engineering. The classification of synthetic polymer-based hydrogels is summarized in Table 2.

4.3 Smart hydrogels

4.3.1 Temperature-responsive hydrogels

Temperature-responsive hydrogels, also known as thermoresponsive hydrogels or temperature-sensitive hydrogels, are hydrogel materials with both hydrophilic and hydrophobic groups on their polymer chains. They exhibit temperature-responsive phase transition properties. When the temperature reaches a certain critical point, the affinity of the thermoresponsive hydrogel towards the solvent changes, leading to a swelling-shrinking transition. This temperature transition point is referred to as the lowest critical solution temperature (LCST) or utmost critical solution temperature (UCST). Injecting thermoresponsive hydrogels into periodontal pockets, they undergo an *in situ* sol-gel transition response under the stimulation of oral temperature. Xu et al. (2019) developed a thermosensitive hydrogel composed of chitosan (CS), sodium glycerophosphate (β-GP), and gelatin, which can sustainably release aspirin and erythropoietin (EPO) when injected. The study demonstrated that CS/β-GP/gelatin hydrogel is a novel drug carrier with easy preparation and excellent biocompatibility. The loaded aspirin/EPO in CS/β-GP/gelatin hydrogel exhibited significant anti-inflammatory and periodontal tissue regeneration-promoting effects. This hydrogel holds promise as a potential candidate for the clinical treatment of periodontitis.

4.3.2 pH-responsive hydrogels

pH-responsive hydrogels are a type of hydrogel material that undergoes swelling or shrinking in response to changes in pH. These hydrogels contain specific acidic groups (such as carboxyl groups) or basic groups (such as amino groups). The physicochemical properties of pH-responsive hydrogels largely depend on the charge changes within the material at different pH values and the interactions between charges. Yu et al. (2022) developed a dual-crosslinked gel system with a polyhedral oligomeric silsesquioxane (POSS) matrix, surrounded by a shell of six dithiol-linked PEG and two 2-ureido-4[1H]-pyrimidinone (UPy) groups. The thiol-disulfide exchange reaction exhibited pH-responsive "on/off" functionality, allowing for controlled structure of the hydrogel. The results showed that the hydrogel improved mechanical strength and had a positive effect on the proliferation, adhesion, and osteogenic ability of periodontal ligament stem cells (PDLSCs). In summary, pH-responsive hydrogels hold great potential for various applications, including drug delivery, tissue engineering, and biomedical devices, due to their ability to respond to changes in pH and provide controlled release and targeted therapy.

4.3.3 Light-responsive hydrogels

Light-responsive hydrogels are a type of hydrogel that undergo changes in their morphology, crosslinking density, and other properties under different light conditions, such as ultraviolet light, near-infrared light, or visible light. There are two different response mechanisms for light-responsive hydrogels: firstly, due to the presence of photosensitive functional groups (such as spiropyran, azobenzene, and other groups) within the hydrogel itself, the properties of the hydrogel change when it absorbs a certain amount of photon energy; secondly, by introducing nanomaterials with photothermal effects (such as gold nanoparticles, graphene oxide, etc.) into thermosensitive hydrogels, the light energy of the nanomaterials is converted into heat energy under light conditions using the photothermal effect, raising the temperature of the hydrogel and thus regulating its properties (Liu et al., 2021b). Zhai et al. (2021) studied a clay-based nanocomposite hydrogel using 4-acryloylmorpholine as a monomer. After exposure to ultraviolet light, the hydrogel exhibited good biocompatibility and mechanical properties. Additionally, animal experimental results demonstrated that the hydrogel had the ability to promote osteoblast differentiation, providing a new clinical approach for bone defect repair. Magalhães et al. (2022) prepared a nanocomposite hydrogel using laponite and polyethylene glycol diacrylate (PEGDA) and utilized ultraviolet radiation to enhance its bone regeneration ability, showcasing its potential application value in the field of bone regeneration. The classification of smart hydrogels is summarized in Table 3.

4.4 Composite hydrogels

Composite hydrogels refer to the incorporation of one or several polymers into a composition consisting of two or more different types or components of polymers, forming a composite system with specific structure and functionality through hydrogen bonding and electrostatic interactions. Clay hydrogels have been representative examples of composite hydrogels in recent years. Dong et al. (2021) uniformly mixed laponite nanoclay with methacrylic acid gelatin to obtain a composite hydrogel. The addition of nanoclay improved the rheological properties, degradation stability, and mechanical strength of the hydrogel. This composite hydrogel scaffold exhibited high proliferation and osteogenic differentiation capacity, making it a promising candidate for bone tissue regeneration biomaterials. Hakimi et al. (2023) developed a novel organic-mineral nanofiber hydrogel composed of chitosan-polyethylene oxide (CS-PEO)/nanoclay-alginate (NC-ALG). The inclusion of NC particles in the hydrogel improved its biocompatibility and promoted bone tissue regeneration. Zhang et al. (2022b) designed a chitosan/polyaniline/lithium polysaccharide (COL) hydrogel, in which aluminum silicate clay material laponite (LAP) was incorporated. This composite hydrogel exhibited good biocompatibility and degradability. Furthermore, the LAP-loaded composite hydrogel demonstrated excellent osteogenic differentiation capacity and could be used for bone defect repair.

5 Application value of hydrogel in promoting periodontal tissue regeneration

The application research of hydrogels in periodontal tissue regeneration has continuously achieved breakthroughs. Early studies mainly focused on the antibacterial activity of hydrogels themselves, aiming to inhibit the development of infection and inflammation by adding antibacterial agents (Chen et al., 2016). However, with further research, it has been found that the effect of a single antibacterial agent is limited. To overcome these problems,

TABLE 3 Classification of smart hydrogels.

Classification	Stimulus condition	Control mechanism	Research and application	Reference
Thermo-responsive	Temperature	By regulating the temperature to control hydrogen bonding within the hydrogel, a sol-gel phase transition is achieved	The smart thermosensitive hydrogel possesses gelation properties and the ability to induce angiogenesis, offering a therapeutic approach for the treatment of bone defects	Lv et al. (2023)
pH-responsive	pH	Changes in pH lead to the ionization of acidic and basic groups, thereby altering the charge density of the hydrogel	The hydrogel demonstrates potent therapeutic efficacy in the treatment of periodontitis, restoration of local immune function, and eradication of pathogens	Yan et al. (2022)
Light-responsive	Light	Light-responsive hydrogels contain photosensitive molecules or groups capable of absorbing light of specific wavelengths	The hydrogel exhibits significant antibacterial properties and can promote cell adhesion and proliferation	Chang et al. (2022)
ROS-responsive	Reactive oxygen species (ROS)	After the reaction of reactive oxygen species with sensitive functional groups in the hydrogel, it will cause the fracture or crosslinking of the hydrogel network structure	ROS-respontive hydrogels can effectively alleviate inflammatory responses in periodontal tissues and reduce bone loss	Gan et al. (2023)
Enzyme-responsive	Matrix metalloproteinase 8 (MMP-8)	Based on the specific functional groups in the hydrogel reacting with specific enzymes, this leads to changes in the hydrogel structure	The MMP-8 hydrogel can inhibit the growth of Porphyromonas gingivalis and maintain its biological activity	Guo et al. (2019)
Glucose-responsive	Glucose	When glucose interacts with these specific functional groups or enzymes, it triggers a chemical or enzymatic reaction, leading to changes in the hydrogel's structure	The hydrogels inhibit the growth of Porphyromonas gingivalis and exhibit strong antibacterial and anti-inflammatory activity	Liu et al. (2022c)

researchers have begun to explore the use of hydrogels as carriers for loading different antibacterial drugs. This loading system can provide a more long-lasting antibacterial effect while reducing the amount of drugs used (Wang et al., 2020). In recent years, hydrogels can be used as carriers for carrying and releasing bioactive molecules, such as growth factors and anti-inflammatory factors. These bioactive molecules can promote tissue regeneration and repair, accelerating the healing process of periodontal tissues (Kuroda et al., 2019). Some studies have also focused on loading growth factors and antibacterial drugs together in hydrogels. This dual-functional hydrogel can not only control infection and inflammation, but also promote the regeneration and repair of periodontal tissues. The potential mechanisms employed by hydrolgel in promoting periodontal tissue regeneration are demonstrated in Figure 3. Tan et al. (2023) prepared a chitosan-based thermosensitive hydrogel loaded with β-tricalcium phosphate, which confirmed the three-dimensional network structure of the hydrogel and demonstrated significant biocompatibility with pre-osteoblastic cells MC3T3-E1 and human gingival fibroblasts, showing great potential in periodontal tissue regeneration. Ammar et al. (2018) incorporated freeze-dried platelet concentrate (FDPC) into chitosan/β-glycerophosphate lipid hydrogel, both showing sustained release of transforming growth factor and platelet-derived growth factors, significantly improving the viability of periodontal ligament stem cells, conducive to periodontal tissue regeneration, and providing essential growth factors and progenitor cells for periodontal tissue regeneration. Fawzy El-Sayed et al. (2015) used gingival-margin-derived stem/progenitor cells (G-MSCs) and hyaluronic acid-synthesized extracellular matrix (HA-sECM) hydrogel loaded with IL-1ra to explore its potential for periodontal regeneration. The results showed that this hydrogel significantly improved periodontal attachment levels, connective tissue adhesion, and alveolar bone regeneration, demonstrating significant periodontal tissue regeneration capability when used in combination with G-MSCs and IL-1-loaded HA-sECM hydrogel. Momose et al. (2016) evaluated the use of collagen hydrogel combined with fibroblast growth factor-2 (FGF2) for healing periodontal defects in beagle dogs. The results showed that periodontal tissues, periodontal ligament-like tissues, and Sharpey's fibers in beagle dogs were repaired, and FGF2-loaded collagen hydrogel guided periodontal regeneration, restoring the function of periodontal tissues.

Currently, hydrogels have enormous potential in the treatment of periodontal tissue regeneration. However, most related research is still at the stage of animal experiments, requiring further exploration of its clinical efficacy and translational applications. With in-depth research on hydrogels and continuous technological improvement, it is believed that their application in the field of periodontal tissue regeneration will be further expanded. We can look forward to hydrogels providing new solutions for the treatment of periodontal tissue diseases, bringing more benefits to periodontal health.

6 Bone defect repair strategy based on hydrogel

Part of periodontitis patients have bone defects, promoting bone regeneration in the area to restore normal chewing function is particularly important for patients with periodontitis combined with bone defects (Li et al., 2023). The repair and regeneration of bone defects is a challenging and highly demanding research.

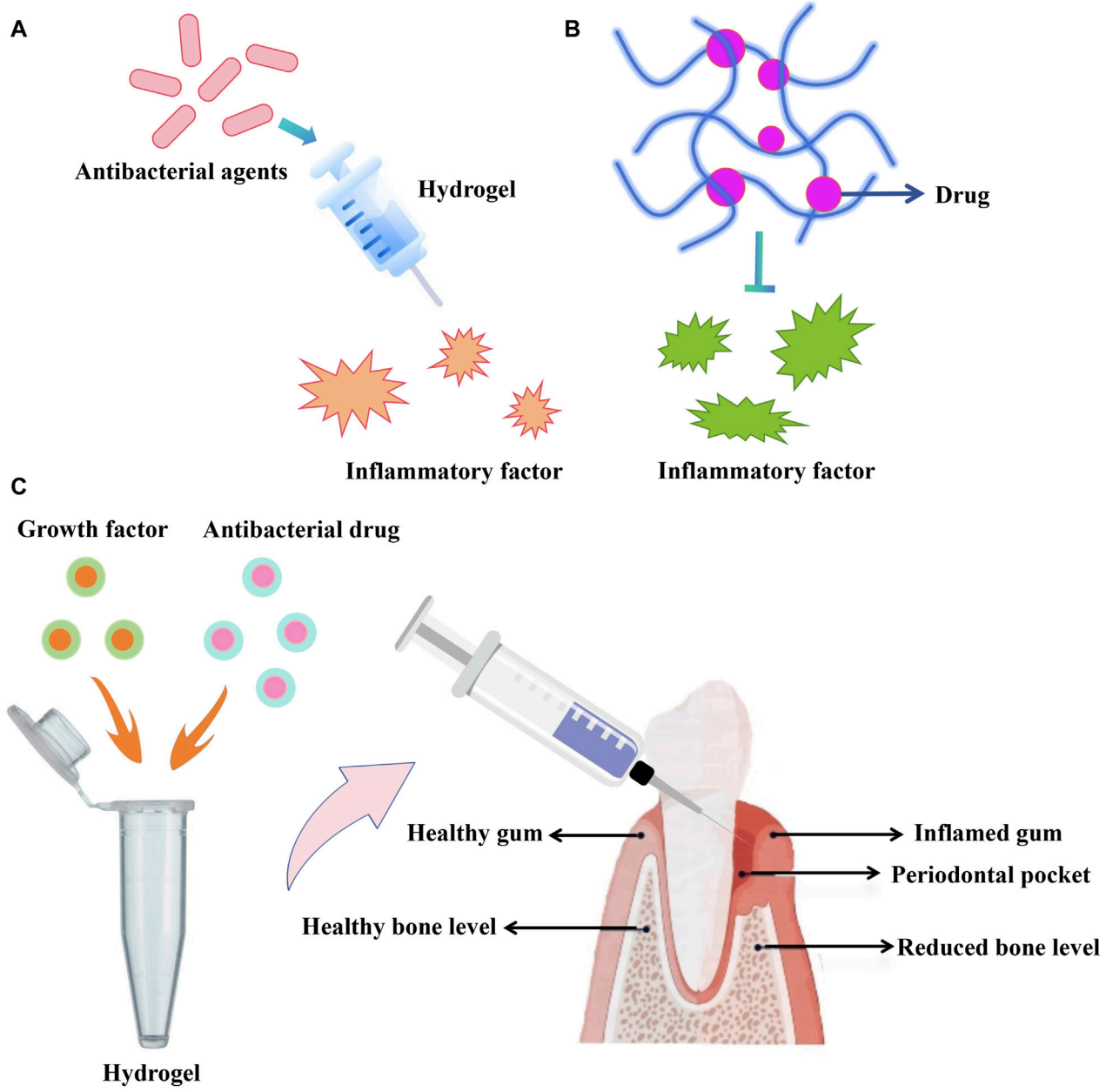

FIGURE 3
(A,B) Antibacterial agents or drugs can be integrated with hydrogel to suppress inflammatory factor. **(C)** Growth factor-loaded hydrogel to promote periodontal tissue regeneration.

6.1 Hydrogels act as carrier to promote bone defect repair

Researchers are constantly exploring new methods to improve the effectiveness of bone defect repair. Hydrogels can encapsulate cells and/or growth factors, effectively protecting them from external environmental influences and maintaining their biological activity. When the hydrogel comes into contact with the site of the bone defect, it selectively transports the encapsulated cells and/or growth factors, thus promoting the proliferation and differentiation of bone cells, accelerating the regeneration and repair of bone tissue (Santos et al., 2023). In addition, hydrogels can also regulate the release rate of cells and growth factors, achieving sustained and controlled release, further enhancing the repair effectiveness (Arpornmaeklong et al., 2021). Tan et al. (2019) prepared a supermolecular hydrogel assembly of NapFFFY with SDF-1 and BMP-2 for the treatment of periodontal bone defects in rats, with a bone regeneration rate as high as 56.7%. Both *in vitro* and *in vivo* results indicated that these two bioactive factors were released synchronously and continuously from the hydrogel under ideal conditions, effectively promoting the regeneration and reconstruction of periodontal bone tissue. It is expected that the SDF-1/BMP-2/NapFFFY hydrogel may soon replace clinical bone transplantation for the repair of periodontal bone defects. Parisi

et al. (2020) introduced adaptors of fibronectin into hyaluronic acid/polyethylene glycol-based hydrogel, evaluating its ability to promote osteogenesis in rats. The hydrogel was found to support osteoblast adhesion, accelerate platelet aggregation and activation, and promote postoperative new bone formation. Chien et al. (2018) applied an injectable thermosensitive chitosan/collagen/glycerophosphate hydrogel to provide a suitable environment for the transplantation of stem cells and enhance their delivery and implantation. In an animal model of maxillary molar defects, the iPSCs-BMP-6 hydrogel-treated group exhibited significant mineralization, increased bone volume, number and thickness of bone trabeculae, and promoted new periodontalligament regeneration as well as the formation of bone and cementum. These findings indicate that the combination of hydrogel-encapsulated iPSCs with BMP-6 provides a new strategy for enhancing periodontal bone regeneration.

6.2 Hydrogels act as scaffold to promote bone defect repair

In recent years, bone tissue engineering (BTE) has played an important role in the treatment of periodontal bone defects (Gao et al., 2024b). The three important elements in BTE include scaffold materials, seed cells, and growth factors. BTE requires the integration of scaffold materials with different types of bioactive substances, including cells, drugs, proteins, and other bioactive molecules, to enhance bone formation effectiveness. Hydrogels, as scaffold materials, provide a living environment for bone cells, which is conducive to bone tissue regeneration (Peng et al., 2023). Hydrogels can simulate the extracellular matrix environment of the human body, providing structural support for new bone formation and enabling bone tissue repair, thus possessing unique advantages. Sowmya et al. (2017) achieved complete regeneration of hard tissues (alveolar bone and tooth bone) at the site of periodontal defect using a three-layered nanocomposite hydrogel scaffold loaded with growth factors. The results demonstrated complete healing of the periodontal bone defect and the formation of new trabecular-like tissue. Histological and immunohistochemical analysis further confirmed the formation of new tooth bone and alveolar bone, with distinct bone trabeculae. Wang et al. (2023) prepared a porous hydrogel scaffold using chitosan and oxidized chondroitin sulfate (OCS) as the matrix, which carried periodontal ligament stem cells (PDLSCs) or gingival mesenchymal stem cells (GMSCs). In a rat model of periodontal defect, the PDLSC and GMSC hydrogels induced bone tissue repair, offering another possibility for clinical application. Kato et al. (2015) investigated the application of bone morphogenetic protein (BMP)/collagen hydrogel scaffold implantation for periodontal bone defect in dogs. The results showed that bone-like tissue was significantly formed after receiving BMP/collagen hydrogel scaffold, and the hydrogel enhanced the regeneration of tooth bone and alveolar bone.

7 Conclusion

The hydrogel is a three-dimensional polymer network characterized by both rigidity and flexibility. Being a rapidly advancing functional polymer material, it possesses distinct advantages that traditional materials lack. It shows significant potential for application in periodontal tissue regeneration and repairing bone defects. Subsequent research should concentrate on enhancing the performance of hydrogels, identifying types with superior performance, and delving deeper into their mechanisms of action. With advancements in medicine, technology, and ongoing research, the utilization of hydrogels in periodontal tissue regeneration and bone defect repair is anticipated to expand new possibilities.

Author contributions

WG: Conceptualization, Data curation, Formal Analysis, Investigation, Writing–original draft. HD: Data curation, Investigation, Writing–original draft. XW: Conceptualization, Project administration, Supervision, Writing–review and editing.

Funding

The author(s) declare that no financial support was received for the research, authorship, and/or publication of this article.

Conflict of interest

The authors declare that the research was conducted in the absence of any commercial or financial relationships that could be construed as a potential conflict of interest.

Publisher's note

All claims expressed in this article are solely those of the authors and do not necessarily represent those of their affiliated organizations, or those of the publisher, the editors and the reviewers. Any product that may be evaluated in this article, or claim that may be made by its manufacturer, is not guaranteed or endorsed by the publisher.

References

Ajlan, S. A., AlHamdan, K. S., and AlQahtani, D. A. (2024). Peri-implant mucosal fenestration and histologic observation of bone xenograft material 7 years after implant installation: a case report. *J. Oral Implantol.* 50, 18–23. doi:10.1563/aaid-joi-d-23-00038

Ammar, M. M., Waly, G. H., Saniour, S. H., and Moussa, T. A. (2018). Growth factor release and enhanced encapsulated periodontal stem cells viability by freeze-dried platelet concentrate loaded thermo-sensitive hydrogel for periodontal regeneration hydrogel for periodontal regeneration. *Saudi Dent. J.*;30(4):355–364. doi:10.1016/j.sdentj.2018.06.002

Arambula-Maldonado, R., Liu, Y., Xing, M., and Mequanint, K. (2023). Bioactive and electrically conductive GelMA-BG-MWCNT nanocomposite

hydrogel bone biomaterials. *Biomater. Adv.*;154:213616. doi:10.1016/j.bioadv.2023.213616

Arpornmaeklong, P., Sareethammanuwat, M., Apinyauppatham, K., and Boonyuen, S. (2021). Characteristics and biologic effects of thermosensitive quercetin-chitosan/collagen hydrogel on human periodontal ligament stem cells ligament stem cells. *J. Biomed. Mater Res. B Appl. Biomater.*;109(10):1656–1670. doi:10.1002/jbm.b.34823

Atia, G. A. N., Shalaby, H. K., Zehravi, M., Ghobashy, M. M., Attia, H. A. N., Ahmad, Z., et al. (2022). Drug-loaded chitosan scaffolds for periodontal tissue regeneration. *Polym. (Basel)* 14 (15), 3192. doi:10.3390/polym14153192

Bastami, F., Safavi, S. M., Seifi, S., Nadjmi, N., and Khojasteh, A. (2024). Addition of bone-marrow mesenchymal stem cells to 3D-printed alginate/gelatin hydrogel containing freeze-dried bone nanoparticles accelerates regeneration of critical size bone defects. *Macromol. Biosci.* 24 (3), e2300065. doi:10.1002/mabi.202300065

Bee, S. L., and Hamid, Z. A. A. (2022). Asymmetric resorbable-based dental barrier membrane for periodontal guided tissue regeneration and guided bone regeneration: a review. *J. Biomed. Mater Res. B Appl. Biomater.* 110 (9), 2157–2182. doi:10.1002/jbm.b.35060

Belgodere, J. A., Lassiter, H. R., Robinson, J. T., Hamel, K. M., Rogers, E. L., Mohiuddin, O. A., et al. (2023). Biomechanical and biological characterization of XGel, a human-derived hydrogel for stem cell expansion and tissue engineering engineering. *Adv. Biol. (Weinh).* ;7(8):e2200332. doi:10.1002/adbi.202200332

Brusentsev, Y., Yang, P., King, A. W. T., Cheng, F., Cortes Ruiz, M. F., Eriksson, J. E., et al. (2023). Photocross-linkable and shape-memory biomaterial hydrogel based on methacrylated cellulose nanofibres. *Biomacromolecules*;24(8):3835–3845. doi:10.1021/acs.biomac.3c00476

Chang, K. C., Chiu, K. C., Chen, W. C., Lan, W. C., Hsia, S. M., et al. (2022). Effects of temoporfin-based photodynamic therapy on the *in vitro* antibacterial activity and biocompatibility of gelatin-hyaluronic acid cross-linked hydrogel membranes. *Pharmaceutics* 14 (11), 2314. doi:10.3390/pharmaceutics14112314

Chen, X., Wu, G., Feng, Z., Dong, Y., Zhou, W., Li, B., et al. (2016). Advanced biomaterials and their potential applications in the treatment of periodontal disease. *Crit. Rev. Biotechnol.* 36 (4), 760–775. doi:10.3109/07388551.2015.1035693

Chen, Y., Sheng, W., Lin, J., Fang, C., Deng, J., Zhang, P., et al. (2022). Magnesium oxide nanoparticle coordinated phosphate-functionalized chitosan injectable hydrogel for osteogenesis and angiogenesis in bone regeneration phosphate-functionalized chitosan injectable hydrogel for osteogenesis and angiogenesis in bone regeneration. *ACS Appl. Mater Interfaces.* ;14(6):7592–7608. doi:10.1021/acsami.1c21260

Chien, K. H., Chang, Y. L., Wang, M. L., Chuang, J. H., Yang, Y. C., Tai, M. C., et al. (2018). Promoting induced pluripotent stem cell-driven biomineralization and periodontal regeneration in rats with maxillary-molar defects using injectable BMP-6 hydrogel injectable BMP-6 hydrogel. *Sci. Rep.*;8(1):114. doi:10.1038/s41598-017-18415-6

Crawford, L., Wyatt, M., Bryers, J., and Ratner, B. (2021). Biocompatibility evolves: phenomenology to toxicology to regeneration. *Adv. Healthc. Mater* 10 (11), e2002153. doi:10.1002/adhm.202002153

Cui, Z. K., Kim, S., Baljon, J. J., Wu, B. M., Aghaloo, T., and Lee, M. (2019). Microporous methacrylated glycol chitosan-montmorillonite nanocomposite hydrogel for bone tissue engineering. *Nat. Commun.* 10 (1), 3523. doi:10.1038/s41467-019-11511-3

Dannewitz, B., Holtfreter, B., and Eickholz, P. Parodontitis – Therapie einer Volkskrankheit Periodontitis-therapy of a widespread disease. *Bundesgesundheitsblatt Gesundheitsforsch. Gesundheitsschutz.* 2021;64(8):931–940. doi:10.1007/s00103-021-03373-2

Dong, L., Bu, Z., Xiong, Y., Zhang, H., Fang, J., Hu, H., et al. (2021). Facile extrusion 3D printing of gelatine methacrylate/Laponite nanocomposite hydrogel with high concentration nanoclay for bone tissue regeneration. *Int. J. Biol. Macromol.* 188, 72–81. doi:10.1016/j.ijbiomac.2021.07.199

Eshwar, S., Konuganti, K., Manvi, S., Bharadwaj, A. N., Sajjan, S., Boregowda, S. S., et al. (2023). Evaluation of osteogenic potential of fucoidan containing chitosan hydrogel in the treatment of periodontal intra-bony defects—a randomized clinical trial containing chitosan hydrogel in the treatment of periodontal intra-bony defects-A randomized clinical trial. *Gels.*;9(7):573. doi:10.3390/gels9070573

Fan, W., Jensen, L. R., Dong, Y., Deloria, A. J., Xing, B., Yu, D., et al. (2023). Highly stretchable, swelling-resistant, self-healed, and biocompatible dual-reinforced double polymer network hydrogels. *ACS Appl. Bio Mater* 6 (1), 228–237. doi:10.1021/acsabm.2c00856

Fatahian, S. A., Motavalizadehkakhky, A., Hosseiny, M., Nouri, S. M. M., Zhiani, R., Sohrabpour, M., et al. (2022). Upregulation of biochemical and biophysical properties of cell-laden microfiber, silk-hyaluronic acid composite. *Int. J. Biol. Macromol.* 211, 700–710. doi:10.1016/j.ijbiomac.2022.05.080

Fawzy El-Sayed, K. M., Mekhemar, M. K., Beck-Broichsitter, B. E., Bähr, T., Hegab, M., Receveur, J., et al. (2015). Periodontal regeneration employing gingival margin-derived stem/progenitor cells in conjunction with IL-1ra-hydrogel synthetic extracellular matrix synthetic extracellular matrix. *J. Clin. Periodontol.*;42(5):448–457. doi:10.1111/jcpe.12401

Fraser, D., and Benoit, D. (2022). Dual peptide-functionalized hydrogels differentially control periodontal cell function and promote tissue regeneration. *Biomater. Adv.* 141, 213093. doi:10.1016/j.bioadv.2022.213093

Fujioka-Kobayashi, M., Schaller, B., Kobayashi, E., Hernandez, M., Zhang, Y., and Miron, R. Hyaluronic acid gel-based scaffolds as potential carrier for growth factors: an *in vitro* bioassay on its osteogenic potential. *J. Clin. Med.* 2016;5(12):112. doi:10.3390/jcm5120112

Gan, Z., Xiao, Z., Zhang, Z., Li, Y., Liu, C., Chen, X., et al. (2023). Stiffness-tuned and ROS-sensitive hydrogel incorporating complement C5a receptor antagonist modulates antibacterial activity of macrophages for periodontitis treatment. *Bioact. Mater* 25, 347–359. doi:10.1016/j.bioactmat.2023.01.011

Gao, P., Kajiya, M., Motoike, S., Ikeya, M., and Yang, J. (2024a). Application of mesenchymal stem/stromal cells in periodontal regeneration: opportunities and challenges. *Jpn. Dent. Sci. Rev.* 60, 95–108. doi:10.1016/j.jdsr.2024.01.001

Gao, X., Ruzbarsky, J. J., Layne, J. E., Xiao, X., and Huard, J. (2024b). Stem cells and bone tissue engineering. *Life (Basel)* 14 (3), 287. doi:10.3390/life14030287

Gu, Z., Qiu, C., Chen, L., and Wang, X. (2024). Injectable thermosensitive hydrogel loading erythropoietin and FK506 alleviates gingival inflammation and promotes periodontal tissue regeneration. *Front. Bioeng. Biotechnol.* 11, 1323554. doi:10.3389/fbioe.2023.1323554

Guo, H., Huang, S., Yang, X., Wu, J., Kirk, T. B., Xu, J., et al. (2021). Injectable and self-healing hydrogels with double-dynamic bond tunable mechanical, gel-sol transition and drug delivery properties for promoting periodontium regeneration in periodontitis. *ACS Appl. Mater Interfaces* 13 (51), 61638–61652. doi:10.1021/acsami.1c18701

Guo, J., Sun, H., Lei, W., Tang, Y., Hong, S., Yang, H., et al. (2019). MMP-8-Responsive polyethylene glycol hydrogel for intraoral drug delivery. *J. Dent. Res.* 98 (5), 564–571. doi:10.1177/0022034519831931

Gupta, P., Sharma, S., Jabin, S., and Jadoun, S. (2024). Chitosan nanocomposite for tissue engineering and regenerative medicine: a review. *Int. J. Biol. Macromol.* 254 (Pt 1), 127660. doi:10.1016/j.ijbiomac.2023.127660

Hakimi, F., Jafari, H., Hashemikia, S., Shabani, S., and Ramazani, A. (2023). Chitosan-polyethylene oxide/clay-alginate nanofiber hydrogel scaffold for bone tissue engineering: preparation, physical characterization, and biomimetic mineralization. *Int. J. Biol. Macromol.* 233, 123453. doi:10.1016/j.ijbiomac.2023.123453

Halperin-Sternfeld, M., Pokhojaev, A., Ghosh, M., Rachmiel, D., Kannan, R., Grinberg, I., et al. (2023). Immunomodulatory fibrous hyaluronic acid-Fmoc-diphenylalanine-based hydrogel induces bone regeneration. *J. Clin. Periodontol.* 50 (2), 200–219. doi:10.1111/jcpe.13725

Hameed, H., Faheem, S., Paiva-Santos, A. C., Sarwar, H. S., and Jamshaid, M. (2024). A comprehensive review of hydrogel-based drug delivery systems: classification, properties, recent trends, and applications. *AAPS PharmSciTech* 25 (4), 64. doi:10.1208/s12249-024-02786-x

He, M., Hou, Y., Zhu, C., Jiang, Y., Feng, G., et al. (2021). 3D-Printing biodegradable PU/PAAM/gel hydrogel scaffold with high flexibility and self-adaptibility to irregular defects for nonload-bearing bone regeneration. *Bioconjug Chem.* 32 (8), 1915–1925. doi:10.1021/acs.bioconjchem.1c00322

Ho, T. C., Chang, C. C., Chan, H. P., Chung, T. W., Shu, C. W., Chuang, K. P., et al. (2022). Hydrogels: properties and applications in biomedicine. *Molecules*;27(9):2902. doi:10.3390/molecules27092902

Hu, Z. C., Lu, J. Q., Zhang, T. W., Liang, H. F., Yuan, H., Su, D. H., et al. (2022). Piezoresistive MXene/Silk fibroin nanocomposite hydrogel for accelerating bone regeneration by Re-establishing electrical microenvironment. *Bioact. Mater* 22, 1–17. doi:10.1016/j.bioactmat.2022.08.025

Kato, A., Miyaji, H., Ishizuka, R., Tokunaga, K., Inoue, K., Kosen, Y., et al. (2015). Combination of root surface modification with BMP-2 and collagen hydrogel scaffold implantation for periodontal healing in beagle dogs. *Open Dent. J.*;9:52–59. doi:10.2174/1874210601509010052

Kuroda, Y., Kawai, T., Goto, K., and Matsuda, S. (2019). Clinical application of injectable growth factor for bone regeneration: a systematic review. *Inflamm. Regen.* 39, 20. doi:10.1186/s41232-019-0109-x

Li, J., Lv, Y., Chen, Z., Zhao, J., and Wang, S. (2024). Citric acid loaded hydrogel-coated stent for dissolving pancreatic duct calculi. *Gels* 10 (2), 125. doi:10.3390/gels10020125

Li, M., Lv, J., Yang, Y., Cheng, G., Guo, S., Liu, C., et al. (2022a). Advances of hydrogel therapy in periodontal regeneration-A materials perspective review. *Gels* 8 (10), 624. doi:10.3390/gels8100624

Li, T., Liang, B., Ye, Z., et al. An integrated and conductive hydrogel-paper patch for simultaneous sensing of Chemical-Electrophysiological signals. *Biosens. Bioelectron.* 2022c 15:113855. doi:10.1016/j.bios.2021.113855

Li, T., Zeng, X., Zou, S., Xu, Y., and Duan, P. Recent advances in horizontal alveolar bone regeneration. *Biomed. Mater.* 2023;18, 052004. doi:10.1088/1748-605x/acd6725).

Li, Z., Li, G., Xu, J., Li, C., Han, S., Zhang, C., et al. (2022b). Hydrogel transformed from nanoparticles for prevention of tissue injury and treatment of inflammatory diseases. *Adv. Mater* 34 (16), e2109178. doi:10.1002/adma.202109178

Liu, J., Liu, H., Jia, Y., Tan, Z., Hou, R., Lu, J., et al. (2022c). Glucose-sensitive delivery of tannic acid by a photo-crosslinked chitosan hydrogel film for antibacterial and anti-inflammatory therapy. *J. Biomater. Sci. Polym. Ed.* 33 (13), 1644–1663. doi:10.1080/09205063.2022.2068948

Liu, S., Lu, S., Sun, S., Hai, J., Meng, G., and Wang, B. (2021b). NIR II light-response Au nanoframes: amplification of a pressure- and temperature-sensing strategy for portable detection and photothermal therapy of cancer cells. *Anal. Chem.* 93 (42), 14307–14316. doi:10.1021/acs.analchem.1c03486

Liu, S., Wang, Y. N., Ma, B., Shao, J., Liu, H., and Ge, S. (2021a). Gingipain-responsive thermosensitive hydrogel loaded with SDF-1 facilitates *in situ* periodontal tissue regeneration. *ACS Appl. Mater Interfaces* 13 (31), 36880–36893. doi:10.1021/acsami.1c08855

Liu, X., Wang, Y., Liang, Z., Lian, X., Huang, D., Hu, Y., et al. (2023). Progress in preparation and application of sodium alginate microspheres. *Sheng Wu Yi Xue Gong Cheng Xue Za Zhi* 40 (4), 792–798. doi:10.7507/1001-5515.202211048

Liu, Y., Li, T., Sun, M., Cheng, Z., Jia, W., Jiao, K., et al. (2022b). ZIF-8 modified multifunctional injectable photopolymerizable GelMA hydrogel for the treatment of periodontitis. *Acta Biomater.* 146, 37–48. doi:10.1016/j.actbio.2022.03.046

Liu, Z., Lin, W., and Liu, Y. (2022a). Macrocyclic supramolecular assemblies based on hyaluronic acid and their biological applications. *Acc. Chem. Res.* 55 (23), 3417–3429. doi:10.1021/acs.accounts.2c00462

Luo, F. Q., Xu, W., Zhang, J. Y., Liu, R., Huang, Y. C., Xiao, C., et al. (2022). An injectable nanocomposite hydrogel improves tumor penetration and cancer treatment efficacy. *Acta Biomater.* 147, 235–244. doi:10.1016/j.actbio.2022.05.042

Lv, Z., Hu, T., Bian, Y., Wang, G., Wu, Z., Li, H., et al. (2023). A MgFe-ldh nanosheet-incorporated smart thermo-responsive hydrogel with controllable growth factor releasing capability for bone regeneration. *Adv. Mater* 35 (5), e2206545. doi:10.1002/adma.202206545

Ma, S., Lu, X., Yu, X., Du, Y., Xu, S., Li, M., et al. (2022). An injectable multifunctional thermo-sensitive chitosan-based hydrogel for periodontitis therapy. *Biomater. Adv.* 142, 213158. doi:10.1016/j.bioadv.2022.213158

Magalhães, LSSM, Andrade, D. B., Bezerra, R. D. S., Morais, A. I. S., Oliveira, F. C., Rizzo, M. S., et al. (2022). Nanocomposite hydrogel produced from PEGDA and laponite for bone regeneration. *J. Funct. Biomater.* 13 (2), 53. doi:10.3390/jfb13020053

Marinho, A., Nunes, C., and Reis, S. (2021). Hyaluronic acid: a key ingredient in the therapy of inflammation. *Biomolecules* 11 (10), 1518. doi:10.3390/biom11101518

Merrill, E. W., Salzman, E. W., Wan, S., Mahmud, N., Kushner, L., Lindon, J. N., et al. (1982). Platelet-compatible hydrophilic segmented polyurethanes from polyethylene glycols and cyclohexane diisocyanate. *Trans. Am. Soc. Artif. Intern Organs* 28, 482–487.

Momose, T., Miyaji, H., Kato, A., Sugaya, T., Kawanami, M., Nishida, E., et al. (2016). Collagen hydrogel scaffold and fibroblast growth factor-2 accelerate periodontal healing of class II furcation defects in dog dog. *Open Dent. J.* ;10:347–359. doi:10.2174/1874210601610010347

Ouyang, Y., Su, X., Zheng, X., Zhang, L., Chen, Z., Yan, Q., et al. (2024). Mussel-inspired "all-in-one" sodium alginate/carboxymethyl chitosan hydrogel patch promotes healing of infected wound. *Int. J. Biol. Macromol.* 261 (Pt 2), 129828. doi:10.1016/j.ijbiomac.2024.129828

Parisi, L., Rivara, F., Costa, C. A., Abuna, R. P., Palioto, D. B., and Macaluso, G. M. Aptamers recognizing fibronectin confer improved bioactivity to biomaterials and promote new bone formation in a periodontal defect in rats. *Biomed. Mater*. 2020;16(1):015016. doi:10.1088/1748-605x/abb6b2

Peng, G., Li, W., Peng, L., Li, R., Wang, Z., Zhou, Y., et al. (2023). Multifunctional DNA-based hydrogel promotes diabetic alveolar bone defect reconstruction. *Small* 20, e2305594. doi:10.1002/smll.202305594

Qiu, H., Wang, J., Hu, H., Song, L., Liu, Z., Xu, Y., et al. (2024). Preparation of an injectable and photocurable carboxymethyl cellulose/hydroxyapatite composite and its application in cranial regeneration. *Carbohydr. Polym.* 333, 121987. doi:10.1016/j.carbpol.2024.121987

Rivera-Hernández, G., Antunes-Ricardo, M., Martínez-Morales, P., and Sánchez, M. L. (2021). Polyvinyl alcohol based-drug delivery systems for cancer treatment. *Int. J. Pharm.* 600, 120478. doi:10.1016/j.ijpharm.2021.120478

Sanchez-Ballester, N. M., Bataille, B., and Soulairol, I. Sodium alginate and alginic acid as pharmaceutical excipients for tablet formulation: structure-function relationship. *Carbohydr Polym.* 2021;270:118399. doi:10.1016/j.carbpol.2021.118399

Santos, M. S., Dos Santos, A. B., and Carvalho, M. S. (2023). New insights in hydrogels for periodontal regeneration. *J. Funct. Biomater.* 14 (11), 545. doi:10.3390/jfb14110545

Sedghi, L. M., Bacino, M., and Kapila, Y. L. (2021). Periodontal disease: the good, the bad, and the unknown. *Front. Cell. Infect. Microbiol.* 11, 766944. doi:10.3389/fcimb.2021.766944

Siddiqui, Z., Sarkar, B., Kim, K. K., Kadincesme, N., Paul, R., Kumar, A., et al. (2021). Angiogenic hydrogels for dental pulp revascularization. *Acta Biomater.*;126:109–118. doi:10.1016/j.actbio.2021.03.001

Smeets, R., Matthies, L., Windisch, P., Gosau, M., Jung, R., Brodala, N., et al. (2022). Horizontal augmentation techniques in the mandible: a systematic review. *Int. J. Implant Dent.* 8 (1), 23. doi:10.1186/s40729-022-00421-7

Sowmya, S., Mony, U., Jayachandran, P., Reshma, S., Kumar, R. A., Arzate, H., et al. (2017). Tri-layered nanocomposite hydrogel scaffold for the Concurrent regeneration of cementum, periodontal ligament, and alveolar bone. *Adv Healthc. Mater*;6. doi:10.1002/adhm.2016012517).

Sun, X., Liang, Y., Ye, L., and Liang, H. (2021). An extremely tough and ionic conductive natural-polymer-based double network hydrogel. *J. Mater Chem. B* 9 (37), 7751–7759. doi:10.1039/d1tb01458g

Suo, L., Wu, H., Wang, P., Xue, Z., Gao, J., and Shen, J. (2023). The improvement of periodontal tissue regeneration using a 3D-printed carbon nanotube/chitosan/sodium alginate composite scaffold D-printed carbon nanotube/chitosan/sodium alginate composite scaffold. *J. Biomed. Mater Res. B Appl. Biomater.* 111 (1), 73–84. doi:10.1002/jbm.b.35133

Tan, J., Zhang, M., Hai, Z., Wu, C., Lin, J., Kuang, W., et al. (2019). Sustained release of two bioactive factors from supramolecular hydrogel promotes periodontal bone regeneration. *ACS Nano* 13, 5616–5622. doi:10.1021/acsnano.9b00788

Tan, N., Sabalic-Schoener, M., Nguyen, L., and D'Aiuto, F. (2023). β-Tricalcium phosphate-loaded chitosan-based thermosensitive hydrogel for periodontal regeneration. *Polym. (Basel).* ;15(20):4146. doi:10.3390/polym15204146

Tian, Y., Cui, Y., Ren, G., Fan, Y., Dou, M., Li, S., et al. (2024). Dual-functional thermosensitive hydrogel for reducing infection and enhancing bone regeneration in infected bone defects. *Mater Today Bio* 25, 100972. doi:10.1016/j.mtbio.2024.100972

Ur Rehman, W., Asim, M., Hussain, S., Khan, S. A., and Khan, S. B. (2020). Hydrogel: a promising material in pharmaceutics. *Curr. Pharm. Des.* 26 (45), 5892–5908. doi:10.2174/1381612826666201118095523

Wang, B., Booij-Vrieling, H. E., Bronkhorst, E. M., Shao, J., Kouwer, P. H., Jansen, J. A., et al. (2020). Antimicrobial and anti-inflammatory thermo-reversible hydrogel for periodontal delivery. *Acta Biomater.* 116, 259–267. doi:10.1016/j.actbio.2020.09.018

Wang, L., Nan, X., Hou, J., Xia, Y., Guo, Y., Meng, K., et al. (2021). Retracted: preparation and biological properties of silk fibroin/nano-hydroxyapatite/hyaluronic acid composite scaffold. *Biomed. Mater* 16, 045045. doi:10.1088/1748-605x/ac08aa

Wang, W., Wang, A., Hu, G., Bian, M., Chen, L., Zhao, Q., et al. (2023). Potential of an aligned porous hydrogel scaffold combined with periodontal ligament stem cells or gingival mesenchymal stem cells to promote tissue regeneration in rat periodontal defects regeneration in rat periodontal defects. *ACS Biomater. Sci. Eng.*;9(4):1961–1975. doi:10.1021/acsbiomaterials.2c01440

Wang, X., Fang, X., Gao, X., Wang, H., Li, S., Li, C., et al. (2022). Strong adhesive and drug-loaded hydrogels for enhancing bone-implant interface fixation and anti-infection properties. *Colloids Surf. B Biointerfaces* 219, 112817. doi:10.1016/j.colsurfb.2022.112817

Wen, B., Dai, Y., Han, X., Huo, F., Xie, L., Yu, M., et al. (2023). Biomineralization-inspired mineralized hydrogel promotes the repair and regeneration of dentin/bone hard tissue. *NPJ Regen. Med.* 8 (1), 11. doi:10.1038/s41536-023-00286-3

Wu, Y., Zhang, X., Tan, B., Shan, Y., Zhao, X., and Liao, J. (2022). Near-infrared light control of GelMA/PMMA/PDA hydrogel with mild photothermal therapy for skull regeneration. *Biomater. Adv.* 133, 112641. doi:10.1016/j.msec.2022.112641

Xia, L., Wang, S., Jiang, Z., Chi, J., Yu, S., Li, H., et al. (2021). Hemostatic performance of chitosan-based hydrogel and its study on biodistribution and biodegradability in rats. *Carbohydr. Polym.* 264, 117965. doi:10.1016/j.carbpol.2021.117965

Xiang, C., Zhang, X., Zhang, J., Chen, W., Li, X., Wei, X., et al. (2022). A porous hydrogel with high mechanical strength and biocompatibility for bone tissue engineering. *J. Funct. Biomater.* 13 (3), 140. doi:10.3390/jfb13030140

Xie, Y., Gan, C., Li, Z., Liu, W., Yang, D., and Qiu, X. (2022). Fabrication of a lignin-copper sulfide-incorporated PVA hydrogel with near-infrared-activated photothermal/photodynamic/peroxidase-like performance for combating bacteria and biofilms. *ACS Biomater. Sci. Eng.* 8 (2), 560–569. doi:10.1021/acsbiomaterials.1c01406

Xu, H., Luo, H., Chen, J., Chen, G., Yu, X., and Ye, Z. (2023). BMP-2 releasing mineral-coated microparticle-integrated hydrogel system for enhanced bone regeneration. *Front. Bioeng. Biotechnol.* 11, 1217335. doi:10.3389/fbioe.2023.1217335

Xu, X., Gu, Z., Chen, X., Shi, C., Liu, C., Liu, M., et al. (2019). An injectable and thermosensitive hydrogel: promoting periodontal regeneration by controlled-release of aspirin and erythropoietin. *Acta Biomater.* 86, 235–246. doi:10.1016/j.actbio.2019.01.001

Yan, N., Xu, J., Liu, G., Bao, L., Cong, Y., et al. (2022). Penetrating macrophage-based nanoformulation for periodontitis treatment. *ACS Nano* 16 (11), 18253–18265. doi:10.1021/acsnano.2c05923

Yu, M. C., Chang, C. Y., Chao, Y. C., Jheng, Y., Yang, C., Lee, N., et al. (2016). pH-responsive hydrogel with an anti-glycation agent for modulating experimental periodontitis. *J. Periodontol.* 87 (6), 742–748. doi:10.1902/jop.2016.150542

Yu, T., Zhang, L., Dou, X., Bai, R., Wang, H., Deng, J., et al. (2022). Mechanically robust hydrogels facilitating bone regeneration through epigenetic modulation. *Adv. Sci. (Weinh)* 9 (32), e2203734. doi:10.1002/advs.202203734

Zhai, X., Ruan, C., Shen, J., Zheng, C., Zhao, X., Pan, H., et al. (2021). Clay-based nanocomposite hydrogel with attractive mechanical properties and sustained bioactive

ion release for bone defect repair. *J. Mater Chem. B* 9 (10), 2394–2406. doi:10.1039/d1tb00184a

Zhang, G., Wang, X., Meng, G., Xu, T., Shu, J., Zhao, J., et al. (2024). Enzyme-Mineralized PVASA hydrogels with combined toughness and strength for bone tissue engineering. *ACS Appl. Mater Interfaces* 16 (1), 178–189. doi:10.1021/acsami.3c14006

Zhang, L., He, G., Yu, Y., Zhang, Y., Li, X., and Wang, S. (2022b). Design of biocompatible chitosan/polyaniline/laponite hydrogel with photothermal conversion capability. *Biomolecules* 12 (8), 1089. doi:10.3390/biom12081089

Zhang, Q., Wang, X., Kang, Y., Yao, C., Li, X., and Li, L. (2022a). Conjugated molecule-assisted supramolecular hydrogel with enhanced antibacterial and antibiofouling properties. *ACS Appl. Bio Mater* 5, 3107–3114. doi:10.1021/acsabm.2c00385

Zhang, Z., Bi, F., and Guo, W. (2023). Research advances on hydrogel-based materials for tissue regeneration and remineralization in tooth. *Gels* 9 (3), 245. doi:10.3390/gels9030245

Zhao, Y., Cui, J., Qiu, X., Yan, Y., Zhang, Z., Fang, K., et al. (2022). Manufacturing and post-engineering strategies of hydrogel actuators and sensors: from materials to interfaces. *Adv. Colloid Interface Sci.*;308:102749. doi:10.1016/j.cis.2022.102749

Zhou, T., Zheng, K., Sui, B., Boccaccini, A. R., and Sun, J. (2020). *In vitro* evaluation of poly (vinyl alcohol)/collagen blended hydrogels for regulating human periodontal ligament fibroblasts and gingival fibroblasts. *Int. J. Biol. Macromol.* 163, 1938–1946. doi:10.1016/j.ijbiomac.2020.09.033

Zor, F., Selek, F. N., Orlando, G., and Williams, D. F. (2019). Biocompatibility in regenerative nanomedicine. *Nanomedicine (Lond).* 14 (20), 2763–2775. doi:10.2217/nnm-2019-0140

frontiers | Frontiers in Bioengineering and Biotechnology

TYPE Original Research
PUBLISHED 26 April 2024
DOI 10.3389/fbioe.2024.1379679

OPEN ACCESS

EDITED BY
Hongye Yang,
Wuhan University, China

REVIEWED BY
Md Shaifur Rahman,
Atomic Energy Research Establishment, Bangladesh
Dingyu Wu,
Central South University, China
Zhanyong Zhu,
Renmin Hospital of Wuhan University, China

*CORRESPONDENCE
Hui Xie,
xiehuijessice@163.com

†These authors have contributed equally to this work

RECEIVED 31 January 2024
ACCEPTED 01 April 2024
PUBLISHED 26 April 2024

CITATION
Wang X, Xiang C, Huang C, Cheng H, Zhou Z, Zhang J and Xie H (2024), The treatment efficacy of bone tissue engineering strategy for repairing segmental bone defects under diabetic condition.
Front. Bioeng. Biotechnol. 12:1379679.
doi: 10.3389/fbioe.2024.1379679

The treatment efficacy of bone tissue engineering strategy for repairing segmental bone defects under diabetic condition

Xiangsheng Wang[1,2†], Can Xiang[3†], Chunhua Huang[1†], Hanxiao Cheng[2], Zhentao Zhou[2], Jufang Zhang[2] and Hui Xie[4*]

[1]Department of Plastic Surgery, Jingshan Union Hospital, Union Hospital, Huazhong University of Science and Technology, Hubei, China, [2]Department of Plastic Surgery, Affiliated Hangzhou First People's Hospital, Zhejiang University School of Medicine, Hangzhou, Zhejiang, China, [3]Department of Research, Union Hospital, Tongji Medical College, Huazhong University of Science and Technology, Wuhan, Hubei, China, [4]Department of Geriatrics, Tongji Hospital, Tongji Medical College, Huazhong University of Science and Technology, Wuhan, Hubei, China

Background: Diabetes mellitus is a systematic disease which exert detrimental effect on bone tissue. The repair and reconstruction of bone defects in diabetic patients still remain a major clinical challenge. This study aims to investigate the potential of bone tissue engineering approach to improve bone regeneration under diabetic condition.

Methods: In the present study, decalcified bone matrix (DBM) scaffolds were seeded with allogenic fetal bone marrow-derived mesenchymal stem cells (BMSCs) and cultured in osteogenic induction medium to fabricate BMSC/DBM constructs. Then the BMSC/DBM constructs were implanted in both subcutaneous pouches and large femoral bone defects in diabetic (BMSC/DBM in DM group) and non-diabetic rats (BMSC/DBM in non-DM group), cell-free DBM scaffolds were implanted in diabetic rats to serve as the control group (DBM in DM group). X-ray, micro-CT and histological analyses were carried out to evaluate the bone regenerative potential of BMSC/DBM constructs under diabetic condition.

Results: In the rat subcutaneous implantation model, quantitative micro-CT analysis demonstrated that BMSC/DBM in DM group showed impaired bone regeneration activity compared with the BMSC/DBM in non-DM group (bone volume: 46 $\pm$ 4.4 mm^3 vs 58.9 $\pm$ 7.15 mm^3, $*p < 0.05$). In the rat femoral defect model, X-ray examination demonstrated that bone union was delayed in BMSC/DBM in DM group compared with BMSC/DBM in non-DM group. However, quantitative micro-CT analysis showed that after 6 months of implantation, there was no significant difference in bone volume and bone density between the BMSC/DBM in DM group (199 $\pm$ 63 mm^3 and 593 $\pm$ 65 mg HA/ccm) and the BMSC/DBM in non-DM group (211 $\pm$ 39 mm^3 and 608 $\pm$ 53 mg HA/ccm). Our data suggested that BMSC/DBM constructs could repair large bone defects in diabetic rats, but with delayed healing process compared with non-diabetic rats.

Conclusion: Our study suggest that biomaterial sacffolds seeded with allogenic fetal BMSCs represent a promising strategy to induce and improve bone regeneration under diabetic condition.

KEYWORDS

diabetes mellitus, bone tissue engineering, mesenchymal stem cells, decalcified bone matrix, bone regeneration

Introduction

Diabetes mellitus (DM) is a chronic metabolic disease characterized by the presence of elevated blood glucose levels, and is of two types: type 1 diabetes, which is due to severe deficiency in insulin synthesis, and type 2 diabetes which is caused by insulin resistance combined with insulin production deficiency (Antar et al., 2023). DM is a systematic disease affecting not only the heart, brain, kidneys, eyes, blood vessels and nerves, but it also causes a negative effect on the skeletal system. It is well known that DM contributes to osteoporosis, increased fracture risk, delayed bone healing and impaired bone regeneration (Antar et al., 2023; Csonka and Lendvay, 2023). In fact, it was reported that diabetic patients had a 6- to 7-fold increased risk of hip fracture, 2.75-fold increased risk of implant failure and 1.6-fold delay in fracture healing compared with non-diabetic population (Hu et al., 2018; Hygum et al., 2019). With the rise in incidence of DM and aging of population, the number of DM patients requiring bone reconstruction procedures rapidly increases. However, the repair of bone fracture and defect in diabetic patients still remains a major clinical challenge (Hu et al., 2018). Thus, it is essential to develop effective methods to accelerate bone regeneration in DM patients.

Bone tissue engineering has recently emerged as a promising treatment strategy for the repair and functional regeneration of large segmental bone defects (Li et al., 2018). Its general principle involves the integration of seed cells, tridimensional biomaterial framework and molecular signals to generate an implantable construct (Perez et al., 2018). This approach has been proved effective in both animal models and clinical trials (Confalonieri et al., 2018; Mazzoni et al., 2023). Nevertheless, most of the studies were performed in healthy recipients with unimpaired bone regeneration activity. There are limited studies on whether bone tissue engineering approach could improve bone regeneration under diabetic condition.

One of the fundamental components of bone tissue engineering strategy is seed cells. Bone marrow-derived mesenchymal stem cells (BMSCs) are a major source of osteoblasts, osteocytes and bone lining cells *in vivo*, and are crucial for bone remodeling via both cellular and paracrine effects. Because of their easy acquisition, potent proliferative and osteogenic potential, well-defined osteogenic differentiation pathway and low immunogenicity, BMSCs are considered as an attractive cellular source for bone tissue engineering applications (Zhang et al., 2012; Grelewski et al., 2023). Although autologous cell sources are generally preferred in clinical trials, it is well documented that BMSCs derived from diabetic patients exhibited decreased proliferative and osteogenic potential (Fijany et al., 2019). In addition, it was reported that diabetic donors possessed fewer BMSCs and that these cells exhibited impaired proliferation and survival *in vitro* (De Vyver, 2017). On the other hand, the use of allogenic BMSCs derived from healthy donors with efficacious osteogenic potential may circumvent the limitations of autologous BMSCs. Besides, allogenic BMSCs can be easily cultured, expanded and cryopreserved, allowing off-the-shelf availability. Investigations into their use in healing critical-sized bone defects in various animal models demonstrated their utility for bone tissue engineering applications (Berner et al., 2013; Arthur and Gronthos, 2020).

Decalcified bone matrix (DBM) is an artificial bone material obtained by decalcifying biological bone. It is considered as an ideal bone regeneration scaffold due to its good biocompatibility and osteogenic activity (Liu et al., 2023). Previously, we have conducted experiments to investigate the potential of allogenic fetal BMSC-based bone tissue engineering strategy for healing critical-sized bone defect in a rabbit model of osteoporosis (Wang et al., 2015). In the current study, we seeded allogenic fetal BMSCs on DBM scaffolds to construct tissue-engineered bone grafts, and investigated their potential to form both ectopic and orthotopic bone in streptozotocin (STZ)-induced type 1 diabetic rat model.

Materials and methods

Isolation and culture of BMSCs

To obtain fetal BMSCs, pregnant SD rats (19 days post conception) were sacrificed. Single-cell suspensions were prepared by flushing the bone marrow out of the femurs of rat fetuses using Dulbecco's Modified Eagle's Medium (DMEM; Hyclone, Logan City, UT, United States of America) containing 10% fetal bovine serum (FBS; Hyclone) under aseptic conditions. Cells were seeded in culture dish and cultured with low-glucose DMEM supplemented with 10% FBS and 1% penicillin-streptomycin antibiotic (Gibco, Grand Island, NY, United States of America) in a humidified incubator with 5% CO_2 at 37°C. After 5 days, the culture medium was changed and non-adherent cells were removed. Cell passaging was performed until the monolayer of the adherent cells reached 80% confluence with trypsin-EDTA (Gibco).

Multilineage differentiation of BMSCs

Osteogenic, adipogenic and chondrogenic differentiation of BMSCs was performed as previously described (Zhang et al., 2009). All chemicals were purchased from Sigma (St Louis, MO, United States of America) unless otherwise stated. For osteogenic differentiation, BMSCs at passage 3 were cultured in osteogenic induction medium (DMEM supplemented with 10% FBS, 1% penicillin-streptomycin antibiotic, 10 mmol/L β-glycerophosphate, 10^{-8} mol/L dexamethasone, and 50 mmol/L ascorbic acid). The medium was changed twice a week for 14 days. After induction, cells were fixed with 10% formalin and then stained with alizarin red.

For adipogenic differentiation, BMSCs at passage 3 were cultured in DMEM supplemented with 10% FBS, 1% penicillin-streptomycin antibiotic, 5 μg/mL insulin, 200 μM indomethacin, 1 μM dexamethasone, and 0.5 mM 3-isobutyl-1-methylxanthine. The medium was changed twice a week. After 21 days of induction, cells were fixed with 10% formalin and then stained with 0.5% oil red O in methanol.

For chondrogenic differentiation, BMSCs at passage 3 were pelleted and cultured in DMEM supplemented with 10% FBS, 1% penicillin-streptomycin antibiotic, 0.1 μM dexamethasone, 0.17 mM ascorbic acid, 1 mM sodium pyruvate, 0.35 mM L-proline, 1% insulin-transferrin sodium-selenite, 1.25 mg/mL bovine serum albumin, 5.33 μg/mL linoleic acid, and 0.01 μg/mL transforming growth factor-β (Cell Science, Canton, MA, United States). The medium was changed twice a week. After 28 days of incubation, the micromass pellets were fixed with 10%

formalin, then embedded in paraffin and sectioned in 10-μm slices. After being dewaxed and rehydrated, the slices were stained with toluidine blue.

Fabrication and characterization of BMSC/DBM construct

DBM scaffolds were prepared from bovine limbs as previously described (Wang et al., 2015). The scaffolds were cut into 10 mm × 5 mm × 3 mm cuboids, and then sterilized with 75% ethanol. BMSCs at passage 3 were harvested with EDTA-trypsin and resuspended with DMEM at a cellular density of 2×10^6/mL. Each DBM cuboid was seeded with 100 μL cell suspension to generate BMSC/DBM construct. After 4 h of incubation in a humidified incubator at 37°C, the BMSC/DBM constructs were replenished with osteogenic induction medium and the medium was changed twice a week. After 14 days of osteogenic induction, BMSC/DBM constructs were ready for transplantation.

For scanning electron microscopic (SEM) analysis, the BMSC/DBM constructs were fixed in 2.5% glutaraldehyde after 14 days of osteogenic induction. The fixed BMSC/DBM constructs were then soaked in 1% osmic acid for 2 h and then rinsed with PBS. After being dehydrated with an ascending sequence of ethanol and dried at room temperature, the samples were sputter-coated with gold and finally observed with an SEM (Hitachi, Tokyo, Japan).

Establishment of DM rat model

All animal protocols were approved by the University Committee on Use and Care of Animals of Huazhong University of Science and Technology. STZ is widely used to produce DM model in rats (Furman, 2021). As previously described with some modifications (Wojcicka et al., 2010), STZ (Sigma) was dissolved in 0.1 M of a citrate buffer (pH 4.5), and injected intraperitoneally into 5-week-old male Sprague-Dawley rats at a dose of 50 mg/kg body weight after overnight fasting. Rats in control group were injected with citrate buffer. Five days after STZ injection, fasting glucose (IFG) level in the blood obtained from the tail was measured using a glucometer (Omron, Kyoto, Japan). IFG >11.1 mmol/L and stable for 2 weeks were considered diabetes.

In vivo study

To test the ability of BMSC/DBM constructs to form ectopic bone, twelve diabetic rats and six age-matched non-diabetic rats were divided into three group: 1) BMSC/DBM in non-DM group (n = 6): BMSC/DBM constructs were implanted subcutaneously into the dorsum of the non-diabetic control rats; 2) BMSC/DBM in DM group (n = 6): BMSC/DBM constructs were implanted subcutaneously into the dorsum of DM rats; 3) DBM in DM group (n = 6): cell-free DBM scaffolds were implanted subcutaneously into the dorsum of DM rats. After 1 and 3 months of implantation, the specimens were harvested and fixed in 4% formalin for further analyses.

To investigate the potential of BMSC/DBM constructs to repair large bone defects under diabetic condition, rat femoral large bone defect model was prepared as previously described (Janko et al., 2019). Twenty diabetic rats and ten age-matched non-diabetic rats were anaesthetized with isoflurane. The left hindlimb of the rat was shaved and cleaned with iodophor, and incision was made from lateral side of the left femur. Next, muscles and subcutaneous tissues were blunt-dissected to expose the left femoral shaft. An internal fixation plate was placed on the surface of the femoral shaft, and four screws fixed the plate to the bone. Afterwards, a 10-mm-long bone defect was created in the femur by an electrical bone saw. Then the rats were divided into three groups as mentioned above, the defects were filled with BMSC/DBM constructs or cell-free DBM scaffolds. The wound was closed and disinfected with iodophor. After the surgery, the rats were given 20,000 U/d gentamycin (Sigma) by intramuscular injection for 3 days. At the 6th month after the surgery, the rats were painlessly killed by overdosed inhalation of carbon dioxide. Femurs were harvested, and fixed in 4% formalin for further analyses.

X-ray and micro-CT analyses

At the 1st, 3rd and 6th month after surgery, plain x-ray images were obtained under anesthesia with isoflurane. For micro-CT (μ-80, Scanco Medical, Zurich, Switzerland) analysis, bone specimens were placed in the sample holder and scanned at multiple longitudinal and transverse sections with 0.05 mm thickness. Then three-dimensional (3D) images were reconstructed. Bone volume (BV), bone volume per tissue volume (BV/TV) and bone density of the specimens was automatically calculated via micro-CT auxiliary software (Volume Graphics GmbH, Heidelberg, Germany).

Histological evaluation

After micro-CT analysis, bone specimens were decalcified with 10% EDTA solution, dehydrated in increasing ethanol concentration, and then embedded in paraffin. Sections were cut into 10-μm-thick sections and stained with hematoxylin and eosin (HE, Sigma) and Van Gieson (VG, Sigma) to visualize tissue morphology and demonstrate collagen formation.

Statistical analysis

All data collected are presented as mean ± standard deviation, and were analyzed using one-way ANOVA analysis. $p < 0.05$ was considered significant.

Results

Characterization of rat BMSCs and BMSC/DBM constructs

Rat fetal BMSCs exhibited a spindle-like morphology at passage 3 (Figure 1A). As shown in Figures 1B–D, MSCs underwent osteogenic, adipogenic, and chondrogenic differentiation, as demonstrated by alizarin red, oil red O and toluidine blue staining. The capacity of BMSCs to undergo multilineage differentiation was thereby established. To fabricate BMSC/DBM

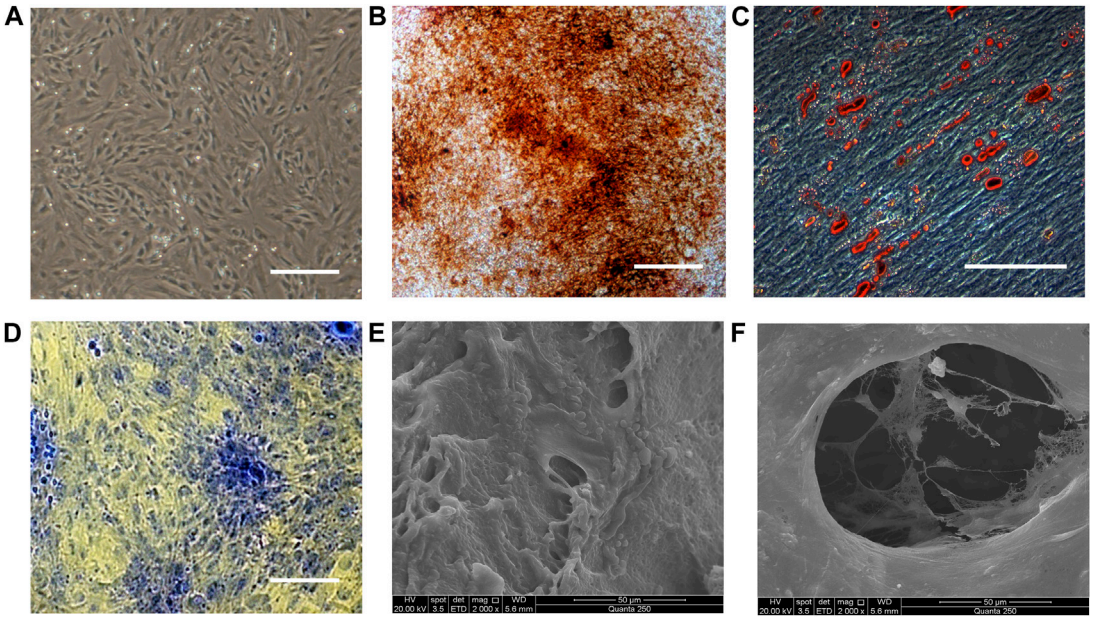

FIGURE 1
Characterization of BMSCs and BMSC/DBM constructs. **(A)**. Typical morphology of rat BMSCs at passage 3. Scale bar: 200 μm. **(B)**. Alizarin red staining of BMSCs after 14 days of osteogeneic induction. Scale bar: 100 μm. **(C)**. Oil red O staining of BMSCs after 21 days of adipogenic induction. Scale bar: 100 μm. **(D)**. Toluidine blue staining of the BMSC-derived micromass after 28 days of chondrogenic induction. Scale bar: 100 μm. **(E,F)**. BMSC/DBM constructs observed under SEM after 14 days of culture. Scale bars: 50 μm.

constructs, BMSCs were seeded on DBM scaffolds and then cultured in osteogenic induction medium for 14 days. SEM showed that after 14 days of culture and osteogenic induction, BMSCs on the DBM scaffolds grew vigorously, secreting abundant extracellular matrix and filling the pores of the scaffolds (Figures 1E, F).

BMSC/DBM constructs form ectopic bone under diabetic condition

To determine whether BMSC/DBM constructs could form ectopic bone under diabetic condition, we implanted BMSC/DBM constructs or cell-free DBM scaffolds subcutaneously into the dorsum of diabetic rats and age-matched non-diabetic rats. At 1 and 3 months after implantation, the specimens were harvested and scanned by micro-CT for evaluation. From the macroscopic view, both the BMSC/DBM in non-DM group and the BMSC/DBM in DM group showed complete tissue morphology, while scaffold degradation had already occurred in the DBM in DM group (Figures 2A, C). The 3D reconstruction of micro-CT images of the specimens showed that obvious mineralized tissue formation can be seen in both the BMSC/DBM in non-DM group and the BMSC/DBM in DM group, while the DBM in DM group showed hardly any mineralized tissue formation (Figures 2B, D). Quantitative micro-CT analysis (Figure 2E) showed that after 1 month of implantation, the BV and BV/TV of the BMSC/DBM in non-DM group (47.75 ± 4.8 mm^3 and 13.3% ± 0.13%) were significantly increased compared with that of the BMSC/DBM in DM group (23.2 ± 2.9 mm^3 and 6.5% ± 0.03%) and DBM in DM group (7.4 ± 1.73 mm^3 and 2.9% ± 0.9%). After 3 months of implantation, the BV and BV/TV of the BMSC/DBM in non-DM group had increased to 58.9 ± 7.15 mm^3 and 19.8% ± 0.25%, followed by the BMSC/DBM in DM group (46 ± 4.4 mm^3 and 12.3% ± 0.41%) and DBM in DM group (11.1 ± 0.9 mm^3 and 5.3% ± 1.2%). Our data demonstrated that BMSC/DBM constructs could form ectopic bone under diabetic condition, however, they showed impaired bone regeneration activity under diabetic condition compared with non-diabetic controls.

BMSC/DBM constructs repair femoral bone defects under diabetic condition

Large bone defects were created in the femurs of both diabetic rats and age-matched non-diabetic rats. To investigate the potential of BMSC/DBM constructs to form orthotopic bone under diabetic condition, BMSC/DBM constructs or cell-free DBM scaffolds were implanted into the defects. X-ray examination showed that dense tissue was formed in both the BMSC/DBM in non-DM group and the BMSC/DBM in DM group at 3 months after surgery, and the BMSC/DBM in non-DM group showed much better new bone formation than the BMSC/DBM in DM group. At 6 months after surgery, bone union was observed in both the BMSC/DBM in non-DM group and the BMSC/DBM in DM group. In contrast, new bone formation did not occur in the DBM in DM group (Figure 3).

Animals were sacrificed at the 6th month post-surgery, femurs were obtained and then subjected to micro-CT analysis. As shown in Figures 4A, B, both macroscopic and 3D reconstructed micro-CT images showed that the defects in BMSC/DBM treated diabetic and non-diabetic group were filled with newly formed bone tissue. However, little new bone formation was observed in the DBM in DM group. Quantitative micro-CT analyses indicated that at

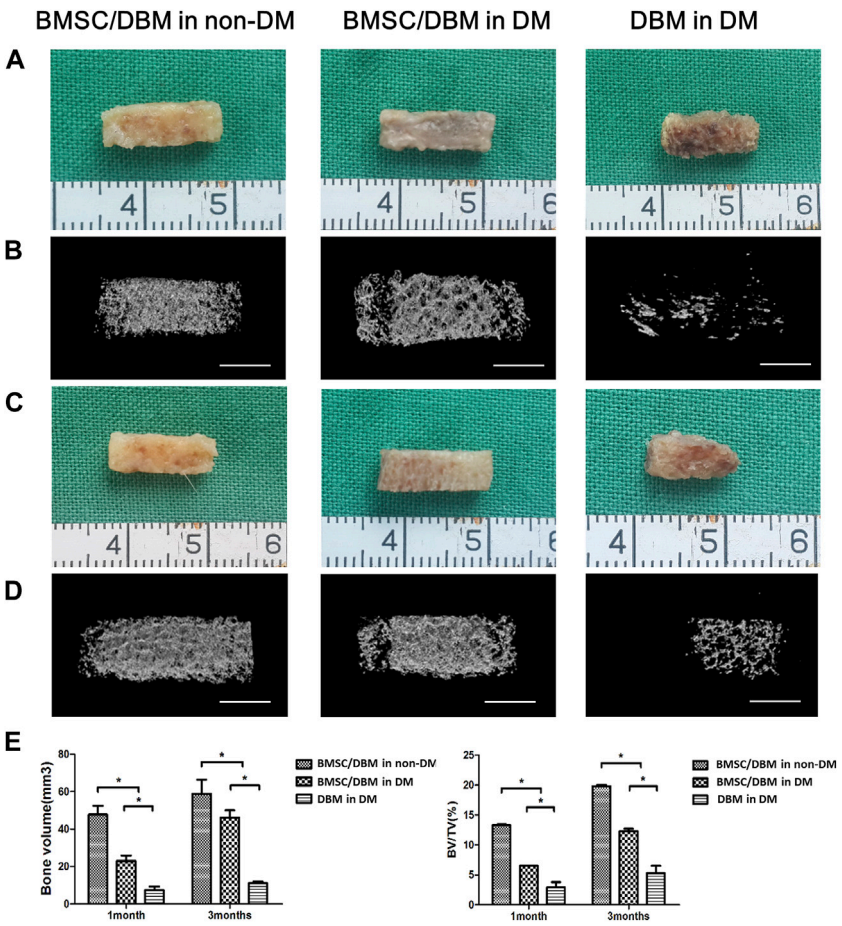

FIGURE 2
BMSC/DBM constructs form ectopic bone under diabetic condition. **(A)**. Macroscopic view of the specimens after 1 month of implantation. **(B)**. 3D reconstruction of micro-CT images of the specimens after 1 month of implantation. Scale bars: 5 mm. **(C)**. Macroscopic view of the specimens after 3 months of implantation. **(D)**. 3D reconstruction of micro-CT images of the specimens after 3 months of implantation. Scale bars: 5 mm. **(E)**. Statistical analyses of bone volume (BV) and bone volume per tissue volume (BV/TV), $*p < 0.05$.

6 months after surgery, there was no significant difference in BV and bone density between the BMSC/DBM in non-DM group (211 ± 39 mm^3 and 608 ± 53 mg HA/ccm) and BMSC/DBM in DM group (199 ± 63 mm^3 and 593 ± 65 mg HA/ccm), although the BV and bone density were slightly higher in the non-diabetic group compared with the diabetic group (Figure 4C). These data suggest that BMSC/DBM constructs could repair large bone defects in diabetic rats, but with delayed healing process compared with non-diabetic rats.

Histological analysis

HE staining and Van Gieson staining were carried out to evaluate new bone formation. As shown in Figure 5, at 6 months post-surgery, newly formed bone tissue was observed in both the BMSC/DBM in non-DM and the BMSC/DBM in DM group. In contrast, the defect area in the DBM in DM group was filled with mostly fibrous connective tissue. Van Gieson staining further demonstrated that well-formed collagen deposition was observed in both the BMSC/DBM in non-DM and the BMSC/DBM in DM group, while hardly any collagen deposition can be seen in the DBM in DM group.

Discussion

Diabetes is a group of metabolic disorders which can cause multiple organ damages. Patients with diabetes are more prone to osteoporosis, bone fracture and impaired bone healing than the non-diabetic population (Hofbauer et al., 2022). The rapidly expanding DM patients requiring bone reconstruction procedures motivated the present study to investigate the potential of bone tissue engineering approach to improve bone regeneration under diabetic condition. We implanted BMSC/DBM constructs or cell-free DBM scaffolds in both ectopic and orthotopic bone formation rat models. Our data suggested that BMSC/DBM constructs could form ectopic and orthotopic bone under diabetic condition, but with impaired bone regeneration activity.

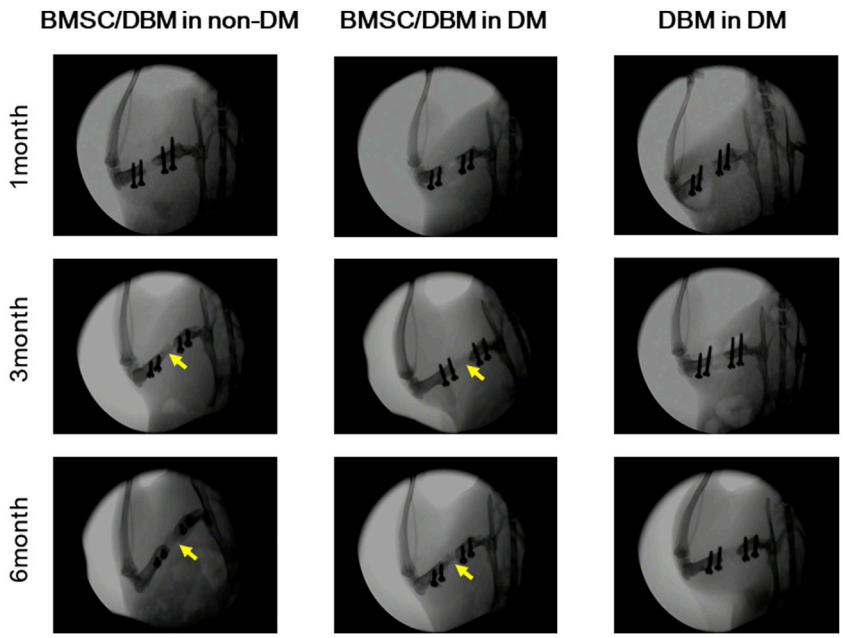

FIGURE 3
Plain X-ray images of the femoral defects at 1, 3 and 6 months after transplantation with BMSC/DBM constructs or DBM scaffolds in diabetic and non-diabetic rats.

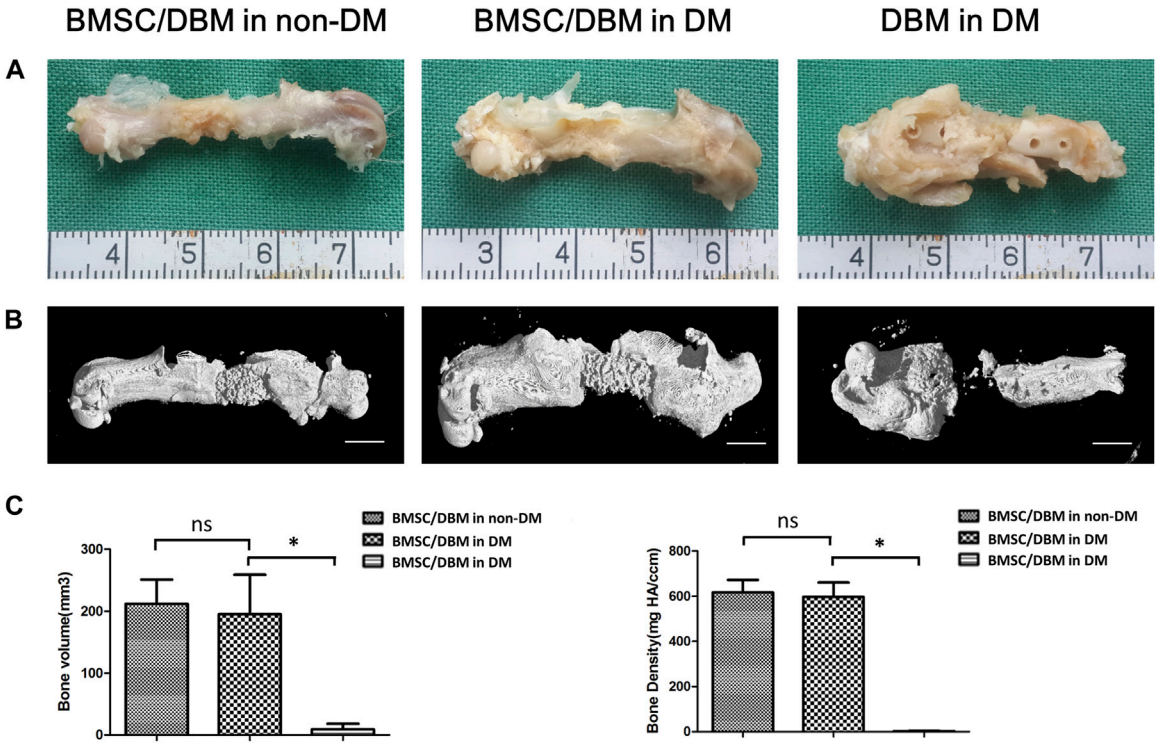

FIGURE 4
BMSC/DBM constructs repair femoral bone defects under diabetic condition. **(A)**. Macroscopic view of the specimens at the 6th month post-surgery. **(B)**. 3D reconstruction of micro-CT images of the specimens at the 6th month post-surgery. Scale bars: 5 mm. **(C)**. Statistical analyses of bone volume (BV) and bone density, $*p < 0.05$.

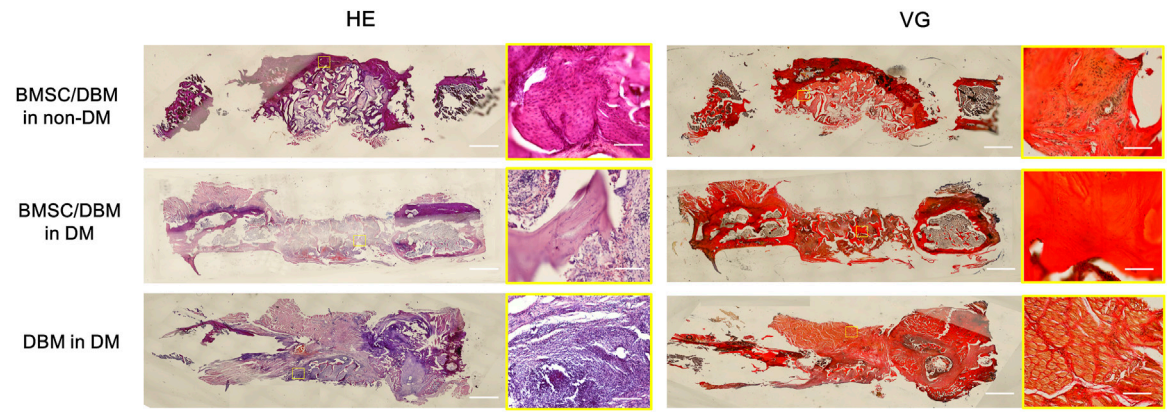

FIGURE 5
Histological analysis: representative images of HE and VG staining of the specimens. Scale bar: low magnifictaion: 2.5 mm; high magnification: 50 μm.

It is well known that BMSCs derived from diabetic patients showed decreased alkaline phosphatase (ALP) activity, mineralization and osteogenic gene expression (Silva et al., 2015). It is also proposed that the balance of BMSC differentiation is switched to favor adipogenic differentiation under diabetic condition (Fijany et al., 2019). Besides, a number of studies suggested that the outcomes of autologous MSC therapy for diabetes-associated complications were variable and not as effective as initially hoped, due to the intrinsic MSC dysfunction (De Vyver, 2017). Therefore, autologous BMSCs may not be the ideal candidate to induce and improve bone regeneration under diabetic condition. Allogenic BMSCs have been shown to be nonimmunogenic in *vivo* transplantation paradigms (Squillaro et al., 2016), and have been used to repair critical-sized bone defects in various animal models (Lin et al., 2019), suggesting their utility for bone tissue engineering applications. In our study, no signs of serious adverse immune reactions were observed. Compared with perinatal and adult sources of MSCs, fetal BMSCs exhibited greater cell proliferative capability, osteogenic potential and lower immunogenicity as reported by previous studies (Zhang et al., 2009; Guillot et al., 2008), thus we chose allogenic fetal BMSCs as our seed cells in the present study.

Our data indicated that BMSC/DBM constructs could form ectopic bone under diabetic condition, but with decreased bone regeneration activity. Previous studies suggested that the osteogenic cells that formed new bone in subcutaneous ectopic bone formation models were mainly of donor origin rather than originated from the local microenvironment (Abdallah et al., 2008; Mankani et al., 2008). Deng et al. demonstrated that BMSCs derived from healthy donors treated with diabetic serum showed a remarkable decrease in osteogenic activity, suggesting that pathologic conditions like diabetes could alter the function of BMSCs derived from healthy donors (Deng et al., 2018). There have been a large number of studies trying to clarify the precise mechanism underlying the detrimental effect of diabetes on BMSCs. It is proved that many factors from the diabetic microenvironment could contribute to the dysfunction of BMSCs, including hyperglycemia, chronic inflammation and increased advanced glycation end-products (AGE) formation (Kume et al., 2005; Li et al., 2007; Yang et al., 2010; Wang et al., 2013; Ko et al., 2015; Qu et al., 2018; Xu and Zuo, 2021). We suggested that the allogenic BMSCs introduced through bone tissue engineering approach were affected by various factors from the diabetic host environment, resulting in the impaired bone regeneration activity. It is worthwhile to track and examine the function of the implanted BMSCs in the future.

Apart from testing the pro-bone regeneration potential of tissue-engineered bone constructs in subcutaneous ectopic bone formation models, we also investigated their potential to repair large segmental bone defects in rat femurs. To our surprise, at 6 months after surgery, BMSC/DBM constructs under diabetic condition showed comparable bone volume and density compared with the non-diabetic controls. However, X-ray analysis at the 1st and 3rd month post-surgery indicated that the healing process was delayed in the diabetic group. The implantation of BMSC-seeded DBM scaffolds enhanced bone formation in orthotopic defects compared with the implantation of unseeded DBM scaffolds, suggesting that the transplanted allogenic BMSCs were able to induce and promote osseous regeneration in orthotopic defect models. However, the delayed healing process compared with non-diabetic controls indicated that the implanted BMSCs were affected by the diabetic host environment, resulting in impaired osteogenic activity. Unlike ectopic bone formation models, previous studies have shown that new bone formation in orthotopic defect models is induced by both host and donor cells, and implantation of donor MSCs can cause recruitment of the host cells (Zhou et al., 2015; Westhauser et al., 2017; Kim et al., 2020). We assume that the implanted BMSCs were able to recruit endogenous stem/progenitor cells to the defect site, and these recruited local stem/progenitor cells together with the transplanted allogenic seed cells were able to induce bone regeneration, eventually leading to bone bridging at the defect site. Future studies could define the origin of the cells that form new bone by labeling the seed cells with fluorescent

marker and investigate the interaction between the host and donor cells. The difference in the outcomes of ectopic bone formation model and orthotopic defect model in our study may be attributed to different local environment (ectopic and orthotopic) as well as different osteogenic process (calcification and new bone formation).

Strategies to promote bone regeneration include providing stem/progenitor cells, growth factors, nutrients, and synthetic materials to the defect site to induce tissue regeneration (Shui-Ling et al., 2018). The concept of bone tissue engineering involves the combination of stem/progenitor cells, tridimensional biomaterial scaffolds and growth factors. Although bone tissue engineering approach seems to hold great potential in improving bone regeneration under diabetic condition, the implanted exogenous seed cells would inevitably be affected by the host diabetic microenvironment. Previous studies on bone regeneration strategy under diabetic condition mainly focused on osteoblasts or osteoclasts by delivering pro-osteogenic factors (such as BMP2, VEGFA, FGF-9, IGF-1, Vitamin D, etc.) (Wang et al., 2010; Wu et al., 2013; De Santana and Trackman, 2015; Wallner et al., 2015) or anti-bone resorption factors like parathyroid hormone-related protein (Ardura et al., 2016). A recent study by Hu et al. highlighted the importance of modulating the diabetic microenvironment. They incorporated interleukin 4 into the nanofibrous heparin-modified gelatin microsphere to polarize proinflammatory M1 macrophages into an anti-inflammatory M2 phenotype that facilitate osteogenic differentiation and bone formation (Hu et al., 2018). Their research demonstrated that modulating the diabetic microenvironment played a crucial role in improving bone regeneration under diabetic condition. Future studies could devote to combining these pro-bone regeneration strategies like modulating the diabetic microenvironment with bone tissue engineering approach to accelerate bone regeneration under diabetic condition.

Conclusion

In the present study, we demonstrated tissue-engineered bone constructs could form both ectopic and orthotopic bone in diabetic rats with impaired bone regeneration activity. Our research suggest that bone tissue engineering approach provides a promising way to accelerate bone regeneration under diabetic condition. In future studies, tissue-engineered cell/scaffold constructs could be combined with pro-osteogenic and immunomodulating factors to accelerate bone regeneration under diabetic condition.

Data availability statement

The raw data supporting the conclusion of this article will be made available by the authors, without undue reservation.

Ethics statement

The animal study was approved by University Committee on Use and Care of Animals of Huazhong University of Science and Technology. The study was conducted in accordance with the local legislation and institutional requirements.

Author contributions

XW: Investigation, Methodology, Writing–original draft. CX: Investigation, Methodology, Writing–original draft. CH: Writing–review and editing. HC: Investigation, Methodology, Writing–original draft, Writing–review and editing. ZZ: Formal Analysis, Writing–original draft, Writing–review and editing. JZ: Formal Analysis, Writing–original draft, Writing–review and editing. HX: Funding acquisition, Project administration, Supervision, Writing–review and editing.

Funding

The author(s) declare that financial support was received for the research, authorship, and/or publication of this article. This work was supported by the National Natural Science Foundation of China (Grant No. 82002060) and the Foundation of Union Jingshan Hospital (2023-XHJS-004, 2023-XHJS-015).

Acknowledgments

The authors wish to thank Wenjie Zhang, Wei Liu, Guangdong Zhou, Zhiyong Zhang and Xiansong Wang (from the Department of Plastic and Reconstructive Surgery, Shanghai 9th People's Hospital) for their kind help during the preparation of this study.

Conflict of interest

The authors declare that the research was conducted in the absence of any commercial or financial relationships that could be construed as a potential conflict of interest.

Publisher's note

References

Abdallah, B., Ditzel, N., and Kassem, K. (2008). Assessment of bone formation capacity using *in vivo* transplantation assays: procedure and tissue analysis. *Methods Mol. Biol.* 455, 89–100. doi:10.1007/978-1-59745-104-8_6

Antar, A., Ashour, N., Sharaky, M., Khattab, M., Ashour, N., Zaid, R., et al. (2023). Diabetes mellitus: classification, mediators, and complications; A gate to identify potential targets for the development of new effective treatments. *Biomed. Pharmacother.* 168, 115734. doi:10.1016/j.biopha.2023.115734

Ardura, J., Portal-Nunez, S., Lozano, D., Gutiérrez-Rojas, I., Sánchez-Salcedo, S., López-Herradón, A., et al. (2016). Local delivery of parathyroid hormone-related protein-derived peptides coated onto a hydroxyapatite-based implant enhances bone regeneration in old and diabetic rats. *J. Biomed. Mater Res. A* 104 (8), 2060–2070. doi:10.1002/jbm.a.35742

Arthur, G., and Gronthos, S. (2020). Clinical application of bone marrow mesenchymal stem/stromal cells to repair skeletal tissue. *Int. J. Mol. Sci.* 21 (24), 9759. doi:10.3390/ijms21249759

Berner, A., Reichert, J. C., Woodruff, M. A., Saifzadeh, S., Morris, A., Epari, D., et al. (2013). Autologous vs. allogenic mesenchymal progenitor cells for the reconstruction of critical sized segmental tibial bone defects in aged sheep, *Acta Biomater.* 9 (8), 7874–7884. doi:10.1016/j.actbio.2013.04.035

Confalonieri, D., Schwab, A., Walles, H., and Ehlicke, F. (2018). Advanced therapy medicinal products: a guide for bone marrow-derived MSC application in bone and cartilage tissue engineering. *Tissue Eng. Part B Rev.* 24 (2), 155–169. doi:10.1089/ten.teb.2017.0305

Csonka, V., and Lendvay, M. (2023). Diabetes mellitus-related musculoskeletal disorders: unveiling the cluster of diseases. *Prim. Care Diabetes* 17 (6), 548–553. doi:10.1016/j.pcd.2023.08.003

Deng, X., Xu, M., Shen, M., and Cheng, J. (2018). Effects of type 2 diabetic serum on proliferation and osteogenic differentiation of mesenchymal stem cells. *J. Diabetes Res.* 2018, 1–9. doi:10.1155/2018/5765478

De Santana, R., and Trackman, P. (2015). Effect of targeted delivery of bone morphogenetic protein-2 on bone formation in type 1 diabetes. *Int. J. Oral Maxillofac. Implants* 30 (3), 707–714. doi:10.11607/jomi.3957

De Vyver, V. (2017). Intrinsic mesenchymal stem cell dysfunction in diabetes mellitus: implications for autologous cell therapy. *Stem Cells Dev.* 26 (14), 1042–1053. doi:10.1089/scd.2017.0025

Fijany, A., Sayadi, L., Khoshab, N., Banyard, D. A., Shaterian, A., Alexander, M., et al. (2019). Mesenchymal stem cell dysfunction in diabetes. *Mol. Biol. Rep.* 46 (1), 1459–1475. doi:10.1007/s11033-018-4516-x

Furman, (2021). Streptozotocin-induced diabetic models in mice and rats. *Curr. Protoc.* 1 (4), e78. doi:10.1002/cpz1.78

Grelewski, P. G., Kwasnicka, M., and Bar, J. K. (2023). Properties of scaffolds as carriers of mesenchymal stem cells for use in bone engineering. *Polim. Med.* 53 (2), 129–139. doi:10.17219/pim/166471

Guillot, P. V., De Bari, C., Dell'accio, F., Kurata, H., Polak, J., and Fisk, N. M. (2008). Comparative osteogenic transcription profiling of various fetal and adult mesenchymal stem cell sources. *Differentiation* 76 (9), 946–957. doi:10.1111/j.1432-0436.2008.00279.x

Hofbauer, L. C., Busse, B., Eastell, R., Ferrari, S., Frost, M., Müller, R., et al. (2022). Bone fragility in diabetes: novel concepts and clinical implications. *Lancet Diabetes Endocrinol.* 10 (3), 207–220. doi:10.1016/s2213-8587(21)00347-8

Hu, Z., Ma, C., Rong, X., Zou, S., and Liu, X. (2018). Immunomodulatory ECM-like microspheres for accelerated bone regeneration in diabetes mellitus. *ACS Appl. Mater Interfaces* 10 (3), 2377–2390. doi:10.1021/acsami.7b18458

Hygum, K., Starup-Linde, J., and Langdahl, B. (2019). Diabetes and bone. *Osteoporos. Sarcopenia* 5 (2), 29–37. doi:10.1016/j.afos.2019.05.001

Janko, M., Dietz, K., Rachor, J., Sahm, J., Schroder, K., Schaible, A., et al. (2019). Improvement of bone healing by neutralization of microRNA-335-5p, but not by neutralization of microRNA-92a in bone marrow mononuclear cells transplanted into a large femur defect of the rat. *Tissue Eng. Part A* 25 (1-2), 55–68. doi:10.1089/ten.tea.2017.0479

Kim, S., Park, J., Kwon, J., Cho, J. G., Park, K. G., Park, C. H., et al. (2020). NIR fluorescence for monitoring *in vivo* scaffold degradation along with stem cell tracking in bone tissue engineering. *Biomaterials* 258, 120267. doi:10.1016/j.biomaterials.2020.120267

Ko, K., Coimbra, L., Tian, C., Alblowi, J., Kayal, R. A., Einhorn, T. A., et al. (2015). Diabetes reduces mesenchymal stem cells in fracture healing through a TNFα-mediated mechanism. *Diabetologia* 58 (3), 633–642. doi:10.1007/s00125-014-3470-y

Kume, S., Kato, S., Yamagishi, S., Inagaki, Y., Ueda, S., Arima, N., et al. (2005). Advanced glycation end-products attenuate human mesenchymal stem cells and prevent cognate differentiation into adipose tissue, cartilage, and bone. *J. Bone Min. Res.* 20 (9), 1647–1658. doi:10.1359/jbmr.050514

Li, J. J., Ebied, M., Xu, J., and Zreiqat, H. (2018). Current approaches to bone tissue engineering: the interface between biology and engineering. *Adv. Healthc. Mater* 7 (6), e1701061. doi:10.1002/adhm.201701061

Lin, H., Sohn, J., Shen, H., Langhans, M. T., and Tuan, R. S. (2019). Bone marrow mesenchymal stem cells: aging and tissue engineering applications to enhance bone healing. *Biomaterials* 203, 96–110. doi:10.1016/j.biomaterials.2018.06.026

Li, Y., Schilling, T., Benisch, P., Zeck, S., Meissner-Weigl, J., Schneider, D., et al. (2007). Effects of high glucose on mesenchymal stem cell proliferation and differentiation. *Biochem. biophysical Res. Commun.* 363 (1), 209–215. doi:10.1016/j.bbrc.2007.08.161

Liu, Z., Jiang, J., Wang, K., Zhou, Y., Li, T., Gao, J., et al. (2023). Preparation of fish decalcified bone matrix and its bone repair effect in rats. *Front. Bioeng. Biotechnol.* 11, 1134992. doi:10.3389/fbioe.2023.1134992

Mankani, M. H., Kuznetsov, S. A., Marshall, G. W., and Robey, P. G. (2008). Creation of new bone by the percutaneous injection of human bone marrow stromal cell and HA/TCP suspensions. *Tissue Eng. Part A* 14 (12), 1949–1958. doi:10.1089/ten.tea.2007.0348

Mazzoni, E., Iaquinta, M. R., Mosaico, M., De Pace, R., D'Agostino, A., Tognon, M., et al. (2023). Human mesenchymal stem cells and innovative scaffolds for bone tissue engineering applications. *Tissue Eng. Part B Rev.* 29 (5), 514–531. doi:10.1089/ten.teb.2022.0217

Perez, J., Kouroupis, D., Li, D., Best, T. M., Kaplan, L., and Correa, D. (2018). Tissue engineering and cell-based therapies for fractures and bone defects. *Front. Bioeng. Biotechnol.* 6, 105. doi:10.3389/fbioe.2018.00105

Qu, B., Gong, K., Yang, H., Li, Y. G., Jiang, T., Zeng, Z. M., et al. (2018). MiR-449 overexpression inhibits osteogenic differentiation of bone marrow mesenchymal stem cells via suppressing Sirt1/Fra-1 pathway in high glucose and free fatty acids microenvironment. *Biochem. biophysical Res. Commun.* 496 (1), 120–126. doi:10.1016/j.bbrc.2018.01.009

Shui-Ling, H., Bolander, R., Rustom, L. E., Johnson, A. W., Luyten, F. P., and Picart, C. (2018). Bone regeneration strategies: engineered scaffolds, bioactive molecules and stem cells current stage and future perspectives. *Biomaterials* 180, 143–162. doi:10.1016/j.biomaterials.2018.07.017

Silva, J., Sampaio, P., Fernandes, M., and Gomes, P. S. (2015). The osteogenic priming of mesenchymal stem cells is impaired in experimental diabetes. *J. Cell. Biochem.* 116 (8), 1658–1667. doi:10.1002/jcb.25126

Squillaro, T., Peluso, G., and Galderisi, U. (2016). Clinical trials with mesenchymal stem cells: an update. *Cell Transpl.* 25 (5), 829–848. doi:10.3727/096368915x689622

Wallner, C., Schira, J., Wagner, J. M., Schulte, M., Fischer, S., Hirsch, T., et al. (2015). Application of VEGFA and FGF-9 enhances angiogenesis, osteogenesis and bone remodeling in type 2 diabetic long bone regeneration. *PLoS One* 10 (3), e0118823. doi:10.1371/journal.pone.0118823

Wang, F., Song, Y., Li, C., Li, D., Zhang, H., Ma, A., et al. (2010). Sustained release of insulin-like growth factor-1 from poly(lactide-co-glycolide) microspheres improves osseointegration of dental implants in type 2 diabetic rats. *Eur. J. Pharmacol.* 640 (1-3), 226–232. doi:10.1016/j.ejphar.2010.04.024

Wang, Z., Chen, C., Zhou, Q., Wang, X. S., Zhou, G., Liu, W., et al. (2015). The treatment efficacy of bone tissue engineering strategy for repairing segmental bone defects under osteoporotic conditions. *Tissue Eng. Part A* 21 (17-18), 2346–2355. doi:10.1089/ten.tea.2015.0071

Wang, L., Zhao, Y., Liu, Y., Akiyama, K., Chen, C., Qu, C., et al. (2013). IFN-Γ and TNF-α synergistically induce mesenchymal stem cell impairment and tumorigenesis via NFκB signaling. *Stem Cells* 31 (7), 1383–1395. doi:10.1002/stem.1388

Westhauser, F., Senger, A., Reible, B., and Moghaddam, A. (2017). *In Vivo*Models for the evaluation of the osteogenic potency of bone substitutes seeded with mesenchymal stem cells of human origin: a concise review. *Tissue Eng. Part C Methods* 23 (12), 881–888. doi:10.1089/ten.tec.2017.0164

Wojcicka, G., Jamroz-Wisniewska, A., Marciniak, A., Łowicka, E., and Bełtowski, J. (2010). The differentiating effect of glimepiride and glibenclamide on paraoxonase 1 and platelet-activating factor acetylohydrolase activity. *Life Sci.* 87 (3-4), 126–132. doi:10.1016/j.lfs.2010.05.018

Wu, Y., Yu, T., Yang, X., Li, F., Ma, L., Yang, Y., et al. (2013). Vitamin D3 and insulin combined treatment promotes titanium implant osseointegration in diabetes mellitus rats. *Bone* 52 (1), 1–8. doi:10.1016/j.bone.2012.09.005

Xu, Z., and Zuo, C. (2021). The fate status of stem cells in diabetes and its role in the occurrence of diabetic complications. *Front. Mol. Biosci.* 8, 745035. doi:10.3389/fmolb.2021.745035

Yang, K., Wang, X., He, Y., Lu, L., Chen, Q. J., Liu, J., et al. (2010). Advanced glycation end products induce chemokine/cytokine production via activation of p38 pathway and inhibit proliferation and migration of bone marrow mesenchymal stem cells. *Cardiovasc Diabetol.* 9, 66. doi:10.1186/1475-2840-9-66

Zhang, Z., Teoh, S., Chong, M., Schantz, J. T., Fisk, N. M., Choolani, M. A., et al. (2009). Superior osteogenic capacity for bone tissue engineering of fetal compared with perinatal and adult mesenchymal stem cells. *Stem Cells* 27 (1), 126–137. doi:10.1634/stemcells.2008-0456

Zhang, Z., Teoh, S., Hui, J., Fisk, N. M., Choolani, M., and Chan, J. K. (2012). The potential of human fetal mesenchymal stem cells for off-the-shelf bone tissue engineering application. *Biomaterials* 33 (9), 2656–2672. doi:10.1016/j.biomaterials.2011.12.025

Zhou, Y., Fan, W., Prasadam, I., Crawford, R., and Xiao, Y. (2015). Implantation of osteogenic differentiated donor mesenchymal stem cells causes recruitment of host cells. *J. Tissue Eng. Regen. Med.* 9 (2), 118–126. doi:10.1002/term.1619

frontiers | Frontiers in Bioengineering and Biotechnology

TYPE Original Research
PUBLISHED 15 May 2024
DOI 10.3389/fbioe.2024.1401032

OPEN ACCESS

EDITED BY
Jian Yu,
University of British Columbia, Canada

REVIEWED BY
Luis Gonzalo Sequeda-Castañeda,
Pontifical Javeriana University, Colombia
Hongbo Zhou,
Xiangya School of Stomatology, Central South University, China

*CORRESPONDENCE
Xinglu Jiang,
jiangxl130@163.com
Wenxia Chen,
angelaxiacw@163.com

†These authors have contributed equally to this work

RECEIVED 14 March 2024
ACCEPTED 16 April 2024
PUBLISHED 15 May 2024

CITATION
Chen Z, Wei Y, Liang L, Wang X, Peng F, Liang Y, Huang X, Yan K, Gao Y, Li K, Huang X, Jiang X and Chen W (2024), Theaflavin –3,3′-digallate/ethanol: a novel cross-linker for stabilizing dentin collagen.
Front. Bioeng. Biotechnol. 12:1401032.
doi: 10.3389/fbioe.2024.1401032

Theaflavin –3,3′-digallate/ethanol: a novel cross-linker for stabilizing dentin collagen

Zhiyong Chen[1,2†], Yingxian Wei[1†], Likun Liang[1], Xu Wang[1], Fangfei Peng[1], Yiying Liang[1], Xin Huang[1], Kaiqi Yan[1], Yunxia Gao[1], Kangjing Li[1,3], Xiaoman Huang[1], Xinglu Jiang[1,4]* and Wenxia Chen[1,3]*

[1]Guangxi Key Laboratory of Oral and Maxillofacial Rehabilitation and Reconstruction, Guangxi Clinical Research Center for Craniofacial Deformity, College & Hospital of Stomatology, Guangxi Medical University, Nanning, China, [2]Department of Prosthodontics, College & Hospital of Stomatology, Guangxi Medical University, Nanning, China, [3]Department of Endodontics, College & Hospital of Stomatology, Guangxi Medical University, Nanning, China, [4]Clinical Laboratory Medicine Department, College & Hospital of Stomatology, Guangxi Medical University, Nanning, China

Objectives: To study the ability of theaflavin-3,3′-digallate (TF3)/ethanol solution to crosslink demineralized dentin collagen, resist collagenase digestion, and explore the potential mechanism.

Methods: Fully demineralized dentin blocks were prepared using human third molars that were caries-free. Then, these blocks were randomly allocated into 14 separate groups (n = 6), namely, control, ethanol, 5% glutaraldehyde (GA), 12.5, 25, 50, and 100 mg/ml TF3/ethanol solution groups. Each group was further divided into two subgroups based on crosslinking time: 30 and 60 s. The efficacy and mechanism of TF3's interaction with dentin type I collagen were predicted through molecular docking. The cross-linking, anti-enzymatic degradation, and biomechanical properties were studied by weight loss, hydroxyproline release, scanning/transmission electron microscopy (SEM/TEM), *in situ* zymography, surface hardness, thermogravimetric analysis, and swelling ratio. Fourier transform infrared spectroscopy (FTIR), X-ray photoelectron spectroscopy (XPS), and Raman spectroscopy were utilized to explore its mechanisms. Statistical analysis was performed using one and two-way analysis of variance and Tukey's test.

Results: TF3/ethanol solution could effectively crosslink demineralized dentin collagen and improve its resistance to collagenase digestion and biomechanical properties ($p < 0.05$), showing concentration and time dependence. The effect of 25 and 50 mg/ml TF3/ethanol solution was similar to that of 5% GA, whereas the 100 mg/mL TF3/ethanol solution exhibited better performance ($p < 0.05$). TF3 and dentin type I collagen are mainly cross-linked by hydrogen bonds, and there may be covalent and hydrophobic interactions.

Conclusion: TF3 has the capability to efficiently cross-link demineralized dentin collagen, enhancing its resistance to collagenase enzymatic hydrolysis and biomechanical properties within clinically acceptable timeframes (30 s/60 s). Additionally, it exhibits promise in enhancing the longevity of dentin adhesion.

KEYWORDS

theaflavin-3,3′-digallate, dentin collagen, cross-linking, collagenase digestion, mechanism

1 Introduction

The basis of dentin bonding lies in the hybrid layer, which is formed when the adhesive penetrates and intertwines with the intricate network of demineralized dentin collagen fibers (Anastasiadis et al., 2021). However, achieving optimal infiltration poses a challenge, often leaving collagen fibers exposed within the hybrid layer and compromising the structural integrity and stability of the dentin bonding interface (Coutinho et al., 2011). Over the long term, these exposed collagen fibers are susceptible to degradation by bacterial enzymes and endogenous dentin collagenases (matrix metalloproteinases, MMPs, and cysteine cathepsins, CCs). This enzymatic hydrolysis undermines the hybrid layer's stability, ultimately leading to a significant reduction in adhesive durability (Fan-Chiang et al., 2023).

For an extended period, scientific research has primarily focused on enhancing the quality of the hybrid layer and bolstering the longevity of the adhesive (Van Meerbeek et al., 2020). For example, through biomimetic remineralization, the exposed collagen fibers are remineralized (Niu et al., 2017; Ma et al., 2021). By applying inhibitors of MMPs and CCs, the enzymatic digestion process of collagen fibers is inhibited (Comba et al., 2019). The physical and chemical characteristics of collagen are optimized through cross-linking, which hides the binding sites of enzymes, thus increasing its resistance to enzymatic hydrolysis (Wang et al., 2022) and so on. Despite these enhancements, issues like biosafety, cumbersome operation, limited durability and ambiguous long-term efficacy persist, leading to no agreed-upon view regarding dentin bonding.

Lately, as it becomes more clearly that maintaining the natural cross-linking condition of dentin collagen is important, attention shifts to stabilizing demineralized dentin collagen through cross-linking, giving rise to the 'dentin biomodification' concept (Cai et al., 2018). Currently, the dentin biomodification is often carried out by chemical synthesis and natural crosslinking agents. Among them, glutaraldehyde (GA) is recognized as a highly efficient chemical crosslinking agent, which is the ' gold standard ' of crosslinking agents and is commonly used for tissue fixation. However, GA has strong cytotoxicity and its clinical application is limited (Cilli and Prakki, 2009; Cai et al., 2018). Therefore, natural polyphenolic cross-linking agents derived from plants have attracted more and more attention due to their strong and low toxicity, such as proanthocyanidins (PA), epigallocatechin gallate (EGCG), etc (Zhao et al., 2022). Studies have shown that naturally occurring polyphenolic compounds can interact with collagen fibers through phenolic hydroxyl and galloyl groups to form covalent, ionic, and hydrogen bonds. They can also alter the spatial conformation of collagen, form cross-links with endogenous MMPs or CCs, obstruct enzyme recognition sites, enhance the mechanical properties of collagen, lessen its sensitivity to enzymes, and locally create a hydrophobic microenvironment that lowers water absorption and swelling ratio (Liu et al., 2015; Reis et al., 2021; Chiang et al., 2023). As mentioned above, recent studies have highlighted the potential of natural polyphenols in dentin biomodification, with PA being particularly noted for its efficacy in this domain (Wang B. et al., 2023). Despite PA's potential in enhancing dentin properties, it is not the ideal collagen cross-linking agent due to limitations: complex molecular structure (Anumula et al., 2022), high molecular weight and low penetration efficiency (Hass et al., 2021), and affecting the curing of the adhesive by scavenging free radicals (Gabetta et al., 2000; Green et al., 2010), plus its dark color causes staining (Gabetta et al., 2000).

Given this, scholars are still committed to finding better natural collagen crosslinking agents. In recent years, the research on theaflavins (TFs) has been increasing due to their ability to crosslink with collagen and produce excellent biological effects, and other biological activities like anti-cancer, anti-bacterial and anti-inflammatory (Vidal et al., 2016; Hass et al., 2021; Guo et al., 2023). TFs is mainly composed of four dimers, namely, theaflavin (TF1), theaflavin-3-gallate (TF2A), theaflavin-3'-gallate (TF2B), and theaflavin-3,3'-digallate (TF3). These four dimers differ from each other based on the number and positioning of the connected gallic acyl groups. However, most of current studies are aimed at TFs, and the role of the four dimers in it is still unknown.

Preliminary studies suggest that among the four dimers of the TFs, TF3 has the largest number of phenolic hydroxyl groups and gallic acyl groups and the most crosslinking potential (Takemoto and Takemoto, 2018). Regrettably, no research has been conducted to assess how TF3 interacts with demineralized dentin collagen and to understand its underlying mechanism. Therefore, our research studied the cross-linking ability of TF3, for the very first time, used in demineralized dentin collagen. Furthermore, we explored the characteristics of TF3, including resistance to internal and external collagenase digestion, biomechanical properties, and its potential mechanism of action, to provide an efficient and clinically feasible new method for improving the longevity of the adhesive. The null hypotheses tested were that TF3 cannot 1) cross-link demineralized dentin collagen by chemical action, 2) enhance the enzymatic hydrolysis resistance of demineralized dentin collagen to internal and external collagenases, or 3) improve the biomechanical characteristics of demineralized dentin collagen.

2 Materials and methods

2.1 Chemicals and reagents

TF3 was purchased from Chengdu Biopurify Phytochemicals Ltd. (Chengdu, China). Ethanol, 25% GA, and phosphate buffer saline were bought from Aladdin (Shanghai, China). 85% phosphoric acid was bought from Shanghai Acmec Biochemical Co., Ltd. (Shanghai, China). Acetic acid was bought from CHRON (Chengdu, China). Ammonium bicarbonate was bought from Macklin (Shanghai, China). 35% Phosphoric-acid gel, Adaper TM Single bond 2 Adhesive, and Resin composite Filtek TM Z250 were bought from 3 M (St. Paul, United States). Figure 1 illustrates the workflow of the experimental process.

2.2 Preparation of solutions

At room temperature and dark conditions, dissolve TF3 in ethanol to prepare TF3 solutions with concentrations of 12.5 mg/mL, 25 mg/mL, 50 mg/mL, and 100 mg/mL. Meanwhile, dilute 25% GA to 5% GA using ethanol. After preparation, dispense 0.5 mL solution into 1.5 mL light-proof Eppendorf tubes for future use. Also, under room temperature and dark conditions, prepare a

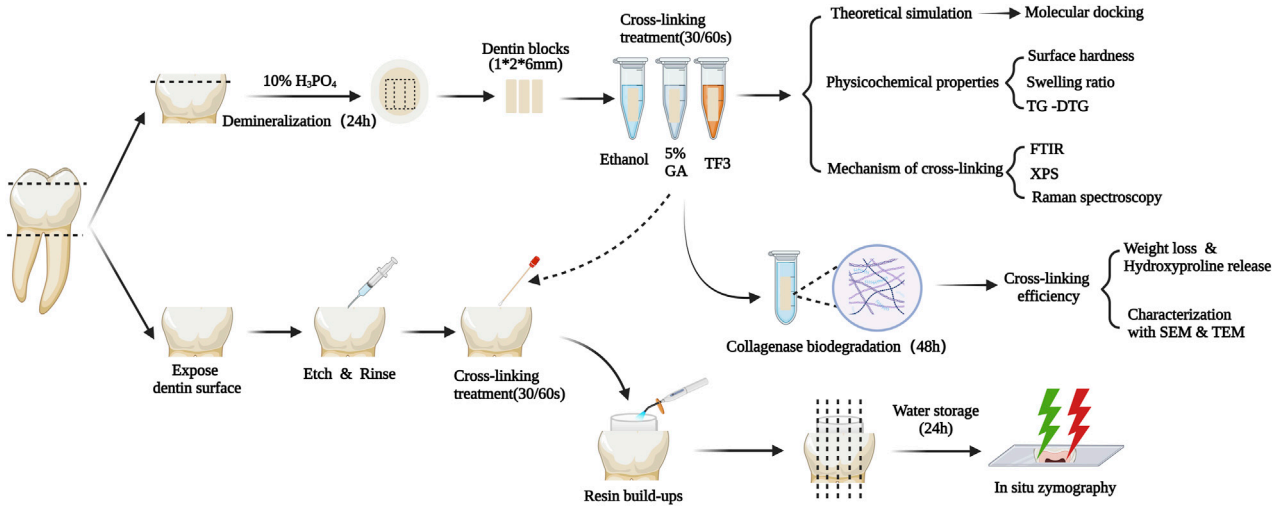

FIGURE 1
Schematic diagram of the experimental design. TG-DTG: Thermogravimetric Analysis and Differential Thermal Gravity. FTIR: Fourier transformed infrared spectroscopy. XPS: X-ray photoelectron spectroscopy. SEM&TEM: Scanning/Transmission electron microscopy.

0.1 mg/mL type I collagenase solution using ammonium bicarbonate buffer. Adjust the pH to 7.1–7.2 by adding glacial acetic acid drop by drop, then weigh and add type I collagenase to the solution, and measure the pH again. All solutions should be prepared and used immediately.

2.3 Theoretical simulation

2.3.1 Molecular docking.

Collagen's X-ray crystallographic formations (PDB: 1QSU, 4OY5, 1CGD) were obtained from the Protein Data Bank. Each compound's protonation state was set to a pH of 7.4, followed by their expansion to three-dimensional structures via Open Babel. The receptor protein and ligands were processed and parameterized using AutoDock Tools (ADT3). Documentation for the docking grid was produced by the Auto Grid of sitemap, and Auto Dock Vina (1.2.0) was utilized for the docking simulation. The most suitable pose was chosen for interaction analysis. Ultimately, PyMOL was responsible for creating the protein-ligand interaction as depicted in Figure 2.

2.4 Cross-linking efficiency

2.4.1 Preparation of experimental materials

Following the acquisition of informed consent from the donors, ninety non-carious human third molars were gathered, adhering to the protocols approved the Ethics Committee for Human Studies of the College and Hospital of Stomatology, Guangxi Medical University. Before usage, the teeth were preserved in the 0.1% thymol solution at a temperature of 4°C for 1 month.

The crown's occlusal segment and the adjacent enamel walls were surgically excised with the aid of a precision low-speed diamond saw equipped with a water-cooling mechanism (EXAKT E300CP, Germany) to obtain dentin blocks. Afterward, 85% phosphoric acid mixed with deionised water to form 10% phosphoric acid, and dentin blocks were placed in a 10% phosphoric acid solution and shaken in a 25°C constant temperature shaking table for 24 h to ensure them were demineralized completely. Subsequently, the demineralized dentin blocks underwent a rigorous washing process, being thoroughly cleansed with distilled water three times, followed by a 1-h hydration period. Finally, these demineralized dentin blocks were cut into 1 × 2 × 6 mm.

2.4.2 Weight loss (WL) and hydroxyproline release (HYP)

The demineralized dentin blocks were randomly allocated into 14 distinct groups, with 6 blocks in each group. At room temperature, the demineralized dentin blocks were cross-linked with 0.5 mL of 12.5 mg/mL, 25 mg/mL, 50 mg/mL, and 100 mg/mL of TF3, 5% GA, and ethanol solutions, respectively, for 30 s or 60 s. Following the cross-linking, the blocks underwent a rigorous cleaning process involving three washes with distilled water. Subsequently, they were subjected to drying in a freeze-vacuum dryer for 12 h to achieve complete dehydration. Three measurements were taken of the demineralized dentin block's mass by electronic balance, with the mean measurement being documented as M0. Subsequently, the dentin blocks underwent hydration using distilled water for 1 hour, followed by immersion in 1 mL of 0.1 mg/mL type I collagenase solution (Sigma-Aldrich, St. Louis, MO, USA) and digestion in a 37°C thermostatic shaker for 48 h. After the end of enzymatic hydrolysis, cleaning, drying, and weighing again, it was recorded as M1. The weight loss rate (d = 0.01 mg) was calculated as per this equation:

$$WL\,\% = \left[(M0 - M1)/M0 \right] \times 100\%.$$

The 0.5 mL enzymatic hydrolysate of collagen from each group was utilized for the determination of HYP release, with reference to the detailed methodology provided in the hydroxyproline kit instructions (Nanjing Jiancheng

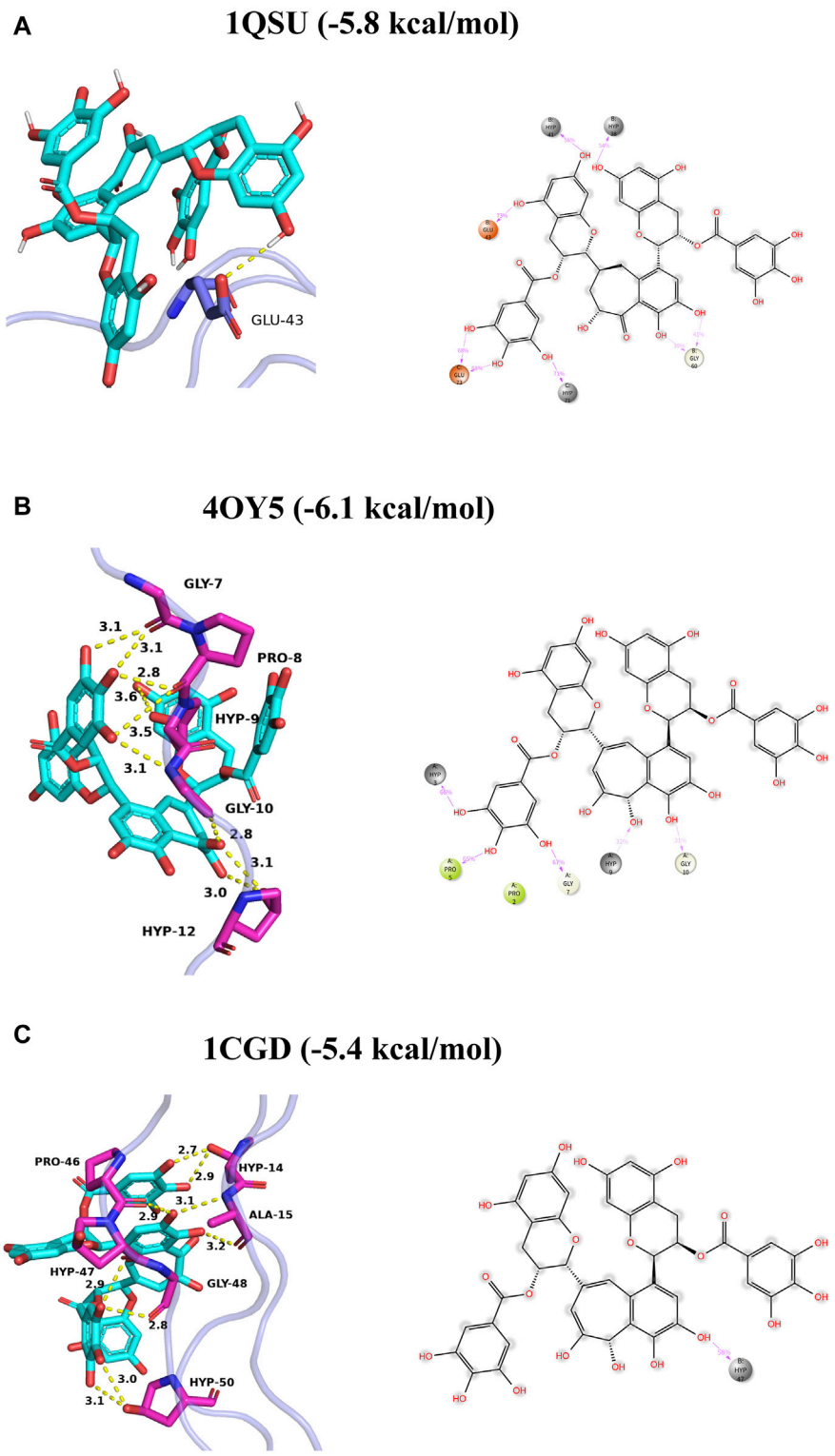

FIGURE 2
Binding mode of TF3 to collagen I **(A–C)**. The left panel shows three-dimensional plots, where hydrogen bonds are depicted by yellow dashed lines and hydrophobic interactions are shown by green dashed lines. The right panel shows two-dimensional plots, where the magenta solid line represents the ion action.

Bioengineering Institute, Nanjing, China). Subsequently, the release of HYP was calculated by measuring the absorbance at 550 nm using a microplate reader.

2.4.3 Scanning electron microscope (SEM)

After cross-linked in 100 mg/ml TF3, 5% GA, and ethanol solutions, the demineralized dentin blocks were hydrolyzed by

collagenase solution, and then underwent overnight fixation in 2.5% glutaraldehyde. Subsequently, they were dehydrated using ethanol solutions of 30%, 50%, 70%, 80%, 90%, and 95%, with each step lasting 15 min. This was followed by two successive 20-min immersions in 100% ethanol. The specimens underwent a 30-min treatment using a blend of ethanol and isoamyl acetate (V/V = 1/1), followed by a 1-h or overnight exposure to solely isoamyl acetate. Subsequent to undergoing critical point drying, the specimens' morphology was meticulously examined utilizing a biological scanning electron microscope (Hitachi SU3800, gold-sprayed by Hitachi MC1000, Japan).

2.4.4 Transmission electron microscopy (TEM)

After cross-linked in 100 mg/ml TF3, 5% GA, and ethanol solutions, the demineralized dentin blocks were hydrolyzed by collagenase solution, and then underwent overnight fixation in 2.5% glutaraldehyde, dehydration using a series of ethanol solutions, and subsequent embedding in epoxy resin as per established guidelines. The specimens were sectioned by Ultramicrotome (EMUC7, Leica Microsystems, Germany) and observed under TEM (Tecnai G2 Spirit, FEI, USA). The accelerating voltage was 80 kV.

2.5 Physicochemical properties

2.5.1 Surface hardness test

According to the above method, 1 mm dentin blocks were prepared, which were cross-linked in 100 mg/ml TF3, 5% GA, and ethanol solutions respectively. Their surfaces were etched using a 35% phosphoric-acid gel for 15 s. Afterward, the blocks were thoroughly rinsed with deionized water and dried. Subsequently, the samples in each group (n = 6) were cross-linked for 30 s and vacuum freeze-dried for 12 h. After being thoroughly dried, observing under a microscope, indentations were produced in the middle of the dentin blocks with a flat surface. Then, the surface Vickers hardness was calculated by loading 15 s at a weight of 50 g with the same indentation process.

2.5.2 Swelling ratio test

At room temperature, demineralized dentin collagen (n = 6) which were cross-linked in 100 mg/ml TF3, 5% GA, and ethanol solutions respectively, were swollen in distilled water and balanced overnight in phosphate buffer. The specimens were immediately weighed after drying with filter paper, which was recorded as wet weight M0. After removing the phosphate by soaking the samples in distilled water for 10 min, they were subjected to vacuum freeze-drying for 12 h. Following this, the specimens were re-weighed and recorded as dry weight M1. This equation is used to compute the swelling ratio:

$$\text{Swelling ratio} = \left[(M0 - M1)/M1 \right] \times 100\,\%$$

2.5.3 Thermogravimetric Analysis and Differential Thermal Gravity (TG-DTG)

The relationship between weight loss and temperature after cross-linking in 100 mg/ml TF3, 5% GA, and ethanol solutions respectively of demineralized dentin was measured by a thermogravimetric analyzer (Netzsch STA-2500), including TG and DTG curves. The parameters are set in the following manner: the nitrogen flow rate is 10 mL/min and the temperature rises to 200°C. Then, the test begins after falling to room temperature. Following this, the temperature rises to 1,000°C at a heating rate of 10°C/min.

2.6 Enzyme inhibition

2.6.1 *In situ* zymography

The enamel of the tooth crown was removed and the dentin was exposed by a low-speed water-cooled diamond saw (EXAKT E300CP Germany). According to the total acid etching dentin bonding process, the dentin surface was treated with acid etching, washing, and drying. Subsequently, the crosslinking agent solutions, which were 100 mg/ml TF3, 5% GA, and ethanol solutions respectively, were applied for 30 s on the dentin surface, following by washing and drying. Then, the Adaper TM Single bond 2 adhesive was evenly applied, blow-thinned and cured, and filled with 2 mm resin composite (Filtek TM Z250). Finally, the samples were immersed in distilled water at 37°C for 24 h. After that, the samples from each group were cut using a low-speed water-cooled diamond saw parallel to the long axis of the tooth, obtaining 1 mm thick tooth slices. Subsequently, the samples were adhered to glass slides and polished wet with silicon carbide papers of 600, 1,200, and 2000 grit sizes in sequence. The final specimens, together with the coverslip, were around 1.13 mm thick. According to the operation steps of the EnzChek Gelatinase/Collagenase Assay Kit (Invitrogen, Carlsbad, United States), Gelatin was diluted using phosphate buffer saline, and 50ul gelatin was dripped onto each specimen before covering with a coverslip to seal the edges. The activity of matrix metalloproteinases in the hybrid layer (λex/λem = 494 nm/521 nm) was observed by confocal laser scanning microscopy (Fluoview FV3000; Olympus, Tokyo, Japan).

2.7 Mechanism of cross-linking

2.7.1 Fourier transform infrared spectroscopy (FTIR)

TF3 powder and demineralized dentin matrixs treated with 100 mg/ml TF3, 5% GA, and ethanol solutions were freeze-dried and then investigated by Fourier transform infrared spectrometer (Thermo Scientific iN10, USA). The spectra were recorded in the wavelength range of 400–4,000 $cm^{-1,}$ with a resolution of 4 cm^{-1}, to capture the detailed vibrational modes of the molecules present. The obtained spectra were analyzed by Thermo Scientific™OMNIC™ software.

2.7.2 X-ray photoelectron spectroscopy (XPS)

The demineralized dentin matrixs treated with 100 mg/ml TF3, 5% GA, and ethanol solutions were freeze-dried and placed in the sample chamber of the XPS instrument (Thermo Scientific K-Alpha, USA). When the sample chamber pressure is lower than 2.0×10^{-7}mbar, the sample is sent to the analysis chamber. The parameters are set as follows: the spot size is 400 μm, the operating voltage is 12 kV, the filament current is 6 mA, the full spectrum scanning energy is 150 eV,

and the step size is 1 eV. Fine spectral scanning of carbon, nitrogen and oxygen elements was carried out with a scanning energy of 50 eV and a step size of 0.1 eV.

2.7.3 Raman spectroscopy

TF3 powder and demineralized dentin collagen treated with 100 mg/ml TF3, 5% GA, and ethanol solutions were freeze-dried and analyzed by Raman spectrometer (Horiba Lab RAM HR Evolution, Japan). The parameters are set as follows: The sample is divided into 1 mm blocks, and three scans lasting 60 s are performed in the specified sample area. Details of the spectrum are captured using a laser beam with a wavelength of 514 nm, ranging from 50 cm^{-1}–4,000 cm^{-1}.

2.8 Statistical analysis

Data on weight loss, hydroxyproline release and swelling ratio were evaluated using two-factor analysis of variance (ANOVA), followed by Tukey's *post hoc* test. The two factors were the solution (factor 1) and treatment duration (factor 2). Data on surface hardness was evaluated using one-factor analysis of variance (ANOVA) and Tukey's *post hoc* test. The significance level was set to 0.05. Statistical analysis was performed using GraphPad Prism 9 (GraphPad Software, San Diego, California, U.S.).

3 Results

3.1 Molecular docking

Grounded in the hypothesis that minimal energy is the best-fitting model, the molecular docking of TF3 with type I collagen was simulated. The binding energy and predicted interaction are shown in Table 1 and binding mode of TF3 to collagen I are shown in Figure 2.

3.2 Cross-linking efficiency

3.2.1 Weight loss and hydroxyproline release

It was suggested that WL rate (Figure 3A) of different TF3 concentrations of 12.5 mg/mL, 25 mg/mL, 50 mg/mL, 100 mg/mL group, and GA group were lower than that of the control and ethanol group ($p < 0.05$). Additionally, between the control group and the ethanol group, there existed no significant difference ($p > 0.05$).

The results of WL rate echoed those of HYP release. There was no difference in HYP release (Figure 3B) between the ethanol group and the control group ($p > 0.05$). With TF3 concentrations increased, the figure of HYP release steadily got close to the positive control GA group. The HYP release showed no significant difference between the 50 mg/ml TF3 and GA groups ($p > 0.05$). The HYP release of 100 mg/ml TF3 group was the lowest in all groups, which was statistically less than the GA group ($p < 0.05$). In all groups except the 12.5 mg/ml TF3 group, the WL rate and HYP release showed no significant difference between those in 30 s and 60 s ($p > 0.05$).

Comprehensive statistical analysis of the experimental results of WL rate and HYP release signified that 100 mg/mL was the best effective concentration of TF3 in biological modification, crosslinking, and anti-enzymatic hydrolysis. By contrast, whether the cross-linking time was 30 s or 60 s, the difference was not statistically significant. Therefore, 100 mg/ml TF3 crosslinking 30 s may be the most suitable concentration and time group for demineralized dentin biomodification crosslinking.

3.2.2 SEM

Figure 3C shows the structure of demineralized dentin collagen in the control and ethanol groups collapsed and gaps appeared after enzymatic hydrolysis by Collagenase type I. However, after cross-linking with 5% GA and 100 mg/ml TF3 for 30 s, the dentin collagen structure and the fiber scaffold were stable. It was confirmed that TF3 cross-linked demineralized dentin collagen can improve the anti-enzymatic hydrolysis ability.

3.2.3 TEM

In Figure 4, there was a typical collagen-striated structure of the demineralized dentin collagen, the original fibers were arranged neatly and the gap was uniform. Compared with the control and ethanol group, after 5% GA and 100 mg/ml TF3 cross-linked for 30 s, the cross-striation structure of collagen became blurred and difficult to distinguish, indicating that the gap between collagen fibers was reduced through cross-linking, resulting in a more compact structure. Following 48 h of digestion with 0.1 mg/mL collagenase (Figure 4), the dentin collagen fibers in both the control and ethanol groups suffered significant damage, leading to their disintegration and the creation of gaps and voids. Some degraded collagen fiber fragments were scattered in gaps. In contrast, the collagen fibers in the GA and TF3 groups were densely arranged and the structure was intact, without gaps due to enzymatic hydrolysis.

3.3 Physicochemical properties

3.3.1 Surface hardness test

Displayed in Figure 5A are the measurements of surface hardness in collagen with varying treatments. Among all groups, the 100 mg/ml TF3 group exhibited the greatest surface hardness.

The 100 mg/ml TF3 group and 5% GA group marked a statistical difference from the control group ($p < 0.05$). No significant difference was shown in HV between the ethanol group and the control group ($p > 0.05$).

3.3.2 Swelling ratio test

Figure 5B shows that the difference between the control group, the ethanol group, the 5% GA group, and the 100 mg/ml TF3 was not statistically significant differences when the cross-linking time was 30 s or 60 s ($p > 0.05$).

3.3.3 TG-DTG

As shown in Figures 5C–F, the TG curve is segmental into three stages, with the initial stage (30°C–200°C) resulting from the depletion of surface-absorbed water, crystal water loss peak in demineralized dentin collagen and other volatile organic

TABLE 1 Predicted interactions of the type I Collagen binding-site Residues with TF3.

Type I Collagen	Binding energy (kcal/mol)	Predicted interactions
1QSU	−5.8	Glu-43, Glu73
4OY5	−6.1	Gly7
1CGD	−5.4	Hyp47

compounds. At this stage, the mass thermal decomposition loss rates of control, ethanol, GA, and TF3 were 4.0%, 5.3%, 6.3%, and 10.1%, respectively. The second stage (200°C–600°C) is the degradation peak of demineralized dentin collagen and the shoulder peak due to the different degrees of cross-linking. At this stage, the weight loss rates of the control, ethanol, GA, and TF groups were 59.3%, 52.8%, 63.3%, and 55.2%, respectively. The third stage (600°C–1,000°C) is the passive thermal region and the slow degradation of carbon-containing substances. In general, the weight loss rates of the control, ethanol, GA, and TF groups were 71.8%, 63.6%, 78%, and 69.3%, respectively, indicating that collagen cross-linking can affect the thermal stability of demineralized dentin collagen.

3.4 Enzyme inhibition

3.4.1 *In situ* zymography

As shown in confocal laser scanning microscopy, the hybrid layer exhibited obvious green fluorescence within the 5% GA-

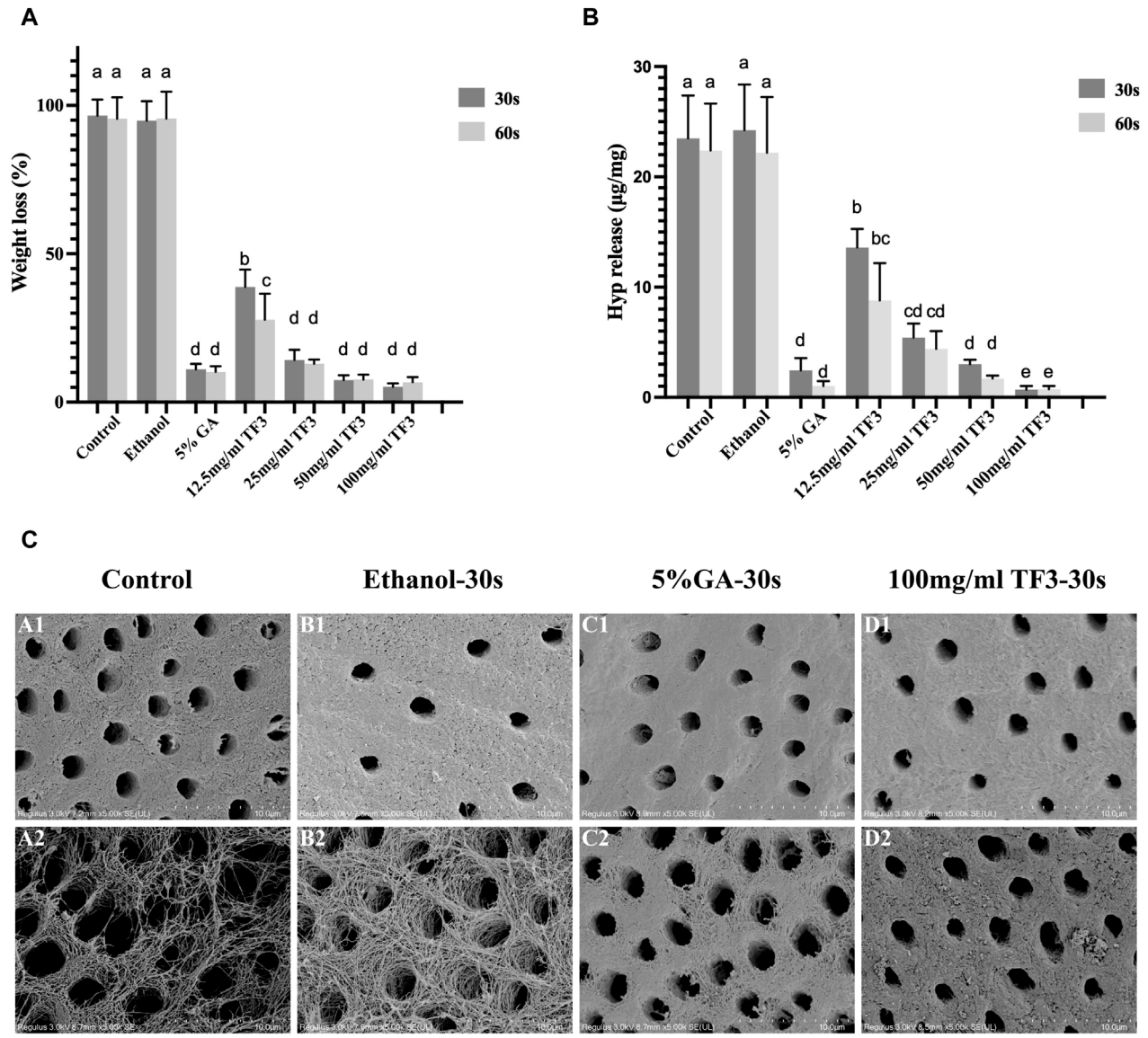

FIGURE 3
Weight loss **(A)** and hydroxyproline release **(B)** of demineralized dentin matrix with different cross-linkers. Variations in lowercase letters signify notable disparities among the groups ($p < 0.05$). Representative SEM images of demineralized dentin matrix with diverse treatments **(C)**: A1 to D1 represent before digestion and A2 to D2 represent after digestion. The scale bar is set at 10 um.

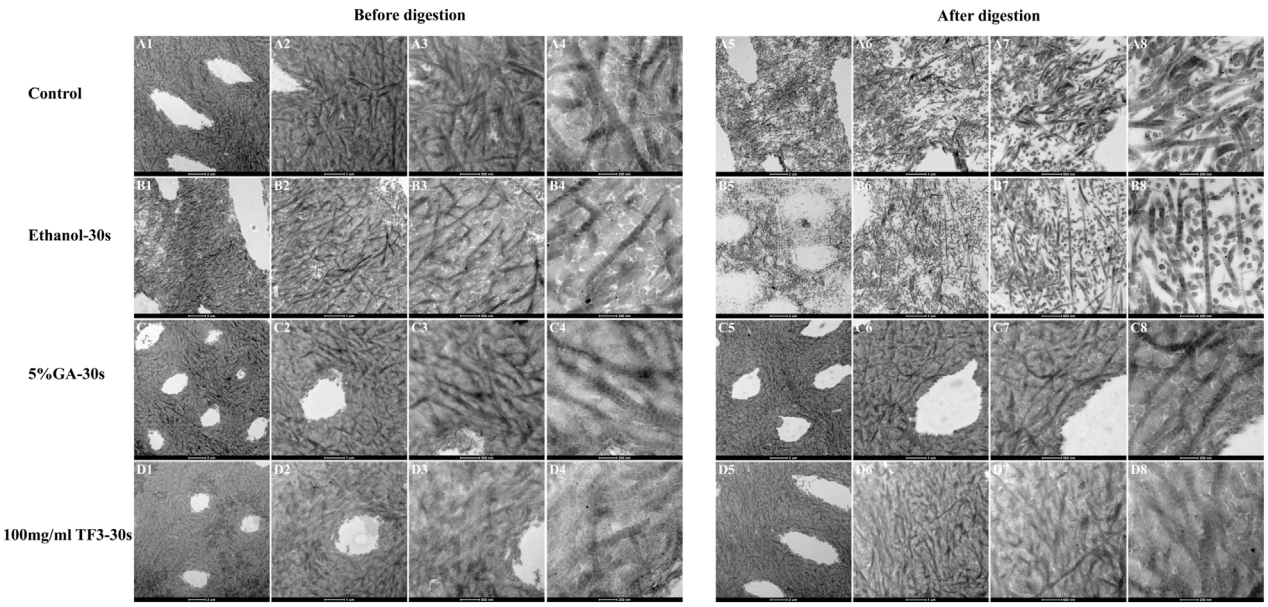

FIGURE 4
Representative TEM images of demineralized dentin matrix with diverse treatments. The scale bar for **(A1–D1)** and **(A5–D5)** is set at 2 um. The scale bar for **(A2–D2)** and **(A6–D6)** is set at 1 um. The scale bar for **(A3–D3)** and **(A7–D7)** is set at 500 nm. The scale bar for **(A4–D4)** and **(A8–D8)** is set at 200 nm. All the specimens were routine serial sections with a thickness of 4 μm, and 5 sections were obtained from each sample.

treated, ethanol-treated, and non-treated control groups. This suggested significant hydrolysis of fluorescein-tagged gelatin by MMPs in the hybrid layer, with effective MMP activity, confirming that the control group, with 5% GA and ethanol, did not inhibit MMPs. In the hybrid layer of 100 mg/ml TF3 in the experimental group, there was almost no green fluorescence, indicating a significant suppression and negligible activity of MMPs, thus confirming the potent inhibitory impact of 100 mg/ml TF3 on MMPs. Representative images are shown in Figure 6.

3.5 Mechanism of cross-linking

3.5.1 Fourier transform infrared spectroscopy

FTIR results (Figure 7A) showed several typical characteristic peaks before and after demineralized dentin collagen treatment: the absorption peak at 3,280 cm^{-1} was the -OH stretching vibration peak, representing amide A, the peaks at 2,940 and 3,060 were assigned to v (CH2) and amide B, respectively (Schmidt et al., 2020). The C=O stretching vibration at 1,633 cm^{-1} represents amide I; the heterogeneous combination of C-N extended vibration and N-H bending vibration at 1,535 cm^{-1} represents the amide II band. The absorption peak at about 1,450 cm^{-1} is caused by the shear vibration absorption of -CH2. At 1,235 cm^{-1}, the combination of C-N vibration and N-H bending vibration represents the amide III band (Antonakos et al., 2007; Nisar et al., 2023). Compared with the untreated demineralized dentin collagen control, TF3 caused significant changes, including the absorption band of OH at 3,280 cm^{-1} at 30 s and 60 s of 100 mg/ml TF3 treatment became wider and the intensity increased. At the same time, the peak position shifted, and a more significant shift occurred at 60 s of 100 mg/ml TF3 treatment. In addition, a new and sharp absorption peak appeared in the cross-linked demineralized dentin collagen of TF powder and 100 mg/ml TF3 at 1,145 cm^{-1} (Liu et al., 2021). Compared with TF powder, the peaks of 100 mg/ml TF3 crosslinked for 30 s and 60 s shifted, and the intensity decreased, especially for 60 s.

3.5.2 XPS

Figure 7C is the C 1s fine spectrum. The peaks at 284.8 eV, 285.9 eV, and 287.1 eV represent C-C/C=C, C-N, and C=N/C=O, respectively (Wang M. et al., 2023). The binding state of C element in different groups was diverse: in ethanol and GA groups, the binding energy of C element was relatively low, indicating that the interaction between C atom and other elements was weak; in the TF3 group, the binding energy of C element was higher, indicating that the interaction between C atom and other elements was stronger. This may be related to the hydrogen bond interaction between the phenolic hydroxyl group in TF3 and the C atom of demineralized dentin collagen (Liu et al., 2021). It is worth noting that with the extension of the action time, the binding energy became larger.

Figure 7D is the N 1s fine spectrum. The peaks at 399.2 and 399.7 eV are associated with N-H and C-N bonds, respectively (Wang M. et al., 2023). The peak position of the ethanol group was close to that of the control group, indicating that the chemical structure of the demineralized dentin collagen was not influenced by the ethanol. In the GA group, the N-H bond slightly shifted to the low binding energy direction, indicating that GA interacted with the N atoms in the demineralized dentin collagen. In the TF group, the peaks of N-H bond and C-N bond shifted significantly in the direction of high binding energy, indicating that TF3 could significantly change the chemical environment of demineralized dentin and affect its molecular structure.

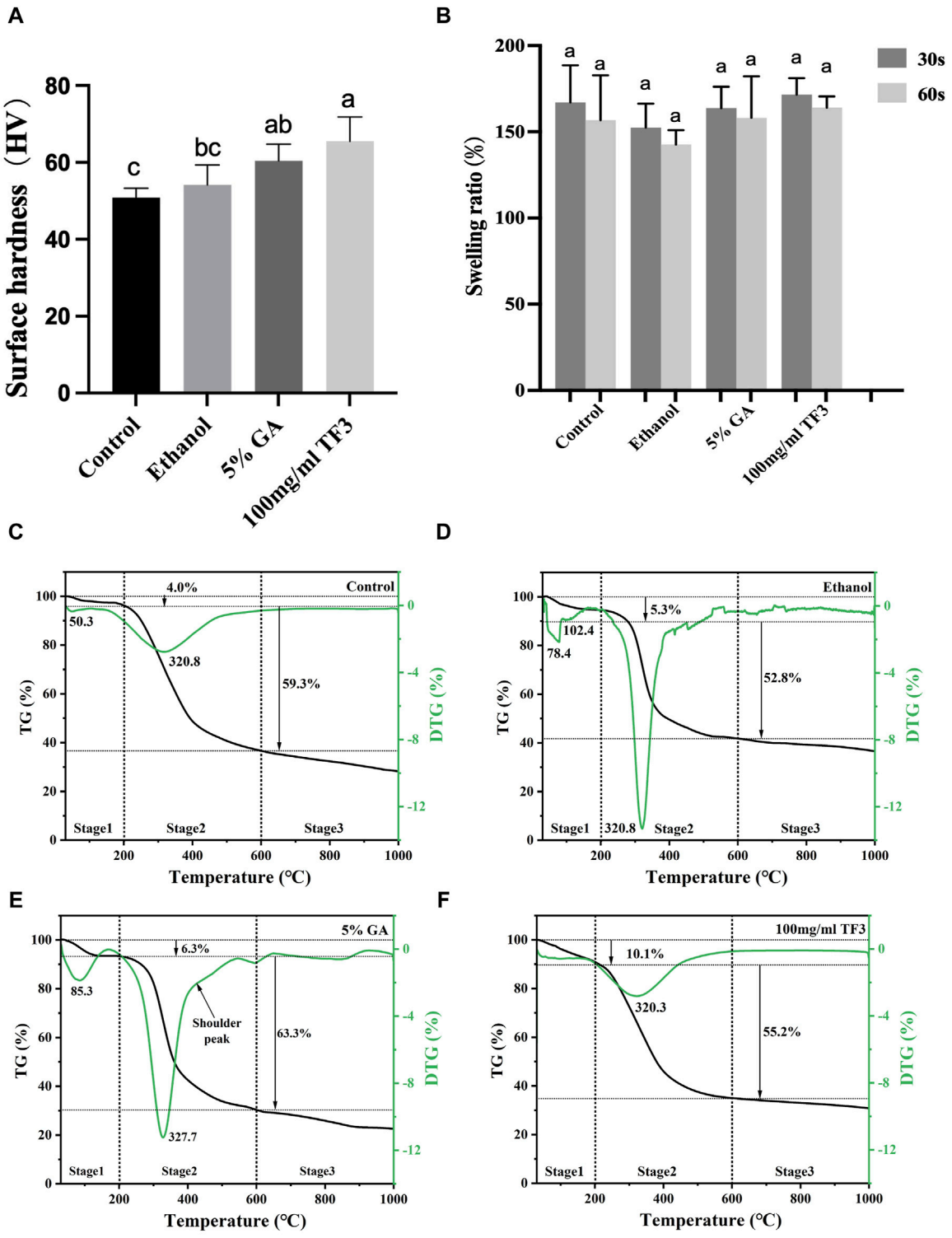

FIGURE 5
Surface hardness **(A)** and swelling ratio **(B)** of demineralized dentin matrix with diverse treatments. Variations in lowercase letters signify notable disparities among the groups ($p < 0.05$). TG-DTG of demineralized dentin matrix with diverse treatments **(C–F)**.

Figure 7E is the O 1s fine spectrum. The peaks at 531.2 eV and 532.6 eV are referred to C-O and C=O, respectively (Wang M. et al., 2023). The chemical state of O in different groups was also significantly different: the peak position of ethanol was close to that of control, indicating that ethanol did not change the chemical structure of demineralized dentin. In the GA group, the C=O double bond did not change significantly, and the C-O bond shifted slightly to the direction of low binding energy, indicating that GA could interact with O atoms in demineralized dentin collagen (Gai et al., 2023). In the TF3 group, the peaks of C-O bond and C=O bond were

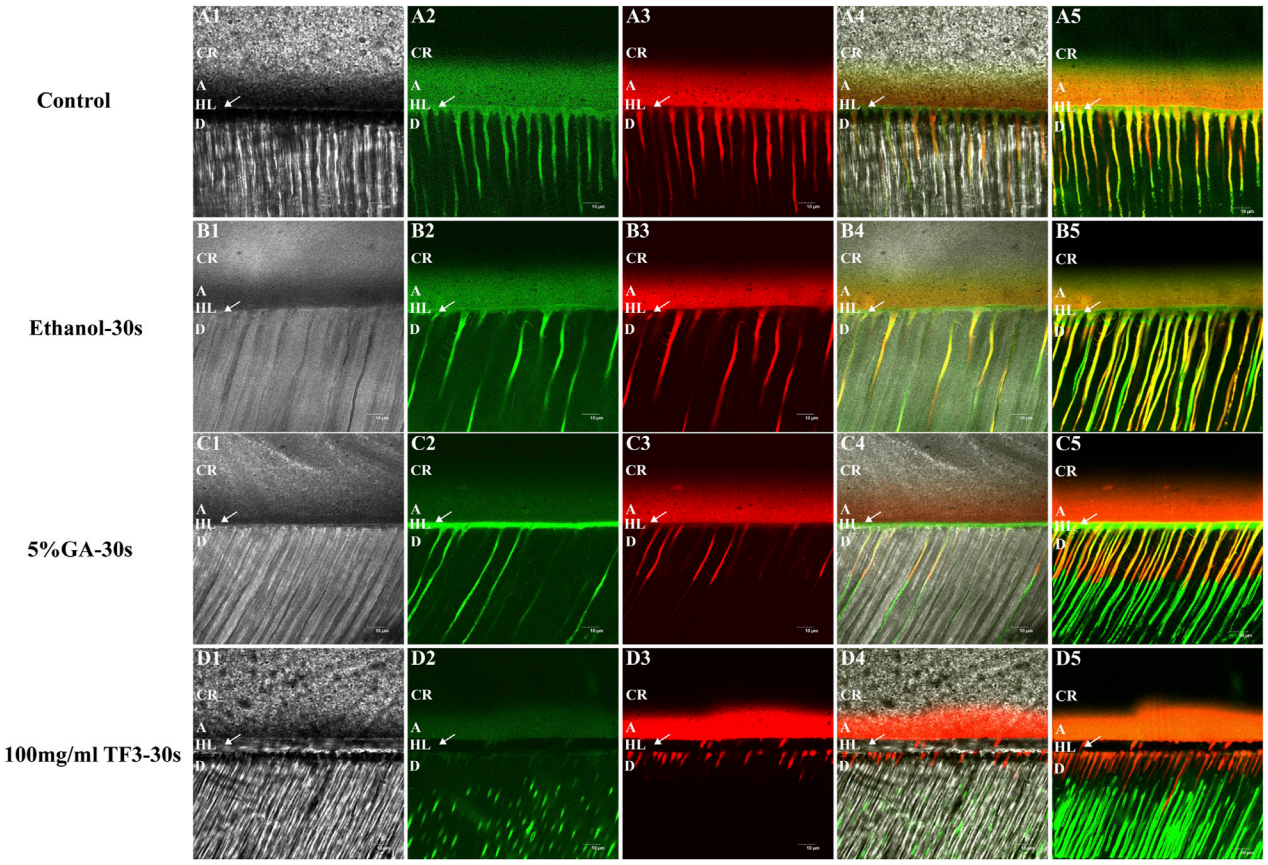

FIGURE 6
Representative confocal laser scanning microscopy images of the resin-dentin interface of demineralized dentin matrix with diverse treatments. **(A1–D1)** represent images under the light microscope. **(A2–D2)** represent the green fluorescence of MMPs. **(A3–D3)** represent the red fluorescence of the adhesive. **(A4–D4)** and **(A5–D5)** are the merged images. CR = Composite-Resin; A = Adhesive; HL = Hybrid Layer; D = Dentin. The arrow refers to HL. The scale bar is set at 10 um.

significantly shifted to the direction of high binding energy. With the prolongation of TF3 treatment time, the shift was more obvious, indicating that TF3 could significantly change the chemical structure of demineralized dentin. More importantly, TF3 can significantly increase the content of C=O bond, indicating that TF and demineralized dentin collagen may form ester bonds through covalent interaction (van den Brand et al., 2004).

3.5.3 Raman spectroscopy

As depicted in Figure 7B, the characteristic peaks at 1,672, 1,530, and 1,234 cm^{-1} are the typical characteristic peaks of the three-dimensional spiral structure of collagen fibers (Xu and Wang, 2012). These peaks were associated with the amide I band, amide II band, and amide III band, respectively, and exhibited sensitivity to the molecular conformation of the polypeptide chain, aligning with the results of infrared spectroscopy (Antonakos et al., 2007; Nisar et al., 2023). The peak at 1,450 cm^{-1} and 2,930 cm^{-1} referred to the C-H bond, reflecting the organic components present in demineralized dentin (Lazar et al., 2005).

The control, ethanol, and GA groups showed similar peaks, indicating that ethanol and GA treatments did not induce significant structural changes in demineralized dentin collagen. However, in the TF3 group, differences emerged compared to the control. Specifically, the amide I, II, and III bands appeared slightly wider, with the amide I band peak experiencing a slight reduction in intensity and a shift towards the lower band region. Conversely, the amide II band peak exhibited an increase in intensity. For the peak of collagen peptide chain C-H bond at 1,450 cm^{-1}, TF3 shifted to the high band area. These observations suggest a robust cross-linking reaction between TF3 and the carboxyl, hydroxyl, and amino groups present in demineralized dentin collagen.

4 Discussion

Theaflavins (TFs) are natural compounds in black tea, which are a general term for a class of benzotropolone compounds containing multiple hydroxyl or phenolic hydroxyl groups. TFs are mainly composed of four dimers, namely, TF1, TF2A, TF2B and TF3, which are different due to the number and location of gallic acid groups. Among them, TF3 contains two gallic acyl groups, which is the most abundant and most active component (Hass et al., 2021). Current research indicates that TFs are capable of rapidly crosslinking demineralized dentin collagen film, safeguarding it against collagenase degradation, and its effect is equivalent to or better

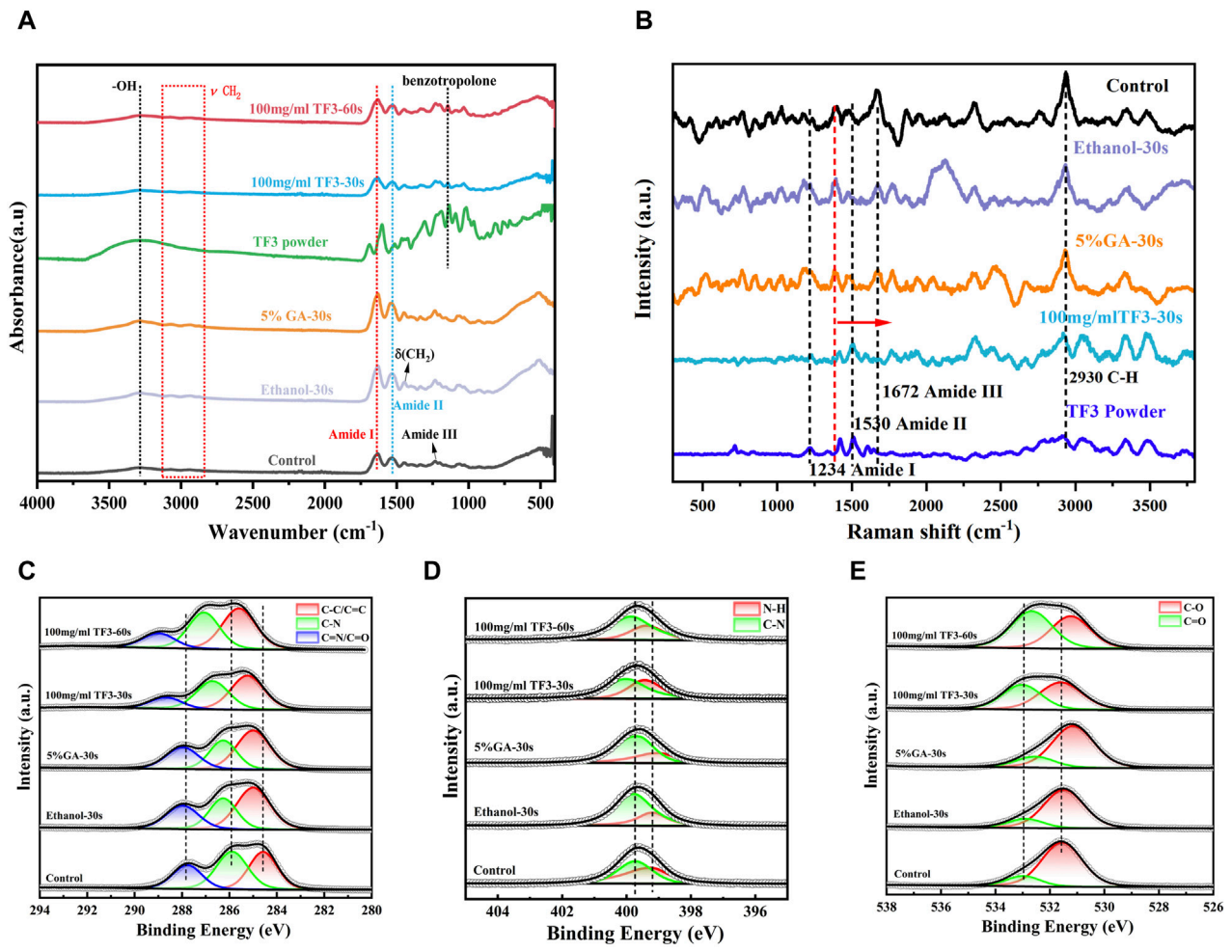

FIGURE 7
FTIR spectrum **(A)**. Raman spectrum **(B)**. XRD spectrum analysis **(C–E)**: Fine spectrum of C 1s **(C)**. Fine spectrum of N 1s **(D)**. Fine spectrum of O 1s **(E)**.

than PA (Liu et al., 2021). The reason lies in the structural difference between TFs and PA. In contrast to the PA dimer, where two catechins are connected by a single C-C bond, the TFs feature two catechin units linked by a benzotropolone skeleton. This unique structure incorporates a carbonyl group positioned near the hydroxyl group. The carbonyl group's ability to form hydrogen bonds with hydrogen donors, such as hydroxyl or amino groups, facilitates the cross-linking of collagen. In addition, TFs have aromatic ring structures, abundant in phenolic hydroxyl groups and gallic acyl groups, which have also been shown to make a crucial contribution to collagen cross-linking (Liu et al., 2013; Vidal et al., 2016). Among the four dimers of TFs, in addition to the same structure, such as benzophenone skeleton and carbonyl group, TF3 has the most phenolic hydroxyl and galloyl groups, which is speculated to have the most crosslinking potential (Truong and Jeong, 2021). However, there are still no studies reporting TF3's cross-linking impact on demineralized dentin collagen. Hence, in this study, we used TF3 as a novel cross-linker and investigated its cross-linking efficacy and mechanism. The results showed that TF3 can effectively cross-link dentin collagen and enhance its enzymatic resistance and biomechanical properties within the clinical time, mainly through hydrogen bonding.

First, we performed theoretical calculations and used molecular docking to predict the interaction between TF3 and type I collagen. The results indicated that the binding energies of TF3 with type I collagen structure 1QSU, 4OY5 and 1CGD were −5.8, −6.1 and −5.4 kcal/mol, respectively, indicating that they could spontaneously bind. This is similar to the predicted result of other studies (Vaidyanathan et al., 2007) using molecular docking to simulate the binding energy between 10-methacryloxy decamethylene phosphate and demineralized dentin type I collagen between −4.5 and −8.9 kcal/mol, which also provides evidence for the interaction between TF3 and collagen. Predictions by MD (Table1) show that TF3 and type I collagen can be combined through various forces, including hydrogen bonds, hydrophobic interactions, and water bridges, among which hydrogen bonds are the most important. For example, the hydrogen bond formation frequency between TF3 and GLU73 in 1QSU structure is as high as 136%, forming two hydrogen bonds with a frequency of 68%. This means that TF3 can spontaneously bind to the active sites of collagen through hydrogen bonds, thereby achieving cross-linking of demineralized dentin collagen. However, it should be noted that the simulation may not fully reflect the real interaction (Bertassoni et al., 2012).

Next, to study the ability of TF3 cross-linked demineralized dentin collagen to resist exogenous collagenase digestion, this study used 0.1 mg/mL exogenous type I bacterial collagenase for collagenase digestion experiment (Liede et al., 1999). Notably, the concentration level of collagenase is two to six orders of magnitude greater than those in human oral fluid (Paivi et al., 2002). Firstly, the overall understanding of the protective relationship of TF3 on dentin collagen was obtained by drying weight loss experiment. This experiment is based on the fact that there is a balance between the degradation rate of soluble dentin collagen small molecule peptides or amino acids and their release rate from the insoluble demineralized dentin matrix that acts as a small molecular sieve (Garnero et al., 2003; Takahashi et al., 2013). So drying weight loss can indirectly evaluate the enzymatic hydrolysis tolerance of demineralized dentin collagen to exogenous type I bacterial collagenase at the overall level. Secondly, given that dentin type I collagen comprises roughly 10% hydroxyproline, the majority of other proteins have minimal or no similar amino acid composition (Marshall et al., 1997). The ability of dentin collagen to withstand collagenase digestion can be specifically detected by measuring hydroxyproline release.

As depicted in Figures 3A,B, WL and HYP release of TF3 were notably less compared to the control and ethanol group, and decreased with the increase in concentration, which was concentration-dependent. Notably, the effect of 100 mg/ml TF3 cross-linking was even better than that of 5% GA, and there was almost no difference in weight loss and hydroxyproline release between 30 s and 60 s. This may be related to the fact that high concentrations of TF3 can penetrate the collagen network more quickly.

In addition, we also detected the impact of TF3 on the activity of endogenous proteases by *in situ* zymography. MMPs exist in the mineralized dentin matrix in the form of zymogens, capable of being activated through acid etching and hydrolyzing the exposed collagen (Mazzoni et al., 2013). The experimental results revealed a prominent green fluorescence at the base of the hybrid layer and within the dentinal tubules in the control group (Figure 6A5), the ethanol group (Figure 6B5), and the GA group (Figure 6C5), signifying that the activity of endogenous dentin MMPs in these regions was uninhibited (Mazzoni et al., 2012). In contrast, there was black at the base of the hybrid layer and within the adjacent dentinal tubules in the TF3 group (Figure 6D5), and no green fluorescence was detected. This suggests that TF3 effectively inhibited the activity of endogenous MMPs. In addition, this also explains the reason why TF3 can effectively resist collagenase digestion, that is, TF3 may interact with the enzyme, inactivate the C-terminal peptidase, and interfere with the binding of collagenase to collagen (Sabatini and Pashley, 2015). In another part of our research on the interaction between TF3 and enzymes, molecular docking simulation showed that the binding energy of TF3 and MMPs was −7.3 ~ −8.7 kcal/mol, and the binding energy of TF3 and cysteine protease was even −9.3 ~ −10.0 kcal/mol. Therefore, it is reasonable to believe that TF3 can inhibit the activity of endogenous proteases.

To further study the impact of TF3 on maintaining the structure of demineralized dentin collagen, we conducted observations using SEM and TEM. The SEM results (Figure 3C) indicate that, compared to the control group and the ethanol group, the surface structure of collagen in the 5% GA and 100 mg/ml TF3 groups appears smoother and denser before enzymatic hydrolysis. However, after enzymatic hydrolysis, the surface becomes slightly rough, yet the collagen structure remains intact, and both intertubular and peritubular dentin remain viable. The TEM results (Figure 4) reveal that the characteristic cross-striation structure of collagen in the 5% GA and 100 mg/ml TF3 groups becomes thicker and blurred. The collagen fibers remain dense and intact with characteristic cross-striations even after enzymatic hydrolysis. These findings corroborate the results of WL and HYP release, suggesting that 100 mg/ml TF3 possesses a crosslinking efficiency similar to that of 5% GA. Both agents can crosslink with dentin collagen and reduce its spacing to maintain structural integrity, thereby enhancing its resistance to enzymatic hydrolysis. Consequently, the first and second null hypotheses were dismissed.

Reports indicated that the surface hardness of demineralized dentin is an important index affecting the bonding durability (Hardan et al., 2022). During the process of dentin bonding, collagen possesses a robust surface, which can resist collagenase digestion and more effectively prevent collagen from collapsing post acid etching-washing, thereby enhancing adhesive penetration (Scheffel et al., 2014). This research focused on testing the surface Vickers hardness of demineralized dentin collagen post-crosslinking. The results showed that (Figure 5A), after crosslinking with ethanol, 5% GA, and 100 mg/ml TF3, the demineralized dentin surface of the 100 mg/ml TF3 group had the highest Vickers hardness, which may be related to the crosslinking effect to shorten the distance between collagen molecules and make its structure denser (Bedran-Russo et al., 2008).

Additionally, collagen's hydrophilicity is influenced by cross-linking agents and the swelling rate is positively correlated with hydrophilicity (Leme et al., 2015). In general, a heightened level of cross-linking between collagen fibers and a decrease in bound water decreases the swelling rate (Miles et al., 2005). However, the study (Figure 5B) revealed no significant difference ($p > 0.05$) among the groups. This suggests that 100 mg/ml TF3 did not change the hydrophilicity of the dentin matrix, also, the inter-collagen fiber-bound water was not reduced during the treatment time (30 s/60 s), which we speculate may be related to the fact that TF3 is soluble in water and the shorter treatment time. Our experimental results were different from those of some studies (Deng et al., 2013; Hiraishi et al., 2013), which showed GA solution's efficacy in diminishing the swelling rate of demineralized dentin matrix, probably because their experimental time (12 h) was much longer than ours (30 s/60 s).

The TG-DTG experiment was conducted to evaluate the thermal stableness of the dentin matrix after cross-linking modification. The denaturation temperature of the dentin matrix is affected by the form, quantity, distribution, and water content of the crosslinking agent. Considering that high temperatures have the potential to disrupt protein-water interactions, break hydrogen bonds, and cause the evaporation of bound water, thermal stability serves as an indicator of a protein structure's resistance to thermal reactions (Rochdi et al., 1999). The second stage of TG-DTG (200°C–600°C) showed a peak of demineralized dentin collagen carbonization degradation and a shoulder peak due to different cross-linking degrees. At this stage, the weight loss rates of the control, ethanol, GA, and TF groups were 59.3%, 52.8%, 63.3%, and

55.2%, respectively. TF3's depletion rate was less than the control group, suggesting that TF3 improved the structural stability and reduced the loss rate of mass thermal decomposition by crosslinking with demineralized dentin. In the GA group at this stage, the main peak of the DTG curve shifts towards the high-temperature region, and a shoulder peak appears at 430°C beyond the main peak at 327.7°C. Additionally, the weight loss rate is relatively high, which may be related to factors such as uneven crosslinking of collagen, multiple thermal decompositions, and additional thermal weight loss caused by the decomposition of the crosslinking agent (Miles et al., 2005).

The results of surface hardness and TG-DTG tests revealed that the biomechanical characteristics of demineralized dentin collagen cross-linked with TF3 have been enhanced. Consequently, the third null hypothesis was likewise dismissed.

To study the mechanism of action of TF3 and type I collagen, we used FTIR, XPS, and Raman spectroscopy. In FTIR detection, the maintenance of amide I, II, and III peaks in TF3 group indicated that TF3 did not disrupt the triple helix structure of dentin collagen. The broadening of amide I (~1,660 cm^{-1}) observed in Figure 7A could be caused by hydrogen bonding interactions between the amino and amide groups of collagen and the phenolic hydroxyl groups of TF3 (He et al., 2011). After TF3 treatment of demineralized dentin collagen, the OH absorption peak at 3,280 cm^{-1} shifted, the absorption band widened and the intensity increased, indicating the formation of intermolecular hydrogen bonds. To further confirm the existence of hydrogen bonds, we increased the cross-linking time of TF to 60 s. The results showed that the absorption peak of OH at 3,280 cm^{-1} shifted more obviously, the absorption band was wider and the intensity increased more obviously (Figure 7A), which confirmed that TF and demineralized dentin collagen formed intermolecular hydrogen bonds. In addition, the ratio of A1235/A1450 at the amide III bond to 1450 cm^{-1} is also an important criterion for evaluating the structural integrity of the collagen triple helix. The collagen A1235/A1450 with complete triple helix structure is about 1 (Figueiró et al., 2006) and the principle of denatured gel is less than 0.6 (Sylvester et al., 1989; Figueiró et al., 2006). In this experiment, the A1235/A1450 of the control group, the ethanol group, the GA group, and the TF3 group were about 1.07, 0.86, 0.97, and 0.66, respectively, all between 0.6-1.0. It also shows that TF3 has a strong interaction with demineralized dentin matrix collagen molecules without changing the triple helix structure. The reason for the decrease of A1235/A1450 caused by TF3 may be that the -CH2 in its structure significantly increases the absorption spectrum at ~ 1,450 cm^{-1}, while the amide III bond at ~ 1,235 cm^{-1} is not strengthened. In addition, in the TF powder and 100 mg ml TF3 group, the C-C (-OH) stretching vibration band at 1,145 cm^{-1} attributed to the benzotropolone structure of TF3 changed, indicating that the benzotropolone structure also played a role in the cross-linking between TF3 and demineralized dentin collagen, which was also verified in the study of Liu's (Liu et al., 2021). When analyzing the reason why the cross-linking effect of low-concentration TF3 is stronger than that of PA, it is speculated that the additional fused ring and/or a great many phenolic hydroxyl groups of benzotropolone in TF3 may have potential influence.

In XPS detection, the peaks at 284.8 eV, 285.9 eV and 287.1 eV in the fine spectrum of C 1s (Figure 7C) represent C-C/C=C, C-N, and C=N/C=O bonds, respectively. The binding energy of ethanol and GA groups is relatively low, while the binding energy of the TF3 group is higher, which is related to the hydrogen bond interaction between phenolic hydroxyl groups in TF3 and demineralized dentin collagen (Gilbert et al., 2013). In the N 1s and O1s fine spectrum (Figures 7D,E), the N - H bond (399.2 eV), C - N bond (399.7 eV), C - O bond (531.2 eV), and C = O bond (532.6 eV) wave peaks were close in position in the ethanol and control groups. In contrast, all of these wave peaks in the TF group were significantly shifted to the high binding energy direction, indicating that the structure of demineralized dentin collagen may be affected by TF3 in molecular aspect. More importantly, the content of C=O bond in the TF3 group increased significantly, suggesting that TF3 and demineralized dentin collagen may form ester bonds through covalent interaction (Nosenko et al., 2015). At the same time, it also indicates the formation of intermolecular hydrogen bonds between TF3 and demineralized collagen to a certain extent.

In the Raman spectroscopy (Figure 7B), the characteristic peaks of 1,672, 1,530 and 1,234 cm^{-1} represent the amide I, II and III bands of the three-dimensional spiral structure of collagen fibers, respectively. The control, ethanol and GA groups showed similar peaks, while in the TF3 group, the amide I band, II band and III band were slightly widened, the amide I band peak was slightly reduced and slightly shifted to the low band region, and the peak of the amide II band was increased, indicating that TF3 preserved the integrity of the dentin collagen triple helix structure (Nosenko et al., 2015). This finding is consistent with the results of FTIR. In addition, in the TF3 group, the peak at 1,450 cm^{-1} representing the C-H bond of the collagen peptide chain shifted to the high-band region, indicating that TF3 had a strong cross-linking reaction with the carboxyl, hydroxyl, and amino groups of the demineralized dentin collagen (Rangan et al., 2020).

FTIR, XPS and Raman studies have shown that TF3 can cross-link demineralized dentin collagen through hydrogen bonds, covalent interactions, etc., further providing strong evidence that TF3 can cross-link demineralized dentin collagen. Consequently, the initial incorrect hypothesis is once more dismissed.

In summary, this study confirmed for the first time that TF3 can efficiently cross-link demineralized dentin collagen, significantly improve its resistance to endogenous and exogenous collagenase digestion, and improve its biomechanical properties. These experiments lay the foundation for the clinical application of TF3 and have very important significance. However, its effectiveness in improving the durability of dentin bonding has not been confirmed in the study, which is slightly regrettable. In subsequent experiments, we will further optimize and study the effect of TF3 on dentin bonding properties, including immediate and durable dentin bonding strength, nanoleakage, fracture mode, *in situ* zymography, etc.

5 Conclusion

Our research revealed that TF3 is capable of efficiently cross-linking demineralized dentin collagen through hydrogen bonds and covalent interactions in clinical time, resisting collagenase digestion, and improving biomechanical properties. At the appropriate treated concentration and time, the safeguarding function of TF3 on dentin

collagen is similar to or even higher than that of GA, which lays a foundation for the subsequent study of the effect of TF3 on dentin and also provides a novel possibility for enhancing the longevity of the adhesive.

Data availability statement

The original contributions presented in the study are included in the article/Supplementary Material, further inquiries can be directed to the corresponding authors.

Ethics statement

The studies involving humans were approved by Approved by the Ethics Committee of the Affiliated Stomatological Hospital of Guangxi Medical University (Certificate of Ethical Approval No. 2023029). The studies were conducted in accordance with the local legislation and institutional requirements. The participants provided their written informed consent to participate in this study.

Author contributions

ZC: Conceptualization, Funding acquisition, Investigation, Writing–original draft. YW: Investigation, Writing–original draft, Conceptualization, Funding acquisition, Validation. XH: Investigation, Resources, Writing–original draft. KY: Methodology, Resources, Writing–original draft. YG: Investigation, Writing–original draft. KL: Visualization, Writing–original draft. XJ: Writing–review and editing. WC: Writing–review and editing. LL: Data curation, Investigation, Writing–original draft, Validation. XW: Formal Analysis, Investigation, Visualization, Writing–original draft. FP: Validation, Writing–original draft. YL: Data curation, Methodology, Writing–original draft. XH: Investigation, Validation, Writing–original draft.

Funding

The author(s) declare that financial support was received for the research, authorship, and/or publication of this article. Financial support comes from Joint Project on Regional High-Incidence Diseases Research of Guangxi Natural Science Foundation (No.2024GXNSFAA010141) and National Clinical Key Specialty Construction Project (No.CZ000037).

Acknowledgments

The authors express gratitude for the drawing materials provided by BioRender.

Conflict of interest

The authors declare that the research was conducted in the absence of any commercial or financial relationships that could be construed as a potential conflict of interest.

Publisher's note

Supplementary material

The Supplementary Material for this article can be found online at: https://www.frontiersin.org/articles/10.3389/fbioe.2024.1401032/full#supplementary-material

References

Anastasiadis, K., Verdelis, K., and Eliades, G. (2021). The effect of universal adhesives on dentine collagen. *Dent. Mater.* 37, 1316–1324. doi:10.1016/j.dental.2021.05.004

Antonakos, A., Liarokapis, E., and Leventouri, T. (2007). Micro-Raman and FTIR studies of synthetic and natural apatites. *Biomaterials* 28, 3043–3054. doi:10.1016/j.biomaterials.2007.02.028

Anumula, L., Ramesh, S., Kolaparthi, V. S. K., Kirubakaran, R., Karobari, M. I., Arora, S., et al. (2022). Role of natural cross linkers in resin–dentin bond durability: a systematic review and meta-analysis. *Materials* 15, 5650. doi:10.3390/ma15165650

Bedran-Russo, A. K. B., Pashley, D. H., Agee, K., Drummond, J. L., and Miescke, K. J. (2008). Changes in stiffness of demineralized dentin following application of collagen crosslinkers. *J. Biomed. Mater. Res. B Appl. Biomater.* 86, 330–334. doi:10.1002/jbm.b.31022

Bertassoni, L. E., Orgel, J. P. R., Antipova, O., and Swain, M. V. (2012). The dentin organic matrix – limitations of restorative dentistry hidden on the nanometer scale. *Acta Biomater.* 8, 2419–2433. doi:10.1016/j.actbio.2012.02.022

Cai, J., Palamara, J. E. A., and Burrow, M. F. (2018). Effects of collagen crosslinkers on dentine: a literature review. *Calcif. Tissue Int.* 102, 265–279. doi:10.1007/s00223-017-0343-7

Chiang, Y.-T., Xiao, Y.-B., Hsu, S., Chang, S.-W., and Chou, C.-C. (2023). Molecular interactions of tannic acid and matrix metalloproteinases 2 and 9. *Comput. Struct. Biotechnol. J.* 21, 2792–2800. doi:10.1016/j.csbj.2023.04.011

Cilli, R., Prakki, A., de Araújo, P. A., and Pereira, J. C. (2009). Influence of glutaraldehyde priming on bond strength of an experimental adhesive system applied to wet and dry dentine. *J. Dent.* 37, 212–218. doi:10.1016/j.jdent.2008.11.017

Comba, A., Maravic, T., Valente, L., Girlando, M., Cunha, S. R., Checchi, V., et al. (2019). Effect of benzalkonium chloride on dentin bond strength and endogenous enzymatic activity. *J. Dent.* 85, 25–32. doi:10.1016/j.jdent.2019.04.008

Coutinho, E., Cardoso, M. V., Fernandes, C. P., Neves, A. A., Gouvea, C. V. D., Landuyt, K. L. V., et al. (2011). Nanoleakage distribution at adhesive-dentin interfaces in 3D. *J. Dent. Res.* 90, 1019–1025. doi:10.1177/0022034511408430

Deng, M., Dong, X., Zhou, X., Wang, L., Li, H., and Xu, X. (2013). Characterization of dentin matrix biomodified by galla chinensis extract. *J. Endod.* 39, 542–547. doi:10.1016/j.joen.2012.12.034

Fan-Chiang, Y.-S., Chou, P.-C., Hsiao, Y.-W., Cheng, Y.-H., Huang, Y., Chiu, Y.-C., et al. (2023). Optimizing dental bond strength: insights from comprehensive literature review and future implications for clinical practice. *Biomedicines* 11, 2995. doi:10.3390/biomedicines11112995

Figueiró, S. D., Macêdo, A. A. M., Melo, M. R. S., Freitas, A. L. P., Moreira, R. A., De Oliveira, R. S., et al. (2006). On the dielectric behaviour of collagen–algal sulfated polysaccharide blends: effect of glutaraldehyde crosslinking. *Biophys. Chem.* 120, 154–159. doi:10.1016/j.bpc.2005.11.001

Gabetta, B., Fuzzati, N., Griffini, A., Lolla, E., Pace, R., Ruffilli, T., et al. (2000). Characterization of proanthocyanidins from grape seeds. *Fitoterapia* 71, 162–175. doi:10.1016/s0367-326x(99)00161-6

Gai, S., Wang, X., Zhang, R., Zeng, K., Miao, S., Wu, Y., et al. (2023). A controllably fabricated polypyrrole nanorods network by doping a tetra-β-carboxylate cobalt phthalocyanine tetrasodium salt for enhanced ammonia sensing at room temperature. *RSC Adv.* 13, 13725–13734. doi:10.1039/d3ra00103b

Garnero, P., Ferreras, M., Karsdal, M., Nicamhlaoibh, R., Risteli, J., Borel, O., et al. (2003). The type I collagen fragments ICTP and CTX reveal distinct enzymatic pathways of bone collagen degradation. *J. Bone Min. Res.* 18, 859–867. doi:10.1359/jbmr.2003.18.5.859

Gilbert, J. B., Rubner, M. F., and Cohen, R. E. (2013). Depth-profiling X-ray photoelectron spectroscopy (XPS) analysis of interlayer diffusion in polyelectrolyte multilayers. *Proc. Natl. Acad. Sci.* 110, 6651–6656. doi:10.1073/pnas.1222325110

Green, B., Yao, X., Ganguly, A., Xu, C., Dusevich, V., Walker, M. P., et al. (2010). Grape seed proanthocyanidins increase collagen biodegradation resistance in the dentin/adhesive interface when included in an adhesive. *J. Dent.* 38, 908–915. doi:10.1016/j.jdent.2010.08.004

Guo, J., Yang, M., and Hu, M. (2023). The roles of theaflavins in reducing dentin erosion. *Sci. Rep.* 13, 9413. doi:10.1038/s41598-023-35382-3

Hardan, L., Daood, U., Bourgi, R., Cuevas-Suárez, C. E., Devoto, W., Zarow, M., et al. (2022). Effect of collagen crosslinkers on dentin bond strength of adhesive systems: a systematic review and meta-analysis. *Cells* 11, 2417. doi:10.3390/cells11152417

Hass, V., Li, Y., Wang, R., Nguyen, D., Peng, Z., and Wang, Y. (2021). Methacrylate-functionalized proanthocyanidins as novel polymerizable collagen cross-linkers – Part 1: efficacy in dentin collagen bio-stabilization and cross-linking. *Dent. Mater. Off. Publ. Acad. Dent. Mater.* 37, 1183–1192. doi:10.1016/j.dental.2021.04.006

He, L., Mu, C., Shi, J., Zhang, Q., Shi, B., and Lin, W. (2011). Modification of collagen with a natural cross-linker, procyanidin. *Int. J. Biol. Macromol.* 48, 354–359. doi:10.1016/j.ijbiomac.2010.12.012

Hiraishi, N., Sono, R., Sofiqul, I., Yiu, C., Nakamura, H., Otsuki, M., et al. (2013). *In vitro* evaluation of plant-derived agents to preserve dentin collagen. *Dent. Mater.* 29, 1048–1054. doi:10.1016/j.dental.2013.07.015

Lazar, G., Zellama, K., Vascan, I., Stamate, M., Lazar, I., and Rusu, I. (2005). Infrared absorption properties of amorphous carbon films. *J. Optoelectron. Adv. Mater.* 7, 647–642.

Leme, A. A., Vidal, C. M. P., Hassan, L. S., and Bedran-Russo, A. K. (2015). Potential role of surface wettability on the long-term stability of dentin bonds after surface biomodification. *J. Biomech.* 48, 2067–2071. doi:10.1016/j.jbiomech.2015.03.016

Liede, K. E., Haukka, J. K., Hietanen, J. H. P., Mattila, M. H., Rönkö, H., and Sorsa, T. (1999). The association between smoking cessation and periodontal status and salivary proteinase levels. *J. Periodontol.* 70, 1361–1368. doi:10.1902/jop.1999.70.11.1361

Liu, H., Guo, J., Wang, R., and Wang, Y. (2021). Theaflavins as a novel cross-linker quickly stabilize demineralized dentin collagen against degradation. *Sci. Rep.* 11, 19699. doi:10.1038/s41598-021-99186-z

Liu, Y., Bai, X., Li, S., Liu, Y., Keightley, A., and Wang, Y. (2015). Molecular weight and galloylation affect grape seed extract constituents' ability to cross-link dentin collagen in clinically relevant time. *Dent. Mater. Off. Publ. Acad. Dent. Mater.* 31, 814–821. doi:10.1016/j.dental.2015.04.006

Liu, Y., Chen, M., Yao, X., Xu, C., Zhang, Y., and Wang, Y. (2013). Enhancement in dentin collagen's biological stability after proanthocyanidins treatment in clinically relevant time periods. *Dent. Mater. Off. Publ. Acad. Dent. Mater.* 29, 485–492. doi:10.1016/j.dental.2013.01.013

Ma, Y., Hoff, S. E., Huang, X., Liu, J., Wan, Q., Song, Q., et al. (2021). Involvement of prenucleation clusters in calcium phosphate mineralization of collagen. *Biominer. Cells Biomater.* 120, 213–223. doi:10.1016/j.actbio.2020.07.038

Marshall, G. W., Marshall, S. J., Kinney, J. H., and Balooch, M. (1997). The dentin substrate: structure and properties related to bonding. *J. Dent.* 25, 441–458. doi:10.1016/s0300-5712(96)00065-6

Mazzoni, A., Nascimento, F. D., Carrilho, M., Tersariol, I., Papa, V., Tjäderhane, L., et al. (2012). MMP activity in the hybrid layer detected with *in situ* zymography. *J. Dent. Res.* 91, 467–472. doi:10.1177/0022034512439210

Mazzoni, A., Scaffa, P., Carrilho, M., Tjäderhane, L., Di Lenarda, R., Polimeni, A., et al. (2013). Effects of etch-and-rinse and self-etch adhesives on dentin MMP-2 and MMP-9. *J. Dent. Res.* 92, 82–86. doi:10.1177/0022034512467034

Miles, C. A., Avery, N. C., Rodin, V. V., and Bailey, A. J. (2005). The increase in denaturation temperature following cross-linking of collagen is caused by dehydration of the fibres. *J. Mol. Biol.* 346, 551–556. doi:10.1016/j.jmb.2004.12.001

Nisar, S., Hass, V., Wang, R., Walker, M. P., and Wang, Y. (2023). Effect of different crosslinkers on denatured dentin collagen's biostability, MMP inhibition and mechanical properties. *Polymers* 15, 3683. doi:10.3390/polym15183683

Niu, L., Jee, S. E., Jiao, K., Tonggu, L., Li, M., Wang, L., et al. (2017). Collagen intrafibrillar mineralization as a result of the balance between osmotic equilibrium and electroneutrality. *Nat. Mater.* 16, 370–378. doi:10.1038/nmat4789

Nosenko, V., Strutynska, N., Vorona, I., Zatovsky, I., Dzhagan, V., Lemishko, S., et al. (2015). Structure of biocompatible coatings produced from hydroxyapatite nanoparticles by detonation spraying. *Nanoscale Res. Lett.* 10, 464. doi:10.1186/s11671-015-1160-4

Paivi, M., Mathias, M., and Denis, F. K. (2002). Gingival crevicular fluid collagenase-2 (MMP-8) test stick for chair-side monitoring of periodontitis. *J. PERIODONTAL Res.* 38, 436–439. doi:10.1034/j.1600-0765.2003.00677.x

Rangan, S., Schulze, H. G., Vardaki, M. Z., Blades, M. W., Piret, J. M., and Turner, R. F. B. (2020). Applications of Raman spectroscopy in the development of cell therapies: state of the art and future perspectives. *Analyst* 145, 2070–2105. doi:10.1039/C9AN01811E

Reis, M., Zhou, B., Alania, Y., Leme-Kraus, A. A., Jing, S., McAlpine, J. B., et al. (2021). Unveiling structure–activity relationships of proanthocyanidins with dentin collagen. *Dent. Mater.* 37, 1633–1644. doi:10.1016/j.dental.2021.08.013

Rochdi, A., Foucat, L., and Renou, J. P. (1999). Effect of thermal denaturation on water-collagen interactions: NMR relaxation and differential scanning calorimetry analysis. *Biopolymers* 50, 690–696. doi:10.1002/(SICI)1097-0282(199912)50:7<690::AID-BIP2>3.0.CO;2-P

Sabatini, C., and Pashley, D. H. (2015). Mechanisms regulating the degradation of dentin matrices by endogenous dentin proteases and their role in dental adhesion. *A Rev.*

Scheffel, D. L. S., Hebling, J., Scheffel, R. H., Agee, K. A., Cadenaro, M., Turco, G., et al. (2014). Stabilization of dentin matrix after cross-linking treatments, *in vitro*. *Dent. Mater. Off. Publ. Acad. Dent. Mater.* 30, 227–233. doi:10.1016/j.dental.2013.11.007

Schmidt, M. M., Fontoura, A. M. D., Vidal, A. R., Dornelles, R. C. P., Kubota, E. H., Mello, R. D. O., et al. (2020). Characterization of hydrolysates of collagen from mechanically separated chicken meat residue. *Food Sci. Technol.* 40, 355–362. doi:10.1590/fst.14819

Sylvester, M. F., Yannas, I. V., Salzman, E. W., and Forbes, M. J. (1989). Collagen banded fibril structure and the collagen-platelet reaction. *Thromb. Res.* 55, 135–148. doi:10.1016/0049-3848(89)90463-5

Takahashi, M., Nakajima, M., Tagami, J., Scheffel, D. L. S., Carvalho, R. M., Mazzoni, A., et al. (2013). The importance of size-exclusion characteristics of type I collagen in bonding to dentin matrices. *Acta Biomater.* 9, 9522–9528. doi:10.1016/j.actbio.2013.07.037

Takemoto, M., and Takemoto, H. (2018). Synthesis of theaflavins and their functions. *Mol. Basel Switz.* 23, 918. doi:10.3390/molecules23040918

Truong, V.-L., and Jeong, W.-S. (2021). Cellular defensive mechanisms of tea polyphenols: structure-activity relationship. *Int. J. Mol. Sci.* 22, 9109. doi:10.3390/ijms22179109

Vaidyanathan, J., Vaidyanathan, T. K., and Kerrigan, J. E. (2007). Evaluation of intermolecular interactions of self-etch dentin adhesive primer molecules with type 1 collagen: computer modeling and *in vitro* binding analysis. *Acta Biomater.* 3, 705–714. doi:10.1016/j.actbio.2007.01.009

van den Brand, J., Blajiev, O., Beentjes, P. C. J., Terryn, H., and de Wit, J. H. W. (2004). Interaction of ester functional groups with aluminum oxide surfaces studied using infrared reflection absorption spectroscopy. *Langmuir ACS J. Surf. Colloids* 20, 6318–6326. doi:10.1021/la049456a

Van Meerbeek, B., Yoshihara, K., Van Landuyt, K., Yoshida, Y., and Peumans, M. (2020). From buonocore's pioneering acid-etch technique to self-adhering restoratives. A status perspective of rapidly advancing dental adhesive technology. *J. Adhes. Dent.* 22, 7–34. doi:10.3290/j.jad.a43994

Vidal, C. M. P., Zhu, W., Manohar, S., Aydin, B., Keiderling, T. A., Messersmith, P. B., et al. (2016). Collagen-collagen interactions mediated by plant-derived proanthocyanidins: a spectroscopic and atomic force microscopy study. *Acta Biomater.* 41, 110–118. doi:10.1016/j.actbio.2016.05.026

Wang, B., Han, F., You, R., Chen, C., and Xie, H. (2023a). Polyphenols can improve resin-dentin bond durability by promoting amorphous calcium phosphate nanoparticles to backfill the dentin matrix. *Int. J. Nanomedicine* 18, 1491–1505. doi:10.2147/IJN.S395631

Wang, M., Chen, Y., Zhao, S., Zhao, C., Wang, G., and Wu, M. (2023b). Nitrogen-doped hierarchical porous carbons derived from biomass for oxygen reduction reaction. *Front. Chem.* 11, 1218451. doi:10.3389/fchem.2023.1218451

Wang, R., Nisar, S., Vogel, Z., Liu, H., and Wang, Y. (2022). Dentin collagen denaturation status assessed by collagen hybridizing peptide and its effect on bio-stabilization of proanthocyanidins. *Dent. Mater.* 38, 748–758. doi:10.1016/j.dental.2022.04.020

Xu, C., and Wang, Y. (2012). Collagen cross linking increases its biodegradation resistance in wet dentin bonding. *J. Adhes. Dent.* 14, 11–18. doi:10.3290/j.jad.a21494

Zhao, S., Hua, F., Yan, J., Yang, H., and Huang, C. (2022). Effects of plant extracts on dentin bonding strength: a systematic review and meta-analysis. *Front. Bioeng. Biotechnol.* 10, 836042. doi:10.3389/fbioe.2022.836042

frontiers | Frontiers in Bioengineering and Biotechnology

TYPE Original Research
PUBLISHED 16 August 2024
DOI 10.3389/fbioe.2024.1409487

OPEN ACCESS

EDITED BY
Wenjie Zhang,
Shanghai Jiao Tong University, China

REVIEWED BY
Zhihao Wang,
Radboud University, Netherlands
Hongbo Zhou,
Central South University, China

*CORRESPONDENCE
Lingyun Xia,
xialingyun200810@163.com
Weidong Leng,
lwd35@163.com

†These authors have contributed equally to this work and share first authorship

RECEIVED 30 March 2024
ACCEPTED 18 July 2024
PUBLISHED 16 August 2024

CITATION
Hu Z, Ren H, Min Y, Li Y, Zhang Y, Mao M, Leng W and Xia L (2024), The effects of antimicrobial peptides buCaTHL4B and Im-4 on infectious root canal biofilms.
Front. Bioeng. Biotechnol. 12:1409487.
doi: 10.3389/fbioe.2024.1409487

The effects of antimicrobial peptides buCaTHL4B and Im-4 on infectious root canal biofilms

Ziqiu Hu[1,2†], Haixia Ren[1,2†], Yifan Min[3†], Yixin Li[1,2], Yuyuan Zhang[1,2], Min Mao[1,2], Weidong Leng[1,2*] and Lingyun Xia[1,2*]

[1]Department of Stomatology, Taihe Hospital, Hubei University of Medicine, Shiyan, China, [2]Institute of Oral Diseases, School of Dentistry, Hubei University of Medicine, Shiyan, China, [3]Department of Stomatology, Zhushan County People's Hospital, Shiyan, China

Purpose: The primary cause of pulp and periapical diseases is the invasion of bacteria into the root canal, which results from the continuous destruction of dental hard tissues. Effective management of infections during root canal therapy necessitates effectively irrigation. This study aims to investigate the effects of two antimicrobial peptides (AMPs), buCaTHL4B and Im-4, on root canal biofilms *in vitro*.

Methods: Two-species biofilms (*Enterococcus faecalis* and *Fusobacterium nucleatum*) were selected and anaerobically cultivated. The following treatments were applied: 10 μg/mL buCaTHL4B, 10 μg/mL Im-4, 5 μg/mL buCaTHL4B, 5 μg/mL Im-4, 1 μg/mL buCaTHL4B, 1 μg/mL Im-4, 1% NaOCl, and sterile water. Each group was treated for 3 min. Subsequently, the two strains were co-cultured with 10 μg/mL buCaTHL4B, 10 μg/mL Im-4, 1% NaOCl, and sterile water for 24, 48, and 72 h. The biofilms were examined using confocal laser scanning microscopy (CLSM) with fluorescent staining, and the percentages of dead bacteria were calculated. Quantitative real-time PCR (qRT-PCR) was employed to assess the variations in bacterial proportions during biofilm formation.

Results: Compared to 1% NaOCl, 10 μg/mL buCaTHL4B or Im-4 exhibited significantly greater bactericidal effects on the two-species biofilms ($p < 0.05$), leading to their selection for subsequent experiments. Over a 48-hour period, 10 μg/mL Im-4 demonstrated a stronger antibiofilm effect than buCaTHL4B ($p < 0.05$). Following a 24-hour biofilm formation period, the proportion of *F. nucleatum* decreased while the proportion of *E. faecalis* increased in the sterile water group. In the buCaTHL4B and 1% NaOCl groups, the proportion of *F. nucleatum* was lower than that of *E. faecalis* ($p < 0.05$), whereas in the Im-4 group, the proportion of *F. nucleatum* was higher than that of *E. faecalis* ($p < 0.05$). The proportions of bacteria in the two AMPs groups gradually stabilized after 24 h of treatment.

Conclusion: buCaTHL4B and Im-4 exhibited remarkable antibacterial and anti-biofilm capabilities against pathogenic root canal biofilms *in vitro*, indicating their potential as promising additives to optimize the effectiveness of root canal treatment as alternative irrigants.

KEYWORDS

antimicrobial peptide, buCaTHL4B, Im-4, apical periodontitis, *Enterococcus faecalis*, *Fusobacterium nucleatum*

1 Introduction

Intact dental hard tissues effectively protect the internal pulp tissues. However, when these hard tissues are destroyed, the invasion of microorganisms can lead to pulp necrosis, followed by periapical lesions (An et al., 2012). Periapical periodontitis is a challenging oral infectious disease, often associated with *E. faecalis* and *F. nucleatum*. *Enterococcus faecalis* is a facultative anaerobic bacterium capable of long-term survival in the root canal due to its resistance to host immunity and various antibacterial treatments (Zhu et al., 2010; Lins et al., 2013; Barbosa-Ribeiro et al., 2016; Bouillaguet et al., 2018). Numerous studies have shown that *F. nucleatum* is frequently found in high prevalence and abundance, primarily linked to primary endodontic infections (Mussano et al., 2018; Hu Z. et al., 2023). As a "bridge bacterium", *F. nucleatum* co-aggregates with most oral bacteria via various cell surface adhesins, contributing to biofilm formation (Haney et al., 2019a; Manoil et al., 2020; Gomes et al., 2021). Additionally, it is reported that *E. faecalis* and *F. nucleatum* can co-adhere, supporting bacterial survival in unfavorable environments, encouraging interspecies communication, and facilitating biofilm production (Yap et al., 2014). These findings prompted us to create a biofilm model resembling those in the infected root canal, using *E. faecalis* and *F. nucleatum* as the dominant species. This biofilms formation is particularly relevant in dental research, they provide insights into how biofilms respond to various disinfection strategies, ensuring that the findings are applicable to actual dental practice.

Research into efficient root canal irrigants that suppress bacterial biofilm is essential to reduce periapical irritation and increase treatment success rates. During the preparation of an infected root canal, sodium hypochlorite (NaOCl), a traditional irrigating solution, is beneficial due to its ability to destroy necrotic tissue and its broad-spectrum antibacterial qualities. (Clarkson and Moule, 1998; Barakat et al., 2024). However, improper use of NaOCl can alter dentinal microhardness and bond strength, and degrade the collagen structure of dentin (Slutzky-Goldberg et al., 2004). Extrusion of NaOCl into periapical tissues may result in pain (Huang et al., 2019). Therefore, there is an urgent need to develop alternative irrigant additives that can effectively inhibit biofilms.

Antimicrobial peptides (AMPs) are effector molecules of innate defense systems. These small molecule products, typically composed of 12–60 amino acids, 2 to 9 positive charges, and an amphiphilic structure, are produced by single genes (Abdi et al., 2019; Grimsey et al., 2020). Antimicrobial peptides may attach to bacterial membranes via cations, causing damage to the membrane through the formation of barrel-stave, carpet, and toroidal pore model structures (Khurshid et al., 2016). By permeabilizing the cell membrane and preventing DNA or protein production, AMPs inhibit bacterial activity (Raheem and Straus, 2019). Additionally, AMPs can target and prevent bacterial biofilm formation (Wang et al., 2018). It has been discovered that peptide 1018 and DJK-5 inhibit a crucial signal molecule (P)ppGpp, involved in biofilm production (de la Fuente-Nunez et al., 2014; Hu J. et al., 2023). To address the limitations of traditional irrigants, AMPs may be employed as agents for suppressing root canal biofilms (Haney et al., 2019b).

In our previous investigation, buCaTHL4B and Im-4 were identified as efficient antibacterial peptides against dental plaque biofilms. buCaTHL4B exhibits significant bactericidal effects with minimal cytotoxicity, distinguished by its high tryptophan concentration. It causes bacterial membranes to rupture rapidly, resulting in noticeable changes such as foaming, budding, and the creation of pore-like structures (Brahma et al., 2015). Im-4, an immune peptide produced by *Drosophila* upon activation of the Toll innate immune system during defense against fungal infections, was found to be particularly effective in reducing biofilm formation. Im-4 shows increased inhibitory effects on filamentous fungi compared to yeasts, Gram-positive bacteria, and Gram-negative bacteria (Cohen et al., 2020). However, uncertainty persists regarding the specific characteristics and effects of these two AMPs on root canal biofilms.

The purpose of this study was to create a type of two-species biofilms with *E. faecalis* and *F. nucleatum*. The antibacterial properties of buCaTHL4B and Im-4 at different concentrations were examined *in vitro* on these formed biofilms. Analyses were also conducted on the impact of two AMPs on biofilm production and the proportion of bacteria during the biofilm development process. The null hypothesis was that: there is no significant difference in the antimicrobial efficacy between buCaTHL4B, Im-4 at different concentrations and NaOCl against the two-species biofilms.

2 Materials and methods

2.1 Antimicrobial peptides synthesis

Peptide buCaTHL4B (AIPWIWIWRLLRKG) and Im-4 (FIGMIPGLIGGLISAIK-NH_2) were synthesized by Sangon Biotech (Shanghai, China) using solid-phase 9-fluorenyl methoxycarbonyl (Fmoc) and purified to 98% using reverse-phase high-performance liquid chromatography (HPLC). The structures and sequences of buCaTHL4B and Im-4 were shown in Supplementary Figure S1. The peptides were resuspended in deionized water and utilized in the present experiments. All stocks remained sterile throughout the duration of the study.

2.2 Culture and growth detection of bacteria

Enterococcus faecalis (ATCC29212) and *F. nucleatum* (ATCC10953) were employed in this study. Bacterial culture conditions were adapted from a previous study (Huang et al., 2015). The strains were subcultured on Brain Heart Infusion (BHI; BectonDickinson, Sparks, MD) agar plates supplemented with 0.5% yeast extract (YE; OXOID, Hampshire, United Kingdom) and 5% defibrillated sheep blood (Solarbio, Beijing, China). The planktonic strains were proliferated in BHI liquid medium containing 0.5% YE. Both bacterial species were incubated at 37°C under anaerobic conditions.

The bacterial suspension of *E. faecalis*, *F. nucleatum*, and the mixed bacteria in equal volumes were adjusted to an optical density at 600 nm (OD_{600}) of 0.10. This was determined using a microplate reader (SpectraMaxi3x, Molecular Devices, United

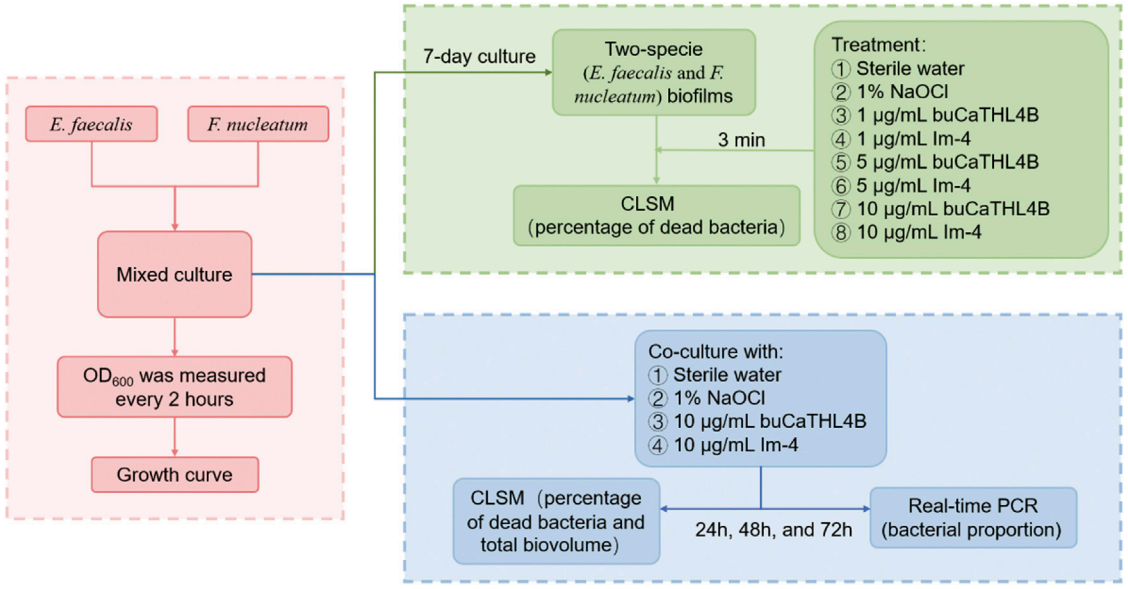

FIGURE 1
The workflow diagram of this study.

States) in a 96-well plate. Subsequently, the bacterial solutions were diluted tenfold and 150 μL of each bacterial suspension was dispensed into each well of the 96-well plate, with three replicates per bacterial suspension. The plate was then incubated under anaerobic conditions at 37°C, and the OD_{600} was measured every 2 h.

2.3 Minimal inhibitory concentration

The minimum inhibitory concentrations (MIC) of buCaTHL4B and Im-4 were determined using the broth microdilution method. The MIC was defined as the peptide concentration at which no bacterial growth was observed. The bacterial suspension of *E. faecalis*, *F. nucleatum* were adjusted to a final concentration of 5×10^5 CFU/mL and added to a 96-well plate, with 100 μL per well. Peptides buCaTHL4B or Im-4 were added to sterile 96-well polypropylene microtiter plates at increasing concentrations (0, 10, 20, 40, and 80 μg/mL), with each concentration tested in triplicate, 10 μL per well. The plates were incubated at 37°C for 24 h, and the absorbance at 630 nm was measured using a microplate reader after 24-hour treatment. Three repeated tests were accomplished for the MIC test.

2.4 Biofilm model

Sterile hydroxyapatite (HA) disks (12 mm in diameter and 2 mm in thickness; Bayamon Bioactive Materials Ltd., Chengdu, China) were used as substrates for biofilm growth. The HA disks were coated with 1 mL of type I collagen solution (10 mg/mL collagen in 0.012M HCl in double-distilled water; Biosharp, Hefei, China) in 24-well plates and incubated overnight at 4°C. The bacterial suspension of *F. nucleatum* and *E. faecalis* was mixed in equal volumes, adjusted to an OD_{600} of 0.10, and then diluted tenfold for biofilm culture. The bacterial biofilms were grown in BHI liquid medium containing 0.5% YE and 1% sucrose (Solarbio, Beijing, China).

2.5 Antimicrobial peptides treat on preformed biofilms

Figure 1 presents the workflow diagram of this study. The two-species biofilms were incubated anaerobically at 37°C on the pre-treated HA disks for 7 days. The disks were then divided into eight treatment groups: (a) sterile water, (b) 1% NaOCl, (c) 1 μg/mL buCaTHL4B, (d) 1 μg/mL Im-4, (e) 5 μg/mL buCaTHL4B, (f) 5 μg/mL Im-4, (g) 10 μg/mL buCaTHL4B, and (h) 10 μg/mL Im-4. Each group contained three disks and treated for 3 min. The test was repeated three times.

2.6 Biofilm inhibition test

The disks were divided into four treatment groups: i) sterile water, ii) 1% NaOCl, iii) 10 μg/mL buCaTHL4B, and iv) 10 μg/mL Im-4. Each group contained three disks. The treatments were added to the mixed bacterial suspensions at the onset of biofilm development and maintained for 3 days under anaerobic incubation at 37°C. The final concentration of the AMPs in the bacterial suspension was 10 μg/mL. The blank group received equal amounts of sterile water, while the positive control group received equal amounts of 1% NaOCl. The disks were subjected to the respective treatments at 24, 48, and 72 h. The test was repeated three times.

2.7 Confocal laser scanning microscopy examination of biofilms

The biofilms on the HA disks were stained using the LIVE/DEAD BacLight Bacterial Viability Kit L-7012 (Molecular Probes, Eugene, OR, United States) for microscopy and quantitative assays following exposure to the different treatments mentioned above (Huang et al., 2019; Yu et al., 2022). Bacteria with intact cell membranes were stained green by SYTO 9, while bacteria with damaged cell membranes were stained red by propidium iodide (PI). Images of the stained samples were captured using confocal laser scanning microscopy (CLSM; FV3000RS, OLYMPUS, Japan). The excitation wavelengths for SYTO 9 and PI were 488 nm and 561 nm, respectively. Four random areas of the biofilm on each disk were scanned, with 50–70 slices of 2.0 μm collected in each area from the top to the bottom of the biofilm. Imaris 9.0.1 software (Bitplane, Zurich, Switzerland) was used for three-dimensional reconstruction and quantitative analysis of each image. The volume ratio of red fluorescence to the total fluorescence (green and red) indicated the percentage of dead bacteria.

2.8 Quantitative real-time PCR

Biofilms co-cultured with AMPs for 24, 48, and 72 h were collected and re-suspended in BHI. The genomic DNA of bacteria was extracted using the Solarbio Bacterial Genomic DNA Extraction Kit (Solarbio, Beijing, China). DNA concentrations were measured with a micro-ultraviolet spectrophotometer (Nanodrop 2000; Thermo, United States). Relevant literature was consulted to determine primers, and the BLAST tool on the NCBI website (http://blast.ncbi.nlm.nih.gov/Blast.cgi) was used to confirm primer specificity for each strain. The primers were as follows: *F. nucleatum*: forward primer GGATTTATCTTTGCTAATTGGGGAAATTATAG, reverse primer ACTATTCCATATTCTCCATAATATTTCCCATTAGA. *Enterococcus faecalis*: forward primer ACCCCGTATCATTGGTTT, reverse primer ACGCATTGCTTTTCCATC. A total of 100 ng DNA from each strain was amplified using species-specific primers (0.4 μM) and DNA Taq Polymerase (TAKARA, TB Green Premix Ex Taq II, Japan). PCR protocol included an initial step at 94°C 5 min, followed by 30 cycles of amplification (94°C for 30 sec, 55°C for 30 sec, and 72°C for 30 sec), and a final elongation step at 72°C for 10 min. Bacteria proportions in the biofilms were calculated using the bacterial quantification algorithm proposed by Livak and Schmittgen, (2001); Huang et al. (2015).

2.9 Statistical analysis

Statistical analysis was conducted using SPSS Statistics 26.0 (IBM Corp, NY, United States). One-way analysis of variance (ANOVA) with *post hoc* pairwise comparisons was performed, and statistical significance was set at $p < 0.05$.

3 Results

3.1 Bacterial growth curve

The bacterial growth curve following a 24-hour culture revealed that *F. nucleatum* grew rapidly between 2 and 10 h, climbed steadily between 10 and 14 h, and stabilized after 14 h. *Enterococcus faecalis* showed rapid growth for 2–12 h before stabilizing. Over the course of 2–16 h, the OD_{600} of the mixed strains was lower than that of the single strains, with mixed bacterial growth tending to stabilize after approximately 16 h (Figure 2).

3.2 Bactericidal effect of antimicrobial peptides on preformed biofilms

For the MIC, we observed that at a concentration as high as 80 μg/mL, neither peptide substantially inhibited the growth of *E. faecalis* and *F. nucleatum* ($p > 0.05$, Supplementary Figure S2). However, different concentrations of buCaTHL4B or Im-4 demonstrated obvious bactericidal effects on the 7-day biofilms (Figure 3A). The bactericidal rates corresponding to 10 μg/mL, 5 μg/mL, and 1 μg/mL concentrations of AMPs were 49.94% ± 2.39%, 42.03% ± 1.37%, and 32.66% ± 1.41% for the buCaTHL4B groups, and 50.18% ± 1.31%, 42.02% ± 1.22%, and 31.81% ± 1.21% for the Im-4 groups, respectively, in comparison to the sterile water controls ($p < 0.05$, Figure 3B). At a concentration of 1 μg/mL, the bactericidal rate of both AMPs was not significantly different from that of the 1% NaOCl group ($p > 0.05$, Figure 3B).

3.3 Antimicrobial peptides inhibit biofilm formation by CLSM

The two-species biofilm formation was inhibited by the two peptides in inhibition experiments (Figure 4A). After 72 h of treatment, the biovolume of the two-species biofilm was significantly reduced by 10 μg/mL buCaTHL4B or Im-4, resulting in approximately 42.78% ± 3.55%, 40.34% ± 2.53%, and 44.74% ± 2.37% residual biofilm biovolume for buCaTHL4B groups, and 36.88% ± 2.10%, 26.87% ± 0.40%, and 37.52% ± 1.79% for Im-4 groups after 24, 48 and 72-hour time intervals, respectively, in comparison to the sterile water controls ($p < 0.05$, Figure 4B). Im-4 exhibited a stronger suppression effect than buCaTHL4B over the 72-hour period, with this difference being statistically significant ($p < 0.05$, Figure 4B).

The percentage of dead bacteria in the developed biofilms was estimated. Following 24, 48, and 72-hour time intervals, the bactericide rates for the buCaTHL4B groups were 41.80% ± 4.02%, 38.31% ± 1.91%, and 38.83% ± 1.78%, while for Im-4 groups were 40.32% ± 2.66%, 42.59% ± 3.24%, and 39.64% ± 1.59%, respectively. These rates were significantly higher than those of the sterile water group ($p < 0.05$). Only at 48-hour mark did the bactericidal effect of Im-4 surpass that of buCaTHL4B ($p < 0.05$), with no significant difference observed at the other time points (Figure 4C). The outcomes demonstrated that both Im-4 and buCaTHL4B could effectively prevent the formation of two-species biofilms.

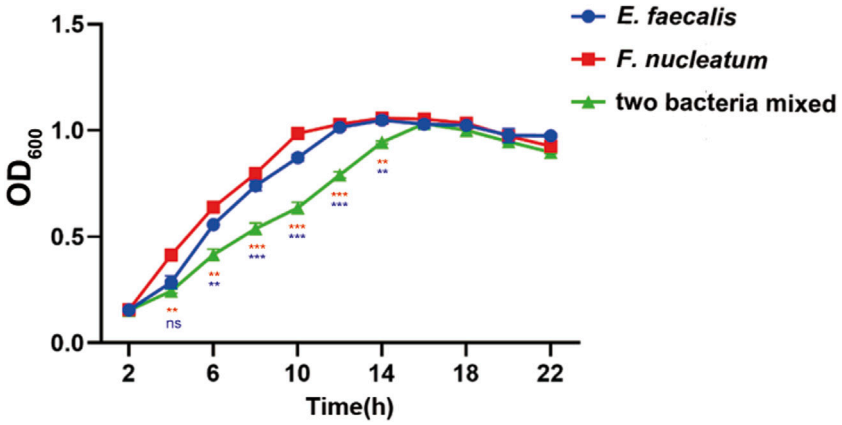

FIGURE 2
Growth curves of *E. faecalis* and *F. nucleatum* in single and mixed cultures. Data are presented as means ± standard deviations. Ns represent $p > 0.05$, *$p < 0.05$, **$p < 0.01$, ***$p < 0.001$. The red values represent the difference between the two species co-culture and the *F. nucleatum* cultured alone, the blue values represent the difference between the two species co-culture and the *E. faecalis* cultured alone.

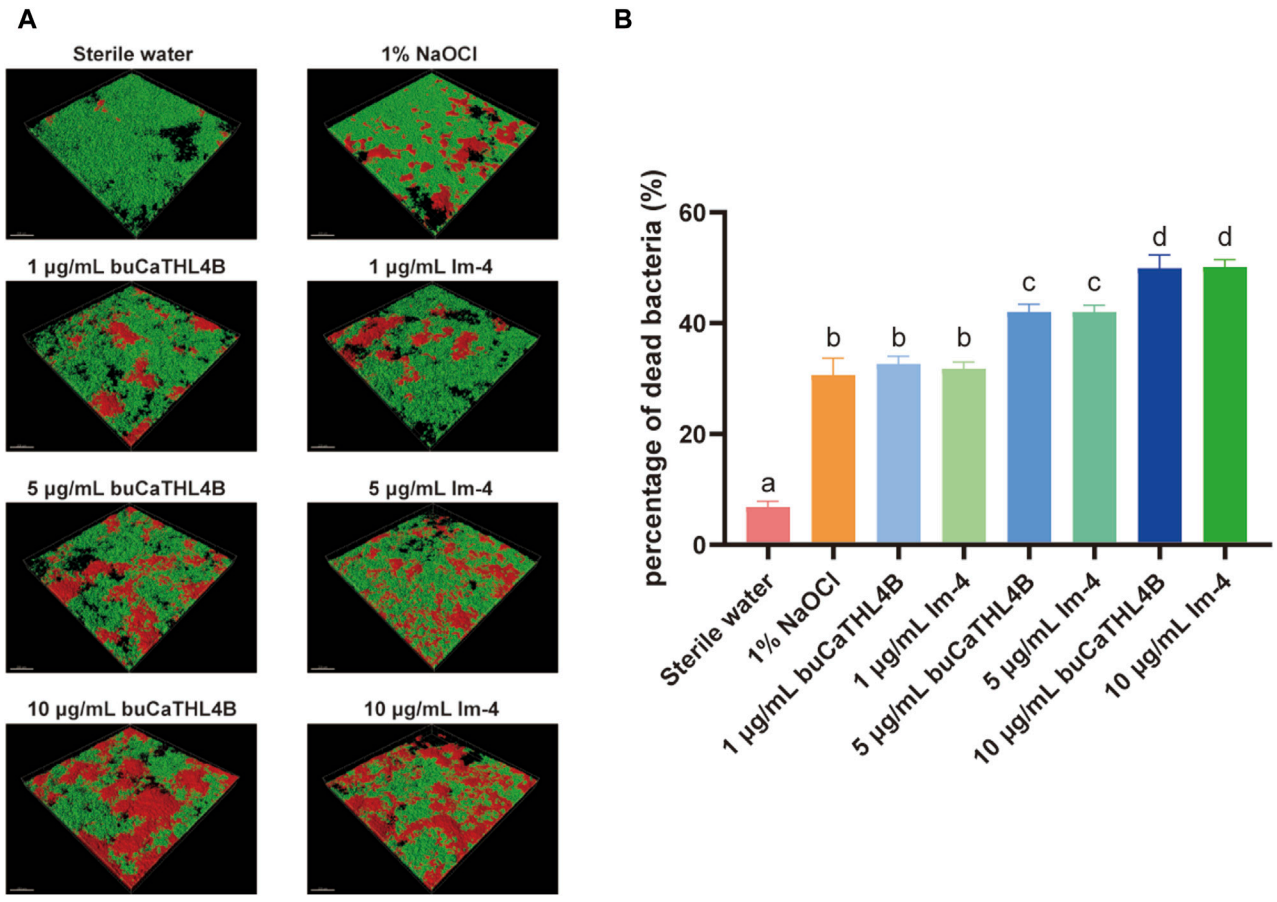

FIGURE 3
The bactericidal effect of buCaTHL4B and Im-4 on two-species biofilms. **(A)** Confocal microscopy images of two-species biofilms on HA discs treated with 10 μg/mL, 5 μg/mL, and 1 μg/mL buCaTHL4B or Im-4. The sterile water group served as blank control, and 1% NaOCl group as the positive control. **(B)** The proportion of dead bacteria as measured by viability staining and CLSM. Data are presented as means ± standard deviations. Different lowercase letters within each group indicate statistically significant difference ($p < 0.05$).

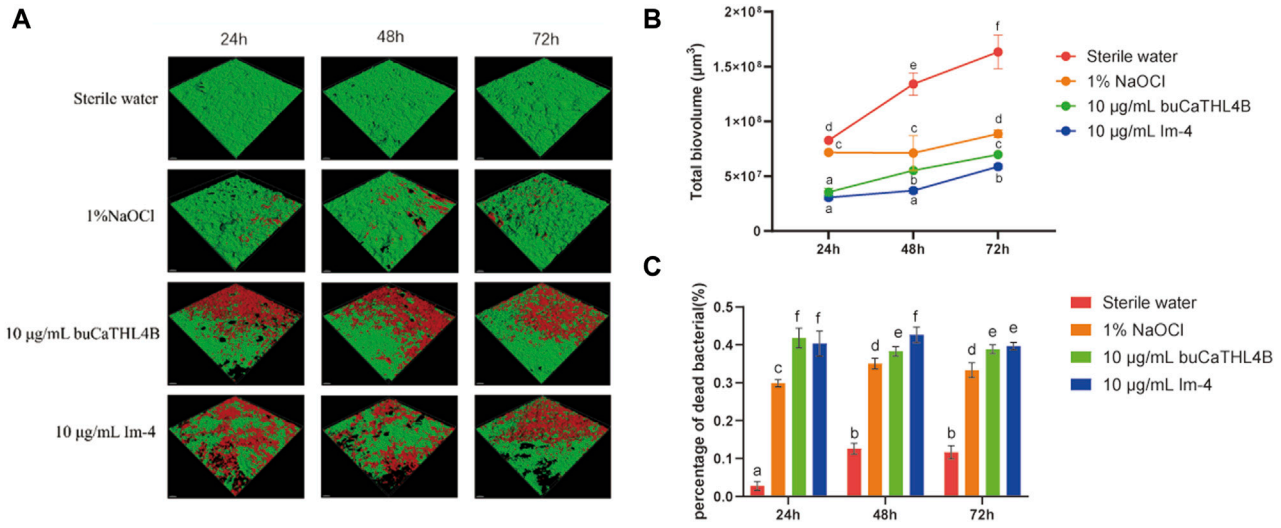

FIGURE 4
The antibiofilm effect of buCaTHL4B and Im-4 during the development of two-species biofilms. **(A)** Confocal microscopy images of biofilm development over 3 days in the presence of 10 μg/mL buCaTHL4B and Im-4. The sterile water group served as blank control, and 1% NaOCl group as the positive control. **(B)** The total biovolume of the biofilm formed over 3 days in the presence of 10 μg/mL buCaTHL4B and Im-4. Data are presented as means ± standard deviations. **(C)** The proportion of dead bacteria in the biofilm formed over 3 days in the presence of 10 μg/mL buCaTHL4B and Im-4. Data are presented as means ± standard deviations. Different lowercase letters within each group indicate statistically significant difference ($p < 0.05$).

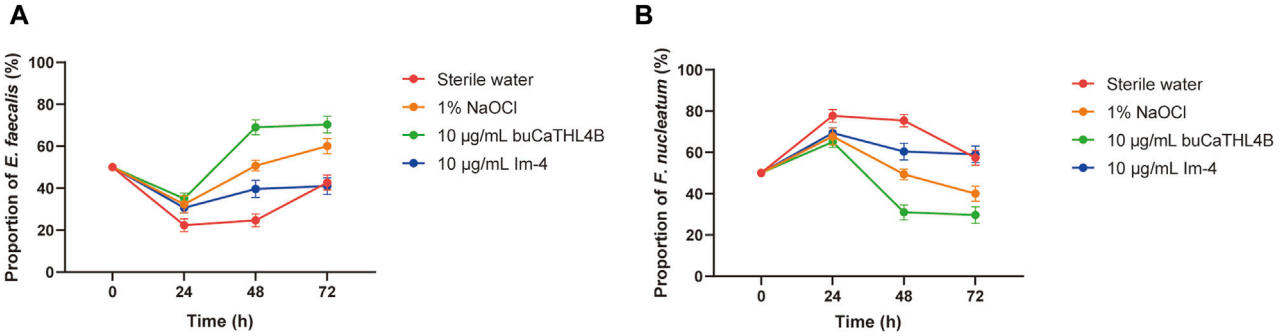

FIGURE 5
The proportion of *E. faecalis* **(A)** and *F. nucleatum* **(B)** in the biofilm of the different treatment groups at 24, 48, and 72 h exanimated by qPCR. Data are presented as means ± standard deviations.

3.4 Antimicrobial peptides inhibit biofilm formation by qPCR

The proportion of the two bacteria in the mixed biofilm following treatment with various agents was determined using a bacterial quantization algorithm. The percentage of *F. nucleatum* increased significantly in all groups at the 24-hour intervals. After 24 h of biofilm development, the proportion of bacterial species changed significantly. In the sterile water group, the proportion of *F. nucleatum* decreased, while the proportion of *E. faecalis* increased. In the buCaTHL4B group, *F. nucleatum* was found in lower proportions compared to *E. faecalis*, whereas in the Im-4 group, *F. nucleatum* was found in higher proportions. The bacterial proportion in both AMP-treated groups gradually stabilized after 48 h of treatment (Figure 5).

4 Discussion

This study evaluated the antibiofilm effects of buCaTHL4B and Im-4 on biofilms formed by *E. faecalis* and *F. nucleatum*. The results demonstrated that both buCaTHL4B and Im-4 at concentrations of 10 μg/mL exhibited significantly higher bactericidal activity compared to 1% NaOCl. Among the two peptides, Im-4 showed superior efficacy against biofilm formation over buCaTHL4B at the same concentration. Therefore, buCaTHL4B and Im-4 at 10 μg/mL are more effective against *E. faecalis* and *F. nucleatum* biofilms than the conventional irrigant solution NaOCl, the null hypothesis was rejected.

The formation of biofilms in a laboratory setting serves as a crucial model for studying microbial behavior and testing the efficacy of various disinfection techniques (Swimberghe et al., 2019). Pathogenic bacteria such as *F. nucleatum* and *E. faecalis*

are commonly found in the root canal wall and dentin tubules as biofilms, contributing significantly to dental root canal infections, posing significant challenges for effective disinfection and treatment. (Razghonova et al., 2022; Hu Z. et al., 2023; Sheng et al., 2023). A two-species biofilm model was developed, mimicking the characteristics of an infected root canal biofilm. In mixed cultures, the time required for the bacteria to reach a stable state was longer compared to single cultures, consistent with previous studies. This delay suggests antagonistic interactions between the two strains, likely due to competition for limited nutrients within the medium. Both species compete for essential nutrients in the limited medium, leading to growth inhibition. This competition is more pronounced in a co-cultured environment than in single cultures (Chavez de Paz et al., 2015).

Fusobacterium nucleatum is known for having more adhesion proteins on its cell membrane compared with other bacteria. These proteins facilitate bacterial aggregation in the early stages of biofilm development (Lima et al., 2019). This early dominance was confirmed by qRT-PCR results, which showed an increase in the proportion of *F. nucleatum* in the biofilm during the initial 24-hour culture stage. This indicates that *F. nucleatum* occupies a dominant niche early in biofilm formation, potentially inhibiting *E. faecalis* growth. After 48 h of culturing, the proportion of *F. nucleatum* began to decrease. This shift can be explained by the creation of an acidic biofilm environment by *E. faecalis*, which inhibits the growth of *F. nucleatum* (Xiang et al., 2023). The sequencing of clinical samples supports these observations, showing *E. faecalis* prevalence in secondary infected root canals and *F. nucleatum* dominance in primary infections (Tennert et al., 2014; Bouillaguet et al., 2018; Qian et al., 2019). These findings highlight the importance of considering bacterial interactions when developing treatment strategies for root canal infections.

In the study, CLSM detection confirmed that *F. nucleatum* and *E. faecalis* could form a biofilm together after 7 days of co-culturing. This indicated that *F. nucleatum* can provide specific links or connections for other co-aggregative microorganisms during biofilm formation (Johnson et al., 2006). *E. faecalis* could co-adhere with *F. nucleatum*, facilitating biofilm formation, promoting interspecies communication, and enhancing bacterial survival in challenging environments (Yap et al., 2014). Further research revealed that *E. faecalis* physically binds to *F. nucleatum* in both planktonic and biofilm environments via the adhesion protein Fap2 (Xiang et al., 2023). Factors such as interactions between microorganisms significantly influence the composition of the microbiota. Laboratory biofilm models are indispensable for the preliminary assessment of root canal disinfection techniques. They provide a controlled environment to study biofilm dynamics, microbial interactions, and the efficacy of new treatments. Our findings highlight the importance of using such models to develop and refine strategies for managing biofilm-related infections in clinical dentistry.

In the study, the efficacy of buCaTHL4B and Im-4 was evaluated using various experimental methods to determine their bactericidal and inhibitory effects on mixed biofilms of *E. faecalis* and *F. nucleatum*. At concentrations significantly lower than 80 μg/mL (10 μg/mL), buCaTHL4B and Im-4 exhibited a significantly higher bactericidal rate in biofilms compared to the 1% NaOCl and markedly reduced biofilms volume. We employed the broth microdilution method to determine the MIC of buCaTHL4B and Im-4 against *E. faecalis* and *F. nucleatum*. However, buCaTHL4B and Im-4 may possess unique bactericidal mechanisms, such as rapidly killing bacteria by disrupting the cell membrane. This rapid and intense action might prevent the traditional MIC determination method from effectively detecting their activity (Wang et al., 2015). Among the two peptides, buCaTHL4B is a tryptophan-rich peptide (Brahma et al., 2015; D'Souza et al., 2021; Necelis et al., 2021). Tryptophan possesses potent hydrophobic qualities that can facilitate the amalgamation of peptides and lipid membranes, as well as cause bacterial mortality by disruption or passage through the bilayer (Shagaghi et al., 2016; Wang et al., 2021; Straus, 2024). Im-4 has been shown to work against Gram-positive bacteria, but the exact mechanism of action remains unclear (Guilhelmelli et al., 2016; Miyashita et al., 2017). Additionally, antimicrobial peptides may exhibit a concentration-dependent bactericidal effect, both buCaTHL4B and Im-4 demonstrated significant bactericidal effects at concentrations of 5 μg/mL and 1 μg/mL, though the efficacy decreased with lower concentrations.

In the 24, 48, and 72-hour experiments, the bactericidal rates in the 10 μg/mL buCaTHL4B and Im-4 treatment groups were significantly higher than those in the 1% NaOCl group. Although the bactericidal effects of the two antimicrobial peptides were similar at most time points, Im-4 exhibited a significantly higher bactericidal rate than buCaTHL4B at 48 h, indicating that Im-4 has a stronger biofilm inhibition capacity during certain time periods. This significant biofilm inhibition effect could be attributed to the unique mechanism of antimicrobial peptides, which cause cell death by disrupting bacterial cell membranes. The higher efficacy of Im-4 might be related to its stronger membrane-penetrating ability and may slow the development of pulp disease by preventing the biofilm from turning into secondary endodontic infections, as suggested by the reduced proportion of *E. faecalis* in the Im-4 group after 24 h. In addition, the inhibitory effect of buCaTHL4B and Im-4 on mixed biofilms of *E. faecalis* and *F. nucleatum* may also include interfering with bacterial signal transduction and hindering the formation of biofilm matrix. The specific role of these mechanisms needs to be further studied.

However, our study has some limitations. First, our model included only two highly abundant bacteria and was grown in a static environment, failing to capture the dynamic and intricate nature of the disease process inside infected root canals. Second, the *in vitro* data presented in this study may not fully replicate the *in vivo* situation. Therefore, further studies on isolated teeth with simulated root canal irrigation and clinical research are required to explore the actual efficacy of root canal irrigant with buCaTHL4B and Im-4 during root canal preparation. In addition, preclinical studies were conducted on animal models to verify the reliability and reproducibility of the laboratory results. This step is crucial to evaluate the effects of antimicrobial peptides in more complex biological settings. Third, more research, including molecular mechanism, is needed to fully understand the anti-biofilm processes of Im-4 and buCaTHL4B.

5 Conclusion

This study demonstrated the effective antibacterial and antibiofilm properties of both buCaTHL4B and Im-4, with Im-4 being more effective than buCaTHL4B in preventing biofilm formation. Im-4 regulates the amount of bacteria involved in biofilm production, which may slow the progression of pulp disease. Im-4 and buCaTHL4B are anticipated to be the potent components of a novel root canal irrigation solution.

Data availability statement

Publicly available datasets were analyzed in this study. This data can be found here: https://figshare.com/articles/code/LCMS_HPLC_buCaTHL4B_Im-4/26530180/2?file=48313975.

Author contributions

ZH: Writing–original draft, Methodology, Investigation, Funding acquisition, Conceptualization. HR: Writing–original draft, Visualization, Methodology, Investigation, Data curation. YM: Writing–original draft, Validation, Resources, Investigation, Formal Analysis. YL: Writing–original draft, Software, Investigation, Formal Analysis. YZ: Writing–original draft, Validation, Methodology, Data curation. MM: Writing–original draft, Validation, Data curation. WL: Writing–review and editing, Supervision, Project administration, Funding acquisition. LX: Writing–review and editing, Supervision, Resources, Project administration, Funding acquisition.

Funding

The author(s) declare that financial support was received for the research, authorship, and/or publication of this article. This work was financially supported by Hubei Provincial Natural Science Foundation (No. 2023AFB842), the Program of Taihe Hospital (No. 2023JJXM038), and Innovative Research Program for Graduates of Hubei University of Medicine (Nos YC2022051 and YC2023057).

Acknowledgments

Experimental instruments involved in the study was provided by Biomedical Research Institute, Hubei University of Medicine.

Conflict of interest

The authors declare that the research was conducted in the absence of any commercial or financial relationships that could be construed as a potential conflict of interest.

Publisher's note

Supplementary material

The Supplementary Material for this article can be found online at: https://www.frontiersin.org/articles/10.3389/fbioe.2024.1409487/full#supplementary-material

References

Abdi, M., Mirkalantari, S., and Amirmozafari, N. (2019). Bacterial resistance to antimicrobial peptides. *J. Pept. Sci.* 25, e3210. doi:10.1002/psc.3210

An, B., Wang, R., and Zhang, D. (2012). Role of crystal arrangement on the mechanical performance of enamel. *Acta. Biomater.* 8, 3784–3793. doi:10.1016/j.actbio.2012.06.026

Barakat, R. M., Almohareb, R. A., Alsuwaidan, M., Faqehi, E., Alaidarous, E., and Algahtani, F. N. (2024). Effect of sodium hypochlorite temperature and concentration on the fracture resistance of root dentin. *BMC Oral Health* 24, 233. doi:10.1186/s12903-024-03954-y

Barbosa-Ribeiro, M., De-Jesus-Soares, A., Zaia, A. A., Ferraz, C. C., Almeida, J. F., and Gomes, B. P. (2016). Antimicrobial susceptibility and characterization of virulence genes of *Enterococcus faecalis* isolates from teeth with failure of the endodontic treatment. *J. Endod.* 42, 1022–1028. doi:10.1016/j.joen.2016.03.015

Bouillaguet, S., Manoil, D., Girard, M., Louis, J., Gaia, N., Leo, S., et al. (2018). Root microbiota in primary and secondary apical periodontitis. *Front. Microbiol.* 9, 2374. doi:10.3389/fmicb.2018.02374

Brahma, B., Patra, M. C., Karri, S., Chopra, M., Mishra, P., De, B. C., et al. (2015). Diversity, antimicrobial action and structure-activity relationship of buffalo cathelicidins. *PLoS One* 10, e0144741. doi:10.1371/journal.pone.0144741

Chavez De Paz, L. E., Davies, J. R., Bergenholtz, G., and Svensater, G. (2015). Strains of *Enterococcus faecalis* differ in their ability to coexist in biofilms with other root canal bacteria. *Int. Endod. J.* 48, 916–925. doi:10.1111/iej.12501

Clarkson, R. M., and Moule, A. J. (1998). Sodium hypochlorite and its use as an endodontic irrigant. *Aust. Dent. J.* 43, 250–256. doi:10.1111/j.1834-7819.1998.tb00173.x

Cohen, L. B., Lindsay, S. A., Xu, Y., Lin, S. J. H., and Wasserman, S. A. (2020). The daisho peptides mediate drosophila defense against a subset of filamentous fungi. *Front. Immunol.* 11, 9. doi:10.3389/fimmu.2020.00009

De La Fuente-Nunez, C., Reffuveille, F., Haney, E. F., Straus, S. K., and Hancock, R. E. (2014). Broad-spectrum anti-biofilm peptide that targets a cellular stress response. *PLoS Pathog.* 10, e1004152. doi:10.1371/journal.ppat.1004152

D'souza, A. R., Necelis, M. R., Kulesha, A., Caputo, G. A., and Makhlynets, O. V. (2021). Beneficial impacts of incorporating the non-natural amino acid Azulenyl-Alanine into the Trp-rich antimicrobial peptide buCATHL4B. *Biomolecules* 11, 421. doi:10.3390/biom11030421

Gomes, B., Bronzato, J. D., Almeida-Gomes, R. F., Pinheiro, E. T., Sousa, E. L. R., and Jacinto, R. C. (2021). Identification of *Fusobacterium nucleatum* in primary and secondary endodontic infections and its association with clinical features by using two different methods. *Clin. Oral. Investig.* 25, 6249–6258. doi:10.1007/s00784-021-03923-7

Grimsey, E., Collis, D. W. P., Mikut, R., and Hilpert, K. (2020). The effect of lipidation and glycosylation on short cationic antimicrobial peptides. *Biochim. Biophys. Acta Biomembr.* 1862, 183195. doi:10.1016/j.bbamem.2020.183195

Guilhelmelli, F., Vilela, N., Smidt, K. S., De Oliveira, M. A., Da Cunha Morales Alvares, A., Rigonatto, M. C., et al. (2016). Activity of scorpion venom-derived antifungal peptides against planktonic cells of Candida spp. and Cryptococcus neoformans and Candida albicans biofilms. *Front. Microbiol.* 7, 1844. doi:10.3389/fmicb.2016.01844

Haney, E. F., Barbosa, S. C., Baquir, B., and Hancock, R. E. W. (2019a). Influence of non-natural cationic amino acids on the biological activity profile of innate defense regulator peptides. *J. Med. Chem.* 62, 10294–10304. doi:10.1021/acs.jmedchem.9b01344

Haney, E. F., Straus, S. K., and Hancock, R. E. W. (2019b). Reassessing the host defense peptide landscape. *Front. Chem.* 7, 43. doi:10.3389/fchem.2019.00043

Hu, J., Yu, J., Liu, H., Wang, Z., Haapasalo, M., Haney, E. F., et al. (2023a). Dynamic killing effectiveness of mouthrinses and a D-enantiomeric peptide on oral multispecies biofilms grown on dental restorative material surfaces. *J. Dent.* 134, 104552. doi:10.1016/j.jdent.2023.104552

Hu, Z., Xiang, Y., Wei, Y., Gu, X., Leng, W., and Xia, L. (2023b). Bacterial diversity in primary infected root canals of a Chinese cohort: analysis of 16S rDNA sequencing. *BMC Oral Health* 23, 932. doi:10.1186/s12903-023-03618-3

Huang, R., Zhang, J., Yang, X. F., and Gregory, R. L. (2015). PCR-based multiple species cell counting for *in vitro* mixed culture. *PLoS One* 10, e0126628. doi:10.1371/journal.pone.0126628

Huang, X., Haapasalo, M., Wang, Z., Hancock, R. E. W., Wei, X., and Shen, Y. (2019). Effect of long-term exposure to peptides on mono- and multispecies biofilms in dentinal tubules. *J. Endod.* 45, 1522–1528. doi:10.1016/j.joen.2019.09.003

Johnson, E. M., Flannagan, S. E., and Sedgley, C. M. (2006). Coaggregation interactions between oral and endodontic *Enterococcus faecalis* and bacterial species isolated from persistent apical periodontitis. *J. Endod.* 32, 946–950. doi:10.1016/j.joen.2006.03.023

Khurshid, Z., Naseem, M., Sheikh, Z., Najeeb, S., Shahab, S., and Zafar, M. S. (2016). Oral antimicrobial peptides: types and role in the oral cavity. *Saudi. Pharm. J.* 24, 515–524. doi:10.1016/j.jsps.2015.02.015

Lima, B. P., Hu, L. I., Vreeman, G. W., Weibel, D. B., and Lux, R. (2019). The oral bacterium Fusobacterium nucleatum binds *Staphylococcus aureus* and alters expression of the staphylococcal accessory regulator sarA. *Microb. Ecol.* 78, 336–347. doi:10.1007/s00248-018-1291-0

Lins, R. X., De Oliveira Andrade, A., Hirata Junior, R., Wilson, M. J., Lewis, M. A., Williams, D. W., et al. (2013). Antimicrobial resistance and virulence traits of *Enterococcus faecalis* from primary endodontic infections. *J. Dent.* 41, 779–786. doi:10.1016/j.jdent.2013.07.004

Livak, K. J., and Schmittgen, T. D. (2001). Analysis of relative gene expression data using real-time quantitative PCR and the 2−ΔΔCT method. *Methods* 25, 402–408. doi:10.1006/meth.2001.1262

Manoil, D., Al-Manei, K., and Belibasakis, G. N. (2020). A systematic review of the root canal microbiota associated with apical periodontitis: lessons from next-generation sequencing. *Proteom. Clin. Appl.* 14, e1900060. doi:10.1002/prca.201900060

Miyashita, M., Kitanaka, A., Yakio, M., Yamazaki, Y., Nakagawa, Y., and Miyagawa, H. (2017). Complete *de novo* sequencing of antimicrobial peptides in the venom of the scorpion Isometrus maculatus. *Toxicon* 139, 1–12. doi:10.1016/j.toxicon.2017.09.010

Mussano, F., Ferrocino, I., Gavrilova, N., Genova, T., Dell'acqua, A., Cocolin, L., et al. (2018). Apical periodontitis: preliminary assessment of microbiota by 16S rRNA high throughput amplicon target sequencing. *BMC Oral Health* 18, 55. doi:10.1186/s12903-018-0520-8

Necelis, M. R., Santiago-Ortiz, L. E., and Caputo, G. A. (2021). Investigation of the role of aromatic residues in the antimicrobial peptide buCATHL4B. *Protein Pept. Lett.* 28, 388–402. doi:10.2174/0929866527666200813202918

Qian, W., Ma, T., Ye, M., Li, Z., Liu, Y., and Hao, P. (2019). Microbiota in the apical root canal system of tooth with apical periodontitis. *BMC Genomics* 20, 189. doi:10.1186/s12864-019-5474-y

Raheem, N., and Straus, S. K. (2019). Mechanisms of action for antimicrobial peptides with antibacterial and antibiofilm functions. *Front. Microbiol.* 10, 2866. doi:10.3389/fmicb.2019.02866

Razghonova, Y., Zymovets, V., Wadelius, P., Rakhimova, O., Manoharan, L., Brundin, M., et al. (2022). Transcriptome analysis reveals modulation of human stem cells from the apical papilla by species associated with dental root canal infection. *Int. J. Mol. Sci.* 23, 14420. doi:10.3390/ijms232214420

Shagaghi, N., Palombo, E. A., Clayton, A. H., and Bhave, M. (2016). Archetypal tryptophan-rich antimicrobial peptides: properties and applications. *World J. Microb. Biot.* 32, 31. doi:10.1007/s11274-015-1986-z

Sheng, X., Yu, J., Liu, H., Wang, Z., Deng, S., and Shen, Y. (2023). Dual effectiveness of a novel all-in-one endodontic irrigating solution in antibiofilm activity and smear layer removal. *Front. Bioeng. Biotechnol.* 11, 1254927. doi:10.3389/fbioe.2023.1254927

Slutzky-Goldberg, I., Maree, M., Liberman, R., and Heling, I. (2004). Effect of sodium hypochlorite on dentin microhardness. *J. Endod.* 30, 880–882. doi:10.1097/01.don.0000128748.05148.1e

Straus, S. K. (2024). Tryptophan- and arginine-rich antimicrobial peptides: anti-infectives with great potential. *Biochim. Biophys. Acta Biomembr.* 1866, 184260. doi:10.1016/j.bbamem.2023.184260

Swimberghe, R. C. D., Coenye, T., De Moor, R. J. G., and Meire, M. A. (2019). Biofilm model systems for root canal disinfection: a literature review. *Int. Endod. J.* 52, 604–628. doi:10.1111/iej.13050

Tennert, C., Fuhrmann, M., Wittmer, A., Karygianni, L., Altenburger, M. J., Pelz, K., et al. (2014). New bacterial composition in primary and persistent/secondary endodontic infections with respect to clinical and radiographic findings. *J. Endod.* 40, 670–677. doi:10.1016/j.joen.2013.10.005

Wang, D., Haapasalo, M., Gao, Y., Ma, J., and Shen, Y. (2018). Antibiofilm peptides against biofilms on titanium and hydroxyapatite surfaces. *Bioact. Mater.* 3, 418–425. doi:10.1016/j.bioactmat.2018.06.002

Wang, Z., De La Fuente-Nunez, C., Shen, Y., Haapasalo, M., and Hancock, R. E. (2015). Treatment of oral multispecies biofilms by an anti-biofilm peptide. *PLoS One* 10, e0132512. doi:10.1371/journal.pone.0132512

Wang, Z., Li, Q., Li, J., Li, J., Shang, L., Chou, S., et al. (2021). The Trp-rich antimicrobial amphiphiles with intramolecular aromatic interactions for the treatment of bacterial infection. *Front. Microbiol.* 12, 733441. doi:10.3389/fmicb.2021.733441

Xiang, D., Dong, P. T., Cen, L., Bor, B., Lux, R., Shi, W., et al. (2023). Antagonistic interaction between two key endodontic pathogens *Enterococcus faecalis* and *Fusobacterium nucleatum*. *J. Oral Microbiol.* 15, 2149448. doi:10.1080/20002297.2022.2149448

Yap, B., Zilm, P. S., Briggs, N., Rogers, A. H., and Cathro, P. C. (2014). The effect of sodium hypochlorite on *Enterococcus faecalis* when grown on dentine as a single- and multi-species biofilm. *Aust. Endod. J.* 40, 101–110. doi:10.1111/aej.12073

Yu, J., Bian, H., Zhao, Y., Guo, J., Yao, C., Liu, H., et al. (2022). Epigallocatechin-3-gallate/mineralization precursors co-delivery hollow mesoporous nanosystem for synergistic manipulation of dentin exposure. *Bioact. Mater.* 23, 394–408. doi:10.1016/j.bioactmat.2022.11.018

Zhu, X., Wang, Q., Zhang, C., Cheung, G. S., and Shen, Y. (2010). Prevalence, phenotype, and genotype of *Enterococcus faecalis* isolated from saliva and root canals in patients with persistent apical periodontitis. *J. Endod.* 36, 1950–1955. doi:10.1016/j.joen.2010.08.053

Frontiers in
Bioengineering and Biotechnology

Accelerates the development of therapies, devices, and technologies to improve our lives

A multidisciplinary journal that accelerates the development of biological therapies, devices, processes and technologies to improve our lives by bridging the gap between discoveries and their application.

Discover the latest Research Topics

See more →

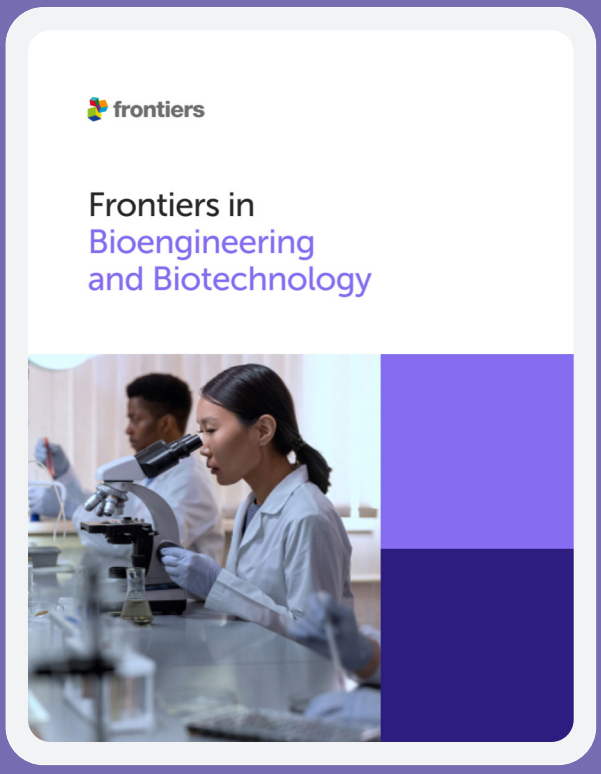

Frontiers

Avenue du Tribunal-Fédéral 34
1005 Lausanne, Switzerland
frontiersin.org

Contact us

+41 (0)21 510 17 00
frontiersin.org/about/contact